PETROGENESIS OF THE NEOGENE-QUATERNARY MAFIC LAVAS FROM THE TUNCELİ-ELAZIĞ REGION (EASTERN TURKEY)

A THESIS SUBMITTED TO
THE GRADUATE SCHOOL OF NATURAL AND APPLIED SCIENCES
OF
MIDDLE EAST TECHNICAL UNIVERSITY

BY

ALİCAN AKTAĞ

IN PARTIAL FULFILLMENT OF THE REQUIREMENTS
FOR
THE DEGREE OF DOCTOR OF PHILOSOPHY
IN
GEOLOGICAL ENGINEERING

JANUARY 2022

Approval of the thesis:

PETROGENESIS OF THE NEOGENE-QUATERNARY MAFIC LAVAS FROM THE TUNCELİ-ELAZIĞ REGION (EASTERN TURKEY)

submitted by **ALİCAN AKTAĞ** in partial fulfillment of the requirements for the degree of **Doctor of Philosophy in Geological Engineering, Middle East Technical University** by,

Prof. Dr. Halil Kalıpçılar
Dean, Graduate School of **Natural and Applied Sciences**

Prof. Dr. Erdin Bozkurt
Head of the Department, **Geological Engineering**

Assoc. Prof. Dr. Kaan Sayıt
Supervisor, **Geological Engineering, METU**

Examining Committee Members:

Prof. Dr. Ercan Aldanmaz
Geological Engineering, Kocaeli University

Assoc. Prof. Dr. Kaan Sayıt
Geological Engineering, METU

Assoc. Prof. Dr. Biltan Kürkçüoğlu
Geological Engineering, Hacettepe University

Assoc. Prof. Dr. Fatma Toksoy-Köksal
Geological Engineering, METU.

Assist. Prof. Dr. Ali İmer
Geological Engineering, METU

Date: 27.01.2022

I hereby declare that all information in this document has been obtained and presented in accordance with academic rules and ethical conduct. I also declare that, as required by these rules and conduct, I have fully cited and referenced all material and results that are not original to this work.

Name Last name : Alican Aktağ

Signature :

ABSTRACT

PETROGENESIS OF THE NEOGENE-QUATERNARY MAFIC LAVAS FROM THE TUNCELİ-ELAZIĞ REGION (EASTERN TURKEY)

Aktağ, Alican
Doctor of Philosophy, Geological Engineering
Supervisor: Assoc. Prof. Dr. Kaan Sayıt

January 2022, 366 pages

The most primitive members of the Late Miocene Tunceli and Pleistocene Elazığ mafic volcanics within the Eastern Anatolian Volcanic Province (EAVP) preserve details regarding the chemical geodynamics of eastern Anatolia. This study, therefore, primarily aims to establish the chemical composition of the source components that have contributed to these volcanics to enhance the understanding of the nature of mantle domains beneath eastern Anatolia.

Quantitative modelings suggest that at least three distinct components have been involved in the genesis Tunceli and Elazığ Volcanics; (i) a depleted asthenospheric mantle component (DM), (ii) an enriched asthenospheric component representing recycled oceanic lithospheric lithologies (i.e., C-like), and (iii) a EMII-type component representing fusible metasomatized SCLM domain(s).

The mixing modelings indicate a common asthenospheric source domain for these volcanics, consisting of a solid-state mixture of ca. 80 a % C-like component and ca. 20% a DM component. This indicates that the asthenosphere beneath eastern Anatolia is heterogeneous, including the recycled oceanic lithologies. In addition, the amount of metasomatized SCLM contribution appears to be larger (ca. 10-30%)

in the Tunceli lavas compared to the Elazığ Volcanics (< 10%). This, in turn, explains the OIB-like and subduction-related signatures observed in the Elazığ and Tunceli Volcanics, respectively.

The melting modelings suggest that the SCLM domain(s) have been detached from the eastern Anatolian lithosphere and occur as fusible pods in the asthenosphere. In this regard, it can be proposed that the delamination process/drip tectonics may be the main driving mechanism of the post-collisional melt generation in eastern Anatolia.

Keywords: Petrogenesis, Intraplate Volcanics, Eastern Anatolia, Mantle Components, Geodynamic Evolution.

ÖZ

TUNCELİ-ELAZIĞ BÖLGESİNDEKİ (DOĞU TÜRKİYE) NEOJEN-KUVATERNER MAFİK LAVLARIN PETROJENEZİ

Aktağ, Aktağ
Doktora, Jeoloji Mühendisliği
Tez Yöneticisi: Doç. Dr. Kaan Sayit

Ocak 2022, 366 sayfa

Doğu Anadolu Volkanik Provensi (DAVP) içerisindeki Geç Miyosen Tunceli ve Pleistosen Elazığ mafik volkanitlerinin en ilksel üyeleri, Doğu Anadolu kimyasal jeodinamiği ile ilgili detaylar barındırmaktadır. Bundan dolayı, bu çalışma, temelde bu volkanitlere katkı yapan kaynak bileşenlerinin kimyasal kompozisyonlarının açığa çıkarılmasıyla Doğu Anadolu altındaki manto alanlarının doğasının daha iyi anlaşılmasını amaçlamaktadır.

Kantitatif modellemeler, Tunceli ve Elazığ volkanitlerinin kökenlerinde en az üç farklı bileşenin olduğunu göstermektedir, bunlar; (i) tüketilmiş bir astenosferik manto bileşeni (DM), (ii) geri dönüştürülmüş okyanusal litosferik litolojileri (C-tipi) temsil eden zenginleştirilmiş bir astenosfer bileşeni ve (iii) kolay ergiyebilir metasomatize SCLM manto alan(lar)ını temsil eden EMII-tipi bir bileşendir.

Karışım modellemeleri, her iki volkanizma için, %80 C-tipi ve %20 DM bileşenlerinin karışımından oluşan ortak bir astenosferik kaynak alanını işaret etmektedir. Bu durum, Doğu Anadolu astenosferik mantosunun geri dönüştürülmüş okyanusal litolojileri ihtiva eden heterojen bir manto olduğunu göstermektedir. Bunun yanında, volkanitlerdeki SCLM katkısının, Tunceli lavlarında (yaklaşık olarak %10-30) Elazığ lavlarına kıyasla (< %10) daha çok olduğu görülmektedir. Bu durum da, Elazığ lavlarında görülen OIB-tipi ve Tunceli lavlarında görülen yitim-ilişkili jeokimyasal izleri açıklamaktadır.

Ergime modellemeleri, söz konusu SCLM manto alan(lar)ının Doğu Anadolu litosferinden ayrık ve ergiyebilir öbekler halinde astenosfer içerisinde olduğunu önermektedir. Bu durumda, Doğu Anadolu çarpışma-sonrası volkanizmasını oluşturan ana mekanizmanın delaminasyon veya drip (damlama) tektoniği olduğu önerilebilir.

Anahtar Kelimeler: Petrojenez, Plakaiçi Volkanitleri, Doğu Anadolu, Manto Bileşenleri, Jeodinamik Evrim.

to all insects, plants, and animals

of Munzur Mountains…

ACKNOWLEDGMENTS

First and foremost, I wish to express my deepest thanks to my supervisor Dr. Kaan Sayıt. Needles to say, the completion of this dissertation would not have been possible without his patience, encouragement, and constant help. I am extremely grateful to him for shaping my ideas and understanding of mantle geochemistry.

I would like to thank Dr. Bradley J. Peters and Dr. Jörg Rickli for carrying out Pb-Hf isotope analyses and for their valuable comments and advice, which improved this work significantly.

I would also like to acknowledge Dr. Özge Karakaş for her help in organizing the isotope analyses at ETH Zürich.

I would like to thank Dr. Tanya Furman for carrying out the microprobe analyses at Penn State and for constructive comments that helped to greatly clarify my thinking around petrogenesis of intraplate lavas.

I also thank S. Bowden and K. Crispin for the EPMA analyses.

I would like to express my appreciation to the thesis committee members Dr. Ercan Aldanmaz, Dr. Biltan Kürkçüoğlu, Dr. Fatma Toksoy-Köksal and Dr. Ali İmer for their help, suggestions, and guidance.

I also thank Dr. Serhat Köksal for carrying out the Sr-Nd isotope analyses at METU.

Special thanks to Onurcan Aktağ and Faruk Berber for their help during the field work.

I owe a debt of gratitude to my parents Haydar and Türkan Aktağ and my brother Onurcan, for their endless encouragement and support in every stage of this journey.

Finally, my deepest thanks must go to Işıl, for her love, patience, encouragement, and understanding through my many struggles. Without her support, this dissertation would not have been accomplished.

This work was supported by a TÜBİTAK grant (118Y280) and METU Scientific Research Project grants (GAP-309-2018-2761 and DKT-309-2018-3705).

TABLE OF CONTENTS

CHAPTERS

APPENDICES

LIST OF TABLES

TABLES

LIST OF FIGURES

FIGURES

LIST OF ABBREVIATIONS

Ab: Albite

AFC: Assimilation-combined Fractional Crystallization

ALM: Arabian Lithospheric Mantle

An: Anorthite

AP: Arabian Platform

Apt: Apatite

ATB: Anatolide-Tauride Block

Bow: Bowlingite

BPB: Bitlis-Pötürge Block

BPLM: Lithospheric Mantle of Bitlis-Pötürge

BPM: Bitlis-Pötürge Crystalline Complex/Massif

BSE: Bulk Silicate Earth

BSZ: Bitlis Suture Zone

C: Common Component

Ca: Calcite

CAVP: Central Anatolian Volcanic Province

CFB: Continental Flood Basalts

CHUR: Chondritic Uniform Reservoir

Cpx: Clinopyroxene

DEM: Digital Elevation Map

DM: Depleted Mantle

DMM: Depleted MORB Mantle

DUPAL: Dupre-Allègre Anomaly, referred to enriched southern hemisphere mantle

E: East

EAAC: Eastern Anatolian Accretionary Complex

EAFZ: Eastern Anatolian Fault Zone

EAP: Eastern Anatolian Platform

EAPCV: Eastern Anatolian Post-collisional Volcanics

EAR: European Asthenospheric Reservoir

EAVP: Eastern Anatolian Volcanic Province

EBB: Eastern Black Sea Basin

EDS: Energy-dispersive Spectroscopy

EMI: Enriched Mantle

EMII: Enriched Mantle II

En: Enstatite

EP: Eastern Pontide

EPMA: Electron Probe Micro Analyses

Fa: Fayalite

FC: Fractional Crystallization

Fo: Forsterite

FOZO: Focal Zone

Fs: Ferrosillite

GCB: Greater Caucasus Basin

GLOSS: Global Subducted Oceanic Sediments

Gt: Garnet

GVP: Galatian Volcanic Province

HFSE: High Field Strength Elements

HIMU: High $\mu=(^{238}\mathrm{U}/^{204}\mathrm{Pb})_{t=0}$

HREE: Heavy Rare Earth Elements

HT: High-temperature

IAESB: İzmir-Ankara-Erzincan Suture Belt

IAESZ: İzmir-Ankara-Erzincan Suture Zone

IB-Irvine and Baragar

ICP-AES: Inductively Coupled Plasma-Atomic Emission Spectrometry

ICP-MS: Inductively Coupled Plasma-Mass Spectrometry

Idd: Iddingsite

Ilm: Ilmenite

KMM: Keban-Malatya Metamorphics

KsM: Kırşehir Massif

LAB: Lithosphere-Asthenosphere Boundary

LC: Lower Crust

LILE: Large Ion Lithophile Elements

LM: Lithospheric Mantle

LOI: Loss on Ignition

LP: Low-pressure

LREE: Light Rare Earth Elements

LVC: Low-Velocity Component

MBB: Maden Back-arc Basin

MBL: Mechanical Boundary Layer

MC-ICP-MS: Multi Collector Inductively Coupled Plasma-Mass Spectrometry

MCP: Munzur Carbonate Platform

METU: Middle East Technical University

Mgt: Magnetite

M-Miyashiro

MoP: Moesian Platform

MORB: Mid-Ocean Ridge Basalt

MREE: Medium Rare Earth Elements

N: North

NAFZ: North Anatolian Fault Zone

NHRL: Northern Hemisphere Reference Line

NMORB: Normal Mid-Ocean Ridge Basalts

NOAA: National Oceanic and Atmospheric Administration

NVZ: Northern Volcanic Zone

OIB: Oceanic Island Basalts

Olv: Olivine

Or: Orthoclase

PAM: peri-Arabian Massif

PHEM: Primitive Helium Mantle

Plg: Plagioclase

PLM: Lithospheric Mantle of Pontide

PM: Primitive Mantle

PoR: Pontides Ranges

PPL: Plane Polarized Light

PREMA: Prevalent Mantle

REE: Rare Earth Elements

RIL: Radiogenic Isotope Laboratory

S: South

SC: Subduction Component

SCLM: Sub-Continental lithospheric Mantle

SCT: Sakarya Composite Terrane

SEAAU: Southeast Anatolian Autochthon Units

SENSB: Southeast Neo-Tethyan Suture Belt

Sp: Spinel

SSB: Sanandaj-Sirjan Block

TaP: Tauride Platform

TBL: Thermal Boundary Layer

TIMS: Thermo-Fisher Triton

Tp: Tephroite

UC: Upper Crust

USA: United States of America

V: Vector

WAVP: Western Anatolian Volcanic Province

WBB: Western Black Sea Basin

Wo: Wollastonite

XPL: Crossed Polarized Light

LIST OF SYMBOLS

C_0^f: initial trace element composition of the melt

C_0^m= trace element composition of the source rock

C_L^m= trace element composition of the melts produced after non-modal batch melting

C_{lc}^{AFC}: trace element composition of the melt affected by assimilation

D_0= bulk partition coefficient of the trace element of minerals in the source

IC_{lc}^{AFC}: isotopic composition of the melt affected by assimilation

Ic_0: initial isotope composition of the melt

Ic_a: isotope composition of the wall rock

P_0= bulk partition coefficient of the trace element of minerals in the melt

°C: degree Celcius

µm: micrometer

C_a: trace element concentration of the wall rock

C_L: trace element concentration (weight) in the remaining melt at any stage of crystallization

cm: centimeter

C_o: trace element concentration (weight) in the parental melt

D: bulk partition coefficient

F: fractionation ratio

g: acceleration of gravity

Ga: giga annum

h: depth (m)

kbar: kilobar

K_D: partition coefficient

kg: kilogramme

km: kilometer

km^2: square kilometer

Kv: kilovolt

m: meter

Ma: mega annum

Mg#: magnesium number

P: pressure

ppm: parts per million

r: ratio of the assimilated material to the crystallized material

T: temperature

vol: volume

wt: weight

ρ: density of the overlying crustal column

CHAPTER 1

INTRODUCTION

1.1 Problem Statement

Since the middle of the 20th century, with the development of new theories on plate tectonics and radical advancements in analytical techniques, investigations concerning the Earth's interior have advanced dramatically. While some of the earlier studies focused on the composition of the mantle domains (e.g., Tatsumoto et al., 1965; Hart, 1971), some others were interested in the nature of the secondary chemical modifications of these mantle sources (e.g., Armstrong, 1968). These researches about the mantle geodynamics of the Earth have been increasingly continued since the early 80s with the availability of a large number of isotope data (e.g., Sun, 1980; Chase, 1981; Hofmann and White, 1982; White, 1985; Zindler and Hart, 1986; Hofmann, 1997; Blichert-Toft et al., 1999; Stracke et al., 2005; Workman et al., 2004; Jackson et al., 2007). Understanding the nature of the Earth's interior is still a natural phenomenon for the earth scientists, and this enigmatic subject still encourages new researches.

Geochemistry and geophysics have been proven to be vital tools to understand the nature of mantle source regions of the solid Earth. In general, the studies related to the chemical geodynamics of the Earth have centered around the limits of these two disciplines. Geochemistry, among these, not only provides information on the present state of the Earth but also develops an evolutionary historical approach (Zindler and Hart, 1986). Within these concepts, major-trace element and isotope systematics are two fundamental methods broadly applied by earth scientists to understand the nature of mantle source regions (Hofmann, 2003). Successful chemical characterization of the Earth's interior depends strongly on the proper application of these methods on suitable materials. In this regard, basaltic rocks from oceanic settings, especially those with primary melt compositions, have been among the favorite materials for the earth scientists. Such lithologies are MgO-rich, and they do not involve any continental addition; thus, they are ideal materials that can carry the messages from the Earth's interior (e.g., Gast et al., 1964; Hart et al., 1973; White and Schilling, 1978; Allègre, 1982; White, 1985; Zindler and Hart, 1986; Hofmann, 1997; Stracke et al., 2005). In continental realms, on the other hand, crustal contamination can be an issue to deal with. However, the primitive basaltic magmas, with negligible post-melting effects, can also provide valuable information about the nature of mantle source regions (Hofmann, 2003; Lustrino and Wilson, 2007), and the large number of studies focusing on the nature of mantle source regions in continental settings has received increasing attention in the literature (e.g., Wörner et al., 1986; Wilson and Downes, 1991; Gibson et al., 1993; Cebrià and Wilson, 1995; Furman and Graham, 1999; Jung and Hoernes, 2000; Jung et al., 2005; Rooney et al., 2012).

Among the Earth's continental intraplate/anorogenic volcanic areas, the anorogenic volcanic provinces within the circum-Mediterranean region offer a great potential to set constraints on the composition of Earth's mantle regions. The anorogenic Cenozoic volcanic provinces of the circum-Mediterranean region cover an extensive area from Iberia to the Middle East (Figure 1.1), and they comprise primitive basaltic rock suites, which reflect the chemical identity of their mantle source regions (Lustrino and Wilson, 2007 and references therein). A geochemical investigation of the nature of the source regions of these volcanic areas will not only contribute to the understanding of mantle-crust evolution of the Earth but also will help to enlighten the geodynamic/tectonomagmatic evolution of the Alpine-Himalayan orogenic belt. Any hypothesis concerning the tectonomagmatic evolution of such volcanic regions will not be methodologically well-grounded without geochemically characterizing the source regions of the volcanism.

Turkey, situated in the eastern termination of the circum-Mediterranean region, and comprises a volumetrically important piece of the anorogenic volcanic fields within this region (Figure 1.1).

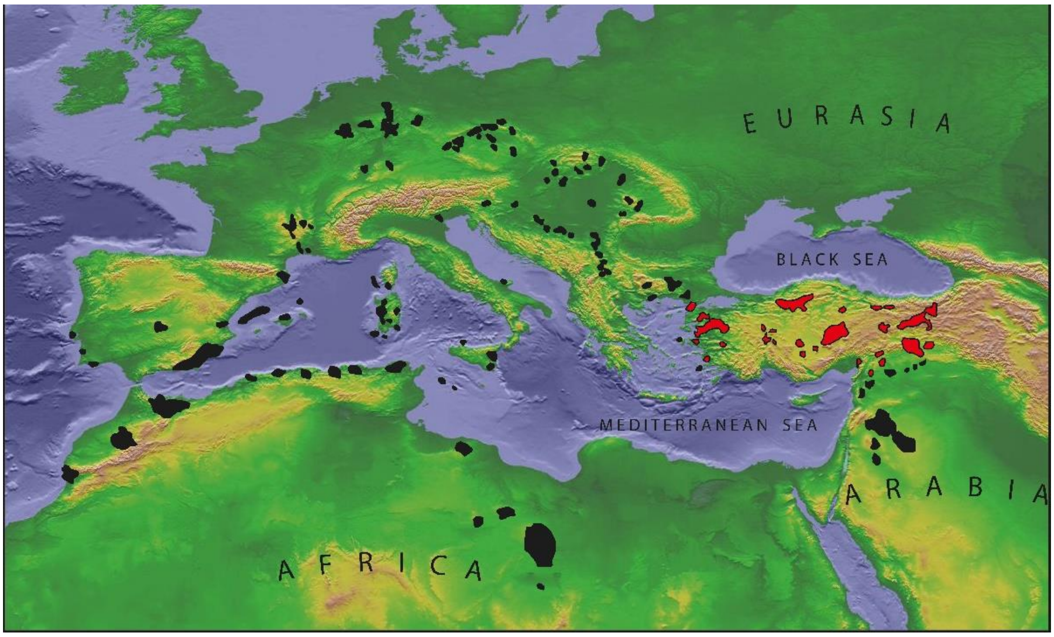

Figure 1.1. Digital elevation map (DEM) of the circum-Mediterranean region showing distributions of the Cenozoic anorogenic volcanic provinces. DEM is from National Oceanic and Atmospheric Administration (NOAA, https://www.ngdc.noaa.gov/mgg/image/2minrelief.html). The locations of the anorogenic volcanic provinces are from Lustrino and Wilson (2007). Red colors represent the anorogenic volcanic provinces of Turkey.

Since various types of spatially and temporally distributed anorogenic magmatism reside on, Turkey can be regarded as one of the key fields to understand the nature of mantle domains beneath the circum-Mediterranean region. Additionally, a chemical characterization of the primitive basaltic members of this anorogenic volcanism will also allow putting constraints on the post-Alpine tectonomagmatic evolution of the region. Since the Cretaceous, the Alpine belt from the Iberia to Turkey, with surrounding areas, have gone through complex tectonic/geodynamics processes, including diachronous plate collisions, subductions, slab-roll back events, slab-tearing events, delaminations, passive upwellings of asthenosphere, and small-scale plume diapirisms (e.g., Lustrino and Wilson, 2007 and references therein). Revealing the source characteristics of the anorogenic volcanics of Turkey, may help to gain further understanding of the nature of geodynamic processes involved in the Alpine belt.

Although the anorogenic volcanism in Turkey/Anatolia occurred between the Late Eocene to Quaternary, volumetrically the most significant pulse of volcanism took place within the Early Miocene-Quaternary time interval (Dilek and Whitney, 2000; Dilek and Altunkaynak, 2010; Dilek et al., 2010). This Neogene-Quaternary anorogenic volcanism, in general, can be subdivided geographically into four main areas: (i) The Western Anatolian Volcanic Province (WAVP), (ii) the Galatian Volcanic Province (GVP), the Central Anatolian Volcanic Province (CAVP), and (iv) the Eastern Anatolian Volcanic Province (EAVP) (Figure 1.2).

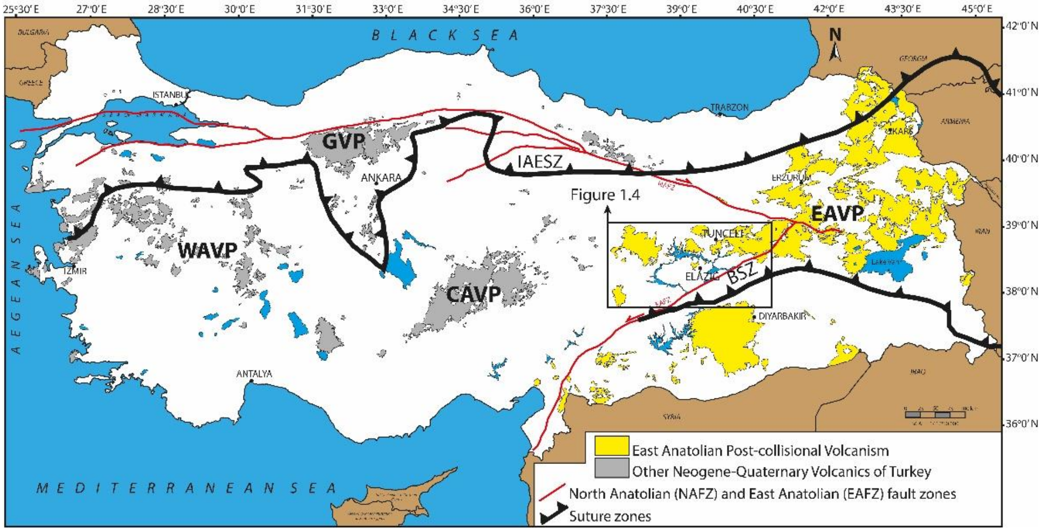

Figure 1.2. Distribution of the Neogene-Quaternary volcanic rocks of Turkey (simplified from Türkecan, 2015). WAVP: Western Anatolian Volcanic Province; GVP: Galatian Volcanic Province; CAVP: Central Anatolian Volcanic Province; EAVP: Eastern Anatolian Volcanic Province; IAESZ: Izmir-Ankara-Erzincan Suture Zone; BSZ: Bitlis Suture Zone; NAFZ: North Anatolian Fault Zone; EAFZ: Eastern Anatolian Fault Zone).

Among the other volcanic provinces, the EAVP can be regarded as a natural laboratory for eliciting both the nature of the diverse mantle source regions and the geodynamic evolution of post-stages of a continent-continent collision event. The widespread volcanic activity in the region started around 11 Ma. ago (Keskin et al.,

1998) after the collision of Arabian and Eurasian plates and has continued until recent times (e.g., 0.01 Ma, Nemrut Volcano; Notsu et al., 1995). These volcanic products cover almost two-thirds of the eastern Anatolia (~43.000 km^2; Keskin, 2007) and are composed of distinct types of lava flows (basalts to rhyolites) and pyroclastic rocks units (Pearce et al., 1990; Keskin et al., 1998; Keskin, 2007). This volcanism has dominated the region with different eruption styles (e.g., fissure type eruptions to Plinian), which created volcanic successions reaching over 1 km thickness in some localities (Keskin, 2007). There are over twenty major volcanic centers (e.g., Mt. Ararat, Mt, Nemrut, Mt. Süphan) that contributed to the development of the volcanostratigraphic evolution of the region (Lambert et al., 1974; Yılmaz et al., 1998; Karaoğlu et al., 2005; Keskin, 2007; Özdemir et al., 2011; Çubukçu et al., 2012). The post-melting magmatic processes such as fractional crystallization (FC) and assimilation-combined fractional crystallization (AFC) are assumed to have played an important role in creating a wide range of compositional variety (basalts to rhyolite) among these volcanics (e.g., Yılmaz et al., 1987; Pearce et al., 1990; Keskin et al., 1998; Keskin, 2007, Önal et al., 2008; Lustrino et al., 2010; Özdemir and Güleç, 2013; Lebedev et al., 2016; Oyan et al., 2016). Including a wide diversity from alkaline to calc-alkaline, it is also possible to find volcanic suites with distinct geochemical characteristics in the region. It is stated that the first episode of the post-collisional volcanics in the region that were emplaced on the north of eastern Anatolia carry calc-alkaline geochemical characteristics with a significant subduction imprint, while the southerly located volcanic areas show increasing alkalinity with a decreasing amount of subduction component (Keskin et al., 1998; Keskin, 2003). The involvement of the subduction component in the post-collisional volcanism of eastern Anatolia is thought to have been inherited from an earlier subduction event in the region (e.g., Pearce et al., 1990). The oceanic lithosphere of the Southern Neo-Tethys was proposed (Pearce et al., 1990) to be a potential source for the slab-derived input observed in the chemistry of the Eastern Anatolian Post-collisional Volcanics (EAPCV).

While their most of petrological features are well-constrained, there is still debate on the nature of the mantle source region(s) and geodynamical evolution of the EAPCV, especially for those situated in the Eurasian sector of eastern Turkey (i.e., those situated in the north of BZS; Figure 1.2). It is important to note that there is a consensus on the triggering mechanism of the volcanicity in the Arabian plate (Karacadağ Volcanism); however, their source characteristics have also not been fully clarified. The Karacadağ Volcanics are assumed to have derived from deep lithospheric mantle source or shallow asthenospheric mantle source (Alıcı-Şen et al., 2004; Lustrino et al., 2010; Keskin et al., 2012a, 2012b), and their melt generation was attributed to the adiabatic decompression melting triggered by fissure systems under the control of N-S directed compressional dynamics (Şengör et al., 1978; Şengör and Yılmaz, 1981). The main geodynamic models proposed to have generated the volcanism in the Eurasian part of the eastern Anatolia (north of the BZS; Figure 1.2), on the other hand, can be subdivided into three major groups: (i) the adiabatic decompression melting (e.g., Şaroğlu and Yılmaz, 1984; Yılmaz et al., 1987) (Figure 1.3a), (ii) the delamination of the lithospheric mantle (e.g., Pearce et al., 1990) (Figure 1.3b) and (iii) the slab break-off (e.g., Keskin, 2003; Şengör et al., 2003) (Figure 1.3c).

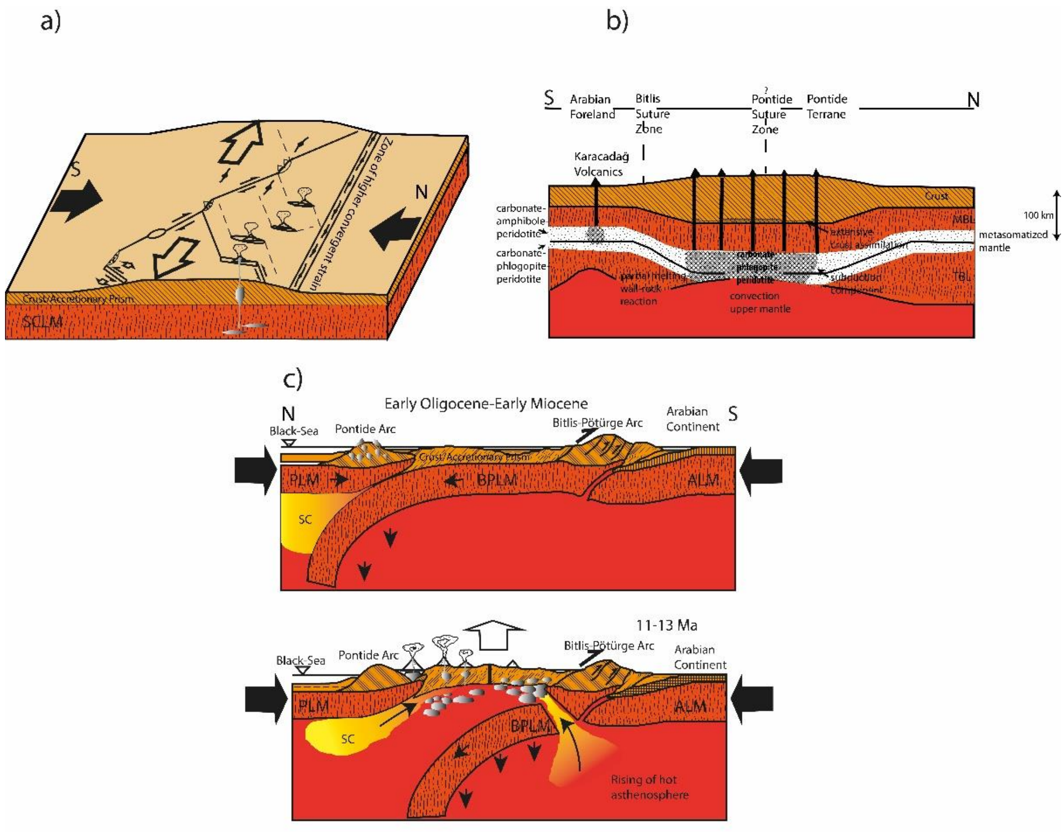

Figure 1.3. (a) The N-S directional fissure system model (modified from Yılmaz et al., 1987). (b) The delamination model (Pearce et al., 1990). (c) The slab break-off model (modified from Keskin, 2003). SCLM: Sub-Continental lithospheric Mantle; MBL: Mechanical Boundary Layer; TBL: Thermal Boundary Layer; PLM: Lithospheric Mantle of Pontide; BPLM: Lithospheric Mantle of Bitlis-Pötürge; ALM: Arabian Lithospheric Mantle.

Yılmaz et al. (1987) linked the widespread volcanism in eastern Anatolia to the systematic adiabatic decompression melting of the lithospheric mantle, initiated by the systematic N-S directional local extensional regions (i.e., fissure systems) under the control of strike-slip fault systems developed after the collision of Arabian and Eurasian plates (Figure 1.3a; Yılmaz et al., 1987). The fissure systems were assumed to be covered by the thick volcanic rock units in the region (Keskin, 1998).

Pearce et al. (1990) envisioned the delamination of the thermal boundary layer of the eastern Anatolian lithospheric mantle as the primary factor that led to melting in the lithospheric mantle. In this view, the collision of Arabian and Eurasian plates created a thickened lithosphere beneath eastern Anatolia, causing the destruction of the thermal boundary layer (TBL). With the loss of TBL, the rising of hot asthenospheric mantle caused melting in the previously metasomatized lithospheric mantle (Figure 1.3b).

Şengör et al. (2003) and Keskin (2003) have proposed the slab break-off model to account for the post-collisional magmatic flare-up in the region. Recent geophysical studies in eastern Anatolia (Gök et al., 2000; 2003; Al-Lazki et al., 2003; Zor et al., 2003; Angus et al., 2006; Özacar et al., 2008; Biryol et al., 2011) revealed that the lithosphere under this region is absent or is very thin (i.e., 15-22 km; Angus et al., 2006; Özacar et al., 2008). These findings led to the development of slab break-off model to explain the generation of EAPCV (Figure 1.3c; Keskin, 2003; Şengör et al., 2003). According to this hypothesis, the steepened oceanic lithosphere of Bitlis-Pötürge detached from eastern Anatolia around 11 Ma. ago, which resulted in the upwelling of hot asthenospheric mantle to shallower depths (Keskin, 2003). This model assumed that a great portion of EAPCV derived from this hot asthenospheric mantle containing the subduction component inherited from earlier events (Keskin, 2003).

In addition to the ideas above, which imply two separate mantle source regions (lithospheric versus asthenospheric mantle) for the EAPCV, there are also studies (e.g., Özdemir and Güleç, 2013; Aktağ et al., 2019) suggesting the melt mixing both from lithospheric and asthenospheric mantle sources as a major process in their genesis. Özdemir and Güleç (2013) underlined that even though the post-collisional volcanism in eastern Anatolia may have been triggered by a number of tectonic dynamics such as slab break-off, delamination, or fissure systems, both mantle sources appear to have contributed to the volcanism, instead solely from a single source region.

Based on the information given above, it can be seen that the main discussions regarding the EAPCV focused, in general, on the determination of the “type” of the mantle source from which the volcanics derived and the main geodynamic mechanism that might have triggered the widespread post-collisional volcanism in the region. The general view about the nature of mantle source region(s) of the EAPCV is that their trace element and isotopic signatures are consistent with an origin involving enriched mantle source component(s) (e.g., Pearce et al., 1990; Keskin et al., 1998; Keskin; 2007; Lebedev et al., 2006; Oyan et al., 2016; Di Giuseppe et al., 2017; Oyan et al., 2017; Kocaarslan and Ersoy, 2018; Lebedev et al., 2018; Aktağ et al., 2019). The enrichment of large ion lithophile elements (LILE) over high field strength elements (HFSE) coupled with negative Nb anomalies in the primitive mantle (PM)- or normal mid-ocean ridge basalts (N-MORB)-normalized spider diagrams can be regarded as a common geochemical pattern of the most of post-collisional volcanics in eastern Anatolia (e.g., Pearce et al., 1990; Keskin et al., 1998; Lustrino et al., 2010; Di Giuseppe et al., 2017). In addition, these volcanics are generally distributed from the depleted quadrant towards the Bulk Silicate Earth (BSE) and/or to Enriched Mantle II (EMII; Zindler and Hart, 1986) and clustered on the EMII field in the Sr-Nd and Pb-Pb isotope spaces, respectively (e.g., Lustrino et al., 2010; Keskin et al., 2012b; Özdemir and Güleç, 2013; Di Giuseppe et al., 2017; Oyan et al., 2017). Such enriched trace element and isotope signatures in the EAPCV have been widely linked to the contributions from the lithospheric mantle metasomatized by earlier subduction events (e.g., Pearce et al., 1990; Keskin et al., 1998; Lustrino et al., 2010; Di Giuseppe et al., 2017; Oyan et al., 2017). However, the lack of extensive discussion on the nature of enriched signatures (e.g., EMII) in this volcanism causes many uncertainties in detailing the characteristics of the mantle source domains in the region. Likewise, it has also been challenging to reach a consensus on the source enrichment process for those EAPCV displaying OIB (oceanic island basalts)-like geochemical signatures without subduction imprint (e.g., Elazığ Volcanics, Di Giuseppe et al., 2017; Karacadağ Volcanics, Lustrino et al., 2010; Keskin et al., 2012b). These volcanics, in general, were regarded to have originated from asthenospheric mantle source (e.g., Di Giuseppe et al., 2017; Alıcı-Şen et al., 2004; Keskin et al., 2012a, 2012b); however, the factors that might have enriched the source region are poorly constrained. Keskin et al. (2012b) implied derivation from the asthenospheric mantle having PREMA-like (the Prevalent Mantle "PREMA" of Zindler and Hart, 1986) characteristics for the Karacadağ Volcanics situated on the Arabian plate, but the idea is not discussed in detail. On the other hand, there is relatively little information regarding the nature of the asthenospheric mantle source beneath the Eurasian portion of eastern Turkey.

The ongoing problems above necessitate a detailed characterization of the mantle source regions of the EAPCV. In the light of this, a successful mantle source characterization of EAPCV can be achieved by:

- Characterization of the effects of mantle processes (e.g., mantle enrichment) on the chemistry of these volcanics, and discrimination of these mantle processes from the modifications of melting and post-melting processes (fractional crystallization, assimilation combined fractional crystallization).
- Determination of the mantle end-members (e.g., DM: Depleted Mantle; EMI: Enriched Mantle 1; EMII; Enriched Mantle 2; HIMU: High $\mu=(^{238}U/^{204}Pb)_{t=0}$ values; PREMA: Prevalent Mantle, Zindler and Hart, 1986) in the petrogenesis of these volcanics and revealing any mixing phenomenon if there is a contribution from multiple end-members. It also necessary to discuss the type of materials that characterizes the mantle end-members, such as (i) recycled altered oceanic crust (e.g., Chase, 1981; Hofmann and White, 1982; Hanan and Graham, 1996; Stracke et al., 2005), (ii) recycled ancient oceanic lithospheric mantle materials (e.g., Workman et al., 2004) (iii) delaminated lithospheric mantle (e.g., McKenzie and O'Nions, 1983; Hawkesworth et al., 1986), (iv) recycled ancient sediment inputs (e.g., Hawkesworth et al., 1979; Weaver, 1991; Chauvel et al., 1992; Rehkämper and Hofmann, 1997) and (v) the recycled of ancient continental crustal materials (e.g., Willbold and Stracke, 2006) in the asthenospheric mantle of the eastern Anatolia.

- Identification of the lithospheric and asthenospheric mantle components. Regarding this, it is crucial to figure out whether the EMII component in these volcanics is related to a recent metasomatic event or the melt contribution from an ancient reservoir residing in the asthenosphere such as recycled ancient sediments, recycled ancient crustal material or recycled ancient metasomatized lithospheric mantle (e.g., Hawkesworth et al., 1979; White and Hofmann, 1982; Willbold and Stracke, 2006; 2010; Widom and Shirey, 1996; Workman et al., 2004).
- Characterization of type of metasomatic agent (melt-dominated or fluid-dominated) that modified the SCLM beneath eastern Anatolia.

Developing a better scientific approach and making contributions to the discussions regarding the chemical evolution of the mantle regions of eastern Anatolia depend strongly on fulfilling these requirements. To obtain this information, the element and isotope systematics of the most primitive lithospheric and asthenospheric mantle-derived melts of eastern Anatolia need to be examined in detail.

1.2 Purpose and Scope

As stated in the “Problem Statement” section of this study, there are still gaps in the evolutionary path of the mantle regions of eastern Anatolia that need to be enlightened.

This study aims to chemically characterize the mantle source regions of eastern Anatolia, specifically beneath the Eurasian sector, in the light of new geochemical data from the post-collisional volcanics that have been contributed from both lithospheric and asthenospheric mantle sources in varying degrees.

This research focuses on the Tunceli-Elazığ region, which yields voluminous outcrops of the post-collisional volcanics (Figure 1.4) that carry chemical signals from both lithospheric and asthenospheric mantle domains beneath eastern Anatolia.

In this region, the Late Miocene Tunceli Volcanics are characterized by high LILE/HFSE ratio, variably enriched Sr-Nd isotopic signatures (e.g., $^{87}Sr/^{86}Sr$: 0.70393-0.7068, $^{143}Nd/^{144}Nd$: 0.51256-0.51279; Di Giuseppe et al., 2017), and negative Nb anomaly (Nb/Nb*=$\sqrt{ThNxLaN}$ < 1; N indicates normalization to PM composition of Sun and McDonough, 1989), indicating a dominant melt contribution from a metasomatically modified lithospheric mantle (Di Giuseppe et al., 2017; Aktağ et al., 2019). On the other hand, the Pleistocene Elazığ Volcanics show OIB-like trace element systematics and relatively low $^{87}Sr/^{86}Sr$ and high $^{143}Nd/^{144}Nd$ isotope ratios (0.70328-0.70375 and 0.51283-0.51290, respectively; Di Giuseppe et al., 2017), exhibiting the chemical characteristics of asthenospheric mantle-derived melts (Di Giuseppe et al., 2017). Also both Tunceli and Elazığ volcanics have not been significantly affected by FC-AFC processes (Di Giuseppe et al., 2017; Aktağ et al., 2019), which makes them good candidates for investigating the mantle processes.

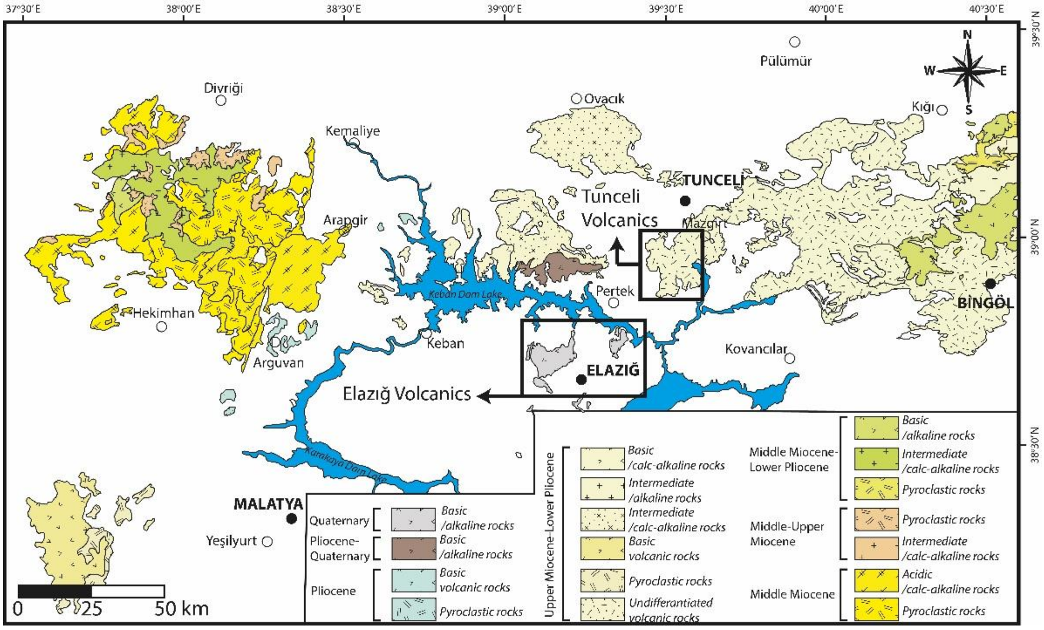

Figure 1.4. Simplified geological map showing the study areas and surrounding post-collisional volcanic units of eastern Anatolia (modified from Türkecan, 2015).

The previous studies related to the Tunceli (Di Giuseppe et al., 2017; Aktağ et al., 2019) and Elazığ Volcanics (Di Giuseppe et al., 2017) particularly concentrated on the role of melting and post-melting processes in the petrogenesis of these extrusives. However, a detailed description of the "nature" of the mantle source region(s), the type of modifications that the mantle source regions underwent (e.g., depletion or enrichment), and the mechanisms involved in this chemical geodynamics (e.g., recycling of ancient reservoirs) have remained unclear.

Therefore, this research mainly focuses on unraveling the:

- Nature of end-member components (e.g., DM, EMI, EMII, HIMU, and PREMA; Zindler and Hart, 1986) involved in the source of these volcanics (Tunceli and Elazığ) and multi-component mixing phenomenon by isotope (Sr-Nd-Pb-Hf) modelings if at least two end-member components have existed in their mantle source regions. These numerical models will also address the questions; (i) whether an ancient lithospheric reservoir existed beneath the region or not and (ii) why a depleted upper mantle component, similar to source of N-MORBs, has not been sampled by the volcanism in the region, even by the asthenosphere-derived melts?". Although the enriched nature of the mantle source regions of both volcanic units was underlined in the previous studies (Di Giuseppe et al., 2017; Aktağ et al., 2019), the petrogenetic processes that caused such enrichment have remained unclear and need to be investigated in detail.
- Nature of the EMII end-member sampled, in general, by the eastern Anatolian post-collisional volcanics. The limited Pb isotope data on both Tunceli and Elazığ Volcanics by Di Giuseppe et al. (2017) cluster toward or on the field of EMII mantle component in the Pb-Pb isotope space. Thus, this research will address whether the EMII signature of the EAPCV is a manifestation of recent metasomatic events or represents the melt contribution from an ancient reservoir.
- Temporal characteristics of the tectonic dynamics (e.g., slab-roll back events, slab-tearing events, delaminations, passive upwellings of asthenosphere and

small-scale plume diapirisms) that have controlled the generation and evolution of the post-collisional anorogenic volcanism of eastern Anatolia. The new geochemical data presented in this study from the Upper Miocene (Tunceli) and Pleistocene (Elazığ) volcanics allow assessing how the melt contributions from different source components and the melting systematics (extent and depth of melting) in the region have changed through time. This will provide significant information regarding the temporal geodynamics of the region.

This study, except the major-trace element data of Tunceli Volcanics, provides new mineral chemistry, whole rock, and Sr-Nd-Hf-Pb isotope data; thus, significantly improving the available dataset on the post-collisional volcanism of eastern Anatolia (see the "Methods of Study" section of this thesis for the details). It is also important to note that this is the first time that the Lu-Hf istotope systematics was applied for the EAPCV. In addition, this research also aims to put constraints on the effects of magmatic modification processes. Characterization and discrimination of the post-melting processes (e.g., FC-AFC) from the source features will avoid misinterpretation of the data and enhance the understanding of the mantle source regions beneath eastern Turkey.

Overall, the integrated elemental and isotopic approach of this research provides new insights into the source characteristics of the post-collisional volcanism of eastern Anatolia and brings additional constraints on the temporal evolution of the dynamic processes that controlled the magma generation in the region. The results presented here also contribute to the basic knowledge of the complex geological history of Turkey and the circum-Mediterranean region.

1.3 Geographic Location

The study areas (Tunceli and Elazığ) are located in eastern Anatolia (Figure 1.2), lying between the coordinates of 38^{o}35’00’’-39^{o}00’00’’ N latitudes and 39^{o}02’00’’-39^{o}36’00’’ E longitudes (Figure 1.4). The study area in the Tunceli regions cover an area of approximately 230 km^2, and it is included in the K42b2 and K43a1 quadrangles of the 1:25000 scaled topographic maps of Turkey. The study area in the Elazığ region occupies approximately 420 km^2, and it is included in the K42: a3-a4-b4-c1-d1-d2, and K43a1quadrangles of the 1:25000 scaled topographic maps of Turkey.

The Elazığ and Tunceli Volcanics are situated between the centrum of the Elazığ and Tunceli provinces (Figure 1.4 and Figure 1.5), and they are located in the north of Elazığ city and south of Tunceli city, respectively. Both areas can be reached by asphalt roads connecting the districts and towns to city centers (Figure 1.5). The Keban Dam Lake separates the two study areas from each other and the ferry service on the dam lake enables the transportation between the two study areas. The nearest airport to the study areas located in the ca. 20 km south of the city center of Elazığ (Figure 1.5) and takes approximately 30 minutes by driving.

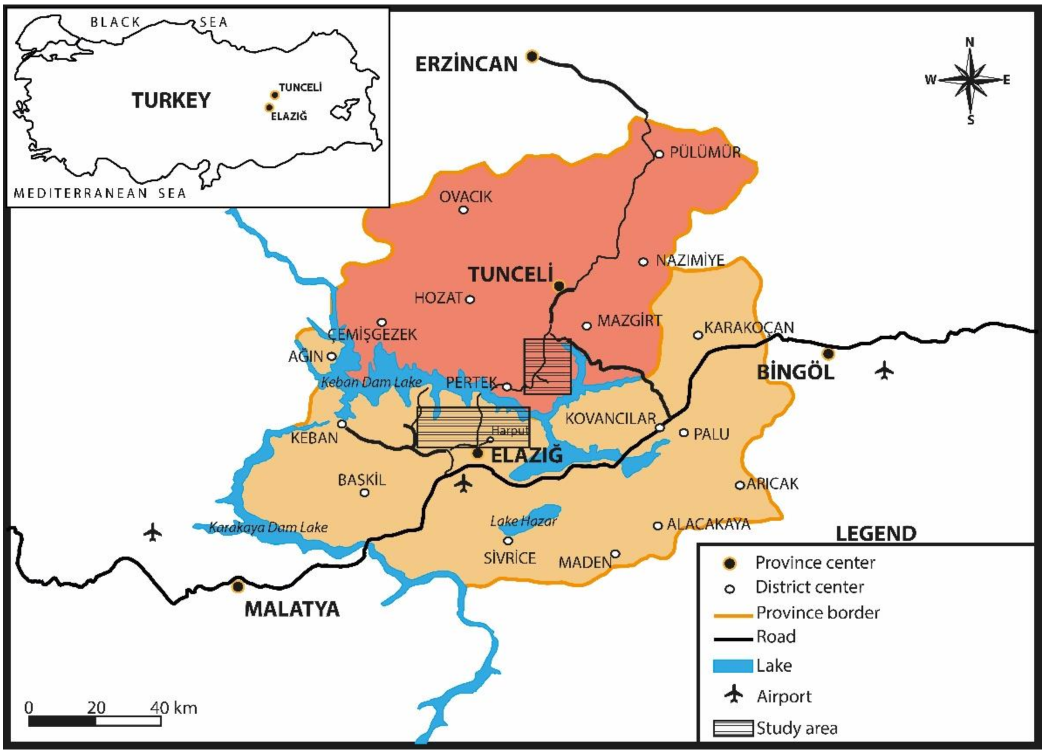

Figure 1.5. Map showing the locations of the study areas in the Elazığ and Tunceli provinces and the main roads connecting the study areas (modified from 8th Division Map of General Directorate of Highways, Republic of Turkey, https://www.kgm.gov.tr/SiteCollectionImages/KGMimages/Haritalar/b8.jpg).

1.4 Methods of Study

This study is composed of three main parts; a) Field Works, b) Analytical Works, and c) Office Works. The details about these parts are explained below.

1.4.1 Field Works

During the field works, the areal distribution of the volcanics and the contact relationships between the volcanics and other lithological units were determined. Also, the lava flow features and textural changes between the volcanic sequences were characterized. The available geological maps of the study areas (Herece, 2016a for the Elazığ region and Aktağ et al., 2019 for the Tunceli region) were modified according to the field observations. The freshest samples, which spatially represent the volcanism, were systematically collected during the field studies (Figure 1.6). A total of 77 samples from the Tunceli Volcanics were collected by Aktağ, 2014, and the same sample set has been used for the laboratory works in this research (Figure 1.6a). A total of 40 samples from the Elazığ Volcanics were collected during the summers of 2017 and 2018 (Figure 1.6b). The coordinates (latitudes and longitudes) of the sample locations can be found in the Table 1.1. Field studies to constrain the distributions of the volcanism in both regions (Tunceli and Elazığ) and obtain additional geological data (lava features, contact relationships, etc.,) were conducted during the summers of 2017, 2018, and 2020.

.

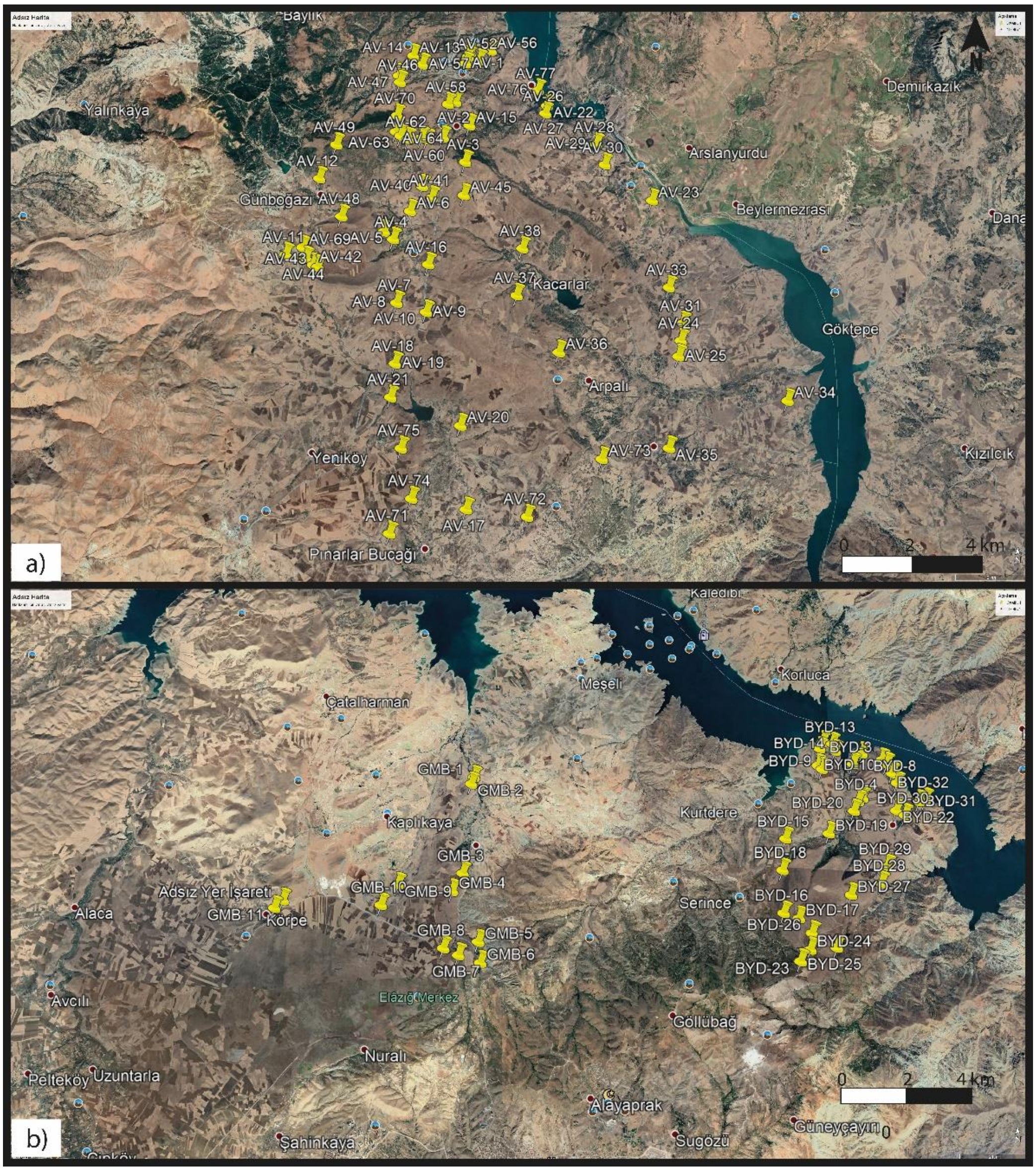

Figure 1.6. Google Earth view showing the sample distribution on (a) Tunceli and (b) Elazığ regions. The coordinates (latitudes and longitudes) of the samples can be found in Table 1.1.

Table 1.1. Coordinates (latitudes and longitudes) of the sample locations. N: north; E: east

Tunceli Volcanics

Sample ID	Latitude (N)	Longitude (E)	Sample ID	Latitude (N)	Longitude (E)
AV1	38º 59′ 38′′	39º 29′ 08′′	**AV40**	38º 57′ 41′′	39º 28′ 22′′
AV2	38º 59′ 01′′	39º 28′ 58′′	**AV41**	38º 57′ 31′′	39º 28′ 33′′
AV3	38º 58′ 04′′	39º 29′ 11′′	**AV42**	38º 56′ 28′′	39º 26′ 22′′
AV4	38º 56′ 52′′	39º 27′ 51′′	**AV43**	38º 56′ 28′′	39º 26′ 27′′
AV5	38º 56′ 53′′	39º 27′ 51′′	**AV44**	38º 56′ 34′′	39º 26′ 13′′
AV6	38º 57′ 19′′	39º 28′ 09′′	**AV45**	38º 57′ 34′′	39º 29′ 10′′
AV7	38º 55′ 56′′	39º 27′ 57′′	**AV46**	38º 59′ 17′′	39º 27′ 52′′
AV8	38º 55′ 56′′	39º 27′ 58′′	**AV47**	38º 59′ 23′′	39º 27′ 51′′
AV9	38º 55′ 48′′	39º 28′ 31′′	**AV48**	38º 57′ 12′′	39º 26′ 51′′
AV10	38º 55′ 48′′	39º 28′ 31′′	**AV49**	38º 58′ 16′′	39º 26′ 43′′
AV11	38º 56′ 37′′	39º 25′ 50′′	**AV50**	38º 59′ 45′′	39º 29′ 10′′
AV12	38º 57′ 46′′	39º 26′ 25′′	**AV51**	38º 59′ 48′′	39º 29′ 13′′
AV13	38º 59′ 43′′	39º 26′ 07′′	**AV52**	38º 59′ 42′′	39º 29′ 24′′
AV14	38º 59′ 43′′	39º 28′ 07′′	**AV53**	38º 59′ 42′′	39º 29′ 24′′
AV15	38º 58′ 39′′	39º 29′ 15′′	**AV54**	38º 59′ 43′′	39º 29′ 24′′
AV16	38º 56′ 31′′	39º 28′ 32′′	**AV55**	38º 59′ 43′′	39º 29′ 24′′
AV17	38º 52′ 58′′	39º 29′ 21′′	**AV56**	38º 59′ 52′′	39º 29′ 37′′
AV18	38º 55′ 03′′	39º 27′ 57′′	**AV57**	38º 59′ 35′′	39º 28′ 17′′
AV19	38º 55′ 03′′	39º 27′ 58′	**AV58**	38º 58′ 58′′	39º 28º 49′′
AV20	38º 54′ 10′′	39º 29′ 13′′	**AV59**	39º 00′35′′	39º 28′ 50′′
AV21	38º 54′ 33′′	39º 27′ 53′′	**AV60**	38º 58′ 24′′	39º 28′ 26′′
AV22	38º 59′ 01′′	39º 30′ 45′′	**AV61**	38º 58′ 25′′	39º 28′ 20′′
AV23	38º 57′ 34′′	39º 32′ 49′′	**AV62**	38º 58′ 23′′	39º 28′ 05′′
AV24	38º 55′ 28′′	39º 33′ 21′′	**AV63**	38º 58′ 26′′	39º 27′ 56′′
AV25	38º 55′ 14′′	39º 33′ 19′′	**AV64**	38º 58′ 30′′	39º 27′ 51′′
AV26	38º 58′ 54′′	39º 30′ 43′′	**AV65**	38º 56′ 60′′	39º 27′ 40′′
AV27	38º 58′ 54′′	39º 30′ 43′′	**AV66**	38º 56′ 59′′	39º 27′ 40′′
AV28	38º 58′ 26′′	39º 31′ 43′′	**AV67**	38º 56′ 59′′	39º 27′ 41′′
AV29	38º 58′ 26′′	39º 31′ 43′′	**AV68**	38º 56′ 59′′	39º 27′ 41′′
AV30	38º 58′ 07′′	39º 31′ 53′′	**AV69**	38º 56′ 43′′	39º 26′ 09′′
AV31	38º 55′ 43′′	39º 33′ 23′′	**AV70**	38º 58′ 44′′	39º 27′ 52′′
AV32	38º 55′ 43′′	39º 33′ 23′′	**AV71**	38º 52′ 37′′	39º 27′ 57′′
AV33	38º 56′ 15′′	39º 33′ 07′′	**AV72**	38º 52′ 53′′	39º 30′ 29′′
AV34	38º 54′ 36′′	39º 35′ 24′′	**AV73**	38º 53′ 43′′	39º 31′ 52′′
AV35	38º 53′ 54′′	39º 33′ 08′′	**AV74**	38º 53′ 07′′	39º 28′ 20′′
AV36	38º 55′ 15′′	39º 31′ 02′′	**AV75**	38º 53′ 50′′	39º 28′ 07′′
AV37	38º 56′ 05′′	39º 30′ 13′′	**AV76**	38º 59′ 16′′	39º 30′ 34′′
AV38	38º 56′ 48′′	39º 30′ 19′′	**AV77**	38º 59′ 16′′	39º 30′ 34′′
AV39	38º 58′ 27′′	39º 28′ 44′′			

Table 1.1. (*Cont'd*)

Elazığ Volcanics

Sample ID	Latitude (N)	Longitude (E)	Sample ID	Latitude (N)	Longitude (E)
BYD1	38º 48´ 06´´	39º 20´ 58´´	**BYD23**	38º 44´ 24´´	39º 19´ 15´´
BYD2	38º 48´ 06´´	39º 20´57´´	**BYD24**	38º 44´ 35´´	39º 19´ 28´´
BYD3	38º 47´ 55´´	39º 20´ 45´´	**BYD25**	38º 44´ 38´´	39º 20´ 01´´
BYD4	38º 47´ 13´´	39º 20´ 47´´	**BYD26**	38º 44´ 52´´	39º 19´ 32´´
BYD5	38º 47´ 59´´	39º 21´ 23´´	**BYD27**	38º 45´ 33´´	39º 20´ 27´´
BYD6	38º 47´ 54´´	39º 21´ 29´´	**BYD28**	38º 45´ 46´´	39º 21´ 09´´
BYD7	38º 47´ 45´´	39º 21´ 35´´	**BYD29**	38º 46´ 04´´	39º 21´ 18´´
BYD8	38º 47´ 34´´	39º 21´ 41´´	**BYD30**	38º 46´ 59´´	39º 21´ 48´´
BYD9	38º 47´ 48´´	39º 20´ 02´´	**BYD31**	38º 47´ 14´´	39º 22´ 08´´
BYD10	38º 47´ 52´´	39º 19´ 57´´	**BYD32**	38º 47´ 16´´	39º 22´ 17´´
BYD11	38º 48´ 11´´	39º 20´ 01´´	**GMB1**	38º 47´ 32´´	39º 12´ 16´´
BYD12	38º 48´ 18´´	39º 20´ 06´´	**GMB2**	38º 47´ 24´´	39º 12´ 13´´
BYD13	38º 48´ 17´´	39º 20´ 18´´	**GMB3**	38º 45´ 48´´	39º 12´ 06´´
BYD14	38º 48´ 08´´	39º 20´ 21´´	**GMB4**	38º 45´ 29´´	39º 11´ 53´´
BYD15	38º 46´ 31´´	39º 19´ 08´´	**GMB5**	38º 44´ 38´´	39º 12´ 29´´
BYD16	38º 45´ 13´´	39º 18´ 59´´	**GMB6**	38º 44´ 17´´	39º 12´ 32´´
BYD17	38º 45´ 08´´	39º 19´ 18´´	**GMB7**	38º 44´ 24´´	39º 12´ 04´´
BYD18	38º 45´ 58´´	39º 19´ 01´´	**GMB8**	38º 44´ 31´´	39º 11´ 45´´
BYD19	38º 46´ 38´´	39º 20´ 06´´	**GMB9**	38º 45´ 34´´	39º 10´ 43´´
BYD20	38º 47´ 03´´	39º 20´ 41´´	**GMB10**	38º 45´ 13´´	39º 10´ 22´´
BYD21	38º 47´ 17´´	39º 20´ 53´´	**GMB11**	38º 45´ 08´´	39º 08´ 06´´
BYD22	38º 47´ 03´´	39º 21´ 37´´			

1.4.2 Analytical Works

The analytical phase of this research comprises four main parts; (i) petrographic examination, (ii) mineral chemistry analysis, (iii) whole-rock major-trace element analysis and (iv) whole-rock Sr-Nd-Pb-Hf isotope analysis. The details of the analytical procedures (i.e., methods) regarding the geochemical analysis is given in the "GEOCHEMISTRY" chapter of this study. The whole-rock major and trace element data of the 23 samples of Tunceli Volcanics were obtained by Aktağ (2014), the data were published in Aktağ et al. (2019). These data have been integrated with the new mineral chemistry and Sr-Nd-Hf-Pb isotope data in the present study. In other words, the mineral chemistry and Sr-Nd-Hf-Pb isotope analysis for the Tunceli Volcanics were performed on the samples with the available major-trace element data. For the Elazığ Volcanics, all the geochemical data were obtained for the first time during this research.

A total of 90 thin sections from both volcanic regions (Tunceli and Elazığ) were petrographically analyzed under Olympus (Model: CX31PF) polarizing microscope and the photomicrographs were acquired by Olympus (Model: SC30) camera at the Crustal Research Laboratory of the Department of Geological Engineering in the Middle East Technical University (Ankara, Turkey).

After the petrographical analyses, a total of 10 representative samples (5 from the Tunceli Volcanics and 5 from the Elazığ Volcanics) were selected for the mineral chemistry analysis. Chemical compositions of the phenocryst phases of both Tunceli and Elazığ Volcanics were determined at the Materials Characterization Laboratory, Pennsylvania State University (Pennsylvania, USA).

A total of 19 relatively unaltered samples from the Elazığ Volcanics were selected for the whole-rock lithogeochemical analyses after the petrographical examination. Major, trace, and rare earth element compositions were determined at the ACME Analytical Laboratories Ltd. (Vancouver, Canada).

10 samples from the Elazığ Volcanics and 15 samples from the Tunceli Volcanics were selected for the whole-rock Sr-Nd-Pb-Hf isotope analysis after evaluating the whole-rock major-trace element data. The Sr and Nd isotope analyses were performed at the Radiogenic Isotope Laboratory (RIL), Middle East Technical University (Ankara, Turkey). After that, the sample pulps left from the Sr-Nd isotope analyses were sent to ETH Zurich for the Pb and Hf isotope analyses. The whole-rock Pb and Hf isotope analyses were performed at the Institute for Geochemistry and Petrology, ETH Zurich, (Zurich, Switzerland).

1.4.3 Office Works

The office work conducted in this thesis basically consists of producing the figures and maps, compiling the geochemical data from the literature for comparison, evaluating and interpreting the numerical data combined with designing the geochemical diagrams and models, and writing the thesis.

1.5 Literature Review

1.5.1 Chemical Geodynamics of the Earth

The concept of "chemical geodynamics" was introduced by Allègre (1982) mainly to describe the chemical evolution of the Earth on the basis of chemical mass transfers between Earth's physical reservoirs (e.g., core, mantle, crust, etc.). Later, the understanding of this concept was expanded (Zindler and Hart, 1986) by investigating the heterogeneity in the mantle through the description of new "mantle components" or "mantle end-members" (e.g., DM, EMI, EMII, HIMU, and PREMA) indicating the existence of ancient geological reservoirs in the mantle having different Rb/Sr, Sm/Nd, Th/Pb, and U/Pb parent-daughter ratios. Therefore, the term "chemical geodynamics" can be regarded to refer to the chemical composition and evolution of the mantle, and in this part of the thesis, a short review of the basic facts and hypothesis regarding the geochemistry of the Earth's convecting mantle will be presented.

1.5.1.1 Heterogeneous Mantle

Since radiogenic isotopes are not fractionated by melting and crystallization, they have been regarded as strong tools to understand the origin of mantle-derived melts and related mantle processes (depletion/enrichment) (e.g., Gast, 1960; White and Schilling, 1978). In other words, isotope ratios of primitive melts are identical to their source regions. This, therefore, makes the isotope systematics unique tracers of mantle composition and processes (Hofmann, 2003). In this regards, with developments in the analytical methods of isotope analyses, a new era began in the early 1960s for the investigation of the mantle domains (Hofmann, 1997).

The early studies concerning mantle geochemistry focused on the differentiation of the Earth, particularly to evolution of the mantle-crust systems (e.g., Gast, 1960; Hurley et al., 1962) by using trace element and radiogenic isotope systematics. Subsequent to the deepening intellectual knowledge about mantle-derived rocks (e.g., Hurley et al., 1962; Faure and Hurley, 1963), a specific interest developed towards the composition of the mantle regions (e.g., Gast et al. 1964; Tatsumoto et al., 1965; Hart, 1971). In this regard, the oceanic basalts became ideal materials for mantle investigations since they are not affected by crustal contamination (Hofmann, 1997). At this early stage of mantle investigations, Gast et al. (1964) showed, based on the Sr isotope data, that the mantle source regions of oceanic basalts are not chemically homogeneous as previously was thought to be. After this groundbreaking finding, many studies have provided scientific evidence to support the mantle heterogeneity (e.g., Hedge, 1966; Tatsumoto, 1966; Allègre, 1982; Zindler and Hart, 1986; Hofmann, 1997; Stracke et al., 2005; Stracke, 2012). In addition, with the availability of a large amount of trace element and isotope data from mantle-derived melts, melt inclusions, and mantle xenoliths, it became increasingly apparent that the mantle heterogeneity occurs within a range from grain-scale to km-scale (e.g., Hofmann and Hart, 1978; Allègre et al., 1980; Zindler and Hart, 1986; Duprè and Allègre, 1983; Allègre and Turcotte, 1986; Saal et al., 1998; Jackson and Hart, 2006; Stracke et al., 2003; Stracke et al., 2005). The diffusion calculations (e.g., Hofmann and Hart, 1978; Allègre, 1982) have shown that these heterogeneities in the mantle, especially larger than "mesoscale" (>1km; according to the definition of Hofmann, 2003), are old (>1.5 Ga; Hofmann and Hart, 1978) and reflect diverse geochemical events in the history of mantle domains (Allègre, 1982).

1.5.1.2 Mantle Components

Starting from the late 1970s, the main effort has been unraveling the nature of the mantle heterogeneities and mapping the chemical structure of the Earth's interior (e.g., DePaolo and Wasserburg, 1976; O'Nions et al., 1979; Allègre et al., 1979; DePaolo, 1980). With the recognition of the inverse correlations between the $^{87}Sr/^{86}Sr$ and $^{143}Nd/^{144}Nd$ isotope ratios of oceanic and continental basalts (e.g., DePaolo and Wasserburg, 1976; Richard et al., 1976), two populations of oceanic basalts emerged in the Sr-Nd isotope space (Figure 1.7): mid-ocean ridge (MORBs) and oceanic island basalts (OIBs) (Allègre, 1982). In general, MORBs are "depleted" in incompatible elements (e.g., Cs, Ba, Rb), and they have lower Sr and Pb, and higher Nd and Hf isotope ratios compared to OIBs (Figure 1.7) (e.g., Stracke et al., 2005; Stracke, 2018). OIBs, on the other hand, with slightly lower Sr and higher Nd isotope ratios than the Bulk Silicate Earth (BSE), exhibited near-primitive geochemical characteristics. The observation of these fundamental differences between two oceanic basalt groups initiated the debate on two different mantle reservoirs in the mantle (e.g., Jacobsen and Wasserburg, 1979, O'Nions et al., 1979; DePaolo, 1980). According to the early mantle models, while MORBs were believed to derive from the depleted upper mantle, OIBs were associated with the "primitive" lower mantle reservoir of the Earth (Jacobsen and Wasserburg, 1979; DePaolo, 1980, Allègre et al., 1980). It was assumed that the lower mantle has remained undisturbed with little or no mass exchange with the upper mantle during the extraction of crust (Jacobsen and Wasserburg, 1979; DePaolo, 1980, Allègre et al., 1980). These ideas, however, soon after were partly modified by the availability of new isotope data from the oceanic basalts. Since these initial observations, recent researches have shown that most of OIBs do not have primitive mantle-like trace element characteristics (e.g., Hofmann and White, 1982), and the isotopic range of OIBs deviate from the "primitive" Earth values (e.g., Zindler and Hart, 1986; Stracke et al., 2005).

It has been recognized that most of OIBs require source regions with non-primitive Sr-Nd-Pb isotope and element ratios such as Nb/U or Ce/Pb (Hofmann, 1997), and their chemistry cannot be explained by only two mantle reservoirs (i.e., a depleted and a primitive one). This isotopic diversity in OIBs has supported the existence of the large-scale heterogeneities in the mantle (e.g., Hofmann and White, 1982; Allègre and Turcotte, 1985) and manifest themselves as deviation from the range of mantle plane of Earth in the isotope ratio-ratio spaces. These extremes found in OIBs have been described as "mantle components" or "mantle end-members" since the early studies (e.g., Zindler et al., 1982; Allègre and Turcotte, 1985; White, 1985; Zindler and Hart; 1986). Although they have been initially recognized by Allègre and Turcotte (1985) and White (1985), Zindler and Hart (1986) have labeled them in the Sr-Nd-Pb isotope spaces with distinct acronyms such as; DM (Depleted Mantle), EMI (Enriched Mantle 1), EMII (Enriched Mantle 2), HIMU (High $\mu=({}^{238}U/{}^{204}Pb)_{t=0}$ values), and PREMA (Prevalent Mantle) (Figure 1.8).

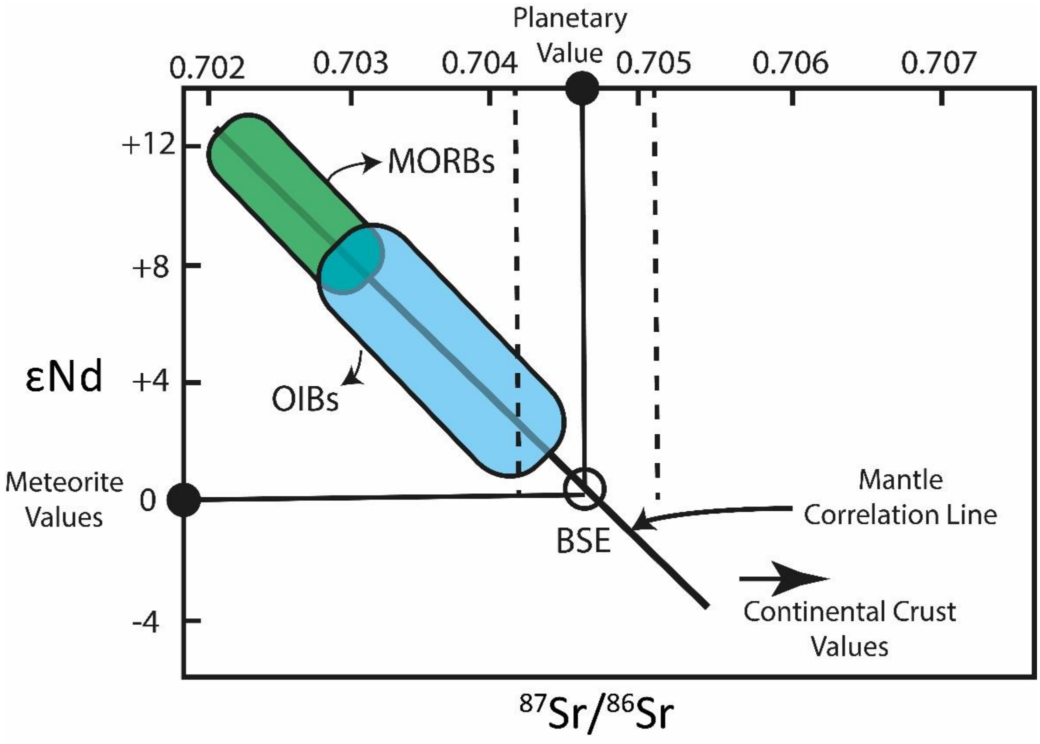

Figure 1.7. Correlation of oceanic basalt in the Sr-Nd isotope space (modified from Allègre, 1982).

The DM component represents the source composition of the “typical” MORBs, which have lower Sr and Pb, and higher Nd isotope compositions in the mantle plane (Zindler and Hart, 1986). The “typical” term here refers explicitly to the depleted mantle source beneath the ridge systems where the plume component is excluded. The plume-interacted ridge systems tend to produce more enriched and heterogeneous magmas with isotope compositions close to BSE in the mantle plane (e.g., Hanan et al. 1986). Although the descriptions of “typical” or “normal” MORB (e.g., N-MORB), which are widely used in the literature to define the depleted volcanics at ridge segments, are somehow problematic for some geoscientists (e.g., Hofmann, 2003) due to the existence of some large-scale MORB populations having extraordinary compositions (e.g., Indian Ocean MORBs, Dupre and Allègre, 1983; Hart, 1984), the DM component has been assumed to be an end-member for most of MORBs (Zindler and Hart, 1986). The different values of DM (DMMa and DMMb) on the plot of $^{87}Sr/^{86}Sr$ versus $^{143}Nd/^{144}Nd$ (Zindler and Hart, 1986) represent the compositional variability of this component in the mantle (Figure 1.8).

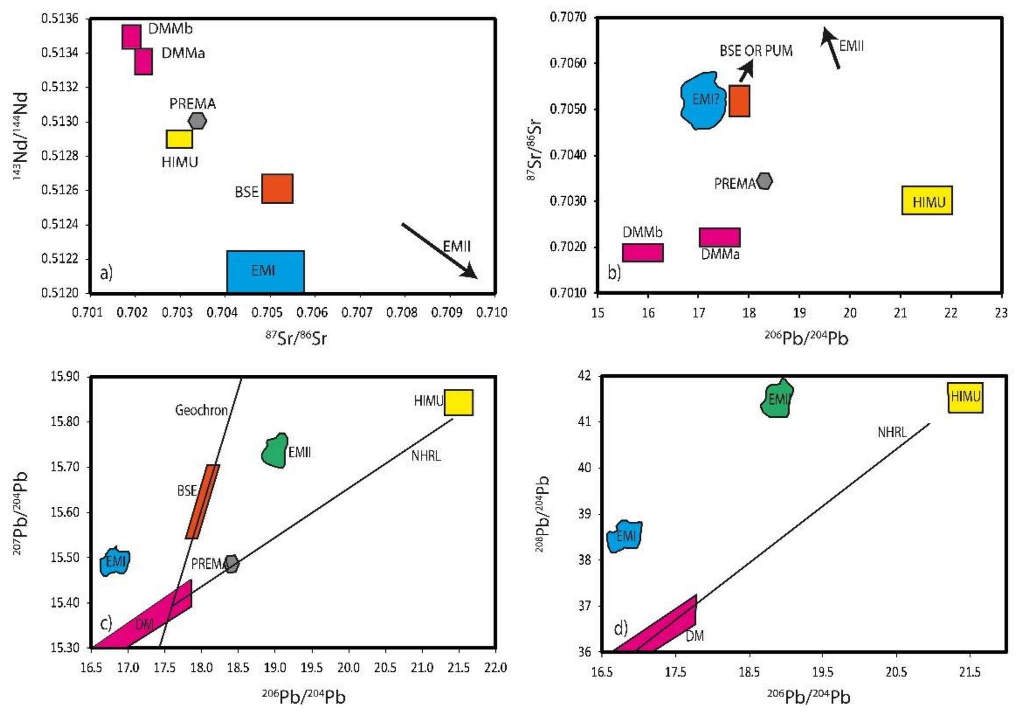

Figure 1.8. Location of mantle end-members in the Sr-Nd-Pb isotope spaces (from Zindler and Hart, 1986).

The HIMU component is one of the extremes found in the mantle and manifests himself with unradiogenic Sr and highly radiogenic Pb isotope contents (e.g., $^{206}Pb/^{204}Pb > 20.5$; Stracke et al., 2005), which require time-integrated evolution of high U/Pb and Th/Pb ratios (Figure 1.8; Zindler and Hart, 1986). The $^{87}Sr/^{86}Sr$ contents of the OIBs sampling the HIMU component are almost as low as those found in MORBs (e.g., 0.702, Zindler and Hart, 1986). Compared to the other mantle components, the pure HIMU component is scarcely sampled by oceanic basalts (Stracke, 2012). St. Helena (Atlantic) and Mangaia (Pasific) islands are the typical localities, where the $^{206}Pb/^{204}Pb$ values exceed 20.5 (e.g., Chaffey et al., 1989;

Reisberg et al., 1993; Woodhead, 1996; Salters and White, 1998; Willbold and Stracke 2006; Salters et al., 2011). However, HIMU is proposed to be a dispersed component in the mantle (e.g., Zindler and Hart, 1986), which likely mixes with other end-members as documented by the isotope spaces (Zindler and Hart, 1986).

The altered and/or subduction-modified ancient oceanic crust has been usually regarded as a potential source reservoir for the HIMU-type volcanism due to its low Sr and high Pb isotopic features (e.g., Chase, 1981; Hofmann and White, 1982; Zindler et al., 1982; Lassiter et al., 2003; Stracke et al., 2003; Day et al., 2010). It is assumed that the alteration and/or subduction processes leading to alkali loss prior to the recycling are plausible mechanisms that can account for the low Rb/Sr and $^{87}Sr/^{86}Sr$ ratios of HIMU-type OIBs. (e.g., Chase, 1981; Hofmann and White, 1982; Zindler and Hart, 1986; Chauvel et al., 1992; Stracke et al., 2003; 2005; Willbold and Stracke, 2006; Stracke, 2012). Stracke et al. (2003) have also shown that this ancient oceanic crust should have been free of its sediment before recycling because even small amounts of the addition of marine sediments would significantly shift its elemental and isotopic budget from the range of HIMU values. Thus, the recycling of pure oceanic crust that modified by sub-arc processes appear to be an ideal source reservoir for the HIMU component (e.g., Chase, 1981; Hofmann and White, 1982; Zindler et al., 1982; Chauvel et al., 1992; Lassiter et al., 2003; Stracke et al., 2003; 2005; Willbold and Stracke, 2006; Day et al., 2010; Stracke, 2012). Alternatively, it is also suggested that recycled metasomatized oceanic or continental lithospheric mantle, which has been fertilized by asthenosphere-derived melts, can also generate the HIMU-like similar isotope compositions (e.g., Sun and McDonough, 1989; Halliday et al., 1995; Niu and O'Hara, 2003; Pilet et al., 2005; 2011). The fundamental principle is based on the long-term isolation of the ancient metasomatized lithospheric mantle and its recycling back into source regions of the oceanic and continental magmatism (Halliday et al., 1995; Niu and O'Hara, 2003; Pilet et al., 2005). The metasomatized portions of the mantle are thought to be entrained into the asthenospheric mantle by subduction or delamination (e.g., Pilet et al., 2005).

The enriched mantle components EMI and EMII (Zindler and Hart, 1986) are the other extreme components widely reported in the genesis of mantle-derived melts. While the EMI-type melts (e.g., basalts on the Islands of Pitcairn, Tristan, and Gough) are characterized by very low $^{143}Nd/^{144}Nd$ and $^{206}Pb/^{204}Pb$ and moderate $^{87}Sr/^{86}Sr$ and $^{208}Pb/^{204}Pb$ isotope ratios, the EMII-type melts (e.g., basalts on the Islands of Sao Miguel, Samoa, and Society) are characterized by very high $^{87}Sr/^{86}Sr$, high $^{207}Pb/^{204}Pb$, $^{208}Pb/^{204}Pb$ and low $^{143}Nd/^{144}Nd$ isotope ratios (Figure 1.8). These distinct extreme isotope characteristics found mostly in OIBs led to the hypothesis that the two different enriched mantle reservoirs exist in the mantle (e.g., Hawkesworth et al., 1979; White and Hoffman, 1982; Cohen and O'Nions, 1982; Zindler and Hart, 1982). Although there is still no consensus on the origins of EM-type volcanism (e.g., Hawkesworth et al., 1979; White and Hofmann, 1982; Cohen and O'Nions, 1982; Zindler and Hart, 1982; Weaver, 1991; Blichert-Toft et al., 1999; Eisele et al., 2002; Willbold and Stracke, 2006), the discussions are mainly centered on the mechanisms including the recycling of different type of lithospheric reservoirs (e.g., whole oceanic lithosphere, crust, and sediments).

According to the diversity in the proposed hypotheses, the source of EMI-type basalts appears to be more controversial than EMII (Hofmann, 2003). The very low $^{143}Nd/^{144}Nd$ and moderately high $^{87}Sr/^{86}Sr$ isotope ratio of the EMI-type magmas require a long-term evolution of a source region with very low Sm/Nd and moderately high Rb/Sr ratios. In order to explain such isotope features, several ancient reservoirs such as metasomatized lithospheric mantle, oceanic crust with pelagic sediments, or lower continental crust have been proposed. The previous models that regard the ancient metasomatized lithospheric mantles as the potential precursor for EMI are mainly based on the isotope ratios of mantle nodules found in the ultramafic massifs (e.g., Hawkesworth et al., 1986). Later, this was also supported by the isotopic evidence found in the lava flows (e.g., Mahoney et al., 1991). It has been suggested that the metasomatic events can significantly lower the Sm/Nd ratio and moderately increase the Rb/Sr ratio mantle materials (Menzies, 1983; Zindler and Jagoutz, 1988; Zindler and Hart, 1986). Hence, the long-term isolation of such material would make it an ideal candidate for the source reservoir of EMI-type volcanism (Zindler and Hart, 1986). Another proposal, suggesting the recycled oceanic crust with the addition of pelagic sediments, was proposed by Weaver (1991). Based on the quantitative trace element calculations, Weaver (1991) showed that the addition of small amounts of pelagic sediments to dehydrated oceanic crust can reproduce the incompatible trace element systematics of the EMI source. Later, this argument was supported by many isotope-based studies (e.g., Chauvel et al., 1992; Rehkämper and Hofmann, 1997; Blichert-Toft et al., 1999; Eisele et al., 2002). Among these, especially the Lu-Hf isotope systematics provided compelling evidence that the EMI-type volcanism may include the ancient pelagic sediments (Blichert-Toft et al., 1999; Eisele et al., 2002). Since the pelagic sediments are zircon-free, they have more radiogenic ^{176}Hf/^{177}Hf ratios than terrigenous sediments (White et al., 1986). Therefore, any involvement of the pelagic sediments in the genesis of volcanics would create a shallower slope than the general trends of OIBs in the Nd-Hf isotope space (e.g., Blichert-Toft et al., 1999). This pattern is well illustrated in the volcanics of Pitcairn Islands (Eisele et al., 2002), which is regarded as one of the typical locations of EMI (e.g., Woodhead and Dewey, 1993). Another idea to explain the origin of EMI is the involvement of the lower crustal material (Escrig et al., 2004; Hanan et al., 2004). Hanan et al. (2004) showed that the distribution of the EMI-type basalts from the Indian ridge in the Hf-Pb isotope space is consistent with the melting of lower crustal granulites with high εHf and low ^{206}Pb/^{204}Pb values. This model assumes that the lower crustal material is incorporated into the MORB mantle during continental rifting and opening of oceanic basins (Hanan et al., 2004). Later, a similar genetic link with the lower crust and the EMI component was shown by Willbold and Stracke (2006). These authors drew attention to the compositional similarities between the upper crustal material (Rudnick and Gao, 2004) and the subducted sediments (Plank and Langmuir, 1998). Based on this, they postulated that instead of sediments, a recycled lower crustal material with lower Sr and Pb isotope contents would provide a plausible explanation for the EMI-type isotope signatures. In their model, unlike the model of continental rifting (Hanan et al., 2004), incorporating the lower crustal material into the mantle region was explained by the subduction erosion (Willbold and Stracke, 2006).

The EMII component, on the other hand, has been widely associated with recycling of upper crust-derived or terrigenous sediments due to its high ^{87}Sr/^{86}Sr and ^{207}Pb/^{204}Pb isotope ratios (e.g., Hawkesworth et al., 1979; White and Hofmann, 1982; Wright and White, 1987; Chauvel et al., 1992; Willbold and Stracke, 2006). However, as in EMI, there is also no consensus on the origin of EMII. Workman et al. (2004) have suggested a recycled metasomatized lithosphere for the origin of EMII. According to their model, an ancient oceanic lithosphere metasomatized by deep asthenospheric melts can produce the isotopic signatures observed in the EMII-type magmas, which can also account for their low ^{187}Os/^{188}Os and high ^{3}He/^{4}He isotope ratios.

Apart from the depleted and enriched components mentioned above, an internal component, which is involved in many OIBs, enriched MORBs, and some continental basalts, was introduced by Zindler and Hart (1986) and labeled as “PREMA” (the Prevalent Mantle). Later, such intermediate component was also introduced by many researchers with different acronyms (e.g., FOZO: Focal Zone; Hart et al., 1992; PHEM: Primitive Helium Mantle; Farley et al., 1992; C: common component, Hanan and Graham, 1996), though they differ from one to another only in detail (Stracke et al., 2005). This component is found as an intermediate component towards which the other mantle components converge in the isotope spaces (Figure 1.8; Zindler and Hart, 1986). Zindler and Hart (1986) postulated two scenarios on the origin of the PREMA; (i) a primitive mantle component and (ii) an ambient component which represents the remixture of the mantle materials (or mantle components such as EMs, HIMU, and DM). The first one assumes a relatively undegassed primordial lower mantle, i.e., PREMA sampled by plumes. This view has widely been reconciled with the high ^{3}He/^{4}He isotope ratios found in some OIBs (e.g., Hawaii, Iceland, Samoa; Zindler and Hart, 1986; Hart et al., 1992; Farley et al., 1992), although it has been suggested that the high ^{3}He/^{4}He ratios can also be produced by intramantle metasomatism in a previously depleted mantle (Zindler and

Hart, 1986). Regardless of whether or not the high $^3He/^4He$ primitive mantle still exists (for a detailed discussion, see Jackson et al., 2008), the hypotheses of the Farley et al. (1992) and Hart et al. (1992) are somewhat consistent with that of Zindler and Hart (1986) since both components FOZO and PHEM are assumed to sample the lower mantle material. On the other hand, the second proposal of Zindler and Hart (1986), which regard PREMA as an "ambient" mantle component, is supported by the convergence of the OIB arrays on the ternary Pb isotope plot (Hanan and Graham, 1996). However, instead of being an external mantle component, PREMA was defined by Hanan and Graham (1996) as a "common" mantle component sampled by most plumes. According to these authors, the common component (called C) represents the melts derived from an oceanic crust (with an age of 300 Ma-2 Ga), which has incorporated some continental Pb before the subduction. Later, Stracke et al. (2005) also postulated a similar argument in their redefined concept of "FOZO". These authors also regard this component as a ubiquitous component in the mantle, produced by continuous subduction and recycling of the oceanic crust. With a little modification, this view was also supported by the study of Stracke (2012), which postulated that the isotope range of the PREMA-type volcanics can be reproduced by recycling subduction-modified oceanic lithosphere (crust plus the residual mantle lithosphere).

Although there are different definitions (e.g., different isotope ranges) and hypotheses on the origin of this intermediate component, it is apparent that most OIB arrays radiate from this component to different directions in the two- or three-dimensional isotope spaces (Hart et al., 1992; Hanan and Graham, 1996; Hofmann, 2003). Therefore, the term "common" appears to be suitable, which is also reinforced by the detection of a similar ubiquitous component beneath the continental areas, such as the Low-Velocity Component (LVC) of Hoernle et al. (1995) or the European Asthenospheric Reservoir (EAR) of Cebriá and Wilson (1995).

1.5.2 The Sub-Continental Lithospheric Mantle (SCLM)

The lithospheric mantle can be described as the upper most portion of the mantle, which is stabilized via isolation from convective mantle flows (McKenzie and Bickle, 1988; Pearson and Nowell, 2002). This portion underlies the Earth’s crust in both oceanic and continental settings (Figure 1.9).

Due to its significant thickness, the sub-continental lithospheric mantle (SCLM) is considered to have potentially contribute to intraplate volcanism. The SCLM has been widely indicated as a common source region for many small-scale magmatic suites (e.g., McDonough, 1990). These suites include basaltic alkaline volcanism and also some particular melt types such as lamproites and kimberlites (e.g., McDonough, 1990). There is also an ongoing discussion whether the SCLM can be the ideal source regions for the large volume of continental volcanism such as continental flood basalts (CFB) or not (e.g., Hawkesworth et al., 1983; Carlson, 1984; Hergt et al., 1991; Menzies, 1992; Anderson, 1994).

These arguments, which attribute the SCLM as the source of intraplate volcanism in continental settings, necessitate a short review regarding the characteristics of the SCLM within the scope of this research.

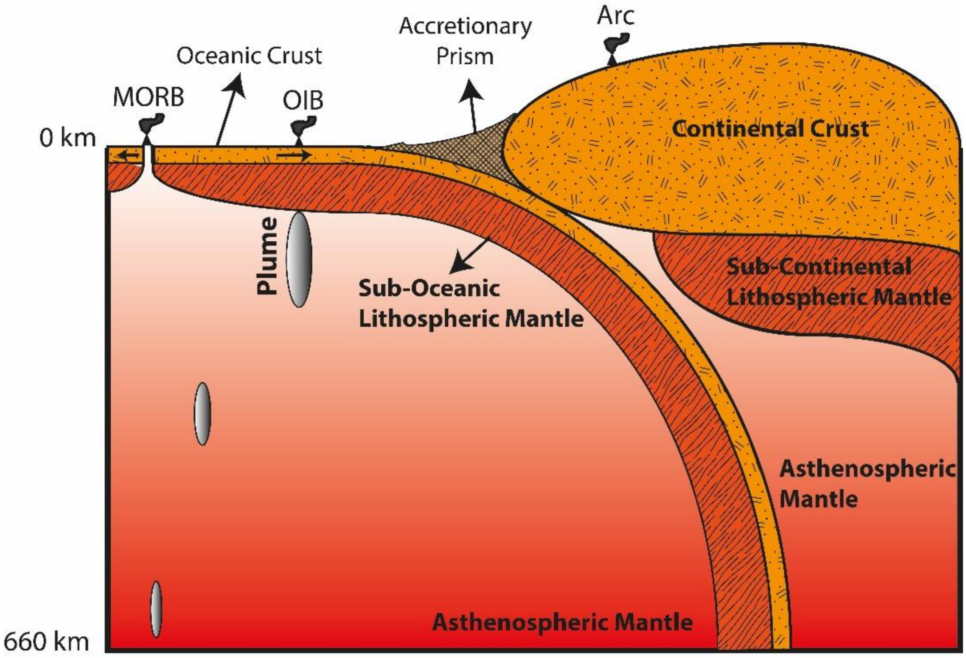

Figure 1.9. Box model showing fundamental structure of the upper mantle. MORB: Mid-Ocean Ridge Basalts; OIB: Ocean Island Basalts.

1.5.2.1 Thickness and Age of the SCLM

The lithospheric mantle extends from the Moho discontinuity to the Lithosphere-Asthenosphere Boundary (LAB) in oceanic and continental settings. The depth of the LAB is around 40-70 km beneath oceanic settings, around 100 km beneath Phanerozoic continental settings, and around 200 or 250 km beneath Precambrian shields (Plomerová et al., 2002). Condie (2016) proposed that while the thickness of the lithosphere in post-Archean regions is around 100-200 km, it commonly exceeds 200 km in the Archean regions. The Sm/Nd ages of the silicate phase inclusions in the diamonds (e.g., Richardson et al., 1993) and Re/Os depletion ages of xenoliths found in some Archean cratons (e.g., Pearson et al., 2002) suggest that the lithospheric mantle beneath old continental setting formed at the same time with their overlying crust (Condie, 2016; Pearson and Nowell, 2002). These suggest that the lithospheric mantle is getting thicker with aging; hence, the lithospheric mantle beneath continental regions is much older and thicker compared to the young sub-oceanic lithospheric mantle. This led the SCLM to be much more prone to secondary modification events in geological history. Due to its old and thick physical nature, the SCLM has recorded the metasomatic and crustal differentiation events since the early history of the Earth. Some progressive events in geological history such as melt extraction (e.g., Hartmann and Wedepohl, 1993), injection of melts and/or fluid derived from plumes (e.g., Rooney et al., 2014), asthenosphere (e.g., Pilet et al., 2011), and subducted slabs (e.g., Zanetti et al., 1999) has created a wide range of compositional diversity in the SCLM. Evidence of these events is frequently found in the lherzolitic and harzburgitic xenoliths from alkaline intraplate volcanics (see Downes, 2001).

1.5.2.2 Composition of the SCLM

Since the chemical budget of the SCLM is affected by aforementioned processes, it is usually difficult to describe its general compositional framework. However, the whole-rock or microprobe data obtained from the xenoliths found in alkaline basalts or kimberlites provide an excellent opportunity to develop a good approach to defining the chemical composition of the SCLM, especially for observing the vertical compositional change in the SCLM (Griffin et al., 2009).

The SCLM is composed of various lithologies ranging from lherzolites (e.g., spinel lherzolites, garnet lherzolites) to harzburgites (Griffin et al., 2009). The mineral assemblages of lherzolites, which make up an essential portion of the SCLM are olivine+orthopyroxene+clinopyroxene±garnet±spinel (Griffin et al., 2009). Among the ultramafic mantle rocks, garnet lherzolites provide important information about the deep parts of the mantle since it is stable below approximately 80 km (e.g., Takahashi and Kushiro, 1983). Spinel lherzolites and other mantle rocks such as harzburgite, on the other hand, represent shallower depths of the lithospheric mantle (Beccaluva et al., 1989; McDonough, 1990; Condie, 2006). Garnet lherzolites are generally sampled by kimberlites, which are assumed to originate at significant depths (>100 km) (e.g., Condie, 2006). Garnet lherzolites are usually depleted in terms of most major and minor elements (e.g., CaO ≈ 0.6-1 wt. %; Al_2O_3 ≈ 1-1. 5wt. %; Griffin et al., 2009) compared to the spinel lherzolites in Archean cratons (McDonough, 1990). This picture somehow changes in the Tecton areas (<1 Ga), where the spinel lherzolites are more depleted (e.g., CaO and Al_2O_3 ≈ 2.5 wt. %) than garnet lherzolites (e.g., CaO ≈ 3.1-3.2 wt. %; Al_2O_3 ≈ 3.5-3.9 wt. %) (Griffin et al., 2009). Regardless of age, however, both lherzolite groups have depleted major and minor element contents relative to the primitive upper mantle (e.g., CaO ≈ 3.6 wt. %; Al_2O_3 ≈ 4.5 wt. %; Griffin et al., 2009). Besides, many harzburgites found in the ultramafic massifs are also strongly depleted in their most major and minor elements (Griffin et al., 2009). These depletions have been widely attributed to the basaltic melt extraction from the SCLM (e.g., McDonough and Frey, 1989; McDonough, 1990; Griffin et al., 2009). The depleted lherzolites and harzburgites have also been reported to display depleted LREE (light rare earth elements) patterns (e.g., Bodinier, 1988; Bodinier et al., 1988; Zangana et el., 1999; Downes, 2001). Such depletions can be observed mainly in the mantle rocks that are isolated from second-stage enrichments. The depletion patterns of mantle rocks show that the melt extraction process, regardless of its depth, is continuous and one of the major processes that have shaped the elemental budget of the SCLM.

The Nd model ages, LREE, and incompatible trace element abundances of many xenoliths found in the Archean and post-Archean fields prove that the melt extraction process is not the only process that shaped the chemical nature of the SCLM (e.g., McDonough, 1990). LREE and incompatible element patterns of various types of xenoliths have indicated that the enrichment process also has a profound effect on the chemistry of the SCLM, at least as much as the depletion process (e.g., Downes, 2001). McDonough (1990) revealed that even the stabilized Archean SCLM underwent post-Archean enrichment subsequent to the depletion events. This was supported by various types of mantle xenoliths found in Europe (e.g., Zangana et al., 1997; Bodinier et al., 1990). Downes (2001) showed that the mantle xenoliths representing different depths of the lithospheric mantle are either LREE-depleted or

-enriched. While the depletions were explained by the melt extraction process, which appears to be the main driving force behind the major and minor element patterns, the enriched patterns were attributed to the second stage enrichment via metasomatism (Downes, 2001).

The contribution of metasomatic agents to the lithospheric mantle is well observed in the most incompatible elements (e.g., LREE, Ba, Rb; McDonough, 1990; Downes, 2001), especially those mobilized by fluids or melts (Downes, 2001). The whole-rock chemistry of most mantle xenoliths or trace element chemistry of pyroxenes from the xenoliths has shown that the fluid and/or melts infiltrated domains of SCLM usually show incompatible element enriched patterns (e.g., Downes, 2001). The types of enrichment, however, strongly depend on the nature of fluid and melt that the SCLM interacts with (Downes, 2001). It is also important that the secondary enrichments not only cause a change in the total chemical budget of the SCLM, but also alter its mineralogy.

For instance, the plume- or asthenosphere-derived melts tend to form amphibole and/or pyroxene-rich peridotites in the SCLM (e.g., Vaselli et al., 1995; Pilet et al., 2008; 2011). While the modifications in major elements are limited during this type of silicate melt metasomatism, the incompatible element systematics of the SCLM is strongly affected. Especially the abundances of highly incompatible elements, which strongly partition into silicate melts (e.g., LREE, Sr, Zr, Hf, and Nb), dramatically increase in the SCLM (Downes, 2001). On the other hand, the carbonatite metasomatism tends to form wehrlites and/or dolomitic veins in the mantle and affects both whole-rock major/minor and trace element chemistry of the mantle (Downes, 2001). An increase in CaO/Al_2O_3 and Ti/Eu ratios, depletion in Zr, and U-shaped REE patterns in the multi-element diagrams were reported from the mantle rocks, which underwent interaction with carbonatite melts (Downes, 2001). Another example is subduction-related metasomatism in the convergent areas, which also has a profound impact on the SCLM. It is widely reported that the lithospheric mantle rocks modified by the slab-derived fluids have high LILE/HFSE and low

Nb/Nb* ratio ($\sqrt{ThNxLaN} < 1$; N indicates normalization to PM composition of Sun and McDonough, 1989), which is characteristic of subduction-related magmas (e.g., Zanetti et al., 1999). Such metasomatic fluids rich in incompatible soluble elements (e.g., Rb, Sr, K, Ba) tend to form amphibole and/or phlogopite minerals in the mantle (Downes, 2001). Hence, in the light of the information above, the metasomatism appears to be a vital process that can alter the bulk composition of the SCLM, and the enrichment characteristics are closely linked to the chemistry of the metasomatic melts and/or fluids.

As mentioned above, both depletion and enrichment processes deeply affect the SCLM, creating elemental and mineralogical diversity. The recent isotope data (e.g., Pearson et al., 1995; Pearson et al., 1999) from the mantle xenoliths have shown that these processes are also responsible for the wide isotopic diversity in the SCLM. The isotope chemistry of the mantle xenoliths indicates time-integrated evolution of low and high Sm/Nd parent-daughter ratios, supporting both long-term depletion and enrichment events in the mantle (Pearson and Nowell, 2002). Hence, most mantle xenoliths plot on an area extending from MORBs fields towards very enriched compositions ($^{87}Sr/^{86}Sr$ > BSE) in the Sr-Nd isotope space (e.g., Downes, 2001). The xenoliths isolated from the enrichment process since their depletion events display highly depleted radiogenic isotope signatures, which overlap with the MORBs (e.g., Downes, 2001). However, those xenoliths that infiltrated by the melts from diverse sources can be more radiogenic than MORBs. Here, it must be noted again that the type of the enrichment also depends on the characteristics of the melt or fluid they have interacted. For instance, the xenoliths that have interacted with the plume-derived melts may have isotope signatures identical to the OIBs, whereas those that interacted with the slab-derived fluids/melts may show highly radiogenic $^{87}Sr/^{86}Sr$ ratios exceeding the BSE value (e.g., Downes, 2001). Thus, as their elemental budget, the isotopic signatures of the mantle xenoliths also give valuable information regarding the major depletion/enrichment events in their geological history.

To sum up, the understanding of the chemical and mineralogical nature of the SCLM is somewhat complicated since the SCLM records all major geological events since its formation. However, this can be an advantage for understanding the geodynamic evolution of the continental regions. Interpreting the geochemical information from the mantle xenoliths or melts derived from the SCLM can provide an excellent opportunity to reveal the nature of the secondary geological events beneath the continents. It is also essential that the in-situ melting of the SCLM is not the only way to contribute to the intraplate volcanism in the continental regions. Removal of the SCLM into the convecting mantle and subsequent recycling of this material into the intraplate volcanism as a mantle component cannot be excluded (e.g., McKenzie and O’Nions, 1983).

1.5.3 Mantle Source Characteristics of Cenozoic Intraplate Volcanism of circum-Mediterranean Region

As mentioned above, the Earth’s mantle is fairly heterogeneous, even on a cm-scale. Hence, drawing a picture regarding the mantle characteristics of a vast region extending from the Atlantic Ocean to the Middle East is complicated and beyond the scope of this research. However, considering that the chemistry of the anorogenic intraplate volcanics in this region may have been affected by similar geodynamic events with the Anatolian anorogenic intraplate volcanics due to their occurrence within the same tectonic belt (the Alpine-Himalayan Orogenic Belt), it can be expected that their mantle sources also share some geochemical similarities. From this point of view, to develop a better understanding of the nature of the mantle source regions of Turkey, the most outstanding chemical features of the mantle sources beneath the surrounding areas should be addressed here. Thus, a short review regarding the nature of the mantle sources of the circum-Mediterranean region will be given in this section. Note that, in this section the petrological evolution of the anorogenic intraplate volcanism is not further discussed. For detailed information regarding the composition, geodynamical evolution and mantle characteristics of the anorogenic intraplate volcanics of the circum-Mediterranean region, the reader is referred to see Wilson and Bianchini (1999), Wilson and Downes (2006), and Lustrino and Wilson (2007).

The term “anorogenic” refers here to those volcanics related to the extensional tectonics, the lithospheric foundering events, or plume activity rather than the products of active subduction events. It is suggested that the extensional tectonics such as the creation of local extension regions under the control of strike-slip faults, reactivation of the older discontinuities (e.g., Permo-Carboniferous sutures and fault systems) in the lithosphere, and orogenic collapse may trigger adiabatic melting either in the lithospheric and/or asthenospheric mantle (e.g., Wilson and Downes, 2006; Lustrino and Wilson, 2007). Likewise, some processes such as lithospheric delamination, slab roll-back, slab break-off, and plume activity can generate thermal anomalies under the continents and trigger mantle melting (Lustrino and Wilson, 2007). It must be also noted that, although these anorogenic volcanics are not related to the active arc-magmatism, some volcanics carry an inherited subduction component (e.g., high LILE/HFSE ratio and negative Nb anomaly in the mantle-normalized diagrams), which is attributed to their derivation from a previously metasomatized lithospheric mantle (e.g., Pearce et al., 1990). Such members of anorogenic volcanics may provide important information regarding the lithospheric mantle.

The intraplate anorogenic volcanism of the circum-Mediterranean region crop out in western Europe (e.g., The Iberia Massif and The Massif Central of France), in central Europe (e.g., Rhenish Massif of Germany, Bohemian Massif and Pannonian Basin), in eastern Europe (e.g., Serbia, Macedonia and Bulgaria), in the Central Mediterranean region (e.g., Sicily Channel, Sardinia, Monte Vulture and Veneto areas of Italy), along North African Foreland, in the Arabian shield, and in the eastern Mediterranean region (e.g., Turkey) (Figure 1.1) (Wilson and Downes, 1991; 2006; Wilson and Bianchini, 1999; Lustrino and Wilson, 2007).

In the circum-Mediterranean region, anorogenic volcanism occurred mainly during the Neogene-Quaternary period (Wilson and Bianchini, 1999). In this region, in general, two distinct groups of lavas have been described; while first one is rich in Si and K ($K_2O/Na_2O>1$; Wilson and Downes, 1991) and with (e.g., the southeast Spain (Tallante), Duggen et al., 2005; Serbia, Prelević et al., 2005) or without (e.g., Massif Central France; Wilson and Downes, 1991) subduction-related trace element patterns, the second group is Si-poor and Na-rich ($K_2O/Na_2O<1$; Wilson and Downes, 1991) and displays OIB-like trace element patterns (e.g., Massif Central France, Rhenish Massif; Wilson et al., 1995a; Wilson and Downes, 1992). The primitive members of the SiO_2-undersaturated group, with their HIMU OIB-like (e.g., St. Helena type) trace element pattern (e.g., peak at Nb in the mantle-normalized diagrams) and depleted Sr-Nd isotope ratios, are thought to represent the products of the asthenospheric source region(s) (i.e., plume melts, e.g., Granet et al., 1995 or melts from plume-contaminated asthenospheric mantle source, e.g., Duggen et al., 2005). These OIB-like volcanics also show a relative depletion at K in their mantle-normalized trace element patterns, which is attributed to the existence of a K-bearing mineral phase (e.g. phlogopite and amphibole) in their source region (e.g., Wilson and Downes, 1991; 1992; Wilson and Bianchini 1999). It has been postulated that the melting of easily fusible, enriched regions at the base of the lithosphere (e.g., thermal boundary layer (TBL); Wilson et al., 1995b), which have been previously infiltrated by plume-contaminated asthenospheric/or plume-derived melts, may have generated the sodic alkaline volcanism of the circum-Mediterranean region (e.g., Wilson et al., 1995a; Jung et al., 2005; Mayer et al., 2013). According to such a model, although melting occurs in the lithosphere-asthenosphere boundary, the parental melts of sodic alkaline volcanics mostly sample the asthenospheric mantle signatures. The K-bearing phases at the base of the lithosphere can be created via percolation of hydrous fluids from former subduction events (during the Variscan or younger subduction events; Wilson and Downes, 2006) or CO_2-H_2O rich silicate melts derived from asthenospheric source (e.g., plume; Wilson et al., 1995b). The potassic magmas, on the other hand, are thought to be derived from an enriched lithospheric mantle source (e.g., Wilson and Bianchini, 1999). Since the chemical characteristics of the lithospheric mantle are strongly linked to the type and duration of the depletion and enrichment processes, the potassic magmas in the region also exhibit a chemical variety. In this regard, the trace element patterns of these volcanics can be roughly divided into two groups: the OIB-like potassic magmas (e.g., leucites and leucite nephelinites in the Massif Central France and Rhenish Massif; Wilson and Downes, 1991), and those with an inherited subduction imprint (e.g., lamproites from Southastern Spain and NW African Margin; Duggen et al., 2005). With DUPAL (enriched southern hemisphere mantle, Hart, 1984)-like trace element patterns, the OIB-like potassic magmas differ from the sodic alkaline anorogenic volcanics (e.g., Wilson and Downes, 1991). The relative depletion in Rb, Ba and K found in sodic alkaline volcanics is not characteristic in the potassic rocks (e.g., Wilson and Downes, 1991). This pattern is assumed to be generated by the complete melting of K-bearing phases (e.g., phlogopite and amphibole) in the lithospheric mantle (Wilson and Downes, 1991). According to the information above, the mantle components found in the circum-Mediterranean anorogenic alkaline mafic and potassic rocks can provide significant information regarding the chemical characteristics of the lithospheric and asthenospheric mantle source domains beneath the region.

According to the Sr-Nd-Pb isotope geochemistry, distinct types of mantle end-members (e.g., DM, HIMU, FOZO/C, EAR/LVC, EMI, and EMII) have been detected in the anorogenic volcanics of the circum-Mediterranean region (Lustrino and Wilson, 2007). While the EM-type (EMI and EMII) mantle components are mostly attributed to the lithospheric mantle-derived melts, the others are thought to reside in the asthenospheric mantle (e.g., Wörner et al., 1986). As an asthenospheric mantle component, the EAR/LVC-type common component is assumed to be the dominant mantle component sampled by the anorogenic volcanism of the circum-Mediterranean region (e.g., Cebriá and Wilson., 1995; Hoernle et al., 1995). The anorogenic volcanics of Europe and the circum-Mediterranean region radiate from this common component in the Sr-Nd-Pb isotope systematics (Cebriá and Wilson., 1995; Hoernle et al., 1995). This was interpreted as the existence of a common component in the asthenospheric mantle source of this region (e.g., Cebriá and Wilson., 1995; Hoernle et al., 1995). Later, many researches, especially those related to the mafic alkaline anorogenic volcanism, have provided compelling evidence regarding the melt contribution from such common component (EAR/LVC) to the anorogenic volcanism of the circum-Mediterranean region (e.g., Wilson and Bianchini, 1999; Bogaard and Wörner, 2003; Jung et al., 2006; Lustrino and Wilson, 2007; Mayer et al., 2013). In contrast to EAR and LVC, the other common components such as FOZO or C have been rarely documented in the genesis of the anorogenic volcanics of European volcanism. For example, for some small anorogenic volcanic provinces, especially in the eastern Mediterranean (northeast Egypt, Endress et al., 2011; western Turkey; Aldanmaz et al., 2015), a C-like common component was suggested to be present in the asthenospheric mantle.

The EAR and LVC show little chemical and conceptional difference with the other common components (e.g. FOZO, C, PHEM, and PREMA), which are mostly defined in the genesis of oceanic basalts. Although the EAR and LVC share similar Sr-Nd isotopic characteristics with the other common components, they specifically differ from them in terms of their slightly radiogenic Pb contents (e.g., LVC: $^{206}Pb/^{204}Pb$= 19.9-20.1, $^{207}Pb/^{204}Pb$=15.62-15.68; Hoernle et al., 1995). The isotopic range of EAR/LVC is rather comparable with the redefined FOZO concept of the Stracke et al. (2005). Due to the radiogenic Pb signatures of the EAR, it has been widely considered as a HIMU-like component (e.g., Jung et al., 2005). It is also important that since some of the most depleted members of the EAR-type volcanics reside between HIMU and DM field in the Sr-Nd isotope space and have $^{206}Pb/^{204}Pb$ values over 19.5 (e.g., Eifel: Wörner et al., 1986; Jung et al., 2006; Westerwald, Siebengebirge; Wedepohl and Baumann, 1999; Polinsky vrch Hill of Bohemian Massif; Ulrych et al., 2016), the dominant source component of such volcanics was also reconciled with the mixture of DM and HIMU components. Due to the geochemical similarities between EAR/LVC and a solid-state mixture of HIMU and DM components, the EAR-type basalts can be indistinguishable from the HIMU-related volcanism. This is inferred from the early studies regarding the anorogenic volcanism of Europe and surrounding areas (e.g., Wörner et al., 1986; Blusztajn and Hart, 1989; Wilson and Downes, 1991; 1992; Wilson et al., 1995b). In these studies, the dominant enriched asthenospheric mantle component of the European anorogenic volcanics, which is now being attributed as EAR or LVC, was thought to be a mixture of DM and HIMU components.

Although the contribution of the HIMU component may not be clearly distinguished from the EAR/LVC-type common component in the genesis of the most of anorogenic volcanics of the circum-Mediterrranean region, the volcanics with typical HIMU-type characteristics (e.g., St. Helena or Mangaia) have been detected in few localities (e.g., North Africa). For instance, the radiogenic Pb isotope contents of some members of the Si-poor group anorogenic volcanics of the Oujda Volcanic Field and Plateau du Rekkam higher than those of LVC, indicate involvement of HIMU component (Duggen et al., 2005). This suggests that the HIMU component, regardless of being a mixture constituent or an individual component, is one of the major asthenospheric mantle components contributing to the circum-Mediterranean volcanism.

One of the remarkable implications from the anorogenic volcanism of the circum-Mediterranean region is that if the EAR or LVC does not represent a possible DM-HIMU mixture, then the DM component may scarcely reside in the asthenospheric mantle. However, this feature either can be related to preferentially melting of the easily fusible enriched pods (e.g., plume-related) or the upper mantle of the circum-Mediterranean region is completely enriched due to mantle dynamics (e.g., lithospheric delamination, plume activity). The widespread detection of the plume-related mantle components (e.g., EAR/LVC, HIMU, and C) in this anorogenic volcanism has been usually linked to the existence of plume activity beneath the region (e.g., Wörner et al., 1986; Stein and Hofmann, 1994; Hoernle et al., 1995; Wilson and Patterson, 2001). Nevertheless, in several locations (e.g., Bohemian Massif, Sicily Channel) in the circum-Mediterranean region, the DM component was sampled by the anorogenic mafic volcanism. For instance, the highly radiogenic Nd isotopic signatures found in the anorogenic alkaline volcanics of southwest Poland suggest the involvement of the DM in their petrogenesis (Blusztajn and Hart, 1989). Similarly, the radiogenic Pb and Nd, and unradiogenic Sr isotope characteristics of the Pantelleria basalts were interpreted as the presence of DM component in the mantle source of the Siciliy Channel (Italy) (Esperança and Crisci, 1995).

In addition to the asthenospheric mantle components defined in the circum-Mediterranean anorogenic volcanism, a large amount of isotope data have also shown that there is also an apparent contribution from enriched mantle components (EMI and EMII) to their genesis (e.g., Wörner et al., 1986; Wilson and Downes, 1991; 1992; Wilson and Bianchini, 1999; Wilson and Downes, 2006). These contributions, in general, are observable in the chemistry of the potassic lavas, which represent the lithospheric melts, and manifest themselves with a shift from the mantle plane towards the crustal lithologies in the isotope spaces. For instance, the lavas that have incorporated enriched components, in general, display a trend from the EAR/LVC field towards the BSE value in the Sr-Nd isotope space (Wilson and Downes, 1991; 1992; Wilson and Bianchini, 1999; Wilson and Downes, 2006). Similarly, in the Pb isotope spaces, their data points shift from the mantle plane towards the DUPAL fields (Wilson and Downes, 1991; 1992; Wilson and Bianchini, 1999; Wilson and Downes, 2006). Since these enriched components (EMI and EMII) are observed mostly in the lithosphere-derived potassic lavas, their origin has been chiefly attributed to the metasomatic processes rather than recycled lithologies. It has been postulated that the slab-derived fluids/melts have modified the lithospheric mantle, and interaction of the lithosphere-derived melts with the EAR/LVC-type asthenospheric melts created the whole chemical variety observed in the anorogenic volcanics of the circum-Mediterranean region (Wilson and Downes, 2006; Lustrino and Wilson, 2007). However, it is also noteworthy that the enriched end-members observed in some volcanic provinces in the circum-Mediterranean region (e.g., Sardinia, Lustrino et al., 2000) exhibit geochemical features that call for contribution from recycled crustal lithologies (EMI) rather than the recently enriched lithospheric mantle.

In summary, the general geochemical features of the primitive anorogenic volcanism of the circum-Mediterranean region provide a significant information regarding the origin of lithospheric and asthenospheric mantle sources involved in the magmatism. The geochemistry of the volcanics suggests that diverse mantle and tectonic processes have been involved during the geochemical evolution of their mantle sources, and locally, each region may have its own geodynamic history, including different proportions of mantle end-members (e.g., DM, HIMU, FOZO/C, EAR/LVC, EMI, EMII). Among these, the EAR or LVC appear to be the most dominant in the asthenospheric mantle source of the region. This probably reflects the effect of extensive dispersion of the recycled lithospheric lithologies in the convecting mantle of the region (e.g., Hoernle et al., 1995; Granet et al., 1995; Wilson and Patterson, 2001). The lithospheric mantle, on the other hand, appears to have been modified by a series of metasomatic events related to the former subduction events and/or melt diapirs from asthenospheric sources (e.g., asthenospheric and/or plume-related).

1.6 Structure of Thesis

This dissertation includes 6 chapters. Following this “INTRODUCTION” chapter, the others can be summarized as follows;

- Chapter 2 include detailed information regarding the geological features of the study area,
- Chapter 3 deals with the petrographic features of the studied rocks,
- Chapter 4 presents all geochemical results obtained during this research,
- Chapter 5 gives a detailed discussion of the data, and
- Chapter 6 presents the overall conclusions of this dissertation.

Note that the petrogenesis of the Elazığ volcanism, which is one of the primary subject this dissertation deals with, is submitted to be published in Lithos as a research article entitled “Interaction of C-like asthenospheric melts and sub-continental mantle lithosphere beneath eastern Turkey”. The co-authors of this article are; Kaan Sayit, Bradley J. Peters, Tanya Furman and Jörg Rickli.

CHAPTER 2

GEOLOGY

2.1 Regional Geology

The current geological configuration of Turkey has been shaped by the amalgamation of several microplates (Şengör and Yılmaz, 1981) or terranes (Göncüoğlu et al., 1997; Göncüoğlu, 2010; 2019) which have been driven by diachronous closure and opening of different seaways (e.g., Şengör and Yılmaz, 1981; Göncüoğlu et al., 1997; Okay and Tüysüz, 1999; Göncüoğlu, 2010; 2019; Okay and Nikishin, 2015). The last episode of these events, called the Alpide orogeny, started during the Late Mesozoic (Okay et al., 2006), and it is currently continuing in some localities (e.g., eastern Mediterranean) in the Alpine-Himalayan orogenic belt. It is characterized by relative convergence of the Africa-Arabian and Eurasian plates (Okay et al., 2006), thereby resulting in the closure of the Neotethyan oceanic branches (e.g., Şengör and Yılmaz, 1981; Göncüoğlu et al., 1997; Robertson et al., 2013; Göncüoğlu, 2019).

In eastern Turkey, the northern branch of the Neo-Tethys ocean was consumed during the Paleocene-Early Eocene (Figure 2.1a), and then the Anatolide-Tauride Block has collided with the eastern Pontides/Sakarya Composite Terrane (e.g., Şengör and Yılmaz, 1981; Keskin et al., 2008; Dilek et al., 2010; Robertson et al., 2013; Okay and Nikishin, 2015). At that time, the southern branch of the Neo-Tethys ocean was still open in the region and was continuing its northward subduction beneath Eurasia (Figure 2.1a; e.g., Şengör and Yılmaz, 1981). Later, during the Early to Middle Miocene period, the last oceanic realm between the Arabian and Eurasian plates was consumed, which is followed by the continental collision along the Bitlis-Zagros Suture Zone (Figure 2.1b) (e.g., Şengör and Yılmaz, 1981; Okay et al., 2010; Cavazza et al., 2018). After the collision of these microplates, the major landmass of

Turkey was nearly created, and a new tectonic era in the region began (e.g., Bozkurt, 2001). This new era is called the Neo-tectonic period and characterized by continental sedimentation, widespread post-collisional volcanism, and development of the major and minor strike-slip faults (Şengör and Yılmaz, 1981; Bozkurt, 2001; Okay, 2008; Göncüoğlu, 2019). In eastern Anatolia, the main volcanic began in the Neo-tectonic period with anorogenic post-collisional characteristics (e.g., Pearce et al., 1990; Keskin et al., 1998).

As mentioned above, the main landmass of Turkey is composed of several continental and oceanic entities. In eastern Anatolia (the gray shaded field in Figure 2.2), from north to south, these terranes can be classified as: (i) the Sakarya Composite Terrane (SCT) (or eastern Pontides; e.g., Ketin, 1966), (ii) the İzmir-Ankara-Erzincan Suture Belt (IAESB), (iii) the Anatolide-Tauride Block (ATB) and/or the Eastern Anatolian Accretionary Complex (EAAC), (iv) the Southeast Neo-Tethyan Suture Belt (SENSB), (v) the Bitlis-Pötürge Crystalline Complex/Massif (BPM) and the Southeast Anatolian Autochthon Units (SEAAU) (Figure 2.2, Göncüoğlu, 2010; 2019).

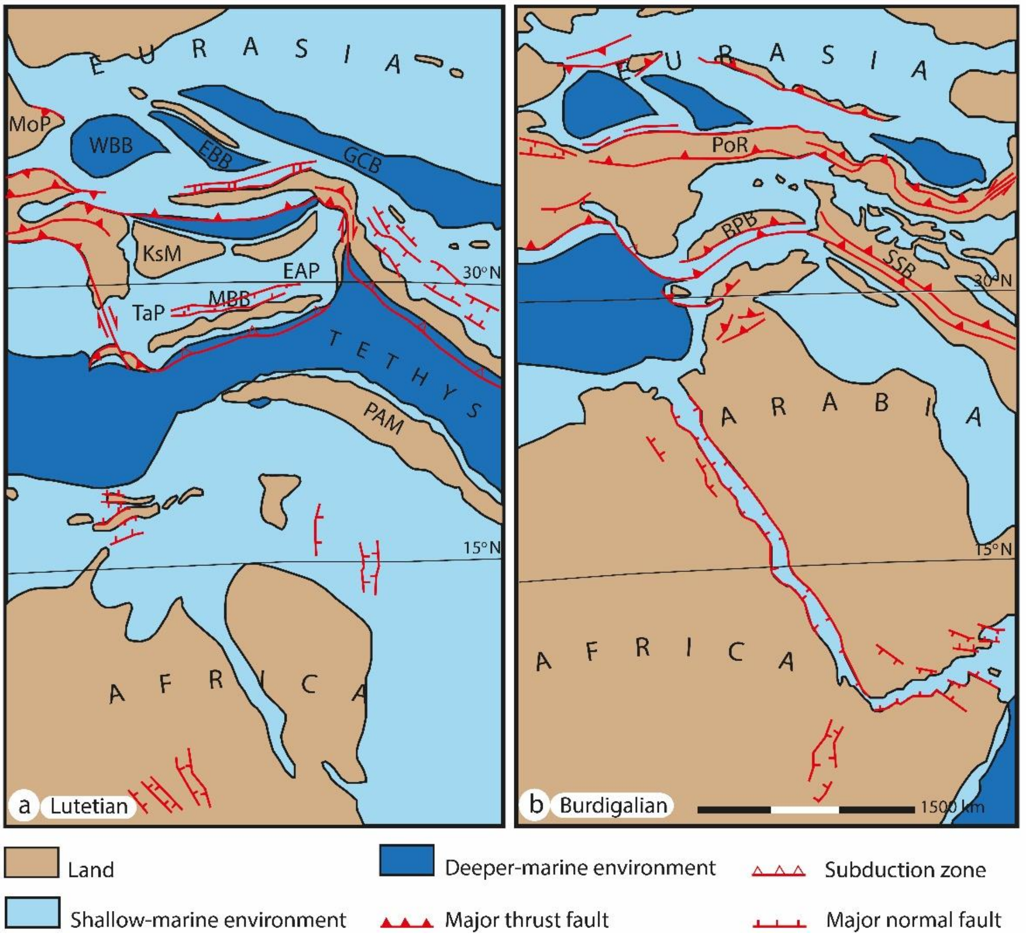

Figure 2.1. Paleogeographic illustrations showing the collision between Arabian and Eurasian plates (modified from Cavazza et al., 2018). BPB: Bitlis-Pötürge Block; EAP: Eastern Anatolian Platform; EBB: Eastern Black Sea Basin; GCB: Greater Caucasus Basin; KsM: Kırşehir Massif; MBB: Maden Back-arc Basin; MoP: Moesian Platform; PAM: peri-Arabian Massif; PoR: Pontides Ranges; SSB: Sanandaj-Sirjan Block; TaP: Tauride Platform; WBB: Western Black Sea Basin.

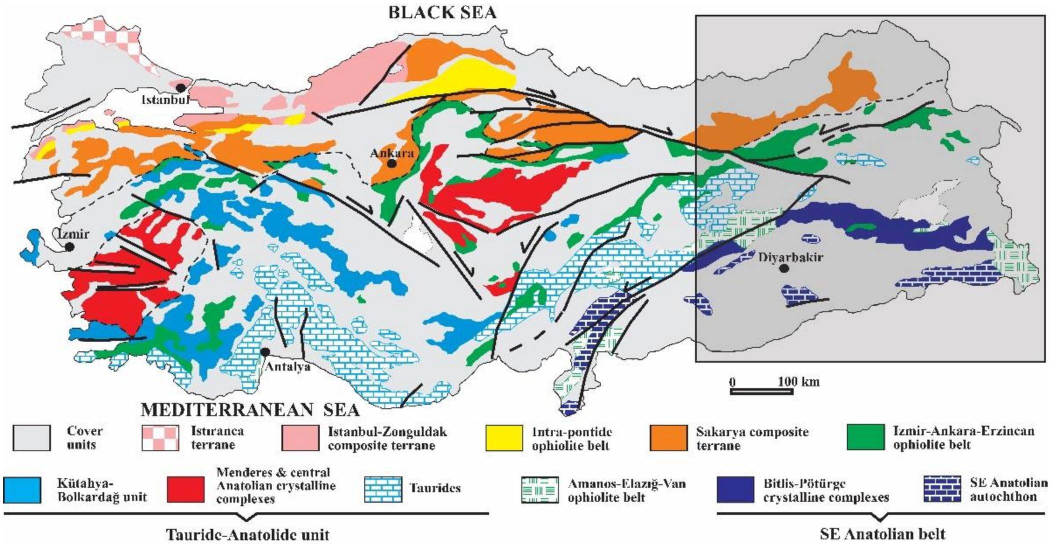

Figure 2.2. The terrane map of Turkey (Göncüoğlu, 2010; 2019).

The eastern SCT, where is also widely defined as eastern Pontides (e.g., Okay and Şahintürk, 1997), is bounded with the IAESB in the south and the eastern Black Sea Basin in the north (Figure 2.2). In the eastern SCT, it is suggested that the southern and the northern parts, which are geographically divided by the Niksar-Gümüşhane-Ardavuç line, exhibit different geological characteristics (e.g., Okay and Şahintürk, 1997). While the pre-Senonian lithologies widely outcrop in the southern part, the Senonian and younger units dominate the main geology of the northern part (Okay and Şahintürk, 1997). The basement rocks, therefore, are found mainly in the southern edge of the eastern SCT (e.g., Topuz et al., 2004). The basement rocks, in general, are composed of the pre-Liassic low-pressure-high-temperature (LP-HT) and high-pressure-low-temperature (HP-LT) metamorphic rocks, granitoids, and molassic sedimentary rocks (e.g., Şengör and Yılmaz, 1981; Okay and Leven, 1996; Okay and Şahintürk, 1997; Okay and Tüysüz, 1999; Okay and Göncüoğlu, 2004; Topuz et al., 2004; 2010; Göncüoğlu, 2010; 2019). These distinct types of basement units are in tectonic contact with each other, and nearly all of them have survived the metamorphism of the Alpine orogeny (Topuz et al., 2010). Triassic sedimentary rocks are absent in the eastern SCT, and the basement rocks are unconformably overlain by Liassic volcanic, volcanoclastic, and sedimentary rocks formed a rift environment (e.g., Görür et al., 1983; 1993; Okay and Şahintürk, 1997). In the region, these Liassic units are conformably overlain by Upper Jurassic-Lower Cretaceous carbonate rocks representing a passive continental margin (e.g., Okay and Şahintürk, 1997). The Late Cretaceous units in the eastern SCT are represented by the volcanic, volcano-sedimentary rocks, granitoids, and flysch sequences related to the northward subduction of the Neo-Tethyan oceanic lithosphere (Topuz et al., 2010). Following the continental collision between the ATB and eastern SCT along the İzmir-Ankara-Erzincan suture zone, the post-Cretaceous geology of the region has mainly been characterized by the post-collisional magmatism and shallow-water sedimentation (Okay and Şahintürk, 1997; Topuz et al., 2004; 2010).

The IAESB, which represent the remnant of the northern branch of the Neo-Tethyan ocean, consist roughly of the lithologies of the oceanic lithosphere and subduction-accretion mélanges (Göncüoğlu, 2010; 2019). The ideas on the age of these oceanic lithologies are somewhat conflicting, thereby, the age of the northern branch of Neo-Tethyan ocean (e.g., Balcı and Sayit, 2020). While some argue that the oceanization started during the Early Jurassic (e.g., Şengör and Yılmaz, 1981; Görür et al., 1983; Rojay, 2013), some others have indicated a Late Triassic or earlier opening of the İzmir-Ankara-Erzincan ocean (Tekin et al., 2002; 2016; Göncüoğlu et al., 2003; Sayit et al., 2015; 2016; 2017; Balcı and Sayit, 2020). These oceanic lithologies are thought to emplaced onto the ATB during the Late Cretaceous period (Göncüoğlu, 2010; 2019; Okay and Tüysüz, 1999). In eastern Turkey, these oceanic lithologies are composed mainly of the serpentinized peridotites, harburgites, dunites, gabbros, sheeted dykes, pillow lavas and deep-sea sediments (e.g., Çimen et al., 2016). The geochemistry of the mantle peridotites, basalts, and gabbros, suggest their formation in an arc-back-arc basin within the northern branch of the Neo-Tethyan ocean (Çimen et al., 2016; Çimen and Öztüfekçi-Önal, 2018).

The ATB, bounded with the IAESB in the north and the SENSB in the south (Figure 2.2; e.g., Göncüoğlu, 2010). It is widely accepted that the ATB represented by Paleozoic-Mesozoic Keban-Malatya Metamorphics (KMM) and a continuous

Middle Triassic-Campanian Munzur Carbonate Platform (MCP) in the western termination of the eastern Anatolia (Kipman 1976; Özgül, 1976; Özgül et al., 1981; Özgül and Turşucu, 1984, Göncüoğlu, 2010). However, there is still no consensus regarding the eastward continuation of the ATB towards the eastern termination of the eastern Anatolia (e.g., Şengör and Yılmaz, 1981; Şengör et al., 2003; Göncüoğlu, 2010; Yılmaz et al., 2010; Topuz et al., 2017). One view assumes that the easternmost edge of the ATB is represented with Munzur (MCP) and Malatya (KMM) digitations (Şengör et al., 2008), and the basement units of most of the eastern Anatolian landmass are composed of the Late Cretaceous oceanic lithologies (e.g., ophiolitic mélanges) and Paleocene to Late Oligocene flysch sequences which have been attributed as a large subduction-accretion prism (EAAC) related to the closure of the multiple branches of the Neo-Tethys ocean (e.g., Şengör and Yılmaz, 1981; Şengör et al., 2003; Keskin, 2007). In this hypothesis, there is no crustal root beneath most of the eastern Anatolia, and the EAAC is devoid of its mantle lithosphere (e.g., Şengör et al., 2003). Hence, the hot asthenospheric mantle is assumed to be in contact with the basement of the EAAC (e.g., Keskin, 2003; Şengör et al., 2003). On the other hand, the other view, suggests that the ATB continues beneath the thick EAAC towards the eastern termination of the eastern Anatolia (Figure 2.2; Göncüoğlu et al., 1997; Yılmaz et al., 2010; Çolakoğlu et al., 2014; Topuz et al., 2017), and in few localities (e.g., Akdağ Metamorphics) the lithologies of the ATB are exposed as tectonic windows (e.g., Yılmaz et al., 2010). For instance, the Akdağ Metamorphics, which consist mainly of marble, clastic and basic rocks, have been correlated with the Mesozoic stratigraphy of the ATB in the central Anatolia (e.g., Central Anatolian Crystalline Complex) based on their lithostratigraphy, age, and metamorphic conditions (Yılmaz et al., 2010; Topuz et al., 2017). Likewise, based on the lithostratigraphic characteristics and fossil contents, the clastic and carbonate rocks in the eastern of Lake Van (e.g., Hasandağ Unit) have been correlated with the non-metamorphic units of the ATB in central Anatolia (e.g., Sarız, Kayseri) and MCP (Yılmaz et al., 2010). According to this view, although the EAAC dominates the main geology of eastern Anatolia, the ATB with a thin mantle lithosphere exists beneath the EAAC as the lithospheric root of the region (Topuz et al., 2017).

The SENSB, which is also known as Amanos-Elazığ-Van Suture (Ophiolite) Belt (e.g., Göncüoğlu, 2010; Göncüoğlu, 2019), represents the lithologies of the southern branch of the Neo-Tethys ocean and separates the ATB and/or EAAC from the Southeast Anatolian Belt (the BPM and SEAAU) in the southeast Anatolia (Figure 2.2; Göncüoğlu, 2010). This belt is characterized by supra-subduction type oceanic lithosphere and consists mainly of ophiolite bodies, arc-related magmatic rocks, and lithologies related to a subduction-accretion prism (Göncüoğlu, 2019). The main lithological members of this belt are; peridotites, chromites, gabbros, basalts, plagiogranites, sheeted-dyke complexes, shales, sandstones, mudstones, pelagic limestones, and cherts (Göncüoğlu, 2019). The age determinations on the oldest radiolarian- and bivalvia-bearing cherts and pelagic limestones associated with OIB-type pillow lavas revealed that the oceanization started earlier than Middle Carnian (Uzunçimen et al., 2011; Varol et al., 2011). Likewise, the age data of the radiolarian cherts associated with arc and back-arc type basaltic rocks suggest the existence of an intra-oceanic subduction system within the southern branch of the Neo-Tethys during the Late Cretaceous (e.g., Yüksekova Complex, Perinçek, 1979; Ural et al., 2015). The oceanic lithologies of the southern branch of the Neo-Tethys are assumed to have obducted onto the Southeast Anatolian Belt also during the Late Cretaceous (Göncüoğlu, 2019).

The BPM separates the autochthon units of the Arabian Foreland (SEAAU) from the units of the ATB and/or EAAC in eastern Anatolia (Figure 2.2). With its Precambrian to Triassic lithostratigraphy, this massif occupies a region approximately 300 km long and 40 km wide and is composed mainly of allochthonous metamorphic rocks (Okay et al., 1985). These metamorphics tectonically overlie an intervening tectonic zone consisting of ophiolites, Tertiary rock series, and sediments of the autochthone Arabian foreland (Hall, 1976; Okay et al., 1985; Oberhänsli et al., 2010). According to Göncüoğlu and Turhan (1984), the basement of the BPM is composed mainly of the pre- to infra-Cambrian gneisses, amphibolites, eclogites, and schists, which are unconformably overlain by the Paleozoic metaclastics, schists, metacarbonates, metavolcanics and metagranites (Göncüoğlu and Turhan, 1984; Oberhänsli et al., 2010). The Triassic units of the BPM starts with recrystallized limestones, calc-schists and slates grade upward into meta-volcanics and –volcanoclastic rocks (Göncüoğlu and Turhan, 1984; Oberhänsli et al., 2010). These Triassic volcanic rocks are assumed to be related to the opening of the southern branch of Neo-Tethys (Göncüoğlu and Turhan, 1984; Göncüoğlu, 2010; 2019). The ideas about the origin of the BPM are contradictory. While some studies (e.g., Göncüoğlu and Turhan, 1984; Oberhänsli et al., 2010; Göncüoğlu, 2019) correlated its lithostratigraphy and its metamorphic conditions with the Arabian platform, some others (e.g., Çetinkaplan et al., 2016) linked its origin to the ATB. Göncüoğlu (2019) suggests that the BPM represented the northernmost edge of the Arabian platform, which was metamorphosed during the closure of the southern branch of the Neo-Tethys.

The SEAAU, which is also known as the Arabian platform, constitutes the southernmost part of eastern Anatolia (Figure 2.2). The basement of this platform is composed of Pan-African Late-Neoproterozoic volcanic and volcanoclastic rocks, and they are transgressively overlain by Lower to Middle Paleozoic siliciclastic rocks (Gürsu et al., 2015, Göncüoğlu, 2019). These units are unconformably overlain by Late Permian shelf-type limestones, which are transitional to Triassic-Early Cretaceous shallow marine sediments (Göncüoğlu, 2019). While the Late Permian unconformity has been interpreted as the manifestation of the opening of the southern branch of the Neo-Tethys ocean or Bitlis-Zagros Ocean (Şengör and Yılmaz, 1981; Altıner, 1989; Göncüoğlu, 2010; 2019), the Triassic-Early Cretaceous marine sediments have been linked to stabilization of the platform conditions in the north of Gondwana (Perinçek, 1990; Perinçek et al., 1991; Göncüoğlu, 2010; 2019). The Late Cretaceous period is mainly characterized by the foreland-type sediment deposition and emplacement of the ophiolites, ophiolitic mélanges and thrust sheets on the northern margin of the SEAAU (Perinçek, 1990; Perinçek et al., 1991; Okay, 2008; Göncüoğlu, 2010; 2019). These allochthonous units are covered by Tertiary sediments, which are tectonically overlain by BPM and underlying mélange units (Perinçek, 1990; Perinçek et al., 1991). The second cycle of the emplacement of the allochthonous units (e.g., BPM) onto the northern margin of the platform is assumed to have occurred during the Miocene period related to the collision of the Arabian and Eurasian continents (e.g., Okay et al., 2010; Göncüoğlu, 2010; 2019; Oberhänsli et al., 2010; 2012).

2.2 Local Geology

This study was conducted in two main areas; the Tunceli region and the Elazığ region. The Tunceli region comprises the Miocene volcanics, which are assumed to be of dominantly lithospheric mantle origin (e.g., Aktağ et al., 2019), whereas the Elazığ region contains the Quaternary volcanics representing the asthenosphere-derived melts (e.g., Di Giuseppe et al., 2017) (Figure 1.4). These two regions share some geological similarities due to their spatial proximity (Figure 1.5). However, since each region has its own lithostratigraphic features, they have been evaluated separately in this section. It is also important to note that, although the Tunceli region was revisited in this research, the samples from this area come from Aktağ (2014).

2.2.1 Tunceli Region

The lithological units of the Tunceli region, from oldest to youngest, are the Permo-Cretaceous Keban Metamorphics, the Bartonian-Early Chattian Kırkgeçit Formation, the Late Miocene Çaybağı Formation, the Late Miocene Tunceli Volcanics, and the Quaternary alluviums (Figure 2.3 and Figure 2.4, Aktağ, 2014, Aktağ et al., 2019).

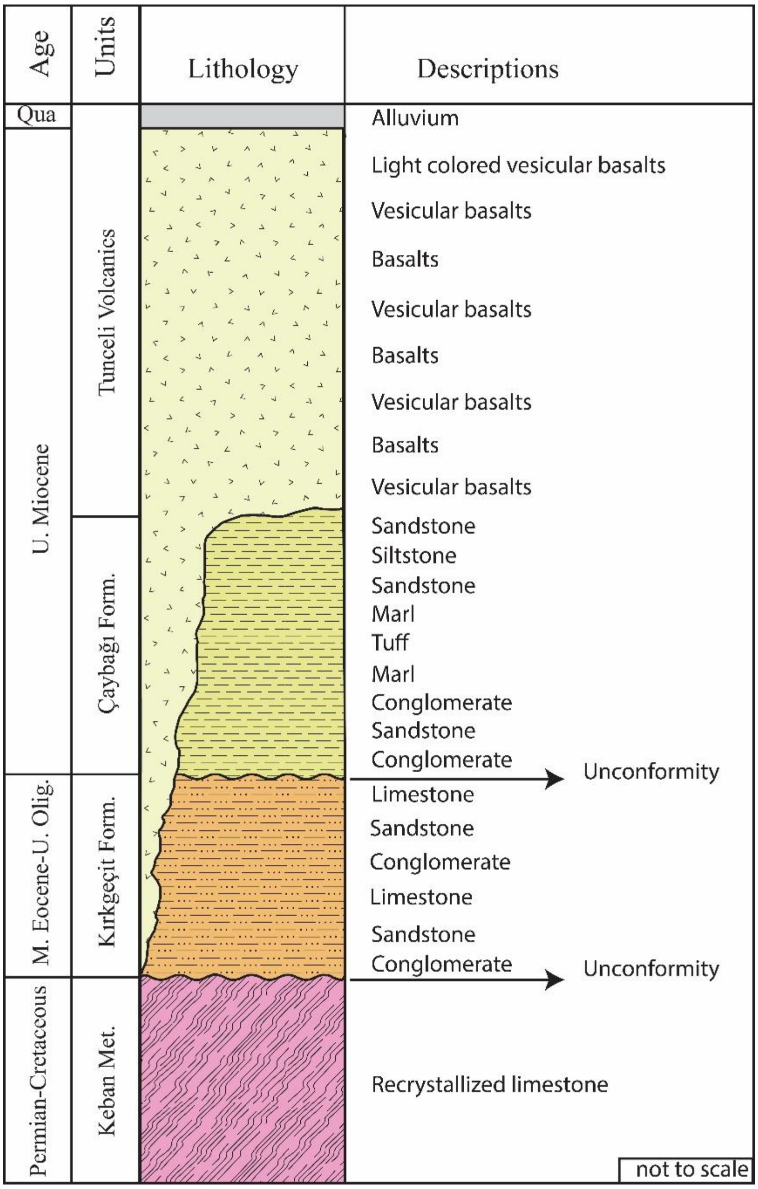

Figure 2.3. The generalized stratigraphic section of the Tunceli region (modified from Aktağ, 2014).

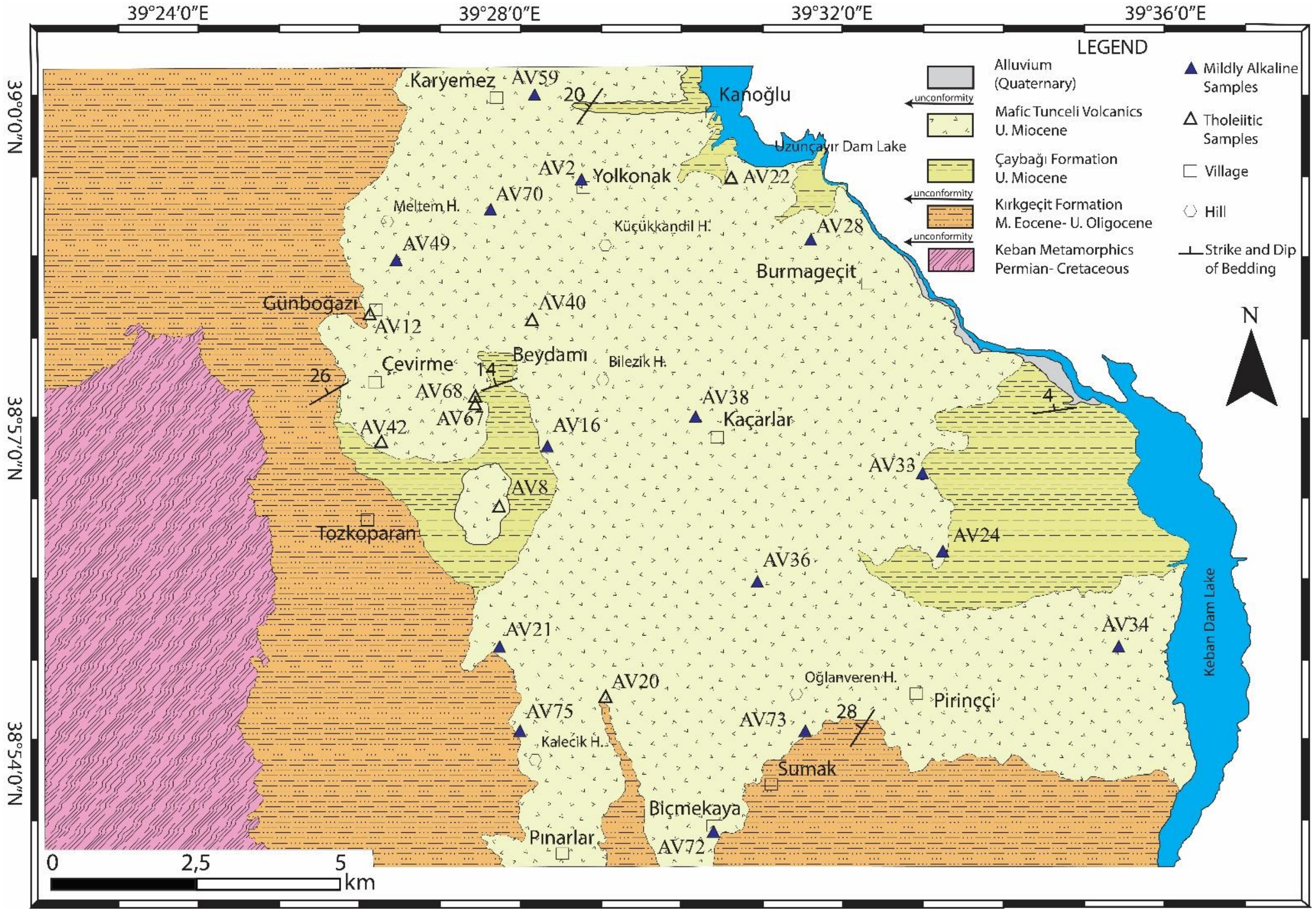

Figure 2.4. The geological map of the Tunceli region (from Aktağ, 2014, Aktağ et al., 2019).

The Permian-Cretaceous Keban Metamorphics was firstly described in the late 70s around the Elazığ and Tunceli provinces (e.g., Kipman, 1976; Özgül, 1976; Perinçek, 1979). This unit mainly crops out as the basement rock units in these areas, and they are primarily characterized by metapelitic and metacarbonate rocks with subordinate amphibolite schists (e.g., Özgül and Turşucu, 1984; Asutay et al., 1986; Bozkaya et al., 2007). The lithostratigraphic section of the Keban Metamorphics has been subdivided into four members; the lower schists (or lower metapelite), the lower marble (or lower metacarbonate), the upper schists (or upper metapelite), and upper marble (or upper metacarbonate) (Asutay et al., 1986; Bozkaya et al., 2007). While the lower metapelite member consists mainly of phyllites and marbles, the upper metapelite member is principally composed of metaconglomerates, phyllites, recrystallized limestones, metamarls, and slates (Bozkaya et al., 2007). The metacarbonate members (lower unit and upper unit), on the other hand, are characterized mainly by recrystallized limestones (Bozkaya et al., 2007). The lower metacarbonate member can be distinguished from the upper member by the presence of the pinkish recrystallized dolomites in its lowest levels. In addition, in the upper metacarbonate level, the metamarls alternate with the recrystallized limestones. Apart from all these, the amphibolites with schistose texture were also reported within the Keban Metamorphics (e.g., Kürüm, 1994; Herece, 2016b; Herece and Acar, 2016). The age of these metamorphic units is unclear. The ages ranging from Permian to Cretaceous were assigned based on the fossil contents found in the different levels of the unit (Herece and Acar, 2016). For instance, while a Permian-Triassic age was assigned based on the fossil contents from the lower levels of the unit (Özgül, 1976), a Campanian age was ascribed to the marbles overlying the upper metapelites (Yılmaz et al., 1993; Herece and Acar, 2016). These low-grade metamorphic units are thought to represent the active southern margin of the ATB which was metamorphosed during the northward subduction of the southern branch of the Neo-Tethys ocean (Göncüoğlu, 2010; 2019).

The Keban Metamorphics outcrop in the Tunceli region as basement rocks (Figure 2.3), and they are mainly characterized by light (cream/beige) colored, and thin- to medium-bedded recrystallized limestones (Figure 2.5a-b). The bedding is well observed in the northwest of the study area. No foliation planes have been observed on the limestones, but they appear to be highly fractured (Figure 2.5b). Kürüm (1994) reported that calcite grains in the recrystallized limestones found near the Çemişgezek district (southwestern Tunceli) are variable in size and show polysynthetic twinning. Additionally, rare quartz and chlorite occurrences were also reported in these limestones (Kürüm, 1994).

Although there is no field evidence regarding the marl alternation along the metacarbonate succession (Bozkaya et al., 2007), the unit may be correlated with the uppermost metacarbonate member of the Keban Metamorphics due to the light-colored appearance of the limestones and absence of the metaconglomerates layer on the top of the unit. The Keban Metamorphics are unconformably overlain by the clastics of the Kırkgeçit Formation in the westernmost edge of the study area (Figure 2.4 and Figure 2.6). No contact relationship has been observed with the Tunceli Volcanics.

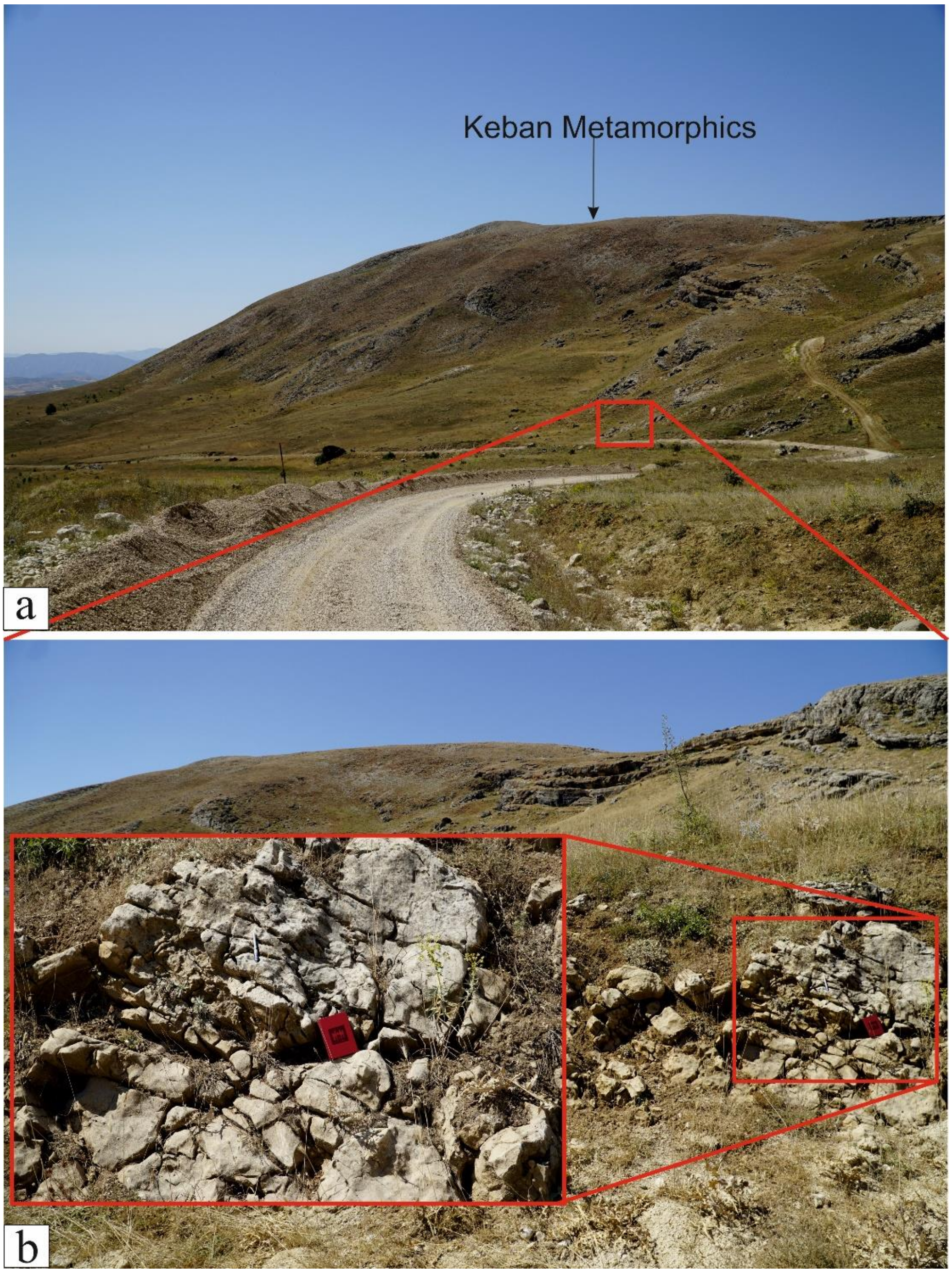

Figure 2.5. (a) A general field and (b) close-up view of the cream-colored recrystallized limestones of the Keban Metamorphics from the northwest of the Çevirme village (view to south).

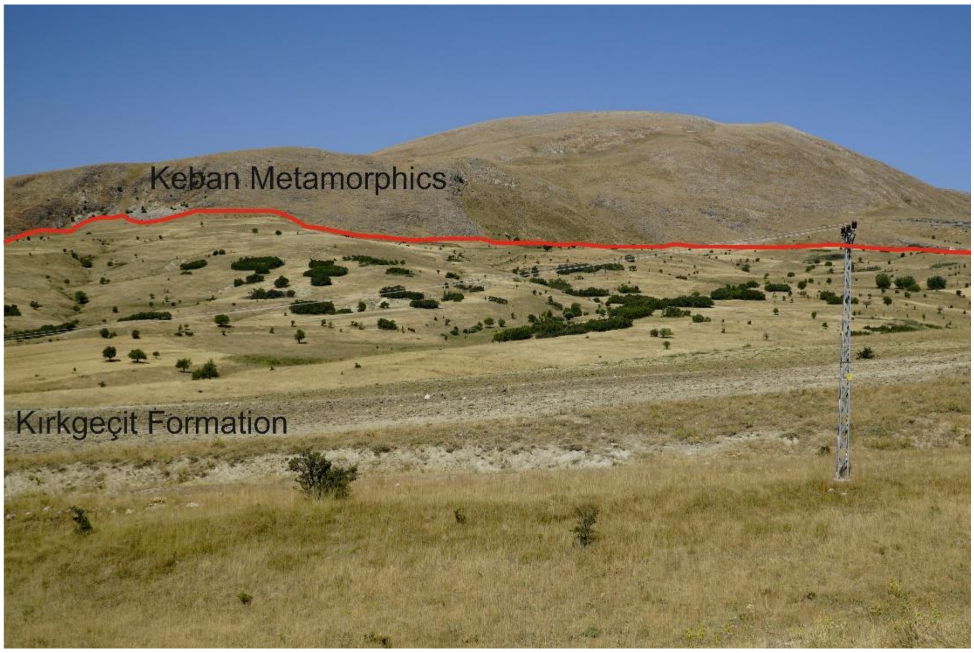

Figure 2.6. Contact relationship between the Keban Metamorphics and Kırkgeçit Formation from the south of the Çevirme village (view to west).

The Middle Eocene-Late Oligocene Kırkgeçit Formation was firstly described by Perinçek (1979) within the Kırkgeçit village, in the south of the Van city, where its typical stratigraphic section can be recognized. Later, it was revealed by many studies that this formation, which composed of the alternation of the conglomerate, sandstone, siltstone, shale, marl, sandy-limestone, limestone (Perinçek, 1979), crops out in a wide area extending from Van city to the Elazığ-Malatya region (e.g., Asutay et al., 1986; Herece et al., 1992; Herece, 2016b; Herece and Acar, 2016, Özcan et al., 2019). The formation has been subdivided into four members in the west of the Elazığ city, where the most extensive outcrop can be recognized (Özkul, 1988; Özcan et al., 2019). These members are (from bottom to top): (i) Marik Member, (ii) Seher Dağı Member, (iii) Keklik Tepe Member, and (iv) Gökbelen Member (Özkul, 1988). The Marik Member represents the lowermost member of the Kırkgeçit Formation, and was initially introduced by Asutay (1985) in the western Baskil (Elazığ). The Marik Member, composed mainly of basal conglomerates involving clasts with different origins and sizes (Asutay, 1985; Özkul, 1988; Herece and Acar, 2016; Özcan et al., 2019). The massive sandstones, which are laterally and vertically transitional with the conglomerates, were also reported within the Marik Member (İnceöz, 1994). The clasts of the conglomerates are thought to have been derived from Cretaceous and pre-Cretaceous units of the region (İnceöz, 1994; Herece and Acar, 2016). The Seher Dağı Member, which overlies the basal conglomerates, is mainly characterized by conglomerates, sandstone, mudstone, and marl alternations (e.g., Asutay, 1985; Özkul, 1988). Asutay (1985) described this unit as a flyschoidal sequence, representing the slope-channel deposition (Özkul, 1988; Özcan et al., 2019). This sequence laterally grades into the units of the Keklik Tepe Member, which is composed of bioclastic limestone involving pelagic fauna and flora (Özcan et al., 2019). The Gökbelen Member overlies the Keklik Tepe Member and chiefly consists of thick-bedded to massive shallow-marine limestones, representing the uppermost units of the sequence (Özcan et al., 2019).

The age findings on the Kırkgeçit Formation are diverse since different sections have been examined in different locations in eastern Anatolia (e.g., Perinçek, 1979; Asutay, 1985; Özkul, 1988; Turan et al., 1995). However, the Middle Eocene-Late Oligocene is the most common age range for the Kırkgeçit Formation (e.g., Özkul, 1988, Herece and Acar, 2016). Recently, based on benthic and planktonic foraminifera found in the units of Kırkgeçit Formation around the Tunceli-Elazığ regions, a Bartonian-Early Chattian age was assigned by Herece and Acar (2016). It is assumed that the lithologies of the Kırkgeçit Formation were deposited in the fore reef and open shelf environments (Herece and Acar, 2016).

The Kırkgeçit Formation is characterized by conglomerates, sandstones, and limestones in the Tunceli region and crops out mainly in the western and southern parts of the study area (Figure 2.4; Aktağ, 2014). The Kırkgeçit Formation in the region does not show lateral continuity, which may indicate the changes in the laterally depositional conditions. However, in some localities, especially within the valleys found in the south of the study area (between the Pınarlar and Biçmekaya villages), it is possible to observe its regular vertical sequences (Figure 2.7). The horizontally bedded sedimentary sequence of the Kırkgeçit Formation starts with a thin-bedded sandstone-conglomerate-limestone alternation at the bottom and ends with a relatively thick-bedded beige-cream colored limestone layer at the top (Figure 2.7).

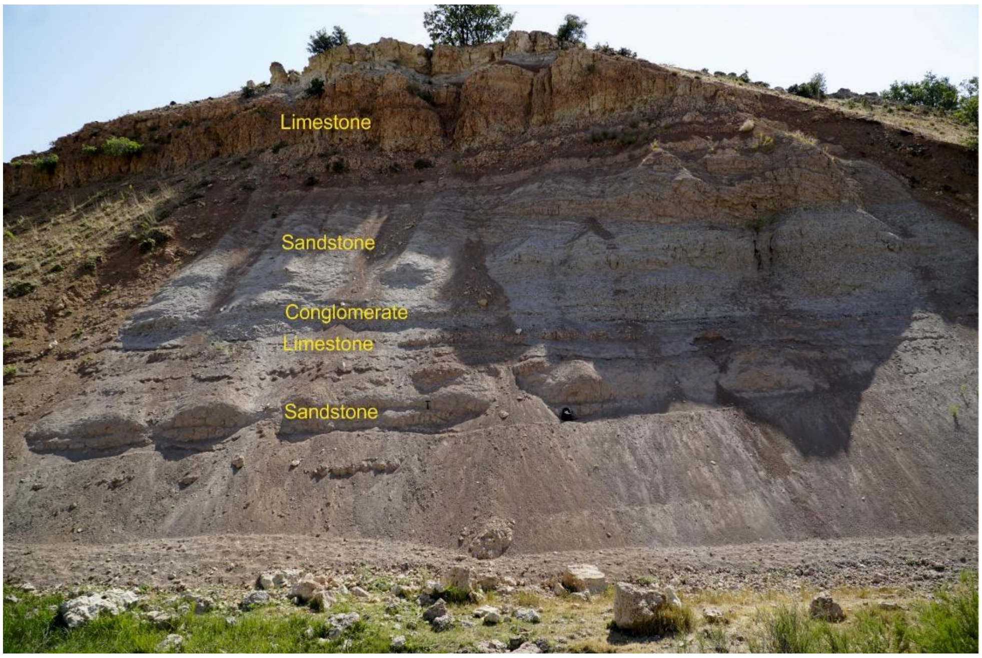

Figure 2.7. Regular section of the Kırkgeçit Formation in the Tunceli region near Pınarlar village (view to east).

The thickness of each unit rarely exceeds 4 m along the sedimentary succession. The sandstones are usually thin-bedded (10 cm to 1 m) and are beige in color (Figure 2.7 and Figure 2.8). They are usually well-sorted and well-rounded, and include mainly quartz and rock fragments. The conglomeratic levels contain intercalations of pebbly sandstones, and their thickness usually does not exceed 4 m in the field (Figure 2.7). They are in light greenish color, poorly-sorted, and consist mainly of well-rounded rock and minerals fragments within a sand-size matrix (Figure 2.9). Limestones are usually cream in color, although they vary from beige to pink in places (Figure 2.7). They have bioclastic depositional texture, and the bioclasts mainly include corals and bivalve fragments with subordinate some algae and sponges (Figure 2.10;

personal communication with S.G. Atasoy, August, 2021). Thin-bedded pinkish carbonate layers can be found as interlayers between sandstones and conglomerates (Figure 2.7).

Figure 2.8. Beige sandstones of the Kırkgeçit Formation in the Tunceli region near Pınarlar village (view to east).

Figure 2.9. Pebbly sandstone and conglomerate alternation of the Kırkgeçit Formation in the Tunceli region near Pınarlar village (view to east).

Figure 2.10. Bioclastic limestone of the Kırkgeçit Formation in the Tunceli region near Pınarlar village (view to east).

However, the limestones usually constitute the top unit of the sequence. The thickness of the limestone layers varies from 2 m to 6 m at some localities within the valleys in the south of the study area (Figure 2.7). Since this sedimentary succession of the Kırkgeçit Formation in the Tunceli region do not contain the thick-bedded limestone and is mainly composed of clastic sedimentary rock alternations with thin-bedded limestone, it may be correlated with the Seher Dağı and Keklik Tepe Members of the Kırkgeçit Formation. However, the pelagic fauna and flora of the limestones in the Tunceli region should be approved to make a robust correlation with these members.

While the unit of Kırkgeçit Formation unconformably overlies the Keban Metamorphics, it is unconformably overlain by the Late Miocene Çaybağı Formation and Tunceli Volcanics (Figure 2.3). The contact relationship between the Kırkgeçit Formation and Tunceli Volcanics can be clearly seen in the south of the study area, near the Pınarlar village (Figure 2.11 and Figure 2.12). In these locations, the limestones represent the uppermost unit of the Kırkgeçit Formation covered by the lava flows of the Tunceli Volcanism.

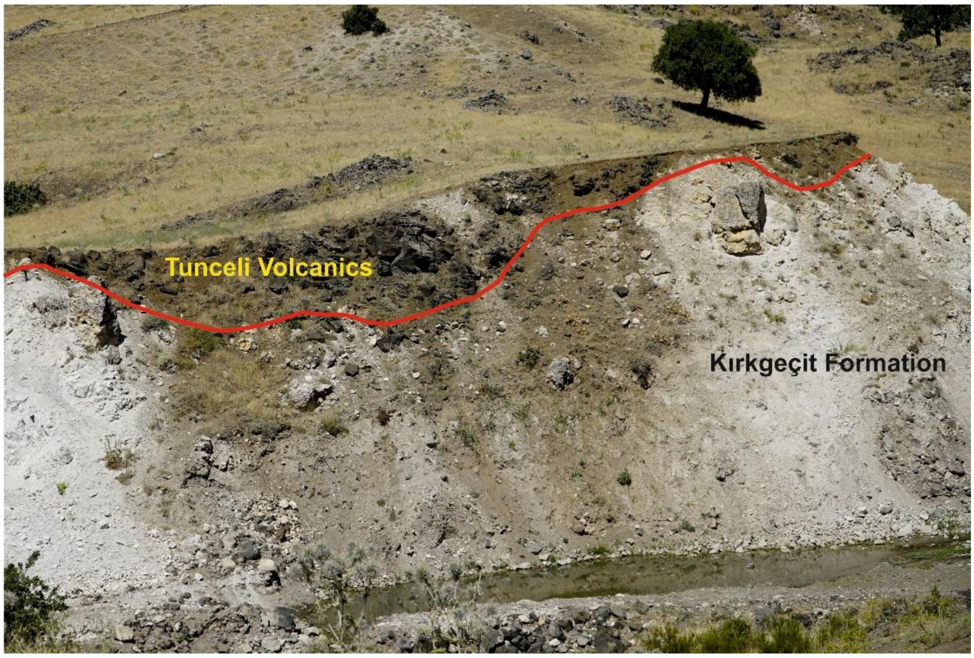

Figure 2.11. Contact relationship between the Kırkgeçit Formation and Tunceli Vocanics near the Pınarlar village (view to north).

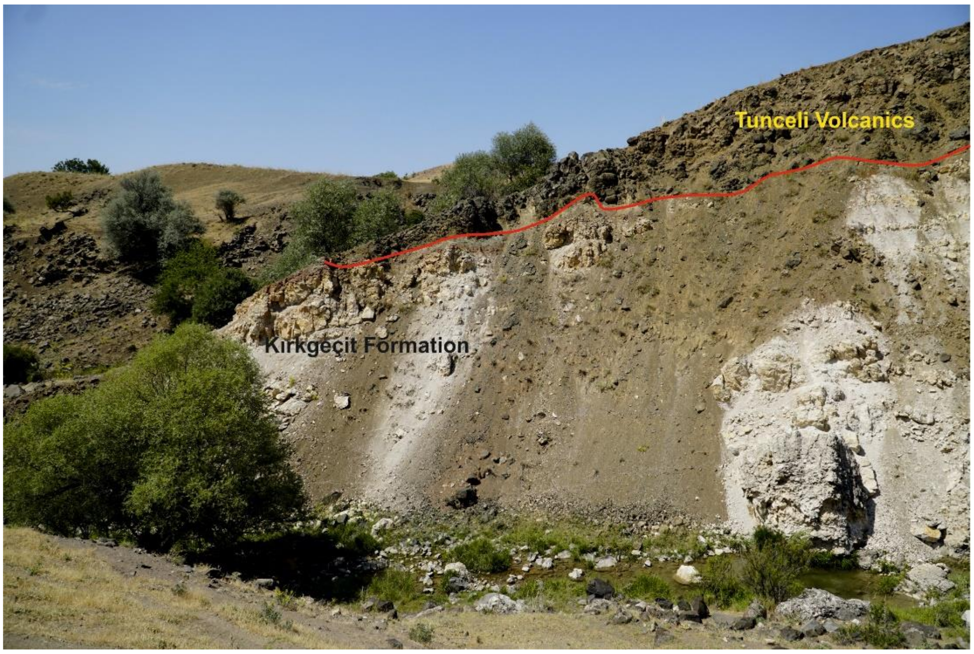

Figure 2.12. Contact relationship between the Kırkgeçit Formation and Tunceli Vocanics near the Pınarlar village (view to north).

The Late Miocene Çaybağı Formation, which crops out mostly in the middle to the western sectors of the study area (Figure 2.4), was originally identified by Türkmen (1991) near the Çaybağı village (Elazığ). In its type locality in the southeast Çaybağı village, the thickness of the Çaybağı Formation reaches up to 700 m, and consist of conglomerate, sandstone, mudstone, marl, claystone interbedded with coal, tuffite, and limestone (Türkmen, 1991). Conglomerates are mostly well-rounded and well-sorted, and composed mainly of volcanic and limestone fragments, which are thought to be mostly derived from the Yüksekova Complex and Kırkgeçit Formation (Türkmen, 1991). Sandstones, on the other hand, occur as light-colored, poorly cemented lithologies containing randomly distributed coarse gravels (Türkmen, 1991). Mudstones are generally reddish and contain coal veins (Türkmen, 1991). The main coal layers are regarded to be interbedded with the claystones containing well-preserved trace fossils of leaves (Türkmen, 1991). Marls within the section, on the other hand, occur as massive layers showing lamination at some places (Türkmen, 1991). Türkmen (1991) also states that the tuffite layers are most apparent at the upper levels of the section and contain fossil, coal, and pyroclastic rock fragments. Limestones, which constitute the uppermost layer of the Çaybağı Formation are characterized as micrites containing scarce fossil contents (Türkmen, 1991).

Around the Çaybağı village, the Çaybağı Formation overlies the Middle Eocene-Late Oligocene Kırkgeçit Formation and Late Cretaceous Yüksekova Complex, and it is unconformably overlain by the Lower Pleistocene Palu Formation (Türkmen, 1991). No suitable fossil assemblages have been found to date the Çaybağı Formation; therefore, its age has been assigned based on the regional correlation. The tuffites found in the upper layers of the section are correlated with the tuff layers of the Pliocene Karabakır Formation in the region (Türkmen, 1991). Since the volcanism is thought to be scarce in the Lower Miocene, a Middle Miocene-Pliocene? age has been assigned to the Formation (Türkmen, 1991). However, in the Tunceli region, the Çaybağı Formation is overlain by the Late Miocene Tunceli Volcanics. This puts an upper age limits of the Çaybağı Formation, and a Late Miocene age is therefore accepted in this study.

The Çaybağı Formation crops out mainly in the east and middle parts of the study area in Tunceli region (Figure 2.4) and is represented by the conglomerate, sandstone, siltstone, marl, and tuff alternation (Figure 2.3). The total thickness of the formation reaches up to 200 m between the Uzunçayır Dam Lake and Karyemez village. Conglomerates can be well observed in the southeast of the Kaçarlar village. Here conglomerates display weakly consolidated crude parallel stratification with the fine-grained sandstones (Figure 2.13). Conglomerates are usually thin-bedded, poorly-sorted, and clast-supported (Figure 2.13).

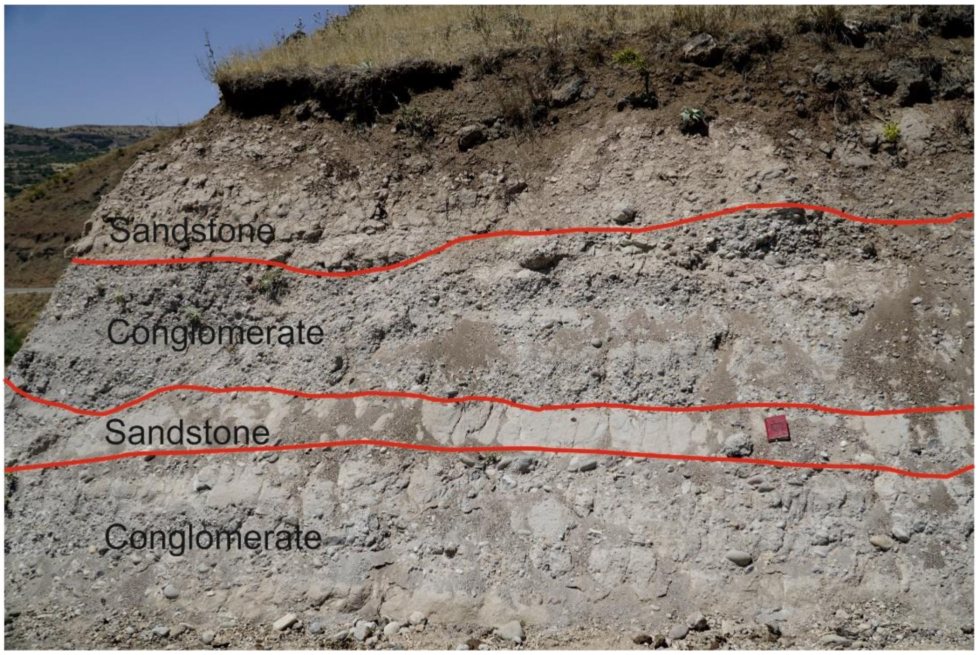

Figure 2.13. Conglomerate-sandstone alternation within the Çaybağı Formation in the southeast of Kaçarlar village (view to west).

Sandstones are usually gray and occasionally white-cream to beige in color. They are usually well-sorted and matrix-supported. Their poorly-sorted, pebble-rich thin beds rarely occur in places, where commonly display alternation with the conglomerates. The clasts are mainly characterized by quartz and feldspar crystals, and rarely by mafic minerals such as amphibole and biotite. Parallel beds of the sandstones with occasional lamination can be seen in the Beydamı village and in the east of the Karyemez village. The sandstone, siltstone, marl and tuff alternation of the Çaybağı Formation can be well observed between the Uzunçayır Dam Lake and Karyemez village, where the thickest succession of the Çaybağı Formation is present (Figure 2.14). Siltstones exhibit colors ranging from light cream to beige, and they are usually very well-sorted. They display thin- to medium- parallel bedding with the sandstones (Figure 2.14).

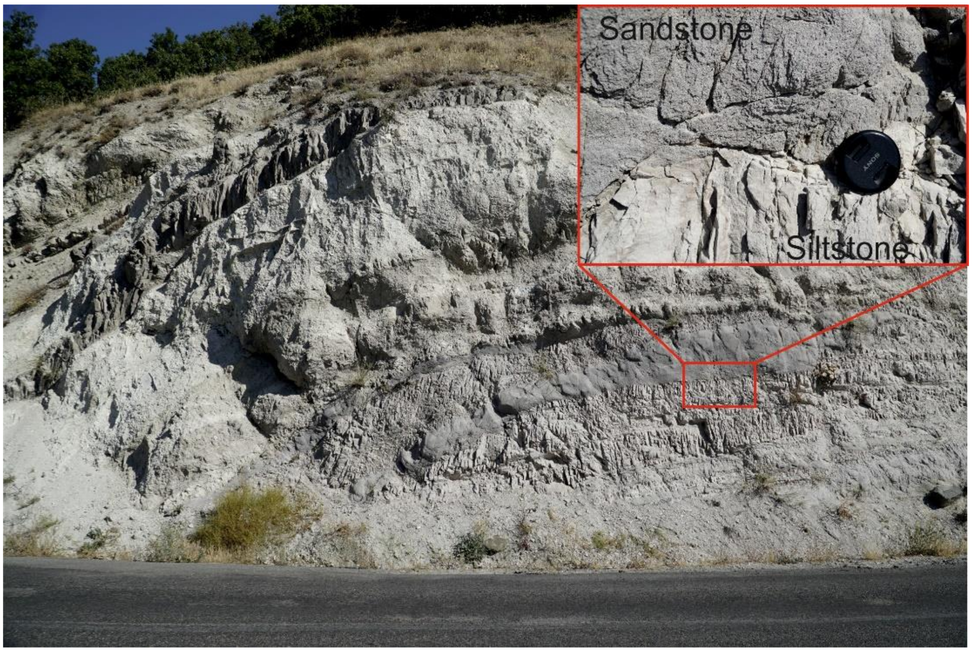

Figure 2.14. Sandstone-siltstone alternation within the Çaybağı Formation in the east of Karyemez village (view to north).

Marls especially crop out between the middle and upper parts of the succession and contain intercalations of tuff beds (Figure 2.15). They are characterized by grayish-greenish colors and thin- to medium-bedded. Tuffs are usually thin-bedded and well-consolidated with fine ash material (Figure 2.15). White-colored angular lapilli-sized pyroclastic fragments constitute the lithic fragments within the tuff units (Figure 2.15). Lithic texture is the main texture of the tuff units. Aktağ (2014) reported that the tuffs within the Çaybağı Formation in the Tunceli region are in andesitic composition, and the main mineralogy is composed of plagioclase, amphibole, and biotite. Additionally, they were proposed to be exhibit typical geochemical features of arc-related volcanism (Aktağ, 2014). The tuff layers in the Tunceli region may be correlated with the upper levels of the Çaybağı Formation.

The Çaybağı Formation is unconformably overlain by the Late Miocene Tunceli Volcanics in the middle parts and along the eastern part of the study area (Figure 2.16). The lava flows are usually in contact with the sandstones of the Çaybağı Formation, and occasionally a thin baked-zone occurs on clastics of the latter unit in the region.

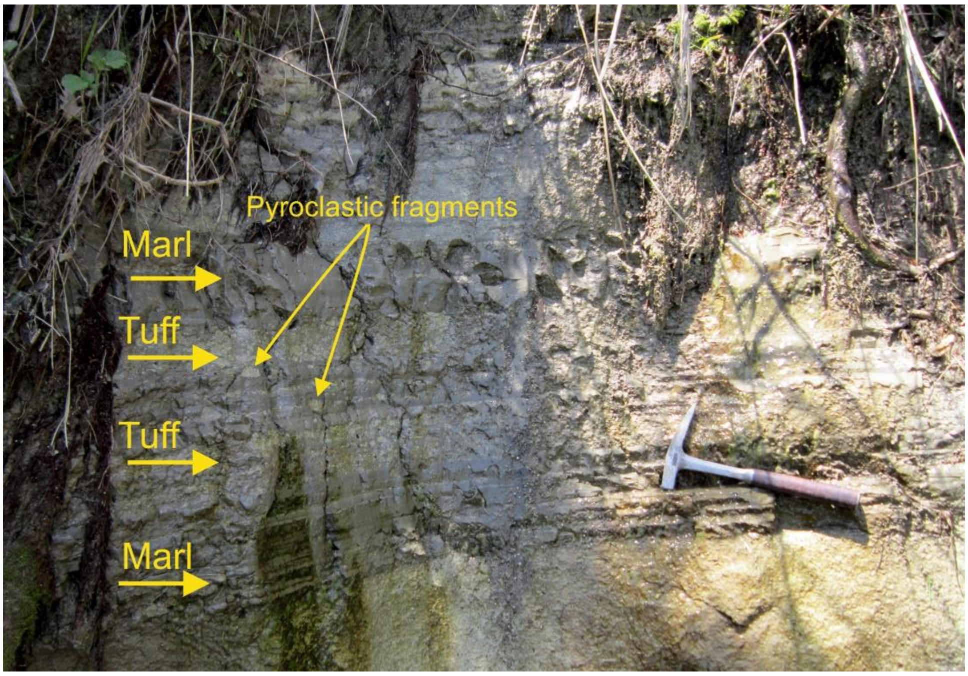

Figure 2.15. Marl-tuff intercalations within the Çaybağı Formation in the east of Karyemez village (view to north).

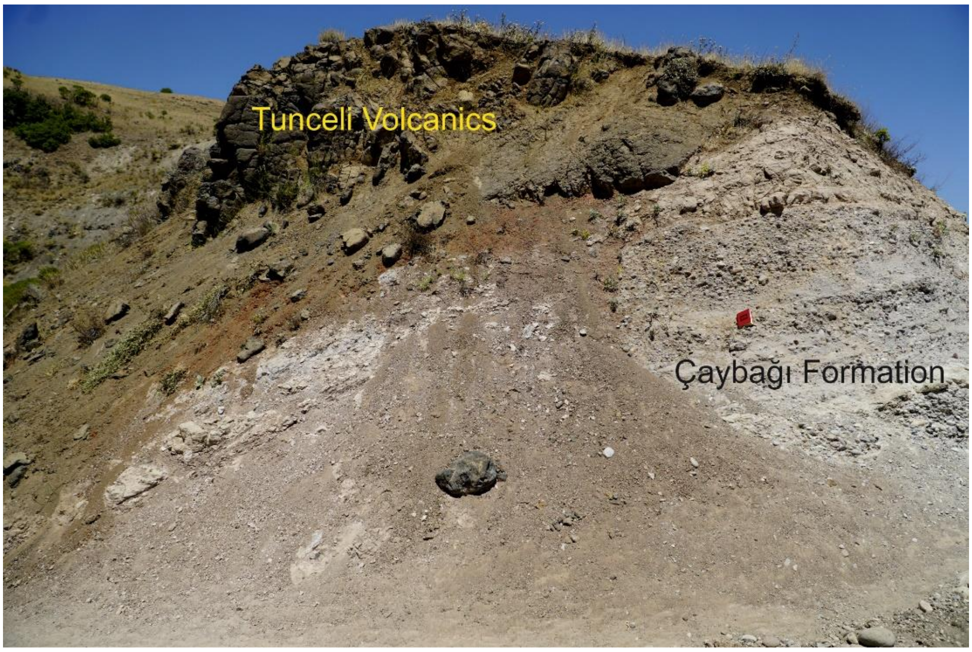

Figure 2.16. Contact relationship between Çaybağı Formation and Tunceli Volcanics in the southeast of Kaçarlar village (view to northwest).

The Late Miocene Tunceli Volcanics cover an area of approximately 100 km^2 with a maximum thickness of 100 m in the study area. The most extensive geological and petrological studies on this volcanicity have been carried out during recent years (e.g., Aktağ, 2014; Di Giuseppe et al., 2017; Aktağ et al., 2019; Agostini et al., 2019). A Late Miocene age, based on Ar-Ar radiometric dating method, was assigned to these volcanics by Di Giuseppe et al. (2017). Apart from the Early-Middle Miocene volcanism in the Tunceli region (e.g., Mazgirt Volcanics), which are mainly intermediate in composition, the Late Miocene Tunceli Volcanics are represented by mafic lava flows (Aktağ, 2014; Di Giuseppe et al., 2017; Aktağ et al., 2019). The Tunceli Volcanics overlie the thick-bedded agglomerates of the Early-Middle Miocene Mazgirt Volcanics near the Burmageçit village (Aktağ, 2014), and represent the youngest volcanic products in the study area. The mafic Tunceli Volcanics have been divided into three members according to their textures and field appearances; the dark-colored vesicular basaltic flows, massive flows and light-colored vesicular basaltic flows containing iddingsitized olivines (Aktağ, 2014).

While the relatively dark-colored lava layers represent the lower and middle parts of the volcanic sequence, the light-colored layers constitute the upper levels. (Aktağ, 2014; Aktağ et al., 2019).

The Tunceli volcanism occupies the field with successive pulses of lava flows, and created a small-scale plateau in the region. Considering the absence of pyroclastic deposits related to the Late Miocene volcanism in the region, it can be suggested that the Late Miocene Tunceli lavas were emplaced on the region by Hawaiian-type or fissure-type eruptions. Based on the topography, these eruptions appear to have been emitted from the monogenetic volcanic center(s) near the Beydamı village (Figure 2.17), as is also proposed by Aktağ (2014). The volcanic center near the Beydamı village has an ellipsoidal caldera-like morphology with a 1.70 x 2.20 km diameter (Figure 2.17). Although the western and eastern walls of this volcanic center appear to be failed, the eastern, northern, and southern walls are well preserved (Figure 2.17). The height of the inner wall of the volcanic center reaches up to 27 m, 33 m, and 10 m in the north, south, and east, respectively (e.g., Figure 2.18). A small dome-like morphology appears at the center of the volcanic center (Figure 2.17). When both current topography and the direction of the lava flows are taken into consideration, the volcanic center in the Beydamı village and Meltem Hill may represent the eruption centers for the Late Miocene Tunceli Volcanism.

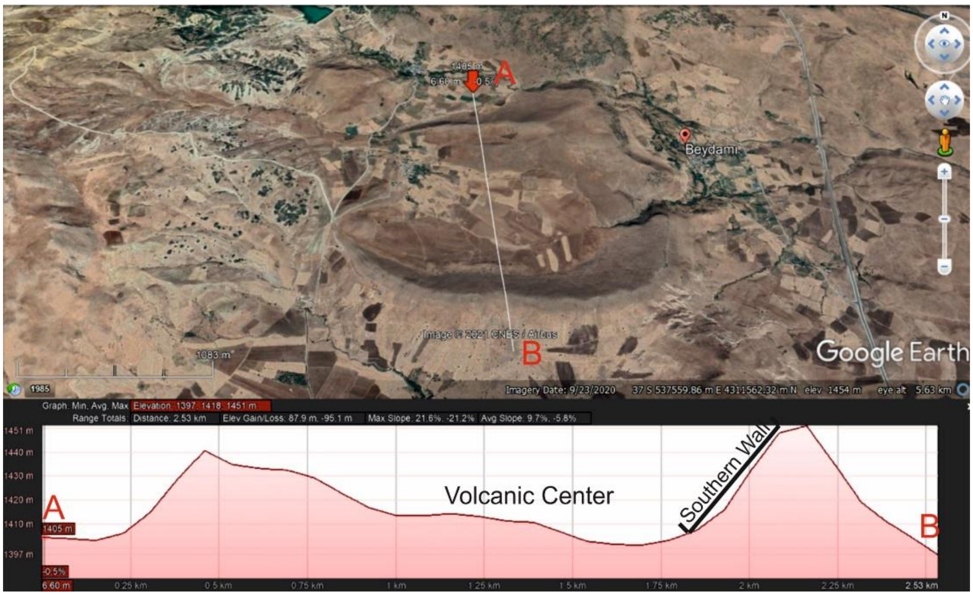

Figure 2.17. Google Earth view of the volcanic center near Beydamı village.

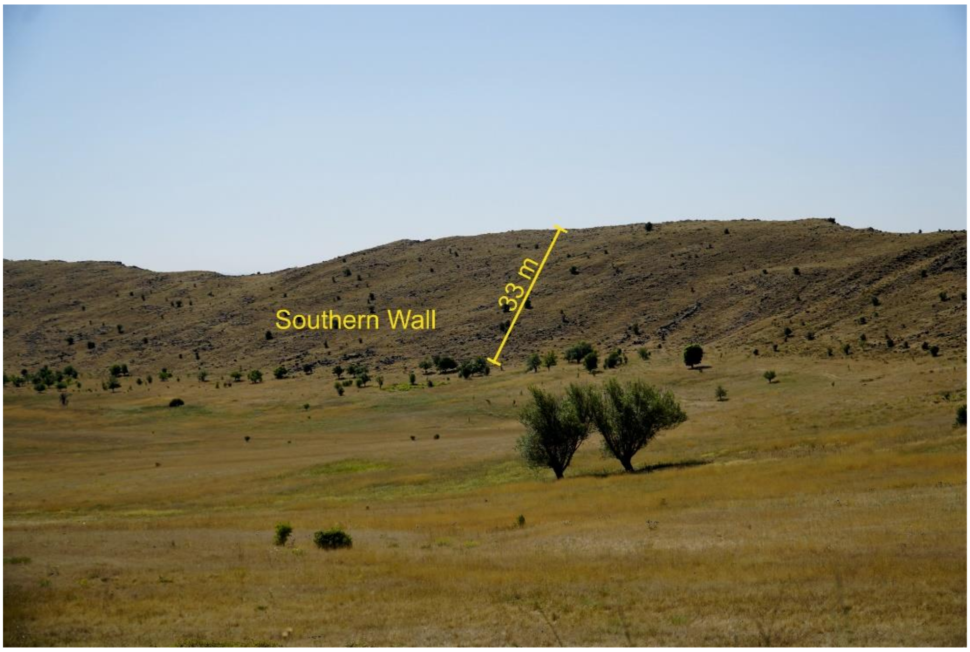

Figure 2.18. Field view of the southern inner wall of the volcanic center near the Beydamı village (view to southeast).

As mentioned in the previous studies (e.g., Aktağ, 2014; Aktağ et al., 2019), the Late Miocene Tunceli Volcanics occur in the region as a succession of diverse pulses of lava flows. Although the thickness of the volcanic unit reaches up to its maximum levels at the base of the succession within the valleys, it decreases to a few meters at some places towards the top of the succession, near the volcanic center. The lava flow pulses vary mainly in terms of their colors and textures in the field. The base of the volcanic succession is mainly made up of vesicular/amygdaloidal gray-dark-colored basalts. These layers display alternation with the massive olivine-bearing basaltic layers along the volcanic succession (Figure 2.19). The thickness of the vesicular/amygdaloidal levels usually does not exceed 2 m along the volcanic succession. Calcite mostly occurs as secondary minerals in the vesicles and fractures. Size of the vesicles vary between 0.5 mm and 3 cm in these lava levels (Figure 2.20).

Figure 2.19. Alternation of vesicular-massif basaltic flows in the east of Pınarlar village (view to northeast).

The alternation of the vesicular/amygdaloidal basaltic lava flows with the massive olivine-bearing basaltic flows continue towards volcanic center and Meltem Hill, representing the top of the volcanic sequence in the study area.

Figure 2.20. Vesicle-filling calcite in the Tunceli basalts from the east of Pınarlar village (view to east).

The massive olivine-bearing basaltic flows constitute the majority of the Late Miocene Tunceli volcanism. They are usually dark in color and cut by sets of platy joints occurring parallel and vertical to their basal surface or flow direction (Figure 2.21). The higher levels of the massive olivine-basalts are relatively non-weathered than the lower levels. In particular, those levels directly overlying the shallow-water sedimentary succession in the eastern part of the study area appear to be more weathered. In some places, there are in-situ basaltic hyaloclastite-like occurences with jigsaw-fit textures, which possibly were developed due to the fragmentation upon interaction with water (Figure 2.22). In these occurrences, basaltic hyaloclastic breccia is encroached by secondary calcite (Figure 2.22). Although the thickness of massive-olivine basaltic layers occasionally decreases to 1 m in some places, mostly due to erosion, at the upper stratigraphic levels, it exceeds 20 m at the lower levels, especially within some valleys (Figure 2.23). Microphaneritic textures, which are characteristically observed in the diabase, can be observed in the basalts situated in the thick lower levels of the volcanic sequence. Relatively slow-cooling rates due to increasing of the depth in these levels may probably have resulted in the formation of these textures in these lavas. Toward the uppermost levels, near the Beydamı volcanic center and Meltrem Hill, these mafic olivine basalts are overlain by light-colored vesicular olivine basalts.

Figure 2.21. Mafic olivine basalts cut by sets of platy joints in the west of Kaçarlar village (view to south).

Figure 2.22. Basaltic hyaloclastite-like occurences with jigsaw-fit textures in the east of Kaçarlar village (view to west).

Figure 2.23. Field view of the thick dark-colored massive olivine basalt layer in the west of Kaçarlar village (view to west).

The light-colored basalts forming the uppermost part of the volcanic sequence characteristically contain iddingsitized olivine crystals indicative of low-grade alteration (Figure 2.24). They are usually light-colored with vesicular textures. Calcite is occasionally present as a secondary mineral within the vesicles, giving rise to amygdaloidal texture in the basalts. Since these levels occur only at the upper levels of the volcanic succession, they probably represent the latest products of the Tunceli volcanism. These basaltic layers overlie the sediments of the Çaybağı Formation between the Tozkoparan and Beydamı villages. Intensely oxidized/altered red basalt layers are observed to occur on the top of sedimentary layers between these villages (Figure 2.25).

The Quaternary alluvium deposits overlie the Tunceli Volcanics as the youngest unit in the study area and are present in the eastern termination of the area, close to the Uzunçayır Dam Lake (Figure 2.4). This unit is characterized mainly by light-colored, well-rounded, poorly-sorted conglomerate levels. They are usually poorly consolidated, and their thickness varies from 1 to 20 m in the study area.

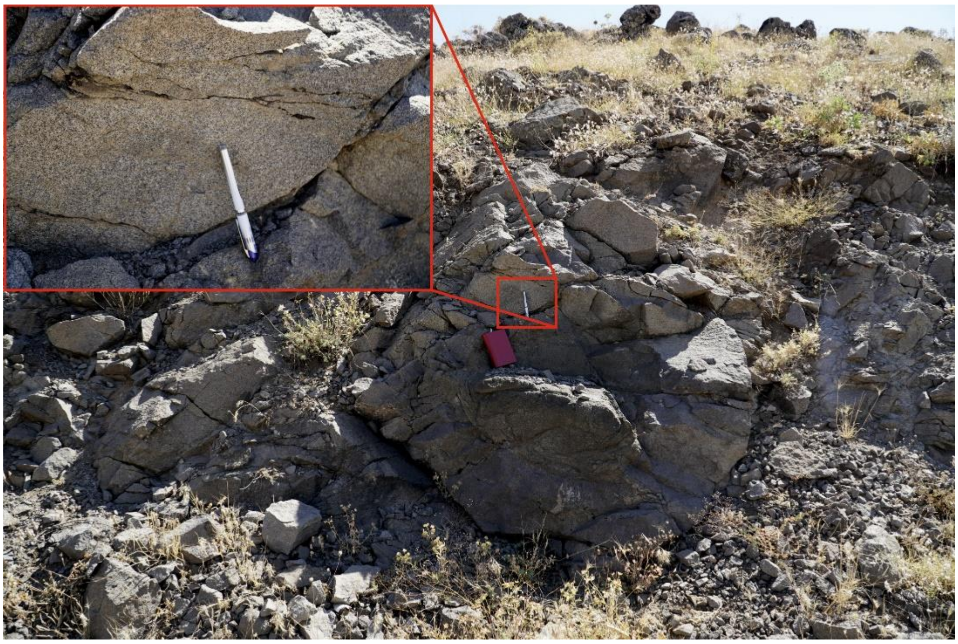

Figure 2.24. Light-colored vesicular olivine basalts in the south of Çevirme village (view to east).

Figure 2.25. Highly oxidized light-colored vesicular olivine basalt layer in the south of Çevirme village (view to east).

2.2.2 Elazığ Region

On a chronological order, the lithological units of the Elazığ region are; the Permo-Cretaceous Keban Metamorphics, the Late Santonian-Early Maastrichtian Elazığ Magmatics, the Late Maastrichtian-Late Paleocene Harami Formation, the Bartonian-Early Chattian Kırkgeçit Formation, the Late Miocene-Pliocene Karabakır Formation, the Early Pleistocene Palu Formation, the Late Pleistocene Elazığ Volcanics, the Late Pleistocene Terrace unit and Holocene Alluviums (Figure 2.26 and Figure 2.27; İnceöz, 1994; Herece, 2016a).

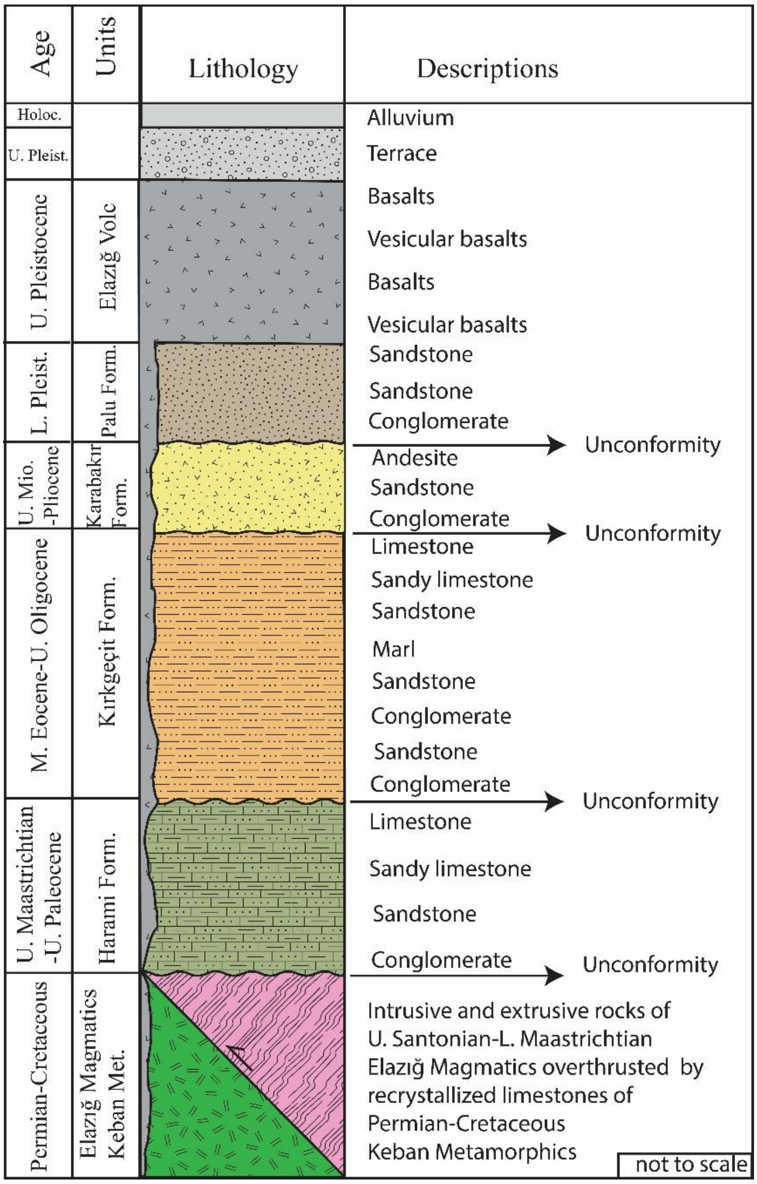

Figure 2.26. Generalized stratigraphic section of the Elazığ region (compiled from İnceöz, 1994; Herece, 2016a; Herece and Acar, 2016).

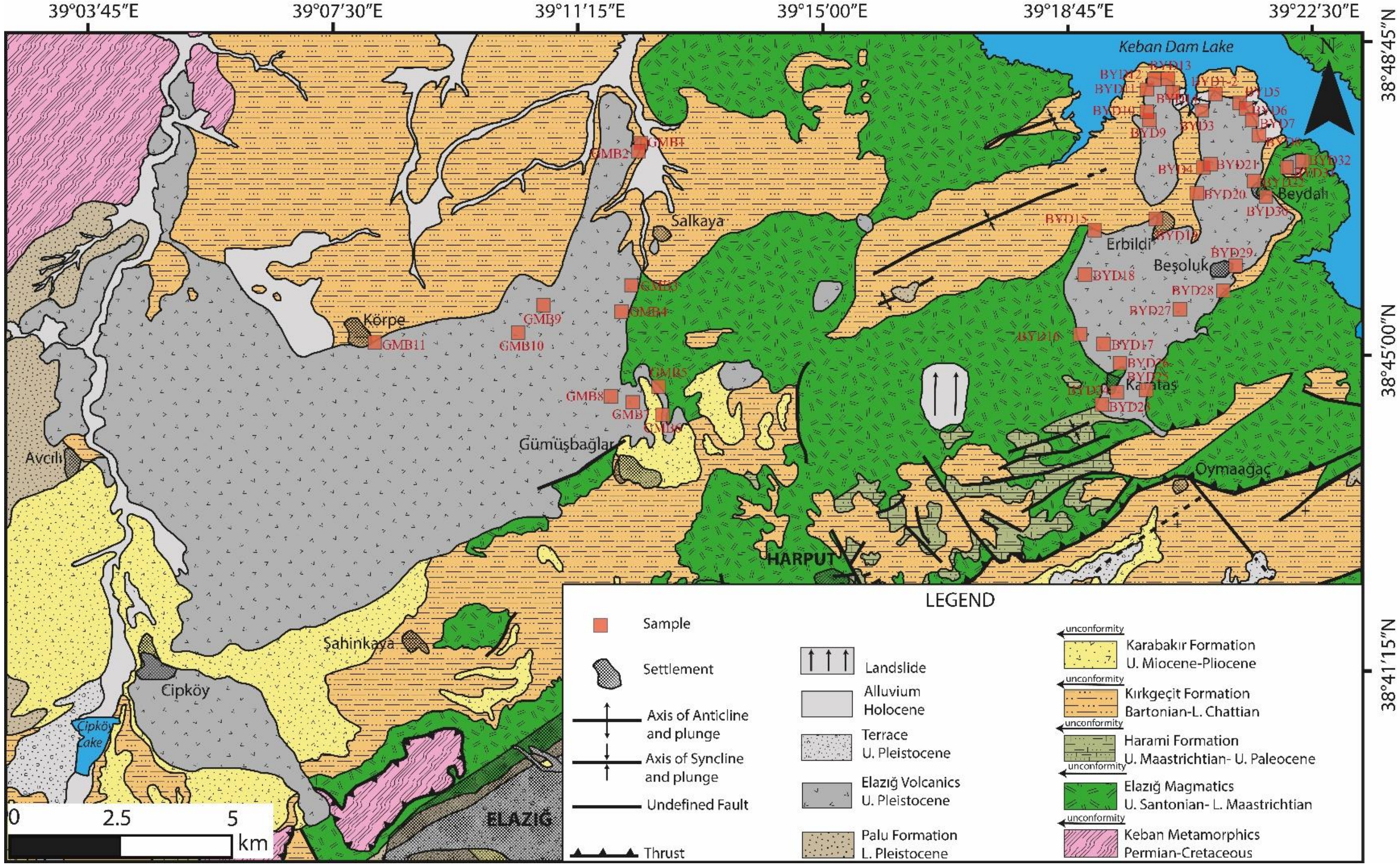

Figure 2.27. The geological map of the Elazığ region (modified from 1:100,000 scale geological map of Turkey (K42), Herece, 2016a).

The basement rocks of the study area in the Elazığ region are made up primarily of Permian-Cretaceous Keban Metamorphics and Late Santonian-Early Maastrichtian Elazığ Magmatics. The Keban Metamorphics, in the Elazığ region are represented by recrystallized limestones as in the Tunceli region. They are usually massive and display white-cream colors in the field (Figure 2.28). In some places, these limestones are observed to be deformed and fractured. Although the fractures are usually irregular on their surface, regular sub-parallel fractures filled with secondary calcites can occasionally be observed at some localities. The Keban Metamorphics crop out mainly in the northwest of the study area and are unconformably overlain by the Cenozoic units. However, they overthrust the Elazığ Magmatics in the south of the study area (Figures 2.26 and 2.27). No contact relationship has been observed between the Keban Metamorphics and the Elazığ Volcanics in the region.

Figure 2.28. The field view of the Keban Metamorphics in the north of the Avcılı village (view to south).

The Late Santonian-Early Maastrichtian Elazığ Magmatics are composed broadly of intra-oceanic arc, back-arc assemblages, which crop out on a wide area across SENSB of Turkey (e.g., Ural et al., 2015; Beyarslan and Bingöl, 2018). The nomenclature and tectonomagmatic evolution of these assemblages are still debated. They were initially defined by Perinçek (1979) as "Yüksekova Complex" due to their lithological similarities to the Late Cretaceous intra-oceanic arc-related magmatics around the Hakkari province (southeast Turkey). This name has later been used in many studies around Elazığ region (e.g., Naz, 1979; Bingöl, 1984; Sungurlu et al., 1985; Turan and Bingöl, 1991; Tekin et al., 2015; Ural et al., 2015). However, in the early 90s, it was postulated that these intra-oceanic magmatics display rather a continuous succession and have distinct lithological-structural features than those exposed around the Hakkari region (Turan and Bingöl, 1991; Turan et al., 1995). Based on these observations, these units around Elazığ region have also been studied under the name of "Elazığ Magmatics" (e.g., Turan and Bingöl, 1991; Turan et al., 1995; Beyarslan and Bingöl, 1996; Beyarslan and Bingöl, 2000, Beyarslan and Bingöl, 2018). Apart from these two widely accepted nomenclatures, there are also different names given to these magmatic units, such as; Elazig Volcanic Complex (e.g., Hempton and Savcı, 1982), Elazığ-Baskil Magmatic Complex (e.g., Robertson et al., 2007), etc.

Elazığ Magmatics are usually associated with the ophiolitic rocks in the region and consist mainly of basic to felsic extrusive (basalt, andesite, dacite, and volcanoclastic) and intrusive (gabbro, diorite, quartz-diorite, monzodiorite, quartz-monzodiorite, monzonite, tonalite, granite, granodiorite) rock units (e.g., Beyarslan and Bingöl, 2018; Sar et al., 2019). A Late Cretaceous age has been assigned to these magmatic rocks based on the zircon U-Pb dating method (e.g., Beyarslan and Bingöl, 2018; Sar et al., 2019). According to recent studies, the emplacement of the magmatics occurred in three stages in the region (Beyarslan and Bingöl, 2018; Sar et al., 2019). The first stage was represented by tholeiitic basalts, gabbros, tonalites, and quartz-diorites, were emplaced between 84 and 81 Ma (Beyarslan and Bingöl, 2018; Sar et al., 2019). On the other hand, the second stage, was characterized by calc-alkaline and high-K series granites, ganodiorites and quartz-monzodiorites, is thought to be emplaced between 80 and 79 Ma (Beyarslan and Bingöl, 2018; Sar et al., 2019). The last stage of magmatism was represented by the shoshonitic quartz-monzonites and monzodiorites, which occurred between 74 and 72 Ma (Beyarslan and Bingöl, 2018; Sar et al., 2019). Although there is also no consensus about the geodynamic evolution of these lithologies, they are, in general, thought to have been formed within the intra-oceanic arc, back-arc settings during the subduction of the southern branch of the Neo-Tethys ocean beneath the Anatolide-Taıride Block (e.g., Ural et al., 2015; Beyarslan and Bingöl, 2018; Sar et al., 2019).

In the study area, while the extrusive rocks are represented mainly by basalt, the intrusive members consist mainly of diabases, diorites and granitoids (granite and granodiorite) (Figure 2.27; Herece, 2016a, Herece and Acar, 2016). The felsic members mainly crop out in the northeast of the study area, whereas the basic members, including both the extrusives and intrusives, largely outcrop out in the southeast of the study area (Figure 2.26 and Figure 2.27). The granitoids are usually altered, displaying pinkish-cream colors (Figure 2.29). K-feldspar, plagioclase, hornblende, and biotite characterize the dominant mineralogy of the granitoids. Both porphyritic and equigranular varieties can be observed in the study area.

Diabases occur as mafic intrusions in the study area. They usually intrude into intermediate and felsic plutonic rocks of the of Elazığ Magmatics (Figure 2.30). They, in general, display dark-greenish color, which may imply low-grade hydrothermal alteration (Figure 2.30). Diabases typically have microphaneritic texture; however, porphyritic varieties also occur occasionally in some places. Diorites, are usually grayish and have holocrystalline/equigranular textures in hand specimen. Their main mineralogical assemblage is represented by plagioclase, hornblende, biotite, and quartz. They are usually intruded by the microdiorites and diabases in the study area (Figure 2.30).

Figure 2.29. The field view of the granitoids of the Elazığ Magmatics near the Beydali village (view to west).

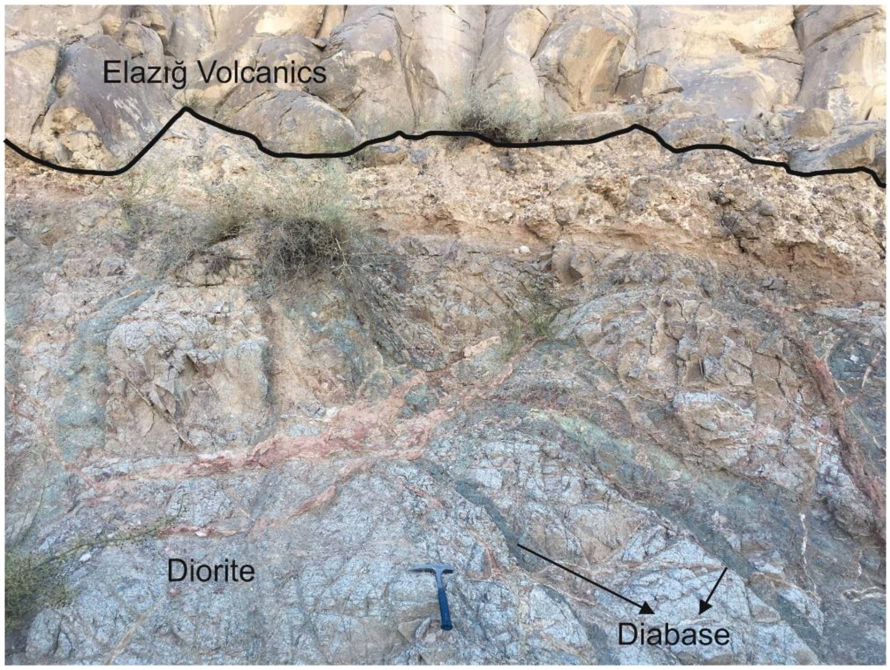

Figure 2.30. The field view of diorite and diabase of the Elazığ Magmatics which are overlain by the Elazığ Volcanics along the Petek-Elazığ road (view to west).

The volcanics of the Elazığ Magmatics are represented predominantly by basaltic rocks in the study area and usually display greenish colors indicative of low-grade hydrothermal alteration (Figure 2.31). Plagioclase and pyroxene characterize the primary mineralogy in these rocks. On the other hand, chlorite and epidote occur as secondary minerals, which can be attributed to the low-grade alteration.

In the study area, the Elazığ Magmatics are unconformably overlain by the Late Maastrichtian-Late Paleocene Harami Formation and Cenozoic sedimentary and volcanic units (e.g., Figure 2.30-2.32).

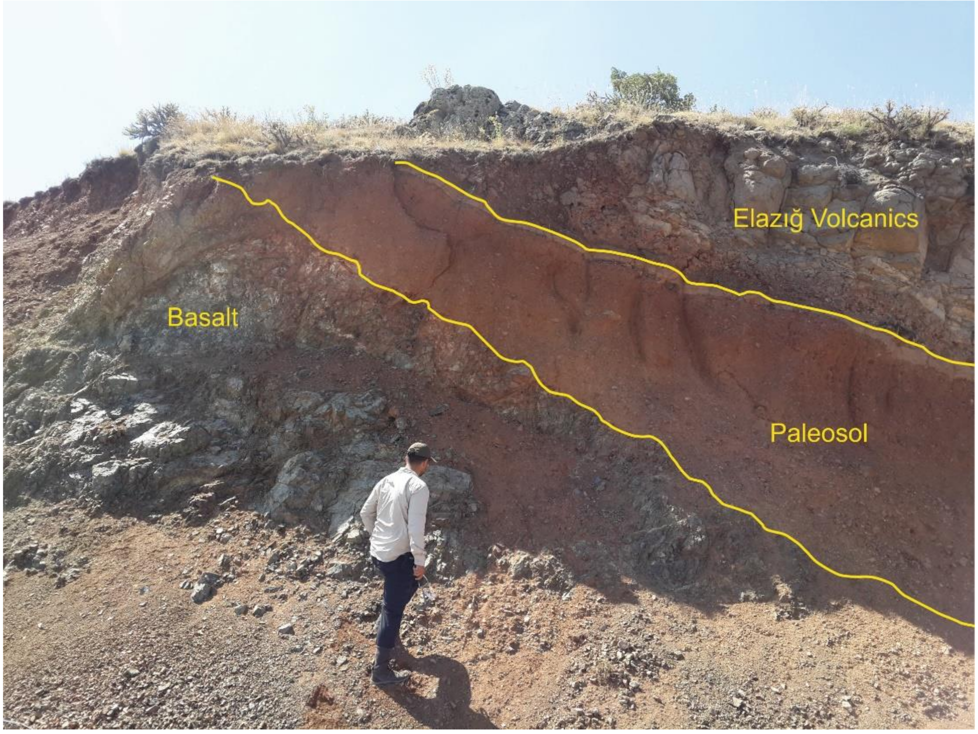

Figure 2.31. The field view of the basalt unit of the Elazığ Magmatics, which are overlain by the Elazığ Volcanics in the south of the study area near Harput district (view to north).

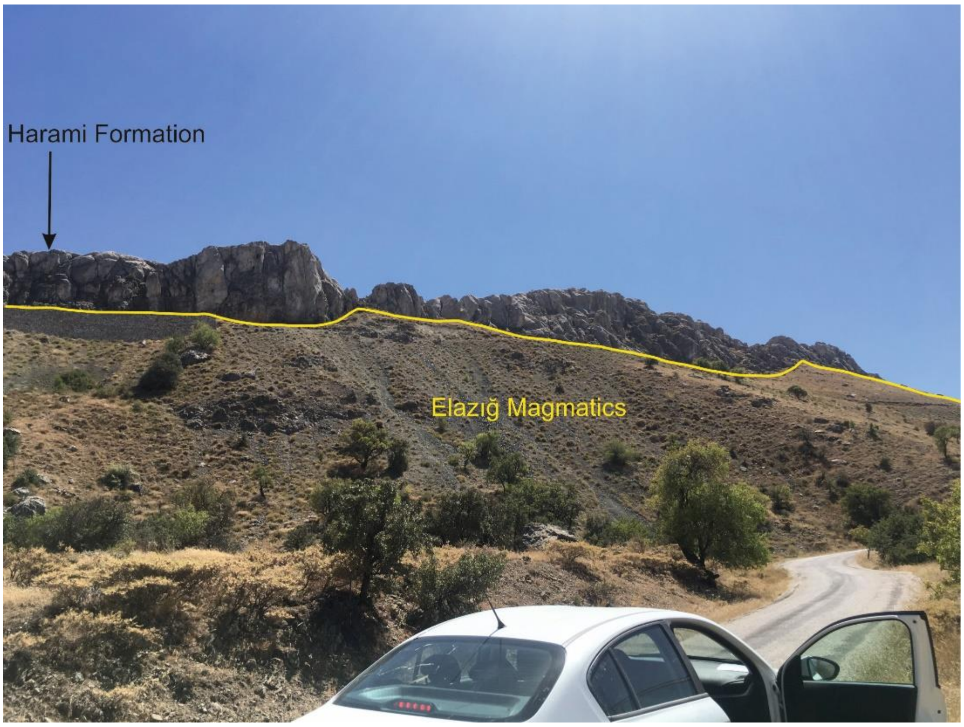

Figure 2.32. Contact relationship between Elazığ Magmatics and Harami Formation in the northeast of Harput district (view to southwest).

The Late Maastrichtian-Late Paleocene Harami Formation was first described and named by Erdoğan (1975) in the north of the Gölbaşı district of Adıyaman province. Later, this name was adopted in many geological studies in the eastern and southeastern Anatolia (e.g., Perinçek, 1979; Naz, 1979; Bingöl, 1984; Sungurlu et al., 1985; Turan et al., 1995; İnceöz, 1994; Herece and Acar, 2016). This formation is broadly characterized by the conglomerate, pebbly sandstone, and limestone units (Herece and Acar, 2016), and crop out in a wide area in eastern Turkey. A Late Maastrichtian-Late Paleocene age was assigned to the Harami Formation based on the benthic foraminifer fossil content determined both from the bottom and top of the limestone unit (Herece et al., 1992; Herece, 2016a; Herece and Acar, 2016). Herece and Acar (2016) suggested that these lithologies were deposited in a shallow shelf environment.

In the study area, the Harami Formation is represented mainly by thick-bedded, white limestone layers largely cropping out around the Harput district (Figure 2.26 and Figure 2.27). The thickness of the limestone sequence reaches up to 60 m in the study area (Herece and Acar, 2016). This unit is unconformably overlain by the Middle Eocene-Late Oligocene Kırkgeçit Formation and Quaternary Elazığ Volcanics in the study area (Figure 2.33).

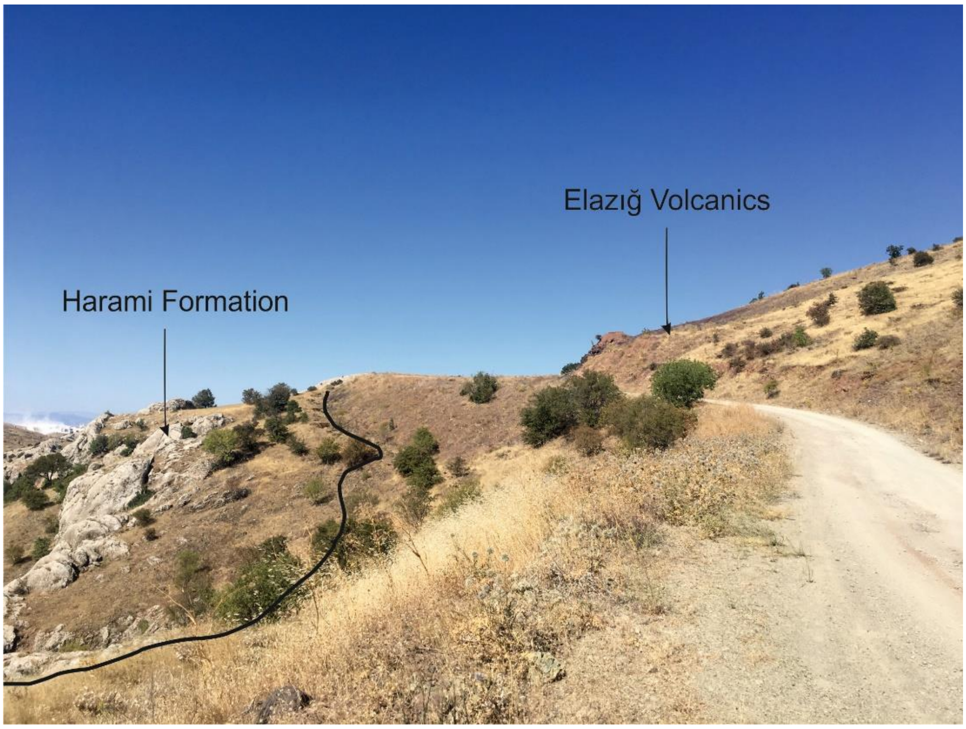

Figure 2.33. Contact relationship between the Harami Formation and Elazığ Volcanics in the east of Harput district (view to west).

The Middle Eocene-Late Oligocene Kırkgeçit Formation also crops out over a wide area in Elazığ region, as in the Tunceli region (Figure 2.27). However, here, almost the entire sedimentary sequence is more completely preserved compared with the Tunceli region. The sedimentary sequence of the Kırkgeçit Formation starts with the Marik Member at the bottom in the study area, similar to its type locality in the Baskil region (İnceöz, 1994). The Marik Member is characterized mainly by conglomerates and subordinate sandstones in the study area. These conglomerates are usually laterally transitional with the massive sandstone levels in the study area (İnceöz, 1994). In the study area, these basal levels are largely exposed in the north of Oymaağaç village and east of Beşoluk village (Figure 2.27). These levels are generally poorly-sorted. The grain size of the conglomerates for the Marik Member varies from pebble-size to boulder-size (Figure 2.34). The Marik Member can be assumed to be genetically related to the pre-Tertiary units in the region (Figure 2.34), as previously reported by İnceöz (1994). The thickness of these unit exceeds 500 m around the Elazığ region (İnceöz, 1994). The Marik Member is conformably overlain by the Seher Dağı Member of the Kırkgeçit Formation in the study area.

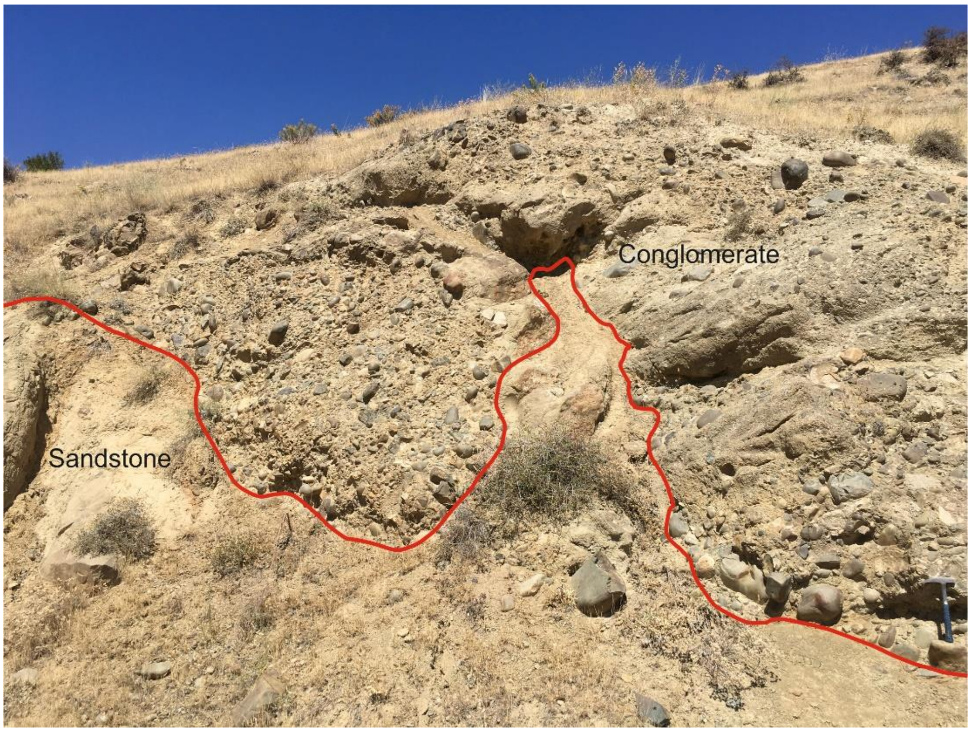

Figure 2.34. Field view of the conglomerate and sandstone from the Marik Member of Kırkgeçit Formation in the east of Beşoluk village (view to west).

The Seher Dağı Member, as in the Baskil region, consists of an alternation of conglomerate, sandstone, mudstone, and marl, representing a flysch-like sequence.

Lithologies of this member are laterally discontinuous in the region. The conglomeratic levels observed in the north of Erbildi village (Figure 2.35). They are overlain by the Elazığ Volcanics in this location (Figure 2.35). Conglomerates are usually poorly-sorted; however, they contain well-rounded clasts (Figure 2.35). These clasts have been chiefly derived from the pre-Tertiary units in the study area. The conglomerate beds are mostly matrix-supported and loosely consolidated (Figure 2.35). Their thickness reaches up to 20 m in the north of the Erbildi village.

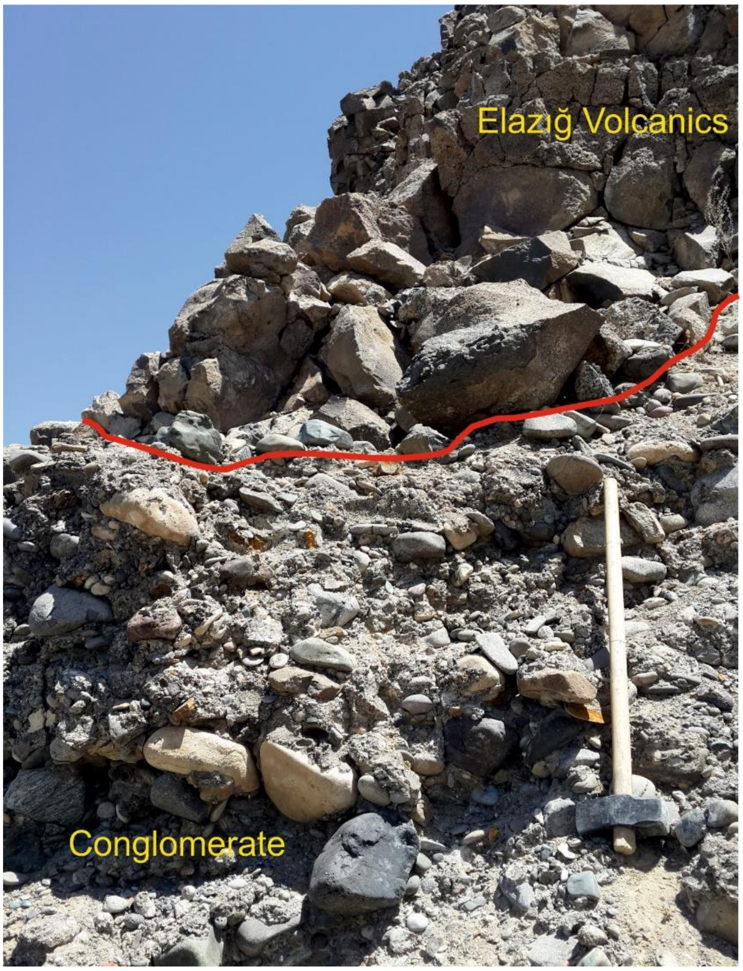

Figure 2.35. Field view of the conglomerates of the Seher Dağı Member of Kırkgeçit Formation overlain by the Elazığ Volcanics in the north of Erbildi village (view to east).

The sandstone-marl alternation mainly crops out between the Erbildi and Salkaya villages, in the north of Gümüşbağlar village and the south of Oymaağaç village (Figure 2.27). Very thick beds (i.e., sandstone-marl alternation), occasionally exceeding 200 m, can be observed in the west of Ebildi village. Sandstones are usually beige in color, well-sorted, and –consolidated. They usually alternate with greenish marl layers in the study area (Figure 2.36). Although the mudstone beds were not observed during the field studies, they were reported to occur as thin intercalations between the conglomerates of Marik Member and the sandstone-marl alternation of Seher Dağı Member (İnceöz, 1994). The lithologies of the Seher Dağı Member are conformably overlain by the limestone of the Keklik Tepe and Gökbelen Members of the Kırkgeçit Formation in the study area.

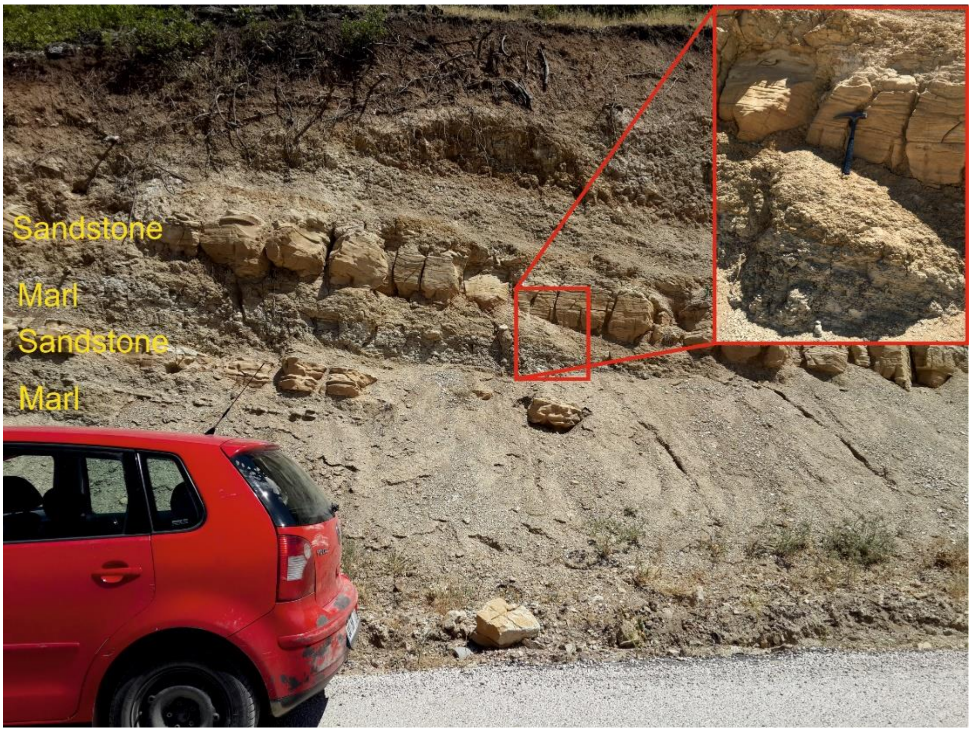

Figure 2.36. Sandstone-marl alternation in the Seher Dağı Member of the Kırkgeçit Formation in the northeast of the Erbildi village (view to east).

The top levels of the Kırkgeçit Formation, mostly represented by limestone beds, are exposed mainly in the northwest of the study area, north of the Körpe village (Figure 2.27). İnceöz (1994) investigated these units under the name of Çömlek Member. However, these units can be correlated with the Keklik Tepe and Gökbelen Members of the Baskil section of Kırkgeçit Formation (Özkul, 1988; Özcan et al., 2019), on the basis of their lithological features and field relations. In the study area, these upper levels are chiefly represented by beige, thick (<400 m; İnceöz, 1994) limestone layers (Figure 2.37).

In the study area, all lithologies of the Kırkgeçit Formation are unconformably overlain by Neogene sedimentary deposits and the Elazığ Volcanics (Figure 2.35 and Figure 2.37).

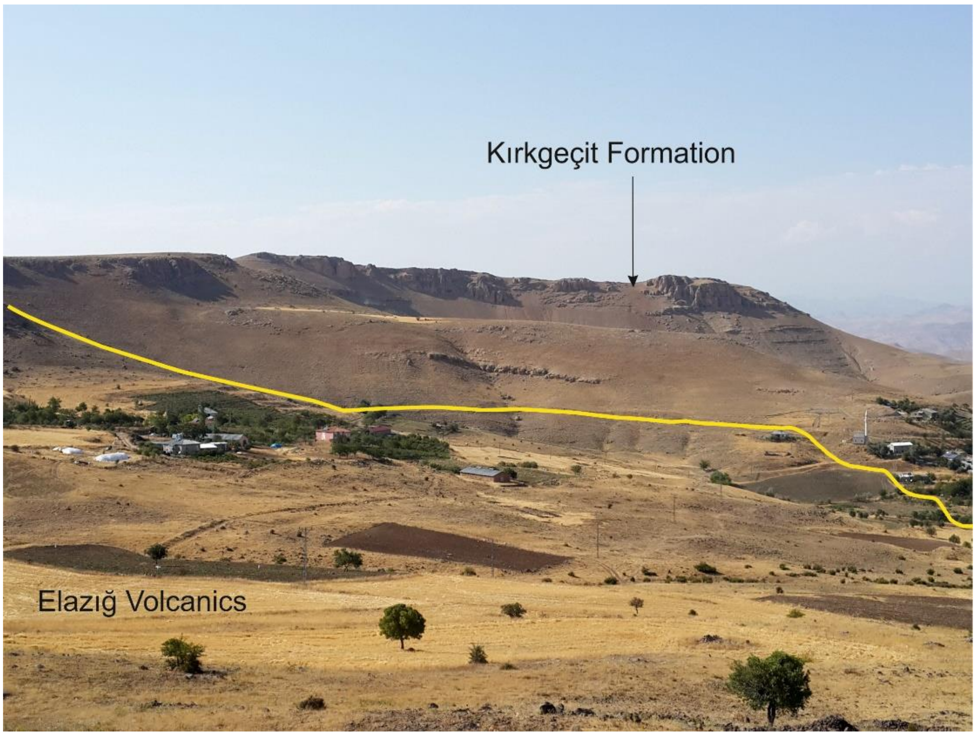

Figure 2.37. Thick massive limestone sequence of the Kırkgeçit Formation unconformably overlain by the Elazığ Volcanics in the northeast of Körpe village (view to northwest).

The Late Miocene-Pliocene Karabakır Formation was initially defined by Naz (1979) in the south of Tunceli region. This formation crops out over a wide area in the Tunceli and Elazığ regions and is mainly characterized by conglomerate, sandstone, mudstone, marl, limestone, volcanoclastic, pyroclastic, epiclastic, andesite and basalt (Naz, 1979; Herece, 2016a; Herece and Acar, 2016). It is suggested that these units are laterally and vertically transitional with each other (Naz, 1979). Later, this name has been adopted by numerous studies concerning the Late Miocene-Pliocene sedimentary and volcanic rocks in the Tunceli and Elazığ regions (e.g., Asutay et al., 1986; Türkmen, 1991; İnceöz, 1994; Kürüm, 1994; Herece, 2016b; Herece and Acar, 2016). Until recent times, the Elazığ Volcanics were also thought to be a member of this formation. However, new radiometric age data (Arger et al., 2000; Seyrek et al., 2008; Demir et al., 2009; Di Giuseppe et al., 2017) from these volcanics showed that the volcanism in the Elazığ region commenced during the Late Pleistocene. Additionally, in the study area, the Elazığ Volcanics overlie the Early Pleistocene Palu Formation, which unconformably overlies the clastic rocks of Karabakır Formation. Therefore, in this study, the Elazığ Volcanics are not included in the Karabakır Formation. The Karabakır Formation is represented mainly by conglomerates in the study area, and largely crops out around the southwest of the study area (Figure 2.27). These conglomerates are generally beige in color, clast-supported, and weakly consolidated.

The Early Pleistocene Palu Formation was initially described and named by Çetindağ (1985) around the Palu district of Elazığ city. Later, this name was used in numerous geological studies in the region (e.g., Kerey and Tükmen, 1991; Türkmen, 1991; Turan and Bingöl 1991; İnceöz, 1994; Herece and Acar, 2016). This formation is mainly characterized by the conglomerate, sandstone, and mudstone levels around Palu region (e.g., Kerey and Türkmen, 1991). However, in the study area, this formation is represented only by the conglomerate levels. These levels contain clasts of different origins and sizes. The clasts were suggested to be mostly derived from the Elazığ Magmatics and Kırkgeçit Formation in the region (İnceöz, 1994). The conglomeratic levels are generally beige colored and poorly-sorted, -rounded, and -

consolidated. They mainly crop out in the west of the study area, around the Avcılı village (Figure 2.27; Herece, 2016a). They overlie the Karabakır Formation with angular unconformity (Herece and Acar, 2016) and overlain by the Late Pleistocene Elazığ Volcanics.

The Late Pleistocene volcanics in the Elazığ region were initially described as "Elazığ Volcanics" by Ercan and Asutay (1993). Later, this name was used in several geological studies in the region to describe this volcanism (e.g., Akgül et al., 2001; Özbulut, 2006). Although the age of this volcanism was thought to be the Late-Miocene-Pliocene based on a regional stratigraphic correlation, the recent radiometric age data (K-Ar and Ar-Ar methods) revealed that the volcanism occurred during the Late Pleistocene (1.47-1.87 Ma, Arger et al., 2000; 1.8-1.9 Ma, Seyrek et al., 2008; 1.8 Ma, Demir et al., 2009; 1.7 Ma, D, Giuseppe et al., 2017).

The Elazığ Volcanics occupies an area of about 90 km^2 in the north of Elazığ city. They mainly crop out in two locations the region; between Avcılar-Gümüşbağlar villages and between Beydalı-Erbildi villages (Figure 2.27; for the sake of simplicity, hereafter they will be referred to as the Gümüşbağlar member and Beydalı member). Similar to in the Tunceli region, the lava flows of this volcanism have created a small-scaled plateau-like morphology in the region (e.g., Figure 2.38).

The volcanism in the Elazığ region is predominantly characterized by successive pulses of lava flows. Scarce pyroclastics can only be observed in few localities as thin to medium agglomerate levels and scoriaceous fragments. These may indicate that the volcanism spread out via Strombolian or Hawaiian-type eruptions in the region. Scoria cones are not observed in the field. They are probably covered by the lava flows in the region. Therefore, eruption centers are not apparent in the field. However, when the topography of the region and the aggregation of the scoriaceous fragments at some particular locations (Figure 2.39) are taken into consideration, one possible eruption center for the Elazığ Volcanics can be situated to the south of the Karataş village. The Beydalı member may have emitted from this location, representing the upper altitude of the topography and spreading out towards the lower altitudes (Figure 2.40). In both locations (Beydalı and Gümüşbağlar), the lavas appear to have flown out from the volcanic centers at higher altitudes and spread towards the lower stratigraphic levels, where the topography becomes much smoother.

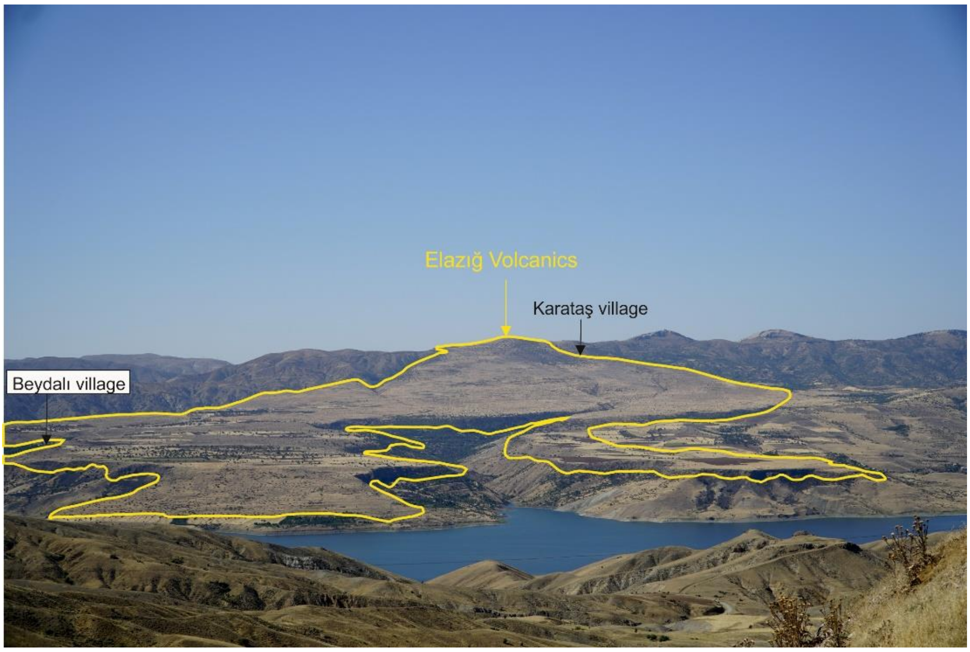

Figure 2.38. Small-scale plateau-like morphology formed by the Quaternary volcanism in the Elazığ region (view to south).

Figure 2.39. Field view of the scoria deposits in the southeast of Karataş village (view to north).

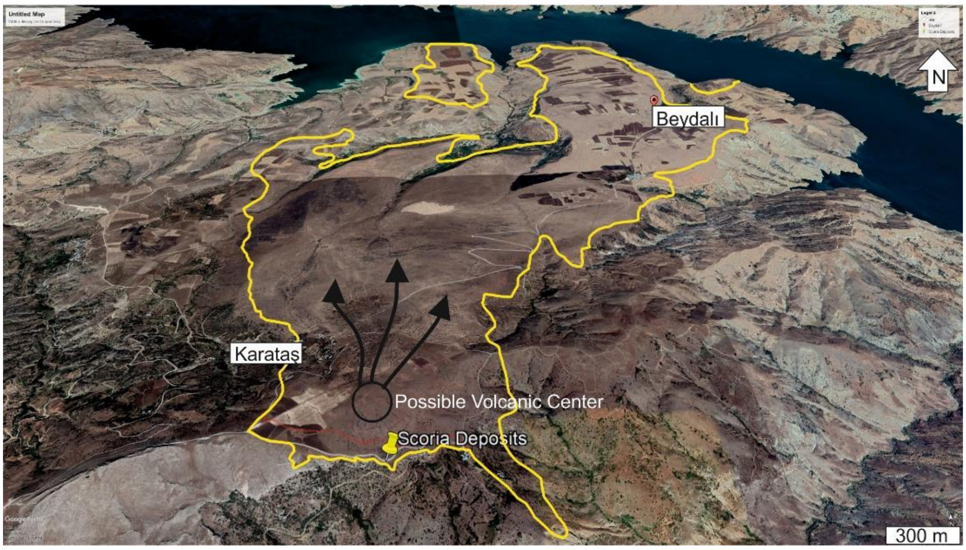

Figure 2.40. Google Earth view of the possible volcanic center for the Beydalı member of the Elazığ Volcanics in the southeast of the Karataş village. The yellow line represents the approximate border of the Beydalı member.

Although the thicknesses of the lava flows decreases to below 1 m at the upper altitudes, they reach up to 30 m at the lower altitudes, towards the valleys (Figure 2.41 and Figure 2.42). The succession of the lava flows is more apparent at the base of the volcanic sequence, where the thickest sections can be observed. The thickness of each lava layer does not exceed 2 m along the sequence (Figure 2.43). At the lower altitudes, the individual lava flows can be differentiated by textural differences among each other. An alternation of the vesicular and massive layers can be observed along the volcanic sequence (Figure 2.43). The vesicles at some levels are intensively filled with calcite, forming amygdaloidal textures in these lavas. Apart from the textural difference, there is no compositional difference among the individual lava layers. Based on the hand specimens, the entire Elazığ Volcanics can be classified as basaltic volcanic lava flows. Olivine occasionally occurs as phenocrysts in some levels, resulting in the formation of porphyritic textures in these rocks.

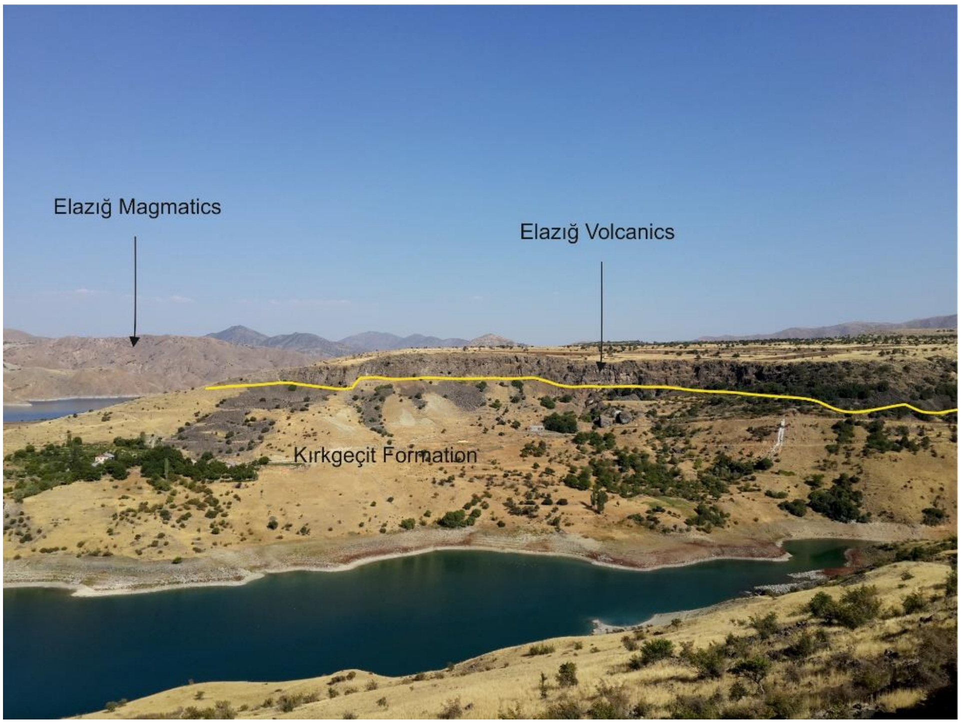

Figure 2.41. Field view of the thick lava flows (~20 m) at the lower altitudes near the Keban Dam Lake in the north of Erbildi village (view to east).

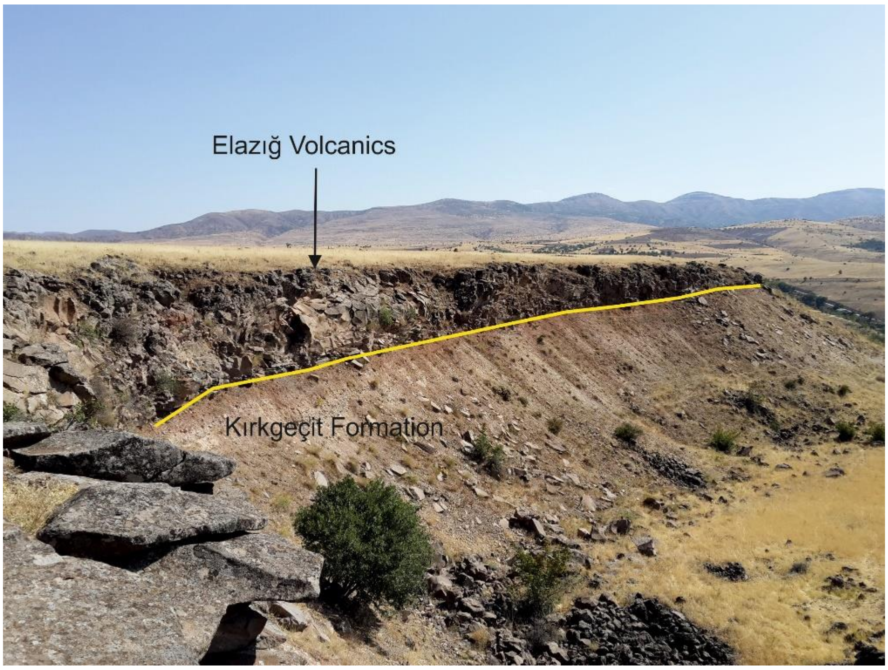

Figure 2.42. Field view of the thick lava flows (~10 m) at the lower altitudes near the Keban Dam Lake in the north of Erbildi village (view to south).

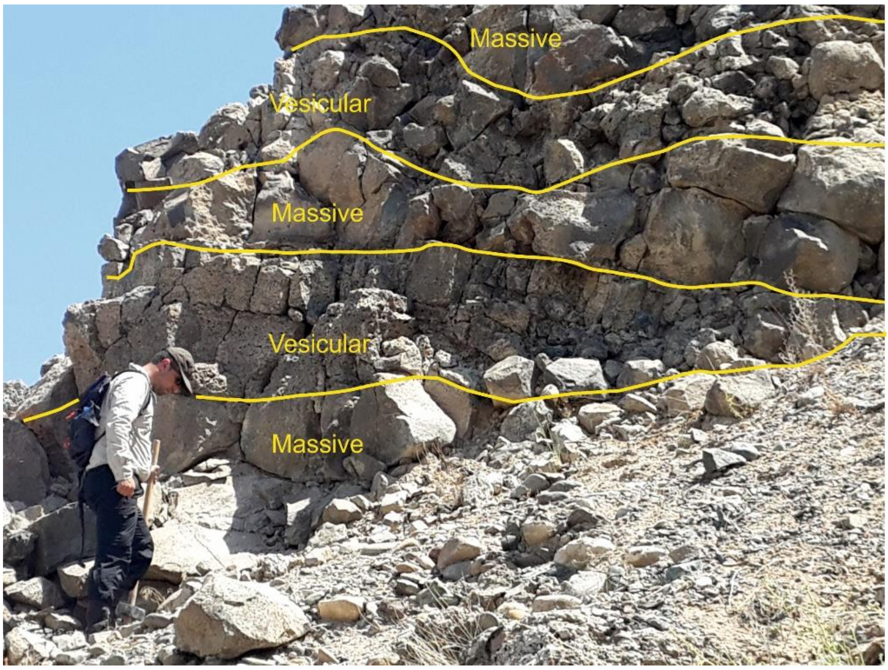

Figure 2.43. Massive and vesicular lava alternation in the north of Erbildi village (view to east).

Although the Elazığ Volcanics are usually fresh, weathered exposures can occasionally be observed in some places. The fresh basaltic lavas generally display a dark gray color compared to their weathered counterparts. The weathered lavas, on the other hand, usually have light gray colors, and include iddingsitized olivine.

At upper the altitudes, near the volcanic center, the basaltic lava flows Elazığ Volcanics contain some crustal xenoliths, probably belonging to the Elazığ Magmatics (Figure 2.44). Sizes of the xenoliths generally vary from 1 cm to 5 cm, and these with angular shapes display gray and black colors (Figure 2.44). It must be noted that at these locations, the Elazığ Volcanics directly overlie the basaltic members of the Elazığ Magmatics. Therefore, it is very likely that the xenoliths represent the basement rocks incorporated into the Elazığ volcanism during the magma ascent. These occurrences may indicate a possible crustal assimilation process during their petrogenetic evolution.

Figure 2.44. Basaltic xenoliths incorporated into the Elazığ Volcanics in the northeast of Karataş village.

At the lower stratigraphic levels, the lava succession both in the Gümüşbağlar and Beydalı region is cut by sets of joints. The joint system appears to have formed mainly parallel to the flow direction (Figure 2.45). These horizontal platy joints in the basalts may have been developed as a result of the internal stress of the flow (Figure 2.45).

The Elazığ Volcanics are the second youngest unit after the Late Pleistocene and Holocene alluvium deposits. The conglomerates of the Late Pleistocene and Holocene alluviums overlie the Elazığ Volcanics in the west of the study area. These alluvium deposits are mainly composed of weakly-consolidated clastic material of various sizes and origins, which developed on riversides (Herece and Acar, 2016).

Figure 2.45. Field view of the platy-joints developed in the Elazığ Volcanics in the north of Erbildi village (view to east).

CHAPTER 3

PETROGRAPHY

In order to unravel the petrographic features of the Tunceli and Elazığ Volcanics, a total of 90 thin sections from both volcanic regions were examined under a polarized light microscope. The petrographic examination indicates that the Tunceli and Elazığ Volcanics are both characterized by basaltic lithologies, including similar mineral assemblages. Therefore, the volcanics from both regions were not internally subdivided into different groups in this chapter.

Petrographic analyses have recorded a distinct combination of phenocryst phases, textures, and secondary mineral products separately in the Tunceli and Elazığ Volcanics. This indicates that the volcanic products in both regions have different crystallization and alteration histories. In this chapter, the primary mineralogical assemblages, textures, and alteration products of the Tunceli and Elazığ Volcanics have been examined in detail.

It is important to note that the petrographical features of the Tunceli samples were given previously in Aktağ (2014) and Aktağ et al. (2019). The same samples are revisited in this chapter.

3.1 Tunceli Volcanics

Petrographically, the Tunceli Volcanics are represented entirely by basaltic rocks. These lavas are mostly aphyric/diabasic (i.e., holocrystalline), and porphyritic to a lesser extent. Therefore, the phenocryst phases, occupying up to ~5 vol.%, appear to be not abundant in these lavas. Nevertheless, the phenocryst mineralogy remains uniform throughout the study area, and includes olivine, clinopyroxene, and plagioclase (in the order of decreasing abundance). Plagioclase, olivine, clinopyroxene, and Fe-Ti oxide phases (in the order of decreasing abundance) represent the groundmass phases in these rocks. The groundmass is usually holocrystalline, as mentioned above, while hypocrystalline mesostasis occurs to a lesser extent (Figure 3.1). In addition, various types of textures, which are mostly typical for volcanic rocks, can also be observed in Tunceli Volcanics. These are; subophitic, glomeroporphyritic, intergranular, intersertal, trachytic and, vesicular/amygdaloidal textures (Figure 3.1).

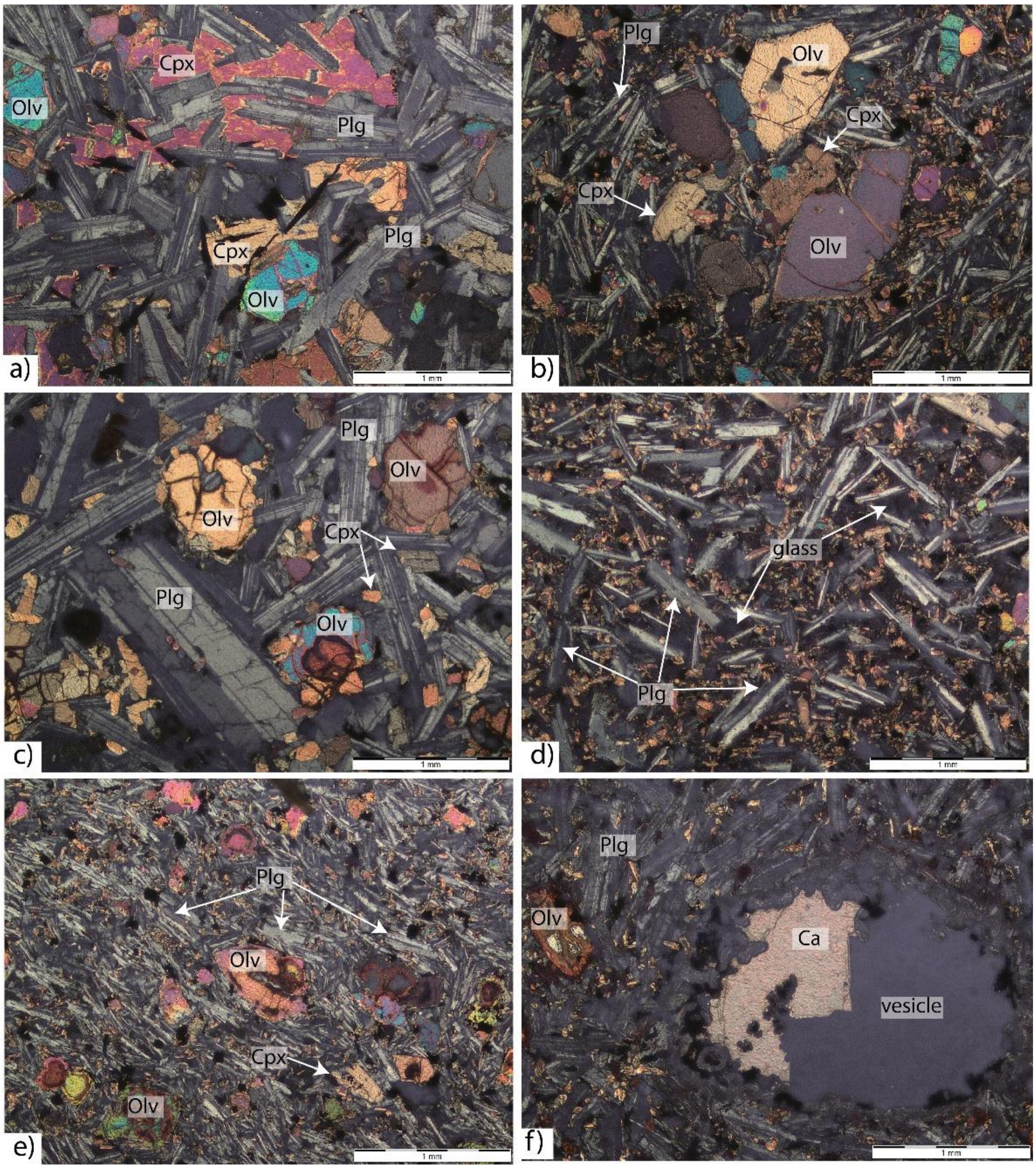

Figure 3.1. Common textures that the Tunceli Volcanics display. a) Subophitic texture (Sample ID: AV4, 4x, XPL). b) Glomeroporphyritic texture (Sample ID: AV33; 4x, XPL). c) Intergranular texture (Sample ID: AV5, 4x, XPL). d) Intersertal texture (Sample ID: AV28, 4x, XPL) e) Trachytic texture (Sample ID: AV49, 4x, XPL). f) Vesicular/amygdaloidal texture (Sample ID: AV7, 4x, XPL). Olv: olivine; Cpx: Clinopyroxene; Plg: Plagioclase; Ca: Calcite.

Olivine is the most abundant phenocryst in the Tunceli lavas and constitutes ~60 vol.% of the total phenocryst content. Olivine phenocrysts are usually found subhedral and euhedral, embedded in a holocrystalline/hypocrystalline groundmass (Figure 3.2). It also occurs as the second most abundant groundmass phase after plagioclase with subhedral and anhedral outlines in these rocks. Occasionally, some olivine grains in the hypocrystalline samples display skeletal and embayed outlines, which may indicate a rapid cooling and/or mineral-melt disequilibrium process (Figure 3.2c-d). Olivine is diagnostic with its colorless appearance and high relief under plane-polarized light (PPL). It is generally fractured and displays interference colors up to third-order under crossed-polarized light (XPL) (Figure 3.2).

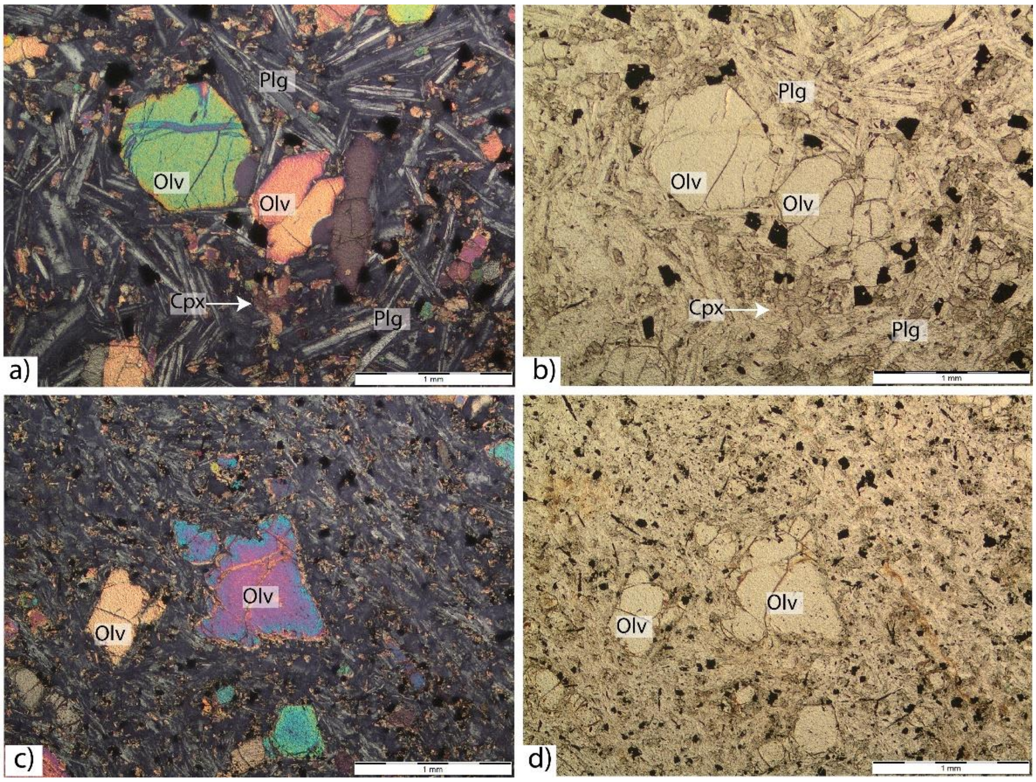

Figure 3.2. (a-b) Microphotographs of the subhedral/euhedral and (c-d) skeletal olivine crystals observed in the Tunceli Volcanics. a) Sample ID: AV33, 4x, XPL. b) Sample ID: AV33; 4x, PPL. c) Sample ID: AV2, 4x, XPL). d) Sample ID: AV2, 4x, PPL. Olv: Olivine; Cpx: Clinopyroxene; Plg: Plagioclase.

Although olivine is usually found fresh in the Tunceli samples, altered grains are also present in some instances. Iddingsite and bowlingite appear to be common secondary products, developing along the rims and fractures of olivine (Figure 3.3). While the bowlingitization occurs mainly at the lower levels of the volcanic sequence, iddingsitzation is more frequent at the upper levels. Occasionally, olivine is totally replaced, giving rise to the formation iddingsite/bowlingite pseudomorphs after olivine. Olivine occasionally forms clusters with pyroxene developing glomeroporphyritic textures (e.g., Figure 3.1b). Also, along with the clinopyroxene, olivine occupies the interstices of plagioclase grains in a holocrystalline groundmass resulting in intergranular texture in these volcanics (Figure 3.1c).

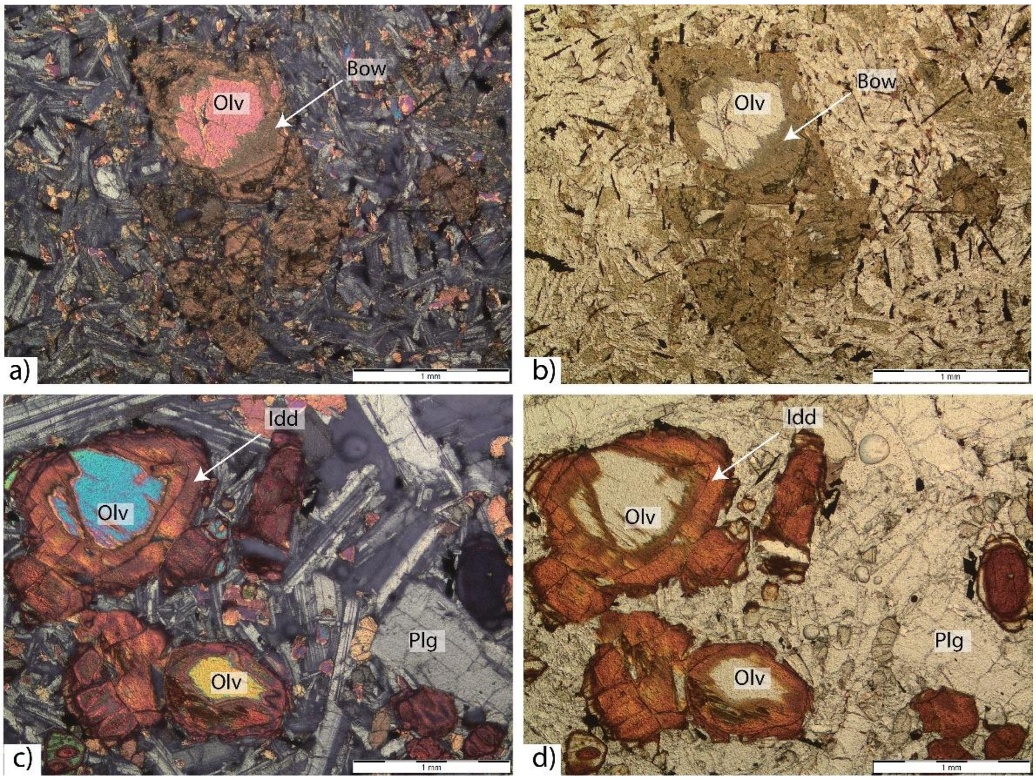

Figure 3.3. Microphotographs of the altered olivines observed in the Tunceli Volcanics. a-b) Replacement of olivine by bowlingite (a: Sample ID: AV25, 4x, XPL; b: Sample ID: AV25; 4x, PPL. c-d) Replacement of olivine by iddingsite (c: Sample ID: AV12, 4x, XPL; d: Sample ID: AV12, 4x, PPL). Olv: Olivine; Cpx: Clinopyroxene; Plg: Plagioclase; Bow: Bowlingite; Idd: Iddingsite.

Clinopyroxene is the second most common phenocryst in the Tunceli Volcanics and constitutes approximately 30-35% of the total phenocryst population. It is pale brownish under PPL, and has moderate to high relief (Figure 3.4). Clinopyroxene grains typically display anhedral and subhedral outlines with second-order interference colors, though some reach up to third-order interference colors (Figure 3.4).

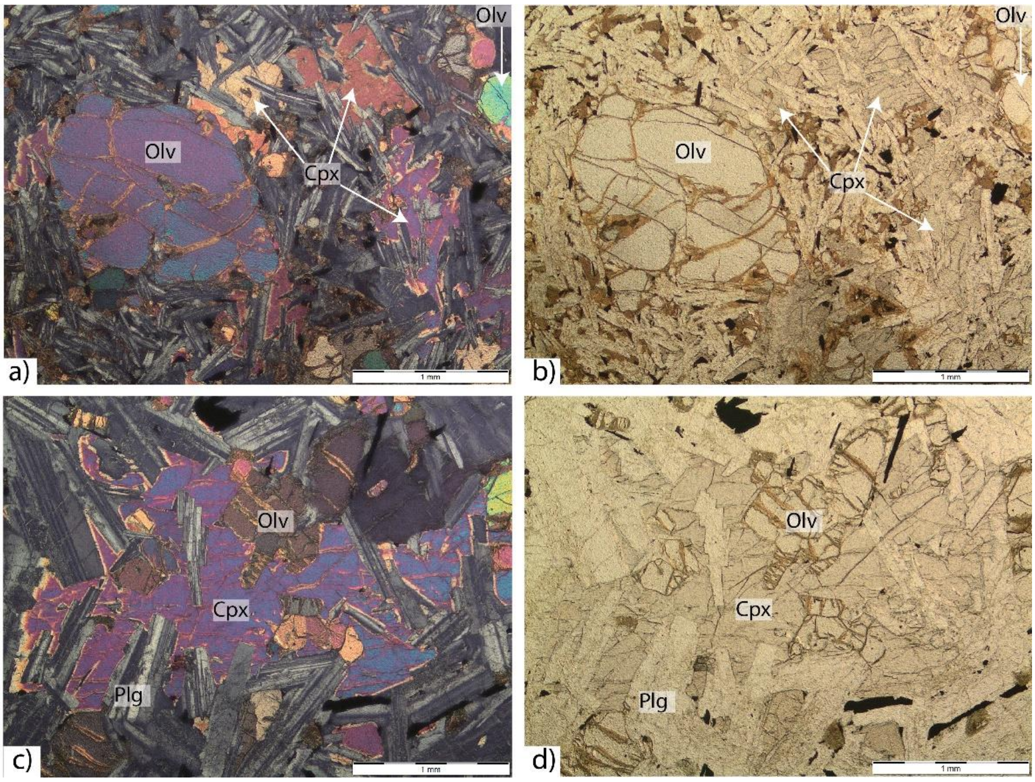

Figure 3.4. Microphotographs of the clinopyroxene crystals observed in the Tunceli Volcanics. a) Sample ID: AV20, 4x, XPL. b) Sample ID: AV20; 4x, PPL. c) Sample ID: AV67, 4x, XPL; d) Sample ID: AV67, 4x, PPL. Olv: Olivine; Cpx: Clinopyroxene; Plg: Plagioclase.

The cleavage planes of clinopyroxenes are barely recognizable in most instances. Well-developed cleavages (mostly in one direction) can occasionally be observed on some grains (Figure 3.5a-b). Twinning is not a common feature of the clinopyroxenes in the Tunceli Volcanics. There are some grains, however, with elongated prismatic shapes displaying simple and polysynthetic twinnings (Figure 3.5c-d). Clinopyroxene grains are usually fresh in the Tunceli lavas; no alteration products were observed on their surfaces. In some instances, the clinopyroxene occurs as anhedral aggregates randomly distributed in a hypocrystalline and holocrystalline groundmass (Figure 3.6). In diabasic samples (i.e., in those with holocrystalline crystallinity), clinopyroxenes enclose the plagioclase crystals forming subophitic texture (e.g., Figure 3.4). This may be indicative of a similar rate of growth and nucleation for these phases. This texture is usually observed in the samples belonging to the thicker parts of the volcanic succession.

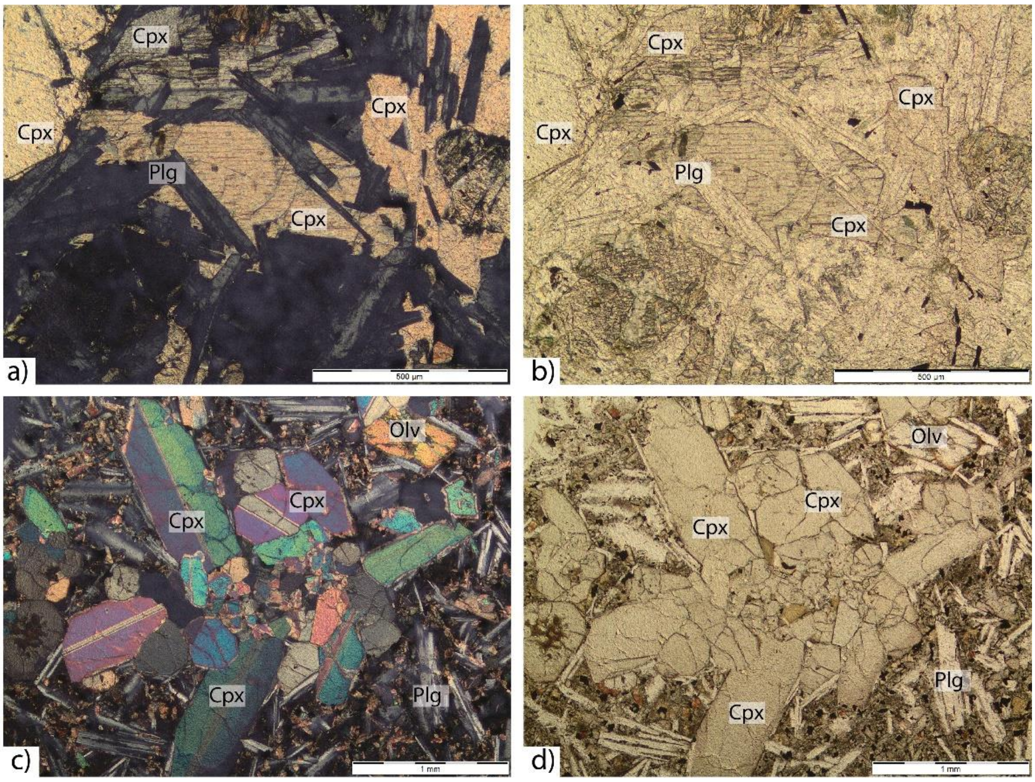

Figure 3.5. Microphotographs of the clinopyroxene crystals showing (a) one-directional cleavage and (b) simple twinning in the Tunceli Volcanics. a) Sample ID: AV23, 10x, XPL. b) Sample ID: AV23; 10x, PPL. c) Sample ID: AV28, 4x, XPL; d) Sample ID: AV28, 4x, PPL. Olv: Olivine; Cpx: Clinopyroxene; Plg: Plagioclase.

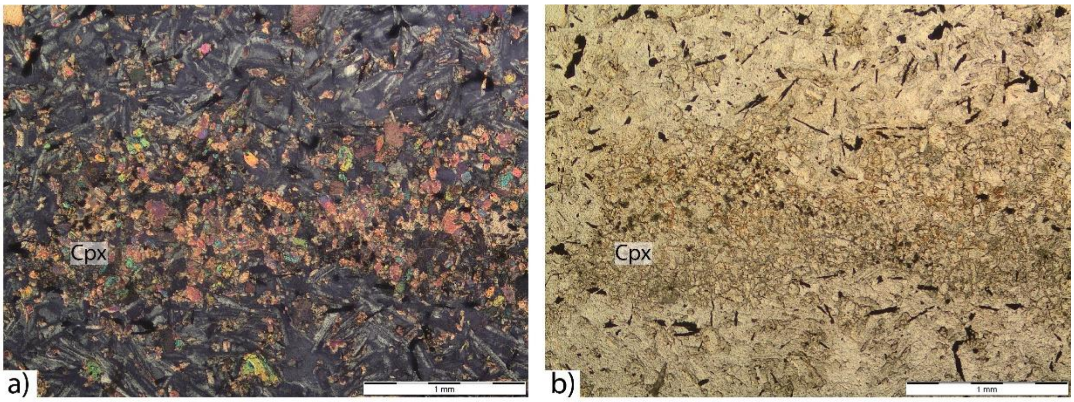

Figure 3.6. Microphotographs of the clinopyroxene aggregates embedded in hypocrystalline groundmass in the Tunceli Volcanics. a) Sample ID: AV29, 4x, XPL. b) Sample ID: AV29; 4x, PPL. Cpx: Clinopyroxene.

Plagioclase rarely occurs as a phenocryst phase in the Tunceli Volcanics. It constitutes nearly 5-10 vol.% of the total phenocryst content in the volcanics. Even though plagioclase is insignificant as a phenocryst phase, it forms a major component of the groundmass. Plagioclase tends to be larger in the groundmass of holocrystalline samples, whereas it is generally found as microliths in the finer-grained varieties. Slow rates at relatively deeper levels probably have resulted in the formation of larger groundmass phases in the holocrystalline samples. Such samples are also characterized by subophitic textures in the volcanics (e.g., Figure 3.1a and Figure 3.4c). Plagioclase grains characteristically are colorless under PPL and display first-order interference colors under XPL (Figure 3.7). They are generally fresh and mostly display subhedral and euhedral outlines (Figure 3.7). Most grains show polysynthetic twinning, a characteristic feature for plagioclase, while combined twins are also present. Oscillatory zoning occasionally observed in plagioclase and restricted to phenocrysts, where it is present (Figure 3.7c).

The Fe-Ti oxide phases occur as both randomly distributed opaque microlites in the groundmass and as inclusions in the silicate phenocrysts (Figure 3.1-3.7). While the cubic and skeletal opaque entities may represent magnetite, those with needle-like outlines may represent ilmenite in these volcanics.

It must also be noted that there are also other secondary occurrences in these rocks besides the iddingsite and bowlingite. These are calcite and zeolite; however, they occur as vesicle-filling minerals in the volcanics rather than an alteration product (Figure 3.8).

The summary of the petrographic features of the Tunceli Volcanics can be found in the Table 3.1.

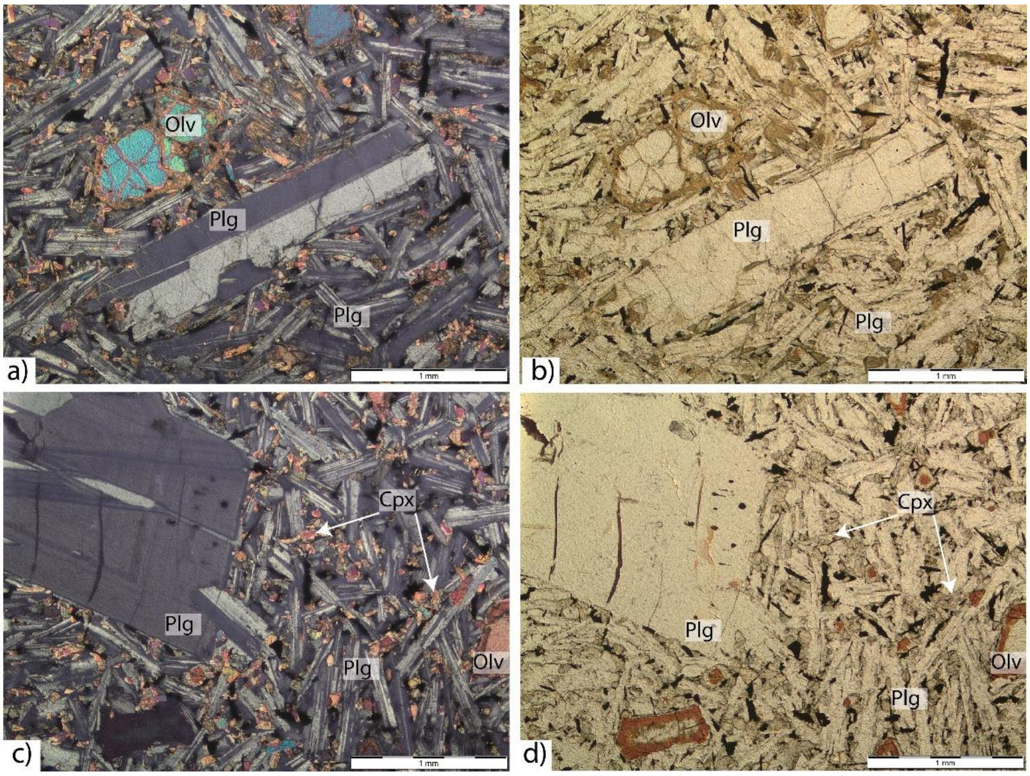

Figure 3.7. Microphotographs of the plagioclase phenocrysts showing (a) multiple twinning and (b) concentric zoning in the Tunceli Volcanics. a) Sample ID: AV21, 4x, XPL. b) Sample ID: AV21; 4x, PPL. c) Sample ID: AV39, 4x, XPL; d) Sample ID: AV39, 4x, PPL. Olv: Olivine; Cpx: Clinopyroxene; Plg: Plagioclase.

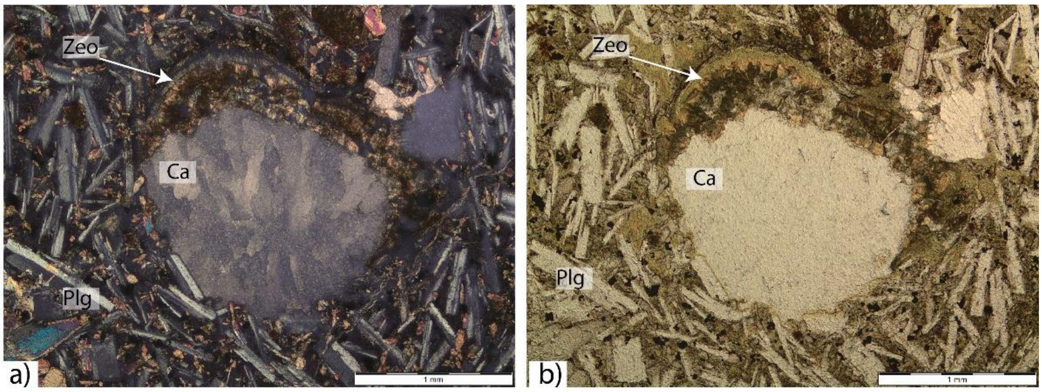

Figure 3.8. Microphotographs of the vesicle filling calcite and zeolite minerals in the Tunceli Volcanics. a) Sample ID: AV28, 4x, XPL. b) Sample ID: AV28; 4x, PPL. Plg: Plagioclase; Ca: Calcite; Zeo: Zeolite.

3.2 Elazığ Volcanics

The Elazığ Volcanics have a similar mineral assemblage as the Tunceli Volcanics, thus characterized by basaltic lithologies. All studies samples are porphyritic with a total phenocryst content of ~20 vol.%, which is chiefly made up by olivine and to a lesser extent by plagioclase. In contrast to Tunceli Volcanics, clinopyroxene does not occur as a phenocryst phase in these lavas. In the Elazığ Volcanics, olivine constitutes approximately ~95 vol.% of the total phenocryst content, while plagioclase constitutes only ~5 vol.%. These phenocryst phases are embedded generally in a hypocrystalline groundmass and, to a lesser extent, in a holocrystalline groundmass. Plagioclase, clinopyroxene, Fe-Ti oxide phases, and olivine (in the order of decreasing abundance) represent the groundmass phases in these rocks. The common textures observed in the Elazığ Volcanics include intersertal, intergranular, glomeroporphyritic, trachytic, vesicular, and amygdaloidal (Figure 3.9).

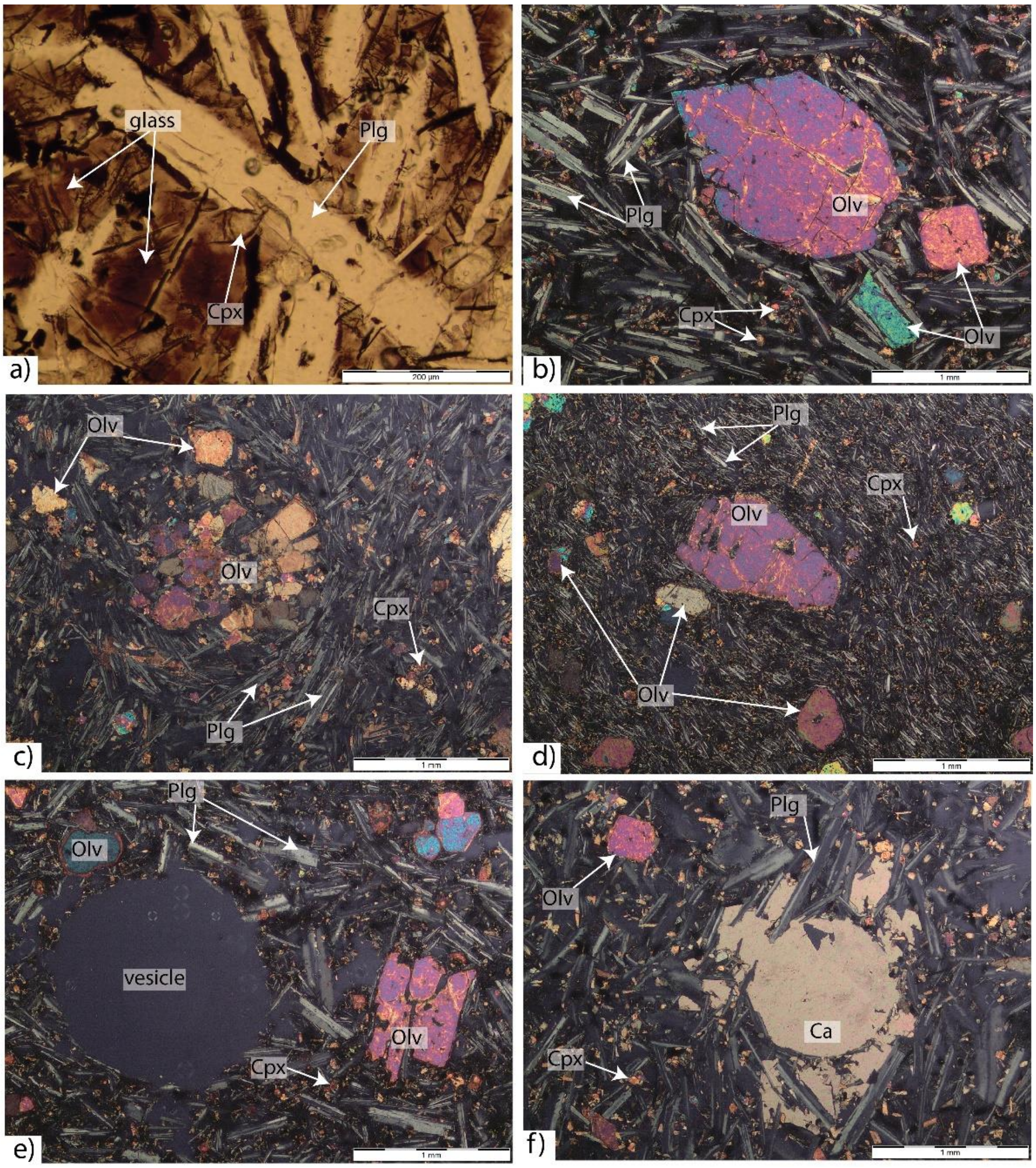

Figure 3.9. Microphotographs of the textures observed in the Elazığ Volcanics. a) Intersertal texture (Sample ID: BYD3, 4x, PPL). b) Intergranular texture (Sample ID: BYD32; 4x, XPL). c) Glomeroporphyritic texture (Sample ID: GMB11, 4x, XPL). d) Trachytic texture (Sample ID: GMB6, 4x, XPL) e) Vesicular texture (Sample ID: BYD28, 4x, XPL). f) Amygdaloidal texture (Sample ID: BYD20, 4x, XPL). Olv: olivine; Cpx: Clinopyroxene; Plg: Plagioclase; Ca: Calcite.

Olivine is the most abundant phenocryst in the Elazığ volcanism. It is usually found as subhedral and euhedral grains embedded in a hypocrystalline crystalline groundmass (Figure 3.10). Olivines are characteristically colorless, fractured, and have high relief under PPL (Figure 3.10). They exhibit a wide range of interference colors, reaching up to third-order, under XPL (Figure 3.10). Compared with the Tunceli Volcanics, the skeletal outlines are more abundant in the Elazığ Volcanics (Figure 3.11). Some skeletal olivines are relatively coarse, reaching up to 8 mm in some samples (Figure 3.11c-d). These coarse olivines generally have elongated shapes and display pinkish and bluish interference colors (Figure 3.11c). The skeletal textures of the olivines in the Elazığ Volcanics may be related to the rapid cooling effect or mineral-melt disequilibrium (e.g., Faure et al., 2003; 2007). Olivine grains are usually fresh; however, iddingsitization can occasionally be found as a secondary alteration product along their rims and fractures (e.g., Figure 3.10c-d). The olivines occasionally occupy the interstices of plagioclases; hence, they form the intergranular texture in the volcanics (Figure 3.9b). In some samples, olivine grains form glomeroporphyritic texture by clustering together in a fine-grained groundmass (Figure 3.9c).

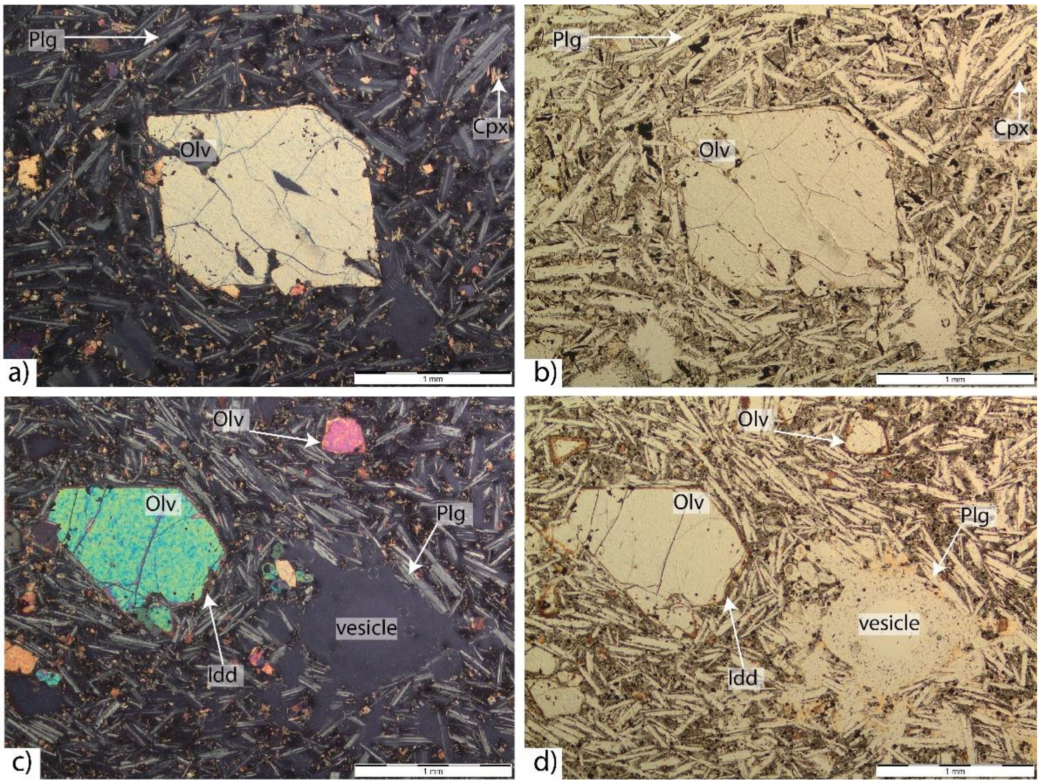

Figure 3.10. Microphotographs of the subhedral and euhedral olivine phenocrysts in the Elazığ Volcanics. a) Sample ID: BYD30, 4x, XPL. b) Sample ID: BYD30; 4x, PPL. c) Sample ID: BYD18, 4x, XPL; d) Sample ID: BYD18, 4x, PPL. Olv: Olivine; Cpx: Clinopyroxene; Plg: Plagioclase; Idd: Iddingsite.

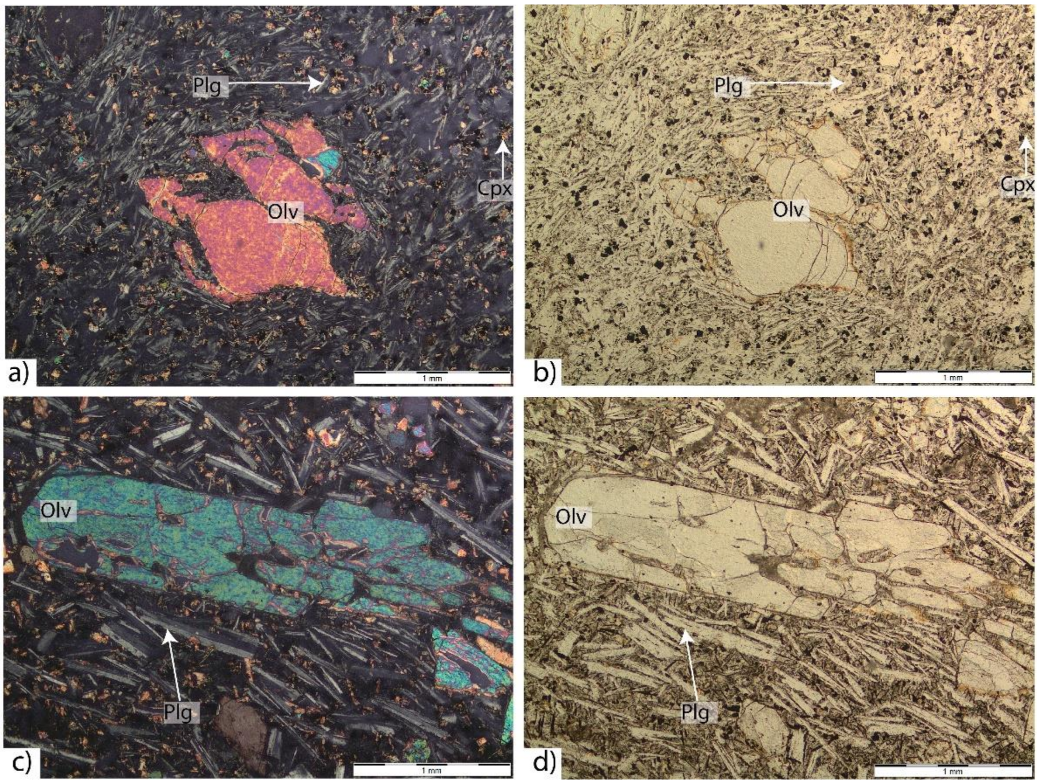

Figure 3.11. Microphotographs of the skeletal olivine phenocrysts in the Elazığ Volcanics. a) Sample ID: GMB10, 4x, XPL. b) Sample ID: GMB10; 4x, PPL. c) Sample ID: BYD1, 4x, XPL; d) Sample ID: BYD1, 4x, PPL. Olv: Olivine; Cpx: Clinopyroxene; Plg: Plagioclase.

Plagioclase occasionally occurs as a phenocryst phase in the Elazığ Volcanics. However, as in the Tunceli Volcanics, it represents the most abundant groundmass phase in the Elazığ Volcanics. They are recognized as colorless, low relief grains under PPL, and display first-order interference colors under XPL (Figure 3.12). They are usually fresh and exhibit subhedral to euhedral outlines (Figure 3.12). In contrast to the Tunceli Volcanics, concentric-zoned crystals are not observed in the Elazığ Volcanics. Multiple twinning is typical and shown by all plagioclase grains (Figure 3.12). Holocrystalline groundmass rarely occurs in the Elazığ Volcanics; therefore, the plagioclase laths are usually embedded in the hypocrystalline groundmass. In some instances, plagioclase laths display parallel/subparallel alignment to each other along the direction of lava flow, forming trachytic texture in these volcanics (e.g.,

Figure 3.9d). Also, as mentioned above, their interstices are occasionally occupied by other grains (e.g., olivine), developing intergranular texture in Elazığ Volcanism (e.g., Figure 3.9b).

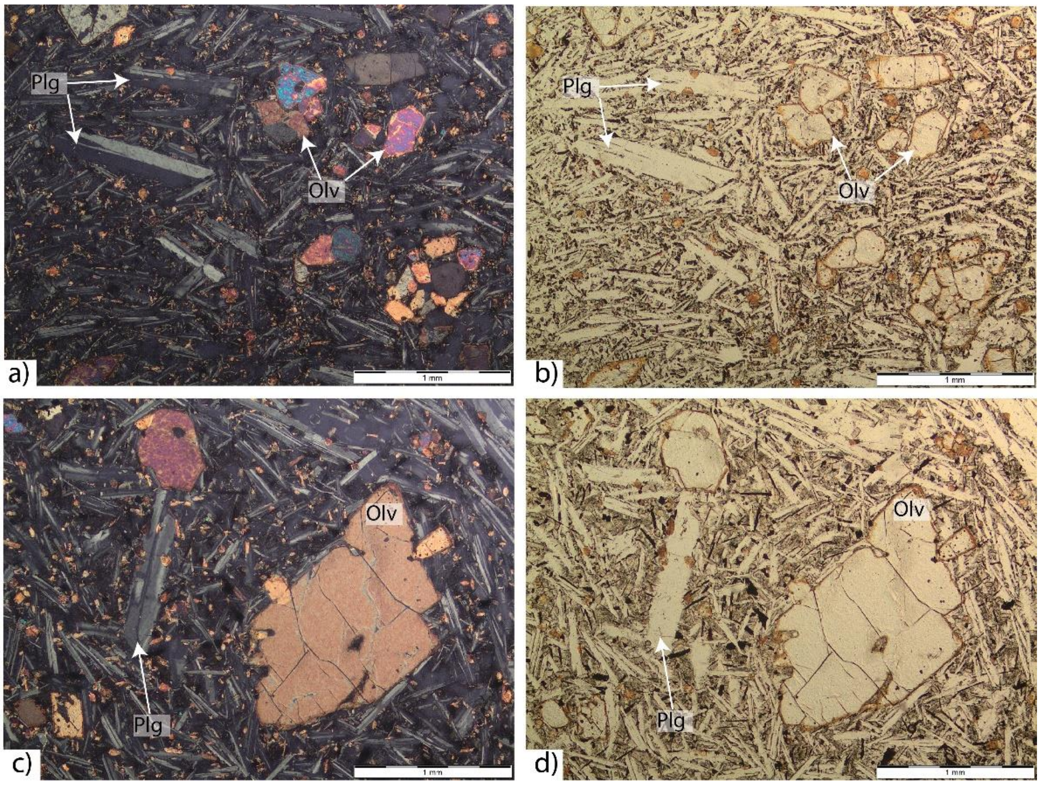

Figure 3.12. Microphotographs of the plagioclase phenocrysts in the Elazığ Volcanics. a) Sample ID: BYD13, 4x, XPL. b) Sample ID: BYD13; 4x, PPL. c) Sample ID: BYD1, 4x, XPL; d) Sample ID: BYD1, 4x, PPL. Olv: Olivine; Cpx: Clinopyroxene; Plg: Plagioclase.

Clinopyroxene is not observed as phenocryst phase in the Elazığ Volcanics. Instead, it is found as small grains with anhedral outlines (Figure 3.13). Clinopyroxene grains are, in generally, randomly distributed in a fine-grained groundmass, even though they can be observed as inclusions in plagioclases (Figure 3.13). Cleavage planes are not observable (Figure 3.13). Although colorless entities occur in these rocks, they usually display pale brownish and pinkish colors under PPL, and have moderate to high relief (Figure 3.13). The clinopyroxenes exhibit generally second-order interference colors under XPL in these rocks (Figure 3.13).

Opaque crystals in the Elazığ Volcanics are represented by cubic and skeletal magnetites and needle-like ilmenites as in Tunceli Volcanics (Figure 3.13). They are randomly embedded in a hypocrystalline/holocrystalline groundmass, and also occasionally found as inclusions in the Elazığ Volcanics (Figure 3.13). The skeletal magnetites, which may indicate the rapid cooling rates of magma, are usually found in the hypocrystalline samples.

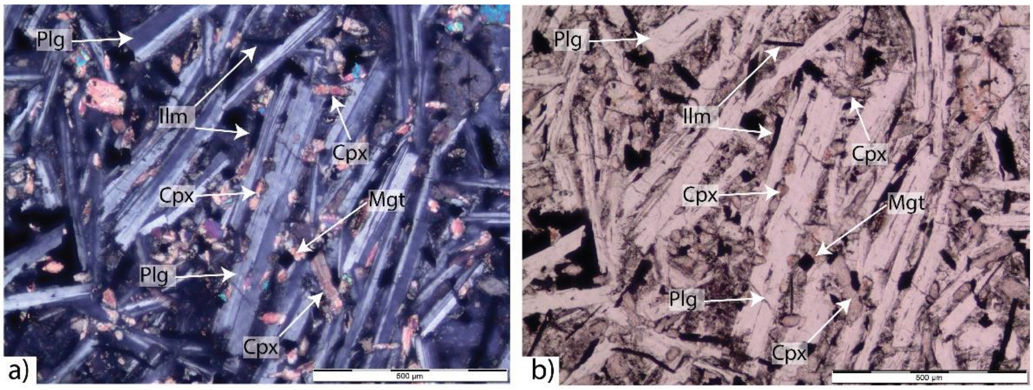

Figure 3.13. Microphotographs of the clinopyroxene aggregates and Fe-Ti oxides in the Elazığ Volcanics. a) Sample ID: BYD11, 10x, XPL. b) Sample ID: BYD11; 10x, PPL. Cpx: Clinopyroxene; Plg: Plagioclase; Mgt: Magnetite; Ilm: Ilmenite.

Apart from these major mineral assemblages mentioned above, apatite is also present in the Elazığ Volcanics, but it occurs as an accessory phase due to its small abundance. Apatite is usually found as euhedral, minute inclusions inside plagioclase phenocrysts (Figure 3.14). They are diagnostic with colorless appearance, moderate relief under PPL, and display first-order interference colors under XPL (Figure 3.14).

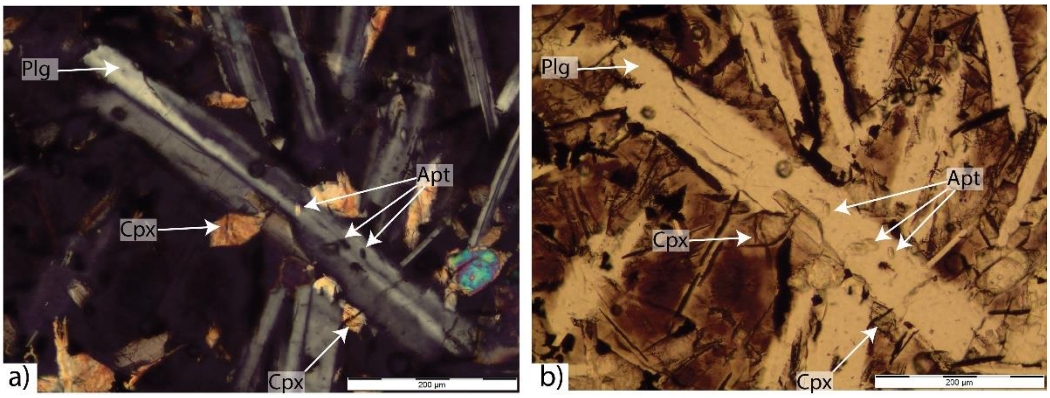

Figure 3.14. Microphotographs of the apatite inclusions in the plagioclase phenocrysts of Elazığ Volcanics. a) Sample ID: BYD3, 20x, XPL. b) Sample ID: BYD3; 20x, PPL. Cpx: Clinopyroxene; Plg: Plagioclase; Apt: Apatite.

Since Elazığ Volcanics rocks also display vesicular texture as Tunceli Volcanics, calcite also occurs as a secondary mineral in these rocks. It usually occurs as fracture-, cavity-, and vesicle-filling minerals in these volcanics (e.g., Figure 3.9f and Figure 3.15a-b). They are characteristically colorless under PPL and display very high birefringence under XPL. Calcite is volumetrically more abundant in the Elazığ Volcanics, when compared with the Tunceli Volcanics. Their widespread occurrence in the Elazığ Volcanics may be indicative of carbonate-rich fluid circulation in these rocks. Signs of possible water-rock interaction are also evident from the fracture networks in these volcanics. Although, this feature is not typical for the Elazığ volcanism; the groundmass in such cases appears to be highly altered throughout minor fracture systems (Figure 3.15c-d). This may also indicate a possible fluid circulation in these volcanics.

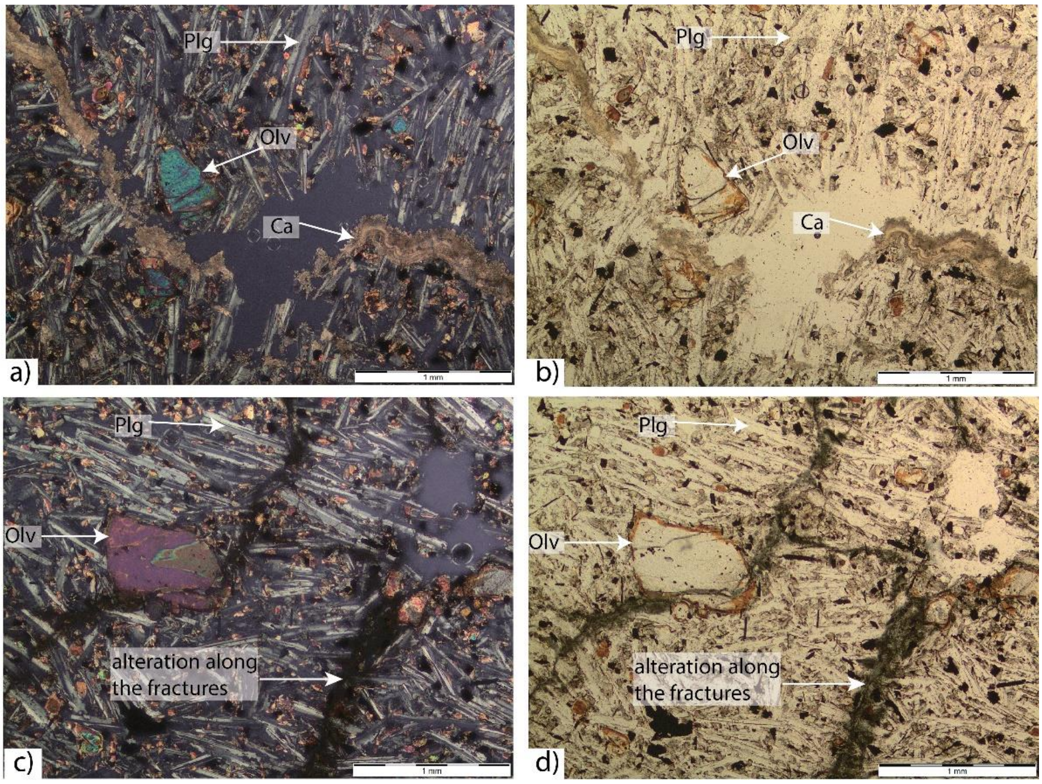

Figure 3.15. Microphotographs of the fracture systems in the Elazığ Volcanics. a) Sample ID: BYD5, 4x, XPL. b) Sample ID: BYD5; 4x, PPL. c) Sample ID: BYD14, 4x, XPL; d) Sample ID: BYD14, 4x, PPL. Olv: Olivine; Plg: Plagioclase; Ca: Calcite.

Another noticeable feature in the Elazığ volcanics is the presence of xenoliths and xenocrysts. The petrographic examination revealed that Elazığ lavas occasionally contain basaltic xenoliths and quartz xenocrysts (Figure 3.16). While sizes of the basaltic xenoliths ranges from 0.5 mm to 2-3 cm, quartz xenocrysts are much smaller, reaching up only to a few mm in the volcanics (Figure 3.16). The basaltic xenoliths in the volcanics are characterized by plagioclase microliths and opacitizated mafic assemblages (Figure 3.16a-b). The identification of these latter phases is possible due to the intensity of opaque replacement (Figure 3.16a-b). Plagioclase, on the other hand, can be recognized its first-order interference color, low relief, and subhedral to euhedral outlines (Figure 3.16a-b). Some plagioclase grains exhibit multiple twinning (Figure 3.16a-b). The quartz xenocrysts appear to have preserved their primary optical features in these basalts (Figure 3.16c-d). They are fresh, unaltered, have low relief and anhedral outlines (Figure 3.16c-d). Wavy extinction is characteristic. Also, these quartz xenocrysts in the Elazığ Volcanics are usually associated with a reaction corona made up of clinopyroxene aggregates (Figure 3.16c-d).

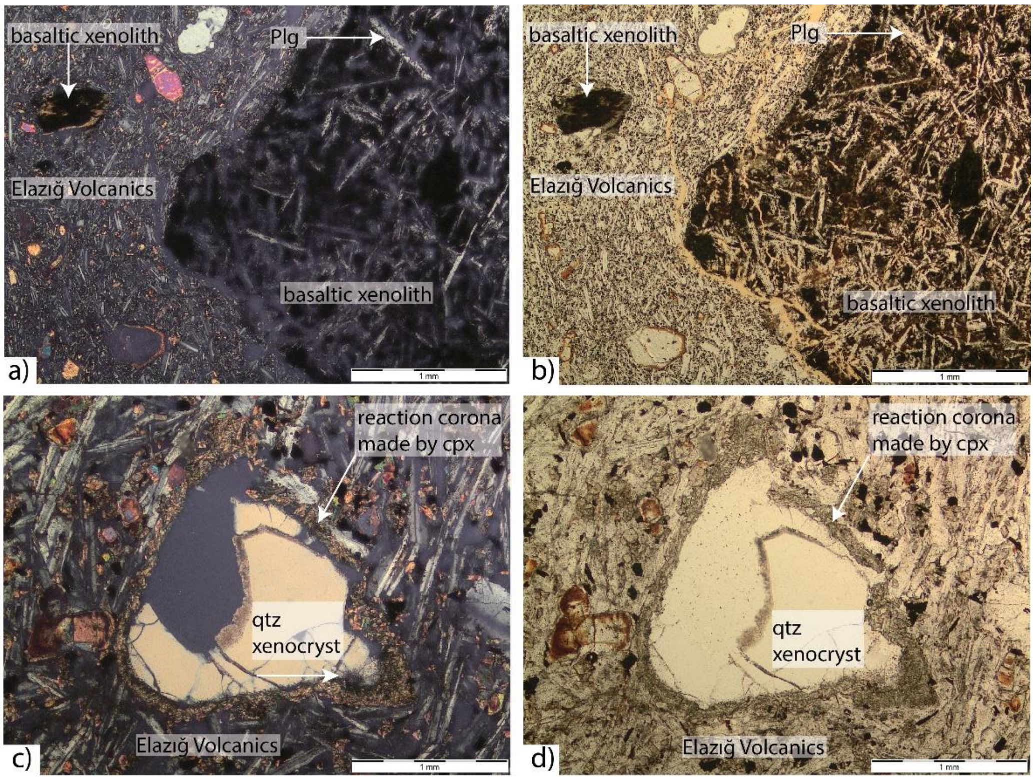

Figure 3.16. Microphotographs of the (a-b) basaltic xenolith and (c-d) quartz xenocryst in the Elazığ Volcanics. a) Sample ID: BYD24, 4x, XPL. b) Sample ID: BYD24; 4x, PPL. c) Sample ID: BYD6, 4x, XPL; d) Sample ID: BYD6, 4x, PPL. Plg: Plagioclase.

The lithology of the xenolith and type of the xenocryst indicate a crustal origin rather than a mantle origin. These crustal fragments are highly possibly incorporated into the Elazığ volcanism during the magma ascent. The basement rocks in the region (e.g., Elazığ Magmatics) may represent a possible candidate for the source of these “foreign” fragments in the Elazığ volcanism. As mentioned in the “GEOLOGY” chapter of this research, their presence probably indicates a possible crustal assimilation process during their petrogenesis.

The summary of the petrographic features of the Elazığ Volcanics can be found in the Table 3.1.

Table 3.1. Petrographic features of Tunceli and Elazığ Volcanics.

			Tunceli Volcanics	**Elazığ Volcanics**
Texture	**dominant**		aphyric/subophitic	porphyritic
	other		glomeroporphyritic, intergranular, intersertal, trachytic, vesicular, amygdaloidal	glomeroporphyritic, intergranular, intersertal, trachytic, vesicular, amygdaloidal
Crystallinity	**dominant**		holocrystalline	hypocrystalline
	other		hypocrystalline	holocrystalline
Phenocryst	**type**		olivine+clinopyroxene ±plagioclase	olivine±plagioclase
	size (mm)		<2	<4
	modal (%)	**total**	ca. 5	ca. 20
		interphase	olivine- ca. 60%; clinopyroxene- ca. 35; plagioclase- ca. 5%	olivine- ca. 95%; plagioclase- ca. 5%
Groundmass			plagioclase+olivine+clinopyroxene+ Fe-Ti oxide phases	plagioclase+clinopyroxene+Fe-Ti oxide phases+olivine
Accessory phases				apatite
Secondary minerals			calcite+zeolite+iddingsite +bowlingite	calcite+iddingsite

CHAPTER 4

GEOCHEMISTRY

4.1 Mineral Chemistry

4.1.1 Analytical Method

Following petrographical analyses, to reveal the chemical compositions of the minerals and their role in the petrogenetic evolution of the studied volcanics, 5 representative samples from Tunceli Volcanics and 5 from the Elazığ Volcanics have been selected for the Electron Probe Micro Analyses (EPMA). The chemical compositions of the minerals both from Tunceli and Elazığ Volcanics were determined at the Materials Characterization Laboratory, Pennsylvania State University (USA) using a CAMECA SX-50 microprobe. The analyses were conducted at 15Kv accelerating voltage and 30 nA beam current. The analytical diameter of the probe was 2 µm during the analyses. Results of the analyses can be found in Appendix A.

4.1.2 Tunceli Volcanics

4.1.2.1 Olivine

As mentioned in the "PETROGRAPHY" chapter, olivine is the most abundant phenocryst phase in the Tunceli Volcanics. The mineral chemistry analyses show that the olivines in Tunceli Volcanics are mainly forsterite-rich, and their compositions range between Fo_{59} and Fo_{85} (Figure 4.1). Although there is no rim measurement in the dataset, their EDS (Energy-dispersive Spectroscopy) chemical maps indicate that the olivines usually show normal zoning with a decrease in Fo towards their rims (Figure 4.2). No reversed-zoned olivines have been observed in the volcanics based on the EDS chemical maps. This may indicate that the magma did not experience an abrupt change in chemical and physical conditions during their crystallization (e.g., van Kooten and Buseck, 1978). This is also supported by the scarcity of the resorbed and skeletal olivines in the volcanics.

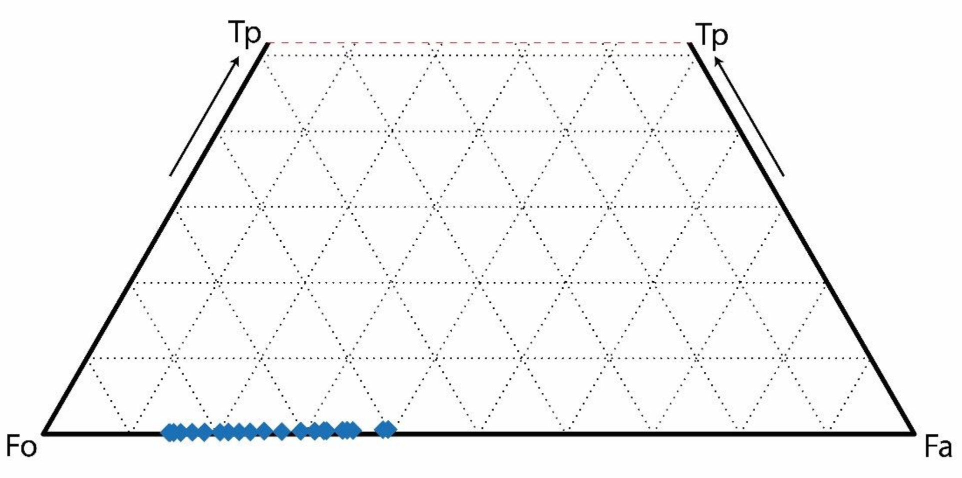

Figure 4.1. The Fo (Forsterite)-Tp (Tephroite)-Fa (Fayalite) ternary diagram showing the compositional range of the olivine crystals found in the Tunceli Volcanics.

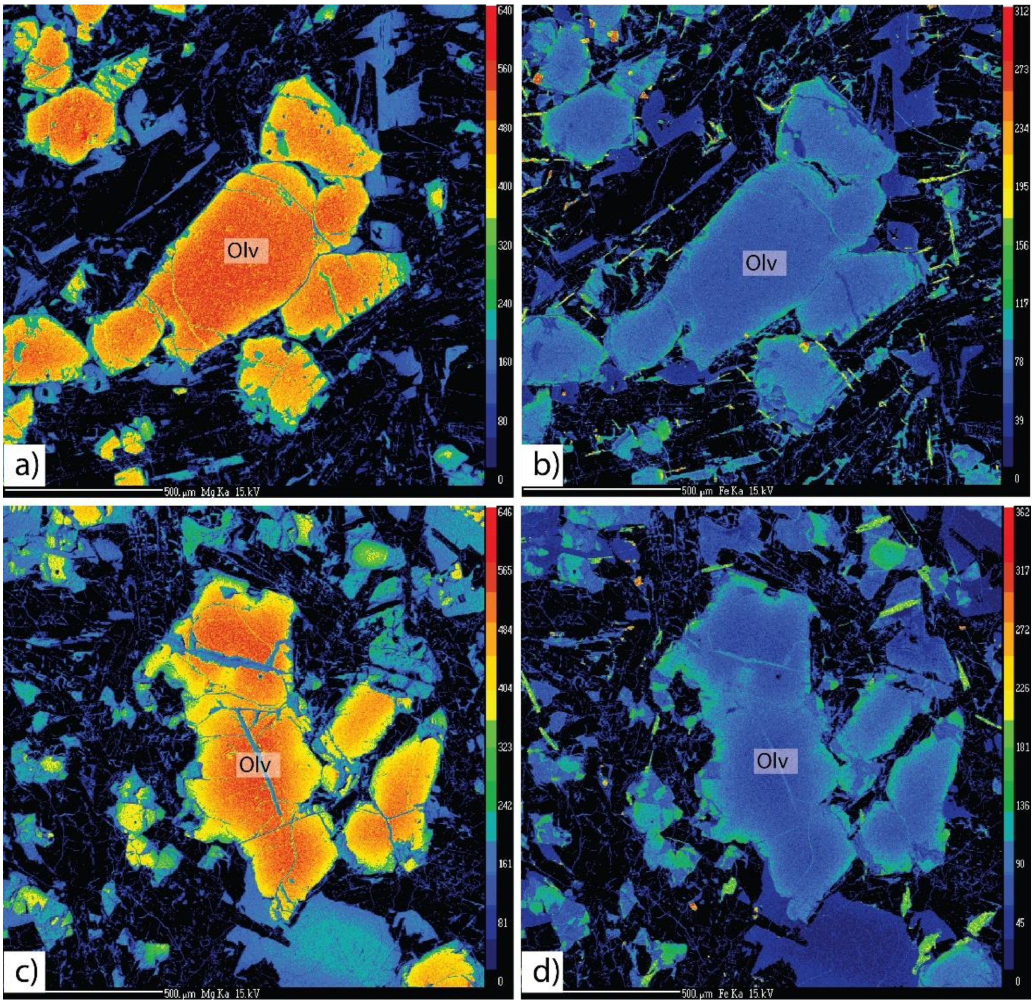

Figure 4.2. EDS chemical maps for the olivine crystals in Tunceli Volcanics. a) Sample ID: AV20, 500µm, for Mg. b) Sample ID: AV20, 500µm, for Fe. c) Sample ID: AV75, 500µm, for Mg. d) Sample ID: AV75, 500µm, for Fe.

Although disequilibrium textures are rare in the Tunceli lavas, a mineral-melt disequilibrium test of Roeder and Emslie (1970) was applied to reveal whether the olivine grains are in equilibrium with their coexisting melts or not (Figure 4.3). The partition coefficient (K_D) of Fe/Mg exchange between olivine and basaltic melt is 0.30 ±0.03 as calculated by Roeder and Emslie (1970). This value is assumed to stay constant under a wide range of chemical and physical conditions (e.g., Ulmer, 1989; Toplis and Carroll, 1995; Damasceno et al., 2002). The mineral-melt equilibrium conditions of olivines is well demonstrated by the plot of Fo content of olivine versus Mg# (Mg# = $100xMg^{+2}/(Mg^{+2}+Fe^{+2})$) assuming that $Fe^{+3}/Fe^{+2}=0.1$) host rock, which includes equilibrium field based on the calculations of Roeder and Emslie (1970) (e.g., Garcia, 1996; Damasceno et al., 2002). When the Fo content of the olivine phases in Tunceli Volcanics are plotted against the Mg# of their host rock, it is observed that while some grains plot within the equilibrium field, the majority fall below the equilibrium field in the diagram (Figure 4.3). Moreover, none of them plot above the equilibrium field (Figure 4.3).

Plotting of the samples above the equilibrium field in the diagram may suggest the addition of high Mg xenocrysts to the melt during the magma ascent or accumulation, whereas plotting below the field may be related to late-crystallization of the groundmass grains or not analyzing the equilibrated core compositions. (Damasceno et al., 2002). The absence of the data distribution above the equilibrium field argues against a xenocryst incorporation or a possible accumulation. This is also consistent with the lack of resorbed olivine grains in the Tunceli lavas. However, when it is considered that all mineral chemistry measurements in Tunceli lavas represent core measurements, the olivine data distributions below the equilibrium field in the plot appear to be most probably related with measurements of the late-crystallizing groundmass phases instead of not analyzing equilibrated core compositions. This, in accordance with the interpretations in the “PETROGRAPHY” chapter, indicates that the most of olivine grains in the holocrystalline groundmass of the Tunceli lavas represent the groundmass phases instead of initially crystallized phenocryst phases.

This also shows that the slow cooling rate may have caused the growth of late crystallized groundmass phases as large as phenocrysts phases in the Tunceli lavas.

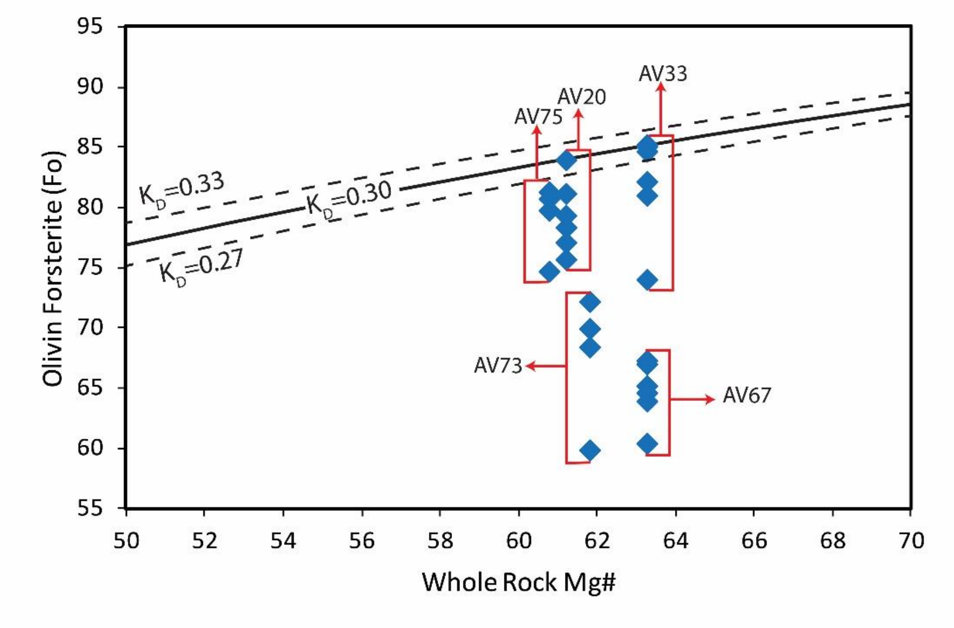

Figure 4.3. Mineral-melt Fe/Mg equilibrium diagram for olivine crystals found in Tunceli Volcanics. The equilibrium field is based on of Fe/Mg exchange partition coefficient (K_D) between olivine and basaltic melt (0.30 ±0.03, Roeder and Emslie, 1970).

4.1.2.2 Clinopyroxene

Clinopyroxene is the second most abundant mafic phase after olivine in the Tunceli Volcanics. Measurements from crystal cores indicate that the clinopyroxene compositions in Tunceli lavas characterized by diopside and augite (Figure 4.4). The majority of the clinopyroxenes plot within the augite field on the ternary plot of Wo-En-Fs with an average composition of $Wo_{42.82}En_{42.73}Fs_{14.45}$ (Figure 4.4). The 9 of the 26 samples, on the other hand, plot within the diopside field in the diagram with an average composition of $Wo_{46.27}En_{42.68}Fs_{11.04}$ (Figure 4.4). The Mg# (Mg# =

$100xMg^{+2}/(Mg^{+2}+Fe^{+2})$) of the clinopyroxenes range between 71.2-85.4. No resorbed or zoned clinopyroxene crystals have been observed in the Tunceli lavas during the petrographic examination. This observation is also consistent with their EDS chemical maps. In the EDS element maps, there is no evidence for a chemical zoning on the clinopyroxenes (Figure 4.5). This may argue against an abrupt change in the chemical conditions during their crystallization, such as secondary melt flux into magma.

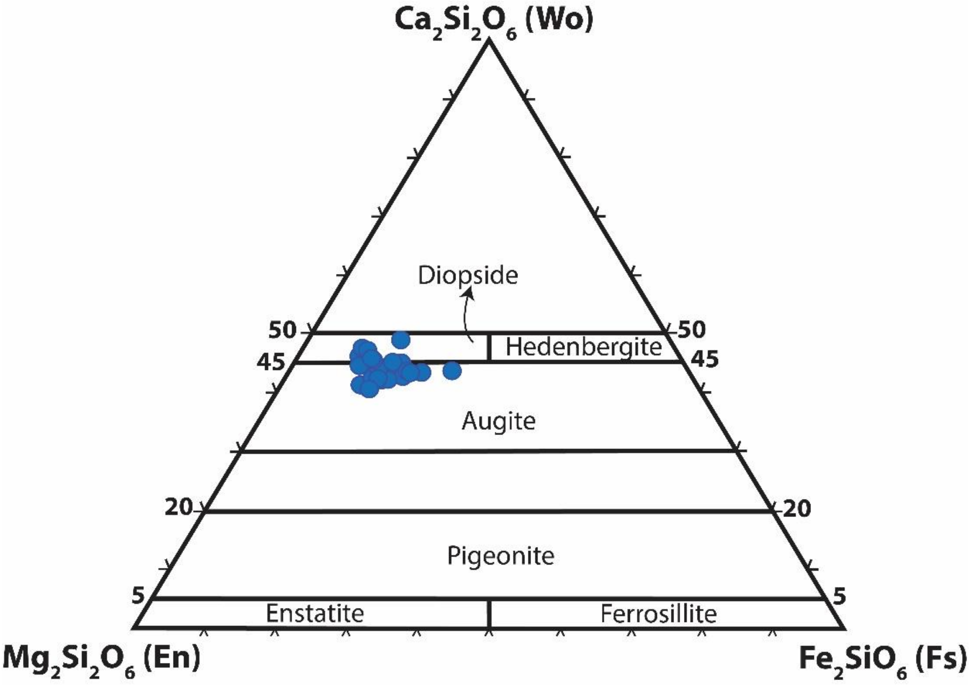

Figure 4.4. The En (Enstatite)-Wo (Wollastonite)-Fs (Ferrosillite) ternary diagram (Morimoto, 1988) showing the compositional range of the clinopyroxene crystals found in the Tunceli Volcanics.

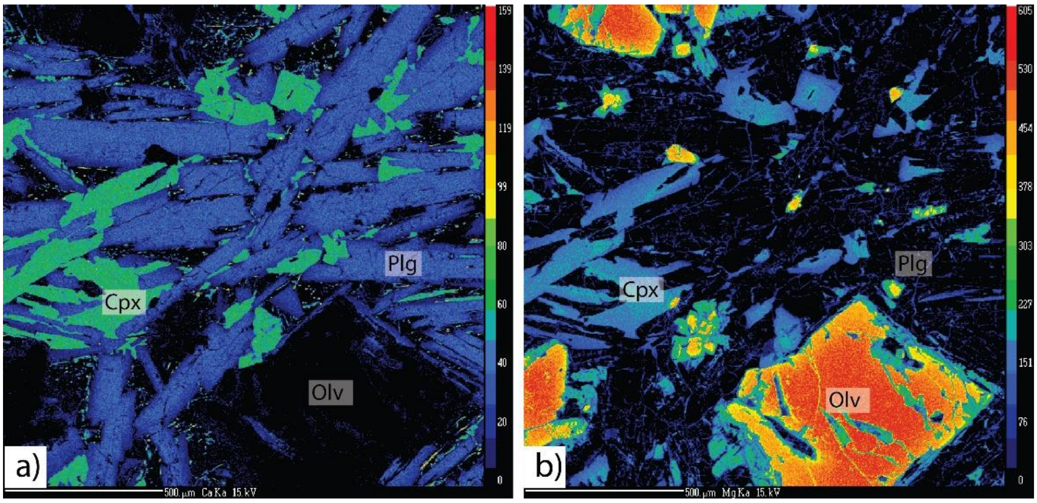

Figure 4.5. EDS chemical maps for the clinopyroxene crystals in the Tunceli Volcanics. a) Sample ID: AV75, 500µm, for Ca. b) Sample ID: AV75, 500µm, for Mg.

4.1.2.3 Plagioclase

Although plagioclase occurs as a major constituent of the groundmass, it is occasionally present as a phenocryst phase in the Tunceli Volcanics. The mineral chemistry analyses on the plagioclase grains have shown that they are primarily characterized by labradorite and andesine (Figure 4.6). Their compositions range between $An_{32.75}$ and $An_{65.91}$.

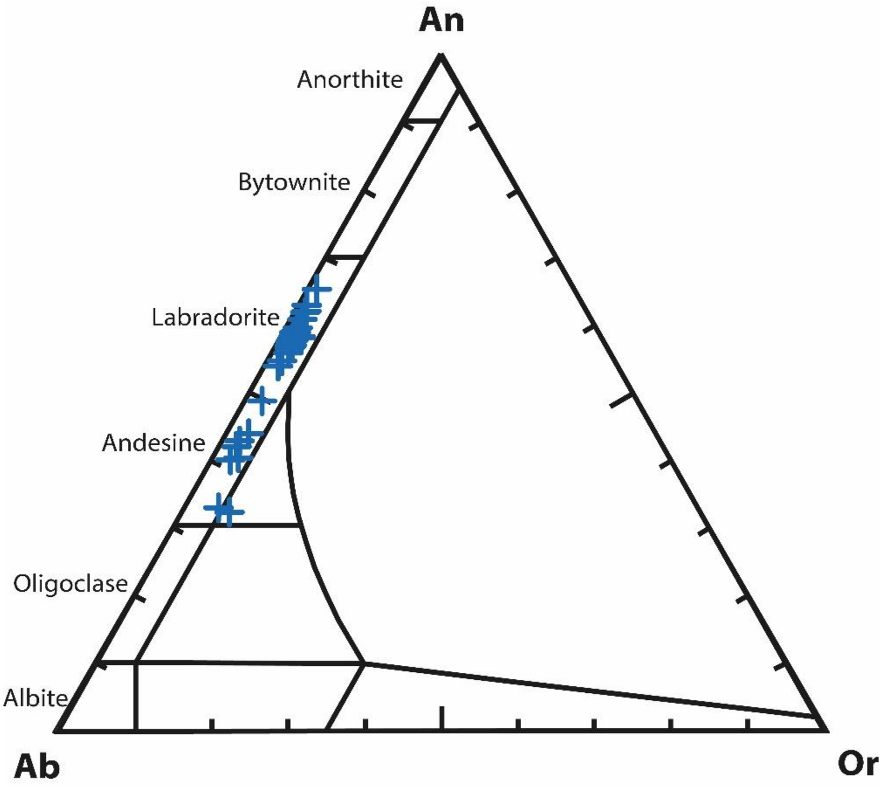

Figure 4.6. The Ab (Albite)-An (Anorthite)-Or (Orthoclase) ternary diagram showing the compositional range of the plagioclase crystals found in the Tunceli Volcanics.

4.1.2.4 Geothermobarometry

Mineral chemistry data provide an excellent opportunity to constrain the crystallization conditions of the minerals. This is very crucial for understanding the evolution of the magmatic systems. In particular, estimating the pressure (*P*) and temperature (*T*) parameters of the mineral crystallization (i.e., geothermobarometry) in volcanic rocks help to elucidate the depth and temperature of magma storage (e.g., Putirka et al., 1996). For that purpose, many calculation methods, which are applicable for the mineral chemistry data, have been proposed to determine the *P*-*T* conditions of the crystallization (e.g., Putirka et al., 1996; Putirka, 2005).

In this study, olivine, clinopyroxene, and plagioclase geothermobarometers of Putirka (2008) were applied to constrain the crystallization conditions of the Tunceli lavas. Note that the geothermobarometers of Putirka (2008) also include calibrations from Putirka (2005) and Putirka et al. (2007). The whole-rock data of the host rocks have been used as melt compositions in the calculations since there is no glass measurements are available.

The olivine-liquid thermometer of the Putirka et al. (2007) (Equation 22 in Putirka, 2008) has been applied on the equilibrium olivines (${}^{Fe/Mg}K_{Dmin/liq}$= 0.30 ±0.03 by Roeder and Emslie, 1970) in the Tunceli lavas. The estimated crystallization temperatures for these olivines range from 1287 to 1295 °C. On the other hand, the clinopyroxene-liquid equilibria geothermobarometer calculations of Putirka (2008) on the mineral chemistry data of the equilibrium clinopyroxenes (having Fe-Mg exchange coefficient (K_D) within range of 0.28 ± 0.08; Putirka, 2008) in the Tunceli lavas yielded crystallization temperatures between 1075 and 1153 °C (Equation 33; Putirka, 2008) and crystallization pressures between 4 and 10.2 kbar (Equation 32c; Putirka, 2008). Lastly, the plagioclase-liquid equilibria thermometer calculation of Putirka (2005) (Equation 23 in Putirka, 2008) yielded crystallization temperatures between 1158 and 1190 °C for the equilibrium plagioclases ($K_{D(Ab\text{-}An)}$ =0.28±0.11; Putirka, 2008) in the Tunceli lavas.

The crystallization temperatures indicate that olivine represents the first crystallizing phase in the Tunceli lavas, followed by plagioclase and clinopyroxene. The close crystallization temperatures of some clinopyroxenes and plagioclases may account for the subophitic textures observed in the Tunceli lavas. The similar nucleation and growth rates at similar temperatures may have given rise to the enclosing of the plagioclases by clinopyroxenes in these lavas.

The pressure estimated for the clinopyroxenes (4-10.2 kbar) enables the calculation of the magma storage depth. When the hydrostatic pressure in the magma chamber is assumed to be equal to surrounding lithostatic pressure, the depth of the magma storage can be revealed by the following equation;

$P: h\rho g$ (Eqn. 1)

P: pressure (pascal)

h: depth (m)

ρ: density of the overlying crustal column ($kg.m^{-3}$)

g: acceleration of gravity ($9.80665\ m.s^{-2}$)

The density of the granitic crustal density is assumed to range between 2600-2700 $kg.m^{-3}$ in the continental areas. When the density of the overlying crustal column is taken as 2700 $kg.m^{-3}$, the magma storage depth for Tunceli lavas ranges between 15-39 km according to the equation (Eqn. 1) above.

The summary of the mineral chemistry results of Tunceli Volcanics can be found in the Table 4.1.

4.1.3 Elazığ Volcanics

4.1.3.1 Olivine

Olivine is not only the most abundant phenocryst in the Elazig Volcanics, but also represents the sole mafic phenocryst phase of these volcanics. Their core measurements show that all olivines from the Elazığ volcanism are forsterite rich, and their composition displays a rather narrow range between Fo_{81-89} (Figure 4.7).

There is no rim measurement available in the data set; however, the EDS chemical maps of the olivines are usually suggestive of normal zoning. According to the EDS chemical maps, the Fo content of the olivines decreases towards their rims (Figure 4.8). This may argue against an abrupt change in the chemical composition of the magma during crystallization, such as secondary magma flux into the magma chamber.

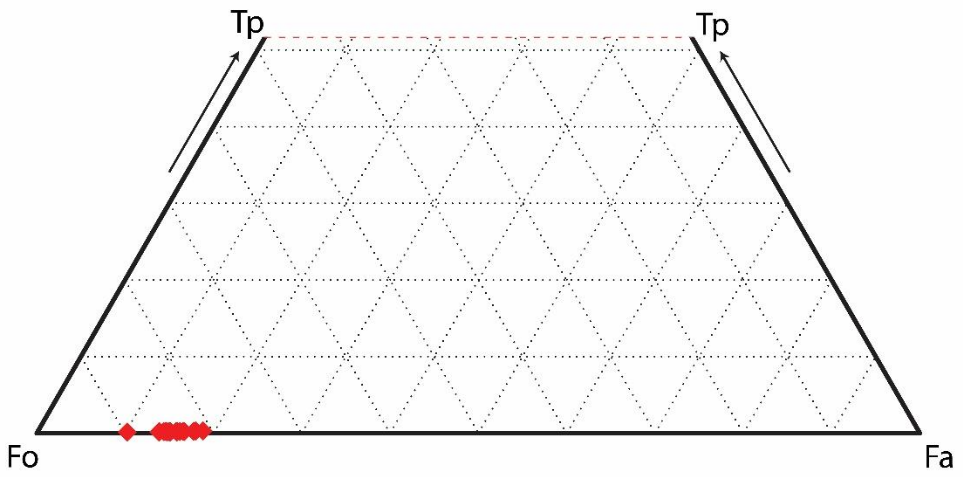

Figure 4.7. The Fo (Forsterite)-Tp (Tephroite)-Fa (Fayalite) ternary diagram showing the compositional range of the olivine phenocrsyts found in the Elazığ Volcanics.

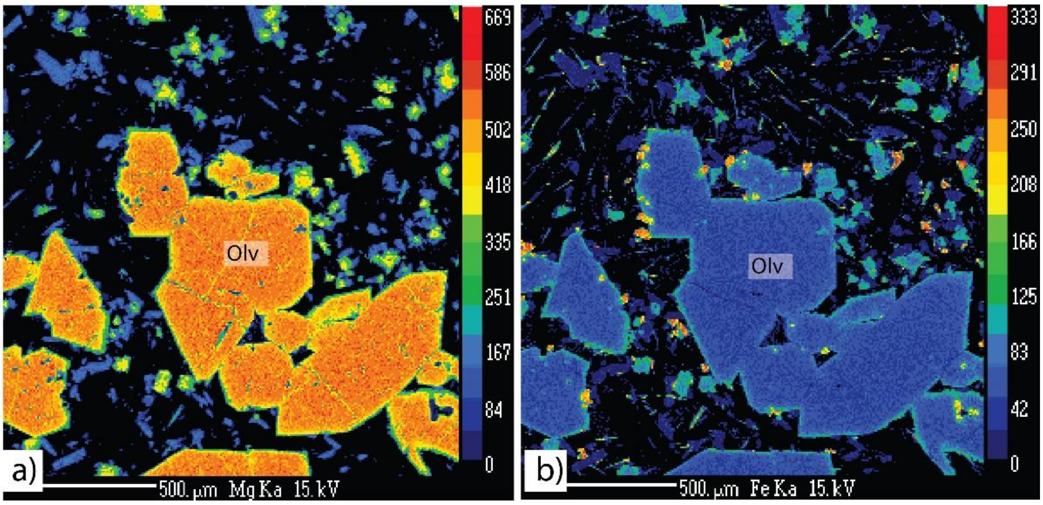

Figure 4.8. EDS chemical maps for the olivine crystals in Elazığ Volcanics. a) Sample ID: BYD10, 500µm, for Mg. b) Sample ID: BYD10, 500µm, for Fe.

As mentioned in the "PETROGRAPHY" chapter, skeletal olivines are abundant in the Elazığ lavas. This may also indicate disequilibrium conditions during crystallization. One possible scenario regarding the existence of skeletal olivines could be the resorption of mantle olivines by the melt during magma ascent. To test this phenomenon, mineral-melt disequilibrium test of Roeder and Emslie (1970) was applied. When the Fo content of the olivine phenocrysts in Elazığ Volcanics are plotted against the Mg# of their host rock, it appears that almost all olivines record mineral-liquid equilibrium (${}^{Fe/Mg}K_{Dmin/liq}$= 0.30 ±0.03; Roeder and Emslie, 1970) (Figure 4.9).

Only one sample is plotted well above the equilibrium field in the diagram (Figure 4.9). This may indicate the scarce addition of mantle xenoliths to the Elazığ volcanism during the magma ascent or accumulation during their evolution. A few samples plotting below the equilibrium field, on the other hand, may suggest analyzing groundmass phases or not analyzing the equilibrated core regions of the olivines (Figure 4.9).

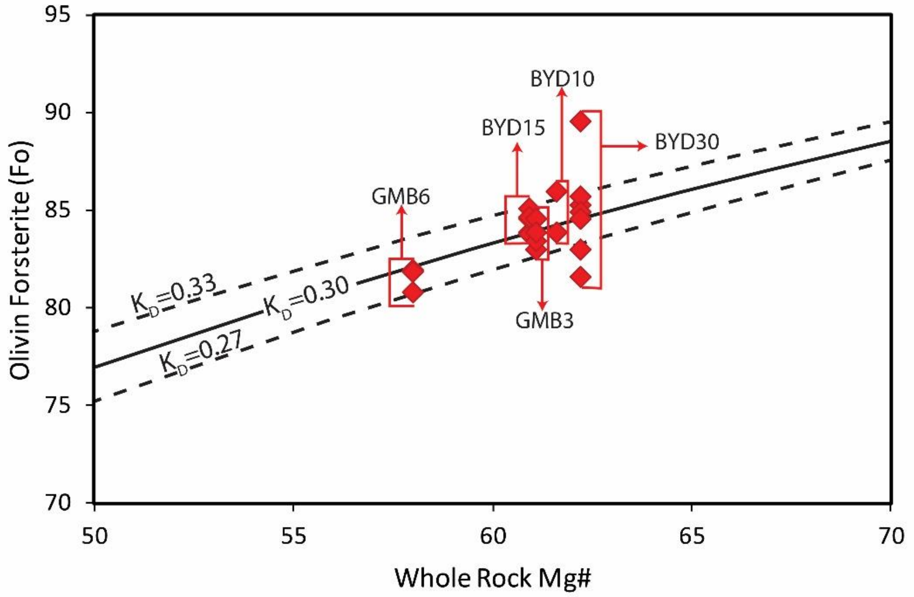

Figure 4.9. Mineral-melt Fe/Mg equilibrium diagram for olivine pohenocrysts found in the Elazığ Volcanics. The equilibrium field is based on of Fe/Mg exchange partition coefficient (K_D) between olivine and basaltic melt (0.30 ±0.03, Roeder and Emslie, 1970).

4.1.3.2 Plagioclase

The mineral chemistry analyses on occasionally found plagioclase phenocryst phases have revealed two distinct populations of plagioclase in the Elazığ lavas. They span a narrow compositional range between labradorite and andesine with an anorthite (An) content between 46-58 (Figure 4.10).

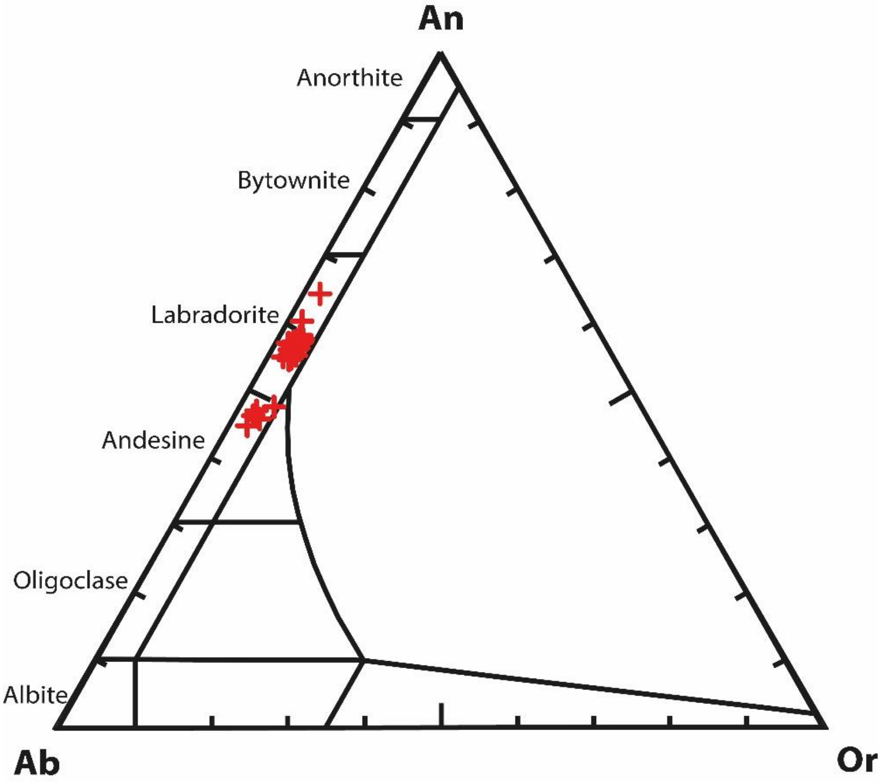

Figure 4.10. The Ab (Albite)-An (Anorthite)-Or (Orthoclase) ternary diagram showing the compositional range of the plagioclase crystals found in the Elazığ Volcanics.

Although the open-system processes such as melt mixing cannot be totally ruled out since there is no rim measurement available on plagioclases, the absence of the zoning patterns on the plagioclases in Elazığ volcanism may argue against such processes. Thus compositional variation in the plagioclase population of Elazığ volcanism may rather be related to the decompression degassing and change in the temperature during magma ascent in a closed-system (Ruprecht and Wörner, 2007).

4.1.3.3 Geothermobarometry

The core compositions of the equilibrium ($^{Fe/Mg}K_{Dmin/liq}$= 0.30 ±0.03 by Roeder and Emslie, 1970) olivines in the Elazığ lavas yielded temperatures of 1258-1289 °C, following the olivine-liquid thermometer of the Putirka et al. (2007) (Equation 22 in Putirka, 2008). The equilibrium ($K_{D(Ab\text{-}An)}$ =0.28±0.11; Putirka, 2008) plagioclase phenocryst compositions, on the other hand, yielded temperatures between 1121 and 1165 °C based on the plagioclase-liquid equilibria thermometer calculation of Putirka (2005) (Equation 23 in Putirka, 2008). Since there is no clinopyroxene phenocryst available in the Elazığ lavas, a robust approximation to magma storage depth cannot be developed. However, the plagioclase-liquid barometer, which is assumed not to be reliable as much as clinopyroxene barometers (Putirka, 2008), suggests magma storage pressures between 12 and 13 kbar, corresponding to depths of 45.3-49.09 km following the Eqn. 1 above.

Although clinopyroxene phenocrysts are not found in the Elazığ lavas in this study, Di Giuseppe et al. (2017) reported some mineral chemistry data in Elazığ Volcanics. They also have reported high-pressure crystallization conditions (9.6- 16.4 kbar; Di Giuseppe et al., 2017) for the Elazığ volcanism. If this is the case, Elazığ volcanism appears to have been crystallized at the base of the crust in Eastern Anatolia (see Angus et al., 2006) and record deeper crystallization conditions compared to the Tunceli volcanism.

The summary of the mineral chemistry results of Elazığ Volcanics can be found in the Table 4.1.

Table 4.1. Summary of the mineral chemistry results of the Tunceli and Elazığ Volcanics. For the P-T calculations the geothermobaramoters of Putirka et al. (1996; 2007); Putirka (2005; 2008) were used.

	Tunceli Volcanics		**Elazığ Volcanics**	
	Composition	T (°C)-P (kbar)	Composition	T (°C)-P (kbar)
Olivine	Fo_{59-85}	1287-1295 °C	Fo_{81-89}	1258-1289 °C
Clinopyroxene	$Wo_{43-46}En_{43}Fs_{11-14}$	1075-1153 °C; 4-10.2 kbar	-	-
Plagioclase	An_{33-66}	1158-1190 °C	An_{46-58}	1121-1165 °C; 12-13 kbar

4.2 Major and Trace Element Geochemistry

4.2.1 Analytical Method

After petrographical examinations, least-altered samples among the volcanics were chosen for the whole-rock major-trace element geochemical analyses. Whole-rock major and trace element concentrations of 23 basaltic samples from Tunceli volcanism and 19 basaltic samples from Elazığ volcanism were determined by Inductively Coupled Plasma-Atomic Emission Spectrometry (ICP-AES) and Inductively Coupled Plasma-Mass Spectrometry (ICP-MS) at the ACME Analytical Laboratories Ltd., Vancouver, Canada.

Before the analysis, each basaltic sample was crushed and powdered using jaw crushers and a tungsten carbide disc mill. Powders of each sample (0.2 gr) were fused using 1.5 gr $LiBO_2$, and then dissolved in 100 ml 5% HNO_3. The loss on ignition (LOI) values were determined according to the weight difference after ignition at 1000 ^{o}C. Detection limits for the major oxides, trace, and rare earth (REE) elements range from 0.002 to 0.04 wt.%, 0.1 to 8 ppm, and 0.01 to 0.1 ppm, respectively. Analytical precision was determined according to the replicate analyses and standard measurement. Reproducibility of the analyses for most of major oxide and trace elements, including the REE, is within 5%. The whole-rock major, trace, and rare element data of the Tunceli and Elazığ Volcanics are available in Table 4.2 and Table 4.3, respectively.

As mentioned in the “INTRODUCTION” chapter, the major-trace element concentrations of the 23 basaltic samples from the Tunceli Volcanics were obtained during the M.Sc. thesis of Aktağ (2014). The whole-rock major-trace element data of the Tunceli Volcanics have been reevaluated with their new whole-rock Sr-Nd-Pb-Hf isotope data within the scope of this research.

Table 4.2. Major (wt.%), trace (ppm) and rare earth (ppm) elements composition for the Tunceli Volcanics. MA: Mildly Alkaline Samples. T: Tholeiitic Samples (from Aktağ et al. 2019).

Charac.	MA	T	T	MA	T	MA	T	MA	MA	MA	MA
ID	**AV2**	**AV8**	**AV12**	**AV16**	**AV20**	**AV21**	**AV22**	**AV24**	**AV28**	**AV33**	**AV34**
SiO_2	48.86	49.29	49.32	48.11	49.14	48.01	51.04	48.55	45.87	46.08	48.90
Al_2O_3	15.10	15.42	16.31	14.99	14.39	14.94	17.44	14.85	14.63	14.64	14.85
Fe_2O_3	11.19	11.93	11.50	10.43	10.84	10.56	7.82	11.09	10.14	10.19	10.96
MgO	7.78	8.20	6.26	8.50	8.62	8.65	3.46	8.48	8.96	8.87	8.33
CaO	6.90	8.96	8.92	8.07	7.67	8.00	10.00	7.45	9.36	9.72	7.39
Na_2O	3.85	3.21	3.38	3.17	3.11	3.17	3.74	3.38	3.16	3.55	3.64
K_2O	1.70	0.59	0.70	1.09	1.07	1.11	1.23	1.40	1.48	1.73	1.28
TiO_2	1.75	1.22	1.30	1.53	1.49	1.55	1.30	1.65	1.67	1.71	1.65
P_2O_5	0.46	0.16	0.18	0.42	0.22	0.45	0.38	0.41	0.94	0.99	0.37
MnO	0.15	0.16	0.15	0.13	0.13	0.15	0.16	0.15	0.15	0.15	0.14
Cr_2O_3	0.030	0.060	0.051	0.041	0.039	0.040	0.007	0.036	0.031	0.032	0.043
LOI	1.9	0.5	1.7	3.2	3.0	3.0	3.2	2.1	3.1	1.8	2.0
Sum	99.67	99.75	99.76	99.68	99.72	99.66	99.74	99.57	99.51	99.50	99.63
Ba	296	165	167	333	162	334	371	786	571	616	257
Co	44.1	51.4	52.3	41.5	47.9	45.2	28.3	48.0	44.3	43.9	46.4
Cs	0.9	0.2	<0.1	0.2	0.2	4.6	0.8	0.5	0.5	1.4	0.5
Ga	18.9	18.1	18.1	18.1	18.5	18.2	18.0	17.7	18.3	18.8	17.6
Hf	4.0	1.9	2.2	2.6	2.7	3.3	3.8	3.4	3.9	4.2	3.2
Nb	21.3	7.6	8.3	16.1	10.9	17.7	14.1	19.1	43.3	41.5	17.6
Rb	33.6	7.0	11.2	19.9	21.6	25.1	22.7	29.4	24.4	30.1	26.2
Sr	642.3	307.6	352.8	609.0	340.7	613.4	618.3	1027.8	1294.2	1345.7	1061.9
Ta	1.4	0.4	0.5	0.7	0.7	0.7	0.8	1.1	2.0	2.0	1.0
Th	3.9	1.5	1.6	5.7	4.1	6.4	7.4	5.1	10.7	10.8	4.0
U	1.6	0.4	0.4	1.2	0.7	1.0	1.6	1.5	2.5	2.5	1.1
V	164	182	205	186	185	202	194	187	175	172	172
Zr	166.3	84.2	86.3	119.1	103.9	126.7	171.2	131.7	178.1	184.7	128.1
Y	20.5	18.7	16.9	20.7	20.8	22.5	24.0	21.1	24.9	26.1	18.8
Mo	1.1	0.2	0.7	0.6	1.0	1.2	0.5	1.2	1.9	2.3	1.1
Cu	57.6	65.3	46.6	34.3	47.1	37.2	51.4	44.8	45.1	50.8	39.4
Pb	5.6	2.9	2.0	4.9	2.7	5.9	2.6	2.2	6.7	7.2	3.2
Zn	84	61	78	65	69	75	57	76	61	68	62
Ni	154.5	219.5	184.5	106.1	171.3	107.4	31.4	166.5	168.5	145.0	140.7
Sc	16	21	20	19	19	19	22	19	17	17	18

Table 4.2. *(Cont'd)*

Charac.	MA	T	T	MA	T	MA	T	MA	MA	MA	MA
ID	**AV2**	**AV8**	**AV12**	**AV16**	**AV20**	**AV21**	**AV22**	**AV24**	**AV28**	**AV33**	**AV34**
La	28.0	10.0	9.6	37.3	15.4	39.2	32.7	31.1	82.1	84.8	29.6
Ce	55.5	18.6	19.7	72.4	31.1	74.5	64.9	59.4	148.9	155.4	58.0
Pr	6.11	2.41	2.46	7.35	3.62	7.68	6.84	6.11	14.76	14.95	5.83
Nd	23.7	11.6	10.7	24.7	14.7	29.4	27.1	22.9	52.0	50.8	21.8
Sm	4.98	2.66	2.66	5.25	3.46	5.42	5.14	4.61	8.07	8.55	4.46
Eu	1.63	0.99	1.01	1.63	1.20	1.57	1.53	1.49	2.43	2.48	1.51
Gd	4.82	3.29	3.04	4.87	3.93	5.06	4.90	4.67	6.96	7.04	4.43
Tb	0.78	0.62	0.57	0.80	0.69	0.79	0.82	0.75	1.00	1.06	0.73
Dy	4.16	3.35	3.11	4.29	3.85	4.31	4.46	3.93	5.09	5.35	3.95
Ho	0.67	0.68	0.61	0.87	0.79	0.84	0.95	0.77	0.90	0.97	0.78
Er	2.09	1.80	1.88	2.21	2.19	2.24	2.49	2.13	2.52	2.59	1.98
Tm	0.26	0.28	0.25	0.32	0.30	0.31	0.36	0.30	0.31	0.34	0.32
Yb	1.80	1.65	1.48	1.74	1.89	1.85	2.62	1.82	2.13	2.03	1.62
Lu	0.24	0.25	0.24	0.28	0.26	0.29	0.35	0.26	0.29	0.30	0.25

Table 4.2. *(Cont'd)*

Charac.	MA	MA	T	T	MA	MA	T	T	MA	MA	MA	MA
ID	**AV36**	**AV38**	**AV40**	**AV42**	**AV49**	**AV59**	**AV67**	**AV68**	**AV70**	**AV72**	**AV73**	**AV75**
SiO_2	48.62	48.72	48.57	48.62	49.09	49.36	48.46	48.34	49.14	48.53	48.34	48.54
Al_2O_3	14.73	14.77	14.93	14.79	15.73	15.48	15.11	15.35	15.91	14.57	14.32	14.93
Fe_2O_3	10.99	10.71	11.72	11.57	11.82	10.98	11.49	12.14	11.37	11.21	11.23	11.28
MgO	8.38	8.54	9.31	9.78	7.61	8.02	10.00	7.85	7.42	8.68	9.18	8.84
CaO	7.57	7.90	8.26	8.16	6.91	8.62	8.21	8.93	8.30	7.69	7.44	7.65
Na_2O	3.28	3.21	3.09	2.98	3.84	3.47	2.95	3.11	3.50	3.18	3.66	3.26
K_2O	1.34	1.09	0.84	0.66	1.77	1.08	0.62	0.65	1.14	1.15	1.20	1.00
TiO_2	1.65	1.57	1.40	1.31	1.83	1.59	1.22	1.29	1.60	1.66	1.79	1.58
P_2O_5	0.38	0.43	0.20	0.16	0.54	0.45	0.15	0.17	0.42	0.26	0.32	0.32
MnO	0.15	0.14	0.16	0.15	0.16	0.15	0.15	0.16	0.15	0.15	0.15	0.14
Cr_2O_3	0.040	0.044	0.045	0.046	0.029	0.040	0.049	0.052	0.045	0.044	0.047	0.038
LOI	2.5	2.5	1.1	1.5	0.3	0.4	1.3	1.7	0.7	2.6	2.0	2.1
Sum	99.67	99.67	99.70	99.72	99.65	99.67	99.72	99.75	99.70	99.70	99.69	99.69
Ba	274	313	132	119	362	345	104	158	300	177	183	233
Co	45.7	43.3	53.5	53.0	47.8	43.2	54.5	52.7	42.4	47.0	49.1	47.4
Cs	0.5	0.4	0.1	0.2	0.7	0.2	0.3	0.2	<0.1	0.1	0.4	0.2
Ga	17.9	18.2	18.1	17.1	21.4	19.5	17.8	17.0	19.0	18.8	18.3	17.8
Hf	3.4	3.1	2.6	1.9	4.7	2.5	2.0	1.9	2.6	3.1	3.3	3.2
Nb	18.3	15.6	10.4	7.6	24.5	16.3	7.0	7.2	15.2	14.2	17.0	13.8
Rb	26.6	20.6	13.6	11.8	30.6	20.1	12.4	11.9	19.1	18.8	20.7	13.5
Sr	724.3	612.0	421.7	312.1	739.4	684.3	303.8	294.4	622.0	505.3	518.2	460.9
Ta	1.1	0.8	0.6	0.4	1.4	0.8	0.4	0.4	0.7	0.8	1.0	0.8
Th	4.3	5.8	1.9	1.7	4.1	6.0	1.4	1.4	5.2	2.5	2.8	4.0
U	1.1	1.4	0.6	0.5	1.6	1.1	0.5	0.5	0.9	0.5	0.7	0.4
V	172	183	191	185	167	194	172	189	186	175	173	194
Zr	134.6	127.5	99.3	86.2	192.8	121.5	79.9	82.4	118.5	113.4	137.2	123.8
Y	19.8	22.1	19.7	18.0	21.6	21.9	16.8	21.6	20.7	18.4	18.5	20.7
Mo	0.3	0.9	0.9	0.6	2.2	1.1	0.7	0.2	1.1	0.4	0.8	0.4
Cu	43.4	31.7	67.5	68.7	54.3	30.7	62.6	35.7	35.9	53.1	50.6	39.3
Pb	2.8	4.7	3.6	2.7	4.9	4.9	2.0	1.0	4.6	4.3	2.3	4.8
Zn	66	70	74	72	87	76	72	76	70	61	69	69
Ni	129.3	98.5	200.0	215.8	160.6	113.2	223.4	225.0	122.6	154.1	181.9	154.5
Sc	18	19	20	20	16	20	20	21	21	18	18	20

Table 4.2. *(Cont'd)*

Charac.	MA	MA	T	T	MA	MA	T	T	MA	MA	MA	MA
ID	**AV36**	**AV38**	**AV40**	**AV42**	**AV49**	**AV59**	**AV67**	**AV68**	**AV70**	**AV72**	**AV73**	**AV75**
La	29.3	38.2	12.5	9.5	30.2	39.2	8.7	12.4	32.8	16.1	18.5	24.7
Ce	57.7	72.8	25.0	19.8	61.0	72.0	18.5	20.2	60.0	32.3	39.8	49.8
Pr	5.87	7.30	2.95	2.44	6.56	7.40	2.16	2.59	6.45	3.81	4.41	5.17
Nd	22.3	28.2	12.6	10.8	25.7	29.0	10.0	10.7	24.5	15.0	16.8	19.9
Sm	4.61	5.11	3.04	2.77	5.45	4.99	2.38	2.97	4.72	3.95	4.05	4.51
Eu	1.48	1.56	1.09	0.98	1.72	1.64	0.95	1.04	1.53	1.27	1.41	1.42
Gd	4.33	4.83	3.60	3.25	5.22	4.98	2.99	3.45	4.58	3.96	4.33	4.43
Tb	0.76	0.83	0.63	0.58	0.85	0.78	0.53	0.62	0.75	0.73	0.73	0.74
Dy	3.87	4.27	3.58	3.29	4.00	4.17	2.96	3.55	4.04	4.02	3.60	3.83
Ho	0.81	0.80	0.73	0.68	0.80	0.84	0.62	0.75	0.76	0.76	0.68	0.82
Er	1.91	2.21	2.12	2.10	2.02	2.01	1.67	2.07	2.23	1.94	1.89	2.21
Tm	0.29	0.34	0.29	0.26	0.27	0.29	0.25	0.27	0.28	0.28	0.28	0.29
Yb	1.31	1.55	1.69	1.66	1.70	2.06	1.38	1.75	1.94	1.52	1.59	1.86
Lu	0.25	0.32	0.25	0.25	0.25	0.26	0.23	0.24	0.27	0.23	0.23	0.24

Table 4.3. Major (wt.%), trace (ppm), and rare earth (ppm) elements composition for the Elazığ Volcanics (this study).

ID	**BYD1**	**BYD3**	**BYD7**	**BYD10**	**BYD14**	**BYD15**	**BYD16**	**BYD18**	**BYD23**
SiO_2	47.49	47.08	48.23	48.09	48.27	49.12	49.09	48.60	45.95
Al_2O_3	16.28	16.17	16.66	16.66	16.68	16.85	16.87	17.01	15.61
Fe_2O_3	9.42	9.60	9.52	9.05	9.20	9.00	8.98	9.04	9.67
MgO	8.13	8.24	7.60	7.33	7.41	7.09	7.25	7.22	7.94
CaO	8.13	8.24	7.40	7.75	7.62	7.37	7.12	7.39	9.33
Na_2O	3.60	3.83	4.31	4.21	4.44	4.41	4.35	4.14	3.17
K_2O	2.59	2.59	2.58	2.51	1.80	2.51	2.53	2.52	2.61
TiO_2	2.12	2.11	1.99	1.88	1.90	1.85	1.85	1.86	2.00
P_2O_5	0.63	0.58	0.71	0.75	0.77	0.73	0.76	0.74	0.67
MnO	0.15	0.15	0.15	0.14	0.14	0.14	0.14	0.14	0.16
Cr_2O_3	0.033	0.039	0.034	0.037	0.033	0.035	0.031	0.034	0.030
LOI	1.0	1.0	0.4	1.2	1.3	0.5	0.6	0.9	2.4
Sum	99.68	99.68	99.66	99.67	99.68	99.68	99.67	99.68	99.66
Ba	392	399	430	441	417	439	430	602	538
Co	33.2	35.8	32.6	30.4	32.2	30.1	32.6	31.6	36.6
Cs	0.4	0.6	0.3	0.4	0.5	0.2	0.4	0.5	0.7
Ga	17.2	17.1	17.5	14.9	16.3	17.8	17.5	17.5	18.9
Hf	4.8	4.6	5.1	5.0	5.4	5.6	5.4	5.5	5.3
Nb	47.0	47.6	60.8	61.4	63.6	63.6	63.0	64.8	62.5
Rb	45.8	42.7	42.2	38.9	31.8	39.8	40.3	40.8	53.1
Sr	672.7	623.1	702.7	734.8	725.6	737.0	760.7	776.0	670.1
Ta	2.9	2.6	3.7	3.8	3.9	3.4	3.3	3.4	3.3
Th	4.6	4.3	4.7	5.1	5.4	5.9	5.5	5.7	5.7
U	0.7	1.1	1.1	1.4	1.6	1.7	1.7	1.4	1.7
V	178	183	160	146	150	149	145	149	193
Zr	240.2	231.3	267.6	282.3	278.4	284.6	294.7	286.6	243.6
Y	21.7	21.6	20.3	21.3	21.3	22.0	23.1	23.0	21.1
Mo	1.9	3.2	2.3	2.0	2.3	2.4	2.7	2.2	3.8
Cu	34.7	41.0	35.1	34.7	30.8	35.1	34.7	36.2	36.8
Pb	3.1	10.9	51.5	5.4	4.5	4.5	2.4	3.9	3.7
Sb	<0.1	0.2	76.9	0.3	4.5	0.2	1.4	0.1	1.1
Zn	46	63	55	55	49	59	54	62	68
Ni	114.7	130.9	129.8	125.5	124.3	122.3	119.0	134.5	119.0
Sc	21	22	19	18	18	18	18	18	21

Table 4.3. *(Cont'd)*

ID	BYD1	BYD3	BYD7	BYD10	BYD14	BYD15	BYD16	BYD18	BYD23
La	30.4	29.0	36.0	38.7	39.0	40.9	41.9	42.7	40.8
Ce	60.3	57.9	71.1	73.3	74.5	76.3	79.1	79.0	77.8
Pr	6.64	6.32	7.58	7.61	7.56	7.91	8.08	8.30	8.09
Nd	26.1	23.4	28.3	29.5	28.6	29.2	32.6	32.2	30.5
Sm	5.20	5.03	5.19	5.19	5.24	5.45	5.30	5.56	5.37
Eu	1.75	1.60	1.73	1.80	1.75	1.85	1.82	1.76	1.88
Gd	4.94	4.64	4.85	5.20	4.83	5.11	4.89	5.32	5.61
Tb	0.72	0.72	0.73	0.72	0.69	0.75	0.73	0.73	0.74
Dy	4.17	4.13	4.01	3.79	4.09	3.99	4.33	4.29	4.57
Ho	0.80	0.74	0.70	0.82	0.76	0.76	0.82	0.75	0.85
Er	2.41	2.20	2.34	2.41	2.27	2.17	2.23	2.35	2.08
Tm	0.30	0.29	0.29	0.32	0.30	0.31	0.28	0.29	0.28
Yb	1.93	1.91	2.06	1.89	1.66	1.92	1.89	1.98	1.92
Lu	0.28	0.26	0.30	0.29	0.27	0.30	0.31	0.26	0.27

Table 4.3. *(Cont'd)*

ID	**BYD26**	**BYD29**	**BYD30**	**BYD31**	**GMB3**	**GMB4**	**GMB6**	**GMB8**	**GMB9**	**GMB10**
SiO_2	48.90	48.56	48.32	48.58	48.20	49.07	49.84	49.56	51.05	50.41
Al_2O_3	16.77	16.63	16.74	16.63	16.77	17.24	17.31	17.40	17.60	17.24
Fe_2O_3	8.94	9.04	9.16	9.05	9.70	9.26	9.04	9.03	9.13	8.72
MgO	7.23	7.47	7.62	7.65	7.69	6.76	6.31	6.38	6.95	6.70
CaO	7.05	7.65	7.53	7.58	7.86	7.03	6.64	6.75	7.19	7.11
Na_2O	4.27	4.31	4.30	4.38	4.23	4.88	4.61	4.65	4.78	4.62
K_2O	2.60	2.55	2.59	2.60	2.29	2.57	2.59	2.63	2.38	2.36
TiO_2	1.84	1.90	1.97	1.96	2.01	1.85	1.75	1.78	1.72	1.67
P_2O_5	0.79	0.73	0.71	0.70	0.59	0.69	0.76	0.75	0.67	0.65
MnO	0.14	0.14	0.14	0.14	0.15	0.15	0.14	0.14	0.14	0.14
Cr_2O_3	0.033	0.032	0.037	0.034	0.027	0.020	0.020	0.021	0.020	0.022
LOI	1.1	0.6	0.5	0.3	0.1	0.1	0.6	0.5	-2.0	0.0
Sum	99.68	99.67	99.68	99.68	99.68	99.68	99.68	99.68	99.69	99.70
Ba	439	458	427	416	408	425	531	544	383	388
Co	32.8	32.6	33.7	33.3	38.1	31.5	31.0	30.0	33.3	31.0
Cs	0.6	0.3	0.4	0.5	0.4	0.8	0.6	0.3	0.4	0.5
Ga	17.5	15.9	17.1	16.7	17.4	17.4	19.9	18.1	18.5	18.7
Hf	5.4	5.6	5.5	5.5	5.3	5.8	5.9	6.0	6.0	5.6
Nb	65.5	64.5	62.5	62.9	49.6	58.6	63.0	65.1	53.2	51.5
Rb	41.6	39.6	42.6	41.5	40.5	43.4	43.9	44.6	39.6	40.5
Sr	709.4	773.7	766.4	740.8	685.8	773.1	827.6	838.6	643.5	668.3
Ta	3.8	3.6	3.7	3.8	3.0	3.5	3.8	3.7	3.1	2.7
Th	5.3	5.4	5.1	5.3	5.7	6.0	7.2	7.2	5.7	6.0
U	1.9	1.6	1.3	1.4	1.3	2.0	2.0	1.7	2.0	1.9
V	150	147	156	151	167	143	132	139	156	150
Zr	283.7	280.4	267.7	272.6	262.7	307.8	323.4	327.5	309.3	308.7
Y	22.0	22.4	22.5	24.2	25.6	22.3	21.9	21.3	22.0	21.6
Mo	3.5	2.3	1.8	2.2	2.1	2.3	2.6	2.3	2.4	2.0
Cu	32.5	33.1	30.3	32.5	33.1	29.5	27.4	30.5	34.0	35.6
Pb	3.7	2.7	2.4	2.2	2.5	2.0	2.1	2.6	1.1	1.5
Sb	0.2	0.6	<0.1	0.4	0.1	0.2	0.2	0.2	0.3	<0.1
Zn	59	54	46	47	47	53	55	57	64	65
Ni	124.6	124.5	115.1	129.2	102.3	90.2	82.9	90.9	101.1	96.6
Sc	18	18	19	19	20	17	16	16	19	18

Table 4.3. *(Cont'd)*

ID	**BYD26**	**BYD29**	**BYD30**	**BYD31**	**GMB3**	**GMB4**	**GMB6**	**GMB8**	**GMB9**	**GMB10**
La	42.3	39.2	40.2	38.5	34.3	40.1	41.6	42.8	37.0	37.0
Ce	75.6	78.0	73.8	74.9	62.7	72.0	76.6	77.6	72.2	71.1
Pr	8.04	7.95	7.83	7.59	6.75	7.80	7.99	8.07	7.48	7.45
Nd	29.5	30.2	29.3	29.5	27.7	27.2	29.2	28.7	28.4	27.9
Sm	5.37	5.62	5.14	5.29	5.08	5.70	5.72	5.46	5.37	5.47
Eu	1.86	1.81	1.74	1.83	1.65	1.76	1.71	1.86	1.69	1.75
Gd	5.24	5.33	5.04	5.22	5.08	5.40	5.38	5.34	5.19	5.27
Tb	0.75	0.73	0.75	0.74	0.74	0.73	0.73	0.74	0.73	0.73
Dy	4.32	4.42	4.57	4.63	4.41	4.01	4.41	3.89	4.47	4.18
Ho	0.77	0.83	0.76	0.77	0.83	0.82	0.80	0.83	0.86	0.82
Er	2.15	2.40	2.31	2.38	2.39	2.43	2.41	2.30	2.28	2.31
Tm	0.30	0.31	0.30	0.31	0.30	0.30	0.34	0.32	0.32	0.32
Yb	1.87	1.85	1.90	1.94	2.12	2.09	2.06	2.00	2.27	2.02
Lu	0.30	0.29	0.30	0.27	0.30	0.30	0.28	0.30	0.32	0.33

4.2.2 Assessment of Alteration

Post-magmatic processes, such as hydrothermal alteration, have potential to disturb the primary chemical budget of the igneous rocks. Particularly, the elements with low ionic potential, such as large ion lithophile elements (LILE; e.g., Cs, K, Rb, Ba; Hart 1969; Jochum and Verma, 1996), are more prone to be affected by such processes. In addition to LILE, the elements Pb, U, Tl, and Sb are also reported to be sensitive to hydrothermal alteration (e.g., McGoldrick et al., 1979; Jochum and Verma, 1996). On the other hand, the high field strength elements (HFSE; e.g., Nb, Ta) and heavy rare earth elements (HREE; e.g., Yb, Lu) are assumed to remain immobile during the water-rock interaction (e.g., Humphris and Thomson, 1978; Jochum and Verma, 1996).

The LOI values of Tunceli and Elazığ Volcanics range between 0.3-3.2 (wt. %) and 0-2.4 (wt. %), respectively. Although most of the samples display low LOI values (<1 wt.%; see Tables 4.2 and 4.3), moderate LOI values (>1 wt.%; see Tables 4.2 and 4.3) also exist for some samples. Considering this with the existence of some alteration products in the volcanics (see PETROGRAPHY chapter), an assessment of alteration is necessary to understand whether the chemical budget of the volcanics has been disturbed by post-magmatic processes or not. Such evaluation will help to understand whether the elements reflect the original (magmatic) chemistry of the rocks, which will in turn allows making reliable petrogenetic implications.

4.2.2.1 Tunceli Volcanics

In order to assess the element mobility in Tunceli Volcanics, various type of elements with low, intermediate, and high ionic potential are plotted against Zr (Figure 4.11), which is assumed to be immobile during low-grade hydrothermal alteration (e.g., Pearce and Cann, 1973). In these diagrams, while the scattered data distribution may be related to the effects of hydrothermal alteration, the parallel/sub-parallel trends preclude modification by post-magmatic processes.

In all plots, it is observed that the volcanics display parallel/ sub-parallel trends (Figure 4.11). This suggests that the elemental budget of the Tunceli Volcanics has not been significantly modified by hydrothermal alteration. Only a slight scattering of the data is observed in the plots of LILE (Ba, Rb), Pb, and U versus Zr (Figure 4.11a-d). This may indicate a slight mobilization in these elements. However, the data still exhibit a linear trends, which argue against a strong modification by alteration. The trends observed in HFSE and REE are smooth, showing high degree of correlation, as is expected. Therefore, the effect of alteration Tunceli Volcanics is only minor, and all elements available in the dataset, including the LILE, can be safely used for petrogenetic interpretations.

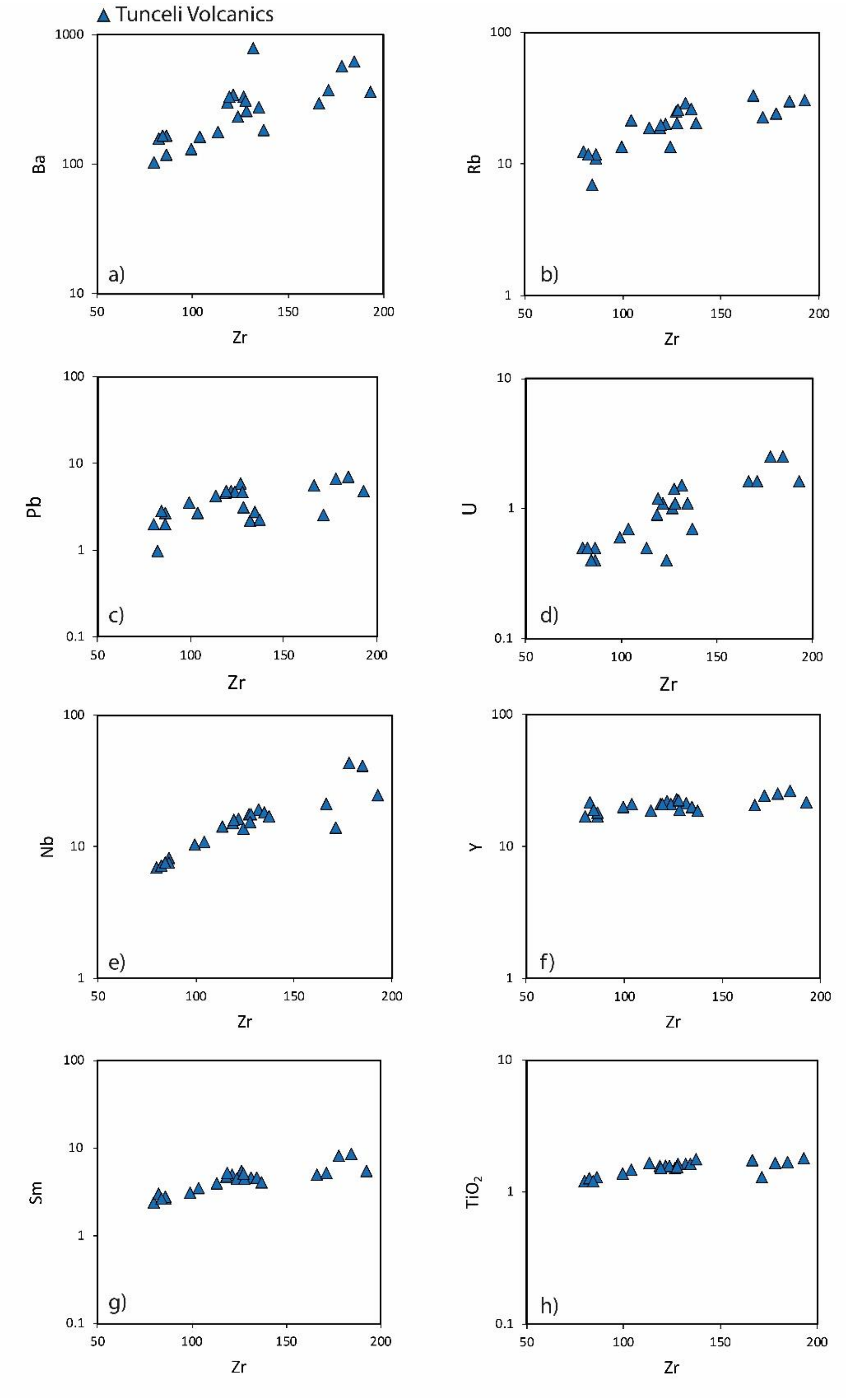

Figure 4.11. Plots of selected trace (ppm) and major elements (wt. %) versus Zr (ppm) for the Tunceli Volcanics.

4.2.2.2 Elazığ Volcanics

To assess the possible effects of alteration on the Elazığ lavas, several selected major-trace elements have also been plotted against Zr (Figure 4.12). Except for the plot of Zr versus Pb (Figure 4.12c), the data distribution exhibit smooth linear trends in all diagrams. It must be noted that this case is also valid for the mobile elements, e.g., the LILE. This suggests that the chemical budget of the Elazığ lavas for most elements remained unaffected during a possible water-rock interaction. However, the scattered Pb pattern may suggest a selective mobilization of this element due to post-magmatic processes. As observed from the plot (Figure 4.12c), some samples (e.g., BYD7) have relatively high Pb concentrations. Apart from the alteration, such elevated Pb concentrations may also indicate possible crustal assimilation. However, their low SiO_2 contents and high Nb/Nb* values (Nb/Nb*= Nb_{PM} / $(Th_{PM}*La_{PM})^{1/2}$, normalizing values from Sun and McDonough, 1989) argue against a possible crustal contamination. Instead, such disturbance appears to be rather related to the low-grade alteration process. The enrichment of Sb in those samples (76.9 ppm for BYD7) is also consistent with this idea. Jochum and Verma (1996) have reported that Sb is one of the best indicators for the water-rock interaction. The Sb content in fresh MORBs usually does not exceed 0.05 ppm, whereas the altered MORBs may contain Sb reaching up to 40 ppm (Jochum and Verma, 1996). Accordingly, the concomitant increase of Pb and Sb can be attributed to the effects of alteration in basalts (Jochum and Verma, 1996). To further assure whether the Pb disturbance in Elazığ lavas is related to alteration, the LOI values plotted against Pb (Figure 4.13). In the diagram, the LOI values display positive correlation with Pb, though some samples deviate from the trend. This may indicate the possible control of alteration on the Pb budget of the basalts. Alternatively, the variable Pb contents among the lavas may be related to the analytical techniques which may have led to artificial excess Pb measurements in some samples. Nevertheless, these elemental behaviors suggest that, with the exception of Pb, all elements in the dataset of Elazığ volcanism are suitable to make petrogenetic interpretations.

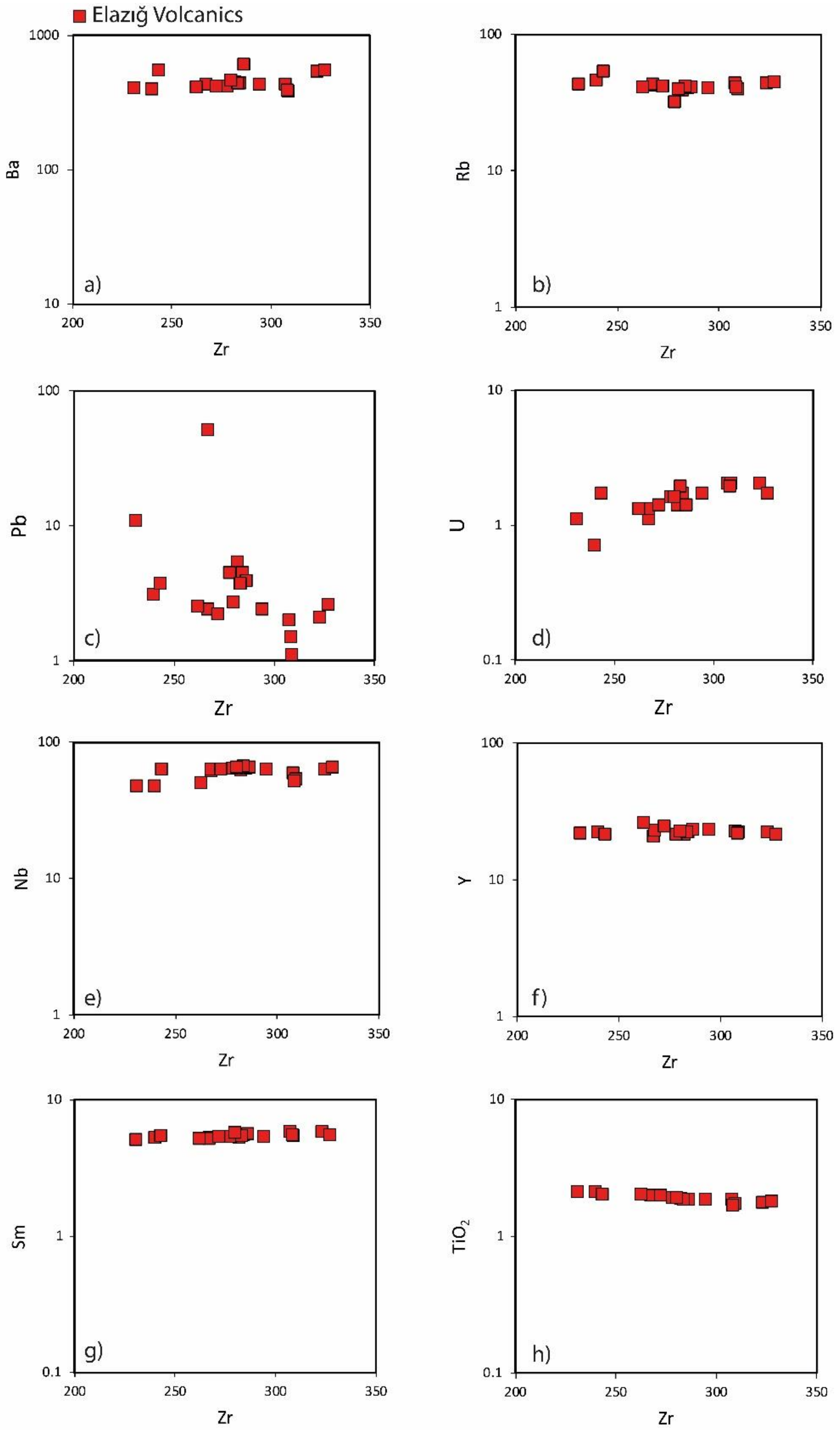

Figure 4.12. Plots of selected trace (ppm) and major elements (wt. %) versus Zr (ppm) for the Elazığ Volcanics.

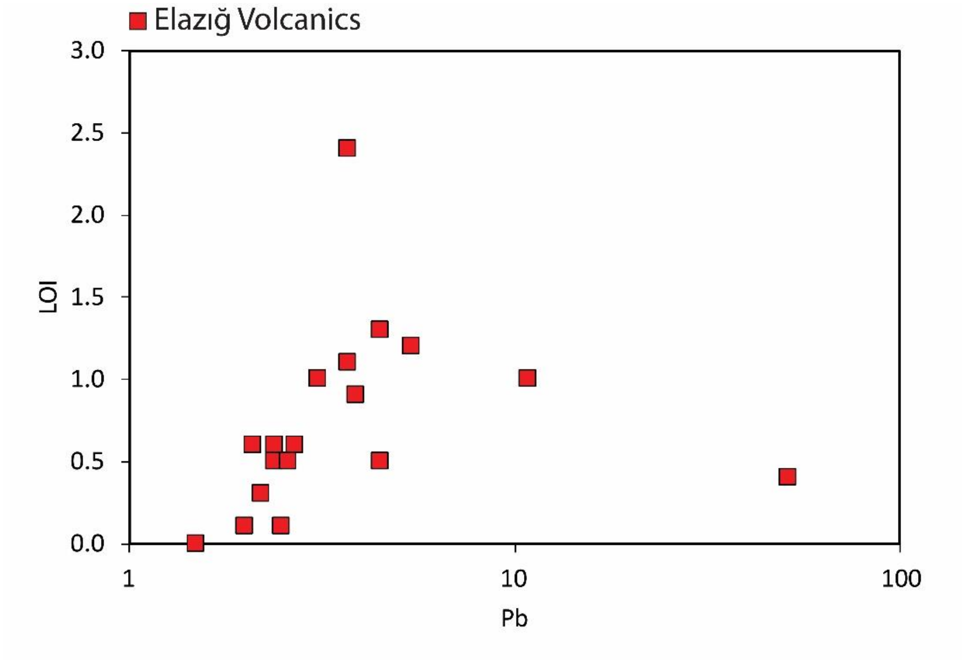

Figure 4.13. Plot of Pb (ppm) versus LOI (wt. %) for the Elazığ Volcanics.

4.2.3 Classification

4.2.3.1 Tunceli Volcanics

As previously reported in Aktağ et al. (2019), all Tunceli samples are of basaltic composition according to their major oxide geochemistry. While the majority of the Tunceli Volcanics plot in the basalt field, a few are distributed in the trachybasalt field on a diagram of SiO_2 versus total alkalis (Na_2O+K_2O) (Figure 4.14; Le Bas et al., 1986). Note that these elements are not significantly affected by post-magmatic processes; thus they were preferred for the chemical classification. Based on the alkaline-subalkaline division line of Miyashiro (1978) in the diagram, 15 samples plot in the alkaline field, whereas the distribution of the remaining 8 samples define subalkaline geochemical characteristics (Figure 4.14). As it is also suggested by Aktağ et al. (2019), strongly alkaline characteristics are not observed among the volcanics; thereby, the alkaline samples can be defined as “mildly alkaline” basalts. The subalkaline samples, on the other hand, exhibit tholeiitic geochemical characteristics instead of calc-alkaline based on the plot of SiO_2 versus FeOt/MgO (Figure 4.15; Miyashiro, 1974), as also mentioned by Aktağ et al. (2019).

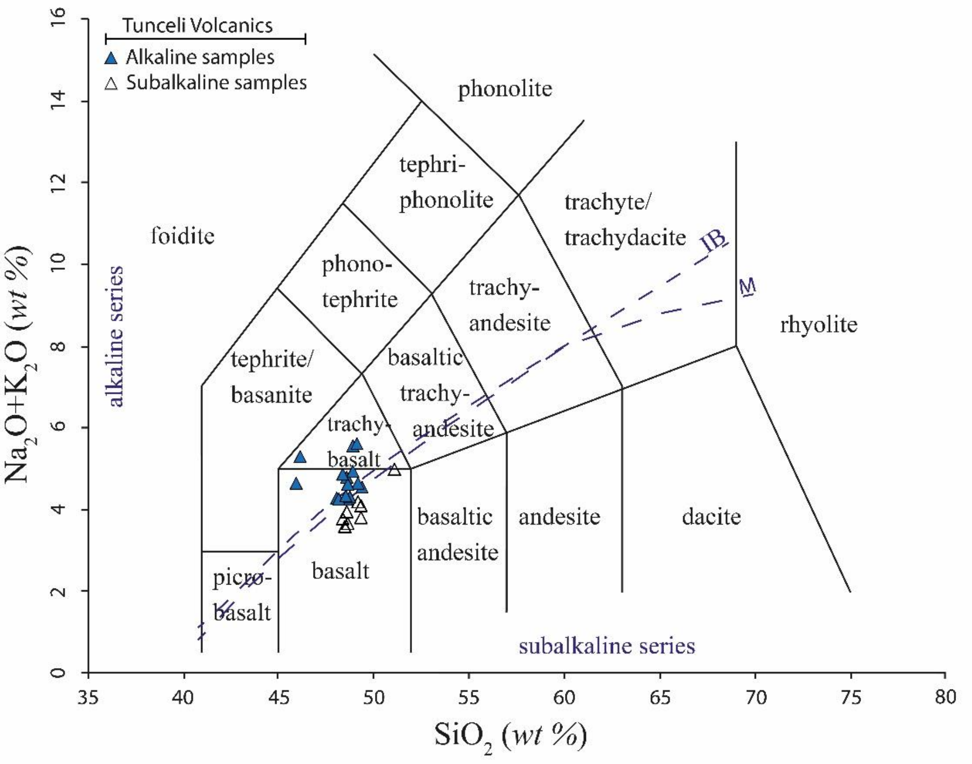

Figure 4.14. Plot of SiO_2 versus total alkalis (Le Bas et al., 1986) for the Tunceli Volcanics. Alkaline-subalkaline division line: IB-Irvine and Baragar (1971); M-Miyashiro (1978).

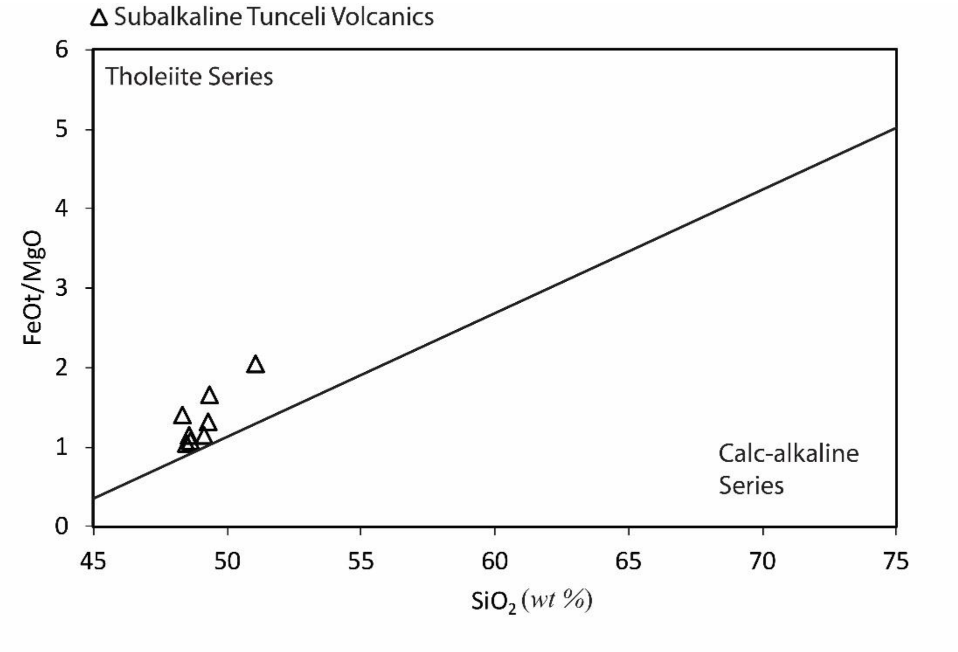

Figure 4.15. SiO_2 versus FeOt/MgO plot illustrating division of tholeiite and calc-alkaline series (Miyashiro, 1974).

Since the Tunceli Volcanics display two distinct geochemical characteristics (i.e., mildly alkaline and tholeiitic), hereafter, they will be subdivided into two groups to enhance the interpretations. Note that these samples have also been evaluated under two groups in the study of Aktağ et al. (2019).

4.2.3.2 Elazığ Volcanics

As mentioned above, with the exception of the Pb, the primary (magmatic) elemental budget of the Elazığ Volcanics appears not to have been significantly affected by hydrothermal alteration. Therefore, their major oxides were used for chemical classification. According to the diagram of SiO_2 versus total alkalis (Na_2O+K_2O) (Figure 4.16; Le Bas et al., 1986), the Elazığ Volcanics are totally alkaline, and their composition predominantly ranges between trachybasalt and basanite. Four samples (GMB6, GMB8, GMB9 and GMB10), on the other hand, display more evolved compositions and plot within the field of basaltic-trachyandesite in the diagram (Figure 4.16).

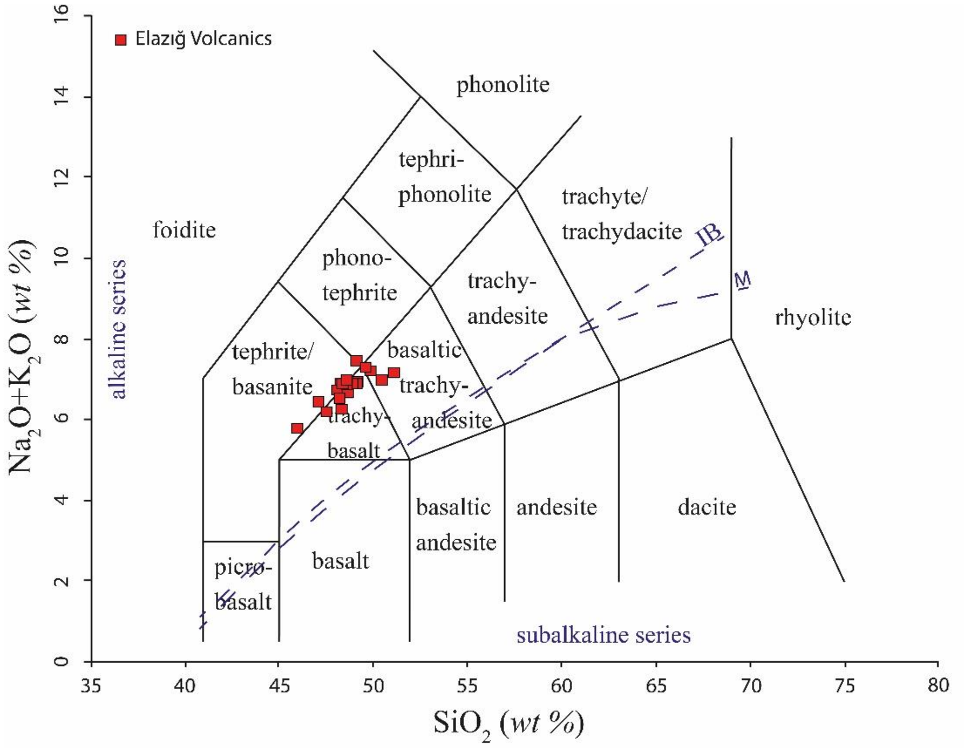

Figure 4.16. Plot of SiO_2 versus total alkalis (Le Bas et al., 1986) for the Elazığ Volcanics. Alkaline-subalkaline division line: IB-Irvine and Baragar (1971); M-Miyashiro (1978).

Although there is a compositional variation among the Elazığ Volcanics, no distinct magma series is present in terms of their silica and total alkali contents. Hence, the Elazığ Volcanics will not be subdivided into any groups in the remainder of the text.

4.2.4 Element Variation

4.2.4.1 Tunceli Volcanics

The mafic Tunceli Volcanics have MgO and SiO_2 contents between 3.46-10 and 45.87-51.04 wt. %, respectively. Note that there is only one sample (AV22; 3.46 wt. %) having MgO content below the value of 6 wt. % in the dataset. While the Mg# (Mg# = $100xMg^{+2}/(Mg^{+2}+Fe^{+2})$ assuming that $Fe^{+3}/Fe^{+2}=0.15$) of this evolved sample (AV22) is 46.7, those of the rest samples range between 51.9-63.6. Excluding the sample AV22, no significant difference in the Mg#s is observed between the mildly alkaline (56.1-63.6) and tholeiitic samples (51.9-63.3). The total alkali (Na_2O+K_2O) content range between 4.26-5.55 wt. % for the alkaline samples, whereas it ranges between 3.57-4.97 wt. % for the tholeiitic samples, as it is reported in Aktağ et al. (2019).

The major element concentrations were plotted against MgO contents to observe the major element variation in the Tunceli Volcanics and give insights into their chemical evolution (Figure 4.17). Except for the SiO_2 and Al_2O_3, no strong correlation is observed between major elements and MgO. The SiO_2 concentrations of the whole lava suite display a negative correlation with the MgO in Figure 4.17a. The samples AV28 and AV33 have the lowest SiO_2 contents (45.87 and 46.08 wt. %, respectively); however, they do not have the highest MgO contents in the dataset. Therefore, these two samples deviate from the general trend in the plot of MgO versus SiO_2. The volcanics have Al_2O_3 contents ranging from 14.32 to 17.44 wt. % forming also a negative trend with the decreasing MgO (Figure 4.17b). While the Na_2O, CaO, Fe_2O_3, TiO_2, K_2O, and P_2O_5 contents of the alkaline lavas do not yield any trend against MgO concentration, those of tholeiitic samples, with the exception of TiO_2, define a slight negative correlation with MgO (Figure 4.17c-h). The concentrations of Na_2O, CaO, Fe_2O_3, TiO_2, K_2O, and P_2O_5 for the whole Tunceli Volcanics range between 2.95-3.85 wt. %, 6.90-10.00 wt. %, 7.82-12.14 wt. %, 1.22-1.83 wt. %, 0.62-1.77 wt. % and 0.15-0.99 wt. %, respectively. Note that the tholeiitic samples have low TiO_2 (1.22-1.49 wt. %), K_2O (0.59-1.23 wt.%), and P_2O_5 (0.15-0.38 wt.%) concentrations at a given MgO content compared to the alkaline samples (1.53-1.83 wt.%, 1.00-1.77 wt.% and 0.26-0.99, respectively).

In order to observe the trace element variations in the Tunceli Volcanics and better understand their chemical evolution, their trace element concentrations are plotted against their MgO content (Figure 4.18). As with most of the major elements, the majority of the trace elements are also not significantly correlated with the MgO on the bivariate Harker diagrams (Figure 4.18). The transition metals Ni and Co of the whole lava suite exhibit a slight positive correlation with MgO (Figure 4.18f and g). The volcanics have Ni and Co contents ranging from 31.4 to 225 ppm and 28.3 to 53.5 ppm, respectively. The Tunceli Volcanics, including both alkaline and tholeiitic members, have Ba, Rb, Sr, Zr, Sc, and V contents ranging from 104 to 786 ppm, 7 to 33.6 ppm, 294.4 to 1345.7 ppm, 79.9 to 192.8 ppm, 16 to 22 ppm and 164 to 202 ppm, respectively. While the Ba and Sr display a very slight negative correlation with the MgO in tholeiitic group, the rest of the elements, both in alkaline and tholeiitic group, do not show an obvious correlation with the MgO on the Harker diagrams (Figure 4.18). No obvious difference is observed in terms of the element abundances between the alkaline and tholeiitic samples.

Note that the sample AV22, which has the lowest MgO content in the data set, has also lowest Fe_2O_3, Ni, an Co concentrations within the Tunceli lava suite. This is obviosly apparent in the Figures 4.17 and 4.18.

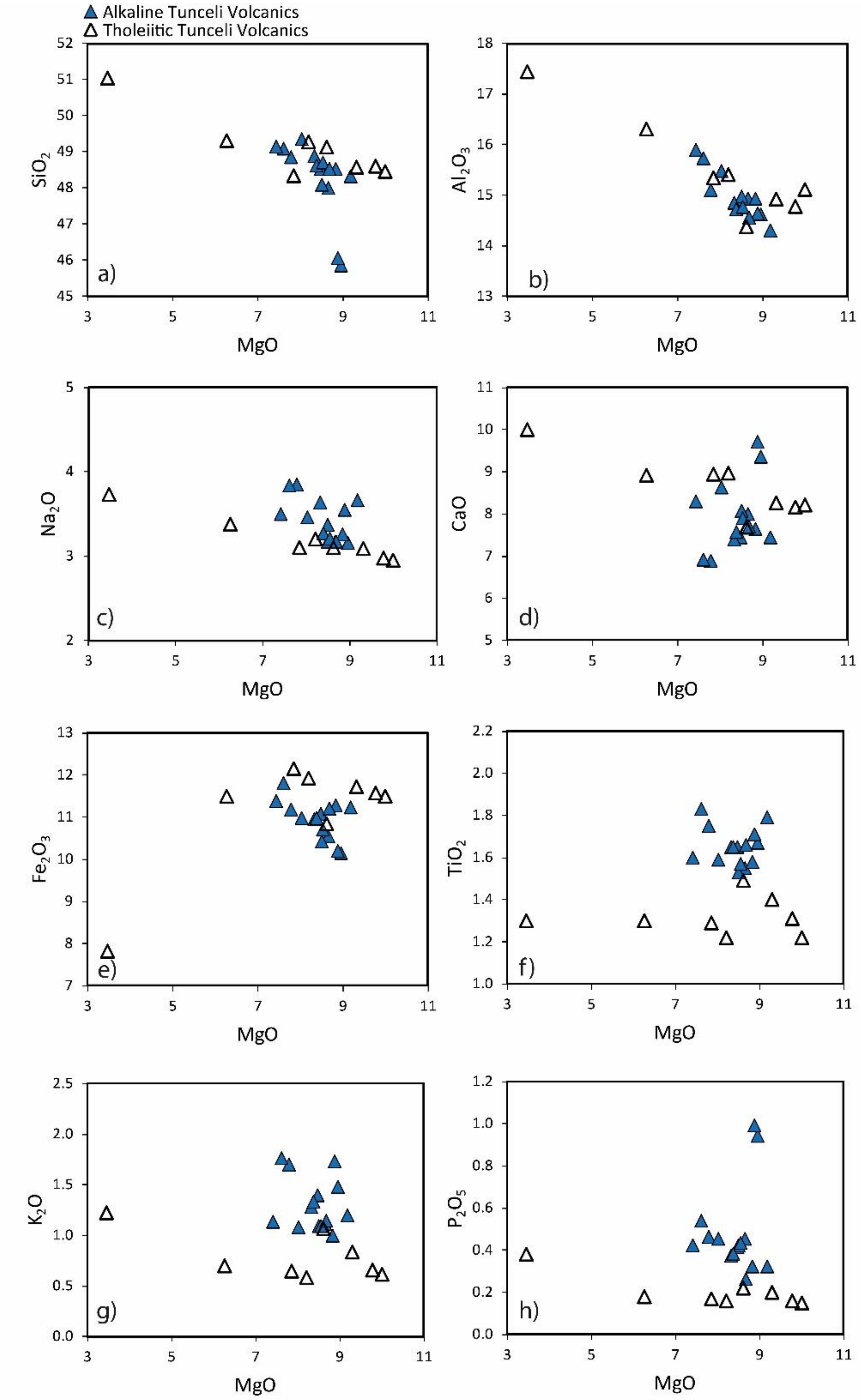

Figure 4.17. Harker diagrams of Tunceli Volcanics showing the behavior of selected major elements (wt. %) with MgO (wt. %).

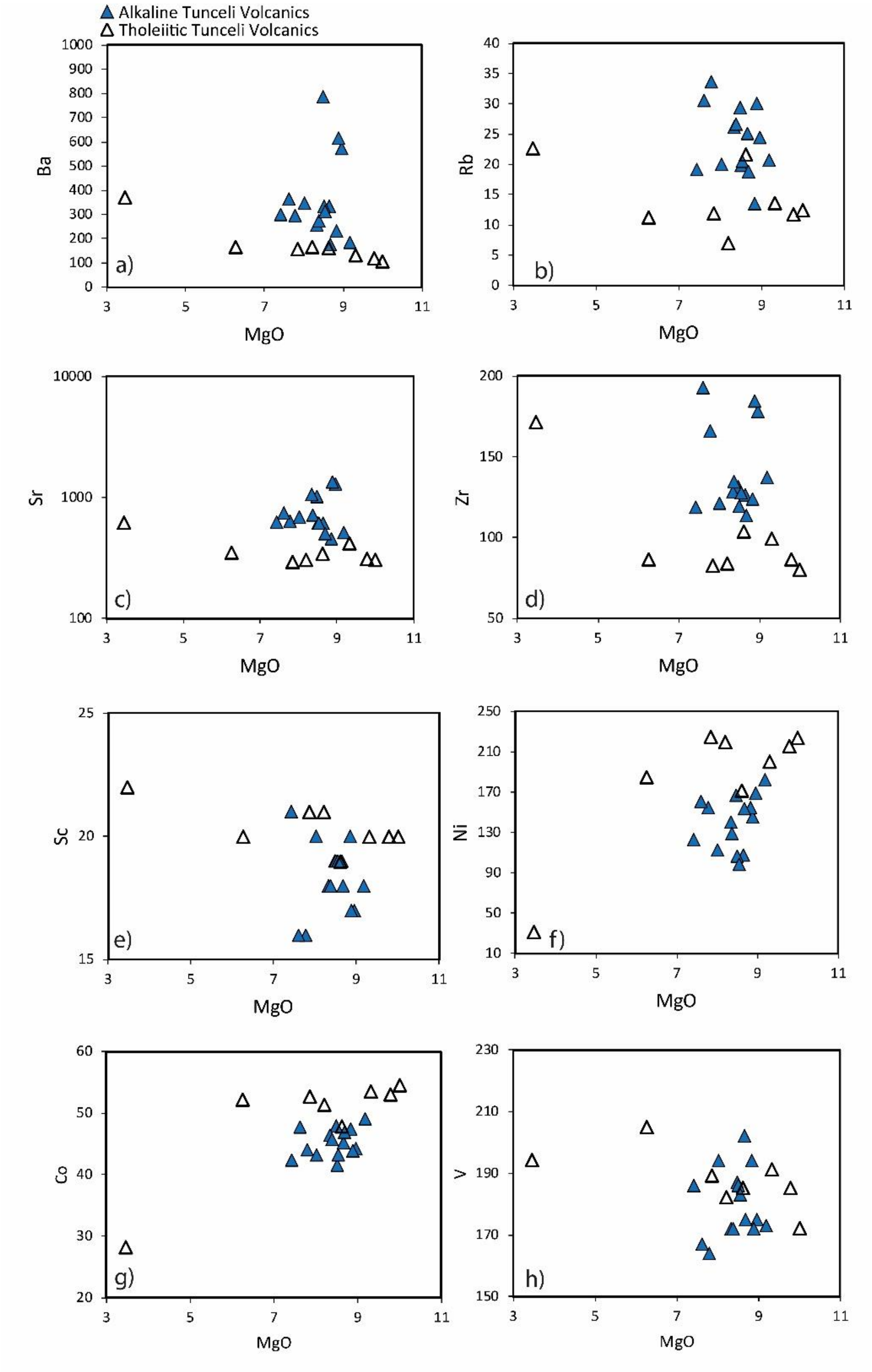

Figure 4.18. Harker diagrams of Tunceli Volcanics showing the behavior of selected trace elements (ppm) with MgO (wt. %).

The primitive mantle (PM) normalized trace element concentrations and chondrite-normalized rare earth element concentrations of Tunceli lavas have been plotted on the multi-element diagrams together with normalized average OIB values (Figure 4.19) to make further petrogenetic implications. The normalization values and the average trace element concentrations of OIB used in the diagram are from Sun and McDonough (1989).

In the PM-normalized multi-element diagram (Figure 4.19a), all Tunceli lavas exhibit enriched trace element abundances relative to PM (Sun and McDonough, 1989). While the abundances of the heavy rare earth elements (HREE; e.g., Yb, Lu), which are expected to be compatible during mantle melting, are 5 to 10 times higher than those of PM, the abundances of highly incompatible LILE (e.g., Rb, Ba) are 10 to 100 times higher than those of PM. Note that, although the general PM-normalized element patterns of the samples are almost identical, the samples display different enrichment levels in the diagram (Figure 4.19a). In general, the alkaline samples appear to be more enriched than tholeiitic samples (e.g., $(Zr/Nb)_N$= 0.26-0.57 and 0.60-0.77 for alkaline and tholeiitic samples, respectively; where N denotes PM normalized based on Sun and McDonough, 1979).

As seen from Figure 4.19a, the elemental patterns of all Tunceli lavas are characterized by the enrichment in LILE (e.g., Rb, Ba, K), Th, and La relative to the HFSE (e.g., Nb, Ti, Zr). The Tunceli Volcanics are characterized by negative Nb anomalies, with Nb/Nb* values between 0.30-0.80. Another outstanding feature in the multi-element diagram (Figure 4.19a) is that all Tunceli lavas display positive spikes at Pb, which may indicate either a possible lithospheric contribution to their petrogenesis or crustal contamination. These scenarios are discussed in detail in the “Petrogenesis” section.

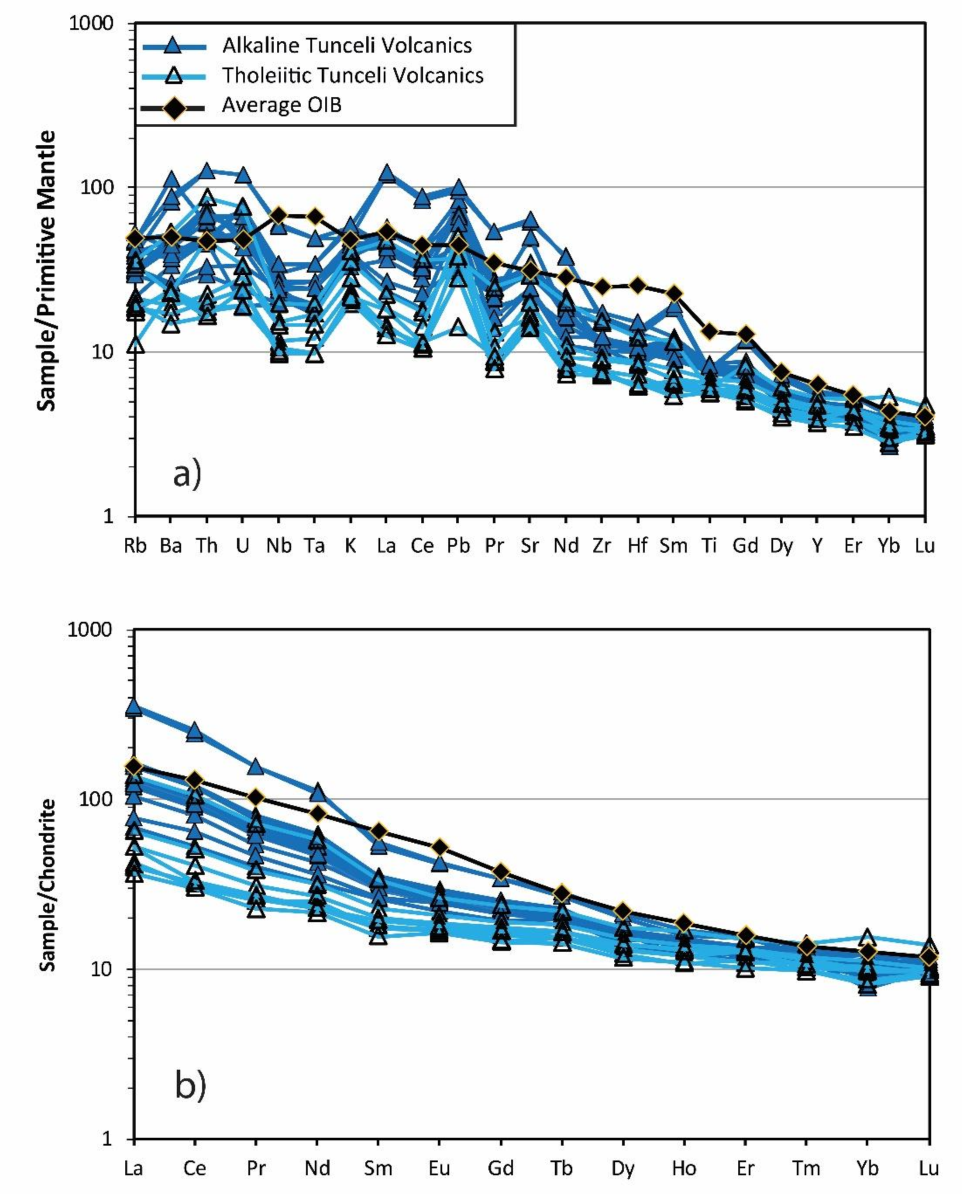

Figure 4.19. (a) Primitive Mantle-normalized multi-element and (b) chondrite-normalized rare earth element diagrams for the Tunceli Volcanics. The normalization values and average OIB values are from Sun and McDonough (1989).

With these elemental characteristics, the Tunceli Volcanics do not resemble the plume-related or asthenosphere-derived within-plates lavas, though the general element patterns of Tunceli lavas are parallel to that of average OIB (Figure 4.19a) (e.g., OIBs; Sun and McDonough, 1989; Weaver, 1991; Jackson et al., 2008; Pilet et al., 2008; Peters and Day, 2014). This is evidenced by the “humped” average OIB pattern in the diagram (Figure 4.19a), which differs from the Tunceli lavas with the positive Nb anomaly. Instead, the Tunceli Volcanics, with their high LILE/HFSE ratios and negative Nb anomalies (Nb/Nb* <1), share geochemical similarities with the arc-related magmas (e.g., active continental margin; e.g., Pearce and Peate, 1995) or intraplate lavas derived from a subduction-modified SCLM (e.g., Pearce et al., 1990). This is also apparent in the PM-normalized multi-element and chondrite-normalized REE diagrams, in which a coherent pattern observed between Tunceli lavas and those lavas derived in the arc settings (e.g., Aeolian arc; Peccerillo et al., 2013) and those intraplate lavas which are presumed to have been derived predominantly from metasomatized SCLM with slab-derived input (e.g., Lavas from the Rio Grande Rift shoulders and some Cenozoic Anatolian lavas; Gibson et al., 1993; Aldanmaz et al., 2000; Oyan et al., 2016; Gall et al., 2021) (Figure 4.20).

In the chondrite-normalized REE diagram, although the Tunceli Volcanics display different enrichment levels, they have similar REE profiles (Figure 4.19b). In general, they display obvious enrichment in LREE relative to MREE (medium rare earth elements) and HREE (Figure, 4.19b; e.g., $(La/Sm)_N$=2.21-6.56, $(La/Yb)_N$= 4.10-29.96, N denotes to chondrite-normalized based on Sun and McDonough, 1989). In detail, the alkaline samples exhibit this element fractionation in a broader spectrum compared to the tholeiitic samples ($(La/Yb)_N$=7.59-27.64 and 4.10-8.95 for alkaline samples and tholeiitic samples, respectively), as also previously reported by Aktağ et al. (2019). Moreover, the fractionation in HREE is greater in alkaline samples than the tholeiitic samples (e.g., $(Tb/Yb)_N$=1.72-2.63 for alkaline samples and 1.42-1.75 for tholeiitic samples). These features may indicate a difference in their degree of melting and source mineralogy. The melting conditions are also discussed in “Petrogenesis” section. It is also important to note that, although the

Tunceli Volcanics generally have lower enrichment levels compared to the OIBs, they show parallel patterns with the average OIB in the diagram (Figure 4.19b). These lavas also display broadly similar REE patterns with the continental arc lavas (e.g., Aeolian lavas, Pecerillo et al., 2013) and with those lavas considered to be predominantly or partly the partial melts of the metasomatized SCLM in the chondrite-normalized REE diagrams (Figure 4.20b and d; e.g., Lavas from the Rio Grande Rift shoulders and some Cenozoic Anatolian lavas; Gibson et al., 1993; Aldanmaz et al., 2000; Oyan et al., 2016; Gall et al., 2021).

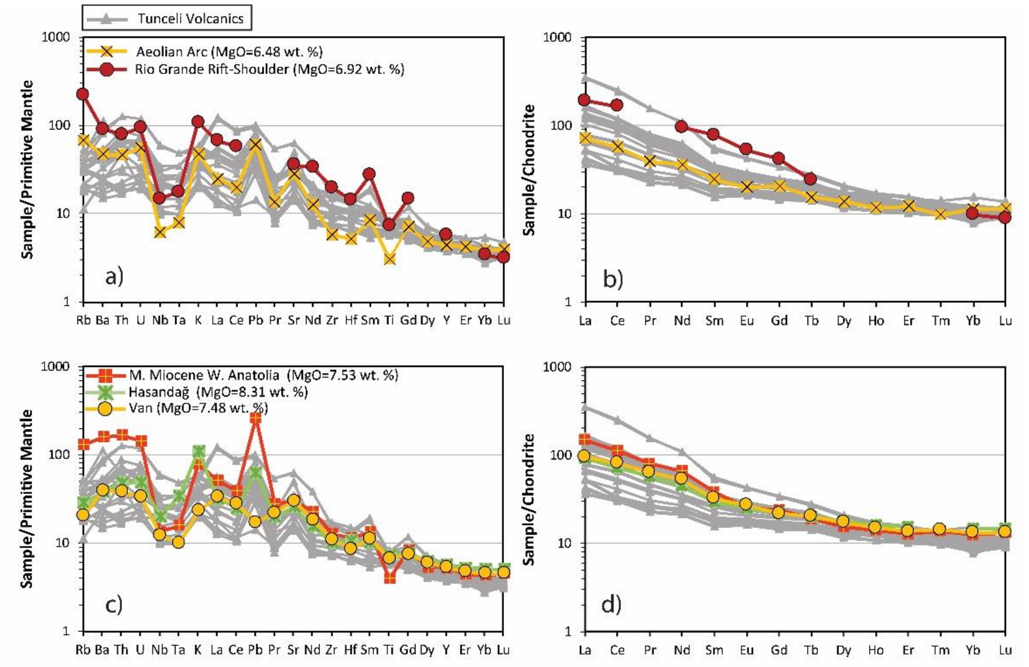

Figure 4.20. (a and c) Primitive Mantle-normalized multi-element and (b and d) chondrite-normalized rare earth element diagrams for the Tunceli Volcanics and those from the modern arc and within plate settings. Normalization values are from Sun and McDonough (1989). Data sources: Aeolian Arc-Peccerillo et al. (2013); Rio Grande Rift (Shoulder of the rift)-Gibson et al. (1993); Middle Miocene western Anatolian lava-Aldanmaz et al. (2000); central Anatolian Hasandağ lava- Gall et al. (2021); lava from Van area (eastern Anatolia)-Oyan et al (2016).

4.2.4.2 Elazığ Volcanics

The MgO and SiO_2 contents of the Elazığ volcanism show variability between 6.31-8.34 wt. % and 45.95-51.05 wt. %, respectively. Mg#s vary in a narrow range from 63.1 to 58.

In order to understand also the element variation in the Elazığ volcanism, their major oxide contents were plotted against MgO on the Harker diagrams (Figure 4.21). The bivariate diagrams have shown that, unlike the Tunceli Volcanism, the major oxide elements of Elazığ Volcanics generally show good correlations with MgO (Figure 4.21). The SiO_2 displays a strong negative correlation with MgO (Figure 4.21a). Similarly, the Elazığ Volcanics have Al_2O_3, Na_2O, and P_2O_5 contents ranging between 15.61.-17.60 wt. %, 3.17-4.78 wt. % and 0.58-0.79 wt. %, respectively, and they display well-defined negative correlations with MgO (Figure 4.21b, c, and h). On the other hand, the CaO, Fe_2O_3, and TiO_2 contents range between 6.64-9.33 wt. %, 8.72-9.70 wt. %, and 1.67-2.12 wt. %, respectively, in the Elazığ Volcanics, and display positive correlations with MgO (Figure 4.21d, e and f). The K_2O concentrations of the volcanics, however, stay constant with decreasing MgO (Figure 4.21g).

When the trace element concentrations of the Elazığ Volcanics are plotted against their MgO contents on the Harker diagrams (Figure 4.22), it is observed that the majority of the trace elements exhibit strong correlations with the MgO. The volcanics have Sr and Zr contents ranging between 623.1-838.6 ppm and 231.3-327.5 ppm, respectively, and these elements are negatively correlated with the MgO (Figure 4.22c and d). On the contrary, the contents of the Sc, Ni, Co, and V range between 16-22 ppm, 82.9-134.5 ppm, 30-38.1 ppm, and 132-183 ppm, respectively, and display positive correlations with MgO in the volcanics (Figure 4.22e, f, g, and h). Note that the correlation of the Co against MgO is not as much as strong compared to others (Figure 4.22g). The Ba and Rb, as the K_2O, do not show any correlation with the MgO in the volcanics (Figure 4.22a-b). They display rather a constant pattern with decreasing MgO.

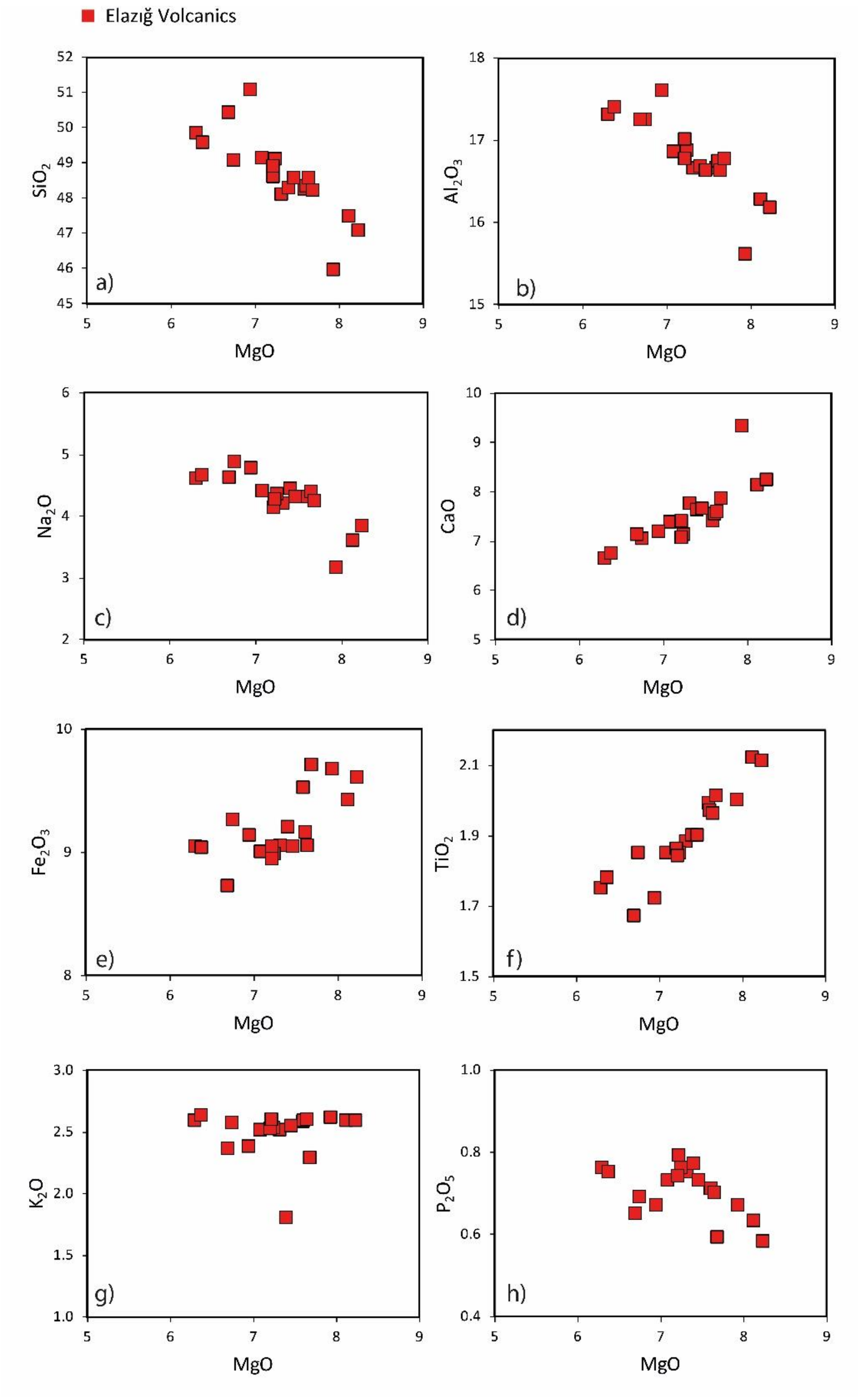

Figure 4.21. Harker diagrams of Elazığ Volcanics showing the behavior of selected major elements (wt. %) with MgO (wt. %).

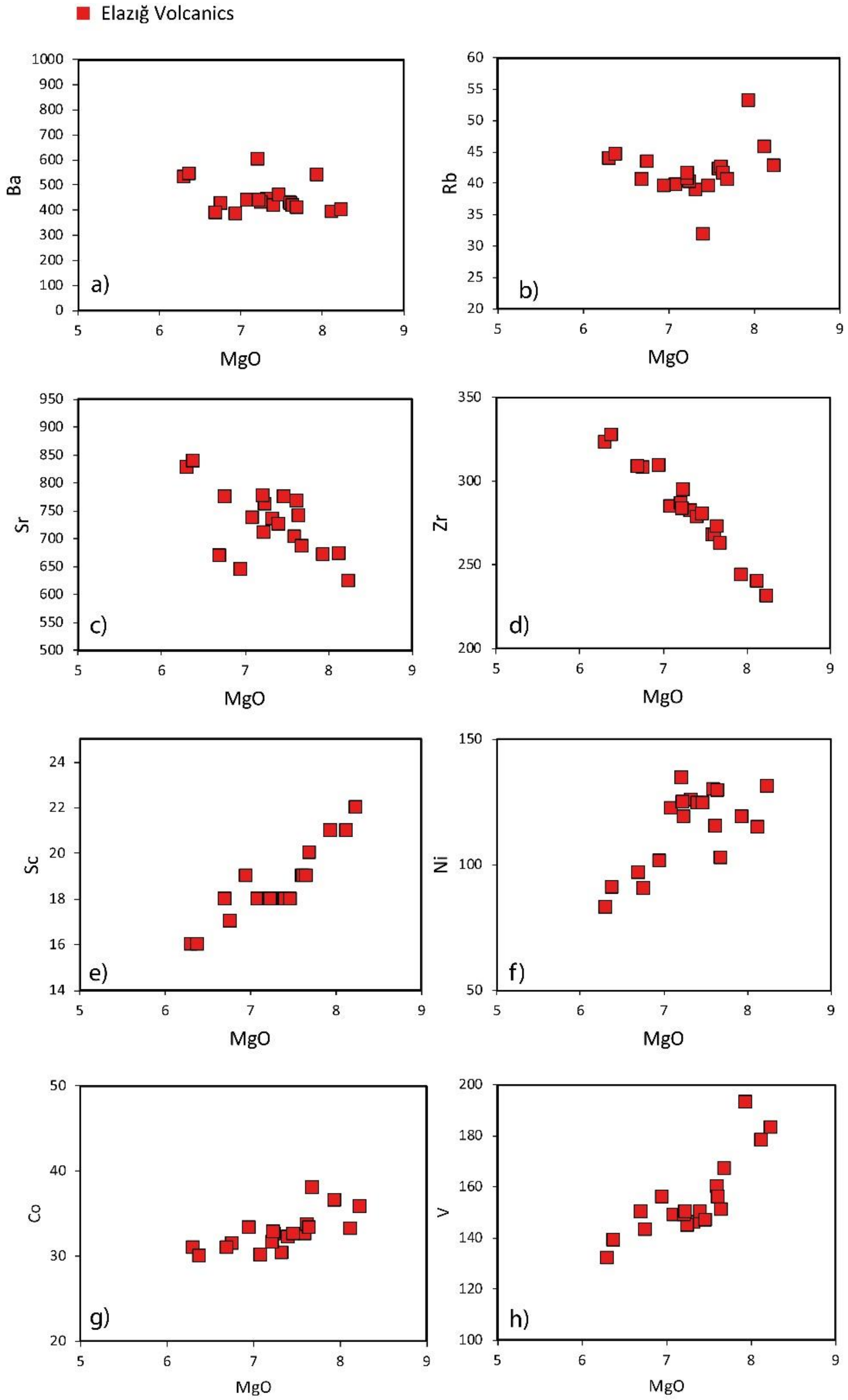

Figure 4.22. Harker diagrams of Elazığ Volcanics showing behavior of selected trace elements (ppm) with MgO (wt. %).

In order to make petrogenetic implications from the trace element systematics, the PM-normalized trace element and chondrite-normalized rare earth element concentrations of Elazığ volcanism were also plotted on the multi-element diagrams (Figure 4.23) with average OIB values and East African Rift sample (Furman, 2007). The normalization values and the average trace element concentrations of OIB used in the diagram are from Sun and McDonough (1989). In the PM-normalized multi-element diagram (Figure 4.23a), the Elazığ Volcanics, with the exception of Pb, display very uniform patterns among each other and exhibit enriched trace element abundances relative to PM (Sun and McDonough, 1989). While the LILEs (e.g., Rb, Ba) of the Elazığ samples appear to be enriched 50 to 100 times higher than those of PM, their HREE (e.g., Yb, Lu) abundances display enrichment levels 3 to 5 times higher than those of PM. The highly variable Pb abundances in the Elazığ Volcanics created a quite variable patterns in the PM-normalized multi-element diagram (Figure 4.23a). The possible reason for variety in the Pb abundances was discussed above in the "Assessment of Alteration" section.

Note that, unlike the Tunceli Volcanics, the HFSEs such as Nb and Ta are also enriched together with LILEs in the Elazığ samples. With Nb/Nb* values between 1.17-1.58, the Elazığ Volcanics are characterized by positive Nb anomalies in the diagram (Figure 4.23a). With these characteristics, the Elazığ volcanism is analogous to most of OIBs (e.g., FOZO/C-type or HIMU-type OIBs; Sun and McDonough, 1989; Woodhead, 1996; Sayit, 2013) and to the continental intraplate lavas originated from asthenospheric mantle sources containing recycled components, similar to the OIB source (e.g., Furman 2007; Endress et al., 2011; Nelson et al., 2012). Elemental similarities between Elazığ volcanism and OIBs and OIB-like intraplate lavas can also be seen from the coherent elemental patterns of average OIB, OIB-like East African Rift lava and Elazığ samples in the multi-element diagram (Figure 4.23a). This may suggest the involvement of similar mantle source and/or petrogenetic processes yielding analogous elemental fractionation for these lavas.

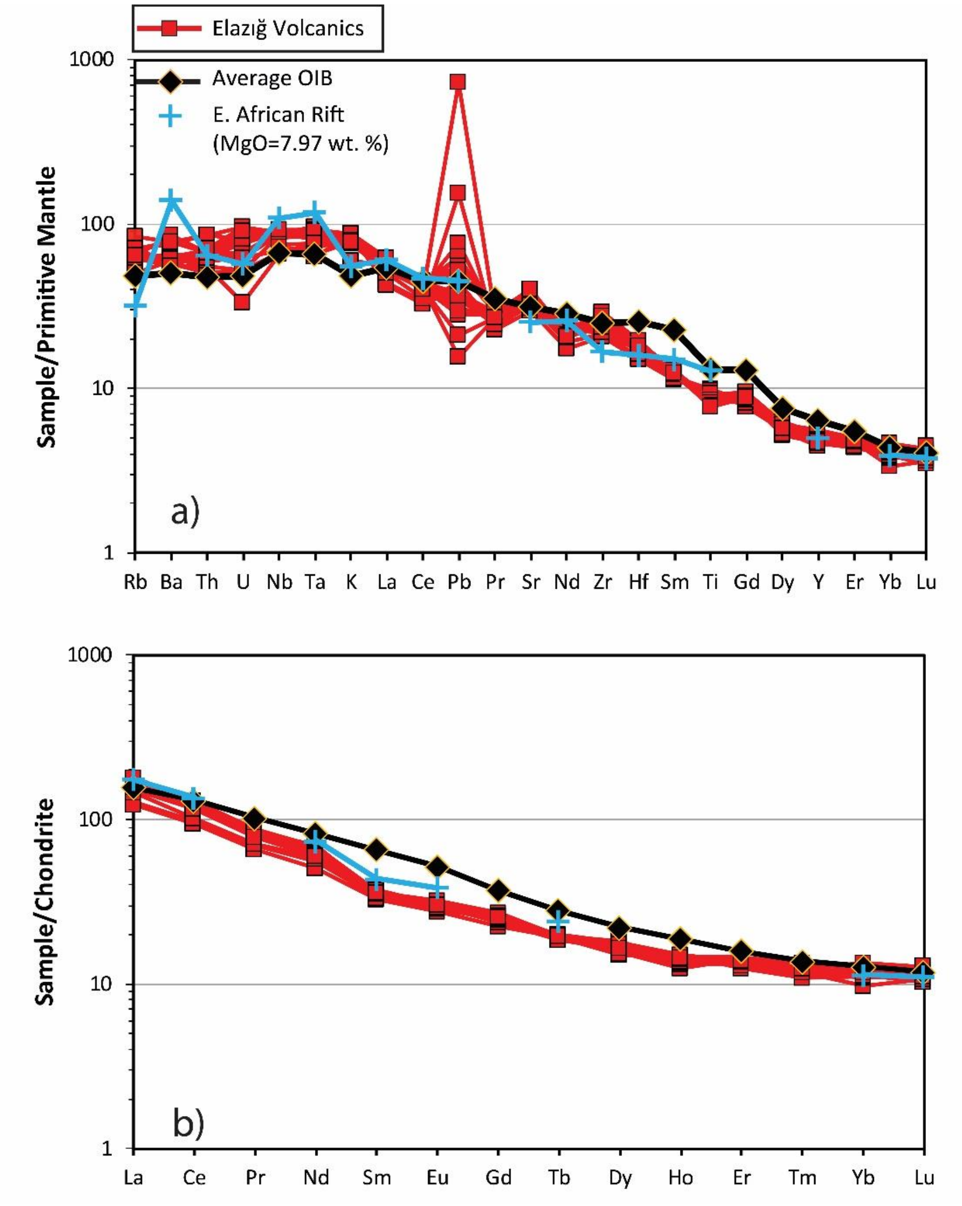

Figure 4.23. (a) Primitive Mantle-normalized multi-element and (b) chondrite-normalized rare earth element diagrams for the Elazığ Volcanics. The normalization values and average OIB values are from Sun and McDonough (1989). The data of East African Rift are from Furman (2007).

Moreover, the Elazığ Volcanics, with their OIB-like trace element characteristics, share also geochemical similarities with the Cenozoic Anatolian (e.g., Late Miocene western Anatolian volcanics, Aldanmaz et al., 2000; Kula Volcanics, Aldanmaz et al., 2015; Karacadağ Volcanics, Keskin et al. 2012b), circum-Mediterranen, and European lavas (e.g., Maghrebian Africa, Duggen et al., 2005; Massif Central France, Pilet et al., 2005; Sicily Channel, Civetta et al., 1998; Vogelsberg, Bogaard and Wörner, 2003) assumed to have been derived predominantly from asthenospheric mantle source region, as also shown by the multi-element diagrams (Figure 4.24). It is also important to note that the recycled asthenospheric mantle components (e.g., C, HIMU, EAR/LVC) have been recognized as playing an important role in the petrogenesis of these Anatolian, Mediterranean, and European (e.g., Wörner et al., 1986; Wilson and Downes, 1991; Cebrià and Wilson, 1995; Hoernle et al., 1995; Keskin et al., 2012b; Aldanmaz et al., 2015).

In the chondrite-normalized (Sun and McDonough, 1989) REE diagram, the Elazığ Volcanics also display very uniform patterns among each other (Figure 4.23b). Moreover, it is observed that LREE are significantly enriched relative to MREE and HREE in the volcanics (Figure 4.23b; e.g., $(La/Sm)_N$=3.72-5.10, $(La/Yb)_N$= 10.89-16.85, N denotes to chondrite-normalized based on Sun and McDonough, 1989). The Elazığ lavas display parallel elemental patterns with the average OIB and East African Rift sample in the diagram (Figure 4.23b). This may reflect similar fractionation histories for these lavas. The strong LREE/HREE fractionation in the lavas and slightly elevated $(Tb/Yb)_N$ (1.46-1.88) and $(Dy/Yb)_N$ (1.28-1.64) may also suggest similar melting conditions and source mineralogies with OIBs worldwide. In addition, the Elazığ lavas also demonstrate REE element patterns very similar to the OIB-like Cenozoic intraplate volcanism of Europe, circum-Mediterranean region, and Turkey in chondrite-normalized REE diagrams, suggesting also similar source features and melting systematics (Figure 4.24b and d). These are also discussed in the “Petrogenesis” section.

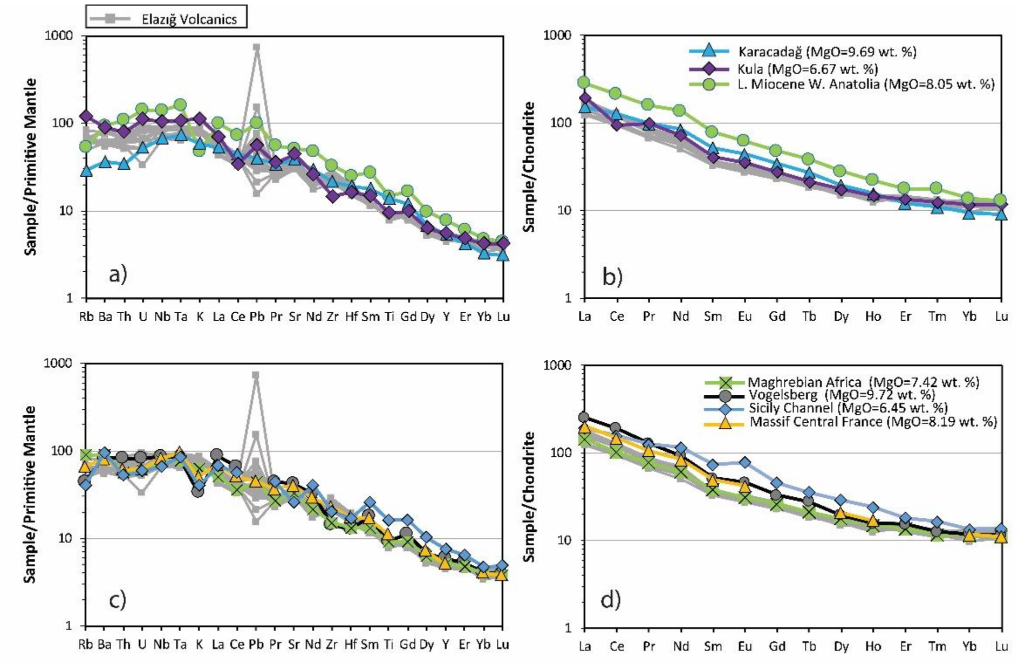

Figure 4.24. (a and c) Primitive Mantle-normalized multi-element and (b and d) chondrite-normalized rare earth element diagrams for the Elazığ Volcanics and the selected Cenozoic intraplate volcanics of the circum-Mediterranean region, Europe, and Anatolia. The normalization values are from Sun and McDonough (1989). Data Sources: Late Miocene western Anatolian volcanics-Aldanmaz et al., 2000; Kula Volcanics-Aldanmaz et al., 2015; Karacadağ Volcanics-Keskin et al. 2012b; Maghrebian Africa-Duggen et al., 2005; Massif Central France-Pilet et al., 2005; Sicily Channel-Civetta et al., 1998; Vogelsberg-Bogaard and Wörner, 2003.

4.3 Sr-Nd-Hf-Pb Isotope Geochemistry

4.3.1 Analytical Method

After evaluation of the major and trace element systematics of the studied rocks, 15 basaltic samples from the Tunceli Volcanics and 10 from the Elazığ Volcanics were selected for the whole rock Sr-Nd-Hf-Pb isotope analyses.

Strontium and Nd isotope analyses of the 25 volcanic samples were performed at the Radiogenic Isotope Laboratory (RIL), Middle East Technical University (METU), Ankara, Turkey. Each basaltic sample was initially powdered before chemical treatment in 100-class clean laboratory. After that, 100 mg powders of each sample were leached using 4 ml HF (52%). Leaching was performed on a hot plate (>100 °C) for 4 days. After the leaching process, the samples were dried and subsequently dissolved on the hotplate using 4 ml 6 N HCl. Afterward, these samples dried again and dissolved in 2.5 N HCL for chromatography. Separation of the Sr and REE from the matrix elements was conducted on the Teflon columns, which contain 2 ml BioRad AG50-W-X8 (100–200 mesh). Before removing the excessive Ba with 2.5 N HNO_3, Sr was separated in 2.5 N HCl. Subsequently, REE fraction (including the Nd) was eluted in 6 N HCl. Finally, the separation of Nd from the REE fraction was conducted on Teflon columns, which contain 2 ml HDEHP-coated BioRad resin in 0.22 N HCl. Before analyses, while the Sr was loaded on single Re filaments combined with 0.005 N H_3PO_4 and Ta activator, the Nd was loaded on double Re filaments with 0.005 N H_3PO_4. At the final stage, analyses were performed using a thermal ionization mass spectrometer (TIMS, Thermo-Fisher Triton). By using exponential law, $^{87}Sr/^{86}Sr$ ratio was normalized to $^{88}Sr/^{86}Sr=0.1194$, whereas $^{143}Nd/^{144}Nd$ ratio was normalized to $^{146}Nd/^{144}Nd=0.7219$. The NBS 987 Sr and the LaJolla Nd standards were measured as 0.710248±10 (n=4) and 0.511845±5 (n=2), respectively, during the analyses. No bias correction has been applied to these measurements. Uncertainties for individual Sr and Nd isotope analyses are at 2-sigma level. The details of the sample digestion, preparation for the chromatography, and isolation of Sr and Nd can be found in Köksal et al. (2017).

After the Sr and Nd isotope analyses, the remainder pulps of the 25 samples (15 from Tunceli Volcanics and 10 from Elazığ Volcanics) were sent to the Institute of Geochemistry and Petrology, ETH Zürich, Zürich, Switzerland for the Pb and Hf analyses. At the first stage, Pb separation was conducted on Teflon columns containing 150 μL BioRad AG1-X8 anion resin (100-200 mesh) in dilute mixtures of HBr and HNO_3, according to a method modified from Strelow and Toerien (1966). Afterward, re-equilibration of the eluted matrix elements was done using HCl for the Hf separation. Hafnium was separated from the major elements using 2 ml BioRad

AG50-X8 cation resin (200-400 mesh) in 1 M HCl-0.1 M HF following the method of Patchett and Tatsumoto (1980). Subsequently, the samples were oxidized with the concentrated $HClO_4$ and HCl. After oxidation, Hf was purified on 1.2 mL Eichrom LN-Spec resin (100-150 mesh) according to a method modified from Münker et al. (2001). At the last stage, subsequent to the elution of Zr in 2M HCl-0.1 M HF, Hf was collected in 6M HCl-0.3M HF. Measurements of the Pb and Hf isotope ratios were performed using multi-collector inductively coupled plasma mass spectrometry (MC-ICP-MS, Thermo-Fisher Neptune Plus). After analyses, corrections for the mass fraction of Pb isotopes were done using Tl doping by calculating a per-session $^{205}Tl/^{203}Tl$ ratio. This calculation is assumed to minimize the total offset of the $^{206,207,208}Pb/^{204}Pb$ and $^{207,208}Pb/^{206}Pb$ ratios of NBS 981 from the accepted values (Baker et al., 2004; c.f., Rehkämper and Halliday, 1998). Data were not accepted when the measured Tl/Pb ratios indicate imperfect homogenization of sample solutions, which corresponds to Tl/Pb ratios more than 10% removed from the sample mean. The corrections for the mass fraction of Hf isotopes, on the other hand, were made using exponential law. During the corrections, the $^{179}Hf/^{177}Hf$ isotope ratio is assumed to be 0.7325, and the sample compositions were normalized to $^{176}Hf/^{177}Hf=0.28216$ (accepted value of JMC-475; c.f., Blichert-Toft and Albarède, 1997) on per-session basis. For standards, average per-session 2 SD was 0.0013 for $^{206}Pb/^{204}Pb$, 0.0022 for $^{207}Pb/^{204}Pb$, and 0.0055 for $^{208}Pb/^{204}Pb$ ($n_{avg}=22$ per session). This was 0.24ε for $^{176}Hf/^{177}Hf$ ($n_{avg}=33$ per session). During the analyses, the NBS 981 was also processed through column chemistry and analyzed. The measurements of NBS 981 yielded 16.9381±0.0032 (2σ; n=13), 15.4939±0.0043 (2σ; n=13) and 36.7090±0.0141 (2σ; n=13), for the $^{206}Pb/^{204}Pb$, $^{207}Pb/^{204}Pb$ and $^{208}Pb/^{204}Pb$, respectively.

The whole rock Sr-Nd-Hf-Pb isotope data of the Tunceli and Elazığ Volcanics are available in Table 4.4.

Table 4.4. Sr-Nd-Hf-Pb isotope compositions of Tunceli and Elazığ Volcanics. Standard errors (s.e.) refer to the last digits in the isotope results.

Sample	**^{87}Sr/^{86}Sr**	2σ s.e.	**^{143}Nd/^{144}Nd**	2σ s.e.	**^{176}Hf/^{177}Hf**	2σ s.e.
Elazığ Volcanics						
BYD10	0.703638	±9	0.512872	±2	0.282998	±1
BYD15	0.703523	±4	0.512896	±2	0.283003	±1
BYD16	0.703525	±4	0.512877	±2	0.283000	±2
BYD26	0.703445	±3	0.512876	±2	0.282998	±3
BYD29	0.703585	±5	0.512871	±2	0.282990	±2
BYD30	0.703516	±5	0.512881	±2	0.283000	±3
BYD31	0.703522	±8	-	-	0.282997	±2
GMB3	0.703534	±12	0.512893	±3	0.283002	±2
GMB6	0.703911	±7	0.512864	±1	0.282992	±2
GMB8	0.703923	±9	0.512855	±2	0.282992	±2
Tunceli Volcanics						
AV2	0.704261	±8	0.512765	±4	0.282976	±2
AV20	0.704419	±8	0.512736	±5	0.282969	±3
AV24	0.704618	±5	0.512695	±3	0.282926	±2
AV33	0.704165	±5	0.512738	±3	0.282967	±2
AV34	0.705040	±6	0.512702	±2	0.282929	±3
AV38	0.704569	±4	0.512681	±2	0.282901	±2
AV40	0.704933	±6	0.512730	±7	0.282941	±2
AV42	0.704577	±8	0.512746	±4	0.282943	±1
AV49	0.704148	±5	0.512791	±4	0.282983	±2
AV59	0.704519	±5	0.512668	±3	0.282903	±3
AV67	0.704447	±9	0.512748	±9	0.282941	±1
AV70	0.704510	±5	0.512693	±6	0.282908	±3
AV72	0.704173	±4	0.512805	±4	0.282979	±3
AV73	0.704258	±5	0.512814	±7	0.282983	±2
AV75	0.704618	±4	0.512678	±5	0.282924	±1

Table 4.4. *(Cont'd)*

Sample	**^{206}Pb/^{204}Pb**	2σ s.e.	**^{207}Pb/^{204}Pb**	2σ s.e.	**^{208}Pb/^{204}Pb**	2σ s.e.
Elazığ Volcanics						
BYD10	18.9498	±13	15.6781	±17	39.0109	±55
BYD15	18.9597	±4	15.6726	±4	38.9966	±13
BYD16	19.0420	±5	15.6684	±4	39.0405	±12
BYD26	18.9942	±4	15.6697	±5	39.0091	±17
BYD29	19.0586	±12	15.6672	±28	39.0513	±40
BYD30	19.0194	±4	15.6678	±5	39.0238	±17
BYD31	19.0450	±3	15.6622	±4	39.0228	±13
GMB3	19.0519	±4	15.6699	±4	39.0643	±10
GMB6	19.0933	±2	15.6676	±2	39.0851	±8
GMB8	19.0860	±74	15.6514	±83	39.0396	±281
Tunceli Volcanics						
AV2	18.7552	±2	15.6915	±1	38.8459	±4
AV20	19.0508	±4	15.7003	±4	39.1682	±13
AV24	19.0845	±5	15.6924	±5	39.2169	±16
AV33	19.0743	±2	15.6777	±2	39.2085	±7
AV34	19.0684	±3	15.6935	±3	39.2038	±12
AV38	18.8469	±5	15.6916	±5	38.9959	±18
AV40	18.9760	±6	15.7145	±6	39.1157	±18
AV42	18.9652	±81	15.6937	±99	39.0521	±330
AV49	18.7256	±73	15.6742	±92	38.7803	±304
AV59	18.8566	±4	15.6917	±5	39.0106	±21
AV67	18.9713	±7	15.7077	±8	39.0866	±29
AV70	18.8255	±39	15.6791	±48	38.9353	±161
AV72	18.8959	±23	15.6437	±27	38.9297	±91
AV73	18.9380	±52	15.6508	±62	38.9754	±207
AV75	18.7686	±75	15.6829	±93	38.8828	±311

4.3.2 Tunceli Volcanics

In general, the mafic Tunceli lavas are characterized by moderately radiogenic $^{87}Sr/^{86}Sr$ and unradiogenic $^{143}Nd/^{144}Nd$ ratios ranging between 0.704148-0.705040 and 0.512668-0.512814, respectively. No systematic Sr-Nd isotopic variation has been observed between the alkaline and tholeiitic samples. With these Sr-Nd isotopic content, the data distribution of the Tunceli Volcanics extends from the depleted quadrant towards the enriched quadrant in the plot $^{87}Sr/^{86}Sr$ versus $^{143}Nd/^{144}Nd$ (Figure 4.25a). While the majority of the samples plot between fields of C/LVC (see the section “The Mantle Components” section in the “INTRODUCTION” chapter) and Bulk Silicate Earth (BSE), few samples follow the trend of EMII beyond the BSE in the diagram (Figure 4.25a). The general trend of the Tunceli Volcanics in the diagram, on the other hand, appear to be consistent with the trends of the western Anatolian lamproitic rocks (Elitok et al., 2010; Prelević et al., 2012), western Anatolian Early-Middle Miocene volcanic rocks (Aldanmaz et al., 2000; 2015), central Anatolian Hasandağ-Karapınar volcanics (Gall et al., 2021) and eastern Anatolian Quaternary Van volcanics (Oyan et al., 2016; 2017) which are assumed to involve melt contributions from the metasomatized-SCLM (Aldanmaz et al., 2000; 2015; Elitok et al., 2010; Prelević et al., 2012).

The Tunceli mafic lavas have $^{176}Hf/^{177}Hf$ ratios ranging between 0.282901-0.282983, and they plot in the depleted quadrant of the $^{143}Nd/^{144}Nd$ versus $^{176}Hf/^{177}Hf$ diagram (Figure 4.25b). They plot slightly above the mantle array ($\varepsilon Hf = 1.59 \varepsilon Nd + 1.28$; Chauvel et al., 2008) between the field of C and the value of “chondritic uniform reservoir” (CHUR; Bouvier et al., 2008) in the diagram (Figure 4.25b). Additionally, in the Nd-Hf isotope space, the Tunceli lavas also define a trend from the C component towards the enriched components EMI/EMII, which is consistent with the trends of western and central (Hasandağ-Karapınar Volcanics) Anatolian lavas. However, the central Anatolian trend deviate from the mantle array towards the terrestrial array (see Gall et al., 2021) (Figure 4.25b).

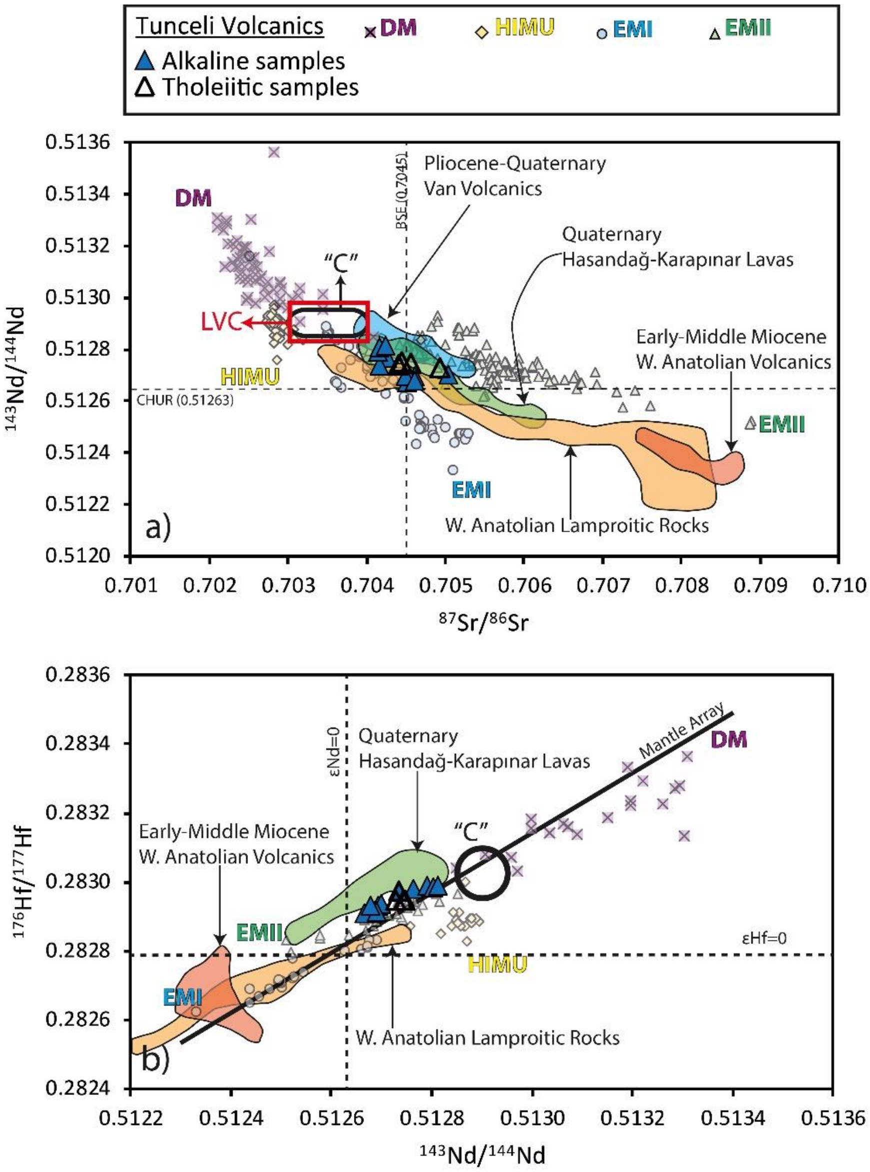

Figure 4.25. (a) ^{87}Sr/^{86}Sr versus ^{143}Nd/^{144}Nd and (b) ^{143}Nd/^{144}Nd versus ^{176}Hf/^{177}Hf plots for the Tunceli Volcanics. The western Anatolian Early-Middle Miocene volcanics (Aldanmaz et al., 2000; 2015), western Anatolian lamproitic rocks (Elitok et al., 2010; Prelević et al., 2012), Quaternary Hasandağ-Karapınar Lavas (Gall et al., 2021), Pliocene-Quaternary Van Volcanics (Oyan et al., 2016; 2017), and oceanic basalts (MORBs and OIBs) representing distinct extreme isotopic compositions in the mantle (HIMU, EMI, EMII and DM) are also plotted into the diagrams for comparison. The value of CHUR (Chondritic Uniform Reservoir) is from Bouvier et al. (2008) and the BSE (Bulk Silicate Earth) value is from Salters and Stracke (2004). The mantle array in the plot of ^{143}Nd/^{144}Nd versus ^{176}Hf/^{177}Hf is from Chauvel et al., 2008. The composition of LVC (Low-Velocity Component) is from Hoernle et al. (1995). The Sr-Nd isotope compositions of "C" (common

component) are from Hanan and Graham (1996). The Hf isotope composition of "C" is from Geldmacher et al. (2011). The data of the MORBs and OIBs are from the compilation of Stracke (2012) and PetDB Database (www.earthchem.org/petdb). The HIMU data are represented by the basalts in the islands of St. Helena and Mangaia (Chaffey et al., 1989; Reisberg et al., 1993; Woodhead, 1996; Salters and White, 1998; Willbold and Stracke 2006; Salters et al., 2011). The EMI data are represented by the basalts in the islands of Pitcairn (Woodhead and McCulloch, 1989; Woodhead and Devey, 1993; Salters and White, 1998; Eisele et al., 2002). The EMII data are represented by the basalts in the island of Samoa (White and Hofmann, 1982; Wright and White, 1987; Workmann et al., 2004; Salters et al., 2011). The DM data are represented by the basalts in the South Atlantic Ridge (Humphris et al., 1985; Hanan et al., 1986; Fontignie and Schilling, 1996; Andres et al., 2004; Agranier et al., 2005; Kelley et al., 2013; Cottrell and Kelley, 2013).

The $^{206}Pb/^{204}Pb$, $^{207}Pb/^{204}Pb$, and $^{208}Pb/^{204}Pb$ ratios of Tunceli Volcanics range between 18.72-19.08, 15.64-15.71 and 38.78-39.21, respectively (Figure 4.26). Although there is not a significant difference between alkaline and tholeiitic samples in terms of the $^{206}Pb/^{204}Pb$ (18.72-19.08 for alkaline samples and 18.96-19.05 for tholeiitic samples) and $^{208}Pb/^{204}Pb$ (38.78-39.21 for alkaline samples and 39.05-39.16 for tholeiitic samples) isotope ratios, the tholeiitic samples are slightly enriched in $^{207}Pb/^{204}Pb$ (15.64-15.69 for alkaline samples and 15.69-15.71 for tholeiitic samples) compared to the alkaline samples. With these Pb isotope compositions, the mafic Tunceli lavas plot above the Northern Hemisphere Reference Line (NHRL; Hart, 1984) in diagrams of $^{206}Pb/^{204}Pb$ versus $^{207}Pb/^{204}Pb$ and $^{206}Pb/^{204}Pb$ versus $^{208}Pb/^{204}Pb$ (Figure 4.26).

In the diagram of $^{206}Pb/^{204}Pb$ versus $^{207}Pb/^{204}Pb$, they define a slightly dispersed cluster above the EMII-type Samoan lavas within the field of the global subducted oceanic sediments (Figure 4.26a; GLOSS; Plank and Langmuir, 1998). Their data distribution in the diagram (Figure 4.26a), also appears to be comparable with the SCLM-related western, central, and eastern Anatolian lavas. In Figure 4.26a, they overlap with the Early-Middle Miocene western Anatolian volcanics, the ^{207}Pb-enriched and ^{206}Pb-depleted members of the western Anatolian lamproitic rocks, central Anatolian Quaternary Hasandağ-Karapınar volcanics, and Pliocene-

Quaternary Van volcanics. In the diagram of $^{206}Pb/^{204}Pb$ versus $^{208}Pb/^{204}Pb$ (Figure 4.26b), they also plot within the field of GLOSS, and overlap predominantly with the EMII-type Samoan lavas and the Anatolian lavas mentioned above. The lamproitic rocks overlapping with the Tunceli lavas in the plot are characterized by unradiogenic $^{206}Pb/^{204}Pb$ ratios (Figure 4.26b).

In addition, although the mafic Tunceli lavas have slightly elevated $^{208}Pb/^{204}Pb$ isotope ratios relative to NHRL, they define a trend between the DM end-member and the component C in plot of $^{206}Pb/^{204}Pb$ versus $^{208}Pb/^{204}Pb$ (Figure 4.26b). It is important to note that, the Tunceli Volcanics have less radiogenic $^{206}Pb/^{204}Pb$ ratios than the C component (e.g., Figure 4.26a and b), though they show relatively marked $^{207}Pb/^{204}Pb$ enrichment (e.g., Figure 4.26a).

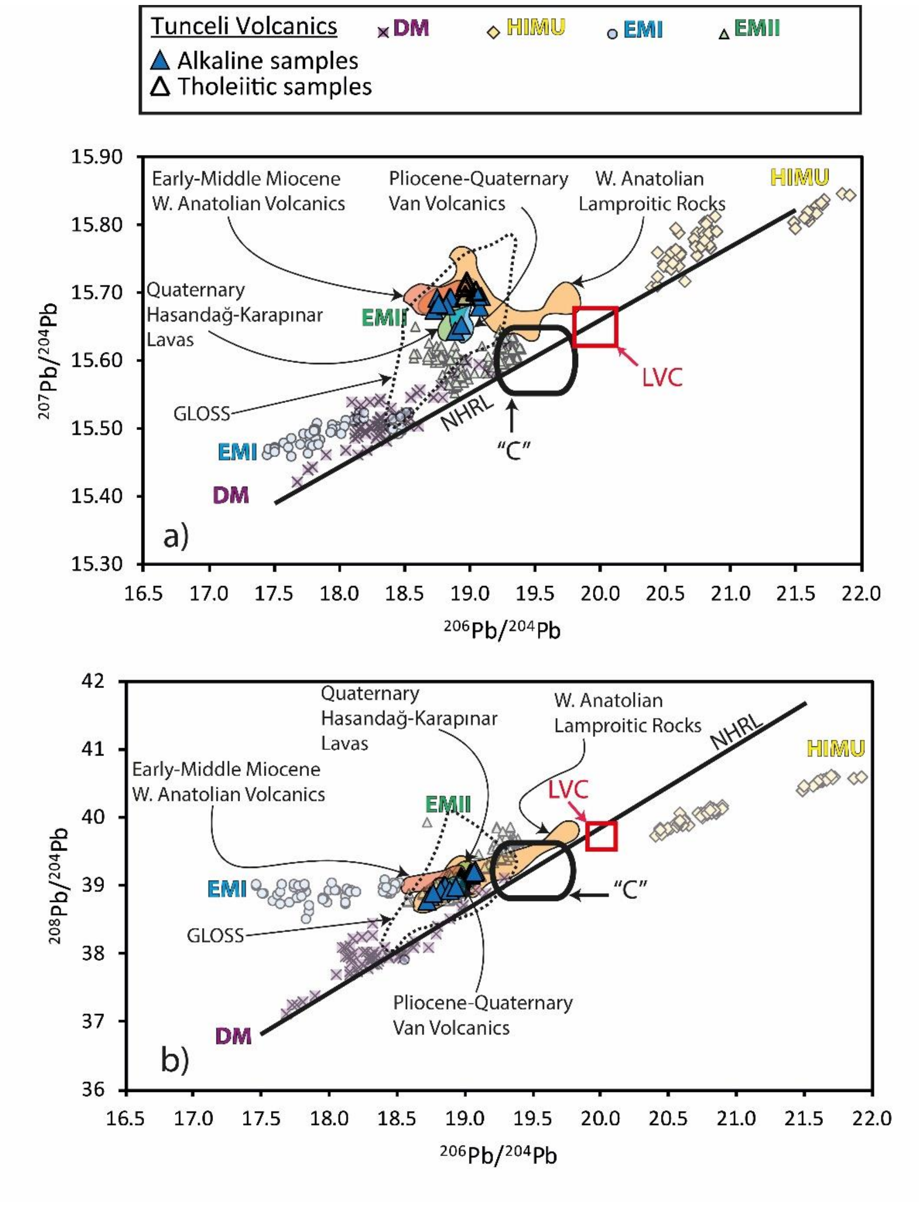

Figure 4.26. The (a) ^{206}Pb/^{204}Pb versus ^{207}Pb/^{204}Pb and (b) ^{206}Pb/^{204}Pb versus ^{208}Pb/^{204}Pb plots for the Tunceli Volcanics. The western Anatolian Early-Middle Miocene volcanics (Aldanmaz et al., 2000; 2015), western Anatolian lamproitic rocks (Elitok et al., 2010; Prelević et al., 2012), Quaternary Hasandağ-Karapınar Lavas (Gall et al., 2021), Pliocene-Quaternary Van Volcanics (Oyan et al., 2016; 2017), and oceanic basalts (MORBs and OIBs) representing distinct extreme isotopic compositions in the mantle (HIMU, EMI, EMII and DM) are also plotted into the diagrams for comparison. NHRL (Northern Hemisphere Reference Line) is from Hart (1984). The GLOSS (Global Subducted Sediments) data are from Plank and Langmuir (1998). The sources of compositions of the components LVC and C are given in the caption of Figure 4.25. Likewise, the locations of oceanic basalts and their data sources are also given in the caption of Figure 4.25.

4.3.3 Elazığ Volcanics

With low $^{87}Sr/^{86}Sr$ (0.70352-0.70392) and high $^{143}Nd/^{144}Nd$ (0.51277-0.51289) ratios relative to BSE, the Elazığ Volcanics plot totally within the depleted quadrant of the diagram of $^{87}Sr/^{86}Sr$ versus $^{143}Nd/^{144}Nd$ (Figure 4.27a). Except two evolved samples (GMB6 and GMB8), they have very uniform Sr-Nd isotope contents, and they define a tight cluster in the fields of C and LVC in the diagram (Figure 4.27a). The diagram (Figure 4.27a) also shows that the Sr-Nd isotope concentrations of the Elazığ lavas fall within the range of the those of other Cenozoic OIB-like intraplate volcanics of Turkey (e.g., Kula Volcanics, Alıcı et al., 2002; Late Miocene Çanakkale-Thrace lavas, Aldanmaz et al., 2000; 2015 and Karacadağ Volcanics, Alıcı-Şen et al., 2004; Keskin et al., 2012b). Likewise, with very uniform $^{176}Hf/^{177}Hf$ ratios (0.282990-0.283003), the Elazığ lavas form a dense cluster predominantly in the field of the C component in the plot of $^{143}Nd/^{144}Nd$ versus $^{176}Hf/^{177}Hf$ diagram (Figure 4.27b). The Elazığ lavas are placed slightly below the mantle array ($\varepsilon Hf = 1.59\varepsilon Nd + 1.28$; Chauvel et al., 2008) in the Nd-Hf isotope space (Figure 4.27b) as many HIMU- and C-type oceanic basalts. The Elazığ lavas also have similar Hf isotope contents with the OIB-like Anatolian lavas, which plot between the low Nd-Hf end of the MORB and high-end Nd-Hf of the EMII arrays in the Nd-Hf isotope space (Figure 4.27b).

The intersect of the Elazığ lavas with compositional space of the LVC component also necessitate a comparison between the Elazığ Volcanics and Cenozoic European and circum-Mediterranean OIB-like intraplate lavas. There is no Hf isotope data available for most European OIB-like intraplate volcanics. However, when their Sr-Nd contents are plotted together with the Elazığ lavas into the diagram of $^{87}Sr/^{86}Sr$ versus $^{143}Nd/^{144}Nd$, it is apparent that the OIB-like intraplate volcanics from these continental sectors are characterized by similar Sr-Nd isotope ratios (Figure 4.28). They overlap together with the compositional space of LVC or EAR in the Sr-Nd isotope space (Figure 4.28), though some volcanic European volcanics deviate from the C/LVC field towards the enriched members (e.g., Vogelsberg).

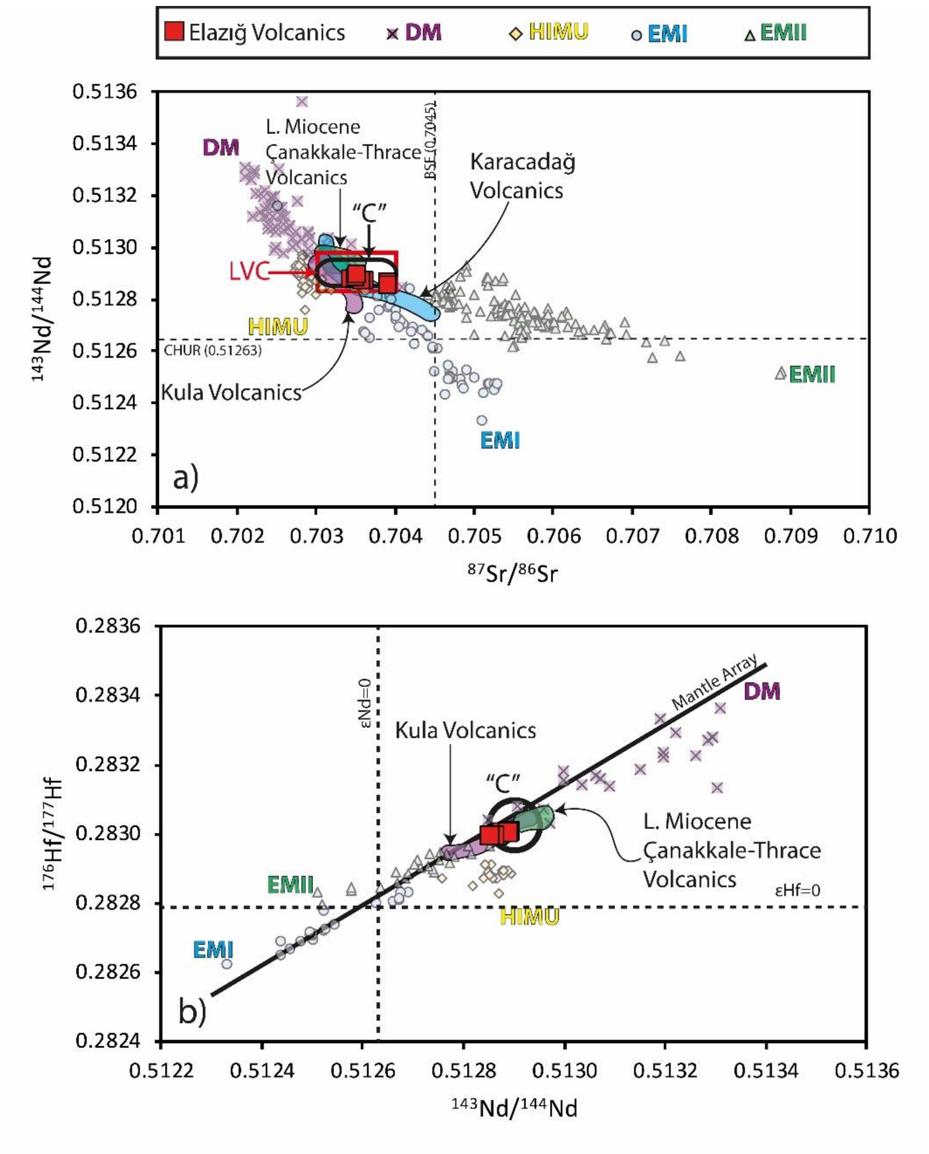

Figure 4.27. (a) $^{87}Sr/^{86}Sr$ versus $^{143}Nd/^{144}Nd$ and (b) $^{143}Nd/^{144}Nd$ versus $^{176}Hf/^{177}Hf$ plots for the Elazığ Volcanics and the Cenozoic OIB-like intraplate Anatolian lavas (Kula Volcanics-Alıcı et al., 2002; Aldanmaz et al., 2015; Late Miocene Çanakkale-Thrace lavas-Aldanmaz et al., 2000; 2015 and Karacadağ Volcanics-Alıcı-Şen et al., 2004; Keskin et al., 2012b). Oceanic basalts (MORBs and OIBs) representing distinct extreme isotopic compositions in the mantle (HIMU, EMI, EMII, and DM) are also plotted into the diagrams for comparison. The sources for the value of CHUR, BSE, mantle array, LVC, C, and oceanic basalts are given in the caption of Figure 4.25.

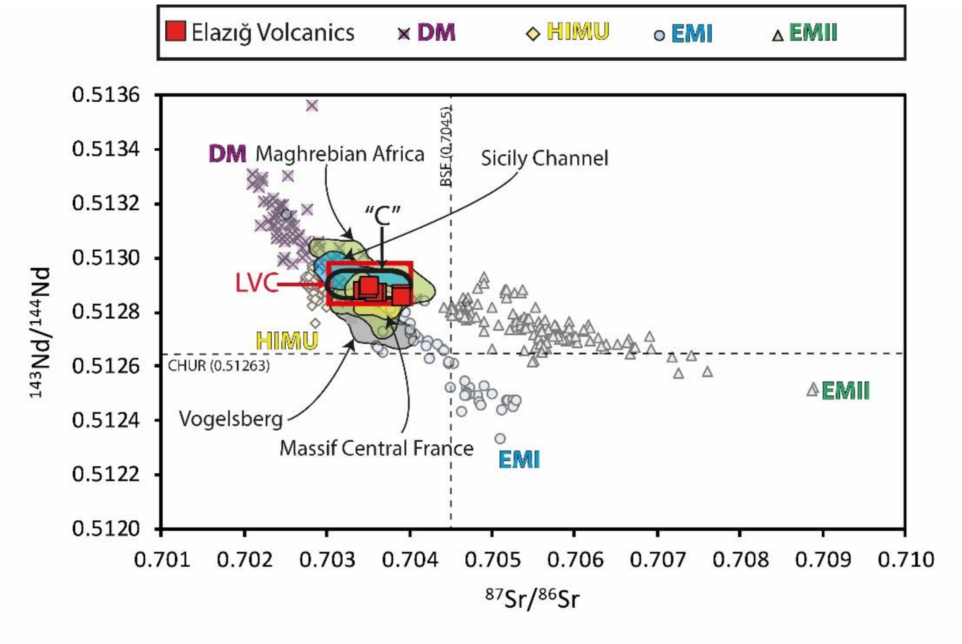

Figure 4.28. The ^{87}Sr/^{86}Sr versus ^{143}Nd/^{144}Nd plot for the Elazığ Volcanics and the Cenozoic OIB-like intraplate circum-Mediterranean and European lavas (Maghrebian Africa-Duggen et al., 2005; Massif Central France-Pilet et al., 2002; 2005; Sicily Channel-Esperença and Crisci, 1995; Civetta et al., 1998 and Vogelsberg-Bogaard and Wörner, 2003). Oceanic basalts (MORBs and OIBs) representing distinct extreme isotopic compositions in the mantle (HIMU, EMI, EMII, and DM) are also plotted into the diagrams for comparison. The sources for the value of CHUR, BSE, LVC, C, and oceanic basalts are given in the caption of Figure 4.25.

The Elazığ Volcanics are characterized by very homogenous ^{206}Pb/^{204}Pb, ^{207}Pb/^{204}Pb, and ^{208}Pb/^{204}Pb ratios, which vary in a narrow range between 18.94-19.09, 15.65-15.67 and 38.99-39.08, respectively.

Such homogenous Pb isotope content may argue that the primary Pb isotope nature of the Elazığ Volcanics, unlike their Pb elemental budget, have not been disturbed by a possible water-rock interaction. Nevertheless, the alteration-modified Pb elemental budget of the Elazığ Volcanics necessitates an assessment of the possible Pb-isotope mobility for these rocks. This assessment will help to understand whether the Pb isotope contents of the volcanics reflect their source feature or not. Therefore, in order to test the possibility of Pb isotope mobility due to alteration in the Elazığ

Volcanics, their Pb element contents and LOI values are plotted against their Pb isotope contents (Figure 4.29). As it can be seen in the figure (Figure 4.29), the ^{206}Pb/^{204}Pb, ^{207}Pb/^{204}Pb, and ^{208}Pb/^{204}Pb ratios of the volcanics remain almost constant independent of Pb element content and with increasing LOI values in the volcanics. This demonstrates that hydrothermal alteration, which may be responsible for the selective Pb element mobility in the Elazığ Volcanics, has not disturbed the Pb isotope contents of these rocks. Hence, the Pb isotope ratios of the Elazığ Volcanics can be used for further petrogenetic interpretations.

With the homogenous Pb isotope contents, the Elazığ lavas plot above the NHRL (Hart, 1984) in both diagrams of ^{206}Pb/^{204}Pb versus ^{207}Pb/^{204}Pb and ^{206}Pb/^{204}Pb versus ^{208}Pb/^{204}Pb (Figure 4.30). The Elazığ lavas have unradiogenic ^{206}Pb/^{204}Pb ratios compared to the C component, and with their elevated ^{207}Pb/^{204}Pb and ^{208}Pb/^{204}Pb relative to NHRL, they plot within the field of GLOSS (Plank and Langmuir, 1998) between the C and DM end-members in the Pb-Pb isotope spaces (Figure 4.30). While the Elazığ lavas define a tight cluster above the EMII-type Samoan lavas in the diagram of ^{206}Pb/^{204}Pb versus ^{207}Pb/^{204}Pb (Figure 4.30a), they plot directly on the EMII-type Samoan lavas in the diagram of ^{206}Pb/^{204}Pb versus ^{208}Pb/^{204}Pb (Figure 4.30b). When the Elazığ Volcanics are plotted together with other Cenozoic OIB-like intraplate volcanics of Turkey into the Pb-Pb spaces, it is observed that the data distribution of the Elazığ lavas is consistent with the compositional trend created by OIB-like Anatolian lavas (Figure 4.30). Their data cluster overlap with these Anatolian lavas (e.g., Kula and Karacadağ Volcanics) in the Pb-Pb isotope spaces (Figure 4.30). This shows that the enrichment in the ratios of ^{207}Pb/^{204}Pb and ^{208}Pb/^{204}Pb relative to the NHRL and slight depletion in the ratio ^{206}Pb/^{204}Pb relative to the C component may be a unique chemical feature for the Anatolian OIB-like intraplate lavas.

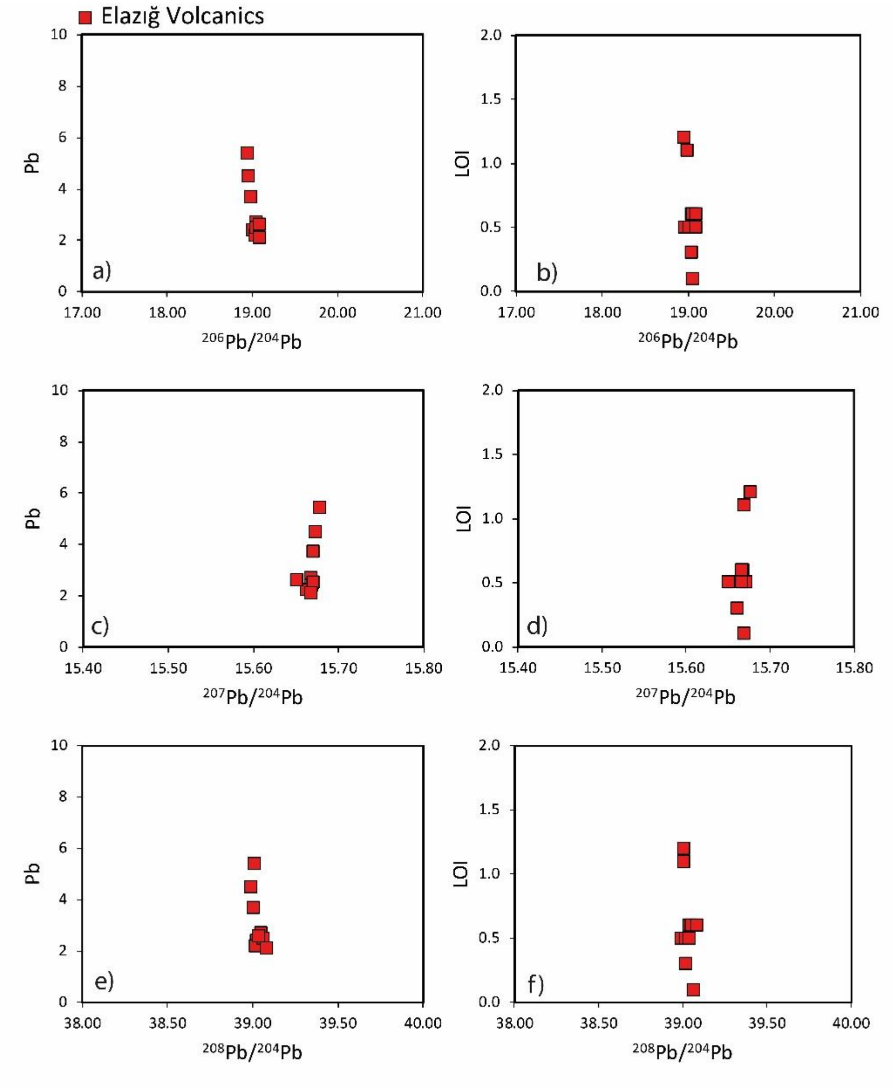

Figure 4.29. Plots of Pb isotope ratios versus Pb (ppm) element abundances and LOI (wt. %) values for the Elazığ Volcanics.

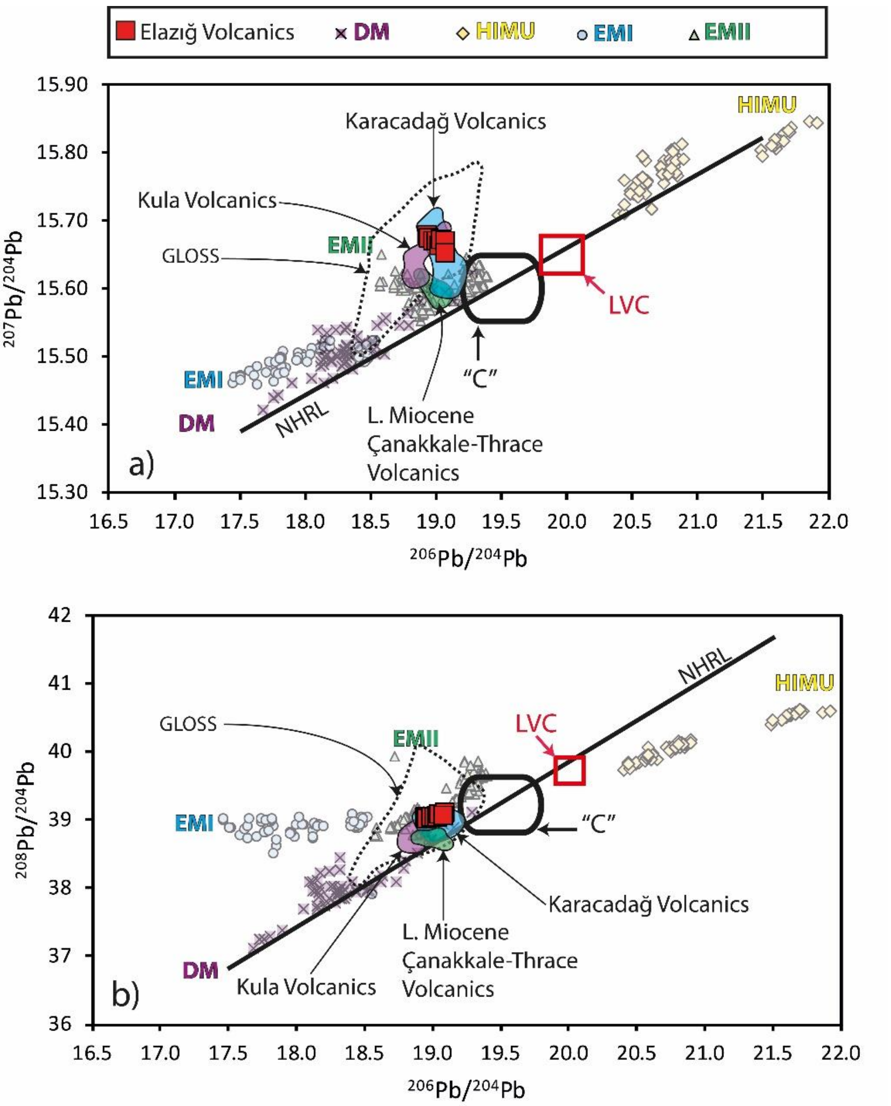

Figure 4.30. The (a) ^{206}Pb/^{204}Pb versus ^{207}Pb/^{204}Pb and (b) ^{206}Pb/^{204}Pb versus ^{208}Pb/^{204}Pb plots for the Elazığ Volcanics and the Cenozoic OIB-like intraplate Anatolian lavas (Kula Volcanics-Alıcı et al., 2002; Aldanmaz et al., 2015; Late Miocene Çanakkale-Thrace lavas-Aldanmaz et al., 2000; 2015 and Karacadağ Volcanics-Alıcı-Şen et al., 2004; Keskin et al., 2012b). Oceanic basalts (MORBs and OIBs) representing distinct extreme isotopic compositions in the mantle (HIMU, EMI, EMII, and DM) are also plotted into the diagrams for comparison. The sources for the NHRL, GLOSS, C, and LVC are given in the captions of Figure 4.25 and Figure 4.26. Likewise, the locations oceanic of basalts and their data sources are also given in the captions of Figure 4.25.

When the OIB-like Elazığ lavas compared with Cenozoic circum-Mediterranean and central European OIB-like intraplate lavas, on the other hand, it can be observed that, despite of their Sr-Nd isotope systematics, they do not share similar Pb isotope characteristics (e.g., Figure 4.31). The circum-Mediterranean and central European Cenozoic OIB-like lavas are characterized generally by more radiogenic $^{206}Pb/^{204}Pb$ isotope ratios relative to Elazığ and other Anatolian OIB-like lavas. They usually deviate from the component LVC, which is characterized by $^{206}Pb/^{204}Pb$ = ~20, towards other enriched and depleted members (Figure 4.31). Moreover, they scarcely plot within the compositional field of GLOSS on the contrary to Elazığ lavas and other Anatolian OIB-like lavas.

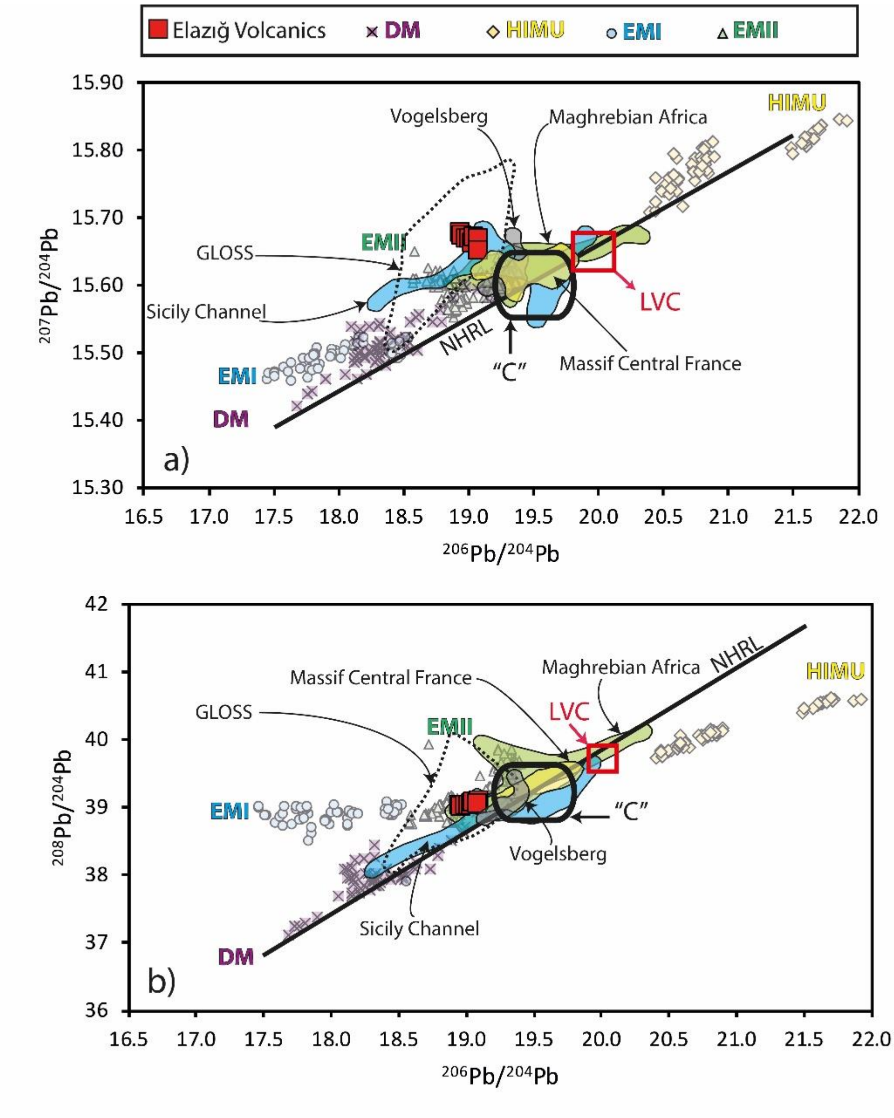

Figure 4.31. The (a) ^{206}Pb/^{204}Pb versus ^{207}Pb/^{204}Pb and (b) ^{206}Pb/^{204}Pb versus ^{208}Pb/^{204}Pb plots for the Elazığ Volcanics and the Cenozoic OIB-like intraplate circum-Mediterranean and European lavas (Maghrebian Africa-Duggen et al., 2005; Massif Central France-Pilet et al., 2002; 2005; Sicily Channel-Esperença and Crisci, 1995; Civetta et al., 1998 and Vogelsberg-Bogaard and Wörner, 2003). Oceanic basalts (MORBs and OIBs) representing distinct extreme isotopic compositions in the mantle (HIMU, EMI, EMII, and DM) are also plotted into the diagrams for comparison. The sources for the NHRL, GLOSS, C, and LVC are given in the captions of Figure 4.25 and Figure 4.26. Likewise, the locations of oceanic basalts and their data sources are also given in the captions of Figure 4.25.

CHAPTER 5

DISCUSSION

5.1 Petrogenesis

5.1.1 Fractional Crystallization

5.1.1.1 Tunceli Volcanics

It has been previously stated that the fractional crystallization process (FC) was not substantially operative during the within-suite petrogenetic evolution of the Tunceli Volcanics (Aktağ et al., 2019). Aktağ et al. (2019) have reported that the major oxide and trace element data of the Tunceli Volcanism is consistent only with minor fractionation of the mafic phases such as olivine and clinopyroxene. Here, in this section of the thesis, the fractionation history of the Tunceli lavas has been revisited using the same major and trace element data reported in the study of Aktağ et al. (2019). In the present study, however, these data have been reevaluated in detail, and is expected to provide a better understanding of their petrogenetic evolution.

As is mentioned above in the "PETROGRAPHY" chapter of this thesis, the main mineral phases in the Tunceli Volcanics are; olivine, clinopyroxene, plagioclase, and the Fe-Ti oxide phases such as ilmenite and magnetite. Removal of one of these phases during the magmatic evolution would control the chemistry of these lavas. Therefore, the major-trace element data are crucial to understand whether the FC was an essential process during the magmatic evolution of the Tunceli volcanism, and the extent to which the FC controlled their chemistry. It is observed that the Tunceli lavas have lower MgO (3.46-10 wt. %) and Ni (31.4-225 ppm) contents compared to the primary basaltic magmas (see Hart and Davies, 1978). In this regard, FC may have led to the evolution of the Tunceli lavas from more magnesian primary magmas. This observation is consistent with the progressive decrease of MgO with increasing SiO_2 in these volcanics, supporting the idea that parental melts of the Tunceli lavas are more magnesian, i.e., more primitive.

The major and trace element variations against MgO in the Tunceli volcanism recorded very limited trends in bivariate diagrams (Figure 4.17 and Figure 4.18). This may argue against an extensive fractional crystallization for these lavas. This is also apparent in their compositional homogeneity. However, a few negative and positive trends in those diagrams may indicate that fractionation of some phases occurred during their magmatic evolution. For instance, the slight decrease in Ni and Co with decreasing MgO in the bivariate diagrams (Figure 4.18f and g) may indicate the removal of mafic phases such as olivine and clinopyroxene in these lavas. However, as mentioned above, these fractionations appear to be not extensive in these lavas. This idea is reinforced by the absence of obvious negative trends in CaO and Sc (Figure 4.17d and 4.18e) with decreasing MgO. In addition, the increase in Al_2O_3 with decreasing MgO may argue against plagioclase fractionation in these lavas (Figure 4.17b). This may also be inferred from the absence of negative trends of CaO and Sr with decreasing MgO (Figure 4.17d and 4.18c).

In order to provide a more detailed approach on this issue, fractionation vectors have been calculated by following the Rayleigh equation (Figures 5.1, 5.2, and 5.3);

$C_L/C_o=F^{(D-1)}$ where (Eqn. 2)

C_L: trace element concentration (weight) in the remaining melt at any stage of crystallization

C_o: trace element concentration (weight) in the parental melt, i.e., starting composition

F: fractionation ratio, i.e., the fraction of the melt remaining

D: bulk partition coefficient for the trace element

Such theoretical modelings, especially those that do not consider the other parameters (e.g., P-T conditions, oxygen fugacity, etc.), do not provide a perfect simulation for the fractional crystallization event. However, they are useful for developing a practical approach to understanding this natural phenomenon. Particularly, the coherency between the trends created by solid geochemical data and the calculated vectors in the models may help to better understand which mineral species dominate the crystallization-based differentiation in the lavas.

Each calculated vector in these models (Figures 5.1, 5.2, and 5.3) represents certain mineral paragenesis (olivine+clinopyroxene+plagioclase), which is consistent with the basic magma composition. Crystallization rates of individual mineral phases in the mineral combination determine the major trends of the vectors in the models. Th was defined as a fractionation index in the models since it is assumed to be highly incompatible during the crystallization of the basaltic magmas (e.g., for basic magmas ${}^{\text{olv-liq}}Kd_{Th}=0.0001$, ${}^{\text{cpx-liq}}Kd_{Th}=0.00026$, ${}^{\text{plg-liq}}Kd_{Th}=0.05$; McKenzie and O'Nions, 1991). Nickel, Sc, and Sr, on the other hand, are selected and set into the Y-axis since they are known to be highly compatible (for the partition coefficients, see Table 5.1) with olivine, clinopyroxene, and plagioclase, respectively. In such modelings, the starting composition is not crucial since the parental melts are not determined. Instead, the main credit has been given to the trends of the calculated vectors (e.g., Keskin, 1994; Aldanmaz, 1998). However, to provide a better demonstration, the composition of the most primitive sample in the data set of Tunceli volcanism (AV67; (Mg#:63,3, MgO: 10,00 w.t.%) was chosen as the starting composition for the calculated vectors.

The model of Th versus Ni was developed to elucidate the extent of olivine crystallization in the lavas since the Ni is known to be highly compatible (Table 5.1; for basic magmas, the ${}^{\text{olv-liq}}Kd_{Ni}=12.2$; Bougault and Hekinian, 1974) with the olivine in the basaltic liquids (Figure 5.1). However, it is also important to note that clinopyroxene has the highest distribution coefficient (Table 5.1; for basic magmas ${}^{\text{cpx-liq}}Kd_{Ni}=4.4$; Bougault and Hekinian, 1974) for Ni after olivine. Therefore, the Ni-based theoretical vectors containing clinopyroxene in their crystallizing mineral paragenesis also give strong insights into the concomitant crystallization of olivine and clinopyroxene. In case of substantial removal of individual olivine or olivine+clinopyroxene pairs from the magma will create a strong negative trend in the Th versus Ni log-log diagrams. This is also well-observed from the calculated vectors consistent with the fractionation of olivine and clinopyroxene. The vectors are consistent with even 5% crystallization of olivine display negative trends in the model (Figure 5.1 e.g., V1, V2 and V3).

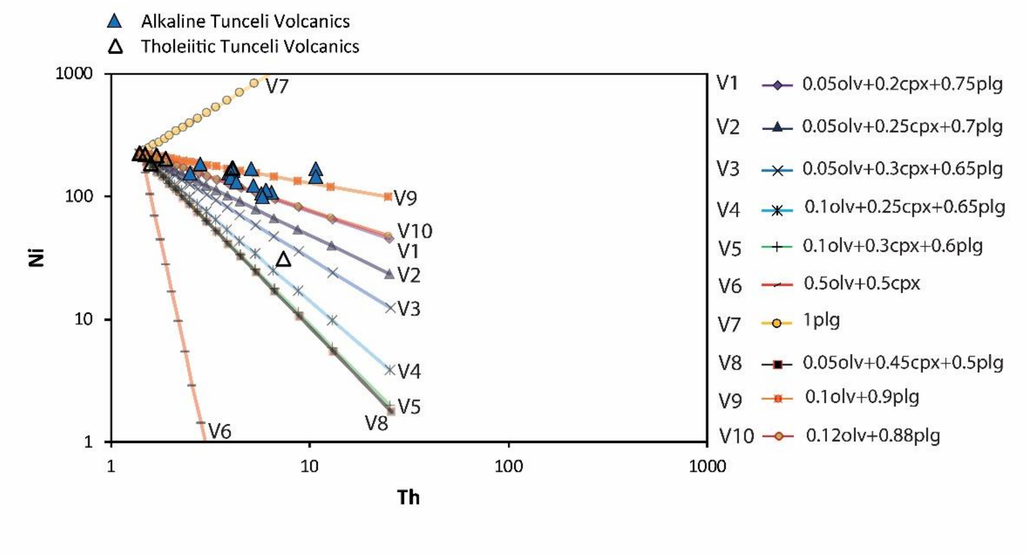

Figure 5.1. The log-log diagram of Th (ppm) versus Ni (ppm) showing the data distribution of Tunceli volcanism and the calculated theoretical Rayleigh vectors. Crystallization ends at 95% for each model, and the tick marks on the vectors correspond to 5% crystallization intervals. The mineral/melt partition coefficients (Kd) for Ni and Th are compiled from GERM K*d* Database (https://earthref.org/). The Kd values and their references are given in Table 5.1. The crystallized mineral phase combinations for each vector are given in the figure. Key to abbreviations: v: vector; olv: olivine; cpx: clinopyroxene; plg: plagioclase.

In the model, it is seen that the Ni displays a slight negative correlation with Th, which can be attributed to olivine or olivine+clinopyroxene crystallization (Figure 5.1). This idea is also supported by the good correlation of the data points with the vectors 1, 9, and 10 in the diagram. While the trend of vector 1 is controlled mainly by concomitant crystallization of olivine and clinopyroxene (5% olivine and 20% clinopyroxene), the trends of vectors 9 and 10 are solely controlled by the crystallization of olivine (vector 9: 10% olivine; vector 10: 12% olivine). Note that the fractionation of plagioclase has no control on the trends due to the low partition coefficient of Ni for plagioclase (Table 5.1; for basic magmas, $^{plg\text{-}liq}Kd_{Ni}$=0,06; Bougault and Hekinian, 1974). Based on the calculated Rayleigh vectors in the diagram of Th versus Ni, two distinct scenarios can be suggested for the crystallization history of Tunceli volcanism. In the first case, fractional crystallization of the Tunceli volcanism is dominated by fractionation of clinopyroxene with subordinate olivine. This can be inferred from the coherent data distribution of the Tunceli volcanics with vector 1 consistent with crystallization 5% olivine and 20% clinopyroxene. In the second scenario, the fractional crystallization-based differentiation of the Tunceli Volcanics is controlled mainly by the removal of olivine from the parental magma. This case, on the other hand, is well supported by the coherent trends between the Tunceli Volcanics and vectors 9 and 10. The trends of these vectors are solely controlled by the crystallization of olivine (~10%). In this case, the removal of olivine around 10% is consistent with trends created by the data distribution of Tunceli volcanism. Extensive crystallization of olivine, however, cannot be suggested based on the Rayleigh modelings. As can be seen from the diagram, more than 10% crystallization of olivine will create strong negative trends (e.g., vector 6), which constrast with the trends of the data points. Note that the sample AV22 display the steeepest negative trend among the Tunceli lavas. This may suggest that relatively more extensive olivine removal may have been occured during the evolution of this unique sample compared to the rest of samples. Such suggestion will be also consistent with its lowest Fe_2O_3, Ni, an Co concentrations within the Tunceli lava suite (Figures 4.17 and 4.18).

Among these two crystallization scenarios, the former requires further evaluation since there is no strong evidence for a clinopyroxene-dominated fractional crystallization event in the trace element systematics of Tunceli lavas. As mentioned above, in their bivariate Harker diagrams, CaO and Sc, which are compatible with the clinopyroxene, do not display any negative trends with decreasing MgO in the Tunceli volcanism (Figure 4.17d and 4.18e). This may argue against a fractionation scenario involving substantial removal of clinopyroxene. Nevertheless, the crystallization of clinopyroxene in these lavas cannot be totally ruled out. Therefore, in order to better understand the role of clinopyroxene removal in the differentiation history of Tunceli Volcanics, the Rayleigh crystallization vectors have been calculated for the diagram Th versus Sc (Figure 5.2). Since Sc is known to be compatible with clinopyroxene (Table 5.1; for basic magmas $^{cpx\text{-}liq}Kd_{Sc}=3.3$; Paster et al., 1974), the Rayleigh modeling of Th versus Sc can provide useful information regarding the control of clinopyroxene removal in evolving an magma.

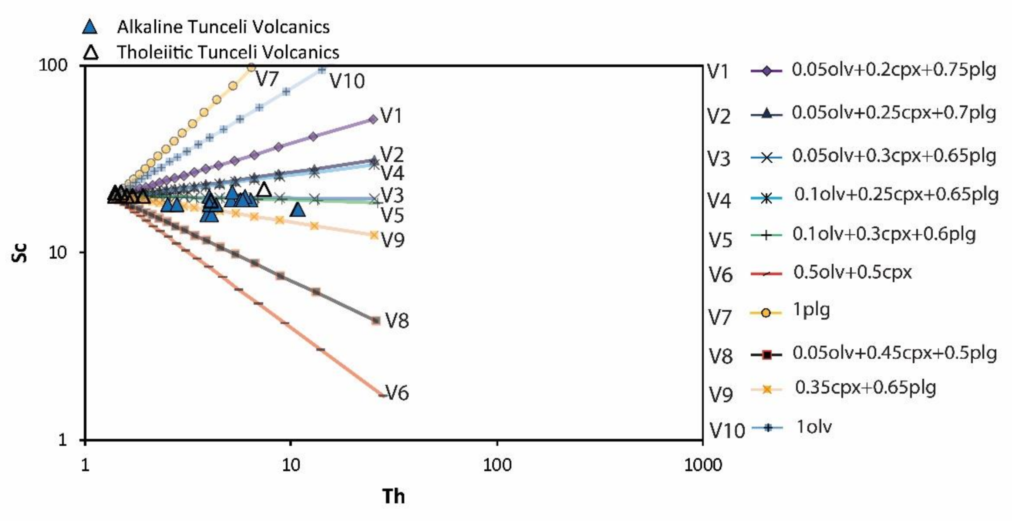

Figure 5.2. The log-log diagram of Th (ppm) versus Sc (ppm) showing the data distribution of Tunceli volcanism and the calculated theoretical Rayleigh vectors. Crystallization ends at 95% for each model, and the tick marks on the vectors correspond to 5% crystallization intervals. The mineral/melt partition coefficients (Kd) for Sc and Th are compiled from GERM K*d* Database (https://earthref.org/). The Kd values and their references are given in Table 5.1. The crystallized mineral phase combinations for each vector are given in the figure. Key to abbreviations: v: vector; olv: olivine; cpx: clinopyroxene; plg: plagioclase.

In the log-log model of Th versus Sc (Figure 5.2), it is observed that the vectors containing no clinopyroxene in their theoretical fractionated mineral assemblage exhibit the steepest positive trends (vector 7: 100% plagioclase fractionation; vector 10: 100% olivine fractionation). These patterns are expected since Sc is not strongly partitioned into olivine and plagioclase (Table 5.1; for basic magmas $^{plg-liq}Kd_{Sc}$=0.008; $^{olv-liq}Kd_{Sc}$=0.33, Paster et al., 1974). Even under 100% fractionation, these incompatible minerals do not create a descending trend between Th and Sc.

However, some interesting trends are reflected by the vectors (vector 1, 2, and 4) consisting of significant fractionation of clinopyroxene. These theoretical Rayleigh vectors have shown that, although Sc is compatible in clinopyroxene with distribution coefficient 3.3 (Paster et al., 1974), even up to %25 fractionation of clinopyroxene do not produce a descending trend between Th and Sc. Moreover, flat trends are created by the vectors consisting of ca. 30% fractionation of clinopyroxene (vector 3 and 5). This suggests that even up to 30% fractionation of clinopyroxene cannot create a negative trend between Th and Sc. In the diagram, the trend of vector 9 indicates that the fractionation of clinopyroxene should exceed 30% in a possible fractional crystallization event to create a negative trend between Sc and Th. The Tunceli lavas, on the other hand, display trends parallel to the flat vectors (vectors 3 and 5) consistent with fractionation of ca. 30% clinopyroxene (Figure 5.2). When considering all these, the first scenario, including concomitant fractionation of clinopyroxene and olivine, cannot be neglected in the petrogenesis of Tunceli lavas, in spite of the absence of positive correlation between CaO and Sc against MgO in the bivariate diagrams (Figure 4.17d and 4.18e).

Apart from olivine and clinopyroxene, an assessment of fractionation using Rayleigh vectors was also conducted for plagioclase, a major phase in the mineralogy of the Tunceli Volcanics (Figure 5.3). Although the trends in the Harker diagrams of Tunceli Volcanics (e.g., Figure 4.17d and 4.18c) argue against plagioclase removal during their magmatic evolution, a correlation between the modeled vectors and the measured data can provide better information on this event. Since Sr has a high distribution coefficient for plagioclase (Table 5.1; for basic magmas, $^{plg-liq}Kd_{Sr}$=2; McKenzie and O’Nions, 1991), its concentration in the melt is assumed to be controlled by fractionation of plagioclase. Therefore, the Rayleigh vectors for certain mineral paragenesis, including different rates of plagioclase fractionation, have been modeled in the log-log diagram of Th versus Sr (Figure 5.3). Nevertheless, the data distribution in this diagram should be carefully interpreted since Sr has low-ionic potential; thereby, more prone to hydrothermal alteration.

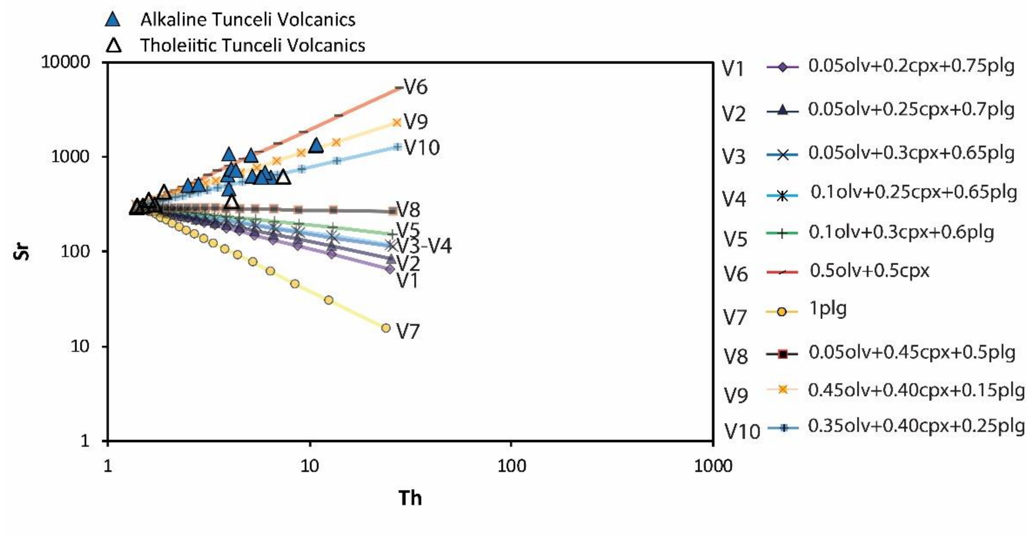

Figure 5.3. The log-log diagram of Th (ppm) versus Sr (ppm) showing the data distribution of Tunceli volcanism and the calculated theoretical Rayleigh vectors. Crystallization ends at 95% for each model, and the tick marks on the vectors correspond to 5% crystallization intervals. The mineral/melt partition coefficients (Kd) for Sr and Th are compiled from GERM K*d* Database (https://earthref.org/). The Kd values and their references are given in Table 5.1. The crystallized mineral phase combinations for each vector are given in the figure. Key to abbreviations: v: vector; olv: olivine; cpx: clinopyroxene; plg: plagioclase.

In the diagram of Th versus Sr (Figure 5.3), the data points of Tunceli lavas, in general, create a positive trend, which is consistent with Rayleigh vectors 6, 9, and 10. Among these vectors, the vector modeled only for the fractionation of olivine and clinopyroxene (vector 6) display the steepest positive trend since both olivine and clinopyroxene have low distribution coefficient for Sr (Table 5.1; for basic magmas $^{olv\text{-}liq}Kd_{Sr}=0.00019$, $^{cpx\text{-}liq}Kd_{Sr}=0.067$; McKenzie and O'Nions, 1991). It can be seen in the diagram, nearly half of the samples follow this plagioclase fractionation-free trend in the diagram. This data distribution in the diagram may support the idea that the fractionation of plagioclase was not significant during the magmatic evolution of Tunceli volcanism. However, there is also a considerable amount of data that follow the trends vectors 9 and 10, which suggest fractionation of plagioclase up to 25% from the magma. This, on the other hand, may argue that, to some extent, plagioclase may have been removed from the parental magma of Tunceli volcanism. These two Rayleigh vectors (V9 and V10) show that, although Sr is compatible in plagioclase, the data distribution displaying a positive trend between Th and Sr is not strictly suggestive for the lack of plagioclase fractionation. Moreover, vector 8 indicate that up to 50 % fractionation of plagioclase cannot create a negative trend between Th and Sr. When considering all these, if the primary (magmatic) elemental budget of Sr in the Tunceli lavas has not been disturbed by a possible water-rock interaction, it can be suggested that to some extent the plagioclase fractionation may have occurred during the magmatic evolution of the Tunceli Volcanics. However, it is also possible that those samples that follow the trends of vector 9 and 10, may have affected by a possible hydrothermal alteration and this result in non-primary trend in the diagram. Note that, Tunceli lavas display a slight dispersed pattern in a diagram of Zr versus Sr (not shown). Therefore, one can still postulate a plagioclase-free fractionation history for Tunceli lavas.

Overall, based on the modelings above, a fractional crystallization history involving olivine-dominant fractionation can be suggested for the Tunceli volcanism. However, the modelings also suggest that, to some extent, the fractionation of clinopyroxene cannot also be totally ruled out. Lastly, in addition to these, if the Tunceli lavas preserve their primary elemental budget for the Sr, a minor fraction of plagioclase may also be suggested for these volcanics. It is also important to note that the data distribution of the Tunceli Volcanics in the bivariate Harker diagrams and log-log Th versus Ni-Sc-Sr modelings indicate that FC process was not extensively involved during their magmatic evolution. This process has created only a minor within-suite compositional diversity in the lavas; indeed, the Tunceli lavas are represented only by basalts.

5.1.1.2 Elazığ Volcanics

The lower MgO (6.31-8.24 wt.%) and Ni (82.9-134.5 ppm) concentrations of Elazığ lavas compared to those of primary basaltic melts (e.g., Hart and Davies, 1978) suggest that the Elazığ lavas may have been differentiated via FC process from more magnesian parental melts. Geochemical trends observed in the bivariate Harker diagrams (Figures 4.21 and 4.22) of Elazığ Volcanics also reveal robust evidence for the involvement of fractional crystallization process. Compared to the Tunceli volcanism, the Elazığ Volcanics display highly correlated trends in the Harker diagrams (Figures 4.21 and 4.22), which can be attributed to a relatively more extensive FC process during their magmatic evolution. Decreasing CaO, Sc, Ni, and Co with decreasing MgO (Figures 4.21d and 4.22e-g) in the Elazığ volcanism are suggestive of fractionation of clinopyroxene and olivine. Moreover, the decrease in Fe_2O_3, TiO_2, and V with decreasing MgO (Figures 4.21e-f and 4.22h) is consistent with the fractionation of oxide phases such as magnetite and ilmenite. In addition to these, the increase in Al_2O_3 and Sr with decreasing MgO (Figures 4.21b and 4.22c) in the Elazığ volcanism indicates that the fractionation of plagioclase was limited or not operative during the magmatic evolution of these lavas, as in the case of Tunceli volcanism.

To test the arguments about the fractionation history of the Elazığ volcanism, the data trends were compared with the modeled Rayleigh vectors in the diagrams of Th versus Ni, Th versus Sc, and Th versus Sr (Figures 5.4, 5.5 and 5.7). These diagrams are assumed to give insights into olivine, clinopyroxene, and plagioclase fractionations, respectively. All modeling parameters, with the exception of starting compositions, are the same as used for Tunceli volcanism above. The related element concentrations of the samples BYD31 (e.g., Mg#:62.6), the most primitive sample of the data set, are set for the starting composition in the modelings.

In the log-log diagram of Th versus Ni (Figure 5.4), the Elazığ Volcanics show a slightly decreasing trend consistent with the trends of vectors 1, 2, and 10. Since the role of plagioclase is limited in determining negative fractionation trends in this diagram, as reflected by vector 7 (also see Table 5.1 for the partition coefficient of plagioclase for Ni in basaltic melts), the trends of these vectors are determined by the fractionation of olivine and clinopyroxene. While vectors 1 and 2 suggest fractionation clinopyroxene-dominated assemblage with subordinate olivine (fractionation of ca. 20-25% clinopyroxene + 5% olivine), the trend of vector 10 is determined solely by fractionation of 10% olivine. The accordance of the Elazığ trend with these vectors, therefore, may imply two possible fractionation paths for the Elazığ volcanism, as in the case of Tunceli volcanism. The first path is consistent with concomitant fractionation of clinopyroxene and olivine, in which the role of clinopyroxene fractionation is dominant in the differentiation of Elazığ volcanism. The latter, on the other hand, suggests only a minor amount of olivine removal from the parental magma of Elazığ lavas. The bulk geochemical trends of Elazığ Volcanics, however, provide compelling evidence for a fractionation assemblage, including clinopyroxene. As mentioned above, the decrease in CaO and Sc with decreasing MgO argue against an FC history in which clinopyroxene is not involved. Therefore, the latter case appears to be not very probable for the Elazığ Volcanism. Nevertheless, the accordance of the data points with vector 10 also necessitates a test for clinopyroxene fractionation in these lavas.

When the Elazığ lavas are plotted in the log-log diagram of Th versus Sc, including modeled Rayleigh fractionation vectors, it is clearly seen that these lavas define a trend showing consistency with the vectors 6 and 8 (Figure 5.5). These Rayleigh vectors in the diagram were modeled for 45-50% removal of clinopyroxene. Hence, the coherent trend of the Elazığ lavas with these vectors can be regarded as a manifestation of substantial fractionation of clinopyroxene in these lavas. This also supports the idea that olivine fractionation alone cannot account for the geochemical trends observed in the Elazığ volcanism.

Overall, the trends created by the Elazığ lavas in the diagrams of Th versus Ni (Figure 5.4) and Th versus Sc (Figure 5.5) suggest fractionation of a clinopyroxene-dominant assemblage with subordinate olivine.

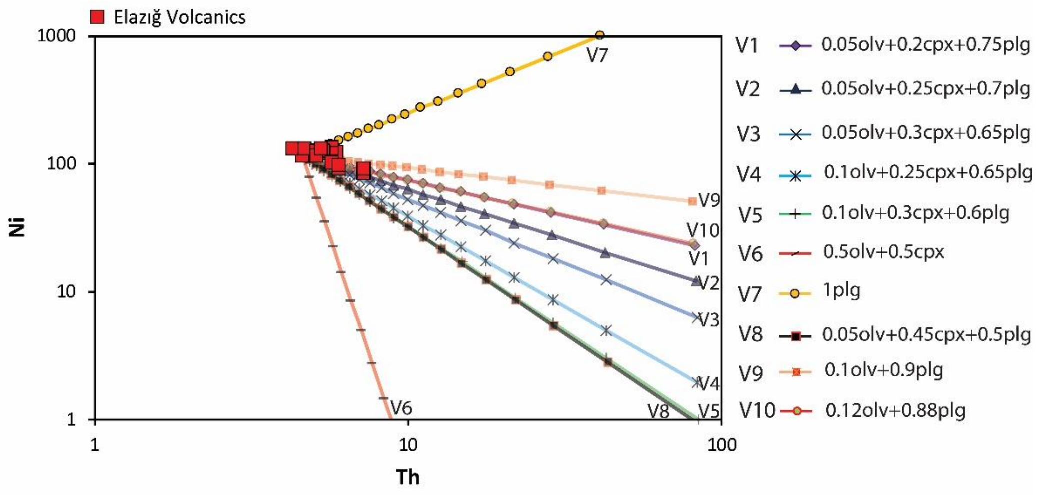

Figure 5.4. The log-log diagram of Th (ppm) versus Ni (ppm) showing the data distribution of Elazığ volcanism and calculated theoretical Rayleigh vectors. Crystallization ends at 95% for each model, and the tick marks on the vectors correspond to 5% crystallization intervals. The mineral/melt partition coefficients (Kd) for Ni and Th are compiled from GERM K*d* Database (https://earthref.org/). The Kd values and their references are given in Table 5.1. The crystallized mineral phase combinations for each vector are given in the figure. Key to abbreviations: v: vector; olv: olivine; cpx: clinopyroxene; plg: plagioclase.

Considering all these with the phenocryst assemblages of Elazığ volcanism and their thermobarometry calculations, it can be suggested that the clinopyroxene removal in these lavas should have been occurred at moderate to high pressures. As it is mentioned in the "PETROGRAPHY" chapter of this thesis, there are no clinopyroxene phenocryst phases available in the Elazığ lavas. This petrographical picture, together with the results of FC modelings implying a significant clinopyroxene removal in these lavas, may suggest a high-P differentiation events. As proven by experiments and modelings, clinopyroxene replaces olivine above the 10 kbar pressures in alkaline and tholeiitic melts (e.g., Bender et al., 1978; Furman et al., 1991). Hence, a high amount of clinopyroxene removal following its crystallization in the Elazığ lavas may have occurred at greater depths (>10 kbar at least; Bender et al., 1978). Such a differentiation process may account for the FC modeling results and mineralogy of the Elazığ lavas.

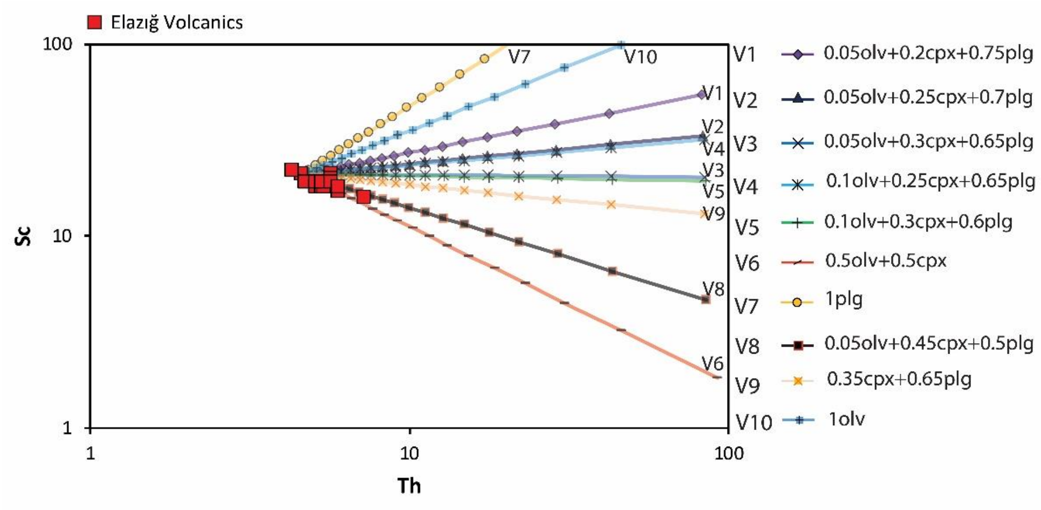

Figure 5.5. The log-log diagram of Th (ppm) versus Sc (ppm) showing the data distribution of Elazığ volcanism and calculated theoretical Rayleigh vectors. Crystallization ends at 95% for each model, and the tick marks on the vectors correspond to 5% crystallization intervals. The mineral/melt partition coefficients (Kd) for Sc and Th are compiled from GERM K*d* Database (https://earthref.org/). The Kd values and their references are given in Table 5.1. The crystallized mineral phase combinations for each vector are given in the figure. Key to abbreviations: v: vector; olv: olivine; cpx: clinopyroxene; plg: plagioclase.

Strong support for a high-P differentiation can be inferred from the olivine-diopside-nepheline pseudo-ternary diagram projected through plagioclase (Figure 5.6; Sack et al., 1987; Furman et al., 1991). When the Elazığ lavas are plotted on this ternary diagram, their data points plot close to experimentally determined moderate to high-pressure (8-30 kbar) multiple saturation surface for alkaline melts. This data distribution in the diagram also suggests a high-P fractionation for the Elazığ lavas. Moreover, in this study and Di Giuseppe et al. (2017), high crystallization pressures have been proposed for the existing phenocryst phases in the Elazığ lavas. Considering this with the absence of clinopyroxene phenocrysts in the Elazığ lavas, high pressures can be suggested for the clinopyroxene fractionation. As in the case of the Surtsey lavas (Furman et al., 1991), the compositional evolution of Elazığ lavas should have occurred *en route* to the surface after substantial differentiation of their primary melts at greater depths.

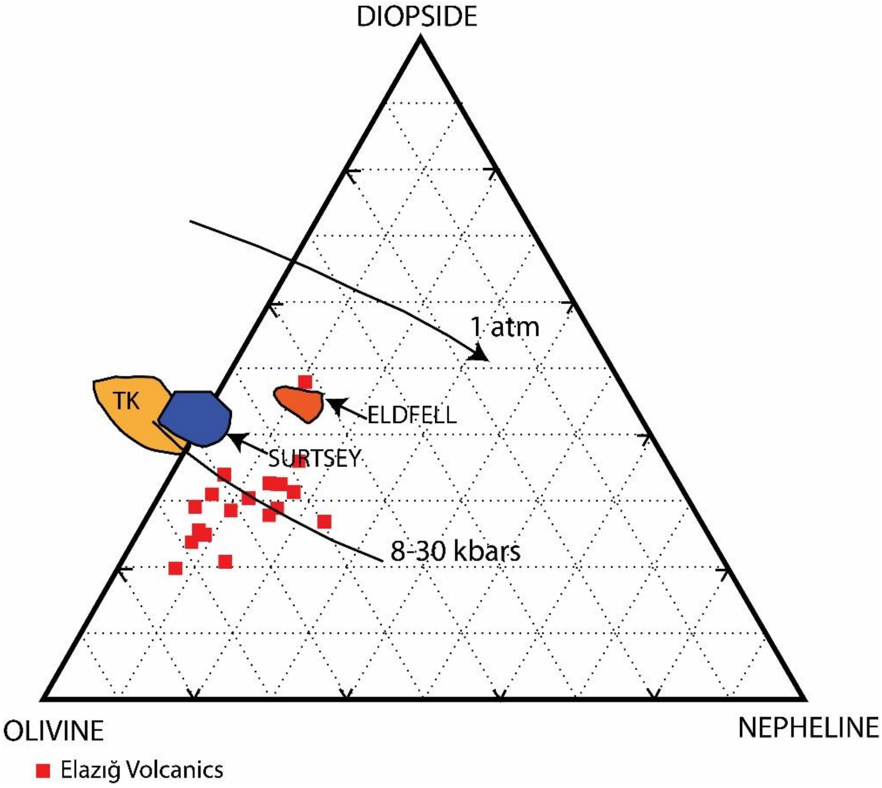

Figure 5.6. Olivine-diopside-nepheline pseudo-ternary diagram including experimentally defined 1 atm olivine+high calcium pyroxene+plagioclase cotectic and moderate to high pressure (8-30 kbar) olivine+orthopyroxene+clinopyroxene cotectic for alkaline melts (Sack et al., 1987). The end-members of the ternary plane represent normative components. All data used in the projection of the experimental cotectics and their sources can be found in Sack et al. (1987). The fields of the Surtsey and Eldfell lavas are from Furman et al. (1991). The field of TK represents moderate to high pressure (8-30 kbar) melts of Takahashi and Kushiro (1983) and Fujii and Scarfe (1985), taken from Furman et al. (1991).

Besides all these implications about mafic phase fractionation in the Elazığ Volcanics, it is also necessary to evaluate the role of plagioclase fractionation in the differentiation history of these lavas since being a largely fractionating phase in the basaltic liquids. As seen in the case of Tunceli volcanism, the increase in Al_2O_3 and Sr with decreasing MgO in the Elazığ volcanism (Figure 4.21b and 4.22c) do not strictly preclude the plagioclase fractionation. Therefore, a detailed evaluation of the Elazığ lavas in the diagram of Th versus Sr (Figure 5.7), which includes calculated

Rayleigh vectors, may provide crucial information regarding the occurrence and extent of plagioclase fractionation during the magmatic evolution of these lavas.

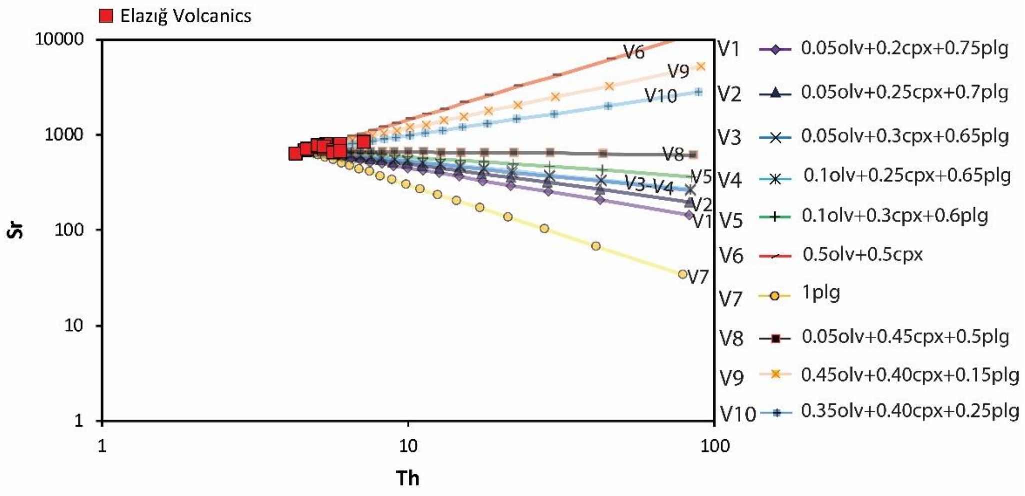

Figure 5.7. The log-log diagram of Th (ppm) versus Sr (ppm) showing the data distribution of Elazığ volcanism and calculated theoretical Rayleigh vectors. Crystallization ends at 95% for each model, and the tick marks on the vectors correspond to 5% crystallization intervals. The mineral/melt partition coefficients (Kd) for Sr and Th are compiled from GERM K*d* Database (https://earthref.org/). The Kd values and their references are given in Table 5.1. The crystallized mineral phase combinations for each vector are given in the figure. Key to abbreviations: v: vector; olv: olivine; cpx: clinopyroxene; plg: plagioclase.

In the log-log diagram of Th versus Sr (Figure 5.7), it is observed that few Elazığ lavas, whit Th contents lower than 5.1 ppm, display a coherent trend with vector 6. Since this vector is consistent with fractionation of a mineral assemblage without plagioclase, it can be suggested that the plagioclase fractionation was not operative during the magmatic evolution of at least some of the samples in the Elazığ data. However, the general increasing trend of the Elazığ lavas appears to stop its increase at 5.1 ppm Th, and get more flattened above this value in the diagram. The samples with Th contents over 5.1 ppm display much more coherent trends with those vectors 9 and 10. This may postulate that the removal of plagioclase in the Elazığ volcanism took place at the point where the Th content of the magma reached around 5 ppm.

Nevertheless, since vectors 9 and 10 are consistent with fractionation of ca. 15-25 % plagioclase, an extensive plagioclase removal cannot be suggested for the Elazığ volcanism.

To sum up the fractionation history of the Elazığ Volcanics in the light of their trends in the bivariate Harker diagrams and log-log FC modeling diagrams, it can be proposed that fractionation of an assemblage containing clinopyroxene, olivine, plagioclase, and Fe-Ti oxide phases played an important role in the differentiation of these rocks. Among these phases, however, the removal of clinopyroxene appears to be relatively extensive during their magmatic evolution. Additionally, this extensive clinopyroxene removal in the Elazığ volcanism seems to have taken place at great depths in the region.

5.1.2 Crustal Assimilation

Magmas that undergo magma storage in the thick continental settings are also simultaneously prone to assimilate the crustal material. It is important to note that around the Tunceli and Elazığ regions, geophysical studies have recorded crustal thickness between 45-50 km (e.g., Zor et al., 2003). Therefore, an assessment is necessary whether the volcanisms both from the Tunceli and Elazığ regions were contaminated by the continental crustal material during their ascent or not. This evaluation would provide crucial information to which extent the volcanics has loosed their primary chemical features if the contamination process were operative during their evolution. Furthermore, according to the implications made in this section, the crustally contaminated samples were eliminated in the assessment of mantle source characteristics. With this elimination, it is expected that the potential misinterpretations regarding the petrogenesis of Tunceli and Elazığ lavas will also be prevented.

5.1.2.1 Tunceli Volcanics

The previous studies argued that the Tunceli lavas had not been affected by potential crustal contamination during their ascent (Di Giuseppe et al., 2017; Aktağ et al., 2019). Rather, it was been postulated that the enriched element and isotope characteristics of the Tunceli Volcanics reflect the derivation of these lavas from a metasomatized SCLM beneath the region. In this section, this discussion has been deepened by reevaluation of their major and trace element data (Aktağ et al., 2019) combined with their new Sr-Nd-Hf-Pb isotope data. It is thought that these new evaluations will bring further aspects to the petrogenesis of Tunceli lavas.

The scattered data distribution of the Tunceli Volcanics in general in the bivariate Harker diagrams (Figure 4.17 and 4.18) may suggest a limited magma residence time in the crust. This is also supported by the results of FC modelings (Figure 5.1, 5.2, and 5.3), arguing against an extensive magma storage processing for these lavas. The low residence time of the magma in the crust may reduce the possibility of crustal assimilation. Therefore, a quick ascent of the Tunceli lavas may have prevented their significant interaction with the eastern Anatolian crust. A rapid rise of magma, however, still cannot totally preclude the possibility of crustal contamination. Even the melts that pass quickly through the thick continental crust may incorporate some crustal xenoliths and/or xenocrysts during their ascent, thus evidencing that crustal contamination might be the case. Although there is no petrographical evidence recognized so far for the incorporation of crustal material during their ascent, a more robust approximation to the role of crustal contamination process in the petrogenesis of Tunceli Volcanics can be developed by the assimilation-sensitive trace element and isotope systematics. Therefore, a detailed evaluation of the crustal assimilation process during the magmatic evolution of Tunceli volcanism is given below.

As an alternative to subduction-related processes, the elevated LILE/HFSE ratio, negative Nb, and positive Pb anomalies observed in the Tunceli Volcanics (Figure 4.19a) may also suggest interaction of the Tunceli melts with the continental crust. Since most incompatible elements (e.g., Cs, Rb, U, Th) are incorporated into the melt during the crust production and the crust is not easily recycled back into the mantle, the crust is regarded as the major geochemical reservoir of the Earth, especially for those elements mobilized during melting (Taylor and McLennan, 1995). Therefore, the crustal domains are enriched in most incompatible/mobile elements (e.g., Taylor and McLennan, 1985; Rudnick and Gao, 2004). This is well demonstrated in Figure 5.8 where the crustal domains (e.g., Upper Crust) are characterized by high contents of Pb, U, and Ba. These elements are known to be more mobile relative to the elements Ce and Nb. Therefore, the crustal reservoirs in the diagram are characterized by low Ce/Pb, Nb/U, and high Ba/Nb ratios.

When considering these, a possible interaction of the lavas with continental crust during their ascent would lead to enrichment in their mobile elemental budget. Therefore, the enriched mobile element profile Tunceli Volcanics may be suggestive for the involvement of the crustal assimilation process in their petrogenesis. This is also supported by the data distribution of the Tunceli Volcanics in the plots of Nb/U versus Ce/Pb (Figure 5.8a) and Ba/Nb versus Ce/Pb (Figure 5.8b). The Tunceli lavas display enrichment in Pb, U, and Ba elements relative to most of the lavas derived from asthenospheric mantle sources (e.g., OIBs and MORBs). This results in a decrease in their Ce/Pb (6.41-24.96), Nb/U (8.81-34.5), and an increase in their Ba/Nb (10.76-41.15) elemental ratios, and deviate their composition from the asthenospheric mantle range (e.g., average of oceanic basalts: Ce/Pb= 25 ± 5, Nb/U=47 ± 10; Hofmann et al., 1986) towards the crustal values (Upper Crust: Nb/U= 8.9, Ce/Pb= 3.2; Taylor and McLennan, 1985) in the diagrams of Nb/U versus Ce/Pb and Ba/Nb versus Ce/Pb (Figure 5.8).

However, it must be noted that such elemental signatures are also apparent in the arc and/or intraplate lavas derived from a mantle source that has been modified by slab-derived melts and fluids (e.g., Ben-Othman et al., 1989; Furman et al., 2021). Hence, the enrichment in the mobile elements may also be related to mantle source characteristics rather than a post-melting process, such as crustal contamination.

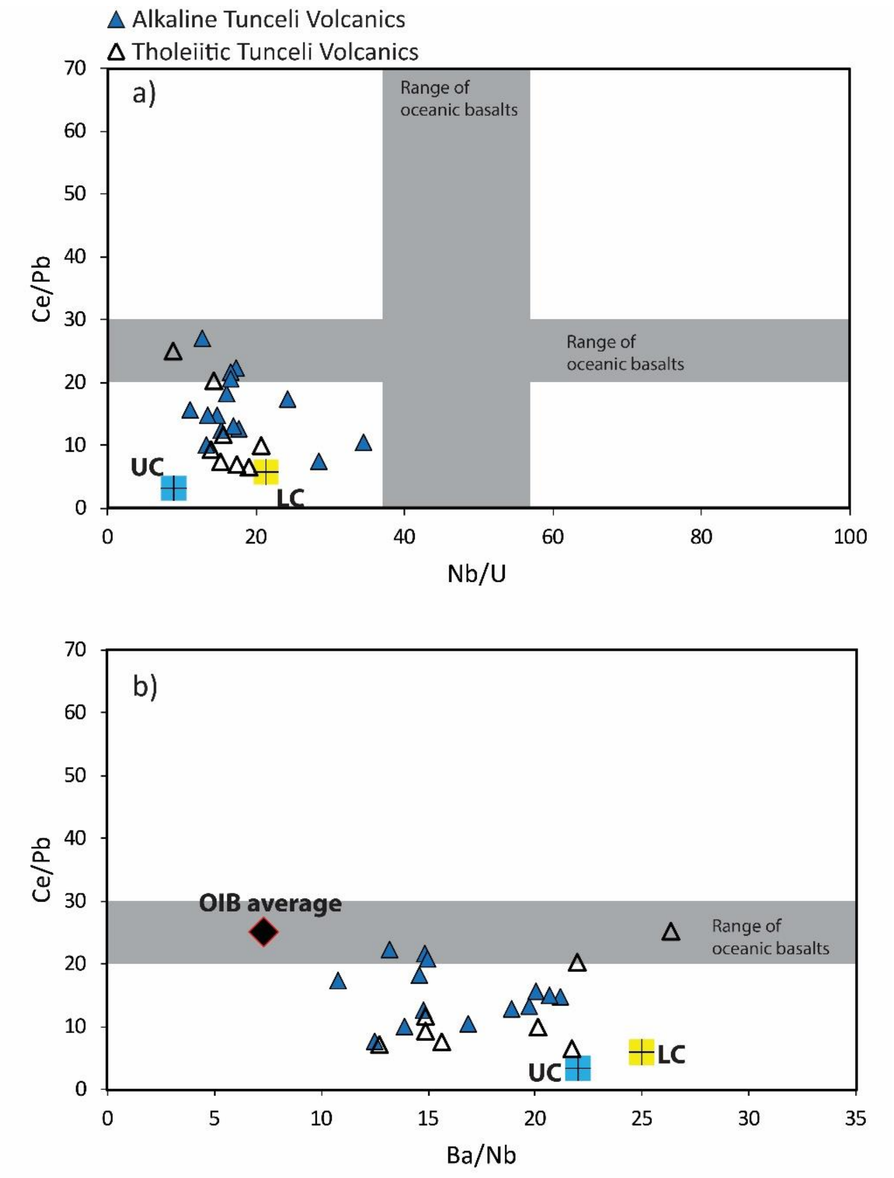

Figure 5.8. The (a) Nb/U versus Ce/Pb (modified from Mayer et al., 2013) and (b) Ba/Nb versus Ce/Pb diagrams for the Tunceli Volcanics. The range of the oceanic basalts (OIBs and MORBs) for the Ce/Pb and Nb/U element ratios are from Hofmann et al. (1986). The average of the crustal values (UC: Upper Crust; LC: Lower Crust) is from Taylor and McLennan (1985). The average of the OIBs is from Sun and McDonough (1989).

If magma interacts with the crustal domains, especially with the upper crust, an increase in their SiO_2 content is also expected since the crustal reservoirs are also characterized by high silica concentrations (e.g., Upper Crust SiO_2: 66.6 wt. %; Rudnick and Gao, 2004). However, when the major oxide element contents of Tunceli lavas are considered, high SiO_2 contents are not observed. Excluding the one evolved sample (AV22), which records 51.04 wt. %, the SiO_2 concentrations range between 45.87-49.36 wt. %. Moreover, a correlation between their SiO_2 contents and mobile elements, which may be indicative of possible crustal contamination, is also not shown by the Tunceli Volcanics. For instance, a positive correlation is expected between SiO_2 and La/Nb or Pb/Ce ratios if these lavas have interacted with crustal material. However, when Tunceli lavas are plotted on the diagrams of SiO_2 versus La/Nb (Figure 5.9a) and SiO_2 versus Pb/Ce (Figure 5.9b), such correlation cannot be observed. In addition to these, as also previously mentioned in the study of Aktağ et al. (2019), the Tunceli lavas are enriched in some mobile elements contents than that of the upper continental crust (e.g., Figure 5.9a). These elemental behaviors argue that their enriched elemental profiles are not acquired via crustal contamination. Therefore, the elemental characteristics of Tunceli volcanism rather suggest a derivation from a source region metasomatized by slab-derived sediment melts or fluids. This is discussed in detail in the further sections of this thesis.

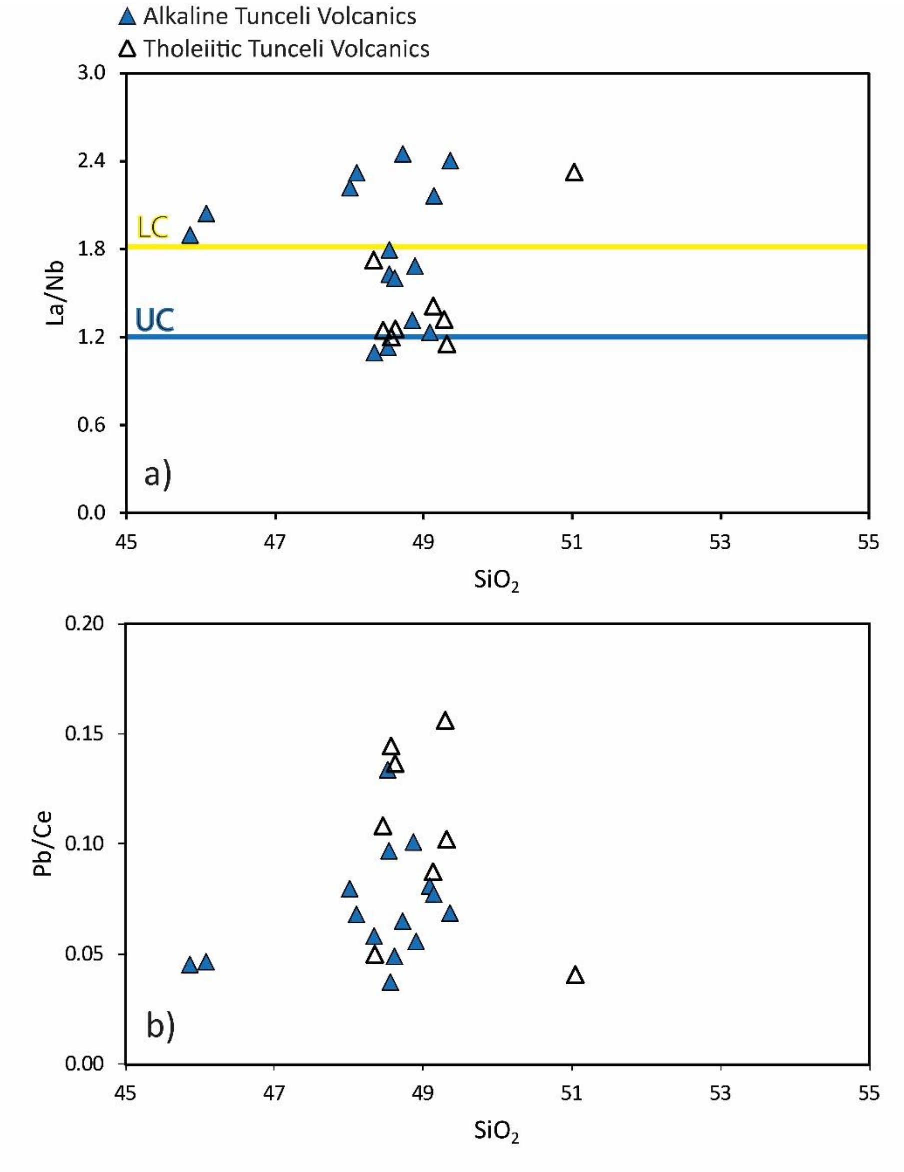

Figure 5.9. The (a) SiO_2 (wt. %) versus La/Nb (modified from Aktağ et al., 2019) and (b) SiO_2 (wt. %) versus Pb/Ce diagrams for the Tunceli Volcanics. The average of the crustal values (UC: Upper Crust; LC: Lower Crust) is from Taylor and McLennan (1985).

Apart from the implications above, a more robust approximation to the possible effects of crustal contamination on the lavas can be developed by using their assimilation-sensitive elements in combination with their isotope ratios. In this regard, the SiO_2 and MgO contents of the Tunceli lavas are plotted against their $^{87}Sr/^{86}Sr$ and $^{143}Nd/^{144}Nd$ isotope ratios (Figure 5.10). Possible crustal assimilation would drive the lavas to more silicic, more radiogenic $^{87}Sr/^{86}Sr$, and more unradiogenic $^{143}Nd/^{144}Nd$ compositions. Therefore, a positive correlation between SiO_2 versus $^{87}Sr/^{86}Sr$ and MgO versus $^{143}Nd/^{144}Nd$, and a negative correlation between SiO_2 versus $^{143}Nd/^{144}Nd$ and MgO versus $^{87}Sr/^{86}Sr$ would be expected in the Tunceli lavas, if they were subjected to crustal contamination process. However, as seen in Figure 5.10, the data points of the Tunceli volcanism display no trends; they rather loosely cluster in the diagrams. This supports the idea that the crustal assimilation did not play a significant role in the petrogenesis of these lavas.

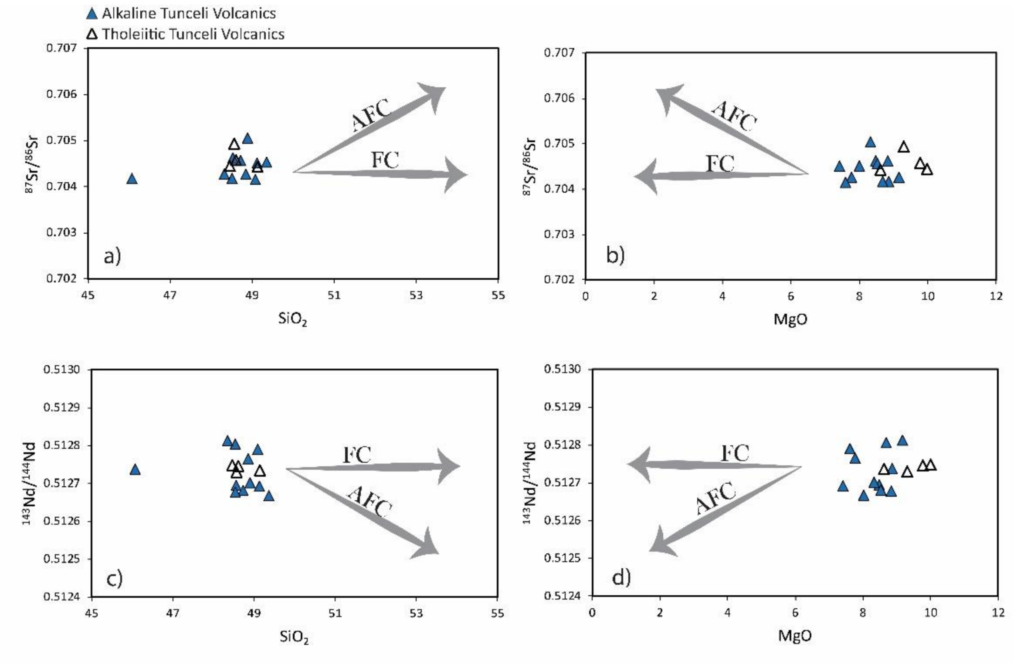

Figure 5.10. The (a) SiO_2 versus $^{87}Sr/^{86}Sr$, (b) MgO (wt. %) versus $^{87}Sr/^{86}Sr$, (c) SiO_2 (wt. %) versus $^{143}Nd/^{144}Nd$, and MgO versus $^{143}Nd/^{144}Nd$ diagrams for the Tunceli Volcanics.

Assimilation combined with fractional crystallization (AFC) modeling is one of the strongest tools to trace the effects of crustal contamination in the chemical budget of the lavas. Therefore, theoretical AFC curves have been modeled on trace elements versus isotope ratio diagrams in order to be sure whether the assimilation process can be ruled out in the petrogenesis of the Tunceli Volcanics or not (Figure 5.11). In addition, a comparison of the Tunceli data with modeled AFC curves can also reveal the extent of the crustal contamination if the Tunceli melts have interacted with the crust.

The AFC curves in the diagrams were modeled based on the formulation of DePaolo (1981), which can be expressed as;

$$C_{lc}^{AFC} = C_0^f \left[F^{-z} + \left(\frac{r}{r-1}\right)\frac{C_a}{zC_0^f}\left(1 - F^{-z}\right)\right] \text{ (for trace elements), and} \qquad \text{(Eqn. 3)}$$

$$IC_{lc}^{AFC} = \frac{\left(\frac{r}{r-1)}\right)\left(\frac{C_a}{z}\right)(1-F^{-z})Ic_a+C_0^f F^{-z} Ic_0}{\left(\frac{r}{r-1}\right)\left(\frac{C_a}{z}\right)(1-F^{-z})+C_0^f F^{-z}} \text{ (for isotope ratios)} \qquad \text{(Eqn. 4)}$$

where

C_{lc}^{AFC}: trace element composition of the melt affected by assimilation

IC_{lc}^{AFC}: isotopic composition of the melt affected by assimilation

C_0^f: initial trace element composition of the melt

C_a: trace element concentration of the wall rock (assimilating material)

Ic_0: initial isotope composition of the melt

Ic_a: isotope composition of the wall rock (assimilating material)

F: Mm/Mi (ratio of the magma mass to initial magma mass)

z: $(r+D-1)/(r-1)$

r: ratio of the assimilated material to the crystallized material

D: bulk partition coefficient

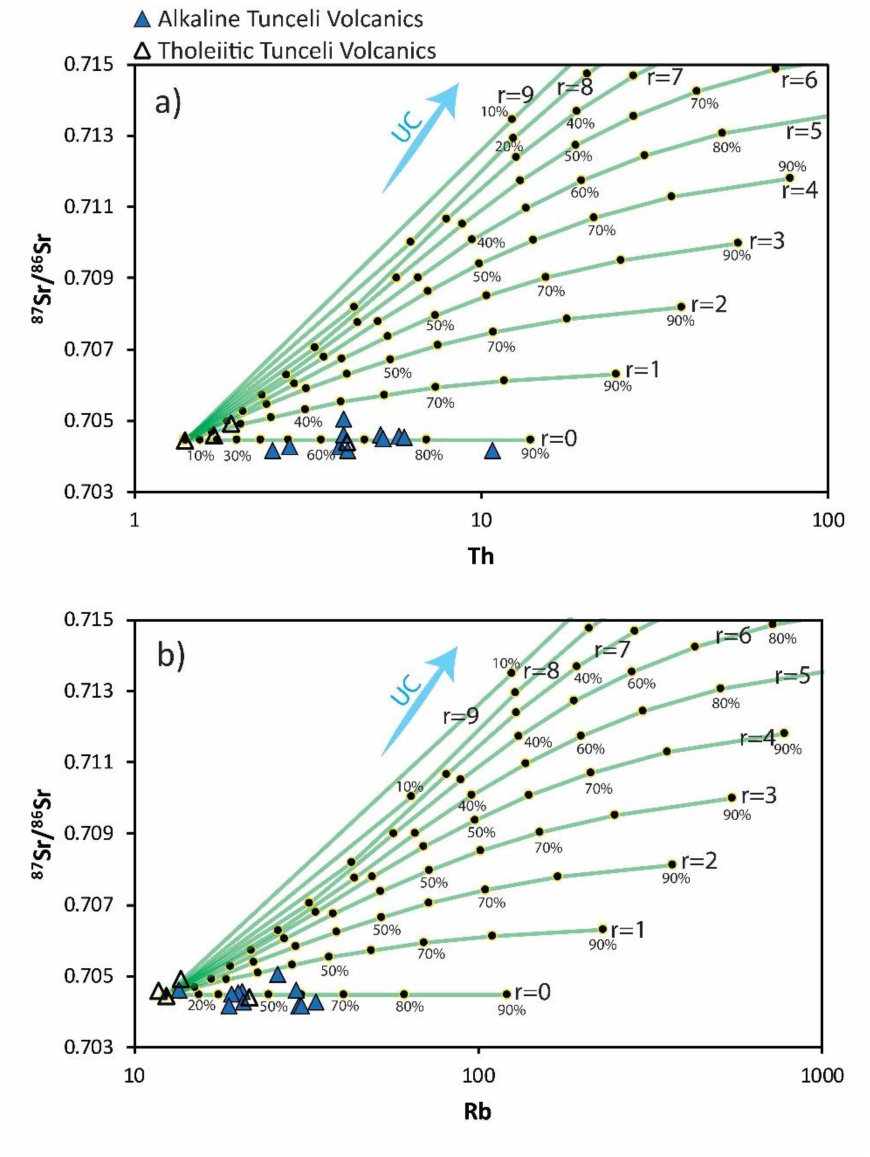

Figure 5.11. The (a) Th (ppm) versus $^{87}Sr/^{86}Sr$ and (b) Rb (ppm) versus $^{87}Sr/^{86}Sr$ diagrams for the Tunceli Volcanics containing calculated AFC curves. The tick marks on the vectors represent the 10% crystallization intervals. The partition coefficients used in the models are given in Table 5.1. The Bulk Distribution Coefficient (D) in the models has been calculated based on a phase combination including no plagioclase fractionation (cpx0.5+olv0.5) since the plagioclase fractionation in the lavas is negligible. The average upper crust (UC) composition of Taylor and McLennan (1985) is chosen as the composition of the assimilating material in the calculations. The composition of the sample AV67 is selected as the starting composition. All parameters used in the models, with the exception of partition coefficients, can be seen in the Table 5.2. Key to abbreviations: r: ratio of mass assimilation rate to fractional crystallization rate.

In the models, the Th (Figure 5.11a) and Rb (Figure 5.11b) were selected as fractionation index and placed onto X-axis. These elements are not compatible with any mineral phase in the lavas, and therefore expected to be steadily increased during the magma evolution (see Table 5.1 for the partition coefficients used in the models). On the other hand, the $^{87}Sr/^{86}Sr$ was selected as the crustal assimilation-sensitive isotope ratio owing to the significant difference in Rb/Sr ratio in the mantle and crustal systems. The $^{87}Sr/^{86}Sr$ isotope ratio is expected to increase in the melt during the assimilation process. Since there is still not a proper upper crust composition available for the eastern Anatolian crust, the average upper crust (UC) composition of the Taylor and McLennan (1985) was chosen for the assimilating end-member composition in the modelings. It should be noted that the composition of the assimilant material in the models could be more mafic (corresponding to the mafic lower crustal granulites; Rudnick and Gao, 2004) since the barometric calculations have recorded high crystallization depths (>15 km) for both Tunceli and Elazığ Volcanics. However, the compositions of the lower crustal material found in some alkaline volcanic fields (Hocheifel, Germany; Stosch and Lugmair, 1984; Loock et al., 1990; Jung et al., 2006) have shown that the lower crustal material widely could also have felsic compositions with higher radiogenic $^{87}Sr/^{86}Sr$ isotope ratios, even than the average upper crust. Therefore, it is thought that the assimilant end-member in the models may also act as a proxy for assimilation in lower crustal depths. In addition to these, the element and isotope contents of the sample AV67 were used for starting composition since it represents the most primitive sample (Mg#=63.3) in the data set. The r values in the plots correspond to the ratio of assimilation rate to the crystallization rate. All parameters used in the models, with the exception of the partition coefficients, can be seen in the Table 5.2.

In the plots of $^{87}Sr/^{86}Sr$ versus Th (Figure 5.11a) and $^{87}Sr/^{86}Sr$ versus Rb (Figure 5.11b), it is observed that the data distribution of the Tunceli lavas defines a flat trend following the calculated AFC vector corresponding to r=0. Since r value 0 indicate a magma storage history without crustal assimilation, these correlations in both diagrams provide compelling evidence that the Tunceli lavas were not significantly contaminated by the crust.

Considering these modeling results with the information above, it can be said that the enriched incompatible element profile of the Tunceli Volcanics is not related to a possible crust-melt interaction process. The new isotope data from the Tunceli volcanism confirm the implications from the previous studies (Di Giuseppe et al., 2017; Aktağ et al., 2019). Instead, these enrichments appear to have been inherited from partial melts of subduction modified source region(s). This will be discussed in detail in the "Mantle Source Characteristics" section of this study. The evaluations above have also shown that, except for the evolved sample (AV22), the compositions of the all available samples are informative for their nature of source regions, and can be used in the remainder of discussion.

5.1.2.2 Elazığ Volcanics

It has been proposed that the Elazığ Volcanics have undergone crustal contamination with an r value (ratio of mass assimilation rate to fractional crystallization rate) around 0.60 despite experiencing a limited extent of fractional crystallization (Di Giuseppe et al., 2017). Although their OIB-like trace element profiles with positive Nb/Nb* values (1.17-1.58) speak against a significant interaction with crustal domains, these previous findings regarding the differentiation history of Elazığ volcanism also necessitate a detailed investigation about the role of crustal assimilation in their petrogenesis.

The Elazığ data trends in the bivariate Harker and log-log FC modeling diagrams, which imply a significant fractional crystallization in their magmatic evolution, may indicate a sufficient magma residence time within the crust for possible crustal contamination. Besides, the xenocrysts found in the lavas (e.g., Figure 3.16) provide compelling evidence that the assimilation has taken place. However, their OIB-like trace element profiles in the PM-normalized diagram (Figure 4.23) suggest that the primitive basaltic Elazığ liquids were not significantly overprinted by the crustal assimilation process. As is stated by Thompson et al. (1982), the Th, Ba, Rb, and La elements can be added to the magma during crustal contamination. Therefore, the positive Nb/Nb* values (1.17-1.58) of the Elazığ lavas argue against significant crustal assimilation during their evolution. Considering these, if these lavas were affected by possible crustal contamination during their magmatic evolution, it could be proposed that the extent of the assimilation should not be very large. Nevertheless, to carry out a detailed evaluation into the role of crustal contamination in their petrogenesis, assimilation-sensitive trace element and isotope contents were plotted on the normal- normal and log-normal diagrams, which can be found below.

Since the primary Pb elemental budget of Elazığ volcanism is significantly disturbed by hydrothermal alteration (e.g., Figure 4.12), Pb has not been used in the evaluations regarding crustal contamination. However, their other mobile elements remained unaffected from water-rock interaction may provide an excellent opportunity to trace the possible modifications of crustal assimilation on the primary chemistry of the lavas. When the Elazığ lavas were plotted on the diagrams of Ba/Nb versus Nb/U (Figure 5.12), it is observed that they do not define any decreasing trends in the diagram. Instead, their data distribution displays a cluster rather than a trend (Figure 5.12). Significant crustal contamination would drive the data distribution to low Nb/U and high Ba/Nb values in the diagram since the elements such as Ba and U are highly enriched in the crust (e.g., Upper Crust: Ba/Nb= 22, Taylor and McLennan, 1985), and Nb stays relatively immobile during mantle melting (Thompson et al., 1982). Therefore, the distribution in the plots may argue against an extensive involvement of the crustal assimilation process in their genesis. Specifically, the Elazığ data on the diagram may totally rule out the possible effects of assimilation on their chemistry, alternatively their data distribution on the diagrams simply could be the reflection of minor assimilation. For the latter case, since the lavas display positive values of Nb/Nb*, which is mostly characteristics of the assimilation-free oceanic basalts, they would not require unusual high incompatible/compatible element ratio (e.g., LILE/HFSE) if these were affected by a nominal crust-melt interaction event. In other words, a minor modification of the crustal contamination would not create a high Ba/Nb ratio in the basalts since these basalts are highly enriched in HFSE such as Nb and Ta. Therefore, the extent of crustal contamination should be small, if any, and this might have affected the primary melt composition of these lavas.

Although the ratio-ratio element diagram (Ba/Nb versus Nb/U) suggests that the crustal contamination process was not extensively involved in the genesis of the Elazığ lavas, such diagrams may not be capable of defining the minimal chemical modification of the crustal contamination on the chemistry of these lavas. In order to make better implications, La/Nb and Nb/U element ratios were plotted against SiO_2 (Figure 5.13).

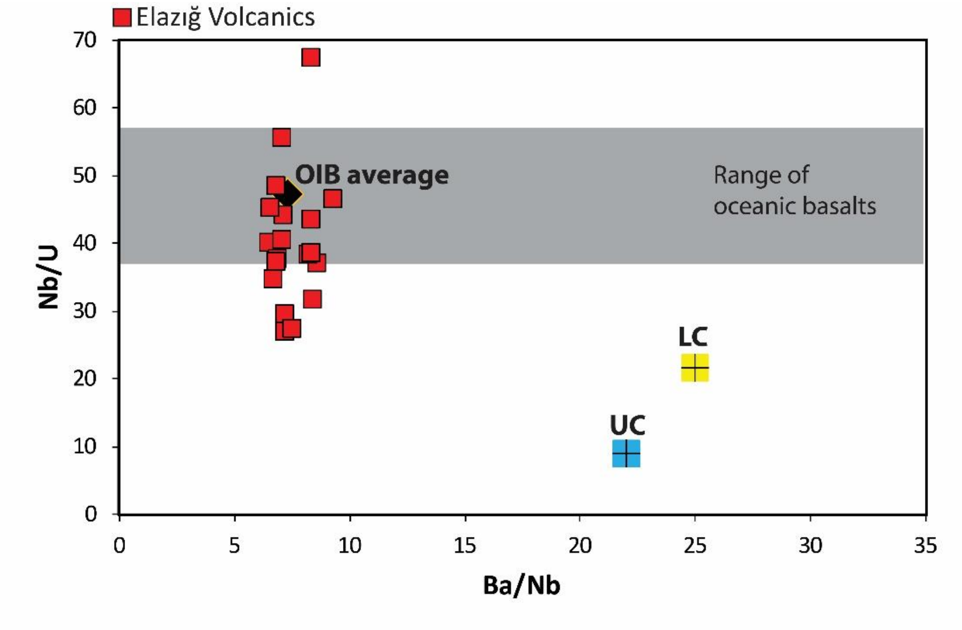

Figure 5.12. The (a) Ba/Nb versus Nb/U diagram for the Elazığ Volcanics. The range of the oceanic basalts (OIBs and MORBs) for the Nb/U element ratio are from Hofmann et al. (1986). The average of the crustal values (UC: Upper Crust; LC: Lower Crust) is from Taylor and McLennan (1985). The average of the OIBs is from Sun and McDonough (1989).

While the Elazığ lavas define a positive trend in the diagram of SiO_2 versus La/Nb (Figure 5.13a), they created a decreasing trend in the diagram of SiO_2 versus Nb/U (Figure 5.13a). Since the crust is presumed to have a silicic composition (e.g., Upper Crust SiO_2: 66.6 wt. %; Rudnick and Gao, 2004) and display enrichment in La/Nb and U/Nb ratios compared to the most mantle-derived melts (e.g., Upper Crust: La/Nb= 1.2; U/Nb=0,112, Taylor and McLennan, 1985; OIB average: La/Nb= 0,77; U/Nb=0.02, Sun and McDonough, 1989), the correlations in both diagrams (Figure 5.13) are consistent with the involvement of crustal contamination in their genesis. However, since only a few samples display an obvious deviation from the data cluster (those samples within the sample; GMB6, GMB8, GMB9, and GMB10), in accordance with the comments above, it can be said the effects of crustal assimilation is limited on the Elazığ volcanism. Moreover, the very narrow variation of La/Nb ratios in the lavas (La/Nb= 0.60-0.71) may also be suggestive for limited assimilation during their evolution.

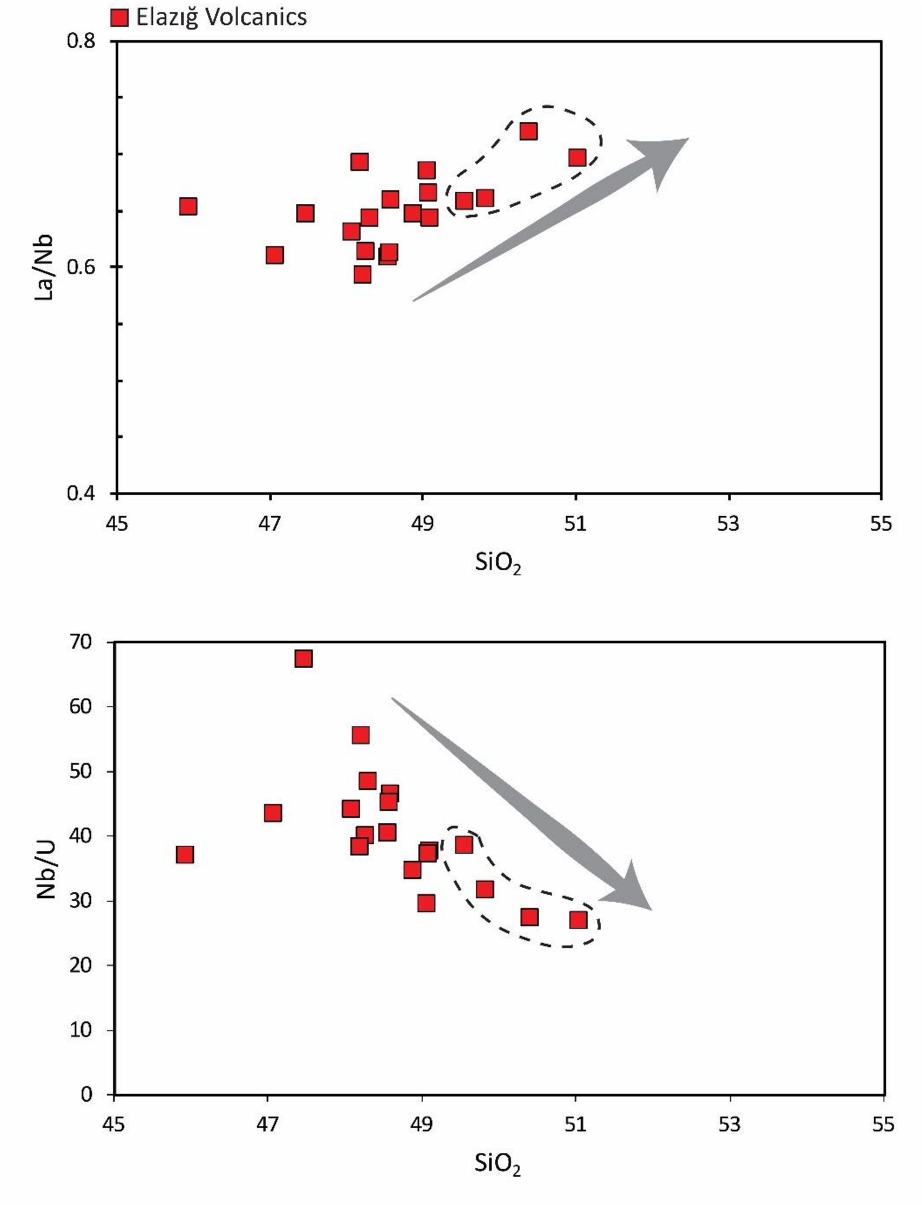

Figure 5.13. The (a) SiO$_2$ (wt. %) versus La/Nb and (b) SiO$_2$ (wt. %) versus Nb/U diagrams for the Elazığ Volcanics. The samples within the dotted field may represent the samples affected by the crustal assimilation process.

The data distribution of the Elazığ lavas in the bivariate element-element variation diagrams above, in general, suggests that the crustal assimilation process in the magmatic evolution of these lavas was operative. However, the same data also indicate that the effects of this process on their chemistry are limited. Only a few samples appear to have experienced this process, and the extent of its chemical modifications on the affected samples seem to be not very large. Nevertheless, as mentioned previously, more robust approximations to these arguments can be made by their isotope contents. Therefore, to define the assimilation modified samples in the data set and determine the extent of the assimilation-related chemical modifications on these samples, the Elazığ lavas were also plotted on the diagrams of SiO_2 versus $^{87}Sr/^{86}Sr$, MgO versus $^{87}Sr/^{86}Sr$, SiO_2 versus $^{143}Nd/^{144}Nd$ and MgO versus $^{143}Nd/^{144}Nd$ (Figure 5.14). It is observed that most of Elazığ Volcanics form linear trends parallel to X-axis (5.14), with fairly constant isotope ratios, which imply an insignificant role of assimilation in their petrogenesis. However, an increase in $^{87}Sr/^{86}Sr$ and a decrease in $^{143}Nd/^{144}Nd$ with increasing SiO_2 or decreasing MgO observed for two evolved samples (GMB6 and GMB8) in the data set suggest minor assimilation of crustal lithologies for these lavas.

In accordance with the comments above, the Elazığ lavas are mainly free of crustal contamination. Since steep arrays between these two evolved samples and the rest of the data points are not observed in these isotope-element spaces, the extent of the crustal contamination for the affected samples appears to be not extensive. Nevertheless, a more detailed look into the extent of crustal assimilation on these evolved lavas can be provided by quantitative modelings. In this regard, the trends of the Elazığ lavas were also compared with the calculated theoretical AFC curves in the element-isotope diagrams (Figure 5.15).

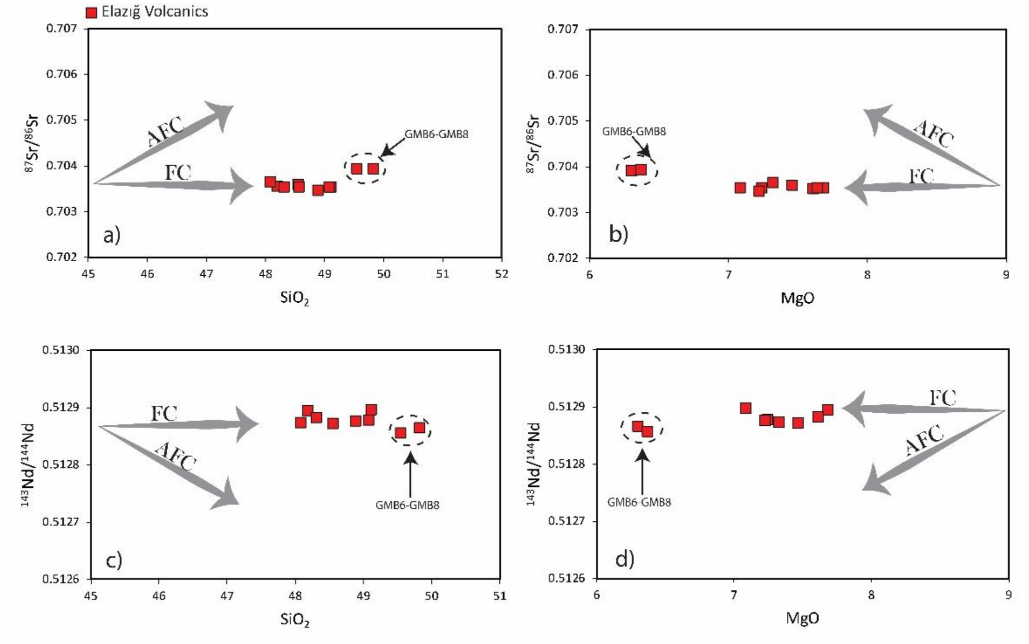

Figure 5.14. The (a) SiO_2 (wt. %) versus $^{87}Sr/^{86}Sr$, (b) MgO (wt. %) versus $^{87}Sr/^{86}Sr$, (c) SiO_2 versus $^{143}Nd/^{144}Nd$, and MgO versus $^{143}Nd/^{144}Nd$ diagrams for the Elazığ Volcanics.

With the exception of starting composition, all parameters in the calculated AFC modelings for Elazığ Volcanism (Figure 5.15) are the same as used in Figure 5.11 (see Tables 5.1 and 5.2). For the starting composition, the related trace element and isotope content of the sample BYD10 were used. Note that most of the Elazığ samples do not create an apparent trend in the diagrams since they have very uniform element and isotope contents. They rather define a tight cluster in the modeling diagrams. Therefore, to make better implications about the extent of crustal contamination on these lavas, the composition of the sample that records low contents in the Th (5.1 ppm) and Rb (38.9 ppm) was selected as the starting composition.

In the plots of $^{87}Sr/^{86}Sr$ versus Th (Figure 5.15a) and $^{87}Sr/^{86}Sr$ versus Rb (Figure 5.15b), as mentioned above, the data distribution of the majority of the Elazığ lavas define a tight cluster instead trending toward the calculated AFC curves. This data distribution also strongly supports the idea that the assimilation of the crustal lithologies was not operative for most of Elazığ Volcanics. However, as also seen in the plots, in accordance with their behavior in Figure 5.14, the two evolved samples (GMB6 and GMB8) display more enriched characteristics, and trend towards the AFC curves. While these two samples lie on the curve corresponding to r value of 1 in the diagram of $^{87}Sr/^{86}Sr$ versus Th (Figure 5.15a), they plot on the curve corresponding to r value of 5 in $^{87}Sr/^{86}Sr$ versus Rb diagram (Figure 5.15b). It must be noted that, since the r value is highly dependent on the chosen end-member compositions and highly variable D (bulk partition coefficient) values in the modelings, it is not capable of perfectly simulating the natural extent of contamination in these lavas. However, the r value in the models can be still be regarded as a proxy of the extent of assimilation with respect to the most primitive composition in the data set. Consequently, it can be suggested that these enriched samples have been affected by low to moderate degree (r values between 1-5) crustal contamination process at least compared to the primitive composition of the lavas. These may confirm the previously suggested crustal assimilation degree (r=6; Di Giuseppe et al., 2017) for the Elazığ volcanism; however, this cannot be envisioned for the whole volcanism in the Elazığ area, since the chemical modifications of crustal assimilation have been solely detected on the volcanics of Gümüşbağlar member of Elazığ Volcanism. The Beydalı member of this volcanism, on the other hand, appear to have not been affected by this process.

In summary, the evaluations above indicate that the majority of the Elazığ volcanism is free of crustal assimilation. In addition to this, only a minor part seems to have been affected by a low to moderate level of contamination during its ascent to the surface. In order to make better implications and prevent misinterpretations regarding the nature of the mantle source regions of the Elazığ Volcanics, the two AFC-modified samples (GMB6 and GMB8) will be excluded from the remainder of the discussion; hereby, the mantle source characterization and melting estimations of Elazığ volcanism will be made by focusing on its uncontaminated samples with no crustal influence.

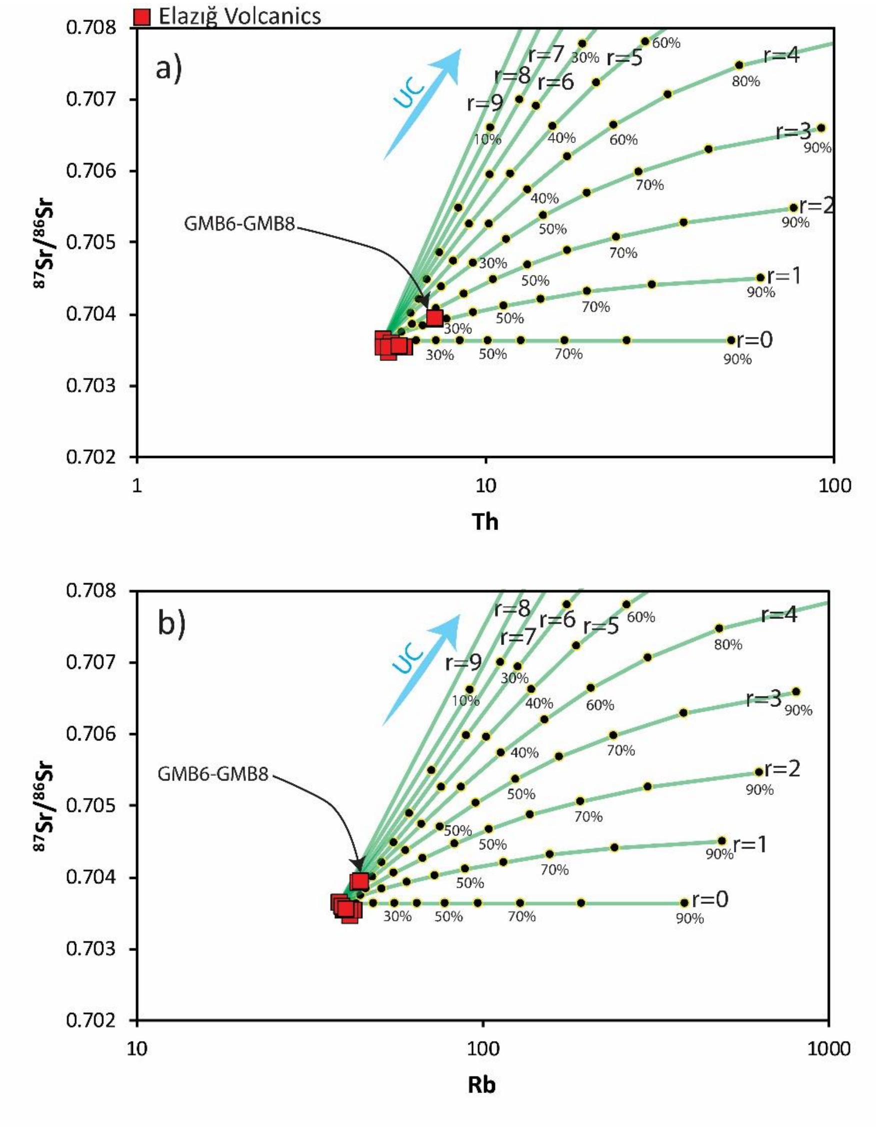

Figure 5.15. The (a) Th (ppm) versus ^{87}Sr/^{86}Sr and (b) Rb (ppm) versus ^{87}Sr/^{86}Sr diagrams for the Elazığ Volcanics containing calculated AFC curves. The tick marks on the vectors represent the 10% crystallization intervals. The partition coefficients used in the models are given in Table 5.1. The Bulk Distribution Coefficient (D) in the models has been calculated based on a phase combination including no plagioclase fractionation (cpx0.5+olv0.5) since the plagioclase fractionation in the lavas is negligible. The average upper crust (UC) composition of Taylor and McLennan (1985) is chosen as the composition of the assimilating material in the calculations. The composition of the sample BYD10 is selected as the starting composition. All parameters used in the models, with exception of partition coefficients, can be seen in Table 5.2. Key to abbreviations: r: ratio of mass assimilation rate to fractional crystallization rate.

Table 5.1. Partition coefficient (K_d) values for the Rayleigh fractionation and assimilation combined fractionation (AFC) models and the data source. The Kd values were compiled from the GERM Partition Coefficient (Kd) Database (https://earthref.org/). Key to abbreviations: olv: olivine; cpx: clinopyroxene; plg: plagioclase.

Elements	**Minerals**	**K_d values for Basic Magma**	**Reference**
Sc	Cpx	3.3	Paster et al., 1974
	Olv	0.33	
	Plg	0.008	
Ni	Cpx	4.4	Bougault and Hekinian, 1974
	Olv	12.2	
	Plg	0.06	
Sr	Cpx	0.067	McKenzie and O'Nions, 1991
	Olv	0.00019	
	Plg	2	
Th	Cpx	0.00026	
	Olv	0.0001	
	Plg	0.05	
Rb	Cpx	0.011	
	Olv	0.00018	
	Plg	0.1	

Table 5.2. Parameters used in the AFC modellings (Figures 5.11 and 5.15). The composition of assimilant is from Taylor and McLennan (1985). Key to abbreviations: Do: Bulk Distribution Coefficient.

		$^{87}Sr/^{86}Sr$	**Sr**	**Th**	**Rb**
Starting Composition	For Tunceli Volcanics	0.704447	303.8	1.4	12.4
	For Elazığ Volcanics	0.703638	734.8	5.1	38.9
Assimilant		0.722	350	10.7	112
Do (Calculated)			0.033595	0.00018	0.00559

5.1.3 Mantle Source Characteristics

5.1.3.1 Tunceli Volcanics

5.1.3.1.1 Constraints from Trace Element Systematics

As it is mentioned in the “GEOCHEMISTRY” chapter of this study, the Tunceli lavas, both their alkaline and tholeiitic members, have enriched trace element abundances compared to the primitive mantle (Figure 4.19). In addition to that, with these enriched element profiles (e.g., LREEs), they strongly argue against predominantly derivation from mantle source region(s) highly depleted in incompatible elements (e.g., DM: depleted upper mantle). Such depleted characteristics arise from the former melt extractions from the melting columns in the mantle domain, and such domains have been widely regarded as the typical source regions for most of MORBs (normal-MORBs; Workman and Hart, 2005) and oceanic arc lavas (Pearce and Peate, 1995). The primitive members of these DM-derived lavas usually reflect their source features and are characterized by depletion in their most incompatible elements with respect to less incompatible ones. These signatures contrast with the trace elements systematics of Tunceli lavas suggesting a relatively enriched source region(s) for the Tunceli volcanism (e.g., Figure 4.19).

The enriched element characteristics of the Tunceli volcanism are also evidenced by their Zr/Nb and Nb/Y ratios. Since Nb is more incompatible than the elements of Zr and Y during upper mantle conditions, it is plausibly enriched in the crust and not abundant in the depleted upper mantle (e.g., Taylor and McLennan, 1985; Workman and Hart, 2005), and therefore the DM-derived lavas display lower Nb/Y and higher Zr/Nb ratios than the lavas predominantly derived from enriched mantle sources (e.g., OIBs, continental intraplate and arc lavas). The Tunceli lavas, on the other hand, display high Nb/Y (0.33-1.73) and low Zr/Nb (4.11-11.44) element ratios relative to DM-derived lavas (e.g., Average N-MORBs Nb/Y= 0.08, Zr/Nb=31.75;

Sun and McDonough, 1989), indicating that the DM component is not an important source component in their petrogenesis.

This is well illustrated in the diagram of Zr/Nb versus Nb/Y (Figure 5.16), where the Tunceli lavas plot on the similar fields with continental arc (e.g., Aeolian Arc) and rift magmas (e.g., East African and Rio Grande Rift) with higher Nb/Y and low Zr/Nb ratios compared to those of N-MORBs (average N-MORB value; Sun and McDonough, 1989) and oceanic arc lavas (e.g., South Sandwich). Also, the Tunceli Volcanics plot very close to the average value of OIBs, consistent with their similar elemental enrichment levels in the PM- and chondrite-normalized diagrams (Figure 4.19 and Figure 4.20). The data distribution in the diagram confirms that the mantle components involved in their genesis were predominantly of enriched nature. However, it is must be noted that the trend of the Tunceli lavas in the diagram of Zr/Nb versus Nb/Y (Figure 5.16) also indicates a minor contribution from a depleted component in their genesis. The Tunceli lavas mainly plot on an area between the average compositions of OIB and MORB (Sun and McDonough, 1989) in the diagram (Figure 5.16), and the high end of the Zr/Nb and low end of the Nb/Y spectrum displayed by Tunceli Volcanics may imply the minor amount of melts contribution from a depleted mantle component. In detail, the tholeiitic samples display elevated Zr/Nb and lower Nb/Y ratios compared to the alkaline samples. This may be a manifestation of tapping a greater amount of the DM component compared to alkaline samples or just a reflection of the difference in the partial melting degrees of these two groups.

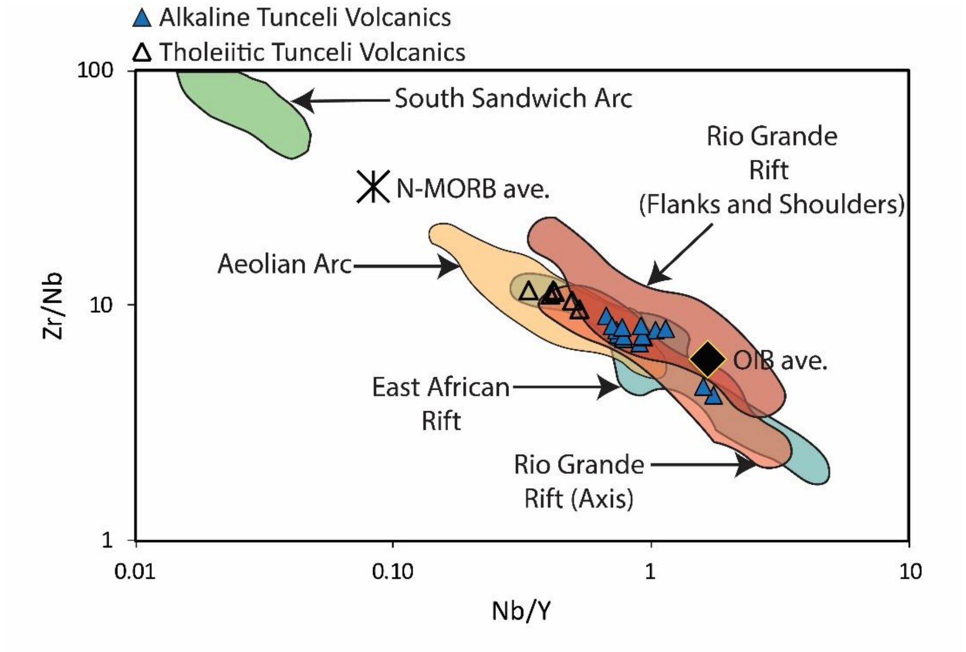

Figure 5.16. The Nb/Y versus Zr/Nb diagram for the Tunceli Volcanics and lavas from modern tectonic settings. The published data used for comparison includes samples with MgO (wt. %) greater than 6 wt. % to avoid the effects of post-melting processes and to make the data set comparable with the Tunceli lavas. The data sources; Average N-MORBs and OIB from Sun and McDonough (1989), East African Rift from Furman et al. (2006), Rio Grande Rift from Gibson et al. (1993), Aeolian Arc from the Peccerillo et al. (2013), and South Sandwich Arc from Pearce et al. (1995).

Based on these, in agreement with the previous arguments (Aktağ et al., 2019), it can be suggested that the elemental signatures of the Tunceli lavas define a composition that lacks significant contribution from DM. In other words, if any depleted component has been involved in their genesis, this involvement must have been not very extensive. In the case of the minor DM involvement in their genesis, the DM contribution must have been overprinted by the contribution(s) of enriched components (e.g., EM, HIMU, FOZO/C, or subduction imprint) during the melt generation.

Among the lavas having an enriched nature with respect to DM-derived melts, the OIB-like melts in oceanic and continental intraplate settings (e.g., St. Helena, Massif

Central France, East African Rift lavas, etc.,) are widely assumed to have been derived from the source region(s) associated with mantle plumes (e.g., Zindler and Hart, 1986; Hoernle et al., 1995; Furman et al., 2006). Moreover, the plume materials that contribute to these volcanics are believed to include distinct recycled lithospheric materials (e.g., Zindler and Hart, 1986, see CHAPTER 1 for detailed information). One general notable feature of the lavas derived from plume-associated source regions; they are not characterized by strong negative Nb/Nb* values (e.g., Weaver, 1991; Jackson et al., 2008; Peters and Day, 2014). On the contrary, the enrichments in HFSE such as Nb and Ta relative to the Th and La are assumed to be a common feature for most of the "typical" OIB-like melts, though some EM-type melts have elevated LILE/HFSE ratios compared to HIMU-type melts (e.g., EMI; see Weaver, 1991). In particular, those melts contributed from the HIMU or FOZO/C type components display strong HFSE enrichments relative to Th and LREEs, which manifest themselves as Nb peak in the PM- or N-MORB-normalized multi-element diagrams.

In the light of the information above, it is apparent that, although the Tunceli lavas display similar elemental enrichment levels with the OIBs (e.g., Figures 4.19 and 5.16), they differ from the OIB-like melts with their strong enrichments in LILE over the HFSE. With the high LILE/HFSE ratios, the Tunceli lavas have a trough at Nb in the primitive mantle (PM) normalized multi-element diagram (Figure 4.19), which is not the case for most OIB-like melts (Sun and McDonough, 1989). These trace element characteristics rather imply derivation from a mantle source that has been modified by slab-derived sediment melts or fluids (e.g., Pearce, 1983). However, the elevated Nb/Nb* values (AV73, ca. 0.80) in some samples may also call a contribution from a mantle source containing plume-related component(s) (e.g., HIMU, FOZO/C). In such a case, contributions both from a mantle source containing plume-related components and a source region modified by slab-derived melt/fluids can be reconciled with the elemental signatures of the Tunceli lavas. To better understand whether the trace elements systematics of Tunceli lavas are consistent with contribution from a mantle component that is widely sampled by OIB-like melts or not, Zr/Nb, Th/Nb, and Ba/Nb ratios were employed. These ratios are also useful in tracing the subduction effects on the lavas due to the different incompatibilities of Nb and Th-LILEs during slab-dehydration.

Similar to LILEs, which are known to fluid-mobile, Th and LREEs are also prone to be transported from subducted slab to the mantle wedge via silicate melts during subduction (Elliot et al., 1997; Class et al., 2000). HFSEs such as Nb and Ta, on the other hand, are retained in the residual slab during subduction due to their low solubility and higher compatibility with some accessory phases (e.g., rutile) (Pearce, 1983; Ayers and Watson, 1993; Pearce and Peate, 1995, Pearce and Stern, 2006). This process results in decoupling between LILEs-Th-LREEs and Nb in the subduction zones. Thus, those lavas derived from subduction-modified source regions will be enriched in the LILEs, LREEs, and Th relative to Nb. In the non-subduction settings, on the other hand, the Th and Nb display similar behavior due to their similar compatibilities during mantle melting. This results in nearly constant Th/Nb ratios among the lavas produced from the source regions free of subduction modification (e.g., average OIB Th/Nb=0.08; average N-MORB Th/Nb= 0.05, Sun and McDonough, 1989). When considering these, derivation from a subduction-modified source region would drive the Th/Nb and Ba/Nb ratios of the melts to higher levels than those of lavas having N-MORB or OIB origin. In the plot shown in Figure 5.17a, the Tunceli lavas, with an increase in their Th/Nb and Ba/Nb ratios, define a trend from the average OIB composition towards the lavas derived from subduction-modified mantle sources (arc lavas and lavas derived from metasomatized SCLM) implying contribution from a mantle domain modified by subduction process. However, it is also apparent in the diagram that the whole Th/Nb and Ba/Nb spectrum displayed Tunceli lavas is somewhat lower than those of arc and metasomatized SCLM-derived lavas, and its lower end plot close to the average OIB value. This may also suggest the involvement of another enriched mantle component related to OIB-type origin (e.g., recycled lithospheric domains).

Similar source contributions into the genesis of Tunceli volcanism are also supported by their Zr/Nb and Ba/Nb spectrum intermediate between those of OIBs and lavas derived from subduction-modified source regions (Figure 5.17b). As mentioned before, the LILE (e.g., Ba) enrichment over Nb is common for subduction zone magmas. Although the Tunceli lavas show enrichment in Ba over Nb compared to the OIB lavas (Figure 5.17b), their total Ba/Nb spectrum, as shown in Figure 5.17b, is lower than arc and SCLM-derived magmas. They mostly cluster between OIB average value and the subduction-related lavas in the diagram (Figure 5.17b). Therefore, contributions both from subduction modified and non-modified (e.g., source domains for OIB-like melts) enriched mantle domains can be suggested for the Tunceli Volcanism. Another notable feature observed in the diagram is that all tholeiitic and some alkaline Tunceli lavas slightly deviate from the OIBs-subduction-related volcanism trend with relatively higher Zr/Nb ratios for a given Ba/Nb ratio.

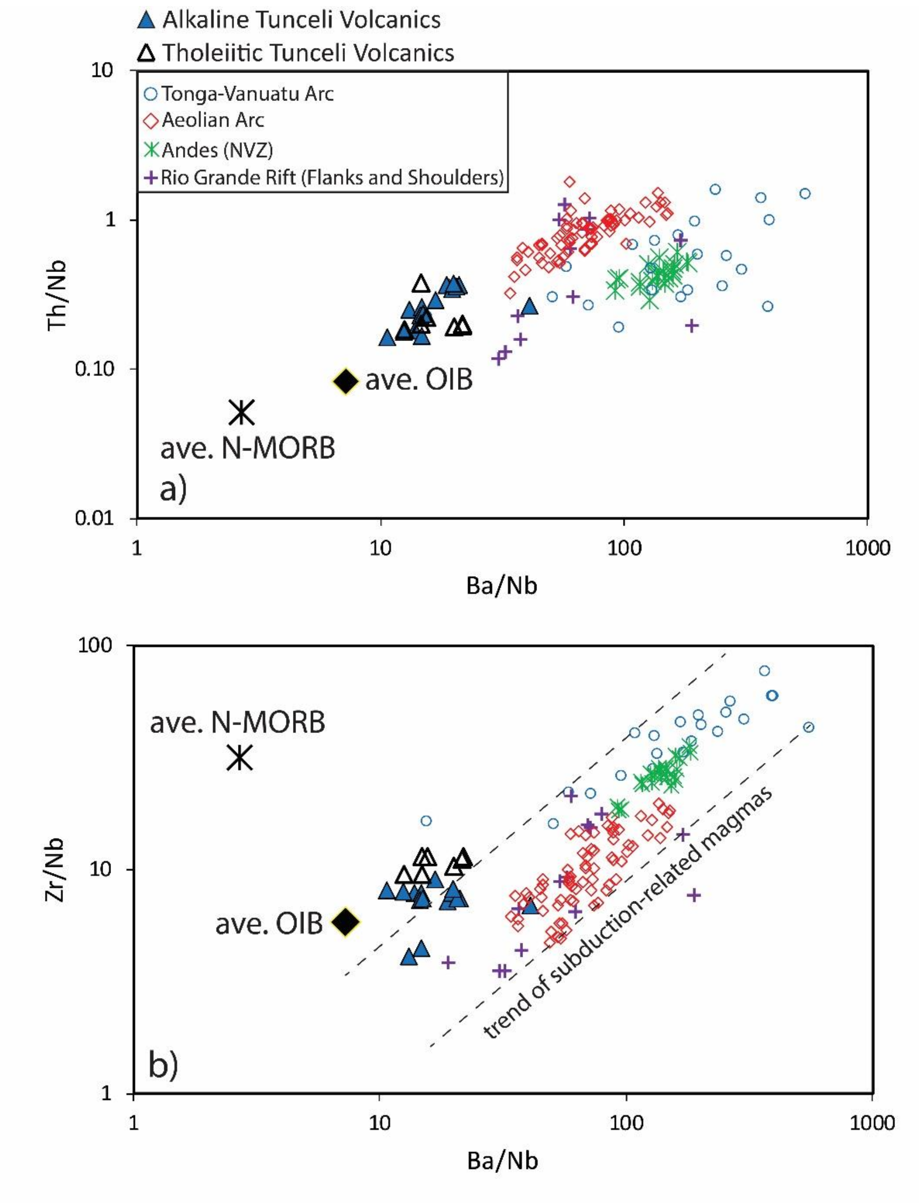

Figure 5.17. The (a) Ba/Nb versus Th/Nb and (b) Ba/Nb versus Zr/Nb diagrams for the Tunceli Volcanics and lavas related with subduction-modified source regions. The published data used for comparison includes samples with MgO (wt. %) greater than 4 wt. % to avoid the effects of post-melting processes and to make the data set comparable with the Tunceli lavas. The data sources; Average N-MORBs and OIB from Sun and McDonough (1989), Tonga-Vanuatu Arc from Pearce et al. (2007), Aeolian Arc from Peccerillo et al. (2013), Andes (NVZ: Northern Volcanic Zone) from Hidalgo et al. (2012), and Rio Grande Rift from Gibson et al. (1993).

As mentioned previously, Zr/Nb ratio is useful for distinguishing between enriched and depleted source regions due to the different bulk distribution coefficients of Zr and Nb during mantle melting. Therefore, this slight deviation in the diagram may also support minor contributions from a DM source domain in the genesis of Tunceli volcanism, which is consistent with the comments above. Nevertheless, solely based on their trace element systematics, it can be argued that the predominant source contributions into the genesis of Tunceli Volcanism appear to be from two distinct enriched source components; while one represents the subduction modified mantle domain, the other is from an enriched asthenospheric mantle domain, which is mostly sampled by OIB-like melts (e.g., recycled lithospheric lithologies).

As detailed above, the PM- and chondrite normalized trace element abundances (Figure 4.19 and 4.20) together with some elemental ratios (Figure 5.16 and 5.17) maintain the idea that distinct types of source components (e.g., depleted and enriched) may have been involved in the petrogenesis of Tunceli lavas. However, their most recognizable source component based on the trace element systematics appear to be the enriched component represents the subduction-modified mantle domain. This, can be further tested by the Th/Yb and Ta/Yb ratios, which are helpful to trace the subduction-related process and highlight the source variations. Since Ta and Yb are subduction immobile and the Th is transported from subducted slab towards the mantle wedge during subduction, a selective Th/Yb enrichment for a given Ta/Yb would be expected in those lavas derived from a subduction-modified mantle region (Pearce, 1983). The non-subduction-related melts (e.g., MORBs and OIBs), on the other hand, display close Th/Yb and Ta/Yb ratios due to the similar behaviors of Th and Ta in subduction-free settings (Pearce, 1983). It is also important to note that, since Ta displays higher incompatibility relative to Yb during melt extraction, a lower Ta/Yb ratio would be observed in the depleted (e.g., DM-derived) subduction-free melts. When considering all these, on a plot of Ta/Yb versus Th/Yb, as shown by Figure 5.18, while the MORBs and OIBs would define an array, the melts derived from subduction-modified source regions are displaced from the array with higher Th/Yb ratios (Pearce, 1983). When the Tunceli data points are plotted on the diagram (Figure 5.18), it is observed that all Tunceli lavas are shifted to high Th/Yb ratios compared to the mantle array, suggesting the incorporation of subduction component into their mantle source regions. Another notable feature in the diagram is that the Tunceli lavas display higher Ta/Yb ratios relative to the DM-derived lavas (average value of N-MORBs and oceanic arc lavas of Tonga-Vanuatu Arc), and therefore forming a trend sub-parallel to an interval of mantle array corresponding to the melts contributed from enriched source region(s). Such enriched source region with high Ta/Yb ratios, as reflected the proximity of the data distribution to the average composition of OIBs, is widely attributed to OIB-type melts (e.g., Sun and McDonough, 1989). The data projection in the diagram, therefore, does not only indicates the contribution from a mantle region hosting subduction component for the Tunceli lavas, but also suggests a contribution from an enriched mantle component widely sampled by OIB-like melts. It is also noteworthy that the tholeiitic Tunceli lavas display slightly lower Ta/Yb ratios compared to the alkaline samples, trending towards the depleted melts (average value of N-MORBs and oceanic arc lavas of Tonga-Vanuatu Arc). This may also support the idea that a depleted component is nominally involved in the genesis of Tunceli lavas.

The enriched trace element characteristics combined with subduction imprint are usually observed in the lavas produced at continental arc-basins and some intraplate settings. In the continental arc-basin systems, the mantle wedge, is assumed to be highly fluxed by melt and/or fluids derived from an actively subducting slab (e.g., Pearce and Peate, 1995). In some continental intraplate settings, on the other hand, the melting is assumed to occur largely in the SCLM, which can be infiltrated by the metasomatic agents from an earlier subduction event (e.g., flanks and shoulders lavas of Rio Grande Rift, Gibson et al., 1993). The enriched trace element systematics of Tunceli lavas with subduction imprint is consistent with of continental arc lavas (e.g., Figure 4.20a-b, Figure 5.18; Aeolian Arc, Peccerillo et al., 2013; the Andes, Hidalgo et al., 2012) and intraplate lavas derived from metasomatized SCLM (e.g., Figure 4.20a-b, Figure 5.18; flanks and shoulders lavas of Rio Grande Rift, Gibson et al., 1993), suggesting possible generation either at the active continental margin or within-plate settings.

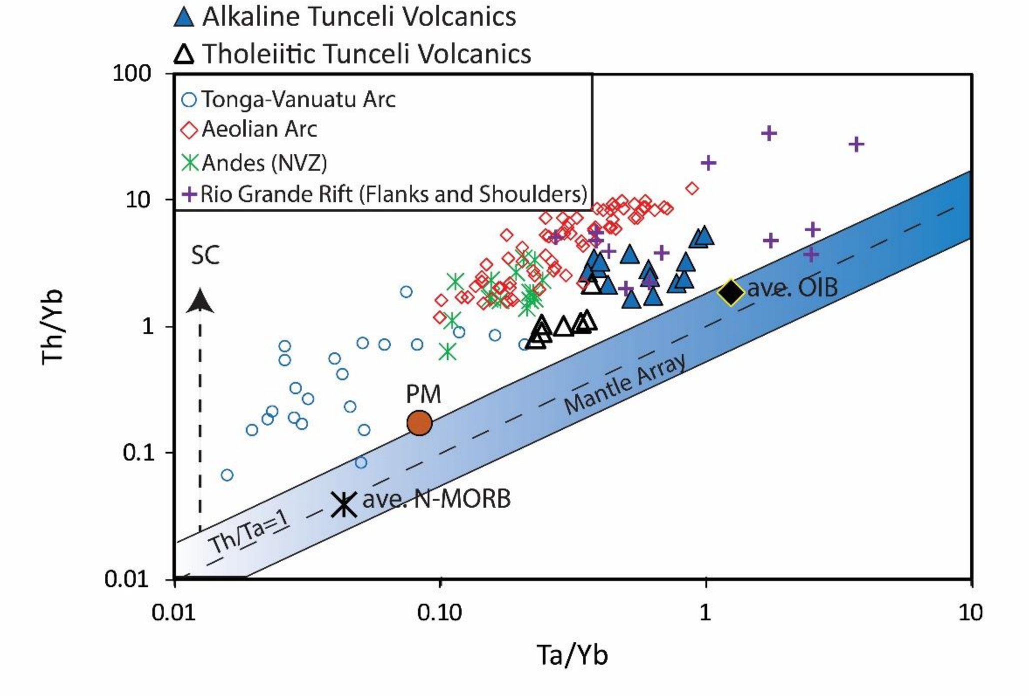

Figure 5.18. The Ta/Yb versus Th/Yb diagram (Pearce, 1983) for the Tunceli Volcanics and lavas related with subduction-modified source regions. The Th/Ta array represents the mantle array defined by non-subduction-related oceanic lavas (MORBs and OIBs). The published data used for comparison includes samples with MgO (wt. %) greater than 4 wt. % to avoid the effects of post-melting processes and to make the data set comparable with the Tunceli lavas. The data sources; Average N-MORBs, OIB and PM from Sun and McDonough (1989), Tonga-Vanuatu Arc from Pearce et al. (2007), Aeolian Arc from Peccerillo et al. (2013), Andes (NVZ: Northern Volcanic Zone) from Hidalgo et al. (2012) and Rio Grande Rift from Gibson et al (1993). Key to abbreviations: SC: subduction component.

However, since the last oceanic realm between Arabian and Eurasian plates was consumed during the Early to Middle Miocene period (e.g., Şengör and Yılmaz, 1981; Okay et al., 2010; Cavazza et al., 2018), the Late Miocene and younger magmatism of eastern Anatolia are assumed to have collision-related or post-collisional geochemical characteristics (see CHAPTER 2 for the details). Hence, they can be attributed to derivation from metasomatized SCLM rather than in a wedge above in an active subduction zone (e.g., Pearce et al., 1990; Keskin, 1994; Keksin et al., 1998). Therefore, the subduction-related signatures of the Late Miocene Tunceli Volcanics can be attributed to contribution from SCLM melts carrying inherited subduction component from an earlier event. This is also evidenced by their similar trace elements pattern with the Anatolian lavas regarded to have been derived from a subduction-modified SCLM (Figure 4.20c-d).

The contribution of metasomatized SCLM appears to have led to the enrichment in most subduction-mobile elements (e.g., LILEs-Th-LREEs) in the Tunceli lavas. Similar to the mantle wedge at active continental margins, the SCLM at subduction zones also tend to be modified by slab-released fluids/melts (e.g., Pearce et al., 1990). As mentioned above, while Th and LREEs are assumed to be largely transported by sediment melts from the top of subducted slab, the fluid-mobile LILEs, such as Ba, are usually expected to be transferred via aqueous fluids released by the altered oceanic crust (Pearce and Peate, 1995; Elliot et al., 1997; Class et al., 2000). Therefore, during subduction, sediment melts and aqueous fluids are not only prone to metasomatize the overlying mantle wedge, but they also tend to be infiltrated by the overlying SCLM domains. Accordingly, the SCLM would be enriched in those elements assumed to be mobile in the subduction zones, and any contribution from the metasomatized SCLM into the genesis of intraplate magmas would enrich their LILEs, Th, and LREEs compared to their HFSE. Such enrichment would create high LILE/HFSE ratios in the lavas; thereby resulting in negative Nb/Nb* values in the lavas, which are usually assumed to be characteristics of the arc-lavas (e.g., Pearce and Peate, 1995). Considering these, the role of metasomatized SCLM in the genesis of Tunceli lavas appears to be necessary, and the contribution of SCLM can indeed be a plausible explanation for the enrichment of Th and La relative to Nb in the Tunceli lavas (e.g., Figure 4.19a). It must also be noted that such elemental enrichments may also be acquired by the crustal contamination process. However, since this possibility has been precluded by the AFC modelings, the relative enrichment in Th and La appears to be rather related to the SCLM contribution. One notable feature in the PM-normalize diagram of the Tunceli lavas (Figure 4.19), the enrichment of their Th relative to LILEs (e.g., Rb, Ba), which may suggest that the metasomatic agents modified the SCLM beneath eastern Anatolia may have plausibly been characterized by sediment melts rather than aqueous fluids. However, this can be well inferred from their Ba/La and Th/Yb ratios rather than enrichment levels in the PM-normalized multi-element diagrams (e.g., Figure 4.19). It has been proposed that the fractionation of Ba from the La can be achieved by mobility in aqueous fluids rather than melting during the subduction; therefore, the high Ba/La ratios observed in the arc lavas have been attributed to derivation from a mantle region metasomatized by slab-derived fluids (e.g., McCulloch and Gamble, 1991; Woodhead et al., 2001). The Th enrichment in the primitive arc lavas, on the other hand, has been associated with slab-derived sediment melt involvement into their source regions (e.g., Johnson and Plank, 1999; Class et al., 2000). Taken together, distinct type of elemental enrichments occurs between the arc lavas derived from fluid-metasomatized mantle regions and those derived from sediment melt-metasomatized mantle regions (e.g., Woodhead et al., 2001). This is well illustrated on a plot of Ba/La versus Th/Yb (Figure 5.19), where two separate trends occur between the oceanic arc lavas assumed to have been derived from mantle regions modified by distinct slab components (sediment melt versus fluid). Although there are still ongoing debates on the effects of post-melting process (e.g., crustal assimilation, see Woodhead et al., 2001) to the lavas of the Lesser Antilles and Sunda arcs, they are characterized by Th/Yb ratios assumed to have been acquired by derivation from sediment-melt modified mantle wedges (e.g., White and Dupre, 1986). The Kermadec, Mariana, and New Britain arc lavas, on the other hand, are characterized high Ba/La ratios, which have been attributed to the involvement of slab-derived fluids in their source regions (e.g., Turner et al., 1997). It must be noted that only the lavas that have MgO (wt. %) higher than 4 wt. % plotted on the diagram to avoid the effects of crustal assimilation.

When the Tunceli lavas are plotted on this diagram (Figure 5.19), it can be observed that they follow the high Th/Yb trend rather than Ba/La, trend suggesting that the

SCLM beneath the eastern Anatolia have been metasomatized by sediment melts rather than aqueous fluids.

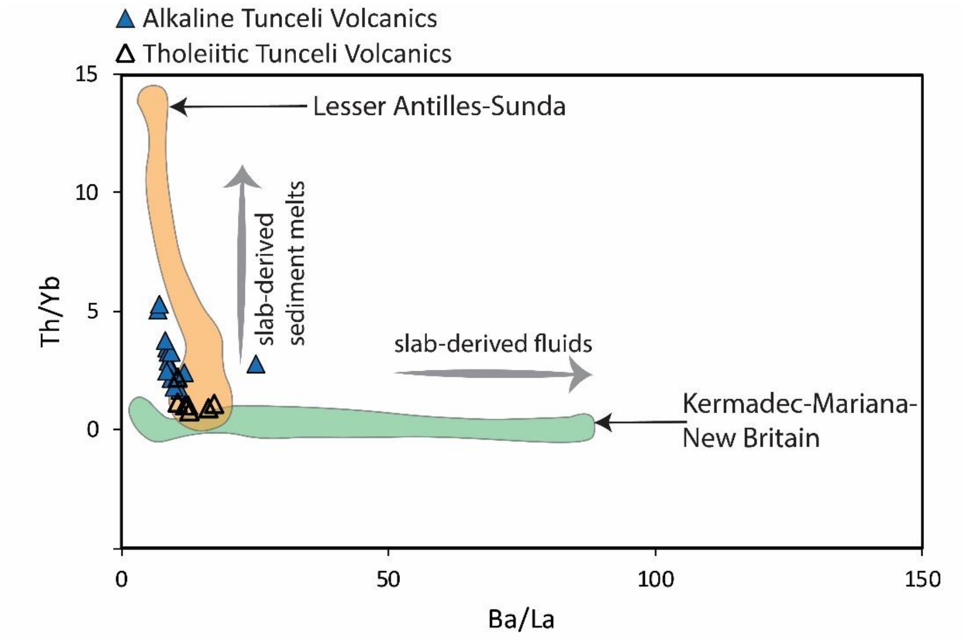

Figure 5.19. The Ba/La versus Th/Yb diagram for the Tunceli Volcanics and lavas related with subduction-modified source regions. The published data used for comparison includes samples with MgO (wt. %) greater than 4 wt. % to avoid the effects of post-melting processes and to make the data set comparable with the Tunceli lavas. The data sources high Th/Yb (the Lesser Antilles and Sunda Arcs) and high Ba/La (Kemadec, Mariana, and New Britain Arcs) arc lavas were taken from the compilation of Woodhead et al. (2001) and all references therein.

To sum up the trace elements constraints on the mantle source characteristics of the Tunceli lavas, at least three mantle components have been involved in Tunceli volcanism. These are; (i) a depleted component which is widely sampled by MORBs and oceanic arc lavas, (ii) enriched component(s) which attributed to the OIBs origin, and (iii) an enriched component represented by an SCLM domain predominantly metasomatized by slab derived sediment melts. Among these, the contribution of DM appears to be limited compared to enriched ones.

The trace element systematics are useful in providing important information regarding the source characteristics of the lavas, especially in differentiating enriched and depleted components in the genesis of the lavas. However, a more robust approximation to the composition of the mantle source regions can be developed by isotope systematics since the isotope ratios of the melts are identical to that of their source regions at magmatic temperatures (Hofmann, 2003). Moreover, the isotope systematics not only provide an excellent opportunity to differentiate the nature source components (e.g., HIMU, FOZO/C) involved in the genesis of the lavas, they also help to elucidate the extent of their involvement. In this regard, in the following section, the details of the geochemical distinctions between the source components of the Tunceli lavas will be considered in the light of Sr-Nd-Hf-Pb isotope data. In addition, more detailed modelings will be presented to constrain the multi-component mixing phenomenon in the genesis of these lavas.

5.1.3.1.2 Constraints from Sr-Nd-Hf-Pb Isotope Systematics

Similar to their trace element systematics, the Sr-Nd-Hf-Pb isotopic range of the Tunceli lavas also indicate heterogeneity in the source regions of Tunceli volcanism. In addition, the isotopic range of the Tunceli lavas display also constitutes several lines of evidence in support of the idea that multi-component mixing has played a role in the genesis of the Tunceli Volcanics. The $^{87}Sr/^{86}Sr$-$^{143}Nd/^{144}Nd$ and $^{143}Nd/^{144}Nd$-$^{176}Hf/^{177}Hf$ correlations (Figure 4.25) suggest that the source region for the Tunceli volcanism can be approximated in general terms as mixing between mantle components with and without time-integrated enrichments in Rb/Sr and Sm/Nd ratios. While the low $^{87}Sr/^{86}Sr$ and high $^{143}Nd/^{144}Nd$ and $^{176}Hf/^{177}Hf$ ratios observed in some Tunceli lavas can be attributed to the possible involvement of several mantle components such as DM, HIMU, and C/LVC (for the details about mantle components, see CHAPTER 1), the elevated $^{87}Sr/^{86}Sr$ and low $^{143}Nd/^{144}Nd$ and $^{176}Hf/^{177}Hf$ ratios in some samples can be associated with the involvement of some continental-lithosphere and/or pelagic sediment-associated mantle components such as EMI and EMII in their genesis (e.g., Zindler and Hart, 1986; Hoernle et al., 1995; Blichert-Toft et al., 1999; Stracke et al., 2005; Willbold and Stracke, 2006). Note that the EM-type enrichments in the intraplate lavas can also be achieved by melt contributions from sediment melt-metasomatized SCLM (e.g., Gall et al., 2021).

Similarly, the intermediate ^{206}Pb/^{204}Pb ratios of the Tunceli lavas between DM and FOZO/C or HIMU end members combined with their elevated ^{207}Pb/^{204}Pb and ^{208}Pb/^{204}Pb ratios relative to the NHRL (Figure 4.26) may also imply the involvement of multiple components in their genesis. The trend of Tunceli lavas towards the MORB samples on the plot of ^{206}Pb/^{204}Pb versus ^{208}Pb/^{204}Pb (Figure 4.26b) suggests the involvement of DM component in their genesis; however, the higher ^{206}Pb/^{204}Pb end of the data trend towards the component C/LVC and also to HIMU indicate also contributions from mantle components associated with recycled oceanic lithospheric lithologies (e.g., Hofmann and White, 1982; Zindler and Hart, 1986; Niu and O'Hara, 2003). This, in general, may imply mixing of DM and a component with more radiogenic ^{206}Pb/^{204}Pb compositions, i.e., C/LVC or HIMU, in the source region of Tunceli lavas. Note that similar ^{206}Pb/^{204}Pb and ^{208}Pb/^{204}Pb compositions are also observed in the lavas of the Gulf of Aden (not shown), which is known to tap a depleted (DM) mantle source polluted by a recycled plume material, i.e., Afar Plume (Schilling et al., 1992; Rooney et al., 2012). Although the physical locations of the source domains of these components are not completely constrained, they are widely assumed to be originated at asthenospheric levels of Earth (e.g., Zindler and Hart, 1986). Thus, the data distribution of Tunceli lavas on the plot of ^{206}Pb/^{204}Pb and ^{208}Pb/^{204}Pb may be supportive for a heterogeneous asthenospheric source region for Tunceli volcanism arising from the mixing of depleted mantle component and a component representing recycled oceanic lithologies (e.g., C/LVC or HIMU component). The steep array defined by the data distribution of Tunceli lavas in the plot of ^{206}Pb/^{204}Pb versus ^{207}Pb/^{204}Pb relative to NHRL (Figure 4.26a), on the other hand, also require an additional enriched source component (e.g., EMII-type) derived from recycled crustal/lithospheric material (e.g., EMII component found in the Samoan lavas; Jackson et al., 2007) or from an SCLM domain fluxed by slab-derived sediment melts (e.g., Gall et al., 2021).

As seen above, besides the trace element systematics, the involvement of multi-component into the genesis of Tunceli lavas, is also evidenced by their isotope systematics. Among the components presumed to have contributed to the Tunceli volcanism, the DM, C/LVC, and HIMU components, as noted above, are regarded as asthenospheric mantle components (e.g., Zindler and Hart, 1986). The EMII-type component, on the other hand, may have two distinct origins. Therefore, to first order, an assessment regarding the origin of EMII signatures observed in the Tunceli lavas is needed to fully understand the nature of the source region(s).

As previously mentioned, the EMII-type isotopic enrichments (high $^{87}Sr/^{86}Sr$ and $^{207}Pb/^{204}Pb$ isotope ratios; Zindler and Hart, 1986) in the intraplate lavas can be acquired by recycling of ancient crustal/lithospheric materials via deep-seated melts/plumes into their source regions (e.g., Samoan lavas, Jackson et al., 2007) or can result from melt contributions from a mantle domain fluxed by continent-derived sediment melts during subduction events (e.g., Gall et al., 2021). In the Pb-Pb isotope spaces (Figure 4.26), the Tunceli lavas plot nearby the Samoan lavas, which are assumed to have been derived from a source region containing ancient crustal material with sediment input or lithospheric material with metasomatic input (e.g., Workman et al. 2004; Jackson et al. 2007). However, it is also apparent in the diagram of $^{206}Pb/^{204}Pb$ versus $^{207}Pb/^{204}Pb$ (Figure 4.26a), the Tunceli lavas with a distinct trend within the field of GLOSS (GLOSS; Plank and Langmuir, 1998) display more radiogenic $^{207}Pb/^{204}Pb$ isotope ratios for a given $^{206}Pb/^{204}Pb$ than the Samoan data cluster (Figure 4.26a). This may argue against the involvement of an EM-type component with a deep mantle origin; instead, it may indicate relatively a shallow source, such as an SCLM domain modified by continental-derived sediment during former subductions beneath the region.

As mentioned in the previous sections, multiple subduction events related to the closure of Neo-Tethyan oceans have contributed to building the main landmass of eastern Anatolia (e.g., Şengör and Yılmaz, 1981). Therefore, the SCLM domains beneath the eastern Anatolian crust are likely to have been infiltrated by the slab-derived metasomatic agents during the subductions of multiple branches of the Neo-Tethys ocean. This process, in particular, manifests itself in the geochemistry of those lavas that have been contributed by melts derived from these SCLM domains. As detailed in the previous section, the Tunceli lavas are among the best candidates for such melts with their subduction-modified trace element budgets (e.g., Nb/Nb* <1). Therefore, the SCLM beneath eastern Anatolia can be regarded as one of the potential candidates for generating EMII-like signatures in the Tunceli lavas. This can be well supported by the Sr-Nd, Nd-Hf, Pb-Pb isotope spaces (Figures 4.25 and 4.26), where the Tunceli lavas follow the trend of Anatolian (from western to eastern Anatolia) lavas assumed to have been derived by melts contributions from metasomatized SCLM. It must be noted that these all SCLM-derived Anatolian lavas display an EMII signature on the plot of $^{206}Pb/^{204}Pb$ versus $^{207}Pb/^{204}Pb$ (Figure 4.26a). If this is the case, the sediment input in the SCLM domains beneath Anatolia should have predominantly been characterized by upper crustal lithologies, which is documented as one of the potential materials to create EMII-like enrichments in the lavas when involved in their genesis (e.g., Willbold and Stracke, 2006). This idea can be further tested by integrating the isotope compositions of young eastern Mediterranean sediments (Klaver et al., 2015) and SCLM-derived western Anatolian lamprophyric and lamproitic lavas (Elitok et al., 2010; Prelević et al., 2012). While the young eastern Mediterranean sediments (Klaver et al., 2015) are appropriate to characterize the metasomatic inputs in the SCLM domains of eastern Anatolia, the western Anatolian potassic lavas are the ideal candidates for the melts derived from the SCLM-domains Anatolia. It is important to note that there is no published data on lamprophyric and/or lamproitic lithologies from eastern Anatolia; therefore, those from western Anatolia (Elitok et al., 2010; Prelević et al., 2012) have been used for comparison. On a plot of $^{206}Pb/^{204}Pb$ vs. $^{207}Pb/^{204}Pb$ (Figure 5.20), the young eastern

Mediterranean lavas displaced from the NHRL towards the above of Samoan lavas with highly radiogenic $^{207}Pb/^{204}Pb$ isotope ratios, and the potassic SCLM-derived lavas of western Anatolia with a broad Pb-spectrum stretch between these sediments and C-type extremes. This may indicate that the EMII-type component is similar to that defined by Mediterranean sediments and can be represent an SCLM domain metasomatized by slab-derived sediment melts. Hence, the compositions of western Anatolian SCLM-derived potassic lavas, Mediterranean sediments, and Tunceli lavas are together consistent with the idea that the EMII-type signatures in the SCLM-related Anatolian lavas have been acquired by melt contributions from an SCLM domain fluxed by slab-derived sediment-melts, rather than contributions from a deep-seated mantle/plume material.

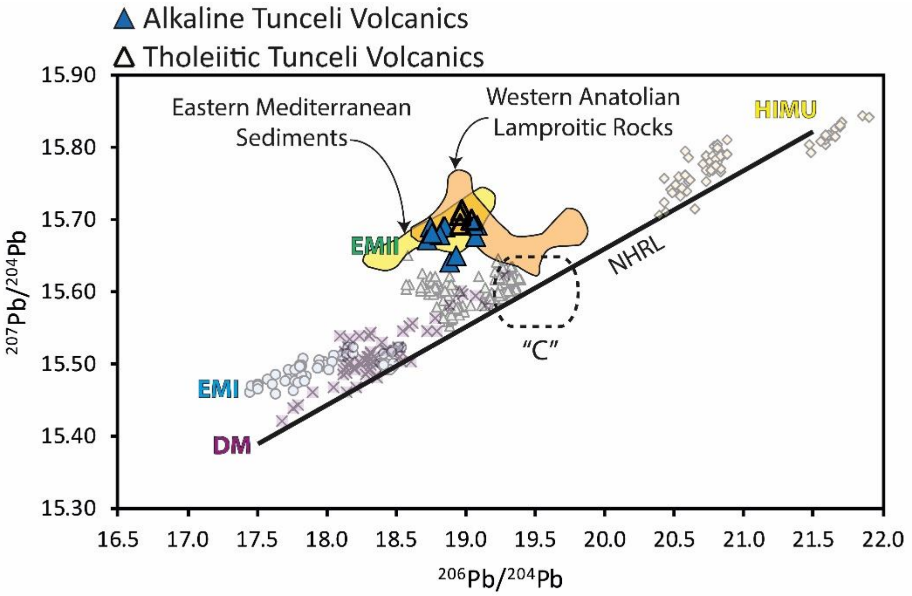

Figure 5.20. The $^{206}Pb/^{204}Pb$ versus $^{207}Pb/^{204}Pb$ plot showing the distribution of the Tunceli Volcanics together with the western Anatolian lamproitic rocks (Elitok et al., 2010; Prelević et al., 2012), eastern Mediterranean sediments (Klaver et al., 2015), global MORBs, and OIBs representing distinct extreme isotopic compositions in the mantle (HIMU, EMI, EMII, and DM). NHRL is from Hart (1984). The sources of compositions of the components LVC and C are given in the caption of Figure 4.25. Likewise, the locations of oceanic basalts and their data sources are also given in the caption of Figure 4.25.

With these arguments, it can be suggested that the Tunceli lavas have been produced by mixing between lithospheric and asthenospheric mantle components. Apart from the lithospheric component (SCLM), an additional asthenospheric multi-component blend containing a depleted and an enriched component is also needed to account for their whole trace element and Sr-Nd-Pb-Hf isotope systematics, as noted above. Therefore, to bring a first-order approximation to the types of asthenospheric mantle components involved in the Tunceli volcanism, a multi-component mixing model was applied using a number of isotope systematics, including ^{87}Sr/^{86}Sr, ^{143}Nd/^{144}Nd, ^{176}Hf/^{177}Hf and ^{206}Pb/^{204}Pb (Figure 5.21).

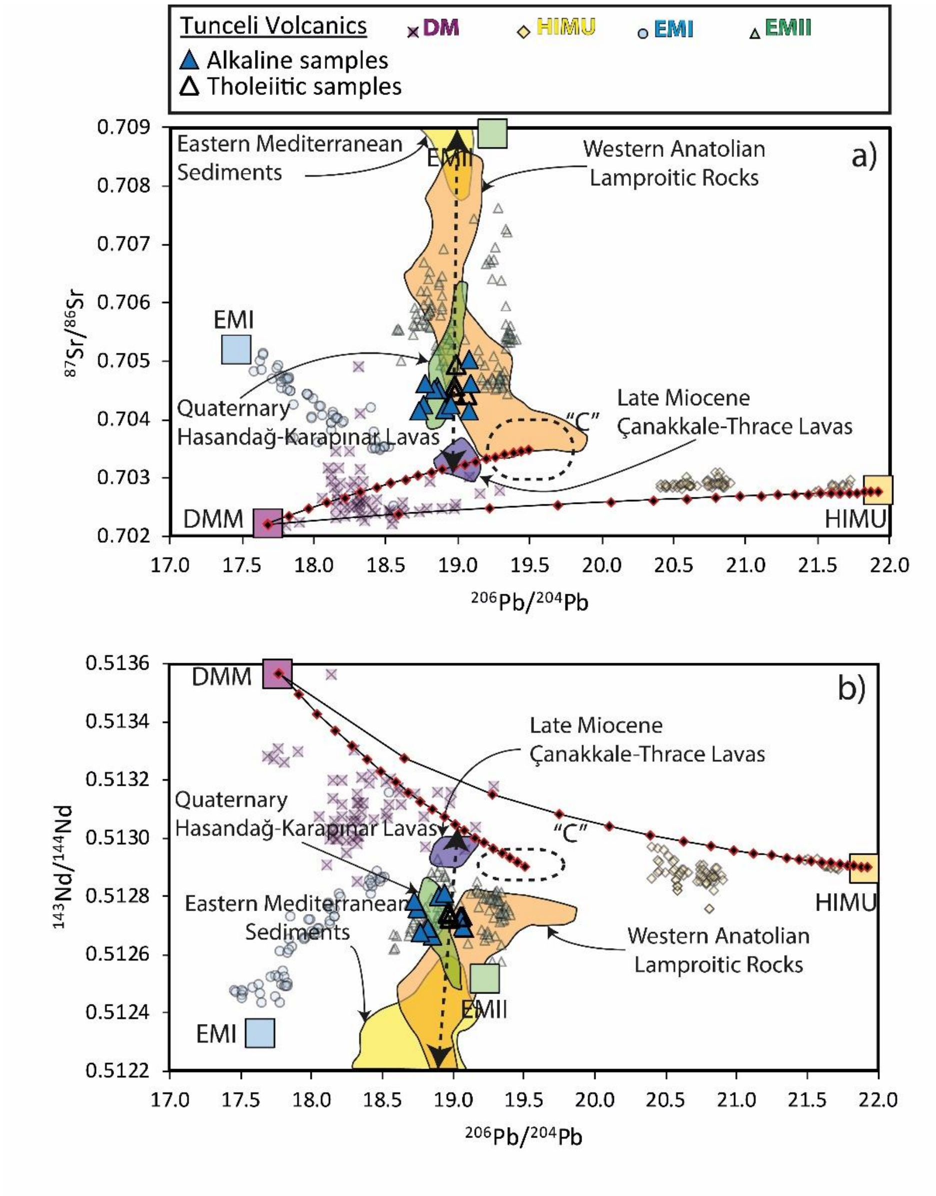

Figure 5.21. The (a) $^{206}Pb/^{204}Pb$ versus $^{87}Sr/^{86}Sr$, (b) $^{206}Pb/^{204}Pb$ versus $^{143}Nd/^{144}Nd$ and (c) $^{206}Pb/^{204}Pb$ versus $^{176}Hf/^{177}Hf$ plots for Tunceli Volcanics showing also the calculated mixing curves between mantle end-members. The western-central Anatolian lavas (Aldanmaz et al., 2000; 2015; Gall et al., 2021; Elitok et al., 2010; Prelević et al., 2012), eastern Mediterranean sediments (Klaver et al., 2015), and oceanic basalts (MORBs and OIBs) representing distinct extreme isotopic compositions in the mantle (HIMU, EMI, EMII and DM) are also plotted into diagram for comparison. The tick marks on each curve correspond to 5% mixing intervals. The isotope compositions of the C are as follows: $^{206}Pb/^{204}Pb$= 19.5; $^{87}Sr/^{86}Sr$= 0.7035; $^{143}Nd/^{144}Nd$= 0.5129; $^{176}Hf/^{177}Hf$= 0.283025. The element concentrations (in ppm) of the C are as follows: Pb= 0.299; Sr= 16.874; Nd= 1.3839; Hf= 0.358. The isotope compositions of the DM are as follows: $^{206}Pb/^{204}Pb$= 17.681

(in Figure 5.21a), 17.762 (in Figures 5.21b and 5.21c); $^{87}Sr/^{86}Sr$= 0.702225; $^{143}Nd/^{144}Nd$= 0.513564; $^{176}Hf/^{177}Hf$= 0.283363. The element concentrations (in ppm) of the DM are as follows: Pb= 0.018; Sr= 7.664; Nd= 0.581; Hf= 0.157. The isotope compositions of the HIMU are as follows: $^{206}Pb/^{204}Pb$= 21.916; $^{87}Sr/^{86}Sr$= 0.702791; $^{143}Nd/^{144}Nd$= 0.512899; $^{176}Hf/^{177}Hf$= 0.2828865. The element concentrations (in ppm) of the HIMU are as follows: Pb= 0.0929; Sr= 67.014; Nd= 8.7196; Hf= 2.32. The all parameters used in the calculation can also be found in the Table 5.3.The sources of composition of the component C is given in the caption of Figure 4.25. Likewise, the locations oceanic basalts and their data sources are also given the caption of Figure 4.25. The compositions of the end-members HIMU, EMI, EMII and DM used in the calculations can be found within the text.

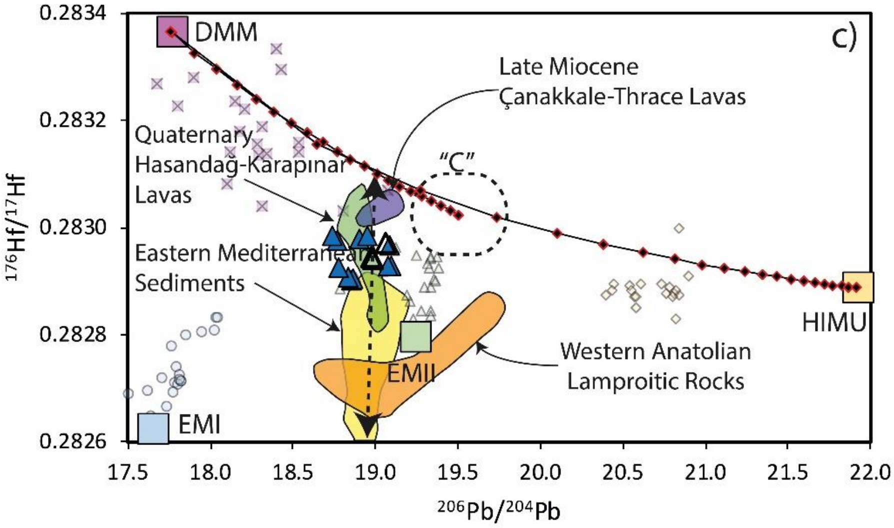

Figure 5.21 *(cont'd).*

In the Sr-Pb, Nd-Pb, and Hf-Pb isotope spaces, shown by Figure 5.21, solid-state mixing curves have been modeled between the end members DM and C and DM and HIMU since their trace element and Sr-Nd-Hf-Pb isotope systematics suggest the involvement of a depleted component and a recycled component possibly of oceanic lithospheric origin. In the calculations, the Sr-Nd-Pb-Hf isotope composition of the common component was estimated from the average isotope composition of "C" from Hanan and Graham (1996) and Geldmacher et al. (2011). The isotope composition of the most depleted lava among the plotted MORB samples is adopted as the isotope composition of the DM. The Sr-Nd-Pb isotope composition of the sample having the most radiogenic $^{206}Pb/^{204}Pb$ among the Mangaian lavas was used as the HIMU composition. The Hf isotope composition of the HIMU was adopted from the average Hf isotope contents of the St. Helena lavas. The trace element concentrations of the mantle end-members used in the models are based on Stracke et al. (2003) and some references articles (i.e., Workman and Hart, 2005). The trace element concentrations of the DM are from Workman and Hart (2005). The trace element contents of the source of “C” were hypothetically calculated from the spreadsheet of Stracke et al. (2003). For the calculation of the trace element content of the “C”, an ancient, sediment-free oceanic lithosphere (90% depleted lithospheric mantle+10% oceanic crust) was assumed to melt in the garnet-stability field. Recycling of such assemblage proposed to have similar isotopic signatures with the common component (Stracke, 2012). The “C” was assumed to be melted by 0.5% degree of non-modal accumulated fractional melting. For the calculation of the trace element content of the “HIMU”, an ancient oceanic crust (0% depleted lithospheric mantle+100% oceanic crust) without any addition of sediment or continental crust was assumed to melt in the garnet-stability field. The “HIMU” (an eclogitic assemblage) was thought to melt by 4% degree of non-modal accumulated fractional melting. The oceanic crust, in the calculations, was regarded to be a package consisting 25% NMORB+25% altered MORB+50% Gabbro, which is exactly the same assemblage used in Stracke et al. (2003). The depleted lithospheric mantle composition in the models is from Salters and Stracke (2004), while the bulk oceanic crust is from Stracke et al. (2003). During the calculations, subduction modifications and sediment-melt alterations were allowed. The coefficient values and associated references in relation to the sub-arc modifications and melting process are given in the spreadsheet of Stracke et al. (2003). All parameters used in the modelings can be found in the caption of Figure 5.21 and Table 5.3.

The calculated mixing arrays together with the loose array defined by Tunceli lavas indicate that the total range of the isotopic data of the Tunceli volcanism requires multi-component mixing involving the DM, C-like and EM-type end-members in varying amounts (Figure 5.21). The data points of Tunceli lavas mainly cluster between the C-DM mixture curve and an EM-type end-member in the plots (Figure 5.21). Since the EM-type component has been attributed to a lithospheric component, i.e., SCLM contribution (see the discussion above), the DM and C-like components appear to be the only asthenospheric mantle components involved in the genesis of Tunceli Volcanism. This also confirms the idea that the asthenospheric mantle beneath eastern Anatolia is fairly heterogeneous. In this multi-component blend, however, there is no requirement for involvement a component with highly radiogenic ^{206}Pb/^{204}Pb ratios such as HIMU or LVC/EAR (^{206}Pb/^{204}Pb= ~20; e.g., Hoernle et al., 1995). Based on the projection of the data points of Tunceli lavas toward the DM-HIMU mixture curve, it is apparent that the contribution of DM would be great (>70%) in the case of involvement components with highly radiogenic Pb isotope compositions in their genesis (e.g., HIMU or LVC/EAR). This, indeed, is not favored by the trace element and isotopic evidence. Therefore, a C-like mantle component appears to be the only enriched asthenospheric mantle component in the genesis of Tunceli volcanism.

Recently a C-like asthenospheric mantle component has also been proposed to be involved in the genesis of western and central Anatolian lavas (e.g., Late Miocene Çanakkale-Thrace lavas, Aldanmaz et al., 2000; 2015; Quaternary Hasandağ-Karapınar lavas, Gall et al., 2021; Furman et al., 2021). In addition, in these lavas, besides the C-like component, the DM is also thought to have been involved in their genesis (e.g., Aldanmaz et al., 2015; Gall et al., 2021; Furman et al., 2021). With these characteristics, they share geochemical similarities with the Tunceli Volcanics. When these lavas are plotted together with Tunceli lavas on the Sr-Pb, Nd-Pb, and Hf-Pb isotope spaces (Figure 5.21), it is observed that they define an array consistent with the mixing scenario suggested for the Tunceli volcanism above. The array of the C-related Anatolian lavas extends from the C-DM mixture curve towards the eastern Mediterranean sediments (Klaver et al., 2015) and western Anatolian potassic lavas (Elitok et al., 2010; Prelević et al., 2012), which are assumed to represent SCLM-type components in most of the Anatolian lavas (Gall et al., 2021).

In addition to these, although the contribution of the SCLM component varies among these Anatolian lavas, the array defined by them converges towards the C-dominant portion of the calculated C-DM mixture curve. This does not only suggests a asthenosheric mantle source dominated by the C-like component for these lavas but also indicate a “common” characteristics for the Anatolian asthenosphere. Moreover, the emergence of the data points Tunceli and other Anatolian C-related lavas towards the EMII-type end member may also simply that pre-mixing between the C-like component and DM component occurred before the involvement of the SCLM component in their genesis. Hence, the asthenospheric mantle source regions of these volcanics appear to be primarily characterized by solid-state mixing of depleted asthenospheric component and a component represented by recycled oceanic lithospheric lithologies (i.e., C-like).

As noted above, the dominance of a C-like component in the C-DM mixture within the asthenosphere is apparent from the convergence of Tunceli lavas towards the C-dominant portion (>60%) of the calculated C-DM mixture curve. However, more robust approximations to which extent these asthenospheric components have mixed with each other can be developed by fixing all end-members in the multi-component mixing (i.e., DM-C-like-EMII-type) presumed for the Tunceli volcanism. This will also help reveal the extent of the SCLM contribution to the genesis of Tunceli volcanism. In this regard, melt-mixing modelings were applied including a component representing the mixture of C-DM, and metasomatized SCLM derived melts by using the Sr-Nd-Hf-Pb isotope systematics (Figure 5.22).

However, it must also be noted that melt-mixing modeling between an asthenospheric component and a lithospheric component is not an easy task due to the highly heterogeneous nature of the SCLM. In addition, in such mixing, the asthenospheric contributions would be dominated by the lithospheric contributions due to the greater Pb, Sr, Nd, and Hf mass proportions of the lithosphere (Furman et al., 2021). As can be seen in Figure 5.22, the Tunceli lavas do not define linear trends; instead, they loosely cluster in the isotope spaces. This likely reflects the melt contributions from a highly heterogeneous SCLM domain, and complicates determining the compositions of the end-member in the modelings. Therefore, the Late Miocene Thrace and Çanakkale lavas of western Anatolia (Aldanmaz et al., 2000; 2015) were also plotted for a more robust approach to detect the composition of the C-DM mixture in the genesis of Tunceli volcanism. As it is apparent in the Sr-Nd-Pb-Hf isotope spaces shown by Figure 5.21, the Late Miocene Çanakkale-Thrace lavas represent the melts with the lowest SCLM contribution within the array defined by the Anatolian C-related lavas. Hence, their trend in the Sr-Nd-Hf-Pb isotope spaces will help fix the C-DM mixture composition in the modelings (Figure 5.22). In addition, to characterize the extent of the heterogeneous SCLM contribution for the Tunceli lavas, multiple SCLM end-members with different Pb isotope compositions were selected for the modelings (Figure 5.22). Hence, multiple mixing curves were modeled in the isotope spaces. Since the Pb isotopes are very sensitive to the addition of sediments (Furman et al., 2021), each mixing curves represent a unique mixing trend between the C-DM source and a sediment-melt metasomatized SCLM domain.

In the modelings, the isotope compositions of C-DM mixtures are obtained from the models designed in Figure 5.21. Since the most coherent melting curves with the Late Miocene Çanakkale-Thrace lava trend were calculated based on a C-DM mixture end-member produced by a C contribution of around 80%, the C-DM end-member containing 80% C and 20% DM was selected as asthenospheric mantle end-member for the Tunceli lavas (Figure 5.22). Such C-DM end-member composition will also be consistent with modelings in Figure 5.21, which favor a dominant involvement of a C-like component in the petrogenesis of the Tunceli volcanism. The curves in the Sr-Pb, Nd-Pb, and Hf-Pb isotope spaces were calculated based on melt-mixing mode. Therefore, for the estimation of the trace element concentrations of the C-DM melt, the solid-state mixture of the C-DM source (80% C and 20% DM) is assumed to have been melted by 0.5 % degree of non-modal fractional melting at the garnet stability field. For the lithospheric melt (LM), on the other hand, the isotope compositions of the most radiogenic samples among the young eastern Mediterranean sediments and western Anatolian lamprophyres/lamproites were chosen as the end-members. The trace element concentrations of the LM end-members used in the modelings are based on the range the western Anatolian lamprophyres/lamproites display and based on the assumptions in Hanan et al. (2008). All parameters regarding the C-DM and LM end-members can be found in the caption of Figure 5.22 and Table 5.4.

The data distribution of the Tunceli lavas on the calculated curves in the Sr-Pb, Nd-Pb, and Hf-Pb isotope spaces (Figure 5.22) indicates that the total range of the isotopic composition of the Tunceli lavas can be generated by mixing of melts derived from an C-DM source, in which the C-like component amount appears to be around 80%, and a sediment melt-metasomatized SCLM domain. In addition, although the amount of the melt contributions from a metasomatized SCLM to Tunceli volcanism varies from one sample to another due to the heterogeneity in the SCLM domain, the calculated mixing curves also suggest that the total amount of SCLM-derived melt contributions to this volcanism vary between 10-30%. These findings, overall, favor a dominant (at least around 70%) involvement of the asthenospheric mantle components in the petrogenesis of the Tunceli volcanism. Moreover, the C-like component, with involvement of at least around 55%, appears to be the most significant component in their genesis.

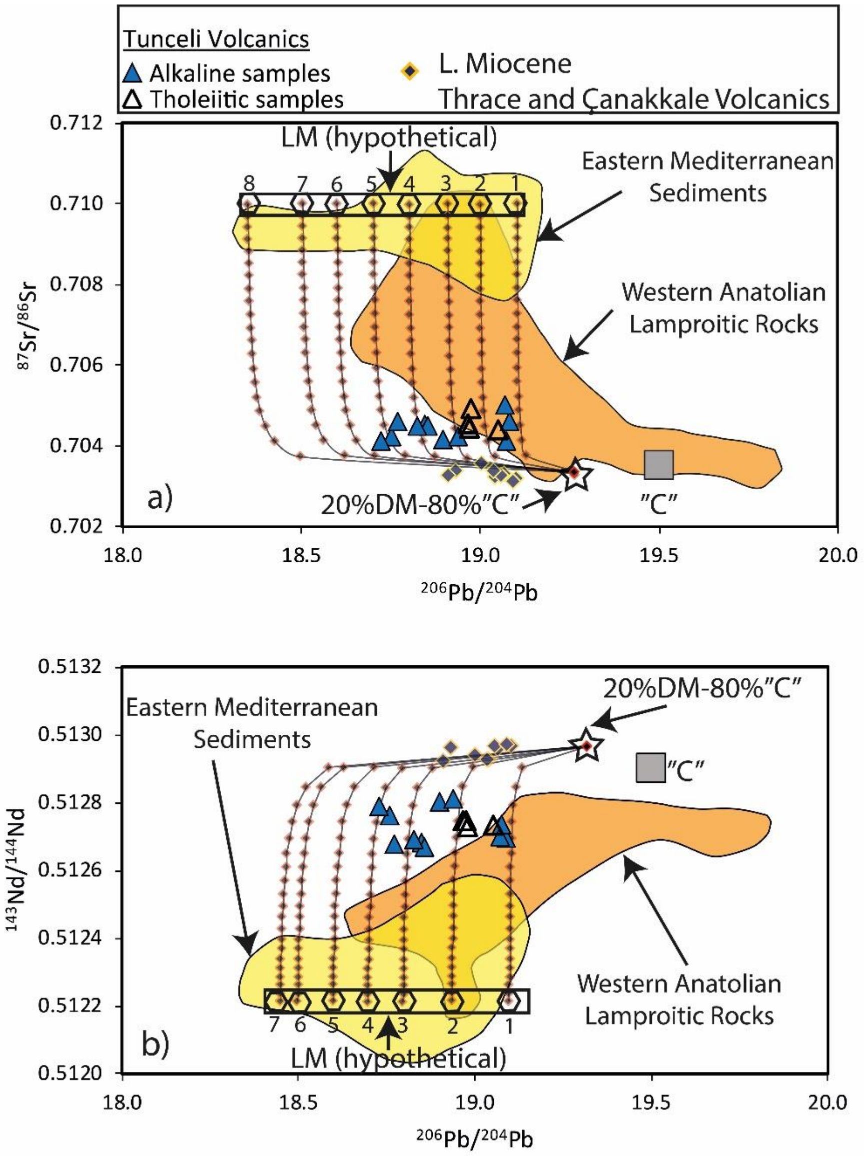

Figure 5.22. The (a) the $^{206}Pb/^{204}Pb$ versus $^{87}Sr/^{86}Sr$, (b) $^{206}Pb/^{204}Pb$ versus $^{143}Nd/^{144}Nd$ and (c) the $^{207}Pb/^{204}Pb$ versus εHf plots for Tunceli Volcanics showing also the calculated mixing curves between mantle C-DM (80% C-20%DM) mixture and SCLM (LM: Lithospheric Mantle) end-members. The representative modern sediments (the eastern Mediterranean Sea; Klaver et al., 2015), western Anatolian lamprophyres/lamproites (Elitok et al., 2010; Prelević et al., 2012) representing LM-derived melts and Late Miocene Çanakkale-Thrace lavas (Aldanmaz et al., 2000; 2015) are also plotted into the diagram for comparison. The tick marks on each curve correspond to 5% mixing intervals. The isotope compositions of the C-DM mixture (80% C-20%DM) are as follows: $^{206}Pb/^{204}Pb$= 19.262 (in Figure 5.22a), 19.32 (in Figure 5.22b); $^{207}Pb/^{204}Pb$= 15.57 (in Figure 5.22c); $^{87}Sr/^{86}Sr$= 0.70337; $^{143}Nd/^{144}Nd$= 0.51296; εHf= 9.667. The element concentrations (in ppm) of the C-

DM mixture are as follows: Pb= 2.41; Sr= 846; Nd= 44.29; Hf= 6.95. The isotope compositions of the Lithospheric Melt (LM) are as follows: ^{206}Pb/^{204}Pb= 19.10 (LM1), 19.00 (LM2), 18.90 (LM3) 18.80 (LM4), 18.70 (LM5), 18.60 (LM6), 18.50 (LM7), 18.35 (LM8) in Figure 5.22a; 19.10 (LM1), 18.94 (LM2), 18.80 (LM3) 18.70 (LM4), 18.60 (LM5), 18.50 (LM6), 18.45 (LM7) in Figure 5.22b; ^{207}Pb/^{204}Pb= 15.75 (LM1), 15.72 (LM2), 15.70 (LM3), 15.68 (LM4), 15.66 (LM5) in Figure 5.22c. ^{87}Sr/^{86}Sr: 0.71001; ^{143}Nd/^{144}Nd: 0.512215; εHf: -9.512. The element concentrations (in ppm) of the LM are as follows: Pb: 241; Sr: 1000; Nd: 74; Hf: 16.65. It is important to note that the Pb element concentration of the lithospheric melt is 100x that of the C-DM mixture, as it is assumed in the study of Hanan et al. (2008). Also, the Sr composition of the lithospheric melt is assumed to be 1000 ppm, which is adoptable for most of lithospheric mantle derived melts. The concentrations of the Nd and Hf elements of the lithospheric end-member have been adopted from the sample 05GUE01 in Prelević et al. (2012). The all parameters used in the models can also be found in the Table 5.4.

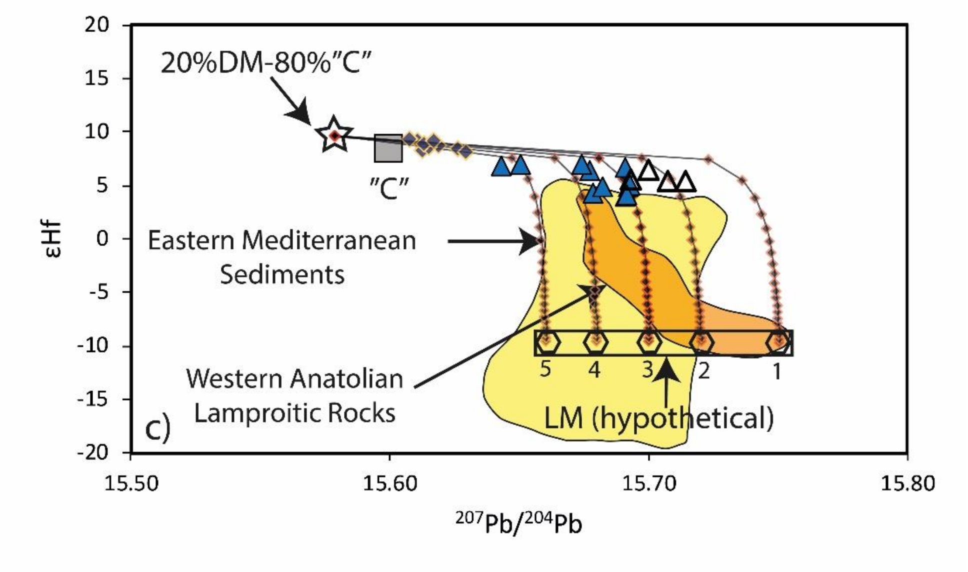

Figure 5.22 *(cont'd).*

Although the SCLM contribution in the genesis of Tunceli volcanism appears to be a maximum of around 30% based on the calculations, these contributions must have significantly modified their elemental budget. Otherwise, no apparent subduction effect (Nb/Nb*<1) would be observed in their PM-normalized trace element patterns. However, the interpretations above raise the question of whether the mixing of 30% SCLM-derived melts and 70% asthenospheric melts (in which the C contribution appears to be around 80%) can create a trough at Nb in the PM-normalized multi-element diagrams or not. To answer this question, a melt-mixing model was applied by using trace element systematics (Figure 5.23). In this model, an asthenospheric mantle source region characterized by solid-state mixing of 80% C and 20% DM was melted by 1 % degree of non-modal batch melting at the garnet-stability field, and subsequently mixed with a melt composition assumed to be derived from a metasomatized SCLM-domain. In the modeling, the trace element concentrations of the DM and C source were calculated by using the supplementary spreadsheets in Stracke et al. (2003). For the lithospheric end-members on the hand, the trace element compositions of a lamproitic sample (05KD012; Prelević et al., 2012) were used. Although adopting a lamproitic sample as a representative lithospheric mantle may be speculative for a distinct point of view, it will help develop an approach to the extent of the lithospheric effects on asthenosphere-derived melts. This modeling will also allow us to check the results obtained from Figure 5.22.

In the figure (Figure 5.23), it is seen that the melt assumed to be derived from a hypothetical C-DM source have very akin geochemical characteristics to the OIB-like melts, although its LILEs are relatively depleted due to the DM contribution. The melts assumed to have been derived from a SCLM domain, on the other hand, with the high LILE/HFSE ratios combined with an apparent trough at Nb mimic the arc lavas (Figure 5.23). If these asthenospheric and lithospheric melts mix with each other at a rate of 70% and 30%, respectively, it can be observed that the lithospheric contribution significantly suppresses the chemistry of the final melt despite its low proportion in the mixture. This is reflected, in particular, by the significant enrichment in LILEs and depletion in HFSE of the final melt. Thus, a trough at Nb in the PM-normalized multi-element diagrams can be produced by mixing between %70 asthenospheric melts and %30 lithospheric melts. Therefore, there is no need for a dominant contribution from a metasomatized SCLM into the genesis of Tunceli lavas to account for their LILE and Th enrichments relative to the HFSE (e.g., Figure

5.23). These findings support interpretations based on the isotopic data (Figure 5.22), suggesting derivation dominantly from an asthenospheric mantle source for the Tunceli lavas.

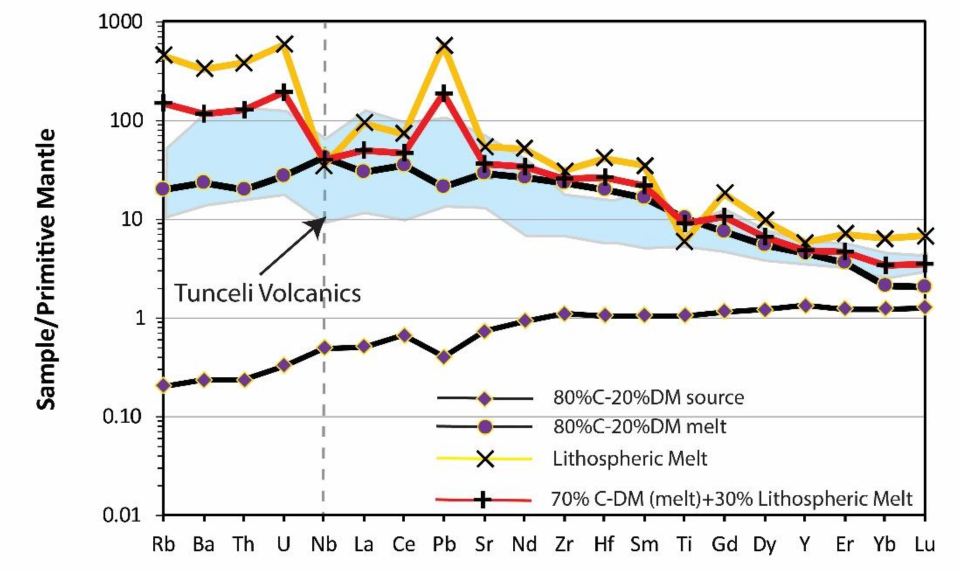

Figure 5.23. Primitive Mantle-normalized (Sun and McDonough, 1989) multi-element diagram showing the melt mixing effect between a sublithospheric source, which is characterized by solid-state mixing of 80% C-like component and DM component, and a metasomatized SCLM domain.

In summary, the isotopic constraints on the nature of the mantle source region of the Tunceli volcanism, in agreement with their trace element systematics, suggest that the Tunceli lavas have been produced by mixing of three distinct components: a depleted asthenospheric component, an enriched asthenospheric component characterized by recycled oceanic lithospheric lithologies (i.e., C-like) and a lithospheric component representing sediment melt metasomatized SCLM domain. At least approximately with an amount of 55%, the contribution of the C-like component into this multi-component blend appears to be dominant compared to other components. In addition to that, contributions at least ca. 15% DM and %30 SCLM components are also needed to explain their full range of isotope systematics.

5.1.3.2 Elazığ Volcanics

5.1.3.2.1 Constraints from Trace Element Systematics

As can be seen in the “GEOCHEMISTRY” chapter of this study, the Elazığ lavas display greater enrichments in their incompatible elements ($(La/Yb)_N$= 10.89-16.85, N denotes to chondrite-normalized based on Sun and McDonough, 1989) compared to those lavas derived from depleted mantle source regions (e.g., average MORBs, $(La/Yb)_N$= 0.58). This is also clearly indicated by their lower Zr/Nb (3.89-5.29) and higher Nb/Y (1.93-2.99) and Zr/Y (10.26-13.18) elemental ratios than those of MORBs (e.g., Average N-MORBs Zr/Nb=31.75, Nb/Y= 0.08, Zr/Y= 2.64; Sun and McDonough, 1989). Note that the Zr/Y ratio is also helpful to track the nature of source regions as the ratios Zr/Nb and Nb/Y (see the discussion above). Since Zr is more incompatible compared to the Y during mantle melting, Zr is expected to be enriched in the mantle-derived melts. Therefore, low Zr/Y ratios are expected in the mantle source regions experienced former melt extractions (e.g., DM=1.52, Workman and Hart, 2005); thereby, also in the lavas derived from such depleted mantle regions (MORBS or oceanic arc lavas). The relatively lower Zr/Nb and higher Nb/Y and Zr/Y elemental ratios of Elazığ lavas compared to the lavas derived from depleted source regions can be well illustrated in the diagrams of Nb/Y versus Zr/Nb (Figure 5.24a) and Zr/Y versus Nb/Y (Figure 5.24b).

In both diagrams (Figure 5.24), the Elazığ lavas displaced from fields of the DM-derived lavas (e.g., average N-MORBs and South Sandwich oceanic arc magmas), and cluster very close to the average value of OIB and the fields defined by the lavas assumed to have been derived from enriched mantle regions. This implies that the contribution of the DM component in the genesis of Elazığ lavas is not significant (if any), and these volcanics dominantly tapped the enriched mantle components.

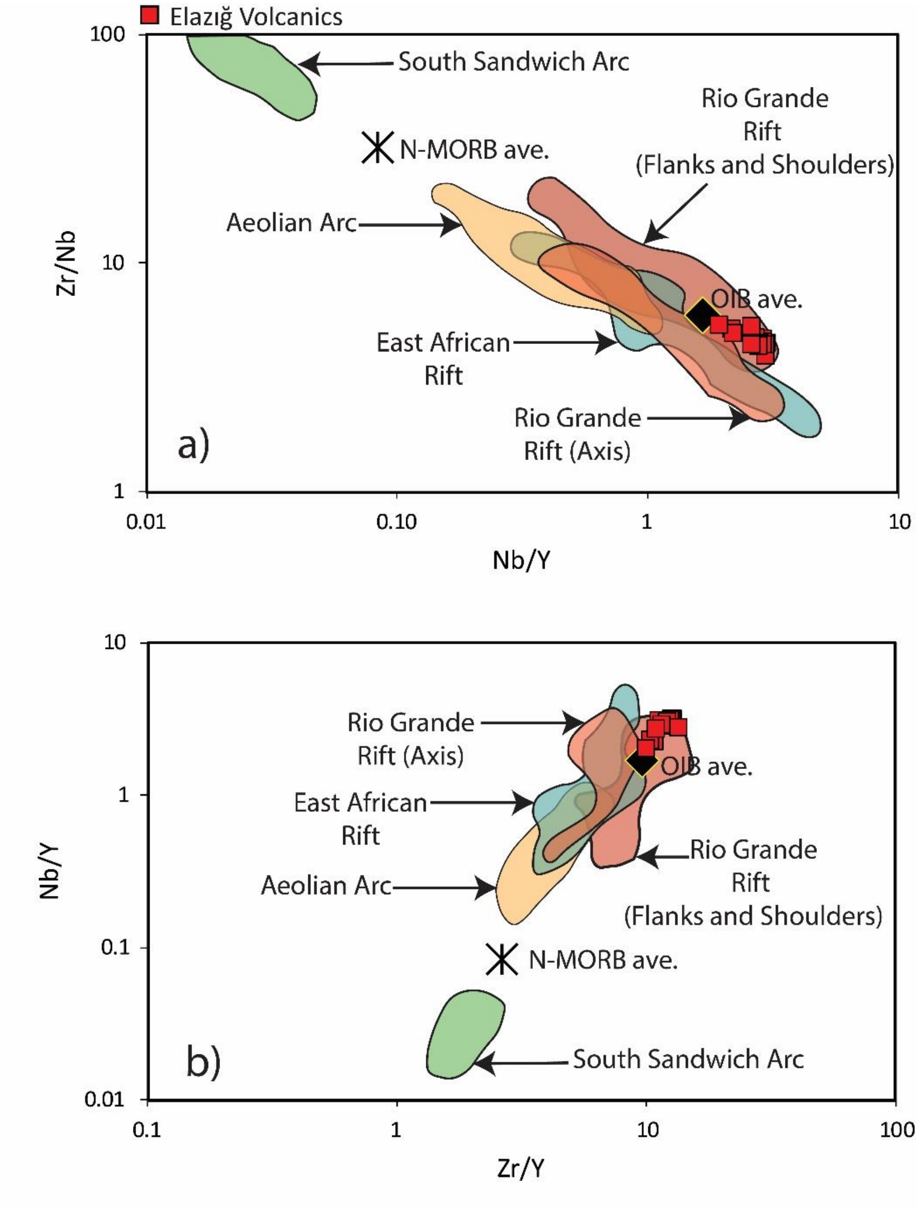

Figure 5.24. The (a) Nb/Y versus Zr/Nb and (b) Zr/Y versus Nb/Y diagrams for the Elazığ Volcanics and lavas from modern tectonic settings. The published data used for comparison includes samples with MgO (wt. %) greater than 6 wt. % to avoid the effects of post-melting processes and to make the data set comparable with the Elazığ lavas. Note that the Elazığ lavas assumed to be affected by a possible crustal assimilation (GMB6, GMB8, GMB9, GMB10) have been excluded from the evaluations. The data sources; Average N-MORBs and OIB from Sun and McDonough (1989), East African Rift from Furman et al. (2006), Rio Grande Rift from Gibson et al. (1993), Aeolian Arc from the Peccerillo et al. (2013), and South Sandwich Arc from Pearce et al. (1995).

Such enrichment levels ($(La/Sm)_N$=3.72-5.10, N denotes to chondrite-normalized based on Sun and McDonough, 1989) observed in the Elazığ volcanism can be rather reconciled with continental arc (e.g., Aeolian Arc or Andes) or intraplate (e.g., St. Helena, Massif Central France, East African Rift lavas, etc.,) lavas. However, both the tectonic configuration of eastern Anatolia during Quaternary and the positive Nb/Nb* values (1.17-1.58) of Elazığ lavas rule out the possibility of the derivation of the parental melts of Elazığ volcanism from a mantle wedge in an active subduction zone. Therefore, the enriched lithospheric and asthenospheric mantle components appear to be the only source components that can be predominantly sampled by the Elazığ volcanism. However, among these, the lithospheric contribution would also enrich the LILE, Th over the HFSE such as Nb in the Elazığ lavas, owing to the metasomatized nature of the SCLM beneath eastern Anatolia (see the discussion for Tunceli Volcanics). As seen in the PM-normalized multi-element diagram of the Elazığ lavas (Figure 4.23), such patterns are not observed. This also speaks against major contributions from a metasomatized SCLM domain. However, minor SCLM contributions in their genesis cannot be totally precluded. In particular, except for the samples believed to have been subjected to crustal assimilation (GMB6, GMB8, GMB9, GMB10), the relatively low Nb/Nb* ratios (< 1.40) observed in some Elazığ samples may imply sampling minor amount of SCLM-related component by the Elazığ volcanism. This idea can be further tested by the plot La/Yb versus Nb/U and Th/Yb versus Nb/U (Figure 5.25). These plots are useful to distinguish the lithospheric (i.e., metasomatized SCLM) contributions, especially those that carry sediment melt-related metasomatic agents, from the asthenospheric contributions in the lavas. Note that the samples assumed to have assimilated the crustal materials (GMB6, GMB8, GMB9, and GMB10) were not plotted on the diagrams to observe solely the source features.

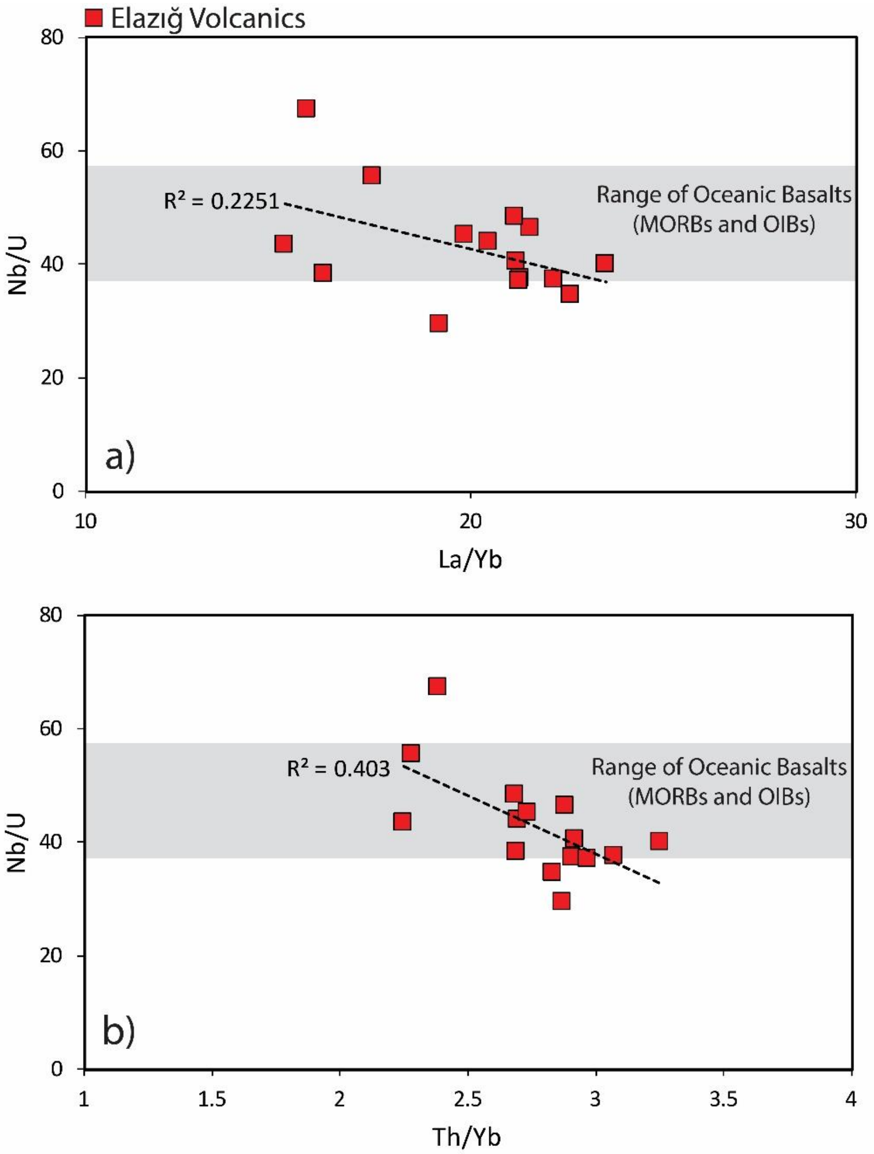

Figure 5.25. The (a) La/Yb versus Nb/U and (b) Th/Yb versus Nb/U diagrams for the Elazığ Volcanics. The Nb/U range for the oceanic basalts (MORBs and OIBs) is from Hofmann et al. (1986). Note that the samples presumed to have been affected by the crustal assimilation process (GMB6, GMB8, GMB9, and GMB10) are excluded from the evaluation to observe only the source features.

As stated previously, contrary to Yb, LREEs and Th are transported to overlying mantle regions (e.g., the base of the SCLM) via slab-derived melts in subduction zones (e.g., Johnson and Plank, 1999; Class et al., 2000). Therefore, those SCLM domains that carry sediment melt-related subduction imprint, as in the case of eastern Anatolian SCLM (see discussion above), would be characterized by high La/Yb and Th/Yb ratios. Accordingly, the same signatures would also be expected in the melts derived from such mantle regions. The Nb/U ratio, on the other hand, is almost constant in the oceanic basalts (MORBs and OIBs Nb/U=47±10, Hofmann et al., 1986), which are regarded to be derived from asthenospheric source regions. In addition, in the case of the sediment melt addition to the SCLM, the Nb/U ratio of the metasomatized domain is expected to decrease since Nb retained in the subducted slab (e.g., Pearce and Peate, 1995; Johnson and Plank, 1999; Class et al., 2000). Therefore, the lavas tapping the sediment melt metasomatized SCLM component are also presumed to be characterized by low Nb/U ratios compared to the MORBs and OIBs. When considering these, negative correlations would be developed between the ratio Nb/U and the ratios La/Yb and Th/Yb of the Elazığ lavas in the case of any contribution from SCLM source regions of eastern Anatolia. In the plots (Figure 5.25), it is clear that the Nb/U ratios of Elazığ lavas are within the range defined by asthenospheric mantle-derived oceanic lavas (OIBs and MORBs; Hofmann et al., 1986), suggesting a dominant contribution from asthenospheric mantle regions beneath eastern Anatolia. However, it must also be noted that a slight decrease in Nb/U with increasing La/Yb and Th/Yb is observed in the Elazığ volcanism. When ruling out the crustal contamination, these elemental behaviors are consistent with the influence of the SCLM contribution in the genesis of Elazığ lavas. It appears, therefore, the enriched trace element characteristics of the Elazığ lavas should have been largely inherited from enriched asthenospheric source contributions. The SCLM contributions, on the other hand, cannot be totally excluded from the genesis of the Elazığ Volcanism. If any enriched component representing the metasomatized SCLM has been involved in the Elazığ volcanism, the trace element systematics of the Elazığ lavas suggest that its contribution is not significant, as in the case of DM.

As mentioned above, the asthenospheric component(s) in the genesis of Elazığ lavas have an enriched nature. Predominant contributions from such enriched asthenospheric component(s) result in OIB-like trace element signatures (Nb/Nb*>1) in the lavas, as it is apparent in the PM-normalized diagrams of Elazığ volcanism (Figure 4.23 and 4.24). This is also evidenced by the data distribution of the Elazığ lavas on the plot of Ta/Nb versus Th/Nb (Figure 5.26). The Elazığ Volcanics display constant Th/Ta ratios and higher Ta/Yb and Th/Yb ratios relative to those of MORBs. With these signatures, they plot very close to the average OIB values and the fields defined by continental rift magmas in the mantle array (Figure 5.26).

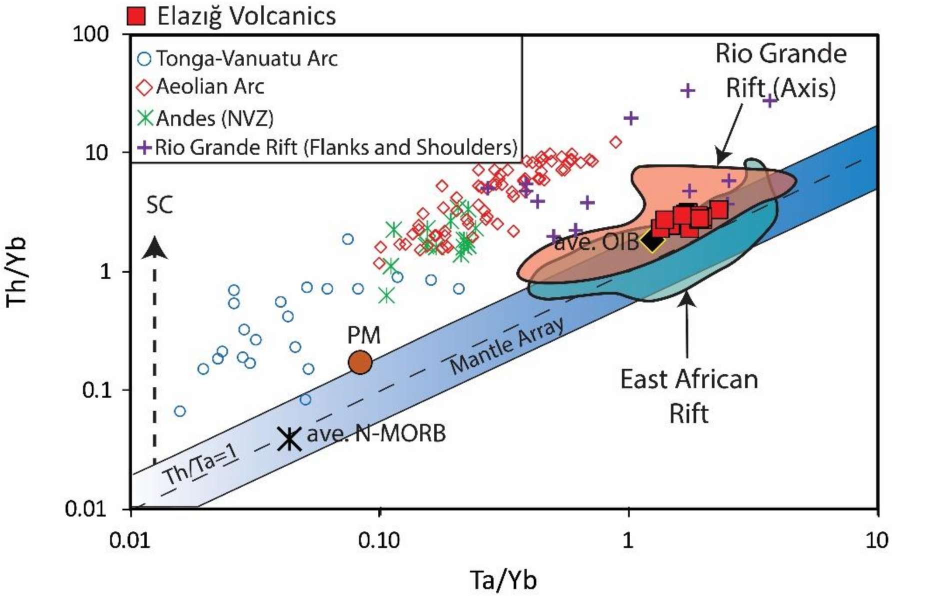

Figure 5.26. The Ta/Yb versus Th/Yb diagram (Pearce, 1983) for the Elazığ Volcanics and from distinct tectonic settings. The Th/Ta array represents the mantle array defined by non-subduction-related oceanic lavas (MORBs and OIBs). The published data used for comparison includes samples with MgO (wt. %) greater than 4 wt. %. The data sources; Average N-MORBs, OIB and PM from Sun and McDonough (1989), Tonga-Vanuatu Arc from Pearce et al. (2007), Aeolian Arc from Peccerillo et al. (2013), Andes (NVZ: Northern Volcanic Zone) from Hidalgo et al. (2012), Rio Grande Rift from Gibson et al. (1993) and East African Rift from Furman et al. (2006). Key to abbreviations: SC: subduction component.

The distribution of the Elazığ lavas on the plot of Ta/Yb versus Th/Yb clearly suggests a dominant contribution from enriched asthenospheric mantle components in their genesis. Such elemental enrichments are not restricted in the intraplate lavas in oceanic settings (e.g., Hawaii, Mangaia, Samoa). In the continental areas, where the lithosphere is thinned due to some tectonic and geodynamic processes (e.g., intraplate deformations of plume impingement etc.,), the melts derive from asthenospheric enriched domains can pass through the lithosphere without lithospheric contamination (e.g., axis of the Rio Grande Rift or East African Rift), thus resulting volcanism with similar trace element signatures to those of OIBs (Gibson et al., 1993; Furman et al., 2006). As can be seen in Figure 5.26, the Elazığ lavas display similar Ta/Yb and Th/Yb ratios with such intraplate lavas (e.g., lavas from the axis of Rio Grande Rift and East African Rift), suggesting similar magmatic histories with these lavas. Likewise, the geochemical similarities between the Elazığ lavas and the OIB-like Cenozoic intraplate volcanism of Europe, the circum-Mediterranean region, including Turkey (Figure 4.24), may imply sampling the similar asthenospheric source components. One other notable feature that can be seen in the diagram is; some Elazığ samples deviate from the mantle array with relatively high Th/Yb ratios. When considering that the crustal contaminated Elazığ samples were removed from the diagram, this deviation may also confirm the minor contributions from the metasomatized SCLM domain(s).

Different enriched components or mantle paradigms have been proposed so far to explain the generation of alkaline OIB-type intraplate lavas. Initially, these types of melts were interpreted as the products of low-degree partial melts of garnet peridotite (e.g., Green, 1973). However, later, it was proposed that the low-degree partial melts of the “dry” peridotites without the addition of H_2O+CO_2 are not capable of generating such magmas (e.g., Eggler and Holloway, 1977; Wyllie, 1977). This proposal later was confirmed by experimental petrology; the low-degree partial melts of 0.1-0.25 wt. % CO_2-added fertile peridotites were suggested as potential parental melts of alkaline OIB-type lavas (e.g., Dasgupta et al., 2007). However, it has been suggested that such a process cannot account for the full range of chemical variants OIB-like magmas, especially trace element systematics, and it has been emphasized that the source area needs additional enrichments for producing OIB-type enriched lavas (e.g., Prytulak and Elliott, 2007). As an alternative hypothesis, Pilet et al. (2011) suggested that the melting of the metasomatic veins in the lithosphere, which were produced by fractional crystallization of low-degree melts from a depleted asthenospheric source (DM) region, can also produce the “typical” geochemical signatures of the OIB-type melts. However, like the other processes above, this process also fails in explaining the total geochemical patterns observed in the OIB-type melts (e.g., the isotopic signatures of HIMU-type OIBs). Therefore, to explain the total range of trace element and isotope data of the OIB-type melts, the recycled oceanic lithospheric materials, such as recycled oceanic crust with or without sediments, recycled oceanic metasomatized mantle lithosphere, or total oceanic lithosphere, has been widely accepted as the primary source components for these lavas (e.g., Hofmann and White, 1982; Zindler and Hart, 1986, Weaver, 1991; Chauvel et al., 1992; Halliday et al., 1992; Niu and O’Hara, 2003; Workman et al., 2004; Pilet et al., 2008, see CHAPTER 1 for the details). When considering these, the OIB-like trace element characteristics of the Elazığ lavas suggest a predominant contribution from an asthenospheric component, most probably representing recycled oceanic lithologies.

To sum up the trace elements constraints on the mantle source characteristics of the Elazığ volcanism, it can be said that an enriched asthenospheric mantle component believed to be widely sampled by OIB was predominantly involved in their genesis. Therefore, the Elazığ Volcanics share obvious geochemical similarities with the OIB-type melts worldwide. In addition, although it is not strongly evidenced, a small amount of SCLM contribution to these volcanics is required to explain some of their trace element patterns. The DM component, on the other hand, appears to be negligible in their genesis based solely on the trace element constraints. More detailed information regarding the DM contributions to this volcanism can be achieved by their isotope systematics.

In order to provide a detailed characterization of the mantle component types in the genesis of Elazığ volcanism and to elucidate the extent of the contributions from each component, the entire range of Sr-Nd-Hf-Pb isotope data of Elazığ lavas has been evaluated in detail via multi-component mixing modelings in the following section. This will not only help to understand the possible role of DM and SCLM components in the genesis of Elazığ lavas (if any), it will also help to reveal the composition of the enriched asthenospheric mantle component (e.g., C/FOZO, HIMU, EMI-EMII) assumed to have predominantly contributed to the Elazığ volcanism.

5.1.3.2.2 Constraints from Sr-Nd-Hf-Pb Isotope Systematics

In agreement with their trace element systematics, the similar range of Sr-Nd-Hf isotope compositions of Elazığ volcanism to those of C/FOZO or LVC/EAR components (Figure 4.27), which are proposed to be the common components of hotspot magmas worldwide (e.g., Hart et al., 1992; Hanan and Graham, 1996; Hoernle et al., 1995), indicate that enriched asthenospheric melts played an essential role in their genesis. However, the lower $^{206}Pb/^{204}Pb$ and higher $^{207}Pb/^{204}Pb$ ratios of the Elazığ lavas relative to the values of the component C and LVC (Figure 4.30) are also consistent with the contributions from an EM-type end-member. This may indicate that the source origin of the Elazığ volcanism cannot be solely within the asthenospheric mantle beneath eastern Anatolia.

As discussed in the former sections, the EM-type isotope characteristics can be acquired either by melting of an ancient plume-related component (e.g., Workman et al. 2004; Jackson et al. 2007) or melt contributions from SCLM domains assumed to have been metasomatized by sediment-melts characterized by time-integrated U/Pb enrichments (e.g., Gall et al., 2021; Furman et al., 2021). It is apparent in the diagram of $^{206}Pb/^{204}Pb$ versus $^{207}Pb/^{204}Pb$ (Figure 4.30a), within the field of GLOSS, the Elazığ lavas plot above the Samoan lavas with relatively more radiogenic $^{207}Pb/^{204}Pb$ ratios for a given $^{206}Pb/^{204}Pb$ composition. As in the case of Tunceli volcanism, this also suggests that the EM-type characteristics of the Elazığ volcanism in the Pb-Pb isotope space most probably reflect the contributions from the metasomatized SCLM domain(s) beneath eastern Anatolia. This idea can be further tested by plotting the Elazığ samples together with the young eastern Mediterranean sediments (Klaver et al., 2015) and SCLM-derived melts such as western Anatolian SCLM-derived melts on the plot of $^{206}Pb/^{204}Pb$ vs. $^{207}Pb/^{204}Pb$ (Figure 5.27).

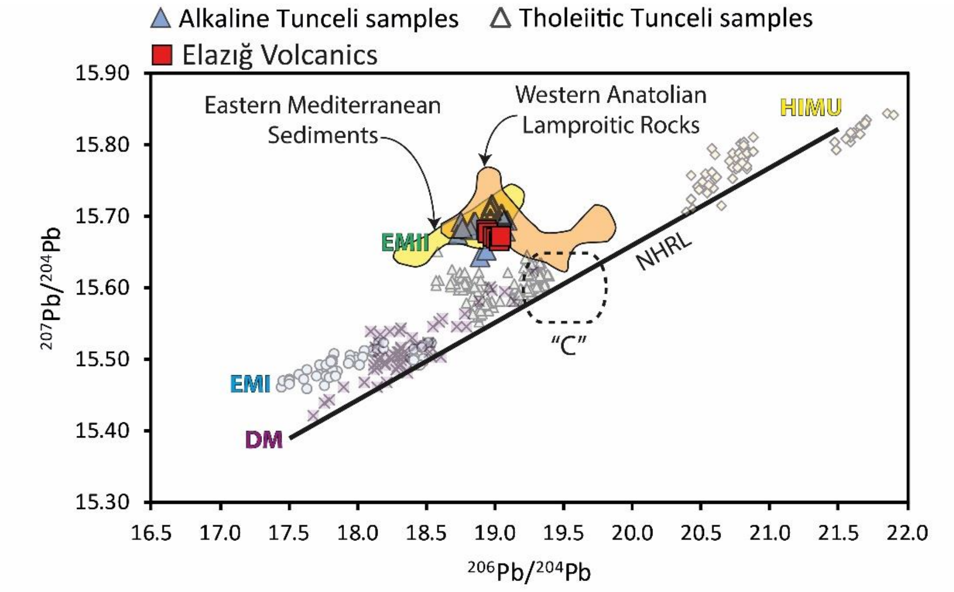

Figure 5.27. The $^{206}Pb/^{204}Pb$ versus $^{207}Pb/^{204}Pb$ plot showing the distribution of the Elazığ Volcanics together with the Tunceli Volcanics, western Anatolian lamproitic rocks (Elitok et al., 2010; Prelević et al., 2012), eastern Mediterranean sediments (Klaver et al., 2015) and global MORBs and OIBs representing distinct extreme isotopic compositions in the mantle (HIMU, EMI, EMII, and DM). NHRL is from Hart (1984). The sources of compositions of the components LVC and C are given in the caption of Figure 4.25. Likewise, the locations of oceanic basalts and their data sources are also given in the caption of Figure 4.25.

As previously mentioned, while the eastern Mediterranean sediments represent the ideal material to be injected in the SCLM of eastern Anatolia, the western Anatolian high-Mg potassic melts can be regarded as the most proper candidates for the SCLM-derived melts of Anatolia carrying sediment-related metasomatic inputs. The distribution of the Elazığ data points on the fields defined by the young eastern Mediterranean sediments (Klaver et al., 2015) and SCLM-derived melts of western Anatolia (e.g., Elitok et al., 2010; Prelević et al., 2012) above the Samoan lavas, therefore, provide compelling evidence that the EM-type signature in the Elazığ lavas is rather related with involvement of SCLM component in their genesis. This finding appears to be also consistent with the interpretations based on their trace element systematics. When considering these all, it can be said that, although the Sr-Nd-Hf isotope systematics of Elazığ samples suggest predominantly involvement of an enriched asthenospheric mantle component (e.g., C/FOZO or LVC/EAR) in their genesis, their Pb isotope systematics rule out a single source origin for these lavas. Several lines of evidence from trace element and Sr-Nd-Hf-Pb isotope systematics suggest contribution from at least two distinct components: one is an enriched asthenospheric mantle component represented probably by recycled oceanic lithospheric lithologies (e.g., FOZO/C or LVC/EAR), and the other is an EM-type component representing the metasomatized SCLM domains beneath eastern Anatolia.

As can be seen in the PM- and chondrite- normalized trace element diagrams (Figure 4.24) and Sr-Nd and Nd-Hf isotope spaces (Figures 4.27 and 4.28), the Elazığ lavas share geochemical similarities with the OIB-like circum-Mediterranean, including central European, and Anatolian volcanics, which have been attributed to derivation from an enriched asthenospheric source region including recycled components with the characteristics of C/FOZO/PREMA or LVC/EAR (e.g., Hoernle et al., 1995; Aldanmaz et al., 2015; Keskin et al., 2012b). These patterns also support the idea that a FOZO/C- or LVC/EAR-like common mantle component was involved in the genesis of Elazığ lavas. However, it must be noted that, although the FOZO/C is are nearly identical to the LVC/EAR, especially in terms of their Sr-Nd isotope systematics, they differ from each other in terms of the Pb isotope systematics. The LVC/EAR component assumed to be the enriched “common” asthenospheric mantle component for most European and circum-Mediterranean intraplate volcanics display more enriched Pb compositions compared to the C or FOZO. Therefore, apart from the contributions from the EM-type SCLM component, the type of the enriched asthenospheric mantle component involved in their genesis is needed also to be characterized. On the other hand, as discussed in the case of Tunceli volcanism, almost all C-related OIB-type volcanics of Anatolia are thought to have also been sampled some DM component during their generation (e.g., Aldanmaz et al., 2015; Gall et al., 2021; Furman et al., 2021). A similar multi-component mixing model has also been proposed for the Tunceli lavas in this study, as can be seen in the former section. Recently, although the lithospheric contribution appears to be greater in their genesis, also the Quaternary Central Anatolian lavas have been linked to derivation from an asthenospheric source region characterized by mixing of a C-like component and a DM component (Gall et al., 2021; Furman et al., 2021). Therefore, although the Elazığ lavas appear to be dominated by contributions from an enriched asthenospheric mantle component, the general isotopic characteristics of the C-related Anatolian lavas necessitate also an investigation regarding the possible involvement of the DM component in the genesis of Elazığ lavas.

In this regard, apart from the lithospheric component (SCLM), to reveal which type of asthenospheric mantle components (e.g., DM, C or LVC) is involved in the genesis of Elazığ lavas, they are plotted together with the Anatolian C-related lavas, eastern Mediterranean sediment, and western Anatolian SCLM-derived melts on the Sr-Pb, Nd-Pb and Hf-Pb isotope spaces including multi-component mixing models (Figure 5.28). Note that the Elazığ lavas have very uniform Sr-Nd-Hf-Pb isotope compositions; thus, they usually define a tight cluster in the isotope spaces rather than a trend. This, accordingly, complicates the specifying the exact members of a multi-component blend in their genesis, even if when the end-members are fixed in the isotope spaces. Hence, the correlation of the Elazığ lavas with the trend defined by those Anatolian lavas assumed to have been generated by multi-component mixing of C-like, DM, and SCLM components will provide significant information regarding the DM involvement. The details of the calculations can be found in the text above regarding the source characteristics of Tunceli volcanism and in the caption of Figure 5.21 and Table 5.3.

Since the Sr-Nd-Hf isotope compositions of the Elazığ lavas suggest the involvement of enriched asthenospheric source components with the characteristics of C-like or LVC/EAR component, in Figure 5.28, the solid-state mixing curves have been modeled between the end members DM and C and DM and HIMU end-members. These mixture scenarios will not only reveal the involvement of DM component in their genesis (if any) but also will provide information for specifying the type of the "common" component (i.e., C-like versus LVC-like) thought to be predominantly sampled by Elazığ volcanism. It must be noted again the LVC or EAR are characterized by radiogenic Pb compositions (^{206}Pb/^{204}Pb= ~20; e.g., Hoernle et al., 1995); therefore, any trend of the Elazığ lavas suggesting the involvement of the HIMU component in Figure 5.28, can also be reconciled with the involvement of LVC/EAR.

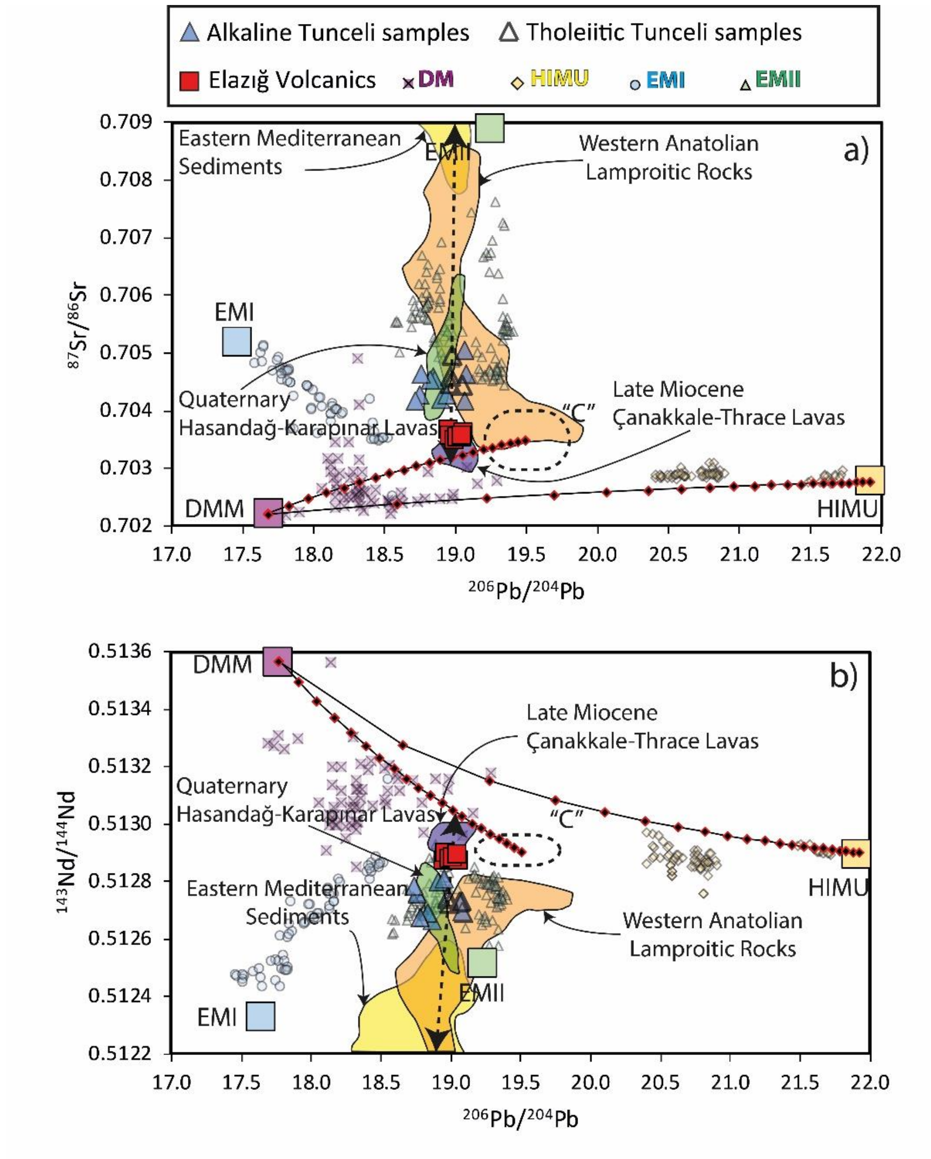

Figure 5.28. The (a) $^{206}Pb/^{204}Pb$ versus $^{87}Sr/^{86}Sr$, (b) $^{206}Pb/^{204}Pb$ versus $^{143}Nd/^{144}Nd$, and (c) $^{206}Pb/^{204}Pb$ versus $^{176}Hf/^{177}Hf$ plots for Elazığ Volcanics and Tunceli Volcanics showing also the calculated mixing curves between mantle end-members. The trace element and isotope compositions of the end-members used in the modelings can be found in the caption of Figure 5.21. The tick marks on each curve correspond to 5% mixing intervals. The sources of the lavas plotted into the diagram for comparison can be found both in the captions of Figure 4.25 and 5.21.

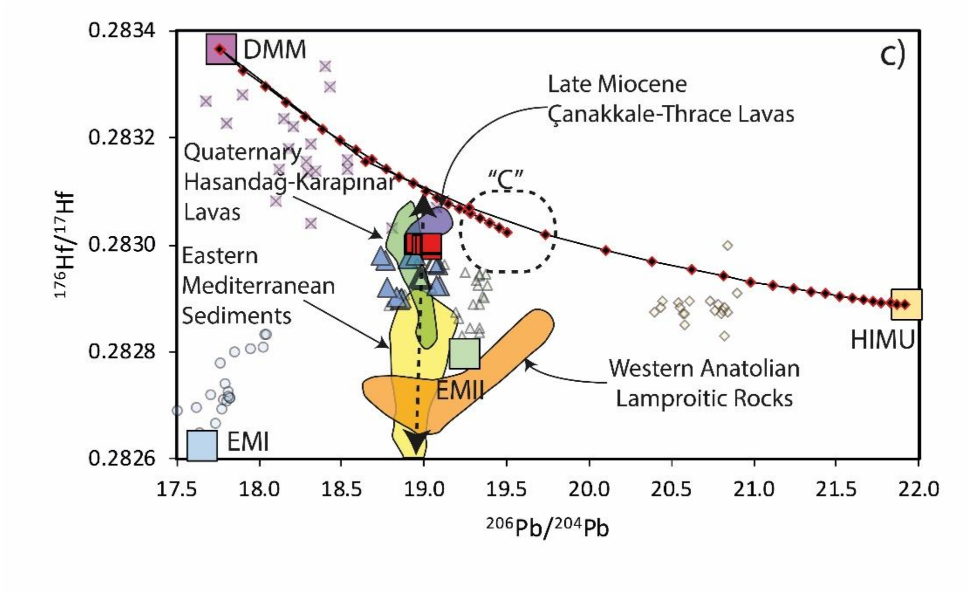

Figure 5.28. *(Cont'd)*

In the Sr-Nd, Nd-Pb, and Hf-Pb isotope spaces, shown by Figure 5.28, the Elazığ Volcanics plot consistently on the trend of Anatolian C-related lavas emerging from the calculated solid-state mixing curve between C and DM towards the fields of eastern Mediterranean sediments and western Anatolian SCLM-derived melts. Although the Elazığ lavas, on the plots (Figure 5.28), do not define an obvious trend due to their uniform isotope compositions, the coherency between their data cluster and the trend of the Anatolian C-related suggest that the total range of the Sr-Nd-Hf-Pb isotope of the Elazığ Volcanism cannot be explained solely by the binary melt mixing between an enriched asthenospheric and an SCLM component. It seems that, in addition to these distinct components, some contribution from the depleted component (i.e., DM) is also required to explain the total isotopic variations in Elazığ lavas. The need for the DM contributions arises from the emergence of the Anatolian C-related lavas from the C-DM mixture curve instead of from the pristine C component in the plots (Figure 5.28). Although their trace element systematics do not imply notable contributions from a DM component, the lower $^{206}Pb/^{204}Pb$ ratios of the Elazığ samples relative to C appear to be not only related to contributions from an SCLM component with low $^{206}Pb/^{204}Pb$ and high $^{207}Pb/^{204}Pb$ compositions. With the DM involvement, the same multi-component blend including C-like, DM, and EM-type SCLM components involved in the genesis of Tunceli lavas appear to have also been played a significant role in the genesis of the Elazığ lavas. This geochemical picture maintains the idea that asthenospheric mantle beneath eastern Anatolia is heterogeneous, and this heterogeneity has been acquired primarily by solid-state mixing of recycled oceanic lithologies with the depleted asthenospheric mantle matrix.

According to data distribution of the Elazığ lavas in Figure 5.28, the recycled oceanic material in the asthenosphere of eastern Anatolia does not seem to have very radiogenic Pb-isotope compositions, which can be reconciled with the components LVC/EAR or HIMU. In the case of LVC or EAR involvement in the genesis of Elazığ lavas, a significant amount of DM contributions would be required to balance a possible EAR/LVC-DM mixture based on the mixture curves. However, such a scenario would contradict the enriched trace element patterns of Elazığ lavas (Figure 4.23). Thus, it can be proposed that despite their identical trace element and Sr-Nd-Hf isotope compositions to most of EAR/LVC-related intraplate lavas, the total range of Sr-Nd-Hf-Pb isotope data of Elazığ lavas is consistent with the involvement of an enriched asthenospheric component with the characteristics of C rather than LVC or EAR. Note that the same geochemical signatures are also observed in the Tunceli (Figures 5.21 and 5.28) and the western and central Anatolian Cenozoic OIB-like lavas. This may suggest that a "common" asthenospheric component is dispersed beneath the whole Anatolia as other areas in the circum-Mediterranean region; however, its geochemistry differs from the EAR or LVC components in terms of Pb isotope compositions.

The Elazığ lavas display very similar isotope compositions with the Late Miocene Çanakkale-Thrace lavas, and plot very close on the C-DM mixture curve. This pattern is suggestive for dominant contributions from melts derived from asthenospheric mantle regions, as in the case of Çanakkale-Thrace lavas. This can also explain the OIB-like trace element systematics of Elazığ lavas (Figure 4.23). Considering the coherency of the Elazığ data with the trend of C-related Anatolian lavas, including Tunceli, the C-like component appears to be also dominant in the genesis of the Elazığ lavas (>60%). All C-related Anatolian lavas appear to define a single array intersecting similar intervals in the calculated C-DM mixture curve (Figure 5.28). Thus, an asthenospheric source region similar to the Tunceli lavas and the other C-related Anatolian lavas (i.e., mixture of ca. %80 C and %20 DM) can also be proposed for the Elazığ volcanism (see Figures 5.22 and 5.28). Interestingly, the whole C-related Anatolian lavas plot on the same array between the C-DM mixture and SCLM component. This may imply that, although the SCLM contributions vary among the C-related lavas of Anatolia, the nearly identical asthenospheric components appear to have been involved in their genesis. This may be related to the preferentially melting of fusible recycled materials (i.e., C-like) relative to the DM matrix, or this may suggest a common asthenospheric component for all Anatolian intraplate lavas.

To test whether a mixture between ca. 80% C-like and 20% DM components can characterize the asthenospheric source region of Elazığ volcanism, melt mixing models have also been applied between the solid-state mixture of 80%C-20%DM source and a SCLM component in the Sr-Nd-Hf-Pb isotope spaces (Figure 5.29). Selecting the potential end-members in this possible multi-component mixing scenario will also help develop a more robust approach to detect the amount of SCLM contributions in the genesis of Elazığ volcanism. The details and parameters regarding the applied modelings can be found in the text regarding the mantle characteristics of Tunceli volcanism, the caption of Figure 5.22, and Table 5.4.

As seen in Figure 5.29, in all models, the Elazığ Volcanics define a coherent trend with the calculated curves between the asthenospheric melt assumed to have been derived a source domain characterized by %80 C and %20 DM component and slab-modified SCLM melts.

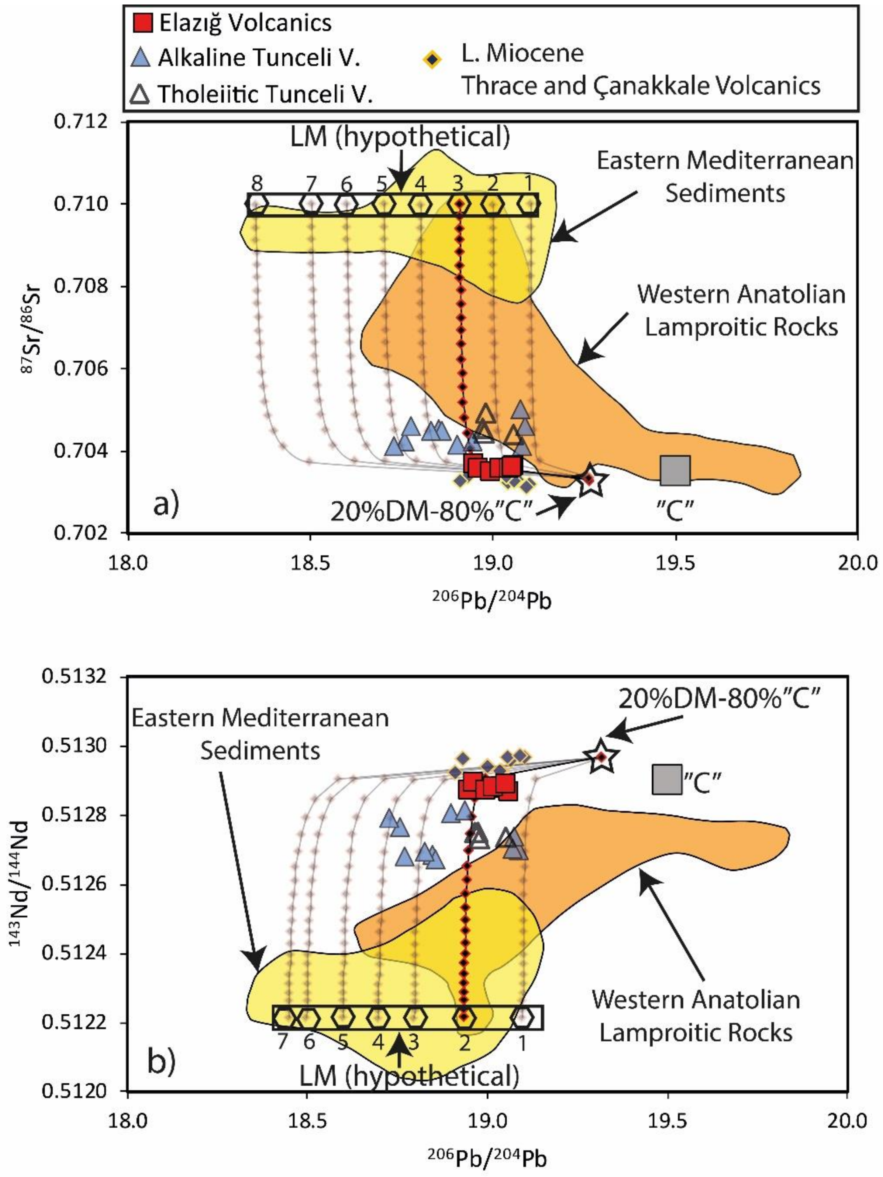

Figure 5.29. The (a) the $^{206}Pb/^{204}Pb$ versus $^{87}Sr/^{86}Sr$, (b) $^{206}Pb/^{204}Pb$ versus $^{143}Nd/^{144}Nd$ and (c) the $^{207}Pb/^{204}Pb$ versus εHf plots for Elazığ Volcanics and Tunceli Volcanics showing also the calculated mixing curves between mantle C-DM (80% C-20%DM) mixture and SCLM (LM: Lithospheric Mantle) end-members. The data sources and all parameters used in the modelings can be found in the caption of Figure 5.22 and Table 5.4.

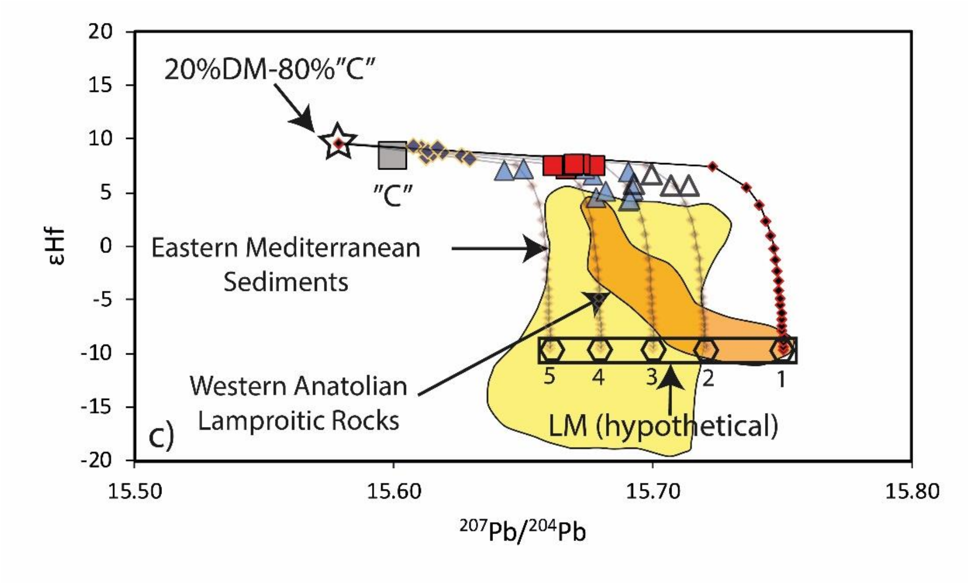

Figure 5.29. *(Cont'd)*

As in Figure 5.28, the trends defined by the Late Miocene Çanakkale-Thrace and Elazığ lavas are consistent with the trends of the calculated mixing curves emerged from a component depleted relative to pristine C. Melt mixing curves between a pristine C and lithospheric melts are not favored by the trends of Çanakkale-Thrace and Elazığ lavas, and at least %20 DM contribution is needed to explain their total isotope variations. This confirms that an asthenospheric source region characterized by %80 C and 20% DM components contributed to the Elazığ Volcanics. As mentioned above, such characteristic appears to be the typical feature of the asthenospheric mantle of eastern Anatolia, and may be suggested as a common asthenospheric mantle reservoir for the Anatolian lavas. As expected, the mixing curves in Figure 5.29 reveal that the lithospheric component was involved in the genesis of Elazığ lavas but appears to be much lower in amount when compared with the Tunceli volcanism. The data distribution on the mixing curves favors less than %10 SCLM derived melt involvement in the genesis of Elazığ lavas. In fact, the mixing curves in the Hf-Pb isotope space suggest (Figure 5.29c) indicate a lithospheric contribution of less than 5%. A low amount of lithospheric contribution is also consistent with the OIB-like trace element patterns of Elazığ lavas. Higher lithospheric melt contributions would create a high LILE/HFSE ratio and negative Nb/Nb* values in the volcanics, as in the case of Tunceli volcanism. Such patterns are not observed in the Elazığ Volcanics.

Nevertheless, the amount of the lithospheric contribution in the genesis of Elazığ lavas can also be tested via trace element-based melt mixing models, as have been done for Tunceli lavas. In order to check whether the melt mixing between the C-DM (80% C+20%DM) and metasomatized SCLM sources can create the trace element patterns of Elazığ lavas or not, a melt-mixing model was applied by using the trace element systematics (Figure 5.30). In the modeling, the C-DM source region presumed for the Elazığ lavas (80% C+20%DM) was melted 0.5 % degree of non-modal batch melting at the garnet-stability field, and subsequently mixed with slab-modified SCLM melts. In this modeling (Figure 5.30), the melting degree is lowered compared to the Tunceli lavas to create similar enrichment levels with those of Elazığ Volcanics. The assumptions and parameters used in the calculations can be found in the discussion above regarding the source characteristics of Tunceli lavas.

In Figure 5.30, it is fairly evident that when 95% of melts derived from the hypothetical C-DM source mixed with the 5% of lithospheric melts, very akin trace element patterns to the Elazığ lavas can be generated. As shown in Figure 5.30, the calculated final melt (shown by red line) has a positive Nb anomaly, which can be attributed to the OIB-like melts in the PM-normalized multi-element diagram. This not only support the findings obtained from the modelings shown by Figure 5.29, but also show that approximately 5% lithospheric contributions to the low-degree melts of the enriched asthenospheric source are not capable of developing negative Nb/Nb* values in the final melt.

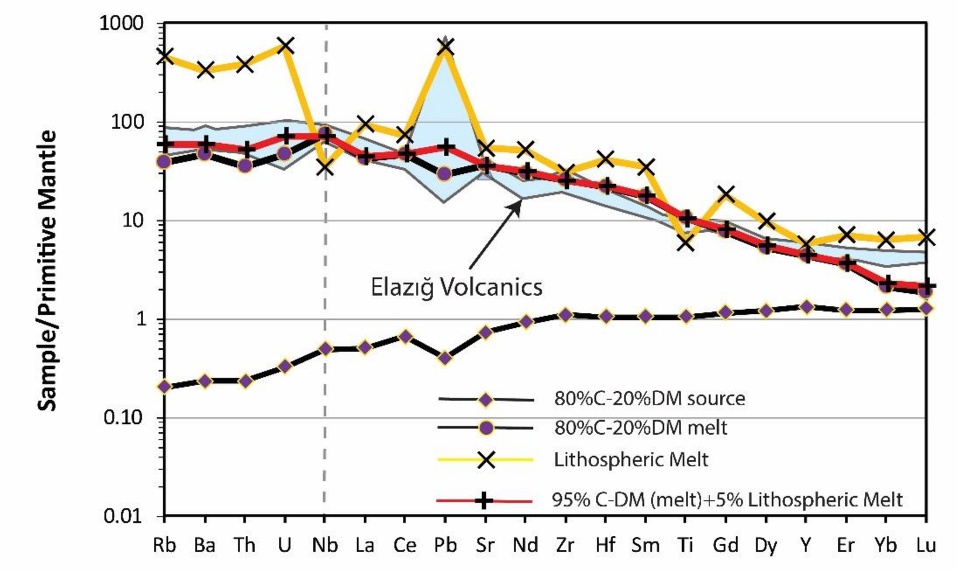

Figure 5.30. Primitive Mantle-normalized (Sun and McDonough, 1989) multi-element diagram showing the melt mixing effect between an asthenospheric source, which is characterized by solid-state mixing of 80% C-like component and DM component, and a metasomatized SCLM domain.

In summary, the isotopic constraints on the nature of the mantle source region of the Elazığ lavas indicated that this volcanism incorporated the same multi-component blend involved in the genesis of the Tunceli volcanism. Accordingly, at least three source components involved in their genesis; a depleted asthenospheric component, a C-like recycled component, and a SCLM component. In this blend, however, the amount of the lithospheric contributions appears to be lower when compared with the Tunceli case. The calculations suggest that the lithospheric contributions should be around 5% or lower than 5%. With predominantly involvement of C-like and DM components, these volcanics represent mainly (ca. 95%) asthenospheric melts. Since the C-like component dominates the eastern Anatolian asthenospheric mantle with a proportion of 80%, the C-like component appears to have played a significant role in the genesis of Elazığ lavas. This account for the OIB-like geochemical signatures observed in the Elazığ Volcanics.

Table 5.3. End-member compositions used in the source mixing models (Figures 5.21 and 5.28). For data sources see related figure captions. Elements in ppm.

	C (Common Comp.)	**DM (Depleted Mantle)**	**HIMU (High μ)**
^{87}Sr/^{86}Sr	0.7035	0.702225	0.702791
^{143}Nd/^{144}Nd	0.5129	0.513564	0.512899
^{176}Hf/^{177}Hf	0.283025	0.283363	0.2828865
^{206}Pb/^{204}Pb	19.50	17.681 (Fig. 5.21a-5.28a)	21.916
		17.762 (Fig. 5.21b-c-5.28b-c)	
Sr	16.874	7.664	67.014
Nd	1.3839	0.581	8.7196
Hf	0.358	0.157	2.32
Pb	0.299	0.018	0.0929

Table 5.4. End-member compositions used in the melt-mixing models (Figures 5.22 and 5.29). For data sources see related figure captions. Elements in ppm.

	Fig.	**80% C-20% DM**	**LM1**	**LM2**	**LM3**	**LM4**	**LM5**	**LM6**	**LM7**	**LM8**
^{87}Sr/^{86}Sr		0.70337	0.71001							
^{143}Nd/^{144}Nd		0.51296	0.512215							
εHf		9.667	-9.512							
^{206}Pb/^{204}Pb	5.22a 5.29a	19.262	19.10	19.00	18.90	18.80	18.70	18.60	18.50	18.35
	5.22b 5.29b	19.32	19.10	18.94	18.80	18.70	18.60	18.50	18.45	-
^{207}Pb/^{204}Pb	5.22c 5.29c	15.57	15.75	15.72	15.70	15.68	15.66	-	-	-
Sr		846	1000							
Nd		44.29	74							
Hf		6.95	16.65							
Pb		2.41	241							

5.1.4 Melting Systematics

Both trace element and isotope systematics show that at least three distinct components involved in the genesis of Tunceli and Elazığ Volcanics. However, it is also crucial to decipher the depth of the residence of these components beneath eastern Anatolia during their partial melting. This will not only help to constrain the magma generation process of the volcanics, but also will help to better understand the geodynamic evolution of eastern Anatolia. In this regard, the REE ratios have been used to elucidate the depth and extent of their partial melting process. REE ratios are useful to trace the extent and the depth of melting since each REE has specific solid-state partitioning for spinel and garnet (e.g., Shaw et al., 2003; McKenzie and O'Nions, 1991). Since the heavy REEs are known to be highly compatible with garnet contrary to the spinel, significant fractions between light-REEs (LREE) and heavy-REEs (HREE) or medium-REEs (MREE) and HREEs are expected in the case of partial melting of garnet-bearing mantle regions (Shaw et al., 2003). This, therefore, lead the LREE/HREE and MREE/HREE ratios useful to monitor both the extent of the melt fraction (i.e., partial melting degree) and also the presence of garnet phase in the source regions (Shaw et al., 2003).

5.1.4.1 Tunceli Volcanics

Based on the information above, the Tunceli Volcanics are plotted on the diagram of $(La/Yb)_N$ versus $(Tb/Yb)_N$ (Figure 5.31, N denotes normalization to PM, normalizing values from Sun and McDonough, 1989). In the diagram, while the Tb/Yb ratio can be used as a proxy of the presence of garnet in the source, the La/Yb ratio is useful to track the amount of melt fraction. Wang et al. (2002) have stated that the value of $(Tb/Yb)_N$ above 1.8 is strongly consistent with the melting in the garnet-stability field. The values of $(Tb/Yb)_N$ below 1.8, on the other hand, are consistent with melting within the spinel stability field (Wang et al., 2002). The $(Tb/Yb)_N$ values of the primitive (MgO> 6 wt. %) Tunceli lavas range from 1.58 to 2.63, suggesting that melts both from spinel- and garnet stability fields are needed to explain the geochemistry of these lavas (Figure 5.31). A remarkable distinction in the $(Tb/Yb)_N$ values can be observed between the alkaline and tholeiitic members of the Tunceli lavas. While the tholeiitic samples have $(Tb/Yb)_N$ values lower than 1.8, the majority of the alkaline samples (except the samples AV59-AV70) have $(Tb/Yb)_N$ values higher than 1.8. This is well observed in Figure 5.31. Such patterns in the diagram suggest that while the tholeiitic samples have been dominated by the melts derived from a source region where spinel is stable, the alkaline members predominantly contributed from melts derived within the garnet stability field. The melting degree, on the other hand, appears to be lower in the alkaline samples since they display much higher $(La/Yb)_N$ values than tholeiitic samples.

In order to test these implications with a more robust approach, a melting REE-based melting modeling (Figure 5.32) has been applied by using non-modal batch melting formulization of Shaw (1970), which can be expressed as;

$$C_L^m = \frac{C_0^m}{D_0 + F(1 - P_0)} \qquad \text{(Eqn. 5)}$$

where

C_L^m= trace element composition of the melts produced after non-modal batch melting

C_0^m= trace element composition of the source rock

D_0= bulk partition coefficient of the trace element of minerals in the source

P_0= bulk partition coefficient of the trace element of minerals in the melt

F = fractionation ratio, i.e., the fraction of the melt remaining

The modeling was applied in the Sm/Yb and Dy/Yb ratio-ratio space. Note that since the absolute element concentrations can be modified by the FC process, using ratios in the modeling is relatively advantageous. In the modeling, Sm/Yb ratio is placed onto X-axis to monitor the amount of melt fraction. Dy/Yb ratio, on the other hand, is placed onto Y-axis to trace the depth of the melting region (i.e., garnet or spinel stability fields). The modes of the source and melt together with the partition coefficients used in the modeling are given in Table 5.5. The references for the parameters are given in the caption of Figure 5.32.

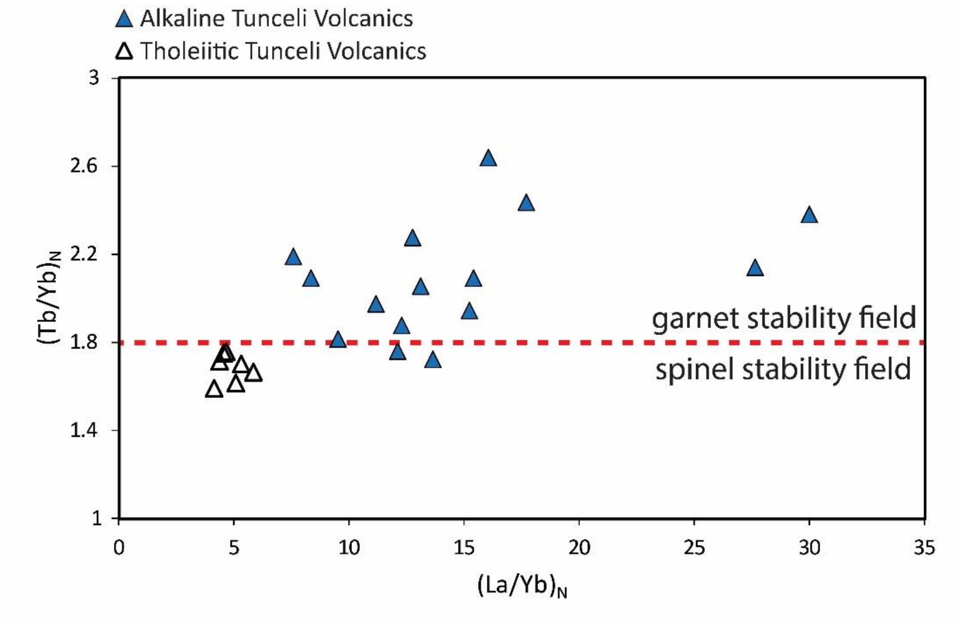

Figure 5.31. The $(La/Yb)_N$ versus $(Tb/Yb)_N$ diagram for the Tunceli Volcanics (modified from Kürkçüoğlu and Yürür, 2021). N denotes normalization to PM (Sun and McDonough, 1989). The garnet- and spinel-lherzolite division value of $(Tb/Yb)_N$ is from Wang et al. (2002).

In Figure 5.32, the Tunceli Volcanics are distributed on an area between the calculated melting curves of garnet- and spinel-peridotite. This data distribution, in accordance with the interpretations above, suggests that melting neither in garnet stability field nor in spinel stability field alone cannot generate the geochemical composition of Tunceli volcanism. Instead, the data points mainly plot on the low degree (0.5-7%) melt mixing curves between garnet and spinel peridotites, implying that melt generation at low degrees in both source regions. Moreover, it is apparent that the alkaline samples plot on the garnet-dominant part of the mixing curves

(>60%), which suggests derivation predominantly from the garnet-stability field for these lavas. The tholeiitic samples, on the other hand, plot on the intervals corresponding approximately to 50-50% melt mixing from garnet and spinel peridotites. Note that, in agreement with the interpretations above, the tholeiitic samples record greater partial melting degrees than the alkaline samples.

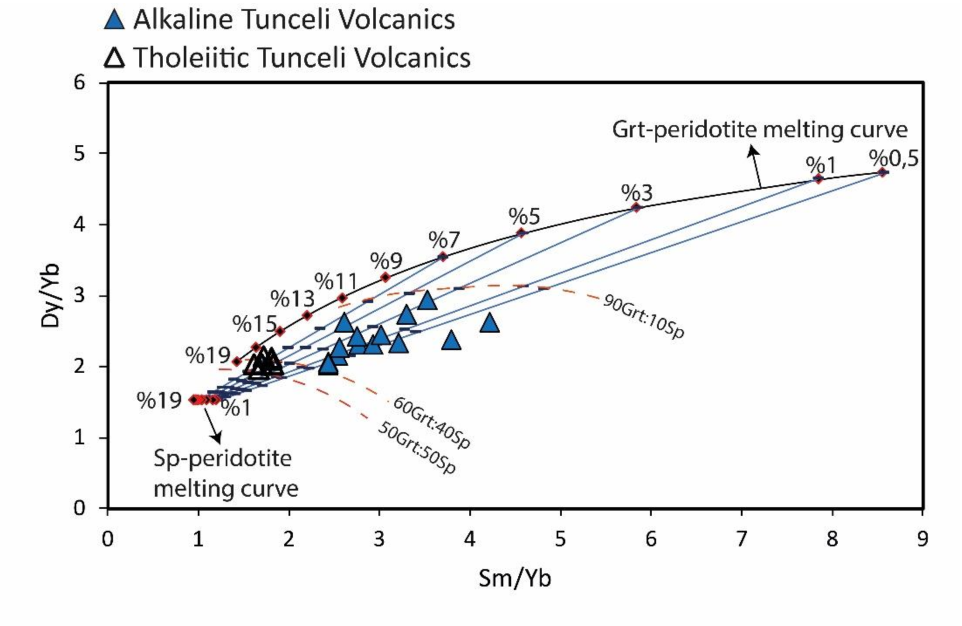

Figure 5.32. The Sm/Yb versus Dy/Yb melt model for the Tunceli Volcanics. For both curves, the source is assumed to have the primitive mantle composition (Sun and McDonough 1989). The source mode, melt mode, and partition coefficients are given in Table 5.5. Source modes and partition coefficients were compiled from McKenzie and O'Nions (1991). The melt modes were taken from Thirlwall et al. (1994). The tick marks on each mixing curve correspond to 10% mixing intervals. Gt: Garnet; Sp: Spinel.

When considering the stability fields of spinel- and garnet-peridotites in the mantle (garnet is stable at ~80 km; e.g., Takahashi and Kushiro, 1983), these results indicate that the Tunceli lavas may be the products of mixing of low-degree melts generated at different depths. In this case, the melts derived from garnet-stability field at greater depths may have been mixed with the melts derived from spinel-dominant source at shallower depths. Alternatively, they may represent partial melts of mantle regions where both the spinel and garnet are stable, such as spinel-garnet transition zone. Based on this scenario, the melting should have occurred at depths of around 80 km beneath eastern Anatolia.

5.1.4.2 Elazığ Volcanics

When the Elazığ Volcanics plotted on the diagram of $(La/Yb)_N$ versus $(Tb/Yb)_N$ (Figure 5.33), it is well observed that the data points of the Elazığ lavas distributed along the garnet-spinel transition line ($(Tb/Yb)_N$=1.8). This indicates that the Elazig volcanism, such as the Tunceli lavas, may be products from mantle domains in spinel and garnet stability areas. The $(La/Yb)_N$ variation (10.89-16-85) that the samples display, on the other hand, may show the difference in the melting degree among the samples. However, the lower array in $(La/Yb)_N$ values suggests that there is no remarkable difference in the melting degrees of the samples when compared with the Tunceli case. Note that the samples that are thought to have been subjected to crustal contamination (GMB6, GMB8, GMB9, GMB10) are excluded from the discussion.

In order to better constrain the melting systematics of the Elazığ lavas, the modeling using the Sm/Yb and Dy/Yb ratios was also applied for the Elazığ Volcanics (Figure 5.34). In the modeling, the Elazığ lavas plot between melting curves garnet and spinel peridotites. This suggests that, as in Tunceli volcanism, melting derived solely from the spinel or garnet stability fields alone cannot account for the geochemical composition of these lavas. At least melts from two mantle regions are needed to explain their total geochemistry. This is well illustrated with the calculated melt mixing curve between the garnet and spinel peridotite (Figure 5.34). The most coherent mixing curve with the trend of the Elazığ lavas corresponds to the mixing of low-degree (1%) spinel- and garnet-peridotite melts. This mixing curve also shows that with a proportion between 60-80%, the garnet-derived melts appear to have made a greater contribution to these volcanics. According to the melt mixing curve, there seems to be not a significant difference in the melting degrees of samples in agreement with the interpretation above. The total lava suite records very-low degree of partial melting, according to the modeling. This is consistent with the OIB-like trace element signatures of the Elazığ lavas.

In general, based on the findings above, the proposed melting model for Tunceli lavas can also be considered for the Elazığ lavas. Accordingly, the Elazığ Volcanics may be the mixing products of garnet and spinel facies melts derived from different depths in the mantle. Alternatively, they may represent the low-degree melts generated in a region in the mantle where both garnet and spinel phases are stable, i.e., at the spinel-garnet transition zone.

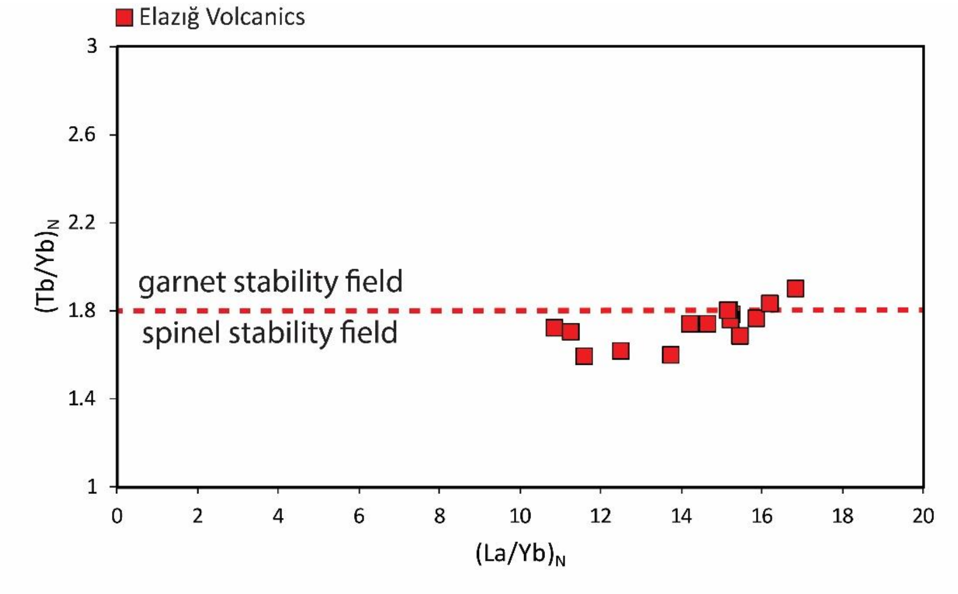

Figure 5.33. The $(La/Yb)_N$ versus $(Tb/Yb)_N$ diagram for the Elazığ Volcanics (modified from Kürkçüoğlu and Yürür, 2021). N denotes normalization to PM (Sun and McDonough, 1989). The garnet- and spinel-lherzolite division value of $(Tb/Yb)_N$ is from Wang et al. (2002).

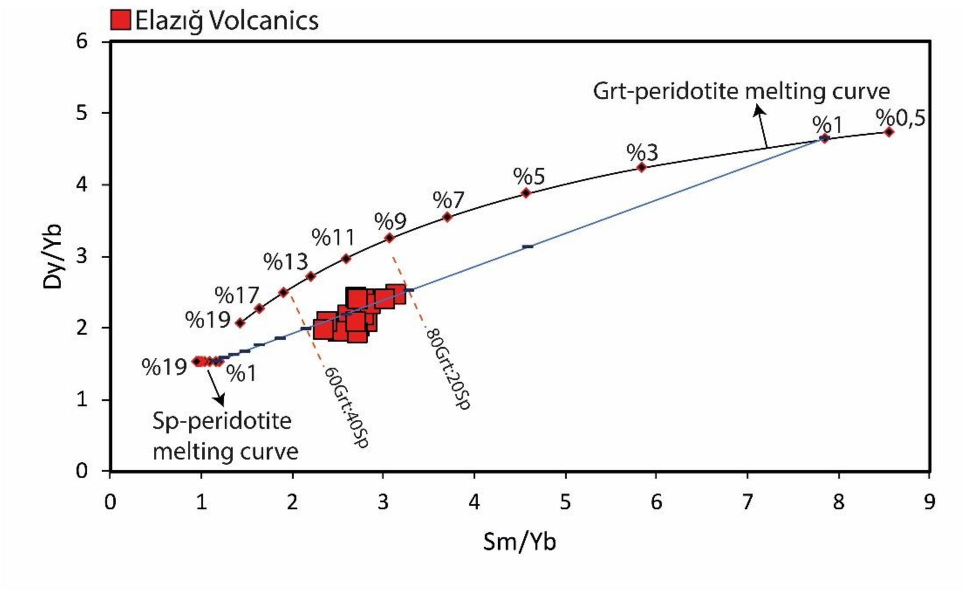

Figure 5.34. The Sm/Yb versus Dy/Yb melt model for the Elazığ Volcanics. For both curves, the source is assumed to have primitive mantle composition (Sun and McDonough 1989). The source mode, melt mode, and partition coefficients are given in Table 5.5. Source modes and partition coefficients were compiled from McKenzie and O'Nions (1991). The melt modes were taken from Thirlwall et al. (1994). The tick marks on each mixing curve correspond to 10% mixing intervals. Gt: Garnet; Sp: Spinel.

Table 5.5. The parameters used in the non-modal batch melting modelings. The references can be found in the related figure caption.

	Source Mode		**Melt Mode**		**K*d* values**		
	Spinel Peridotite	**Garnet Peridotite**	**Spinel Peridotite**	**Garnet Peridotite**	**Dy**	**Sm**	**Yb**
Olivine	0.578	0.598	0.1	0.05	0.0017	0.0013	0.0015
Orthopyroxene	0.27	0.211	0.27	0.2	0.022	0.01	0.049
Clinopyroxene	0.119	0.076	0.5	0.3	0.33	0.26	0.28
Spinel	0.033		0.13		0.01	0.01	0.01
Garnet		0.115		0.45	1.06	0.217	4.03

5.2 Regional Geodynamics

Despite the idea that eastern Anatolia is free of its SCLM (e.g., Şengör et al., 2003; Keskin, 2003), the low-velocity seismic anomalies (*P* and *S* waves) inferred from more recent geophysical studies indicated that the SCLM beneath eastern Anatolia exists but appears to be very thin (i.e., 15-22 km) than expected in continental areas (e.g., Angus et al., 2006; Özacar et al., 2008; Biryol et al., 2011). Following Angus et al. (2006), around the Tunceli and Elazığ region, the total thickness of the lithosphere appears to be approximately 70 km, and the hot asthenospheric mantle occurs at shallower depths. This indicates that the spinel-garnet transition zone (~80 km; e.g., Takahashi and Kushiro, 1983) is located within the asthenospheric mantle rather than the SCLM beneath the study area. When considering these with the melting scenarios proposed for the Tunceli and Elazığ lavas, the spinel-facies melt contributions in the lavas may have been derived from SCLM root attached to the eastern Anatolian crust or may have been derived from the spinel-garnet transition zone located in the asthenosphere. However, in the first case, the lavas dominated by spinel-facies melts (e.g., tholeiitic members of Tunceli lavas) would also be dominated by SCLM contributions. In fact, such signatures are not observed in those lavas (e.g., Figure 5.22). Therefore, the melting region(s) of the studied lavas should be located within the asthenosphere, where both spinel and garnet phases are stable. In this regard, it can be proposed that the components involved in the genesis (i.e., C-like, DM, and SCLM components) of the Tunceli and Elazığ lavas should be located totally within the asthenosphere.

Melting of a C-like or DM component in the asthenospheric depths can be easily explained by their nature since they are widely attributed to asthenospheric mantle components. However, to melt an SCLM component completely within the asthenosphere, the SCLM domains needed to be detached from the lithosphere and presumed to occur as fusible pods in the asthenosphere. The detachment of SCLM domains can plausibly be driven by delamination process or drip tectonics (e.g., Elkins-Tanton, 2005; 2007; Furman et al., 2016; Göğüş et al., 2017). Therefore, combining the proposed geophysical findings with the geochemical data of volcanism in the Tunceli and Elazığ region, it can be suggested that the thickened lithosphere after the collision of Arabian and Eurasian continents lost its structural integrity, and SCLM detachment(s) occurred beneath eastern Anatolia. A similar geodynamic model previously proposed by Pearce et al. (1990); however, as mentioned in “CHAPTER 1” of this study, in that model, the melting is assumed to occur in the domains intrinsic to the lithosphere. Note that a delamination or drip model appears to be also consistent with the thickness of the lithospheric mantle beneath the region. These indicate that the slab break-off process (Şengör et al., 2003; Keskin, 2003) or other mechanisms such as adiabatic decompression melting (Yılmaz et al., 1987) cannot account alone for the geophysical and geochemical data obtained from the region. The delamination or drip dynamics are needed at least to explain the geochemical composition of the volcanism in the Tunceli-Elazığ region.

The lithospheric mantle beneath the eastern Anatolian crust appears thin beneath the whole area between Arabian and Pontide microcontinents (e.g., Angus et al., 2006). Therefore, the lithospheric thickness in the region suggests that if SCLM delamination occurred in the region, it should have been catastrophic instead of small-scaled individual detachments. It was proposed that the widespread post-collisional volcanic activity in eastern Anatolia started in the Late Miocene (Keskin et al., 1998; Keskin, 2003; Keskin, 2007). Therefore, the Late Miocene Tunceli volcanism may represent one of the initial products of this plausible catastrophic SCLM delamination in the region. This may also explain the great SCLM contributions in the Tunceli lavas (ca. 30%). If this is the case, it can be proposed that; following a catastrophic SCLM delamination beneath the region, during the Late Miocene, the detached SCLM domain may have sunk into the asthenosphere, and major melting occurred within the spinel-garnet transition zone (Figure 5.35a). In such a process, the heat required to melt the fusible detached SCLM mass may have been provided by the rising of the hot asthenosphere (Figure 5.35a). After that, the mixing of the melts derived from C-DM and SCLM-sources finally generated the Tunceli lavas, as well as most of the Late Miocene lavas in the region. The

Quaternary Elazığ melts, on the other hand, may represent the melt mixing between the C-DM asthenospheric source and small-scaled slivered SCLM pods that remained after the destabilization of the large scale SCLM mass in the mantle (Figure 5.35b). Melting of such small pods within the spinel-garnet transition zone can account for the dominance of the asthenospheric partial melts in the genesis of Elazığ lavas.

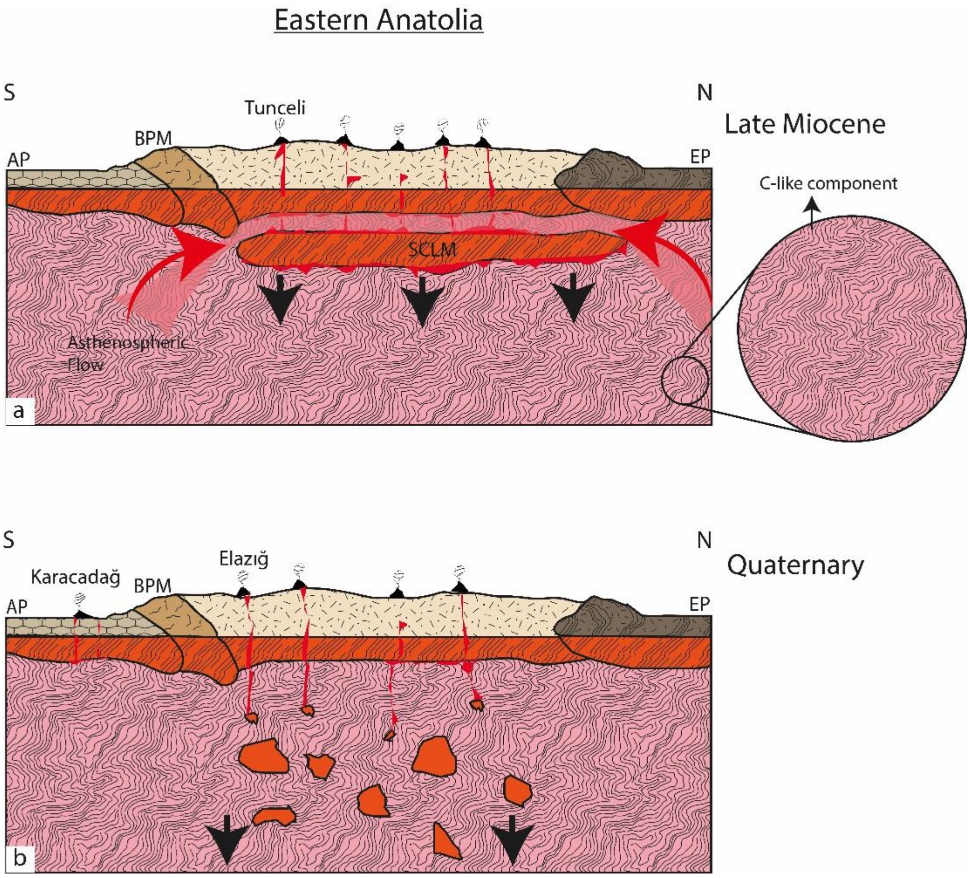

Figure 5.35. The Late Miocene-Quaternary geodynamic evolution model for eastern Anatolia inferred from the geochemistry of Tunceli and Elazığ Volcanics. AP: Arabian Platform; BPM: Bitlis-Pötürge Massif; EP: Eastern Pontide; SCLM: Sub-continental Lithospheric Mantle.

Recently a delamination/drip model has also been proposed for the central Anatolian lavas (Karapınar, Hasandağ and Sivas volcanics; Furman et al., 2021; Gall et al., 2021). It has been proposed that the central Anatolian intraplate lavas represent the products of melt mixing between an asthenospheric mantle, including the C-like recycled component and lithospheric component modified by slab-derived sediment melts (Furman et al., 2021; Gall et al., 2021). It is thought that, similar to the proposed model in this study, this multi-component blend in their genesis has been involved by lithospheric drip melting beneath central Anatolia (e.g., Gall et al., 2021).

To test whether the lavas from these two Anatolian sectors have undergone similar geodynamic process, they were plotted together on a ternary Pb isotope plot (Figure 5.36). For comparison, the anorogenic western Anatolian lavas were plotted on the ternary Pb diagram. The total Pb isotope systematics (^{206}Pb/^{204}Pb, ^{207}Pb/^{204}Pb, and ^{208}Pb/^{204}Pb) are useful to trace the similar source interaction if similar crustal reservoirs such as C-like component or subducted sediments modified SCLM component involved in the lavas (e.g., Hanan and Graham, 1996; Furman et al., 2021). In the diagram, it is apparent that the lavas from the Tunceli-Elazığ region define a coherent trend with the central Anatolian lavas. The lavas from western Anatolia, on the other hand, are characterized by the different trend. These regional difference in the total Pb isotope systematics (western Anatolia versus central-eastern Anatolia) indicate melting of source domains with different Pb characteristics (Furman et al., 2021). It is known that the C-like component is also present in the ambient depleted asthenospheric mantle of western Anatolia (e.g., Late Miocene Thrace-Çanakkale lavas, Aldanmaz et al., 2015). However, it is clear from the diagram that the total Pb-isotope characteristics of other source components involved (i.e., SCLM component) in the western Anatolian lavas have distinct total Pb-isotope signatures than other central and eastern Anatolian lavas. This, in particular, can be confirmed by the trend of the Early-Middle Miocene western Anatolian volcanics (Aldanmaz et al., 2000). These lavas are assumed to have been predominantly derived from metasomatized SCLM (Aldanmaz et al., 2000); however, the sediment flux in their genesis appears to be characterized by distinct Pb isotope systematics, especially in terms of ^{207}Pb, than the eastern Mediterranean young sediments (Figure 5.36). Besides these, difference in the melting systematics controlled mainly by the geodynamic factor may also control the tapping of similar source domains by the lavas. Melting of SCLM domain modified by the sediments with the characteristics of eastern Mediterranean sediments totally within the asthenospheric mantle region characterized by a solid-state mixture of C-like and DM components will result in a multi-component blend as in the cases of central (Karapınar, Hasandağ and Sivas volcanics; Furman et al., 2021; Gall et al., 2021) and eastern Anatolian (e.g., Tunceli and Elazığ lavas, this study) lavas (Figure 5.35). This is evidenced by the coherent trend of the central and eastern Anatolian lavas in the Pb-ternary diagram (Figure 5.36). These all, in turn, suggest that the lavas from central and eastern Anatolia tapped similar source domains induced by a similar geodynamic process. Based on this information, it can be proposed that the lithospheric drip or delamination process, as in central Anatolia, has predominantly triggered the mantle melting in eastern Anatolia.

Such a regional geodynamic process can also be evidenced by the isotope composition of the other eastern Antolian post-collisional volcanism. When the isotope systematics of Late Miocene Tunceli and Quaternary Elazığ Volcanics compared with selected other post-collisional volcanics of eastern Anatolia, it can be cleary observed that the post-collisional volcanism in other sectors of the eastern Anatolia highly possible tapped also the similar source components involved in the Tunceli and Elazığ Volcanics (Figure 5.37). Although the amount of the individual component contributions vary from one sector to another, the C-DM-SCLM multiple component blend can be also suggested for the whole post-collisional volcanic system in eastern Anatolia. Such geochemical similarity reinforce the the idea that a catastrophic geodynamic process (i.e. delamination/drip tectonics) has mainly controlled the the generation of the post-collisional volcanic activity in the region. Nevertheless, to make better a better assumption regarding the regional chemical geodynamic perspective, a detailed comparative study involving the all post-collisional volcanic suites of the region need to be conducted.

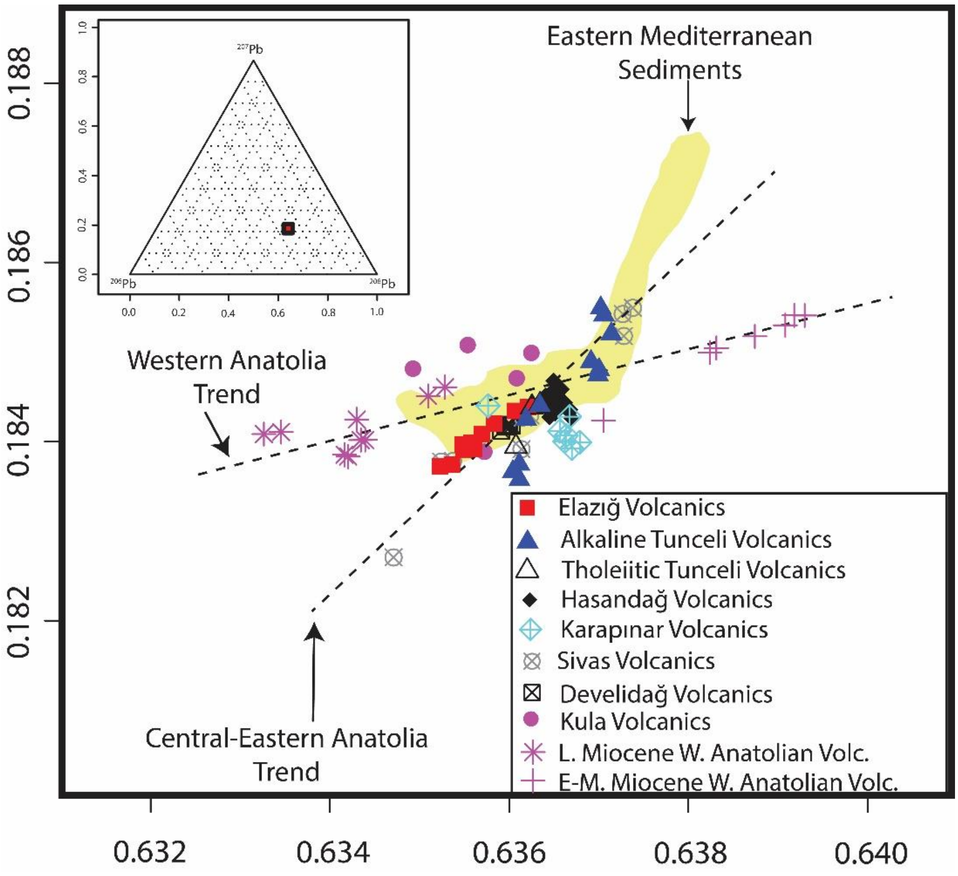

Figure 5.36. The ternary Pb isotope diagram for the selected Anatolian mafic lavas (after Hanan et al., 1986 and Furman et al., 2021). This figure represents the zoomed-in view of the location of the data distribution in the ternary inset. The location of the data is labeled as red-black square in the ternary inset. The expanded slice of x-y coordinates can also be seen in the ternary inset. The data of the Hasandağ and Karapınar volcanics are from Gall et al. (2021). The data of Sivas and Develidağ Volcanics are from Furman et al. (2021). The data of Kula volcanics are from Alıcı et al. (2002) and Aldanmaz et al. (2015). The data of Late Miocene (Thrace and Çanakkale) and Early-Middle Miocene (Foça, Bergama, Ayvalık, Y. Şakran, Ayvalık and Assos) western Anatolian volcanics are from Aldanmaz et al. (2000; 2006; 2015). The data of eastern Mediterranean sediments are from Klaver et al. (2015).

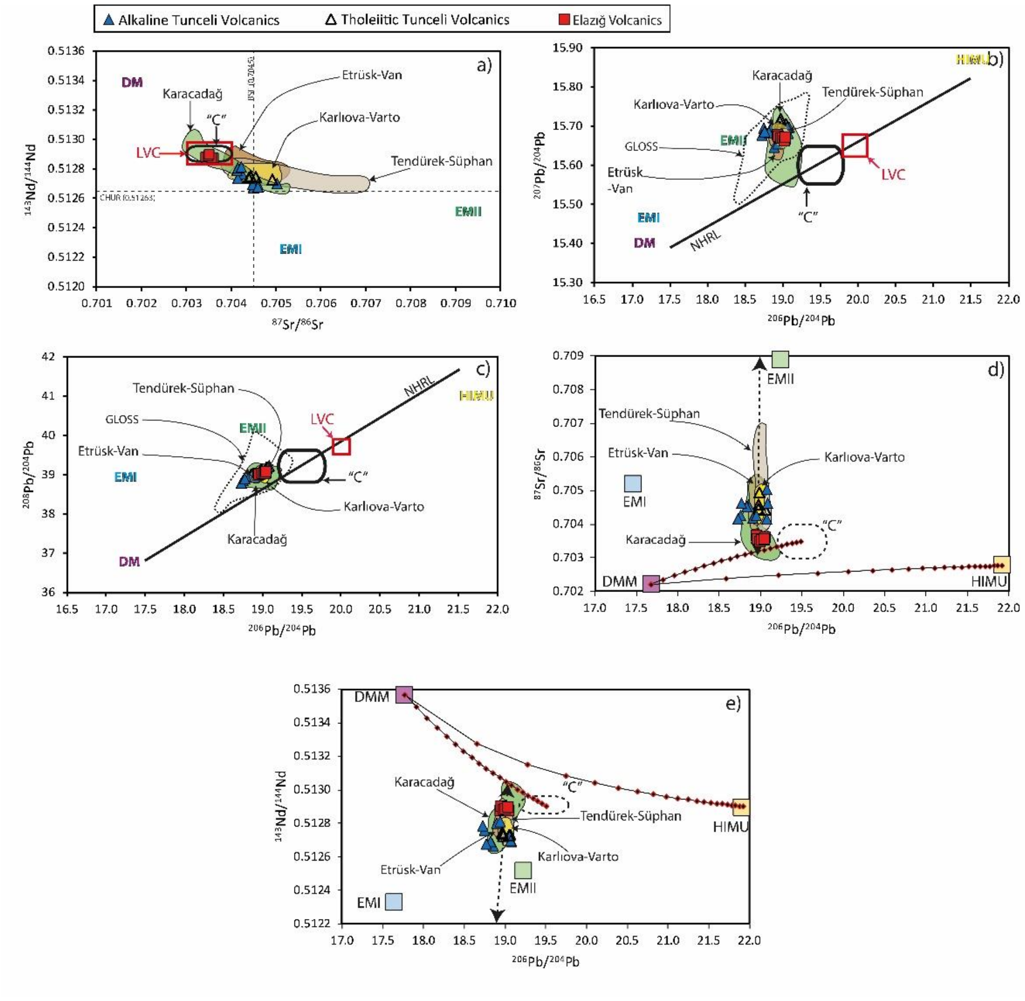

Figure 5.37. Distribution of the selected eastern Anatolian post-collisional volcanics together with the Tunceli and Elazığ Volcanics in Sr-Nd, Pb-Pb, Pb-Sr, and Pb-Nd isotope spaces. The published data used for comparison includes samples with MgO (wt. %) greater than 4 wt. % to avoid the effects of post-melting processes and to make the data set comparable with the Tunceli and Elazığ lavas. Data sources: Karacadağ Volcanics-Keskin et al., 2012b, Ekici et al., 2014; Tendürek Volcanics-Lebedev et al., 2016; Süphan Volcanics-Özdemir and Güleç, 2013; Etrüsk Volcanics-Oyan et al., 2016; Van Volcanics-Oyan et al., 2017; Karlıova-Varto Volcanics-Karaoğlu et al., 2020. The data sources of the source components, parameters regarding the source mixing curves can be seen in the Figures 4.25, 4.26, and 5.21 and Table 5.3.

5.3 Recycling

As it is explained in detail in the “CHAPTER 1, although there are views linking the origin of C-like material to the remixing of end-members in the mantle (e.g., Zindler and Hart, 1986) or to undegassed primordial lower mantle component (e.g., Hart et al., 1992; Farley et al., 1992), it has been widely attributed to the recycled oceanic lithospheric lithologies (e.g., Zindler and Hart, 1986; Hoernle et al., 1995; Hanan and Graham, 1996; Stracke et al., 2005, Stracke, 2012). The recycled oceanic crust/lithosphere that incorporated some continental Pb before its subduction (Hanan and Graham, 1996) or affected by sub-arc alteration during its subduction (Stracke et al., 2005; Stracke, 2012) have been proposed to explain the total isotopic range of such “common” component. Such recycled component, apart from its protolith, is thought reside in the lower mantle or lower-upper mantle transition zone, and entrained into plumes to be transported into the source regions of intraplate oceanic or continental lavas (e.g., Hoernle et al., 1995; Hanan and Graham, 1996).

The total Sr-Nd-Hf-Pb isotope range of Tunceli and Elazığ Volcanics indicates that the C-like mantle component, which could be attributed to ancient oceanic lithologies, is present beneath eastern Anatolia, and has been extensively sampled (55-70%) by the eastern Anatolian post-collisional volcanism. This implies that, therefore, recycling of the ancient materials from the deep mantle regions has occurred beneath eastern Anatolia. However, in eastern Anatolia, no structural or geophysical evidence consistent with a single plume model has been proposed so far (see Keskin, 2007 for detailed information). Thus, such recycled materials beneath the eastern Anatolia, or maybe beneath the whole Anatolian microcontinent, should have been recycled via diapiric upwelling of small-scale instabilities from the deep mantle regions. Such model, on the other hand, is consistent with the “mantle hot fingers” model of Wilson and Patterson (2001) suggested for the European intraplate volcanics. In such a model, the physical evidence for the recycling process may be poor, but the chemistry of primitive basaltic rocks can provide compelling evidences, as in the Tunceli and Elazığ case. In this regard, it can be proposed that the C-like component has been recycled by small-scale diapiric upwellings from the deep mantle regions (i.e., 660 km seismic discontinuity or lower mantle) rather than via a single plume to the shallow regions beneath eastern Anatolia, and mixed with depleted asthenospheric mantle matrix. Considering these with all results obtained from this study, it can be suggested that the eastern Anatolian asthenospheric mantle became fairly heterogeneous with the involvement of C-like component with recycling and SCLM domains with delamination. The mixing models indicate that the premixing between C and DM components should have occurred before the SCLM contributions into the mantle.

It must be noted that, the C-like material is assumed to have also been involved in the genesis of western Anatolian (Kula volcanics; Aldanmaz et al., 2015), central Anatolian (Karapınar, Hasandağ and Sivas volcanics; Furman et al., 2021; Gall et al., 2021) and southeastern Anatolian (Karacadağ volcanics; Keskin et al., 2012) intraplate volcanics. This indicates that such material is disseminated in the whole Anatolian asthenospheric mantle. Considering this, a common geodynamic process should have been recycled this ancient material beneath all sectors of Anatolia. One possible candidate for a common geodynamic process for these lavas could be the recycling of Neo-Tethyan oceanic lithospheres beneath Anatolia. Biryol et al. (2011) proposed that the subducted Neo-Tethyan oceanic lithosphere is currently lying on the 660 km transition zone beneath the whole Anatolia. After a somewhat long residence time (>300 Ma), melts derived from this oceanic lithosphere may have isotope characteristics similar to component C (e.g., Hanan and Graham, 1996). Therefore, recycling of the Neo-Tethyan lithosphere may account for C signatures found in the Cenozoic OIB-like Anatolian lavas. Note that such a recycling process may also explain the isotopic difference of the “common” components found in the European and Anatolian lavas (i.e., EAR versus C-like components). Since the initial composition and the age of the subducted material affect the final composition of the recycled component (e.g., Stracke et al., 2005), the compositional difference in the “common” components found in the lavas from different sectors of circum-Mediterranean region may arise from the difference in the composition and age of the initial subducted material. In this regard, the EAR component with high Pb isotope compositions may be related to the recycling of an older and compositionally different subducted material than the Neo-Tethyan lithosphere.

CHAPTER 6

CONCLUSIONS

The major concluding remarks drawn from this dissertation are summarized as follows;

1. The Late Miocene Tunceli and Quaternary Elazığ mafic volcanics, representing the temporal volcanic phases of post-collisional volcanicity of eastern Anatolia, are the second-youngest units after Quaternary alluvium deposits in the Tunceli and Elazığ regions, respectively. The volcanism in both regions is characterized by successive pulses of lava flows, which vary mainly in terms of their colors and textures in the field. The lava succession in both areas is mainly made up of an alternation of vesicular/amygdaloidal and massive lava flows.
2. Based on the petrographic and mineral chemistry evaluations, both the Tunceli and Elazığ Volcanics are made up of basaltic lithologies with similar mineralogical assemblages. Olivine, clinopyroxene, plagioclase, and Fe-Ti oxide phases characterize the main mineralogy in these lavas. The Tunceli lavas are mostly aphyric/diabasic (i.e., holocrystalline) and porphyritic to a lesser extent. Therefore, the phenocryst phases, are not abundant (~5 vol.%) in these lavas. Nevertheless, the phenocryst mineralogy in the Tunceli Volcanics includes, in general, olivine, clinopyroxene, and plagioclase (in the order of decreasing abundance). The Elazığ Volcanics, on the other hand, are entirely porphyritic, and phenocryst content reaches up to ~20 vol.% in these lavas. The phenocryst assemblage is chiefly made up of olivine and to a lesser extent plagioclase in the Elazığ Volcanics. In contrast to the Tunceli Volcanics, clinopyroxene does not occur as a phenocryst phase in the Elazığ Volcanics.

3. The major element geochemistry also confirms that both Tunceli and Elazığ Volcanics are basaltic in composition. While the Tunceli lavas are totally composed of alkaline and tholeiitic basalts, the composition of the Elazığ lavas, with an alkaline geochemical affinity range predominantly between trachybasalt and basanite.
4. The bivariate Harker diagrams and log-log FC modelings suggest that fractional crystallization has played a role in the genesis of both Tunceli and Elazığ Volcanics. However, its effects on the chemistry of Tunceli lavas appear to be limited compared to the Elazığ lavas. In general, it can be proposed that while minor amount of fractionation of olivine and clinopyroxene phases occurred during the magmatic evolution of Tunceli lavas, relatively more extensive fractionation of clinopyroxene, olivine, and Fe-Ti oxide phases played an important role in the differentiation of the Elazığ Volcanics. It is also important to note that, although the element variation of both volcanic suites in the bivariate Harker diagrams argues against a plagioclase fractionation, the FC modelings indicate that a minor amount of plagioclase fractionation during their magmatic evolution cannot be totally ruled out.
5. The AFC modelings showed that the Tunceli and Elazığ Volcanics are free of significant crustal contamination. According to the trace element and Sr-Nd isotope systematics, while the Tunceli lavas do not appear to have interacted with the continental crust, only a minor part of the Elazığ Volcanics seems to have been affected from low to moderate level contamination during their ascent to the surface. Nevertheless, for the majority of the Elazığ Volcanics, the effects of AFC seem to be negligible. Thus, it can be said that the geochemical signatures in the most primitive members of the Tunceli and Elazığ Volcanics closely reflect the geochemical features of their source regions.
6. Both the Tunceli and Elazığ Volcanics display enriched trace element signatures, suggesting derivation predominantly from enriched mantle source

region(s) for the two volcanic suites. While the Tunceli lavas are characterized by the enrichment in LILE (e.g., Rb, Ba, K), Th, and La relative to the HFSE (e.g., Nb, Ti, Zr), the Elazığ lavas exhibit enrichment in LILEs together with HFSE. LREE enrichment over HREE is characteristic in both volcanics.

7. The total range of trace element and Sr-Nd-Hf-Pb isotope data requires the involvement of three distinct components in the genesis of Tunceli and Elazığ Volcanics; a depleted asthenospheric mantle component (DM), an enriched asthenospheric component representing recycled oceanic lithospheric lithologies (i.e., C-like), and EMII-type component. According to the mixing modelings in the Sr-Nd-Hf-Pb isotope spaces, an asthenospheric source domain that is made up of solid-state mixture of a C-like component and a DM component appears to be a common asthenospheric source region for the both Tunceli and Elazığ Volcanics. The modelings suggest that the involvement of the C-like component in this mixture is significant, with around 80%. This indicates that the asthenosphere beneath eastern Anatolia is heterogeneous, consisting of recycled oceanic lithologies. Based on the findings in this study, it can be proposed that the recycling of oceanic lithologies with the characteristic of C is dispersed in the eastern Anatolian asthenosphere as fusible schlieren and mixed with the depleted asthenospheric matrix.
8. The trace element and Sr-Nd-Hf-Pb isotope systematics together with geodynamic configuration of the eastern Anatolia suggest that the EMII-type component in the genesis of these lavas represent fusible SCLM domain(s), metasomatized by sediment melt dominated slab-derived inputs from Tethyan slab. The mixing modelings suggest that the amount of metasomatized SCLM contribution appears to be larger (ca. 10-30%) in the Tunceli lavas compared to the Elazığ Volcanics (< 10%). This, in turn, makes the C contribution larger (ca. 70-80%) in the genesis of Elazığ lavas compared to the Tunceli lavas (ca. 55-70%). Such involvement can account

for the OIB-like and subduction-related signatures in the Elazığ and Tunceli Volcanics, respectively.

9. The melting modelings indicate that the melts of both the Tunceli and Elazığ Volcanics have derived from a region where garnet and spinel are stable, i.e., spinel-garnet transition zone. When the lithospheric thickness of eastern Anatolia is taken into consideration, this indicates that all source components (i.e., DM, C-like, and SCLM components) involved in the genesis of Tunceli and Elazığ lavas have been melted totally in the asthenosphere. This, in turn, requires the SCLM domain(s) to be detached from the eastern Anatolian lithosphere and occur as fusible pods in the asthenosphere. In this regard, it can be proposed that the delamination process or drip tectonics may be the main driving mechanism of the post-collisional melt generation in eastern Anatolia.
10. From a temporal perspective, it can be speculated that a catastrophic SCLM delamination beneath the region occurred during the Late Miocene, and a large amount of SCLM component involved in the genesis of the volcanics in eastern Anatolia during this time. Later, with the melting of small-scaled slivered SCLM pods that remained after the destabilization of the large-scale SCLM mass in the mantle, the SCLM contribution in the lavas was diminished. However, such a scenario, should be reconciled with the geochemical data from the other post-collisional volcanics in the region.

REFERENCES

Agostini, S., Savaşçın, M. Y., Di Giuseppe, P., Di Stefano, F., Karaoğlu, Ö., Lustrino, M., Manetti, P., Ersoy, Y., Kürüm, S., and Öztufekçi Önal, A. (2019). Neogene volcanism in Elazig-Tunceli area (eastern Anatolia): geochronological and petrological constraints. Italian Journal of Geosciences, 138(3), 433–455. https://doi.org/10.3301/ijg.2019.18

Agranier, A., Blichert-Toft, J., Graham, D., Debaille, V., Schiano, P., and Albarède, F. (2005). The spectra of isotopic heterogeneities along the mid-Atlantic Ridge. Earth and Planetary Science Letters, 238(1–2), 96–109. https://doi.org/10.1016/j.epsl.2005.07.011

Akgül, B., Kürüm, S., and Erdem, E. (2001). Elazığ volkanitlerinin (Alt Pliyosen) petrografik ve jeokimyasal özellikleri. Yerbilimleri, 39, 69–83.

Aktağ, A. (2014). Tunceli Güneyindeki Tersiyer Volkanitlerinin Petrografisi ve Jeokimyası. Yüksek Lisans Tezi, Tunceli Üniversitesi, Fen Bilimleri Enstitüsü, Tunceli, 109s.

Aktağ, A., Önal, A. Ö., and Sayit, K. (2019). Geochemistry of the post-collisional Miocene mafic Tunceli Volcanics, Eastern Turkey: Implications for the nature of the mantle source and melting systematics. Chemie Der Erde, 79(1), 113–129. https://doi.org/10.1016/j.geoch.2018.11.004

Al-Lazki, A. I., Seber, D., Sandvol, E., Turkelli, N., Mohamad, R., and Barazangi, M. (2003). Tomographic Pn velocity and anisotropy structure beneath the Anatolian plateau (eastern Turkey) and the surrounding regions. Geophysical Research Letters, 30(24), 4–7. https://doi.org/10.1029/2003GL017391

Aldanmaz, E. (1998). Petrogenesis of late cenozoic collision volcanism in western Anatolia, Turkey. PhD Thesis, Durham University, Durham.

Aldanmaz, E., Pearce, J. A., Thirlwall, M. F., and Mitchell, J. G. (2000). Petrogenetic evolution of late Cenozoic, post-collision volcanism in western Anatolia, Turkey. Journal of Volcanology and Geothermal Research, 102(1–2), 67–95. https://doi.org/10.1016/S0377-0273(00)00182-7

Aldanmaz, E., Köprübaşi, N., Gürer, Ö. F., Kaymakçi, N., and Gourgaud, A. (2006). Geochemical constraints on the Cenozoic, OIB-type alkaline volcanic rocks of NW Turkey: Implications for mantle sources and melting processes. Lithos, 86(1–2), 50–76. https://doi.org/10.1016/j.lithos.2005.04.003

Aldanmaz, E., Pickard, M., Meisel, T., Altunkaynak, Ş., Sayıt, K., Şen, P., Hanan, B. B., and Furman, T. (2015). Source components and magmatic processes in the genesis of Miocene to Quaternary lavas in western Turkey: constraints from HSE distribution and Hf–Pb–Os isotopes. Contributions to Mineralogy and Petrology, 170(2). https://doi.org/10.1007/s00410-015-1176-x

Alıcı, P., Temel, A., and Gourgaud, A. (2002). Pb–Nd–Sr isotope and trace element geochemistry of Quaternary extension-related alkaline volcanism: a case study of Kula region (western Anatolia, Turkey). Journal of Volcanology and Geothermal Research, 115(3–4), 487–510. https://doi.org/10.1016/S0377-0273(01)00328-6

Alıcı Şen, P., Temel, A., and Gourgaud, A. (2004). Petrogenetic modelling of Quaternary post-collisional volcanism: a case study of central and eastern Anatolia. Geological Magazine, 141(1), 81–98. https://doi.org/10.1017/S0016756803008550

Allègre, C. J. (1982). Chemical geodynamics. Tectonophysics, 81(3–4), 109–132. https://doi.org/10.1016/0040-1951(82)90125-1

Allègre, C. J., Ben Othman, D., Polve, M., and Richard, P. (1979). The Nd-Sr isotopic correlation in mantle materials and geodynamic consequences. Physics of the Earth and Planetary Interiors, 19(4), 293–306. https://doi.org/10.1016/0031-9201(79)90002-5

Allègre, C. J., Brevart, O., Dupre, B., and Minster, J. F. (1980). Isotopic and Chemical Effects Produced in a Continuously Differentiating Convecting Earth Mantle. Philosophical Transactions of the Royal Society A: Mathematical, Physical and Engineering Sciences, 297(1431), 447–477. https://doi.org/10.1098/rsta.1980.0225

Allègre, C. J., and Turcotte, D. L. (1985). Geodynamic mixing in the mesosphere boundary layer and the origin of oceanic islands. Geophysical Research Letters, 12(4), 207–210. https://doi.org/10.1029/GL012i004p00207

Allègre, C. J., and Turcotte, D. L. (1986). Implications of a two-component marble-cake mantle. Nature, 323(6084), 123–127. https://doi.org/10.1038/323123a0

Altiner, D. (1989). An Example for the Tectonic Evolution of the Arabian Platform Margin (SE Anatolia) during Mesozoic and some Criticisms of the Previously Suggested Models BT - Tectonic Evolution of the Tethyan Region (A.M.C. Şengör (ed.); pp. 117–129). Springer Netherlands. https://doi.org/10.1007/978-94-009-2253-2_7

Anderson, D. L. (1994). The sublithospheric mantle as the source of continental flood basalts; the case against the continental lithosphere and plume head reservoirs. Earth and Planetary Science Letters, 123(1–3), 269–280. https://doi.org/10.1016/0012-821X(94)90273-9

Andres, M., Blichert-Toft, J., and Schilling, J. G. (2004). Nature of the depleted upper mantle beneath the Atlantic: Evidence from Hf isotopes in normal mid-ocean ridge basalts from 79°N to 55°S. Earth and Planetary Science Letters, 225(1–2), 89–103. https://doi.org/10.1016/j.epsl.2004.05.041

Angus, D. A., Wilson, D. C., Sandvol, E., and Ni, J. F. (2006). Lithospheric structure of the Arabian and Eurasian collision zone in eastern Turkey from S-wave receiver functions. Geophysical Journal International, 166(3), 1335–1346. https://doi.org/10.1111/j.1365-246X.2006.03070.x

Arger, J., Mitchell, J., and Westaway, R. W. C. (2000). Neogene and Quaternary volcanism of southeastern Turkey. Geological Society Special Publication, 173, 459–487. https://doi.org/10.1144/GSL.SP.2000.173.01.22

Armstrong, R. L. (1968). A model for the evolution of strontium and lead isotopes in a dynamic Earth. Reviews of Geophysics, 6(2), 175. https://doi.org/10.1029/RG006i002p00175

Asutay, H. J. (1985). Baskil (Elazığ) çevresinin jeolojik ve petrografik incelenmesi. Doktora Tezi, Ankara Üniversitesi, Fen Bilimleri Enstitüsü, Ankara, 156s.

Asutay, H. J., Turan, M., Poyraz, N., Orhan, H., Tarı, E., and Yazgan, E. (1986). Doğu Toroslar-Keban-Baskil dolaylarının jeolojisi. MTA Raporu, No: 8008.

Ayers, J. C., and Watson, E. B. (1993). Rutile solubility and mobility in supercritical aqueous fluids. Contributions to Mineralogy and Petrology, 114(3), 321–330. https://doi.org/10.1007/BF01046535

Baker, J., Peate, D., Waight, T., and Meyzen, C. (2004). Pb isotopic analysis of standards and samples using a ^{207}Pb-^{204}Pb double spike and thallium to correct for mass bias with a double-focusing MC-ICP-MS. Chemical Geology, 211(3–4), 275–303. https://doi.org/10.1016/j.chemgeo.2004.06.030

Balcı, U., and Sayit, K. (2020). Diabase dykes from Boğazkale (Çorum), Central Anatolia: Geochemical insights into the geodynamical evolution of the northern branch of Neotethys. Chemie Der Erde, 80(2), 125602. https://doi.org/10.1016/j.chemer.2020.125602

Beccaluva, L., Macciotta, G., Siena, F., and Zeda, O. (1989). Harzburgite-lherzolite xenoliths and clinopyroxene megacrysts of alkaline basic lavas from Sardinia (Italy). Chemical Geology, 77(3–4), 331–345. https://doi.org/10.1016/0009-2541(89)90082-X

Ben Othman, D., White, W. M., and Patchett, J. (1989). The geochemistry of marine sediments, island arc magma genesis, and crust-mantle recycling. Earth and Planetary Science Letters, 94(1–2), 1–21. https://doi.org/10.1016/0012-821X(89)90079-4

Bender, J. F., Hodges, F. N., and Bence, A. E. (1978). Petrogenesis of basalts from the project FAMOUS area: experimental study from 0 to 15 kbars. Earth and Planetary Science Letters, 41(3), 277–302. https://doi.org/10.1016/0012-821X(78)90184-X

Beyarslan, M., and Bingöl, A. F. (1996). Kömürhan ofiyolit biriminin petrografik ve petrolojik incelenmesi. F.Ü. Fen ve Müh. Bilimleri Dergisi, 8(2), 1–16.

Beyarslan, M., and Bingöl, A. F. (2000). Petrology of a supra-subduction zone ophiolite (Elazığ, Turkey). Canadian Journal of Earth Sciences, 37(10), 1411–1424. https://doi.org/10.1139/e00-041

Beyarslan, M., and Bingöl, A. F. (2018). Zircon U-Pb age and geochemical constraints on the origin and tectonic implications of late cretaceous intra-oceanic arc magmatics in the Southeast Anatolian Orogenic Belt (SE-Turkey). Journal of African Earth Sciences, 147(July), 477–497.

https://doi.org/10.1016/j.jafrearsci.2018.07.001

Bingöl, A. F. (1984). Geology of the Elazığ area in the Eastern Taurus region. In O. Tekeli and M. C. Göncüoğlu (Eds.), Geology of the Taurus Belt (pp. 209–217).

Biryol, C. B., Beck, S. L., Zandt, G., and Özacar, A. A. (2011). Segmented African lithosphere beneath the Anatolian region inferred from teleseismic P-wave tomography. Geophysical Journal International, 184(3), 1037–1057. https://doi.org/10.1111/j.1365-246X.2010.04910.x

Blichert-Toft, J., and Albarède, F. (1997). The Lu-Hf isotope geochemistry of chondrites and the evolution of the mantle-crust system. Earth and Planetary Science Letters, 148(1–2), 243–258. https://doi.org/10.1016/S0012-821X(97)00040-X

Blichert-Toft, J., Frey, F. A., and Albarede, F. (1999). Hf Isotope Evidence for Pelagic Sediments in the Source of Hawaiian Basalts. Science, 285, 879–883. https://doi.org/10.1126/science.285.5429.879

Blusztajn, J., and Hart, S. R. (1989). Sr , Nd , and Pb isotopic character of Tertiary basalts from southwest Poland. Geochimica et Cosmochimica Acta, 53, 2689–2696.

Bodinier, J. L. (1988). Geochemistry and petrogenesis of the Lanzo peridotite body, western Alps. Tectonophysics, 149(1–2), 67–88. https://doi.org/10.1016/0040-1951(88)90119-9

Bodinier, J. L., Dupuy, C., and Dostal, J. (1988). Geochemistry and petrogenesis of Eastern Pyrenean peridotites. Geochimica et Cosmochimica Acta, 52(12), 2893–2907. https://doi.org/10.1016/0016-7037(88)90156-1

Bodinier, J. L., Vasseur, G., Vernieres, J., Dupuy, C., and Fabries, J. (1990). Mechanisms of Mantle Metasomatism: Geochemical Evidence from the Lherz Orogenic Peridotite. Journal of Petrology, 31(3), 597–628. https://doi.org/10.1093/petrology/31.3.597

Bogaard, P. J. F., and Wörner, G. (2003). Petrogenesis of Basanitic to Tholeiitic Volcanic Rocks from the Miocene Vogelsberg , Central Germany. Journal of Petrology, 44(3), 569–602.

https://doi.org/https://doi.org/10.1093/petrology/44.3.569

Bougault, H., and Hekinian, R. (1974). Rift Valley in the Atlantic Ocean near 36°50′N: petrology and geochemistry of basaltic rocks. Earth and Planetary Science Letters, 24(2), 249–261. https://doi.org/10.1016/0012-821X(74)90103-4

Bouvier, A., Vervoort, J. D., and Patchett, P. J. (2008). The Lu-Hf and Sm-Nd isotopic composition of CHUR: Constraints from unequilibrated chondrites and implications for the bulk composition of terrestrial planets. Earth and Planetary Science Letters, 273(1–2), 48–57. https://doi.org/10.1016/j.epsl.2008.06.010

Bozkaya, Ö., Yalçin, H., Başibüyük, Z., Özfirat, O., and Yilmaz, H. (2007). Origin and evolution of the southeast Anatolian metamorphic complex (Turkey). Geologica Carpathica, 58(3), 197–210.

Bozkurt, E. (2001). Neotectonics of turkey–a synthesis. Geodinamica Acta, 14(1–3), 3–30. https://doi.org/10.1080/09853111.2001.11432432

Carlson, R. W. (1984). Isotopic constraints on Columbia River flood basalt genesis and the nature of the subcontinental mantle. Geochimica et Cosmochimica Acta, 48(11), 2357–2372. https://doi.org/10.1016/0016-7037(84)90231-X

Cavazza, W., Cattò, S., Zattin, M., Okay, A. I., and Reiners, P. (2018). Thermochronology of the Miocene Arabia-Eurasia collision zone of southeastern Turkey. Geosphere, 14(5), 2277–2293. https://doi.org/10.1130/GES01637.1

Cebriá, J. M., and Wilson, M. (1995). Cenozoic mafic magmatism in Western/Central Europe: a common European asthenospheric reservoir. Terra Nova Abstract Supplement 7, 162.

Çetindağ, B. (1985). Palu-Kovancılar (Elazığ) dolayının hidrojeolojik incelenmesi. Yüksek Lisans Tezi, Fırat Üniversitesi, Fen Bilimleri Enstitüsü, Elazığ, 117s.

Çetinkaplan, M., Pourteau, A., Candan, O., Koralay, O. E., Oberhänsli, R., Okay, A. I., Chen, F., Kozlu, H., and Şengün, F. (2016). P–T–t evolution of eclogite/blueschist facies metamorphism in Alanya Massif: time and space relations with HP event in Bitlis Massif, Turkey. International Journal of Earth

Sciences, 105(1), 247–281. https://doi.org/10.1007/s00531-014-1092-8

Chaffey, D. J., Cliff, R. A., and Wilson, B. M. (1989). Characterization of the St Helena magma source. Geological Society Special Publication, 42, 257–276. https://doi.org/10.1144/GSL.SP.1989.042.01.16

Chase, C. G. (1981). Oceanic island Pb: Two-stage histories and mantle evolution. Earth and Planetary Science Letters, 52(2), 277–284. https://doi.org/10.1016/0012-821X(81)90182-5

Chauvel, C., Hofmann, A. W., and Vidal, P. (1992). HIMU-EM: The French Polynesian connection. Earth and Planetary Science Letters, 110(1–4), 99–119. https://doi.org/10.1016/0012-821X(92)90042-T

Chauvel, C., Lewin, E., Carpentier, M., Arndt, N. T., and Marini, J. C. (2008). Role of recycled oceanic basalt and sediment in generating the Hf-Nd mantle array. Nature Geoscience, 1(1), 64–67. https://doi.org/10.1038/ngeo.2007.51

Civetta, L., Antonio, M. D., Orsi, G., and Tilton, G. R. (1998). The Geochemistry of Volcanic Rocks from Pantelleria Island , Sicily Channel : Petrogenesis and Characteristics of the Mantle Source Region. Journal of Petrology, 39(8), 1453–1491.

Class, C., Miller, D. M., Goldstein, S. L., and Langmuir, C. H. (2000). Distinguishing melt and fluid subduction components in Umnak Volcanics, Aleutian Arc. Geochemistry, Geophysics, Geosystems, 1(6), 1004. https://doi.org/10.1029/1999GC000010

Cohen, R. S., and O’nions, R. K. (1982). The lead, neodymium and strontium isotopic structure of ocean ridge basalts. Journal of Petrology, 23(3), 299–324. https://doi.org/10.1093/petrology/23.3.299

Condie, K. C. (2016). The Mantle. In Earth as an Evolving Planetary System. https://doi.org/10.1016/b978-0-12-803689-1.00004-3

Cottrell, E., and Kelley, K. A. (2013). Redox Heterogeneity in Mid-Ocean Ridge Basalts as a Function of Mantle Source. Applied Physics Letters, 340(6138), 1314–1317. https://doi.org/10.1063/1.4852615

Çimen, O., Toksoy-Köksal, F., Öztüfekçi-Önal, A., and Aktağ, A. (2016). Depleted to refertilized mantle peridotites hosting chromitites within the Tunceli ophiolite, Eastern Anatolia (Turkey): Insights on the back-arc origin. Ofioliti, 41(1), 1–20. https://doi.org/10.4454/ofioliti.v41i1.439

Çimen, O., and Öztüfekçi-Önal A. (2018). Preliminary geochemical data of the mafic rocks from the Ovacik and Pülümür Ophiolite Zone (Eastern Anatolia, Turkey): Implications for the geodynamic evolution of the northern Neotethyan Ocean. Ofioliti, 42(3), 103–116. https://doi.org/10.4454/ofioliti.v43i2.458

Çolakoğlu, A. R., Günay, K., Göncüoğlu, M. C., Oyan, V., and Erdoğan, K. (2014). Geochemical evaluation of the late Maastrichtian subduction-related volcanism in the southern Neotethys in Van area, and a correlation across the Turkish-Iranian border. Ofioliti, 39(2), 51–65. https://doi.org/10.4454/ofioliti.v39i2.429

Çubukçu, H. E., Ulusoy, I., Aydar, E., Ersoy, O., Şen, E., Gourgaud, A., and Guillou, H. (2012). Mt. Nemrut volcano (Eastern Turkey): Temporal petrological evolution. Journal of Volcanology and Geothermal Research, 209–210, 33–60. https://doi.org/10.1016/j.jvolgeores.2011.08.005

Damasceno, D., Scoates, J. S., Weis, D., Frey, F. A., and Giret, A. (2002). Mineral chemistry of mildly alkalic basalts from the 25 Ma Mont Crozier section, Kerguelen Archipelago: Constraints on phenocryst crystallization environments. Journal of Petrology, 43(7), 1389–1413. https://doi.org/10.1093/petrology/43.7.1389

Dasgupta, R., Hirschmann, M. M., and Smith, N. D. (2007). Partial Melting Experiments of Peridotite + CO_2 at 3 GPa and Genesis of Alkalic Ocean Island Basalts. Journal of Petrology, 48(11), 2093–2124. https://doi.org/10.1093/petrology/egm053

Day, J. M. D., Pearson, D. G., Macpherson, C. G., Lowry, D., and Carracedo, J. C. (2010). Evidence for distinct proportions of subducted oceanic crust and lithosphere in HIMU-type mantle beneath El Hierro and La Palma, Canary Islands. Geochimica et Cosmochimica Acta, 74(22), 6565–6589. https://doi.org/10.1016/j.gca.2010.08.021

Demir, T., Seyrek, A., Guillou, H., Scaillet, S., Westaway, R., and Bridgland, D. (2009). Preservation by basalt of a staircase of latest Pliocene terraces of the River Murat in eastern Turkey: Evidence for rapid uplift of the eastern

Anatolian Plateau. Global and Planetary Change, 68(4), 254–269. https://doi.org/10.1016/j.gloplacha.2009.02.008

DePaolo, D. J. (1980). Crustal growth and mantle evolution : inferences from models of element transport and Nd and Sr isotopes. Geochimica et Cosmochimica Acta, 44, 1185–1196. https://doi.org/https://doi.org/10.1016/0016-7037(80)90072-1

DePaolo, D. J. (1981). Trace element and isotopic effects of combined wallrock assimilation and fractional crystallization. Earth and Planetary Science Letters, 53(2), 189–202. https://doi.org/10.1016/0012-821X(81)90153-9

DePaolo, D. J., and Wasserburg, G. J. (1976). Inferences about Magma Sources and Mantle Structure from Variations of ^{143}Nd/^{144}Nd. Geophysical Research Letters, 3(12). https://doi.org/10.1029/GL003i012p00743

Di Giuseppe, P., Agostini, S., Lustrino, M., Karaoglu, Ö., Savaşçin, M. Y., Manetti, P., and Ersoy, Y. (2017). Transition from compression to strike-slip tectonics revealed by miocene-pleistocene volcanism west of the karliova triple junction (east anatolia). Journal of Petrology, 58(10), 2055–2087. https://doi.org/10.1093/petrology/egx082

Dilek, Y., and Altunkaynak, S. (2010). Geochemistry of Neogene-Quaternary alkaline volcanism in western Anatolia, Turkey, and implications for the Aegean mantle. International Geology Review, 52(4–6), 631–655. https://doi.org/10.1080/00206810903495020

Dilek, Y., Imamverdiyev, N., and Altunkaynak, Ş. (2010). Geochemistry and tectonics of Cenozoic volcanism in the Lesser Caucasus (Azerbaijan) and the peri-Arabian region: Collision-induced mantle dynamics and its magmatic fingerprint. International Geology Review, 52(4–6), 536–578. https://doi.org/10.1080/00206810903360422

Dilek, Y, and Whitney, D. L. (2000). Cenozoic crustal evolution in Central Anatolia: extension, magmatism and landscape development. Third International Conference on the Geology of the Eastern Mediterranean, Proceedings, January, 183-192\r376.

Downes, H. (2001). Formation and modification of the shallow sub-continental lithospheric mantle: A review of geochemical evidence from ultramatic xenolith suites and tectonically emplaced ultramafic massifs of Western and Central Europe. Journal of Petrology, 42(1), 233–250. https://doi.org/10.1093/petrology/42.1.233

Duggen, S., Hoernle, K., van den Bogaard, P., and Garbe-Schönberg, D. (2005). Post-collisional transition from subduction-to intraplate-type magmatism in the westernmost Mediterranean: Evidence for continental-edge delamination of subcontinental lithosphere. Journal of Petrology, 46(6), 1155–1201. https://doi.org/10.1093/petrology/egi013

Dupré, B., and Allègre, C. J. (1983). Pb–Sr isotope variation in Indian Ocean basalts and mixing phenomena. Nature, 303(5913), 142–146. https://doi.org/10.1038/303142a0

Eggler, D. ., and Holloway, J. R. (1977). Partial melting of peridotite in the presence of H_2O and CO_2 : Principles and review. In H. J. . Dick (Ed.), Magma Genesis (pp. 15–36). Oregon Department of Geology and Mineral Industries Bulletin 96.

Eisele, J., Sharma, M., Galer, S. J. G., Blichert-Toft, J., Devey, C. W., and Hofmann, A. W. (2002). The role of sediment recycling in EM-1 inferred from Os, Pb, Hf, Nd, Sr isotope and trace element systematics of the Pitcairn hotspot. Earth and Planetary Science Letters, 196(3–4), 197–212. https://doi.org/10.1016/S0012-821X(01)00601-X

Ekici, T., Macpherson, C. G., Otlu, N., and Fontignie, D. (2014). Foreland magmatism during the Arabia-Eurasia collision: Pliocene-Quaternary activity of the Karacadağ volcanic complex, SW Turkey. Journal of Petrology, 55(9), 1753–1777. https://doi.org/10.1093/petrology/egu040

Elitok, Ö., Özgür, N., Drüppel, K., Dilek, Y., Platevoet, B., Guillou, H., Poisson, A., Scaillet, S., Satr, M., Siebel, W., Bardintzeff, J. M., Deniel, C., and Ylmaz, K. (2010). Origin and geodynamic evolution of late Cenozoic potassium-rich volcanism in the Isparta area, southwestern Turkey. International Geology Review, 52(4–6), 454–504. https://doi.org/10.1080/00206810902951411

Elkins-Tanton, L. T. (2005). Continental magmatism caused by lithospheric delamination. In Plates, plumes and paradigms (Vol. 2388, Issue 27, pp. 449–461). Geological Society of America. https://doi.org/10.1130/0-8137-2388-

4.449

Elkins-Tanton, L. T. (2007). Continental magmatism, volatile recycling, and a heterogeneous mantle caused by lithospheric gravitational instabilities. Journal of Geophysical Research, 112(B3), B03405. https://doi.org/10.1029/2005JB004072

Elliott, T., Plank, T., Zindler, A., White, W., and Bourdon, B. (1997). Element transport from slab to volcanic front at the Mariana arc. Journal of Geophysical Research: Solid Earth, 102(B7), 14991–15019. https://doi.org/10.1029/97JB00788

Endress, C., Furman, T., El-Rus, M. A. A., and Hanan, B. B. (2011). Geochemistry of 24 Ma basalts from NE Egypt: Source components and fractionation history. Geological Society Special Publication, 357(1), 265–283. https://doi.org/10.1144/SP357.14

Ercan, T., and Asutay, H. J. (1993). Malatya-Elazığ-Tunceli-Bingöl-Diyarbakır dolaylarındaki Neojen-Kuvaterner yaşlı volkanitlerin petrolojisi. A. Suat ERK Jeoloji Sempozyumu, 291–302.

Erdoğan, T. (1975). Gölbaşı yöresinin jeolojisi. TPAO Raporu, No: 229, 18s.

Escrig, S., Capmas, F., Dupré, B., and Allègre, C. J. (2004). Osmium isotopic constraints on the nature of the DUPAL anomaly from Indian mid-ocean-ridge basalts. Nature, 431(7004), 59–63. https://doi.org/10.1038/nature02904

Esperança, S., and Crisci, G. M. (1995). The island of Pantelleria: A case for the development of DMM-HIMU isotopic compositions in a long-lived extensional setting. Earth and Planetary Science Letters, 136(3–4), 167–182. https://doi.org/10.1016/0012-821X(95)00178-F

Farley, K. A., Natland, J. H., and Craig, H. (1992). Binary mixing of enriched and undegassed (primitive?) mantle components (He, Sr, Nd, Pb) in Samoan lavas. Earth and Planetary Science Letters, 111(1), 183–199. https://doi.org/10.1016/0012-821X(92)90178-X

Faure, F., Schiano, P., Trolliard, G., Nicollet, C., and Soulestin, B. (2007). Textural evolution of polyhedral olivine experiencing rapid cooling rates. Contributions to Mineralogy and Petrology, 153(4), 405–416. https://doi.org/10.1007/s00410-006-0154-8

Faure, F., Trolliard, G., Nicollet, C., and Montel, J.-M. (2003). A developmental model of olivine morphology as a function of the cooling rate and the degree of undercooling. Contributions to Mineralogy and Petrology, 145(2), 251–263. https://doi.org/10.1007/s00410-003-0449-y

Faure, G., and Hurley. (1963). The Isotopic Composition of Strontium in Oceanic and Continental Basalts : Application to the Origin of Igneous Rocks. 4(1), 31–50. https://doi.org/https://doi.org/10.1093/petrology/4.1.31

Fontignie, D., and Schilling, J. G. (1996). Mantle heterogeneities beneath the South Atlantic: A Nd-Sr-Pb isotope study along the Mid-Atlantic Ridge (3°S-46°S). Earth and Planetary Science Letters, 142(1–2), 209–221. https://doi.org/10.1016/0012-821x(96)00079-9

Fujii, T., and Scarfe, C. M. (1985). Composition of liquids coexisting with spinel lherzolite at 10 kbar and the genesis of MORBs. Contributions to Mineralogy and Petrology, 90(1), 18–28. https://doi.org/10.1007/BF00373037

Furman, T. (2007). Geochemistry of East African Rift basalts : An overview. Journal of African Earth Sciences, 48, 147–160. https://doi.org/10.1016/j.jafrearsci.2006.06.009

Furman, T., Frey, F. A., and Park, K. H. (1991). Chemical constraints on the petrogenesis of mildly alkaline lavas from Vestmannaeyjar, Iceland: the Eldfell (1973) and Surtsey (1963-1967) eruptions. Contributions to Mineralogy and Petrology, 109(1), 19–37. https://doi.org/10.1007/BF00687198

Furman, T., and Graham, D. (1999). Erosion of lithospheric mantle beneath the East African Rift system: geochemical evidence from the Kivu volcanic province. Lithos, 48(1–4), 237–262. https://doi.org/10.1016/S0024-4937(99)00031-6

Furman, T., Hanan, B. B., Pickard Sjoblom, M., Kürkcüoğlu, B., Sayit, K., Şen, E., Alıcı Şen, P., and Yürür, T. (2021). Evolution of mafic lavas in Central Anatolia: Mantle source domains. Geosphere. https://doi.org/10.1130/GES02329.1

Furman, T., Kaleta, K. M., Bryce, J. G., and Hanan, B. B. (2006). Tertiary Mafic Lavas of Turkana , Kenya : Constraints on East African Plume Structure and the Occurrence of High-μ Volcanism in Africa. 47(6), 1221–1244. https://doi.org/10.1093/petrology/egl009

Furman, T., Nelson, W. R., and Elkins-Tanton, L. T. (2016). Evolution of the East African rift: Drip magmatism, lithospheric thinning and mafic volcanism. Geochimica et Cosmochimica Acta, 185, 418–434. https://doi.org/10.1016/j.gca.2016.03.024

Gall, H., Furman, T., Hanan, B., Kürkcüoğlu, B., Sayıt, K., Yürür, T., Sjoblom, M. P., Şen, E., and Şen, P. A. (2021). Post-delamination magmatism in south-central Anatolia. Lithos, 398–399, 106299. https://doi.org/10.1016/j.lithos.2021.106299

Garcia, M. O. (1996). Petrography and olivine and glass chemistry of lavas from the Hawaii Scientific Drilling Project. Journal of Geophysical Research: Solid Earth, 101(B5), 11701–11713. https://doi.org/10.1029/95JB03846

Gast, P. W. (1960). Limitations on the Composition of the Upper Mantle. Journal of Geophysical Research, 65(4), 1287–1297.

Gast, P. W., Tilton, G. R., and Hedge, C. (1964). Isotopic Composition of Lead and Strontium from Ascension and Gough Islands. Science, 145(3637), 1181–1185. https://doi.org/10.1126/science.145.3637.1181

Geldmacher, J., Hoernle, K., Hanan, B. B., Blichert-Toft, J., Hauff, F., Gill, J. B., and Schmincke, H. (2011). Hafnium isotopic variations in East Atlantic intraplate volcanism. Contributions to Mineralogy and Petrology, 162(1), 21–36. https://doi.org/10.1007/s00410-010-0580-5

Gibson, S. A., Thompson, R. N., Leat, P. T., Morrison, M. A., Hendry, G. L., Dickin, A. P., and Mitchell, J. G. (1993). Ultrapotassic magmas along the flanks of the oligo-miocene rio grande rift, USA: Monitors of the zone of lithospheric mantle extension and thinning beneath a continental rift. Journal of Petrology, 34(1), 187–228. https://doi.org/10.1093/petrology/34.1.187

Gök, R., Sandvol, E., Türkelli, N., Seber, D., and Barazangi, M. (2003). Sn attenuation in the Anatolian and Iranian plateau and surrounding regions.

Geophysical Research Letters, 30(24), 3–6. https://doi.org/10.1029/2003GL018020

Gök, R., Türkelli, N., Sandvol, E., Seber, D., and Barazangi, M. (2000). Regional wave propagation in Turkey and surrounding regions. Geophysical Research Letters, 27(3), 429–432. https://doi.org/10.1029/1999GL008375

Göğüş, O. H., Pysklywec, R. N., Şengör, A. M. C., and Gün, E. (2017). Drip tectonics and the enigmatic uplift of the Central Anatolian Plateau. Nature Communications, 8(1), 1538. https://doi.org/10.1038/s41467-017-01611-3

Göncüoğlu, M.C. (2010). Introduction to the Geology of Turkey: Geodynamic Evolution of the pre-Alpine and Alpine Terranes. MTA Monography Series, 5(January), 1–69.

Göncüoğlu, M. C. (2019). A Review of the Geology and Geodynamic Evolution of Tectonic Terranes in Turkey BT - Mineral Resources of Turkey (F. Pirajno, T. Ünlü, C. Dönmez, and M. B. Şahin (eds.); pp. 19–72). Springer International Publishing. https://doi.org/10.1007/978-3-030-02950-0_2

Göncüoğlu, M. C., Dirik, K., and Kozlu, H. (1997). Pre-Alpine and Alpine Terranes in Turkey: explanatory notes to the terrane map of Turkey. Annales Geologique de Pays Hellenique, 37, 515–536.

Göncüoğlu, M.C., and Turhan, N. (1984). Geology of the Bitlis Metamorphic Belt. In O. Tekeli and M. C. Göncüoğlu (Eds.), Proceed. Intern. Symp. Geology of the Taurus Belt (pp. 237–244). MTA Publications.

Göncüoglu, M. C., Turhan, N., and Tekin, U. K. (2003). Evidence for the Triassic rifting and opening of the Neotethyan Izmir-Ankara Ocean and discussion on the presence of Cimmerian events at the northern edge of the Tauride-Anatolide Platform, Turkey. Bollettino Della Societa Geologica Italiana, 2(1), 203–212.

Görür, N., Sengor, A. M. C., Akkok, R., and Yılmaz, Y. (1983). Pontidlerde Neo - Tetis ’ in kuzey kolunun açılmasına ilişkin sedimentolojik veriler. Türkiye Jeoloji Bülteni, February, 11–20.

Görür, N., Tuysuz, O., Aykol, A., Sakinc, M., Yigitbas, E., and Akkok, R. (1993). Cretaceous red pelagic carbonates of northern Turkey: their place in the opening history of the Black Sea. Eclogae Geologicae Helvetiae, 86(3), 819–838.

Granet, M., Wilson, M., and Achauer, U. (1995). Imaging a mantle plume beneath the French Massif Central. Earth and Planetary Science Letters, 136(3–4), 281–296. https://doi.org/10.1016/0012-821X(95)00174-B

Green, D. H. (1973). Conditions of melting of basanite magma from garnet peridotite. Earth and Planetary Science Letters, 17(2), 456–465. https://doi.org/10.1016/0012-821X(73)90214-8

Griffin, W. L., O'Reilly, S. Y., Afonso, J. C., and Begg, G. C. (2009). The composition and evolution of lithospheric mantle: A re-evaluation and its tectonic implications. Journal of Petrology, 50(7), 1185–1204. https://doi.org/10.1093/petrology/egn033

Gürsu, S., Möller, A., Göncüoglu, M. C., Köksal, S., Demircan, H., Köksal, F. T., Kozlu, H., and Sunal, G. (2015). Neoproterozoic continental arc volcanism at the northern edge of the Arabian Plate, SE Turkey. Precambrian Research, 258, 208–233. https://doi.org/10.1016/j.precamres.2014.12.017

Hall, R. (1976). Ophiolite emplacement and the evolution of the Taurus suture zone, southeastern Turkey. Bulletin of the Geological Society of America, 87(7), 1078–1088. https://doi.org/10.1130/0016-7606(1976)87<1078:OEATEO>2.0.CO;2

Halliday, A. N., Davies, G. R., Lee, D. C., Tommasini, S., Paslick, C. R., Fitton, J. G., and James, D. E. (1992). Lead isotope evidence for young trace element enrichment in the oceanic upper mantle. Nature, 359(6396), 623–627. https://doi.org/10.1038/359623a0

Halliday, A. N., Lee, D., Tommasini, S., Davies, G. R., Paslick, C. R., Godfrey Fitton, J., and James, D. E. (1995). Incompatible trace elements in OIB and MORB and source enrichment in the sub-oceanic mantle. Earth and Planetary Science Letters, 133(3–4), 379–395. https://doi.org/10.1016/0012-821X(95)00097-V

Hanan, B.B, and Graham, D. (1996). Lead and Helium Isotope Evidence from Oceanic Basalts for a Common Deep Source of Mantle Plumes. Science, 272.

Hanan, B. B., Blichert-Toft, J., Pyle, D., and Christie, D. (2004). Constrasting origins of the upper mantle revealed by hafnium and lead isotopes from the Southeast Indian Ridge. Nature, 432, 91–94.

Hanan, B. B., Kingsley, R. H., and Schilling, J. G. (1986). Pb isotope evidence in the South Atlantic for migrating ridge - Hotspot interactions. Nature, 322(6075), 137–144. https://doi.org/10.1038/322137a0

Hanan, B. B., Shervais, J. W., and Vetter, S. K. (2008). Yellowstone plume-continental lithosphere interaction beneath the Snake River Plain. Geology, 36(1), 51–54. https://doi.org/10.1130/G23935A.1

Hart, S. R. (1969). K, Rb, Cs Contents and K/Rb, K/Cs Ratios of Fresh and Altered Submarine Basalts. Earth and Planetary Science Letters, 6, 295–303. https://doi.org/https://doi.org/10.1016/0012-821X(69)90171-X

Hart, S. R. (1971). K, Rb, Cs, Sr and Ba Contents and Sr Isotope Ratios of Ocean Floor Basalts. Philosophical Transactions of the Royal Society A: Mathematical, Physical and Engineering Sciences, 268(1192), 573–587. https://doi.org/10.1098/rsta.1971.0013

Hart, S. R. (1984). A large-scale isotope anomaly in the Southern Hemisphere mantle. Nature, 309(5971), 753–757. https://doi.org/10.1038/309753a0

Hart, S. R., and Davies, K. E. (1978). Nickel Partitioning Between Olivine and Silica Melt. Earth and Planetary Science Letters, 40, 203–219. https://doi.org/10.1016/0012-821X(78)90091-2

Hart, S. R., Hauri, E. H., Oschmann, L. A., and Whitehead, J. A. (1992). Mantle Plumes and Entrainment: Isotopic Evidence. Science, 256(5056), 517–520. https://doi.org/10.1126/science.256.5056.517

Hart, S. R., Schilling, J. G., and Powell, J. L. (1973). Basalts from Iceland and Along the Reykjanes Ridge: Sr Isotope Geochemistry. Nature Physical Science, 246(155), 104–107. https://doi.org/10.1038/physci246104a0

Hartmann, G., and Wedepohl, K. H. (1993). The composition of peridotite tectonites from the Ivrea Complex, northern Italy: Residues from melt extraction. Geochimica et Cosmochimica Acta, 57(8), 1761–1782.

https://doi.org/10.1016/0016-7037(93)90112-A

Hawkesworth, C. J., Erlank, A. J., Marsh, J. S., Menzies, M. A., and V.Calsteren, P. (1983). Evolution of the continental lithosphere: evidence from volcanics and xenoliths from southern Africa. In C. J. . Hawkesworth and M. J. Norry (Eds.), Continental basalts and mantle xenoliths (pp. 111–138). Shiva.

Hawkesworth, C. J., Mantovani, M. S. M., Taylor, P. N., and Palacz, Z. (1986). Evidence from the Parana of south Brazil for a continental contribution to Dupal basalts. Nature, 322(6077), 356–359. https://doi.org/10.1038/322356a0

Hawkesworth, C. J., Norry, M. J., Roddick, J. C., and Vollmer, R. (1979). ^{143}Nd/^{144}Nd and ^{87}Sr/^{86}Sr ratios from the Azores and their significance in LIL-element enriched mantle. Nature, 280(5717), 28–31. https://doi.org/10.1038/280028a0

Hedge, C. E. (1966). Variations in radiogenic strontium found in volcanic rocks. Journal of Geophysical Research, 71(24), 6119–6126. https://doi.org/10.1029/jz071i024p06119

Hempton, M. R., and Savci, G. (1982). Elazığ volkanik karmaşığının petrolojik ve yapısal özellikleri. TJK Bülteni, 25, 143–150.

Herece, E. (2016a). 1:100.000 ölçekli Türkiye Jeoloji Haritaları Serisi, Elazığ K-42 Paftası No: 234. MTA Genel Müdürlüğü Yayınları.

Herece, E. (2016b). Altınkuşak (Elazığ) ile Pertak (Tunceli) arasındaki alanın jeolojisi. MTA Raporu, No: 11907.

Herece, E., Akay, E., Küçümen, Ö., and Sarıaslan, M. (1992). Elazığ-Sivrice-Palu dolayının jeolojisi. MTA Raporu, No: 9634.

Herece, E. İ., and Acar, Ş. (2016). Upper Cretaceous-Tertiary Geology/Stratigraphy of Pertek and Its Vicinity Tunceli, Turkey). Bulletin Of The Mineral Research and Exploration, 153, 1–44. https://doi.org/10.19111/bmre.38353

Hergt, J. M., Peate, D. W., and Hawkesworth, C. J. (1991). The petrogenesis of Mesozoic Gondwana low-Ti flood basalts. Earth and Planetary Science Letters, 105(1–3), 134–148. https://doi.org/10.1016/0012-821X(91)90126-3

Hidalgo, S., Gerbe, M. C., Martin, H., Samaniego, P., and Bourdon, E. (2012). Role of crustal and slab components in the Northern Volcanic Zone of the Andes (Ecuador) constrained by Sr–Nd–O isotopes. Lithos, 132–133, 180–192. https://doi.org/10.1016/j.lithos.2011.11.019

Hoernle, K., Zhang, Y.S., and Graham, D. (1995). Seismic and Geochemical Evidence for Large-scale Mantle Upwelling Beneath the Eastern Atlantic and Western and Central Europe. Nature, 374, 34–39. https://doi.org/https://doi.org/10.1038/374034a0

Hofmann, A. W. (1997). Mantle geochemistry: the message from oceanic magmatism. Nature, 385, 219–229.

Hofmann, A W. (2003). Sampling Mantle Heterogeneity through Oceanic Basalts: Isotopes and Trace Elements (H. D. Holland and K. K. B. T.-T. on G. (Second E. Turekian (eds.); pp. 61–101). Elsevier. https://doi.org/https://doi.org/10.1016/B978-0-08-095975-7.00203-5

Hofmann, A. W., and Hart, S. R. (1978). An assessment of local and regional isotopic equilibrium in the mantle. Developments in Petrology, 5(C), 44–62. https://doi.org/10.1016/B978-0-444-41658-2.50008-0

Hofmann, A.W., Jochum, K. P., Seufert, M., and White, W. M. (1986). Nb and Pb in oceanic basalts: new constraints on mantle evolution. Earth and Planetary Science Letters, 79(1–2), 33–45. https://doi.org/10.1016/0012-821X(86)90038-5

Hofmann, A. W., and White, W. M. (1982). Mantle plumes from ancient oceanic crust. Earth and Planetary Science Letters, 57(2), 421–436. https://doi.org/10.1016/0012-821X(82)90161-3

Humphris, S. E., and Thompson, G. (1978). Trace element mobility during hydrothermal alteration of oceanic basalts. Geochimica et Cosmochimica Acta, 42(1), 127–136. https://doi.org/10.1016/0016-7037(78)90222-3

Humphris, S. E., Thompson, G., Schilling, J. G., and Kingsley, R. H. (1985). Petrological and geochemical variations along the Mid-Atlantic Ridge between

46°S and 32°S: Influence of the Tristan da Cunha mantle plume. Geochimica et Cosmochimica Acta, 49(6), 1445–1464. https://doi.org/10.1016/0016-7037(85)90294-7

Hurley, P. M., Hughes, H., Fauae, G., Fairbairn, H. W., and Pinson, W. H. (1962). Radiogenic Strontium-87 Model of Continent Formation. Journal of Geophysical Research, 67(13), 5315–5334.

İnceöz, M. (1994). Harput (Elazığ) Yakın Kuzeyi ve Doğusunun Jeolojik Özellikleri. Doktora Tezi, Fırat Universitesi, Fen Bilimleri Enstitüsü, Elazığ, 112s.

Irvine, T. N., and Baragar, W. R. A. (1971). A Guide to the Chemical Classification of the Common Volcanic Rocks. Canadian Journal of Earth Sciences, 8(5), 523–548. https://doi.org/10.1139/e71-055

Jackson, M. G., and Hart, S. R. (2006). Strontium isotopes in melt inclusions from Samoan basalts : Implications for heterogeneity in the Samoan plume. 245, 260–277. https://doi.org/10.1016/j.epsl.2006.02.040

Jackson, M. G., Hart, S. R., Koppers, A. A. P., Staudigel, H., Konter, J., Blusztajn, J., Kurz, M., and Russell, J. A. (2007). The return of subducted continental crust in Samoan lavas. Nature, 448(7154), 684–687. https://doi.org/10.1038/nature06048

Jackson, M. G., Hart, S. R., Saal, A. E., Shimizu, N., Kurz, M. D., Blusztajn, J. S., and Skovgaard, A. C. (2008). Globally elevated titanium, tantalum, and niobium (TITAN) in ocean island basalts with high ^{3}He/^{4}He. Geochemistry, Geophysics, Geosystems, 9(4). https://doi.org/10.1029/2007GC001876

Jacobsen, S. B., and Wasserburg, G. J. (1979). The Mean Age of Mantle and Crustal Reservoirs. Journal of Geophysical Research, 84, 7411–7428. https://doi.org/https://doi.org/10.1029/JB084iB13p07411

Jochum, K. P., and Verma, S. P. (1996). Extreme enrichment of Sb, Tl and other trace elements in altered MORB. Chemical Geology, 130(3–4), 289–299. https://doi.org/10.1016/0009-2541(96)00014-9

Johnson, M. C., and Plank, T. (1999). Dehydration and melting experiments constrain the fate of subducted sediments. Geochemistry, Geophysics, Geosystems, 1(12), n/a-n/a. https://doi.org/10.1029/1999GC000014

Jung, C., Jung, S., Hoffer, E., and Berndt, J. (2006). Petrogenesis of Tertiary Mafic Alkaline Magmas in the Hocheifel, Germany. Journal of Petrology, 47(8), 1637–1671. https://doi.org/10.1093/petrology/egl023

Jung, S., and Hoernes, S. (2000). The major- and trace-element and isotope (Sr, Nd, O) geochemistry of Cenozoic alkaline rift-type volcanic rocks from the Rhön area (central Germany): Petrology, mantle source characteristics and implications for asthenosphere-lithosphere interactions. Journal of Volcanology and Geothermal Research, 99(1–4), 27–53. https://doi.org/10.1016/S0377-0273(00)00156-6

Jung, S., Pfänder, J. A., Brügmann, G., and Stracke, A. (2005). Sources of primitive alkaline volcanic rocks from the Central European Volcanic Province (Rhön, Germany) inferred from Hf, Os and Pb isotopes. Contributions to Mineralogy and Petrology, 150(5), 546–559. https://doi.org/10.1007/s00410-005-0029-4

Karaoğlu, Ö., Gülmez, F., Göçmengil, G., Lustrino, M., Di Giuseppe, P., Manetti, P., Savaşçın, M. Y., and Agostini, S. (2020). Petrological evolution of Karlıova-Varto volcanism (Eastern Turkey): Magma genesis in a transtensional triple-junction tectonic setting. Lithos, 364–365, 1–15. https://doi.org/10.1016/j.lithos.2020.105524

Karaoğlu, Ö., Yavuz, Ö., Tolluoğlu, Ü., Karabıyıkoğlu, M., Köse, O., and Froger, J. L. (2005). Stratigraphy of the volcanic products around Nemrut caldera: Implications for reconstruction of the caldera formation. Turkish Journal of Earth Sciences, 14(2), 123–143.

Kelley, K. A., Kingsley, R., and Schilling, J. (2013). Composition of plume-influenced mid-ocean ridge lavas and glasses from the Mid-Atlantic Ridge, East Pacific Rise, Galápagos Spreading Center, and Gulf of Aden. 14(1). https://doi.org/10.1029/2012GC004415

Kerey, E., and Türkmen, İ. (1991). Palu Formasyonu'nun (Pliyosen-Kuvaterner) Sedimantolojik özellikler, Elazığ Doğusu. TJK Bülteni, 34(February), 21–26.

Keskin, M. (1994). Genesis of collision-related volcanism on the Erzurum-Kars Plateau, Northeastern Turkey. PhD Thesis, University of Durham, Durham, 391pp.

Keskin, M. (1998). Erzurum - Kars Platosunun Çarpışma Kökenli Volkanizmasının Volkanostratigrafisi ve Yeni K/Ar Yaş Bulguları Işığında Evrimi, Kuzeydoğu Anadolu. MTA Dergisi, 120, 135–157.

Keskin, M.. (2003). Magma generation by slab steepening and breakoff beneath a subduction-accretion complex: An alternative model for collision-related volcanism in Eastern Anatolia, Turkey. Geophysical Research Letters, 30(24), 7–10. https://doi.org/10.1029/2003GL018019

Keskin, M.. (2007). Eastern Anatolia: A hotspot in a collision zone without a mantle plume. Special Paper of the Geological Society of America, 430, 693–722. https://doi.org/10.1130/2007.2430(32)

Keskin, M., Chugaev, A. V., Lebedev, V. A., Sharkov, E. V., Oyan, V., and Kavak, O. (2012a). The geochronology and origin of mantle sources for late cenozoic intraplate volcanism in the frontal part of the Arabian plate in the Karacadağ neovolcanic area of Turkey. Part 1. The results of isotope-geochronological studies. Journal of Volcanology and Seismology, 6(6), 352–360. https://doi.org/10.1134/S0742046312060036

Keskin, M., Chugaev, A. V., Lebedev, V. A., Sharkov, E. V., Oyan, V., and Kavak, O. (2012b). The geochronology and origin of mantle sources for late cenozoic intraplate volcanism in the frontal part of the Arabian plate in the Karacadağ neovolcanic area of Turkey. Part 2. The results of geochemical and isotope (Sr-Nd-Pb) studies. Journal of Volcanology and Seismology, 6(6), 361–382. https://doi.org/10.1134/S0742046312060048

Keskin, M., Genç, Ş. C., and Tüysüz, O. (2008). Petrology and geochemistry of post-collisional Middle Eocene volcanic units in North-Central Turkey: Evidence for magma generation by slab breakoff following the closure of the Northern Neotethys Ocean. Lithos, 104(1–4), 267–305. https://doi.org/10.1016/j.lithos.2007.12.011

Keskin, M., Pearce, J. A., and Mitchell, J. G. (1998). Volcano-stratigraphy and geochemistry of collision-related volcanism on the Erzurum-Kars Plateau, northeastern Turkey. Journal of Volcanology and Geothermal Research, 85(1–4), 355–404. https://doi.org/10.1016/S0377-0273(98)00063-8

Ketin, I. (1966). Anadolu’nun tektonik birlikleri. Maden Tetkik ve Arama Dergisi, 66(66), 23-34 (in Turkish). https://doi.org/10.19076/MTA.18509

Kipman, E. (1976). Keban’ın jeolojisi ve volkanitlerinin petrolojisi. Doktora Tezi, İstanbul Ünivesitesi, Fen Bilimleri Enstitüsü, 91s.

Klaver, M., Djuly, T., de Graaf, S., Sakes, A., Wijbrans, J., Davies, G., and Vroon, P. (2015). Temporal and spatial variations in provenance of Eastern Mediterranean Sea sediments: Implications for Aegean and Aeolian arc volcanism. Geochimica et Cosmochimica Acta, 153, 149–168. https://doi.org/10.1016/j.gca.2015.01.007

Kocaarslan, A., and Ersoy, E. Y. (2018). Petrologic evolution of Miocene-Pliocene mafic volcanism in the Kangal and Gürün basins (Sivas-Malatya), central east Anatolia: Evidence for Miocene anorogenic magmas contaminated by continental crust. Lithos, 310–311, 392–408. https://doi.org/10.1016/j.lithos.2018.04.021

Köksal, S., Toksoy-Köksal, F., and Göncüoglu, M. C. (2017). Petrogenesis and geodynamics of plagiogranites from Central Turkey (Ekecikdağ/Aksaray): new geochemical and isotopic data for generation in an arc basin system within the northern branch of Neotethys. International Journal of Earth Sciences, 106(4), 1181–1203. https://doi.org/10.1007/s00531-016-1401-5

Kürkcüoğlu, B., and Yürür, M. T. (2021). Source constraints for the young basaltic rocks from the northernmost end of Cappadocian region, Turkey: Melting evidence from peridotite and pyroxenite source domains. Geochemistry, 125838. https://doi.org/10.1016/j.chemer.2021.125838

Kürüm, S. (1994). Elazığ Kuzeybatısındaki Genç Volkanitlerin Petrolojik Özellikleri. Doktora Tezi, Fırat Üniversitesi, Fen Bilimleri Enstitüsü, 106s.

Lambert, R. S. J., Holland, J. G., and Owen, P. F. (1974). Chemical petrology of a suite of calc-alkaline lavas from Mount Ararat, Turkey. The Journal of Geology, 82(4), 419–438.

Lassiter, J. C., Blichert-Toft, J., Hauri, E. H., and Barsczus, H. G. (2003). Isotope and trace element variations in lavas from Raivavae and Rapa, Cook-Austral islands: Constraints on the nature of HIMU- and EM-mantle and the origin of mid-plate volcanism in French Polynesia. Chemical Geology, 202(1–2), 115–138. https://doi.org/10.1016/j.chemgeo.2003.08.002

Le Bas, M. J., Maitre, R. W. L., Streckeisen, A., and Zanettin, B. (1986). A chemical classification of volcanic rocks based on the total alkali-silica diagram. Journal of Petrology, 27(3), 745–750. https://doi.org/10.1093/petrology/27.3.745

Lebedev, V. A., Parfenov, A. V., and Yakushev, A. I. (2018). Neogene–Quaternary Magmatism of the Çaldıran Plain and its Vicinity (Eastern Turkey): an Example of Post-Collisional Transition from Subduction to Intraplate Type. Petrology, 26(5), 469–491. https://doi.org/10.1134/s0869591118050053

Lebedev, V. A., Sharkov, E. V., Ünal, E., and Keskin, M. (2016). Late Pleistocene Tendürek Volcano (Eastern Anatolia, Turkey): I. Geochronology and Petrographic Characteristics of Igneous Rocks. Петрология, 24(2), 142–167. https://doi.org/10.7868/s0869590316020047

Loock, G., Stosch, H.-G., and Seck, H. A. (1990). Granulite facies lower crustal xenoliths from the Eifel, West Germany: petrological and geochemical aspects. Contributions to Mineralogy and Petrology, 105(1), 25–41. https://doi.org/10.1007/BF00320964

Lustrino, M., Keskin, M., Mattioli, M., Lebedev, V. A., Chugaev, A., Sharkov, E., and Kavak, O. (2010). Early activity of the largest Cenozoic shield volcano in the circum-Mediterranean area: Mt. Karacadağ, SE Turkey. European Journal of Mineralogy, 22(3), 343–362. https://doi.org/10.1127/0935-1221/2010/0022-2024

Lustrino, M., Melluso, L., and Morra, V. (2000). The role of lower continental crust and lithospheric mantle in the genesis of Plio–Pleistocene volcanic rocks from Sardinia (Italy). Earth and Planetary Science Letters, 180(3–4), 259–270. https://doi.org/10.1016/S0012-821X(00)00185-0

Lustrino, M., and Wilson, M. (2007). The circum-Mediterranean anorogenic Cenozoic igneous province. Earth-Science Reviews, 81(1–2), 1–65. https://doi.org/https://doi.org/10.1038/nature06688002

Mahoney, J., Nicollet, C., and Dupuy, C. (1991). Madagascar basalts: tracking oceanic and continental sources. Earth and Planetary Science Letters, 104(2–4), 350–363. https://doi.org/10.1016/0012-821X(91)90215-4

Mayer, B., Jung, S., Romer, R. L., Stracke, A., Haase, K. M., and Garbe-Schönberg, C. D. (2013). Petrogenesis of tertiary hornblende-bearing lavas in the rhön, germany. Journal of Petrology, 54(10), 2095–2123. https://doi.org/10.1093/petrology/egt042

McCulloch, M. T., and Gamble, J. A. (1991). Geochemical and geodynamical constraints on subduction zone magmatism. Earth and Planetary Science Letters, 102(3–4), 358–374. https://doi.org/10.1016/0012-821X(91)90029-H

McDonough, W. F. (1990). Constraints on the composition of the continental lithospheric mantle. Earth and Planetary Science Letters, 101(1), 1–18. https://doi.org/10.1016/0012-821X(90)90119-I

McDonough, W. F., and Frey, F. . (1989). REE in upper mantle rocks. In B. Lipin and G. R. McKay (Eds.), Geochemistry and Mineralogy of Rare Earth Elements (pp. 99–145). Mineral. Soc. Am.,.

McGoldrick, P. J., Keays, R. R., and Scott, B. B. (1979). Thallium: a sensitive indicator of rock/seawater interaction and of sulfur saturation of silicate melts. Geochimica et Cosmochimica Acta, 43(8), 1303–1311. https://doi.org/10.1016/0016-7037(79)90120-0

Mckenzie, D., and Bickle, M. J. (1988). The volume and composition of melt generated by extension of the lithosphere. Journal of Petrology, 29(3), 625–679. https://doi.org/10.1093/petrology/29.3.625

McKenzie, D., and O’Nions, R. K. (1983). Mantle reservoirs and ocean island basalts. Nature, 301(5897), 229–231. https://doi.org/10.1038/301229a0

McKenzie, D., and O’Nions, R. K. (1991). Partial Melt Distributions from Inversion of Rare Earth Element Concentrations. Journal of Petrology, 32(5), 1021–1091. https://doi.org/10.1093/petrology/32.5.1021

Menzies, M. A. (1983). Mantle ultramafic xenoliths in alkaline magmas : evidence for mantle heterogeneity modified by magmatic activity. In C. J. Hawkesworth and M. J. Norry (Eds.), Continental Basalts and Mantle Xenoliths (pp. 91–110). Cheshire, Engl: Shiva. 272 pp.

Menzies, M. A. (1992). The lower lithosphere as a major source for continental flood basalts: A re-appraisal. Geological Society Special Publication, 68(68), 31–39. https://doi.org/10.1144/GSL.SP.1992.068.01.03

Miyashiro, A. (1974). Volcanic rock series in island arcs and active continental margins. American Journal of Science, 274(4), 321–355. https://doi.org/10.2475/ajs.274.4.321

Miyashiro, A. (1978). Nature of alkalic volcanic rock series. Contributions to Mineralogy and Petrology, 66(1), 91–104. https://doi.org/10.1007/BF00376089

Morimoto, N. (1988). Nomenclature of Pyroxenes. Mineralogy and Petrology, 39(1), 55–76. https://doi.org/10.1007/BF01226262

Münker, C., Weyer, S., Scherer, E., and Mezger, K. (2001). Separation of high field strength elements (Nb, Ta, Zr, Hf) and Lu from rock samples for MC-ICPMS measurements. Geochemistry, Geophysics, Geosystems, 2(12). https://doi.org/10.1029/2001GC000183

Naz, N. (1979). Elazığ-Palu dolayının jeolojisi. TPAO Raporu, No: 1360.

Nelson, W. R., Furman, T., van Keken, P. E., Shirey, S. B., and Hanan, B. B. (2012). OsHf isotopic insight into mantle plume dynamics beneath the East African Rift System. Chemical Geology, 320–321, 66–79. https://doi.org/10.1016/j.chemgeo.2012.05.020

Niu, Y., and O’Hara, M. J. (2003). Origin of ocean island basalts: A new perspective from petrology, geochemistry, and mineral physics considerations. Journal of Geophysical Research: Solid Earth, 108(B4). https://doi.org/10.1029/2002jb002048

Notsu, K., Fujitani, T., Ui, T., Matsuda, J., and Ercan, T. (1995). Geochemical features of collision-related volcanic rocks in central and eastern Anatolia, Turkey. Journal of Volcanology and Geothermal Research, 64(3–4), 171–191. https://doi.org/10.1016/0377-0273(94)00077-T

O’Nions, R. K., Evensen, N. M., and Hamilton, P. J. (1979). Geochemical modeling of mantle differentiation and crustal growth. Journal of Geophysical Research, 84(B11), 6091–6101. https://doi.org/10.1029/JB084iB11p06091

Oberhänsli, R., Bousquet, R., Candan, O., and Okay, A. I. (2012). Dating subduction events in East Anatolia, Turkey. Turkish Journal of Earth Sciences, 21(1), 1–17. https://doi.org/10.3906/yer-1006-26

Oberhänsli, R, Candan, O., Bousquet, R., Rimmele, G., Okay, A. I., and Goff, J. (2010). Alpine high pressure evolution of the eastern Bitlis complex , SE Turkey. Geological Society, London, Special Publications, 340, 461–483. https://doi.org/10.1144/SP340.20

Okay, A. I. (2008). Geology of Turkey : A Synopsis. Anschnitt, 21, 19–42.

Okay, A. I., Arman, M. B., and Göncüoglu, M. C. (1985). Petrology and phase relations of the kyanite-eclogites from eastern Turkey. Contributions to Mineralogy and Petrology, 91(2), 196–204. https://doi.org/10.1007/BF00377767

Okay, A. I., and Göncüoğlu, C. (2004). The Karakaya Complex: A review of data and concepts. Turkish Journal of Earth Sciences, 13(2), 77–95.

Okay, A. I., and Leven, E. J. (1996). Stratigraphy and Paleontology of the Upper Paleozoic Sequences in the Pulur (Bayburt) Region, Eastern Pontides. Turkish Journal of Earth Sciences, 5, 145–155. https://doi.org/1300-0985 / 1303-619X

Okay, A. I., and Nikishin, A. M. (2015). Tectonic evolution of the southern margin of Laurasia in the Black Sea region. International Geology Review, 57(5–8), 1051–1076. https://doi.org/10.1080/00206814.2015.1010609

Okay, A. I., Satir, M., and Siebel, W. (2006). Pre-Alpide Palaeozoic and Mesozoic orogenic events in the Eastern Mediterranean region. Geological Society Memoir, 32, 389–405. https://doi.org/10.1144/GSL.MEM.2006.032.01.23

Okay, A. I., and Şahintürk, Ö. (1997). Geology of the Eastern Pontides. In A. G. Robinson (Ed.), Regional and Petroleum Geology of the Black Sea and Surrounding Region (Vol. 68, pp. 291–311). American Association of Petroleum Geologists. https://doi.org/10.1306/M68612C15

Okay, A. I., and Tüysüz, O. (1999). Tethyan sutures of northern Turkey. Geological Society Special Publication, 156, 475–515. https://doi.org/10.1144/GSL.SP.1999.156.01.22

Okay, A. I., Zattin, M., and Cavazza, W. (2010). Apatite fission-track data for the Miocene Arabia-Eurasia collision. Geology, 38(1), 35–38. https://doi.org/10.1130/G30234.1

Önal, A., Boztuğ D., Arslan M., Spell T., and S., K. (2008). Petrology and ^{40}Ar-^{39}Ar Age of the Bimodal Orduzu volcanics (Malatya) from the Western end of the Eastern Anatolia Neogene Volcanism, Turkey. Turkish Journal of Earth Sciences, 17(85–109), 85–109.

Oyan, V., Keskin, M., Lebedev, V. A., Chugaev, A. V., and Sharkov, E. V. (2016). Magmatic evolution of the Early Pliocene Etrüsk stratovolcano, Eastern Anatolian Collision Zone, Turkey. Lithos, 256–257, 88–108. https://doi.org/10.1016/j.lithos.2016.03.017

Oyan, V., Keskin, M., Lebedev, V. A., Chugaev, A. V., Sharkov, E. V., and Ünal, E. (2017). Petrology and geochemistry of the quaternary mafic volcanism to the NE of Lake Van, Eastern Anatolian collision zone, Turkey. Journal of Petrology, 58(9), 1701–1728. https://doi.org/10.1093/petrology/egx070

Özacar, A. A., Gilbert, H., and Zandt, G. (2008). Upper mantle discontinuity structure beneath East Anatolian Plateau (Turkey) from receiver functions. Earth and Planetary Science Letters, 269(3–4), 427–435. https://doi.org/10.1016/j.epsl.2008.02.036

Özbulut, E. (2006). Harput (Elazığ) Kuzeydoğusundaki Alt Pliyosen Yaşlı Piroklastik Kayaçların İncelenmesi. Yüksek Lisans Tezi, Fırat Üniversitesi, Fen Bilimleri Ensitüsü, Elazığ, 62s.

Özcan, E., Less, G., Jovane, L., Catanzariti, R., Frontalini, F., Coccioni, R., Giorgioni, M., Rodelli, D., Rego, E. S., Kayğılı, S., and Asgharian Rostami, M. (2019). Integrated biostratigraphy of the middle to upper Eocene Kırkgeçit Formation (Baskil section, Elazığ, eastern Turkey): larger benthic foraminiferal perspective. In Mediterranean Geoscience Reviews (Vol. 1, Issue 1). Springer International Publishing. https://doi.org/10.1007/s42990-019-00004-6

Özdemir, Y., Blundy, J., and Güleç, N. (2011). The importance of fractional crystallization and magma mixing in controlling chemical differentiation at Süphan stratovolcano, eastern Anatolia, Turkey. Contributions to Mineralogy and Petrology, 162(3), 573–597. https://doi.org/10.1007/s00410-011-0613-8

Özdemir, Y., and Güleç, N. (2013). Geological and geochemical evolution of the quaternary süphan stratovolcano, Eastern Anatolia, Turkey: Evidence for the lithosphere-asthenosphere interaction in post-collisionalvolcanism. Journal of Petrology, 55(1), 37–62. https://doi.org/10.1093/petrology/egt060

Özgül, N. (1976). Torosların bazı temel jeoloji özellikleri. TJK Bulletin, 19(1), 65–78.

Özgül, N., and Turşucu, A. (1984). Stratigraphy of the Mesozoic carbonate sequence of the Munzur Mountains (Eastern Taurides). In O. Tekeli and M. C. Göncüoğlu (Eds.), Geology of the Taurus Belt (pp. 173–181).

Özgül, N., Turşucu, A., Özyardımcı, N., Şenol, M., Bingöl, İ., and Uysal, Ş. (1981). Munzur Dağlarının Jeolojisi. MTA Raporu, No: 6995.

Özkul, M. (1988). Elazığ batısında Kırkgeçit Formasyonu üzerine sedimantolojik incelemeler. Doktora Tezi, Fırat Üniversitesi, Fen Bilimleri Enstitüsü, Elazığ, 186s.

Paster, T. P., Schauwecker, D. S., and Haskin, L. A. (1974). The behavior of some trace elements during solidification of the Skaergaard layered series. Geochimica et Cosmochimica Acta, 38(10), 1549–1577. https://doi.org/10.1016/0016-7037(74)90174-4

Patchett, P. J., and Tatsumoto, M. (1980). Hafnium isotope variations in oceanic basalts. Geophysical Research Letters, 7(12), 1077–1080. https://doi.org/10.1029/GL007i012p01077

Pearce, J. A. (1983). Role of the sub-continental lithosphere in magma genesis at active continental margins. In C. J. Hawkesworth and M. J. Norry (Eds.), Continental basalts and mantle xenoliths (pp. 230–249).

Pearce, J. A., Baker, P. E., Harvey, P. K., and Luff, I. W. (1995). Geochemical Evidence for Subduction Fluxes, Mantle Melting and Fractional Crystallization Beneath the South Sandwich Island Arc. Journal of Petrology, 36(4), 1073–1109. https://doi.org/10.1093/petrology/36.4.1073

Pearce, J. A., Bender, J. F., De Long, S. E., Kidd, W. S. F., Low, P. J., Güner, Y., Saroglu, F., Yilmaz, Y., Moorbath, S., and Mitchell, J. G. (1990). Genesis of collision volcanism in Eastern Anatolia, Turkey. Journal of Volcanology and Geothermal Research, 44(1–2), 189–229. https://doi.org/10.1016/0377-0273(90)90018-B

Pearce, J.A., and Cann, J. R. (1973). Tectonic setting of basic volcanic rocks determined using trace element analyses. Earth and Planetary Science Letters, 19(2), 290–300. https://doi.org/10.1016/0012-821X(73)90129-5

Pearce, J A, Kempton, P. D., and Gill, J. B. (2007). Hf – Nd evidence for the origin and distribution of mantle domains in the SW Pacific. 260, 98–114. https://doi.org/10.1016/j.epsl.2007.05.023

Pearce, J. A., and Peate, D. W. (1995). Tectonic Implications of the Composition of Volcanic Arc Magmas. Annual Review of Earth and Planetary Sciences, 23(1), 251–285. https://doi.org/10.1146/annurev.ea.23.050195.001343

Pearce, J. A., and Stern, R. J. (2006). Origin of back-arc basin magmas: Trace element and isotope perspectives. Geophysical Monograph Series, 166, 63–86. https://doi.org/10.1029/166GM06

Pearson, D. G. (1999). Evolution of cratonic lithospheric mantle: an isotopic perspective. In C. . Bertka, B. . Mysen, and Y. Fei (Eds.), Mantle petrology: field observations and high pressure experimentation (pp. 57–78). Geochemical Society Special Publication.

Pearson, D. G., Irvine, G. J., Carlson, R. W., Kopylova, M. G., and Ionov, D. A. (2002). The development of lithospheric keels beneath the earliest continents: Time constraints using PGE and Re-Os isotope systematics. Geological Society Special Publication, 199, 65–90. https://doi.org/10.1144/GSL.SP.2002.199.01.04

Pearson, D. G., and Nowell, G. M. (2002). The continental lithospheric mantle: Characteristics and significance as a mantle reservoir. Philosophical Transactions of the Royal Society A: Mathematical, Physical and Engineering Sciences, 360(1800), 2383–2410. https://doi.org/10.1098/rsta.2002.1074

Pearson, D. G., Shirey, S. B., Carlson, R. W., Boyd, F. R., Pokhilenko, N. P., and Shimizu, N. (1995). Re-Os, Sm-Nd, and Rb-Sr isotope evidence for thick Archaean lithospheric mantle beneath the Siberian craton modified by multistage metasomatism. Geochimica et Cosmochimica Acta, 59(5), 959–977. https://doi.org/10.1016/0016-7037(95)00014-3

Peccerillo, A., De Astis, G., Faraone, D., Forni, F., and Frezzotti, M. L. (2013). (Chapter 15) Compositional variations of magmas in the Aeolian arc: implications for petrogenesis and geodynamics. Geological Society, London, Memoirs, 37(1), 491–510. https://doi.org/10.1144/M37.15

Perincek, D. (1990). Hakkari ili ve dolayının stratigrafisi, Güneydoğu Anadolu, Türkiye. Türkiye Petrol Jeologları Derneği Bülteni, 2(21–68).

Perinçek, D. (1979). The Geology of Hazro-Korudağ-Çüngüş-Maden-Ergani-Hazar-Elazığ-Malatya area: Guide Book. TJK Publications, 33.

Perinçek, D., Duran, O., Bozdoğan, N., and Çoruh, T. (1991). Stratigraphy and paleogeographical evolution of the autochthonous sedimentary rocks in the SE Anatolia. In S. Turgut (Ed.), Ozan Sungurlu Symposium Proceedings (pp. 274–305). O. Sungurlu Foundation.

Peters, B. J., and Day, J. M. D. (2014). Assessment of relative Ti, Ta, and Nb (TITAN) enrichments in ocean island basalts. Geochemistry, Geophysics, Geosystems, 15(11), 4424–4444. https://doi.org/10.1002/2014GC005506

Pilet, S., Baker, M. B., Müntener, O., and Stolper, E. M. (2011). Monte Carlo simulations of metasomatic enrichment in the lithosphere and implications for the source of alkaline basalts. Journal of Petrology, 52(7–8), 1415–1442. https://doi.org/10.1093/petrology/egr007

Pilet, S., Baker, M. B., and Stolper, E. M. (2008). Metasomatized Lithosphere and the Origin of Alkaline Lavas. Science, 320(5878), 916–919. https://doi.org/10.1126/science.1156563

Pilet, S., Hernandez, J., Sylvester, P., and Poujol, M. (2005). The metasomatic alternative for ocean island basalt chemical heterogeneity. Earth and Planetary Science Letters, 236(1–2), 148–166. https://doi.org/10.1016/j.epsl.2005.05.004

Pilet, S, Hernandez, J., and Villemant, B. (2002). Evidence for high silicic melt circulation and metasomatic events in the mantle beneath alkaline provinces : the Na ± Fe-augitic green-core pyroxenes in the Tertiary alkali basalts of the

Cantal massif (French Massif Central). Mineralogy and Petrology, 76, 39–62. https://doi.org/10.1007/s00710-001-0184-x

Plank, T., and Langmuir, C. H. (1998). The chemical composition of subducting sediment and its consequences for the crust and mantle. Chemical Geology, 145(3–4), 325–394. https://doi.org/10.1016/S0009-2541(97)00150-2

Plomerová, J., Kouba, D., and Babuška, V. (2002). Mapping the lithosphere-asthenosphere boundary through changes in surface-wave anisotropy. Tectonophysics, 358(1–4), 175–185. https://doi.org/10.1016/S0040-1951(02)00423-7

Prelević, D., Akal, C., Foley, S. F., Romer, R. L., Stracke, A., and Van den Bogaard, P. (2012). Ultrapotassic mafic rocks as geochemical proxies for post-collisional dynamics of orogenic lithospheric mantle: The case of southwestern Anatolia, Turkey. Journal of Petrology, 53(5), 1019–1055. https://doi.org/10.1093/petrology/egs008

Prelević, D., Foley, S. F., Romer, R. L., Cvetković, V., and Downes, H. (2005). Tertiary ultrapotassic volcanism in Serbia: Constraints on petrogenesis and mantle source characteristics. Journal of Petrology, 46(7), 1443–1487. https://doi.org/10.1093/petrology/egi022

Prytulak, J., and Elliott, T. (2007). TiO_2 enrichment in ocean island basalts. Earth and Planetary Science Letters, 263(3–4), 388–403. https://doi.org/10.1016/j.epsl.2007.09.015

Putirka, K. D. (2005). Igneous thermometers and barometers based on plagioclase + liquid equilibria: Tests of some existing models and new calibrations. American Mineralogist, 90(2–3), 336–346. https://doi.org/10.2138/am.2005.1449

Putirka, K. D. (2008). Thermometers and barometers for volcanic systems. Reviews in Mineralogy and Geochemistry, 69, 61–120. https://doi.org/10.2138/rmg.2008.69.3

Putirka, K. D., Perfit, M., Ryerson, F. J., and Jackson, M. G. (2007). Ambient and excess mantle temperatures, olivine thermometry, and active vs. passive upwelling. Chemical Geology, 241(3–4), 177–206. https://doi.org/10.1016/j.chemgeo.2007.01.014

Putirka, K., Johnson, M., Kinzler, R., Longhi, J., and Walker, D. (1996). Thermobarometry of mafic igneous rocks based on clinopyroxene-liquid equilibria, 0- 30 kbar. Contributions to Mineralogy and Petrology, 123(1), 92–108. https://doi.org/10.1007/s004100050145

Rehkämper, M., and Halliday, A. N. (1998). Accuracy and long-term reproducibility of lead isotopic measurements by multiple-collector inductively coupled plasma mass spectrometry using an external method for correction of mass discrimination. International Journal of Mass Spectrometry, 181(1–3), 123–133. https://doi.org/10.1016/s1387-3806(98)14170-2

Rehkämper, M., and Hofmann, A. W. (1997). Recycled ocean crust and sediment in Indian Ocean MORB. Earth and Planetary Science Letters, 147(1–4), 93–106. https://doi.org/10.1016/s0012-821x(97)00009-5

Reisberg, L., Zindler, A., Marcantonio, F., White, W., Wyman, D., and Weaver, B. (1993). Os isotope systematics in ocean island basalts. Earth and Planetary Science Letters, 120(3–4), 149–167. https://doi.org/10.1016/0012-821X(93)90236-3

Richard, P., Shimizu, N., and Allègre, C. J. (1976). ^{143}Nd/^{146}Nd, a natural tracer: an application to oceanic basalts. Earth and Planetary Science Letters, 31(2), 269–278. https://doi.org/10.1016/0012-821X(76)90219-3

Richardson, S. H., Harris, J. W., and Gurney, J. J. (1993). Three generations of diamonds from old continental mantle. Nature, 366(6452), 256–258. https://doi.org/10.1038/366256a0

Robertson, A. H. F., Parlak, O., Rízaoğlu, T., Ünlügenç, Ü., İnan, N., Tasli, K., and Ustaömer, T. (2007). Tectonic evolution of the South Tethyan ocean: evidence from the Eastern Taurus Mountains (Elaziğ region, SE Turkey). Geological Society, London, Special Publications, 272(1), 231–270. https://doi.org/10.1144/GSL.SP.2007.272.01.14

Robertson, A., Parlak, O., Ustaömer, T., Tasli, K., Inan, N., Dumitrica, P., and Karaoğlan, F. (2013). Subduction, ophiolite genesis and collision history of Tethys adjacent to the Eurasian continental margin: New evidence from the Eastern Pontides, Turkey. Geodinamica Acta, 26(3–4), 230–293. https://doi.org/10.1080/09853111.2013.877240

Roeder, P. L., and Emslie, R. F. (1970). Olivine-liquid equilibrium. Contributions to Mineralogy and Petrology, 29(4), 275–289. https://doi.org/10.1007/BF00371276

Rojay, B. (2013). Tectonic evolution of the Cretaceous Ankara Ophiolitic Mélange during the Late Cretaceous to pre-Miocene interval in Central Anatolia, Turkey. Journal of Geodynamics, 65, 66–81. https://doi.org/10.1016/j.jog.2012.06.006

Rooney, T. O., Hanan, B. B., Graham, D. W., Furman, T., Blichert-Toft, J., and Schilling, J. G. (2012). Upper mantle pollution during Afar plume-continental rift interaction. Journal of Petrology, 53(2), 365–389. https://doi.org/10.1093/petrology/egr065

Rooney, T. O., Nelson, W. R., Dosso, L., Furman, T., and Hanan, B. (2014). The role of continental lithosphere metasomes in the production of HIMU-like magmatism on the northeast African and Arabian plates. Geology, 42(5), 419–422. https://doi.org/10.1130/G35216.1

Rudnick, R. L., and Gao, S. (2004). Composition of the Continental Crust. In R. L. Rudnick (Ed.), Treatise on Geochemistry, vol. 3, The Crust (Vol. 3, pp. 1–64). Elsevier, New York.

Ruprecht, P., and Wörner, G. (2007). Variable regimes in magma systems documented in plagioclase zoning patterns: El Misti stratovolcano and Andahua monogenetic cones. Journal of Volcanology and Geothermal Research, 165(3–4), 142–162. https://doi.org/10.1016/j.jvolgeores.2007.06.002

Saal, A. E., Rudnick, R. L., Ravizza, G. E., and Hart, S. R. (1998). Re–Os isotope evidence for the composition, formation and age of the lower continental crust. Nature, 393(6680), 58–61. https://doi.org/10.1038/29966

Sack, R. O., Walker, D., and Carmichael, I. S. E. (1987). Experimental petrology of alkalic lavas: constraints on cotectics of multiple saturation in natural basic liquids. Contributions to Mineralogy and Petrology, 96(1), 1–23. https://doi.org/10.1007/BF00375521

Salters, V. J. M., Mallick, S., Hart, S. R., Langmuir, C. E., and Stracke, A. (2011). Domains of depleted mantle: New evidence from hafnium and neodymium isotopes. Geochemistry, Geophysics, Geosystems, 12(8).

https://doi.org/10.1029/2011GC003617

Salters, V. J. M., and Stracke, A. (2004). Composition of the depleted mantle. Geochemistry, Geophysics, Geosystems, 34(5). https://doi.org/10.1029/2003GC000597

Salters, V. J. M., and White, W. M. (1998). Hf isotope constraints on mantle evolution. Chemical Geology, 145(3–4), 447–460. https://doi.org/10.1016/S0009-2541(97)00154-X

Sar, A., Ertürk, M. A., and Rizeli, M. E. (2019). Genesis of Late Cretaceous intra-oceanic arc intrusions in the Pertek area of Tunceli Province, eastern Turkey, and implications for the geodynamic evolution of the southern Neo-Tethys: Results of zircon U–Pb geochronology and geochemical and Sr–Nd isotop. Lithos, 350–351, 105263. https://doi.org/10.1016/j.lithos.2019.105263

Sayit, K. (2013). Immobile trace element systematics of oceanic island basalts: The role of oceanic lithosphere in creating the geochemical diversity. Ofioliti, 38(1), 101–120. https://doi.org/10.4454/ofioliti.v38i1.419

Sayit, K., Bedi, Y., Tekin, U. K., Göncüoglu, M. C., and Okuyucu, C. (2017). Middle Triassic back-arc basalts from the blocks in the Mersin Mélange, southern Turkey: Implications for the geodynamic evolution of the Northern Neotethys. Lithos, 268–271, 102–113. https://doi.org/10.1016/j.lithos.2016.10.032

Sayit, K., Göncüoglu, M. C., and Kagan Tekin, U. (2015). Middle carnian arc-type basalts from the lycian nappes, southwestern anatolia: Early late triassic subduction in the northern branch of Neotethys. Journal of Geology, 123(6), 561–579. https://doi.org/10.1086/683664

Sayit, K., Marroni, M., Göncüoglu, M. C., Pandolfi, L., Ellero, A., Ottria, G., and Frassi, C. (2016). Geological setting and geochemical signatures of the mafic rocks from the Intra-Pontide Suture Zone: implications for the geodynamic reconstruction of the Mesozoic Neotethys. International Journal of Earth Sciences, 105(1), 39–64. https://doi.org/10.1007/s00531-015-1202-2

Schilling, J. G., Kingsley, R. H., Hanan, B. B., and McCully, B. L. (1992). Nd-Sr-Pb isotopic variations along the Gulf of Aden: Evidence for Afar Mantle Plume-Continental Lithosphere Interaction. Journal of Geophysical Research, 97(B7), 10927. https://doi.org/10.1029/92JB00415

Seyrek, A., Westaway, R., Pringle, M., Yurtmen, S., Demir, T., and Rowbotham, G. (2008). Timing of the quaternary Elaziğ volcanism, eastern Turkey, and its significance for constraining landscape evolution and surface uplift. Turkish Journal of Earth Sciences, 17(3), 497–541.

Shaw, D. M. (1970). Trace element fractionation during anatexis. Geochimica et Cosmochimica Acta, 237–243. https://doi.org/https://doi.org/10.1016/0016-7037(70)90009-8

Shaw, J. E., Baker, J. A., Menzies, M. A., Thirlwall, M. F., and Ibrahim, K. M. (2003). Petrogenesis of the Largest Intraplate Volcanic Field on the Arabian Plate (Jordan): a Mixed Lithosphere–Asthenosphere Source Activated by Lithospheric Extension. Journal of Petrology, 44(9), 1657–1679. https://doi.org/10.1093/petrology/egg052

Stein, M., and Hofmann, A. W. (1994). Mantle plumes and episodic crustal growth. Nature, 372(6501), 63–68. https://doi.org/10.1038/372063a0

Stosch, H. G., and Lugmair, G. W. (1984). Evolution of the lower continental crust: Granulite facies xenoliths from the Eifel, West Germany. Nature, 311(5984), 368–370. https://doi.org/10.1038/311368a0

Stracke, A. (2012). Earth's heterogeneous mantle: A product of convection-driven interaction between crust and mantle. Chemical Geology, 330–331, 274–299. https://doi.org/10.1016/j.chemgeo.2012.08.007

Stracke, A. (2018). Mantle Geochemistry. In William M White (Ed.), Encyclopedia of Geochemistry. Encyclopedia of Earth Sciences Series (pp. 867–878). Springer International Publishing. https://doi.org/10.1007/978-3-319-39312-4_286

Stracke, A., Bizimis, M., and Salters, V. J. M. (2003). Recycling oceanic crust: Quantitative constraints. Geochemistry, Geophysics, Geosystems, 4(3). https://doi.org/10.1029/2001GC000223

Stracke, A., Hofmann, A. W., and Hart, S. R. (2005). FOZO, HIMU, and the rest of the mantle zoo. Geochemistry, Geophysics, Geosystems, 6(5).

https://doi.org/10.1029/2004GC000824

Strelow, F. W. E., and Toerien, F. S. (1966). Separation of Lead(II) from Bismuth(III), Thallium(III), Cadmium(II), Mercury(II), Gold(III), Platinum(IV), Palladium(II), and Other Elements by Anion Exchange Chromatography. Analytical Chemistry, 38(4), 545–548. https://doi.org/10.1021/ac60236a006

Sun, S. S. (1980). Lead Isotopic Study of Young Volcanic Rocks from Mid-Ocean Ridges, Ocean Islands and Island Arcs. Philosophical Transactions of the Royal Society A: Mathematical, Physical and Engineering Sciences, 297(1431), 409–445. https://doi.org/10.1098/rsta.1980.0224

Sun, S. S., and McDonough, W. F. (1989). Chemical and isotopic systematics of oceanic basalts: Implications for mantle composition and processes. Geological Society Special Publication, 42(1), 313–345. https://doi.org/10.1144/GSL.SP.1989.042.01.19

Sungurlu, O., Perinçek, D., Kurt, G., Tuna, E., Dülger, S., Çelikdemir, E., and Naz, H. (1985). Elazığ-Hazar-Palu Alanının Jeolojisi. Petrol İşleri Genel Müdürlüğü Dergisi, 29, 83–191.

Şaroğlu, F., and Yılmaz, Y. (1984). Doğu Anadolu'nun Neotektoniği ve İlgili Magmatizması. TJK Ketin Sempozyumu Bildiriler Kitabı, 149–162.

Şengör, A. M. C., Burke, K., and Dewey, J. F. (1978). Rifts at high angles to orogenic belts; tests for their origin and the Upper Rhine Graben as an example. American Journal of Science, 278(1), 24–40. https://doi.org/10.2475/ajs.278.1.24

Şengör, A. M. C., Özeren, S., Genç, T., and Zor, E. (2003). East Anatolian High Plateau as a mantle-supported, north-south shortened domal structure. Geophysical Research Letters, 30(24), 2–5. https://doi.org/10.1029/2003GL017858

Şengör, A. M. C., Özeren, M. S., Keskin, M., Sakinç, M., Özbakir, A. D., and Kayan, I. (2008). Eastern Turkish high plateau as a small Turkic-type orogen: Implications for post-collisional crust-forming processes in Turkic-type orogens. Earth-Science Reviews, 90(1–2), 1–48.

https://doi.org/10.1016/j.earscirev.2008.05.002

Şengör, A. M. C., and Yılmaz, Y. (1981). Tethyan evolution of Turkey: A plate tectonic approach. Tectonophysics, 75(3–4), 737. https://doi.org/10.1016/0040-1951(81)90275-4

Takahashi, E., and Kushiro, I. (1983). Melting of a dry peridotite at high pressures and basalt magma genesis. American Mineralogist, 68(9–10), 859–879.

Tatsumoto, M. (1966). Genetic Relations of Oceanic Basalts as Indicated by Lead Isotopes. Science, 153(3740), 1094–1101. https://doi.org/10.1126/science.153.3740.1094

Tatsumoto, M., Hedge, C. E., and Engel, A. E. J. (1965). Potassium, Rubidium, Strontium, Thorium, Uranium, and the Ratio of Strontium-87 to Strontium-86 in Oceanic Tholeiitic Basalt. Science, 150(3698), 886–888. https://doi.org/10.1126/science.150.3698.886

Taylor, S. R., and McLennan, S. M. (1985). The Continental Crust: Its Composition and Evolution (1st ed.). Oxford, UK: Blackwell.

Taylor, S. R., and McLennan, S. M. (1995). The geochemical evolution of the continental crust. Reviews of Geophysics, 33(2), 241–265. https://doi.org/10.1029/95RG00262

Tekin, U. K., Bedi, Y., Okuyucu, C., Göncüoglu, M. C., and Sayit, K. (2016). Radiolarian biochronology of upper Anisian to upper Ladinian (Middle Triassic) blocks and tectonic slices of volcano-sedimentary successions in the Mersin Mélange, southern Turkey: New insights for the evolution of Neotethys. Journal of African Earth Sciences, 124, 409–426. https://doi.org/10.1016/j.jafrearsci.2016.09.039

Tekin, U. K., Goncuoglu, M. C., and Turhana, N. (2002). First evidence of Late Carnian radiolarians from the Izmir-Ankara suture complex, central Sakarya, Turkey: Implications for the opening age of the Izmir-Ankara branch of Neo-Tethys. Geobios, 35(1), 127–135. https://doi.org/10.1016/S0016-6995(02)00015-3

Tekin, U. K, Ural, M., Göncüoğlu, M. C, Arslan, M., and Kürüm, S. (2015). Upper

Cretaceous Radiolarian ages from an arc–back-arc within the Yüksekova Complex in the southern Neotethys mélange, SE Turkey. Comptes Rendus Palevol, 14(2), 73–84. https://doi.org/10.1016/j.crpv.2014.10.002

Thirlwall, M. F., Upton, B. G. J., and Jenkins, C. (1994). Interaction between Continental Lithosphere and the Iceland Plume--Sr-Nd-Pb Isotope Geochemistry of Tertiary Basalts, NE Greenland. Journal of Petrology, 35(3), 839–879. https://doi.org/10.1093/petrology/35.3.839

Thompson, R. N., Dickin, A. P., Gibson, I. L., and Morrison, M. A. (1982). Elemental fingerprints of isotopic contamination of hebridean Palaeocene mantle-derived magmas by archaean sial. Contributions to Mineralogy and Petrology, 79(2), 159–168. https://doi.org/10.1007/BF01132885

Toplis, M. J., and Carroll, M. R. (1995). An experimental study of the influence of oxygen fugacity on Fe-Ti oxide stability, phase relations, and mineral-melt equilibria in ferro-basaltic systems. Journal of Petrology, 36(5), 1137–1170. https://doi.org/10.1093/petrology/36.5.1137

Topuz, G., Altherr, R., Satir, M., and Schwarz, W. H. (2004). Low-grade metamorphic rocks from the Pulur complex, NE Turkey: Implications for the pre-Liassic evolution of the Eastern Pontides. International Journal of Earth Sciences, 93(1), 72–91. https://doi.org/10.1007/s00531-003-0372-5

Topuz, G., Altherr, R., Siebel, W., Schwarz, W. H., Zack, T., Hasözbek, A., Barth, M., Satir, M., and Şen, C. (2010). Carboniferous high-potassium I-type granitoid magmatism in the Eastern Pontides: The Gümüşhane pluton (NE Turkey). Lithos, 116(1–2), 92–110. https://doi.org/10.1016/j.lithos.2010.01.003

Topuz, G., Candan, O., Zack, T., and Yilmaz, A. (2017). East Anatolian plateau constructed over a continental basement: No evidence for the East Anatolian accretionary complex. Geology, 45(9), 791–794. https://doi.org/10.1130/G39111.1

Turan, M., Aksoy, E., and Bingöl, A. F. (1995). Doğu Toroslar'ın jeodinamik evriminin Elazığ civarındaki özellikleri. Fırat Üniversitesi, Fen ve Mühendislik Bilimleri Dergisi, 7(2), 177–199.

Turan, M., and Bingöl, A. F. (1991). Kovancılar-Baskil (Elazığ) arası bölgenin tektono-stratigrafik özellikleri. Ç. Ü. Ahmet Acar Jeoloji Sempozyumu, Tebliğler, 213–227.

Türkecan, A. (2015). Türkiye'nin Senozoyik Volkanitleri. MTA Genel Müdürlüğü Yayınları, Ankara.

Türkmen, İ. (1991). Elazığ Doğusunda Çaybağı Formasyonu (Üst Miyosen-Pliyosen?) stratigrafisi ve sedimantolojisi. Türkiye Jeoloji Bülteni / Geological Bulletin of Turkey, 34, 45–53.

Turner, S., Hawkesworth, C., Rogers, N., Bartlett, J., Worthington, T., Hergt, J., Pearce, J., and Smith, I. (1997). ^{238}U-^{230}Th disequilibria, magma petrogenesis, and flux rates beneath the depleted Tonga-Kermadec island arc. Geochimica et Cosmochimica Acta, 61(22), 4855–4884. https://doi.org/10.1016/S0016-7037(97)00281-0

Ulmer, P. (1989). The dependence of the Fe^{2+}-Mg cation-partitioning between olivine and basaltic liquid on pressure, temperature and composition - An experimental study to 30 kbars. Contributions to Mineralogy and Petrology, 101(3), 261–273. https://doi.org/10.1007/BF00375311

Ulrych, J., Krmíček, L., Tomek, Č., Lloyd, F. E., Ladenberger, A., Ackerman, L., and Balogh, K. (2016). Petrogenesis of Miocene alkaline volcanic suites from western Bohemia: Whole rock geochemistry and Sr-Nd-Pb isotopic signatures. Chemie Der Erde, 76(1), 77–93. https://doi.org/10.1016/j.chemer.2015.11.003

Ural, M., Arslan, M., Göncüoğlu, M. C., Tekin, U. K., and Kürüm, S. (2015). Late Cretaceous arc and back-arc formation within the southern neotethys: whole-rock, trace element and Sr-Nd-Pb isotopic data from basaltic rocks of the Yüksekova Complex (Malatya-Elazığ, SE Turkey). Ofioliti, 40(1), 52–72. https://doi.org/http10.4454/ofioliti.v40i1.435

Uzuncimen, S., Tekin, U. K., Bedi, Y., Perincek, D., Varol, E., and Soycan, H. (2011). Discovery of the Late Triassic (Middle Carnian-Rhaetian) radiolarians in the volcano-sedimentary sequences of the Kocali Complex, SE Turkey: Correlation with the other Tauride units. Journal of Asian Earth Sciences, 40(1), 180–200. https://doi.org/10.1016/j.jseaes.2010.08.004

van Kooten, G. K., and Buseck, P. R. (1978). Interpretation of olivine zoning: Study of a maar from the San Francisco volcanic field, Arizona. Geological Society of America Bulletin, 89(5), 744. https://doi.org/10.1130/0016-7606(1978)89<744:IOOZSO>2.0.CO;2

Varol, E., Bedi, Y., Tekin, U. K., and Uzuncimen, S. (2011). of Late Triassic Basic Volcanic Rocks From the Kocali Complex , Se Turkey : Implications for the Triassic Evolution of Southern Tethys. Ofioliti, 36(1), 101–115. https://doi.org/https://doi.org/10.4454/ofioliti.v36i1.396

Vaselli, O., Downes, H., Thirlwall, M., Dobosi, G., Coradossi, N., Seghedi, I., Szakacs, A., and Vannucci, R. (1995). Ultramafic xenoliths in plio-pleistocene alkali basalts from the eastern transylvanian basin: Depleted mantle enriched by vein metasomatism. Journal of Petrology, 36(1), 23–53. https://doi.org/10.1093/petrology/36.1.23

Wang, K., Plank, T., Walker, J. D., and Smith, E. I. (2002). A mantle melting profile across the Basin and Range, SW USA. Journal of Geophysical Research: Solid Earth, 107(B1), ECV 5-1-ECV 5-21. https://doi.org/10.1029/2001JB000209

Weaver, B. L. (1991). The origin of ocean island basalt end-member compositions: trace element and isotopic constraints. Earth and Planetary Science Letters, 104(2–4), 381–397. https://doi.org/10.1016/0012-821X(91)90217-6

Wedepohl, K. H., and Baumann, A. (1999). Central European Cenozoic plume volcanism with OIB characteristics and indications of a lower mantle source. Contributions to Mineralogy and Petrology, 136(3), 225–239. https://doi.org/10.1007/s004100050534

White, W. M. (1985). Sources of oceanic basalts: radiogenic isotopic evidence. Geology, 13(2), 115–118. https://doi.org/10.1130/0091-7613(1985)13<115:SOOBRI>2.0.CO;2

White, W. M., and Dupré, B. (1986). Sediment subduction and magma genesis in the Lesser Antilles: Isotopic and trace element constraints. Journal of Geophysical Research, 91(B6), 5927. https://doi.org/10.1029/JB091iB06p05927

White, W. M., and Hofmann, A. W. (1982). Sr and Nd isotope geochemistry of oceanic basalts and mantle evolution. Nature, 296(5860), 821–825. https://doi.org/10.1038/296821a0

White, W. M., Patchett, J., and BenOthman, D. (1986). Hf isotope ratios of marine sediments and Mn nodules: evidence for a mantle source of Hf in seawater. Earth and Planetary Science Letters, 79(1–2), 46–54. https://doi.org/10.1016/0012-821X(86)90039-7

White, W. M., and Schilling, J. G. (1978). The nature and origin of geochemical variation in Mid-Atlantic Ridge basalts from the Central North Atlantic. Geochimica et Cosmochimica Acta, 42(10), 1501–1516. https://doi.org/10.1016/0016-7037(78)90021-2

Widom, E., and Shirey, S. B. (1996). Os isotope systematics in the Azores: Implications for mantle plume sources. Earth and Planetary Science Letters, 142(3–4), 451–465. https://doi.org/10.1016/0012-821x(96)00111-2

Willbold, M., and Stracke, A. (2006). Trace element composition of mantle end-members: Implications for recycling of oceanic and upper and lower continental crust. Geochemistry, Geophysics, Geosystems, 7(4), 1–30. https://doi.org/10.1029/2005GC001005

Willbold, M., and Stracke, A. (2010). Formation of enriched mantle components by recycling of upper and lower continental crust. Chemical Geology, 276(3–4), 188–197. https://doi.org/10.1016/j.chemgeo.2010.06.005

Wilson, M., and Bianchini, G. (1999). Tertiary-Quaternary magmatism within the Mediterranean and surrounding regions. Geological Society Special Publication, 156, 141–168. https://doi.org/10.1144/GSL.SP.1999.156.01.09

Wilson, M., and Downes, H. (1991). Tertiary-Quaternary Extension-Related Alkaline Magmatism in Western and Central Europe. Journal of Petrology, 32(4), 811–849. https://doi.org/10.1093/petrology/32.4.811

Wilson, M., and Downes, H. (1992). Mafic alkaline magmatism associated with the European Cenozoic rift system. Tectonophysics, 208(1–3), 173–182. https://doi.org/10.1016/0040-1951(92)90343-5

Wilson, M., and Downes, H. (2006). Tertiary-Quaternary intra-plate magmatism in

Europe and its relationship to mantle dynamics. Geological Society Memoir, 32, 147–166. https://doi.org/10.1144/GSL.MEM.2006.032.01.09

Wilson, M., Downes, H., and Cebriá, J. M. (1995a). Contrasting Fractionation Trends in Coexisting Continental Alkaline Magma Series; Cantal, Massif Central, France. Journal of Petrology, 36(6), 1729–1753. https://doi.org/10.1093/oxfordjournals.petrology.a037272

Wilson, M., and Patterson, R. (2001). Intraplate magmatism related to short-wavelength convective instabilities in the upper mantle: Evidence from the Tertiary-Quaternary volcanic province of Western and Central Europe. In R. E. Ernst and K. . Buchan (Eds.), Mantle plumes: their identification through time (pp. 37–58). Geological Society of America 352. https://doi.org/10.1130/0-8137-2352-3.37

Wilson, M., Rosenbaum, J. M., and Dunworth, E. A. (1995b). Melilitites: partial melts of the thermal boundary layer? Contributions to Mineralogy and Petrology, 119(2–3), 181–196. https://doi.org/10.1007/BF00307280

Woodhead, J. D. (1996). Extreme HIMU in an oceanic setting: The geochemistry of Mangaia Island (Polynesia), and temporal evolution of the Cook-Austral hotspot. Journal of Volcanology and Geothermal Research, 72(1–2), 1–19. https://doi.org/10.1016/0377-0273(96)00002-9

Woodhead, J. D., and Devey, C. W. (1993). Geochemistry of the Pitcairn seamounts, I: source character and temporal trends. Earth and Planetary Science Letters, 116(1–4), 81–99. https://doi.org/10.1016/0012-821X(93)90046-C

Woodhead, J. D., Hergt, J. M., Davidson, J. P., and Eggins, S. M. (2001). Hafnium isotope evidence for ‘conservative’ element mobility during subduction zone processes. Earth and Planetary Science Letters, 192(3), 331–346. https://doi.org/10.1016/S0012-821X(01)00453-8

Woodhead, J. D., and McCulloch, M. T. (1989). Ancient seafloor signals in Pitcairn Island lavas and evidence for large amplitude, small length-scale mantle heterogeneities. Earth and Planetary Science Letters, 94(3–4), 257–273. https://doi.org/10.1016/0012-821X(89)90145-3

Workman, R. K., and Hart, S. R. (2005). Major and trace element composition of the depleted MORB mantle (DMM). Earth and Planetary Science Letters, 231(1–2), 53–72. https://doi.org/10.1016/j.epsl.2004.12.005

Workman, R. K., Hart, S. R., Jackson, M., Regelous, M., Farley, K. A., Blusztajn, J., Kurz, M., and Staudigel, H. (2004). Recycled metasomatized lithosphere as the origin of the Enriched Mantle II (EM2) end-member: Evidence from the Samoan Volcanic Chain. Geochemistry, Geophysics, Geosystems, 5(4), 1–44. https://doi.org/10.1029/2003GC000623

Wörner, G., Zindler, A., Staudigel, H., and Schmincke, H. U. (1986). Sr, Nd, and Pb isotope geochemistry of Tertiary and Quaternary alkaline volcanics from West Germany. Earth and Planetary Science Letters, 79(1–2), 107–119. https://doi.org/10.1016/0012-821X(86)90044-0

Wright, E., and White, W. M. (1987). The origin of Samoa: new evidence from Sr, Nd, and Pb isotopes. Earth and Planetary Science Letters, 81(2–3), 151–162. https://doi.org/10.1016/0012-821X(87)90152-X

Wyllie, P. J. (1977). Mantle Fluid Compositions Buffered by Carbonates in Peridotite-CO_2-H_2O. The Journal of Geology, 85(2), 187–207. https://doi.org/10.1086/628285

Yilmaz, A., Yilmaz, H., Kaya, C., and Durmus, B. (2010). The nature of the crustal structure of the Eastern Anatolian Plateau, Turkey. Geodinamica Acta, 23(4), 167–183. https://doi.org/10.3166/ga.23.167-183

Yilmaz, Y., Güner, Y., and Şaroğlu, F. (1998). Geology of the quaternary volcanic centres of the east Anatolia. Journal of Volcanology and Geothermal Research, 85(1–4), 173–210. https://doi.org/10.1016/S0377-0273(98)00055-9

Yilmaz, Y, Saroglu, F., and Güner, Y. (1987). Initiation of the neomagmatism in East Anatolia. Tectonophysics, 134, 177–199.

Yilmaz, Y., Yiğitbaş, E., and Genç, Ş. C. (1993). Ophiolitic and metamorphic assemblages of southeast Anatolia and their significance in the geological evolution of the orogenic belt. Tectonics, 12(5), 1280–1297. https://doi.org/10.1029/93TC00597

Zanetti, A., Mazzucchelli, M., Rivalenti, G., and Vannucci, R. (1999). The Finero phlogopite-peridotite massif: An example of subduction-related metasomatism. Contributions to Mineralogy and Petrology, 134(2–3), 107–122. https://doi.org/10.1007/s004100050472

Zangana, N. A., Downes, H., Thirlwall, M. F., and Hegner, E. (1997). Relationship between deformation, equilibration temperatures, REE and radiogenic isotopes in mantle xenoliths (Ray Pic, Massif Central, France): An example of plume-lithosphere interaction? Contributions to Mineralogy and Petrology, 127(1–2), 187–203. https://doi.org/10.1007/s004100050275

Zangana, N. A., Downes, H., Thirlwall, M. F., Marriner, G. F., and Bea, F. (1999). Geochemical variation in peridotite xenoliths and their constituent clinopyroxenes from Ray Pic (French Massif Central): Implications for the composition of the shallow lithospheric mantle. Chemical Geology, 153(1–4), 11–35. https://doi.org/10.1016/S0009-2541(98)00150-8

Zindler, A., and Hart, S. R. (1986). Chemical Geodynamics. Annual Review of Earth and Planetary Sciences, 14(1), 493–571. https://doi.org/10.1146/annurev.earth.14.1.493

Zindler, A., and Jagoutz, E. (1988). Mantle cryptology. Geochimica et Cosmochimica Acta, 52(2), 319–333. https://doi.org/10.1016/0016-7037(88)90087-7

Zindler, A., Jagoutz, E., and Goldstein, S. (1982). Nd, Sr and Pb isotopic systematics in a three-component mantle: a new perspective. Nature, 298, 519. https://doi.org/10.1038/298519a0

Zor, E., Sandvol, E., Gürbüz, C., Türkelli, N., Seber, D., and Barazangi, M. (2003). The crustal structure of the East Anatolian plateau (Turkey) from receiver functions. Geophysical Research Letters, 30(24), 2–5. https://doi.org/10.1029/2003GL018192

APPENDICES

A. Microprobe analyses of the minerals in Tunceli and Elazığ Volcanics (oxides: wt%; elements: at%$_{corrected}$). olv: olivine; cpx: clinopyroxene; plg: plagioclase.

Tunceli Volcanics							
olivine							
S. ID	**AV20**						**AV33**
	Olv-1	**Olv-2**	**Olv-3**	**Olv-4**	**Olv-5**	**Olv-6**	**Olv-1**
Na_2O	0.0167	0.0016	0.0226	0.0076	0.0378	0.0061	0.0214
MgO	41.2905	41.7851	43.3811	45.3503	40.564	39.1089	46.2637
Al_2O_3	0.0341	0.0269	0.0303	0.0575	0.0605	0.0221	0.0415
SiO_2	39.3283	39.2816	39.6057	40.0899	38.9515	38.7941	40.4612
K_2O	0.0072	0.0000	0.0105	0.0024	0.0000	0.0124	0.0000
CaO	0.2476	0.2446	0.2152	0.2296	0.2354	0.3672	0.2465
TiO_2	0.0177	0.0000	0.0000	0.0176	0.0065	0.0112	0.0105
Cr_2O_3	0.0226	0.0207	0.0212	0.0175	0.0265	0.0131	0.013
MnO	0.2521	0.2374	0.2179	0.1892	0.2548	0.2751	0.1904
FeO	19.7852	18.8729	17.4368	15.0749	20.8879	21.6344	13.8259
Total	101.00	100.47	100.94	101.04	101.02	100.24	101.07
Na	0.0118	0.0011	0.0158	0.0052	0.0267	0.0043	0.0146
Mg	22.3516	22.649	23.2335	23.9927	22.0684	21.5469	24.3271
Al	0.0146	0.0115	0.0128	0.0241	0.026	0.0096	0.0172
Si	14.2809	14.2826	14.2286	14.2274	14.2149	14.3372	14.2718
K	0.0034	0.0000	0.0048	0.0011	0.0000	0.0058	0.0000
Ca	0.0963	0.0953	0.0828	0.0873	0.092	0.1454	0.0932
Ti	0.0048	0.0000	0.0000	0.0047	0.0018	0.0031	0.0028
Cr	0.0065	0.0059	0.006	0.0049	0.0076	0.0038	0.0036
Mn	0.0776	0.0731	0.0663	0.0569	0.0788	0.0861	0.0569
Fe	6.0083	5.7387	5.2388	4.4741	6.3749	6.6866	4.0784
O	57.1443	57.1459	57.1128	57.1217	57.1105	57.171	57.1403
Total	100	100	100	100	100	100	100

Appendix A. *(Cont'd)*

Tunceli Volcanics							
olivine							
S. ID	**AV33**					**AV67**	
	Olv-2	**Olv-3**	**Olv-4**	**Olv-5**	**Olv-6**	**Olv-1**	**Olv-2**
Na_2O	0.0076	0.0015	0.0209	0.0273	0.0377	0.0113	0.0064
MgO	46.3229	43.2196	45.8365	38.2252	43.7377	33.7051	31.8753
Al_2O_3	0.0317	0.035	0.0553	0.0538	0.0353	0.0374	0.0383
SiO_2	40.3557	39.7065	40.2331	38.3637	39.6796	37.3102	36.9799
K_2O	0.0089	0.0157	0.0101	0.0000	0.0121	0.0000	0.0000
CaO	0.2344	0.2974	0.24	0.4286	0.2849	0.3294	0.3442
TiO_2	0.0173	0.0131	0.0091	0.0207	0.0000	0.0191	0.0353
Cr_2O_3	0.0181	0.0000	0.0189	0.0128	0.0072	0.0086	0.0242
MnO	0.1881	0.2726	0.1902	0.3653	0.2317	0.3951	0.4332
FeO	13.9714	17.4076	14.3087	23.0454	15.9222	28.4634	30.366
Total	101.16	100.97	100.92	100.54	99.95	100.28	100.10
Na	0.0052	0.001	0.0144	0.0196	0.0264	0.0083	0.0048
Mg	24.352	23.1462	24.1939	21.1488	23.5112	19.2071	18.3829
Al	0.0132	0.0148	0.0231	0.0235	0.015	0.0168	0.0175
Si	14.2309	14.2643	14.2452	14.2379	14.3079	14.2621	14.3059
K	0.004	0.0072	0.0046	0.0000	0.0056	0.0000	0.0000
Ca	0.0886	0.1145	0.091	0.1704	0.1101	0.1349	0.1427
Ti	0.0046	0.0035	0.0024	0.0058	0.0000	0.0055	0.0103
Cr	0.005	0.0000	0.0053	0.0037	0.002	0.0026	0.0074
Mn	0.0562	0.0829	0.057	0.1148	0.0708	0.1279	0.142
Fe	4.1203	5.2298	4.2369	7.1527	4.8014	9.0992	9.8242
O	57.12	57.1356	57.1262	57.1241	57.1501	57.137	57.1633
Total	100	100	100	100	100	100	100

Appendix A. *(Cont'd)*

Tunceli Volcanics							
olivine							
S. ID	**AV67**				**AV73**		
	Olv-3	**Olv-4**	**Olv-5**	**Olv-6**	**Olv-1**	**Olv-2**	**Olv-3**
Na_2O	0.0021	0.0088	0.0171	0.0127	0.0102	0.009	0.0239
MgO	32.3415	33.4737	29.4131	31.6376	35.5771	37.025	34.3656
Al_2O_3	0.0153	0.0392	0.0123	0.0152	0.0316	0.0323	0.032
SiO_2	37.0454	37.4647	36.5284	36.8897	37.8129	38.2521	37.8527
K_2O	0.0000	0.0000	0.0000	0.0079	0.0111	0.0000	0.0103
CaO	0.3426	0.2731	0.3201	0.2998	0.3521	0.2481	0.2855
TiO_2	0.0224	0.0039	0.0427	0.0164	0.0415	0.032	0.0271
Cr_2O_3	0.0047	0.0058	0.0006	0.0033	0.0269	0.0116	0.0075
MnO	0.4102	0.3819	0.4843	0.4229	0.3408	0.2951	0.35
FeO	30.0852	28.6854	33.4168	30.9994	26.5172	24.7832	27.638
Total	100.27	100.34	100.24	100.30	100.72	100.69	100.59
Na	0.0016	0.0065	0.013	0.0095	0.0074	0.0065	0.0175
Mg	18.5853	19.0778	17.2052	18.2563	19.9773	20.6074	19.427
Al	0.007	0.0177	0.0057	0.0069	0.014	0.0142	0.0143
Si	14.2802	14.3231	14.3331	14.2792	14.2428	14.2815	14.3538
K	0.0000	0.0000	0.0000	0.0039	0.0053	0.0000	0.005
Ca	0.1415	0.1119	0.1346	0.1243	0.1421	0.0992	0.116
Ti	0.0065	0.0011	0.0126	0.0048	0.0118	0.009	0.0077
Cr	0.0014	0.0018	0.0002	0.001	0.008	0.0034	0.0023
Mn	0.1339	0.1237	0.1609	0.1387	0.1087	0.0933	0.1124
Fe	9.6987	9.1714	10.9657	10.0349	8.353	7.7381	8.7647
O	57.1454	57.1654	57.1717	57.1406	57.1296	57.1483	57.1793
Total	100	100	100	100	100	100	100

Appendix A. *(Cont'd)*

Tunceli Volcanics							
olivine							**c.pyroxene**
S. ID	**AV73**	**AV75**					**AV20**
	Olv-4	**Olv-1**	**Olv-2**	**Olv-3**	**Olv-4**	**Olv-5**	**Cpx-1**
Na_2O	0.0089	0.0162	0.0187	0.0237	0.015	0.0046	0.3735
MgO	29.1114	38.7649	42.3691	43.1971	42.0819	43.1478	14.9861
Al_2O_3	0.0218	0.0448	0.0491	0.0691	0.051	0.0578	2.8142
SiO_2	36.1204	38.5036	39.7268	39.5332	39.312	39.5527	50.7139
K_2O	0.0012	0.0072	0.0032	0.0125	0.0000	0.0000	0.0105
CaO	0.3956	0.3571	0.2076	0.2702	0.2386	0.225	20.6792
TiO_2	0.043	0.0112	0.0183	0.0155	0.0256	0.0089	1.4198
Cr_2O_3	0.0067	0.0173	0.0184	0.022	0.0155	0.0158	0.0631
MnO	0.505	0.3113	0.2297	0.2402	0.2351	0.2169	0.1795
FeO	33.9305	22.7351	18.6437	17.7856	18.5115	17.2514	8.4806
Total	100.14	100.77	101.28	101.17	100.48	100.48	99.72
Na	0.0068	0.0116	0.013	0.0165	0.0105	0.0032	0.2699
Mg	17.0984	21.3512	22.7363	23.1226	22.7679	23.2011	8.3252
Al	0.0101	0.0195	0.0208	0.0292	0.0218	0.0246	1.236
Si	14.231	14.2258	14.3002	14.1949	14.2673	14.2664	18.8984
K	0.0006	0.0034	0.0015	0.0057	0.0000	0.0000	0.005
Ca	0.167	0.1414	0.0801	0.104	0.0928	0.0869	8.2564
Ti	0.0128	0.0031	0.005	0.0042	0.007	0.0024	0.3979
Cr	0.0021	0.0051	0.0052	0.0062	0.0045	0.0045	0.0186
Mn	0.1685	0.0974	0.07	0.0731	0.0723	0.0663	0.0567
Fe	11.1798	7.0248	5.6124	5.3407	5.6185	5.2038	2.6429
O	57.1231	57.1168	57.1555	57.1029	57.1423	57.1409	59.893
Total	100	100	100	100	100	100	100

Appendix A. *(Cont’d)*

Tunceli Volcanics							
clinopyroxene							
S. ID	**AV20**					**A33**	
	Cpx-2	**Cpx-3**	**Cpx-4**	**Cpx-5**	**Cpx-6**	**Cpx-1**	**Cpx-2**
Na_2O	0.3667	0.2878	0.2908	0.4463	0.3869	0.4753	0.4695
MgO	15.2627	16.7539	16.0931	13.8583	15.5018	15.7627	15.4886
Al_2O_3	2.7818	1.7425	1.5463	2.7481	3.5955	3.6984	4.0818
SiO_2	51.1556	52.4825	52.4395	50.1422	50.7172	51.379	50.7537
K_2O	0.0152	0.002	0.0000	0.0023	0.0000	0.0000	0.0000
CaO	20.8037	20.2039	20.7952	20.5847	20.2582	22.3144	22.1113
TiO_2	1.2533	0.7073	0.8405	1.7957	1.2816	0.8523	1.1826
Cr_2O_3	0.1132	0.2964	0.0784	0.0115	0.3951	0.152	0.0207
MnO	0.1663	0.1685	0.1743	0.2119	0.1734	0.1234	0.1314
FeO	7.9427	6.9769	7.7312	9.9041	7.4235	5.274	6.4676
Total	99.86	99.62	99.99	99.71	99.73	100.03	100.70
Na	0.2638	0.206	0.2084	0.325	0.278	0.3382	0.3336
Mg	8.4439	9.2229	8.8685	7.7593	8.5633	8.6239	8.4599
Al	1.2167	0.7584	0.6737	1.2165	1.5702	1.5997	1.7626
Si	18.9843	19.3802	19.3846	18.8325	18.7933	18.8559	18.5956
K	0.0072	0.0009	0.0000	0.0011	0.0000	0.0000	0.0000
Ca	8.2719	7.9936	8.2361	8.2834	8.0428	8.7742	8.68
Ti	0.3498	0.1964	0.2337	0.5072	0.3571	0.2352	0.3258
Cr	0.0332	0.0865	0.0229	0.0034	0.1158	0.0441	0.006
Mn	0.0523	0.0527	0.0546	0.0674	0.0544	0.0384	0.0408
Fe	2.4651	2.1546	2.39	3.1108	2.3005	1.6187	1.9817
O	59.9118	59.9478	59.9324	59.8933	59.9281	59.872	59.8213
Total	100	100	100	100	100	100	100

Appendix A. *(Cont'd)*

Tunceli Volcanics							
clinopyroxene							
S. ID	**AV33**				**AV67**		
	Cpx-3	**Cpx-4**	**Cpx-5**	**Cpx-6**	**Cpx-1**	**Cpx-2**	**Cpx-3**
Na_2O	0.4327	0.4475	0.5765	0.5251	0.4874	0.3629	0.4151
MgO	16.0703	15.2988	12.767	15.0147	14.129	15.3697	15.0576
Al_2O_3	3.2006	4.0586	5.7044	4.6753	1.806	2.5164	2.3477
SiO_2	51.4281	50.4841	47.8103	50.0423	51.2981	51.2519	51.1121
K_2O	0.0242	0.0047	0.0027	0.0000	0.0101	0.0133	0.0000
CaO	21.5877	22.8503	22.8021	22.5703	20.5371	20.2989	20.4313
TiO_2	0.8122	0.8857	2.3954	1.1012	1.2935	1.1091	1.4543
Cr_2O_3	0.265	0.422	0.0086	0.169	0.0076	0.0924	0.0476
MnO	0.1365	0.1015	0.1309	0.1087	0.2222	0.1964	0.1954
FeO	5.826	5.0874	7.7673	5.653	10.0898	8.4122	9.0228
Total	99.78	99.64	99.97	99.86	99.88	99.62	100.08
Na	0.309	0.3204	0.4179	0.3757	0.354	0.2619	0.2993
Mg	8.8232	8.4217	7.1155	8.2602	7.8896	8.5285	8.3468
Al	1.3892	1.7663	2.5135	2.0334	0.7973	1.1039	1.0289
Si	18.9405	18.6417	17.8742	18.4673	19.2148	19.0768	19.0054
K	0.0114	0.0022	0.0013	0.0000	0.0048	0.0063	0.0000
Ca	8.5184	9.0403	9.1336	8.9241	8.242	8.0952	8.1398
Ti	0.2249	0.2459	0.6735	0.3056	0.3643	0.3104	0.4067
Cr	0.0772	0.1232	0.0025	0.0493	0.0023	0.0272	0.014
Mn	0.0426	0.0317	0.0414	0.034	0.0705	0.0619	0.0615
Fe	1.7944	1.571	2.4285	1.7446	3.1606	2.6186	2.8058
O	59.8692	59.8355	59.7981	59.8157	59.8997	59.9094	59.8919
Total	100	100	100	100	100	100	100

Appendix A. *(Cont'd)*

Tunceli Volcanics							
clinopyroxene							
S. ID	**AV67**			**AV73**			
	Cpx-4	**Cpx-5**	**Cpx-6**	**Cpx-1**	**Cpx-2**	**Cpx-3**	**Cpx-4**
Na_2O	0.3356	0.3267	0.2903	0.4237	0.425	0.5196	0.5343
MgO	15.1234	15.6063	16.5072	14.9322	15.1577	13.6076	14.0327
Al_2O_3	2.9635	1.7291	1.691	3.7086	3.36	3.4072	3.3482
SiO_2	51.2121	52.0942	52.4984	50.2856	50.3831	49.3522	49.3014
K_2O	0.0059	0.0023	0.0027	0.007	0.0000	0.0225	0.0074
CaO	21.2461	20.656	19.9669	21.6094	22.0283	21.3564	21.4133
TiO_2	1.0374	0.963	0.723	1.5134	1.3058	2.3852	2.2867
Cr_2O_3	0.2359	0.0607	0.1923	0.5038	0.4897	0.0086	0.0296
MnO	0.1557	0.1775	0.1954	0.1488	0.1254	0.1662	0.1469
FeO	7.6036	8.1444	8.0306	6.6291	6.4424	9.1116	8.3535
Total	99.92	99.76	100.10	99.76	99.72	99.94	99.45
Na	0.2412	0.2352	0.2076	0.3047	0.3057	0.3775	0.3887
Mg	8.3575	8.6379	9.0771	8.2567	8.3833	7.6004	7.8497
Al	1.2948	0.7566	0.7351	1.6212	1.4692	1.5045	1.4807
Si	18.9842	19.3414	19.3647	18.6515	18.6921	18.4906	18.4996
K	0.0028	0.0011	0.0013	0.0033	0.0000	0.0108	0.0035
Ca	8.4384	8.2169	7.8911	8.5876	8.7562	8.573	8.6089
Ti	0.2892	0.2689	0.2005	0.4221	0.3643	0.672	0.6453
Cr	0.0692	0.0178	0.0561	0.1477	0.1436	0.0026	0.0088
Mn	0.0489	0.0558	0.0611	0.0467	0.0394	0.0528	0.0467
Fe	2.3572	2.5288	2.4773	2.0563	1.9989	2.855	2.6214
O	59.9167	59.9397	59.9282	59.902	59.8575	59.861	59.8467
Total	100	100	100	100	100	100	100

Appendix A. *(Cont’d)*

Tunceli Volcanics							
clinopyroxene					**plagioclase**		
S. ID	**AV75**				**AV20**		
	Cpx-1	**Cpx-2**	**Cpx-3**	**Cpx-4**	**Plg-1**	**Plg-2**	**Plg-3**
Na_2O	0.5633	0.4877	0.4179	0.4252	4.5818	6.4363	4.0956
MgO	10.9726	12.7138	13.5032	13.3102	0.1281	0.0576	0.237
Al_2O_3	4.1596	3.9289	3.4274	3.3704	29.655	26.4171	30.4135
SiO_2	46.9545	48.443	49.3811	49.9457	53.4199	58.4145	53.094
K_2O	0.0046	0.0000	0.0179	0.0000	0.2716	0.6083	0.2282
CaO	19.9132	20.2384	20.5822	20.3293	12.3152	8.5376	12.8884
TiO_2	3.0071	2.4015	2.075	2.1066	0.0994	0.1571	0.0748
Cr_2O_3	0.0043	0.0197	0.0634	0.0302	0.0000	0.0000	0.0007
MnO	0.2608	0.2316	0.2085	0.2222	0.0068	0.0043	0.0000
FeO	13.3517	11.169	10.0026	10.3016	0.4947	0.577	0.6119
Total	99.19	99.63	99.68	100.04	100.97	101.21	101.64
Na	0.4205	0.3581	0.3049	0.3092	3.0705	4.2628	2.7311
Mg	6.2982	7.1763	7.5749	7.441	0.066	0.0293	0.1215
Al	1.8876	1.7533	1.52	1.4896	12.0805	10.6354	12.3279
Si	18.079	18.3419	18.582	18.7298	18.4643	19.9541	18.2605
K	0.0023	0.0000	0.0086	0.0000	0.1198	0.2651	0.1001
Ca	8.2148	8.2101	8.2982	8.168	4.5607	3.1247	4.7493
Ti	0.8707	0.6838	0.5872	0.5941	0.0258	0.0404	0.0193
Cr	0.0013	0.0059	0.0189	0.0089	0.0000	0.0000	0.0002
Mn	0.085	0.0743	0.0664	0.0706	0.002	0.0013	0.0000
Fe	4.2993	3.5366	3.1478	3.2307	0.143	0.1648	0.176
O	59.8414	59.8642	59.891	59.9596	61.4676	61.5237	61.5141
Total	100	100	100	100	100	100	100

Appendix A. *(Cont'd)*

Tunceli Volcanics							
plagioclase							
S. ID	**AV20**				**AV33**		
	Plg-4	**Plg-5**	**Plg-6**	**Plg-7**	**Plg-1**	**Plg-2**	**Plg-3**
Na_2O	4.8262	4.8454	4.6321	4.2402	6.9299	4.5888	4.4965
MgO	1.7579	0.3751	0.0794	0.148	0.0196	0.0606	0.0784
Al_2O_3	26.4337	28.6035	29.3131	29.9912	25.584	29.4962	29.5083
SiO_2	53.8644	54.7196	53.5366	53.1063	60.9967	53.9465	53.4169
K_2O	0.3462	0.3204	0.2703	0.2463	1.0994	0.3241	0.3106
CaO	8.8931	11.3045	12.1199	12.6953	6.7446	11.6139	11.9023
TiO_2	0.0976	0.1172	0.1059	0.0785	0.1363	0.1356	0.0878
Cr_2O_3	0.0023	0.0031	0.0000	0.0053	0.003	0.0000	0.0000
MnO	0.0312	0.0028	0.0035	0.0096	0.0000	0.0048	0.0035
FeO	3.3643	0.8019	0.7248	0.3974	0.2557	0.5461	0.4716
Total	99.62	101.09	100.78	100.92	101.77	100.72	100.27
Na	3.2905	3.2384	3.1116	2.8447	4.5413	3.0786	3.0314
Mg	0.9215	0.1928	0.041	0.0764	0.0099	0.0313	0.0406
Al	10.9551	11.6205	11.9695	12.2306	10.1911	12.0291	12.0926
Si	18.9411	18.8623	18.5485	18.3757	20.616	18.6669	18.5736
K	0.1553	0.1409	0.1195	0.1087	0.474	0.1431	0.1378
Ca	3.3506	4.175	4.499	4.7065	2.4424	4.3057	4.4341
Ti	0.0258	0.0304	0.0276	0.0204	0.0346	0.0353	0.023
Cr	0.0006	0.0008	0.0000	0.0014	0.0008	0.0000	0.0000
Mn	0.0093	0.0008	0.001	0.0028	0.0000	0.0014	0.001
Fe	0.9894	0.2312	0.21	0.115	0.0723	0.158	0.1371
O	61.3609	61.5068	61.4726	61.5177	61.6195	61.5525	61.5291
Total	100	100	100	100	100	100	100

Appendix A. *(Cont’d)*

Tunceli Volcanics							
plagioclase							
S. ID	**AV33**						**AV67**
	Plg-4	**Plg-5**	**Plg-6**	**Plg-7**	**Plg-8**	**Plg-9**	**Plg-1**
Na_2O	4.2228	4.5595	4.2609	4.567	4.6451	4.702	6.281
MgO	0.3227	0.0557	0.05	0.0461	0.0521	0.0441	0.0723
Al_2O_3	29.3723	29.3896	29.0099	29.4666	29.5422	29.6384	26.9311
SiO_2	52.9089	53.6057	53.986	53.7919	53.7509	54.0451	58.2025
K_2O	0.4318	0.3387	0.4093	0.3194	0.3402	0.3631	0.4155
CaO	11.5883	11.7566	11.732	11.7328	11.8653	11.5836	9.0744
TiO_2	0.1002	0.1096	0.1424	0.105	0.1394	0.1138	0.1478
Cr_2O_3	0.0006	0.0000	0.0000	0.0022	0.0026	0.0035	0.0039
MnO	0.0086	0.0079	0.0025	0.002	0.0025	0.0000	0.0006
FeO	0.7698	0.6176	0.5778	0.5945	0.5116	0.5205	0.5667
Total	99.73	100.44	100.17	100.63	100.85	101.01	101.70
Na	2.8658	3.07	2.8768	3.0681	3.114	3.1445	4.1426
Mg	0.1684	0.0288	0.0259	0.0238	0.0268	0.0227	0.0367
Al	12.1166	12.0286	11.9056	12.0331	12.0386	12.0486	10.7971
Si	18.519	18.6155	18.7988	18.6384	18.5849	18.6416	19.7987
K	0.1928	0.1501	0.1818	0.1412	0.1501	0.1598	0.1803
Ca	4.3458	4.3743	4.377	4.3557	4.3956	4.2809	3.3073
Ti	0.0264	0.0286	0.0373	0.0274	0.0363	0.0295	0.0378
Cr	0.0002	0.0000	0.0000	0.0006	0.0007	0.0009	0.001
Mn	0.0025	0.0023	0.0007	0.0006	0.0007	0.0000	0.0002
Fe	0.2253	0.1794	0.1683	0.1723	0.1479	0.1501	0.1612
O	61.5372	61.5239	61.6294	61.539	61.5044	61.5219	61.5371
Total	100	100	100	100	100	100	100

Appendix A. *(Cont’d)*

Tunceli Volcanics							
plagioclase							
S. ID	**AV67**						
	Plg-2	**Plg-3**	**Plg-4**	**Plg-5**	**Plg-6**	**Plg-7**	**Plg-8**
Na_2O	6.3085	3.7357	4.0248	6.4304	4.0609	6.072	4.4618
MgO	0.0516	0.0922	0.1685	0.2993	0.1533	1.5796	0.0869
Al_2O_3	26.7349	30.683	30.2078	26.0947	30.0809	22.405	29.5821
SiO_2	58.2999	51.6889	52.3858	59.1928	52.5652	61.4282	53.1008
K_2O	0.4165	0.1775	0.158	0.4463	0.2145	0.6886	0.2332
CaO	8.8082	13.4778	13.0137	8.2868	12.6718	5.9216	12.2561
TiO_2	0.1505	0.0281	0.0507	0.1119	0.0894	0.0837	0.0748
Cr_2O_3	0.0006	0.0026	0.0000	0.003	0.0000	0.0000	0.0000
MnO	0.0091	0.0000	0.0000	0.0095	0.0098	0.014	0.0011
FeO	0.7007	0.5475	0.4645	0.6844	0.5686	1.122	0.6943
Total	101.48	100.43	100.47	101.56	100.41	99.31	100.49
Na	4.1693	2.5256	2.7148	4.2394	2.7403	4.0771	3.0065
Mg	0.0262	0.0479	0.0874	0.1517	0.0796	0.8155	0.045
Al	10.7403	12.6092	12.3858	10.4575	12.3388	9.1447	12.1167
Si	19.8723	18.0231	18.2247	20.1275	18.2947	21.2733	18.4544
K	0.1811	0.079	0.0701	0.1936	0.0952	0.3042	0.1034
Ca	3.2168	5.0351	4.8507	3.019	4.7253	2.1972	4.5636
Ti	0.0386	0.0074	0.0133	0.0286	0.0234	0.0218	0.0195
Cr	0.0002	0.0007	0.0000	0.0008	0.0000	0.0000	0.0000
Mn	0.0026	0.0000	0.0000	0.0027	0.0029	0.0041	0.0003
Fe	0.1997	0.1596	0.1351	0.1946	0.1655	0.325	0.2018
O	61.553	61.5166	61.5192	61.5844	61.5348	61.8382	61.4887
Total	100	100	100	100	100	100	100

Appendix A. *(Cont'd)*

Tunceli Volcanics							
plagioclase							
S. ID	**AV73**	**AV75**					
	Plg-1	**Plg-1**	**Plg-2**	**Plg-3**	**Plg-4**	**Plg-5**	**Plg-6**
Na$_2$O	6.0253	4.3839	3.8472	4.056	4.4346	4.5813	4.4644
MgO	0.0506	0.1505	4.5396	1.949	0.1949	0.231	0.1442
Al$_2$O$_3$	27.3128	29.6949	26.3071	26.9668	29.475	28.9173	29.3578
SiO$_2$	57.5616	53.2479	49.3038	52.9683	53.7871	54.0283	53.7237
K$_2$O	0.5202	0.2509	0.2345	0.27	0.2643	0.2925	0.2577
CaO	9.2195	12.43	8.6667	11.0885	12.2521	11.72	12.1528
TiO$_2$	0.1428	0.0917	0.0918	0.1221	0.092	0.0924	0.1153
Cr$_2$O$_3$	0.0000	0.0004	0.0069	0.0276	0.0155	0.0117	0.0048
MnO	0.0074	0.0067	0.0742	0.0218	0.0034	0.0006	0.0021
FeO	0.497	0.4436	7.8068	1.8934	0.538	0.5734	0.4523
Total	101.34	100.70	100.88	99.36	101.06	100.45	100.68
Na	3.9905	2.9461	2.6398	2.7712	2.9691	3.0824	2.9987
Mg	0.0258	0.0778	2.395	1.0239	0.1003	0.1195	0.0745
Al	10.9957	12.1303	10.9724	11.1997	11.9957	11.8269	11.987
Si	19.6623	18.456	17.4483	18.6653	18.5736	18.749	18.6121
K	0.2267	0.111	0.1059	0.1214	0.1165	0.1295	0.1139
Ca	3.3742	4.616	3.2861	4.1865	4.533	4.3576	4.5109
Ti	0.0367	0.0239	0.0244	0.0324	0.0239	0.0241	0.03
Cr	0.0000	0.0001	0.0019	0.0077	0.0042	0.0032	0.0013
Mn	0.0021	0.002	0.0222	0.0065	0.001	0.0002	0.0006
Fe	0.142	0.1286	2.3105	0.558	0.1554	0.1664	0.131
O	61.5441	61.5083	60.7935	61.4275	61.5273	61.5411	61.54
Total	100	100	100	100	100	100	100

Appendix A. *(Cont'd)*

Elazığ Volcanics							
olivine							
S. ID	**BYD10**			**BYD15**			
	Olv-1	**Olv-2**	**Olv-3**	**Olv-1**	**Olv-2**	**Olv-3**	**Olv-4**
Na_2O	0.0169	0.0203	0.0347	0.0122	0.0087	0.0152	0.013
MgO	45.2211	45.8891	46.761	45.0648	45.1593	45.1061	46.1767
Al_2O_3	0.0458	0.0612	0.013	0.0699	0.0277	0.0507	0.052
SiO_2	40.1165	40.0969	40.3914	40.2806	40.1122	40.1181	40.1767
K_2O	0.0004	0.004	0.0000	0.0000	0.0000	0.0105	-0.004
CaO	0.1808	0.2058	0.1302	0.1872	0.1862	0.1886	0.2071
TiO_2	0.0285	0.0086	0.0000	0.0271	0.0081	0.0214	0.0018
Cr_2O_3	0.0109	0.0157	0.01	0.0183	0.01	0.0195	0.0237
MnO	0.2135	0.1986	0.1715	0.2212	0.209	0.2032	0.1971
FeO	15.0835	14.3069	13.2991	15.006	15.0126	15.1361	13.9951
Total	100.92	100.81	100.81	100.89	100.73	100.87	100.84
Na	0.0116	0.014	0.0238	0.0084	0.006	0.0105	0.0089
Mg	23.9545	24.2489	24.586	23.8746	23.9608	23.9124	24.3567
Al	0.0192	0.0256	0.0054	0.0293	0.0116	0.0213	0.0217
Si	14.2547	14.2129	14.2457	14.3148	14.2765	14.2665	14.2154
K	0.0002	0.0018	0.0000	0.0000	0.0000	0.0047	-0.0018
Ca	0.0689	0.0782	0.0492	0.0713	0.071	0.0719	0.0785
Ti	0.0076	0.0023	0.0000	0.0072	0.0022	0.0057	0.0005
Cr	0.0031	0.0044	0.0028	0.0051	0.0028	0.0055	0.0066
Mn	0.0642	0.0596	0.0512	0.0666	0.063	0.0612	0.0591
Fe	4.4823	4.2411	3.9226	4.4598	4.4685	4.5014	4.1412
O	57.1338	57.1112	57.1178	57.169	57.1427	57.139	57.1133
Total	100	100	100	100	100	100	100

Appendix A. *(Cont'd)*

Elazığ Volcanics							
olivine							
S. ID	**BYD15**	**BYD30**					
	Olv-5	**Olv-1**	**Olv-2**	**Olv-3**	**Olv-4**	**Olv-5**	**Olv-6**
Na_2O	0.0333	0.0162	0.0079	0.0189	0.0108	0.0111	0.012
MgO	45.7508	46.2302	46.6602	44.407	43.4225	45.855	49.4177
Al_2O_3	0.0398	0.0473	0.0746	0.058	0.042	0.051	0.0093
SiO_2	40.1669	40.2342	40.5741	39.8676	39.6564	40.1599	41.0909
K_2O	0.0000	0.0000	0.017	0.0129	0.0113	0.0000	0.0057
CaO	0.1686	0.1935	0.2272	0.176	0.2369	0.1924	0.0906
TiO_2	0.0063	0.0064	0.0289	0.0167	0.0323	0.0078	-0.0053
Cr_2O_3	0.0233	0.0159	0.0169	0.0108	0.0196	0.018	0.008
MnO	0.2054	0.2045	0.1801	0.2171	0.2611	0.1952	0.1415
FeO	14.4804	13.7679	13.3621	15.8031	16.898	14.0666	9.9818
Total	100.87	100.72	101.15	100.59	100.59	100.56	100.75
Na	0.0229	0.0111	0.0054	0.0131	0.0076	0.0076	0.0081
Mg	24.1801	24.3927	24.4621	23.6862	23.2905	24.269	25.596
Al	0.0166	0.0197	0.0309	0.0245	0.0178	0.0213	0.0038
Si	14.2402	14.2403	14.2687	14.2644	14.2681	14.2577	14.2766
K	0.0000	0.0000	0.0076	0.0059	0.0052	0.0000	0.0025
Ca	0.064	0.0734	0.0856	0.0675	0.0913	0.0732	0.0337
Ti	0.0017	0.0017	0.0076	0.0045	0.0087	0.0021	0.0000
Cr	0.0065	0.0045	0.0047	0.0031	0.0056	0.0051	0.0022
Mn	0.0617	0.0613	0.0536	0.0658	0.0796	0.0587	0.0416
Fe	4.2933	4.0752	3.9298	4.7286	5.0845	4.1764	2.9003
O	57.1237	57.1256	57.1439	57.1366	57.1411	57.1364	57.1365
Total	100	100	100	100	100	100	100

Appendix A. *(Cont’d)*

Elazığ Volcanics							
olivine							
S. ID	**BYD30**	**GMB3**				**GMB6**	
	Olv-7	**Olv-1**	**Olv-2**	**Olv-3**	**Olv-4**	**Olv-1**	**Olv-2**
Na_2O	0.0000	0.0776	0.0225	0.0146	0.0053	0.0056	0.015
MgO	45.6473	44.0154	45.093	45.8837	45.2938	42.9919	43.6557
Al_2O_3	0.0473	0.1895	0.0576	0.047	0.0581	0.0296	0.0456
SiO_2	40.1852	39.4432	39.9189	40.2519	40.1924	39.6943	39.6183
K_2O	0.0036	0.0105	0.0000	0.002	0.0153	-0.0105	0.0113
CaO	0.1812	0.2913	0.1895	0.2346	0.1957	0.2027	0.1828
TiO_2	0.0174	0.0299	0.028	0.0197	0.0215	0.0173	0.0109
Cr_2O_3	0.0131	0.0203	0.0194	0.0149	0.0159	0.0131	0.0141
MnO	0.2015	0.2403	0.218	0.2083	0.2087	0.2821	0.231
FeO	14.3617	15.4931	15.4667	14.4139	15.047	17.6814	16.7099
Total	100.66	99.81	101.01	101.09	101.05	100.91	100.49
Na	0.0000	0.0542	0.0155	0.01	0.0037	0.0039	0.0104
Mg	24.1655	23.6526	23.9085	24.1889	23.9562	23.0627	23.4103
Al	0.0198	0.0805	0.0241	0.0196	0.0243	0.0125	0.0193
Si	14.2704	14.2179	14.1975	14.2342	14.2598	14.2837	14.2512
K	0.0016	0.0048	0.0000	0.0009	0.0069	0.0000	0.0052
Ca	0.0689	0.1125	0.0722	0.0889	0.0744	0.0781	0.0704
Ti	0.0046	0.0081	0.0075	0.0053	0.0057	0.0047	0.003
Cr	0.0037	0.0058	0.0054	0.0042	0.0045	0.0037	0.004
Mn	0.0606	0.0734	0.0657	0.0624	0.0627	0.086	0.0704
Fe	4.2652	4.6705	4.6004	4.2627	4.4645	5.321	5.0268
O	57.1441	57.1198	57.1069	57.123	57.1373	57.1485	57.129
Total	100	100	100	100	100	100	100

Appendix A. *(Cont’d)*

Elazığ Volcanics							
olivine		**plagioclase**					
S. ID	**GMB6**	**BYD10**					
	Olv-3	**Plg-1**	**Plg-2**	**Plg-3**	**Plg-4**	**Plg-5**	**Plg-6**
Na_2O	0.0153	4.5812	4.475	4.6484	4.5382	4.7432	4.8509
MgO	43.8397	0.1111	0.151	0.0872	0.0974	0.0851	0.0939
Al_2O_3	0.0382	28.9223	29.4116	29.2504	29.467	28.9351	28.9789
SiO_2	39.7339	53.1185	53.5038	53.6915	53.631	54.0726	54.1928
K_2O	0.0125	0.4696	0.3675	0.5241	0.4709	0.5245	0.5017
CaO	0.1969	12.5188	11.0556	11.7135	11.8708	11.3253	11.4203
TiO_2	0.0232	0.1508	0.1181	0.1729	0.1747	0.1664	0.1745
Cr_2O_3	0.0136	0.0032	0.0000	0.0000	0.0006	0.0031	0.0000
MnO	0.2407	0.0071	0.0000	0.0000	0.0025	0.0038	0.0059
FeO	16.8212	0.539	0.5908	0.4271	0.5297	0.5379	0.5164
Total	100.94	100.42	99.67	100.52	100.78	100.40	100.74
Na	0.0106	3.0926	3.0308	3.1268	3.0464	3.1923	3.254
Mg	23.4132	0.0577	0.0786	0.0451	0.0503	0.044	0.0484
Al	0.0161	11.8682	12.1087	11.9603	12.0241	11.8377	11.8163
Si	14.2346	18.4945	18.6898	18.6278	18.5685	18.7699	18.7493
K	0.0057	0.2086	0.1638	0.232	0.208	0.2323	0.2214
Ca	0.0756	4.67	4.1378	4.3541	4.4035	4.2121	4.2333
Ti	0.0062	0.0395	0.031	0.0451	0.0455	0.0434	0.0454
Cr	0.0039	0.0009	0.0000	0.0000	0.0002	0.0009	0.0000
Mn	0.0731	0.0021	0.0000	0.0000	0.0007	0.0011	0.0017
Fe	5.0397	0.157	0.1726	0.1239	0.1534	0.1562	0.1494
O	57.1213	61.409	61.5887	61.4865	61.4994	61.5102	61.4822
Total	100	100	100	100	100	100	100

Appendix A. *(Cont'd)*

Elazığ Volcanics							
plagioclase							
S. ID	**BYD10**				**BYD15**	**BYD30**	
	Plg-7	**Plg-8**	**Plg-9**	**Plg-10**	**Plg-1**	**Plg-1**	**Plg-2**
Na_2O	4.5239	4.5727	4.5271	4.4103	4.619	4.4841	4.4443
MgO	0.0899	0.0971	0.0934	0.1146	0.0943	0.101	0.1596
Al_2O_3	29.4635	29.4001	29.4385	29.2219	29.2917	29.3079	29.4555
SiO_2	53.6019	53.8111	53.6925	53.8452	53.7883	53.5354	53.4788
K_2O	0.49	0.4977	0.4405	0.4357	0.5177	0.529	0.5441
CaO	11.7944	11.7934	11.9813	11.9471	11.6607	11.822	11.8211
TiO_2	0.1143	0.1345	0.1437	0.1449	0.1239	0.157	0.1523
Cr_2O_3	0.003	0.0000	0.0029	0.0000	0.0015	0.0035	0.0000
MnO	0.0015	0.0000	0.0000	0.0000	0.0032	0.0091	0.0115
FeO	0.4451	0.43	0.4592	0.554	0.4728	0.5746	0.9075
Total	100.53	100.74	100.78	100.67	100.57	100.52	100.97
Na	3.0428	3.069	3.0386	2.9641	3.1048	3.019	2.983
Mg	0.0465	0.0501	0.0482	0.0592	0.0487	0.0523	0.0824
Al	12.0461	11.9944	12.011	11.9382	11.9686	11.9942	12.0178
Si	18.5947	18.6271	18.5874	18.6646	18.6479	18.5897	18.5132
K	0.2169	0.2198	0.1945	0.1927	0.229	0.2343	0.2403
Ca	4.3837	4.374	4.444	4.4371	4.3314	4.3983	4.3845
Ti	0.0298	0.035	0.0374	0.0378	0.0323	0.041	0.0397
Cr	0.0008	0.0000	0.0008	0.0000	0.0004	0.001	0.0000
Mn	0.0005	0.0000	0.0000	0.0000	0.0009	0.0027	0.0034
Fe	0.1291	0.1245	0.133	0.1606	0.1371	0.1668	0.2627
O	61.5091	61.5074	61.5071	61.5465	61.4989	61.5008	61.4746
Total	100	100	100	100	100	100	100

Appendix A. *(Cont'd)*

Elazığ Volcanics							
plagioclase							
S. ID	**BYD30**						
	Plg-3	**Plg-4**	**Plg-5**	**Plg-6**	**Plg-7**	**Plg-8**	**Plg-9**
Na_2O	4.5606	4.4849	4.4338	4.648	4.59	4.8799	5.7627
MgO	0.0942	0.0968	0.0981	0.0894	0.0925	0.0915	0.0863
Al_2O_3	29.1553	29.3081	29.5102	29.5195	29.3365	29.1748	27.5046
SiO_2	53.7964	53.7751	53.5933	54.0301	54.0741	54.1004	57.0136
K_2O	0.5467	0.5337	0.5294	0.2639	0.4827	0.3313	0.4135
CaO	11.6579	11.846	11.9943	11.776	11.8242	11.4316	9.539
TiO_2	0.1576	0.1256	0.1451	0.1599	0.1678	0.1893	0.229
Cr_2O_3	0.0046	0.0002	0.0013	0.0000	0.0000	0.0000	0.001
MnO	0.0098	0.0000	0.0057	0.0048	0.0000	0.0027	0.0063
FeO	0.5138	0.4745	0.4617	0.5371	0.5082	0.604	0.5727
Total	100.50	100.64	100.77	101.03	101.08	100.81	101.13
Na	3.0691	3.0142	2.9772	3.1091	3.0713	3.2706	3.8288
Mg	0.0487	0.05	0.0507	0.046	0.0476	0.0472	0.0441
Al	11.9268	11.9732	12.0453	12.0028	11.9324	11.8858	11.1084
Si	18.6725	18.6401	18.5609	18.6403	18.6617	18.7009	19.5374
K	0.2421	0.236	0.2339	0.1162	0.2125	0.1461	0.1808
Ca	4.3354	4.3995	4.4506	4.3529	4.3722	4.2338	3.5023
Ti	0.0411	0.0327	0.0378	0.0415	0.0435	0.0492	0.059
Cr	0.0013	0.0001	0.0003	0.0000	0.0000	0.0000	0.0003
Mn	0.0029	0.0000	0.0017	0.0014	0.0000	0.0008	0.0018
Fe	0.1491	0.1376	0.1337	0.155	0.1467	0.1746	0.1641
O	61.511	61.5172	61.508	61.5352	61.5146	61.4921	61.573
Total	100	100	100	100	100	100	100

Appendix A. *(Cont'd)*

Elazığ Volcanics							
plagioclase							
S. ID	**BYD30**	**GMB3**					
	Plg-10	**Plg-1**	**Plg-2**	**Plg-3**	**Plg-4**	**Plg-5**	**Plg-6**
Na_2O	4.6441	4.7071	4.6053	5.2052	3.7331	5.1975	4.3033
MgO	0.1209	0.0861	0.0774	0.1805	0.0948	0.1126	0.0767
Al_2O_3	28.9524	29.0924	29.3455	27.493	30.5221	30.514	29.987
SiO_2	54.0667	53.785	53.5829	56.689	52.1016	53.6383	53.0016
K_2O	0.5878	0.4453	0.3692	0.7878	0.3313	0.736	0.294
CaO	11.3955	11.3752	11.9351	9.8393	13.1577	9.4606	12.569
TiO_2	0.1979	0.1686	0.1486	0.2515	0.0921	0.1481	0.1747
Cr_2O_3	0.0000	0.0000	0.0046	0.0001	0.0000	0.0028	0.0024
MnO	0.0000	0.0059	0.0000	0.0000	0.0073	0.0033	0.0017
FeO	0.6691	0.5884	0.6264	0.9943	0.5828	0.7084	0.6706
Total	100.63	100.25	100.70	101.44	100.62	100.52	101.08
Na	3.1215	3.1731	3.0949	3.4613	2.5185	3.4811	2.8858
Mg	0.0625	0.0446	0.04	0.0923	0.0491	0.058	0.0396
Al	11.8292	11.9212	11.988	11.113	12.5167	12.4231	12.2238
Si	18.7432	18.7001	18.5727	19.4425	18.1289	18.5288	18.3319
K	0.26	0.1975	0.1632	0.3447	0.147	0.3244	0.1297
Ca	4.2326	4.2375	4.4324	3.6156	4.9052	3.5015	4.6578
Ti	0.0516	0.0441	0.0387	0.0649	0.0241	0.0385	0.0454
Cr	0.0000	0.0000	0.0013	0.0000	0.0000	0.0008	0.0007
Mn	0.0000	0.0018	0.0000	0.0000	0.0022	0.001	0.0005
Fe	0.194	0.1711	0.1816	0.2852	0.1696	0.2047	0.194
O	61.5091	61.5096	61.4885	61.5804	61.5392	61.4382	61.4909
Total	100	100	100	100	100	100	100

Appendix A. *(Cont'd)*

Elazığ Volcanics							
plagioclase							
S. ID	**GMB3**		**GMB6**				
	Plg-7	**Plg-8**	**Plg-1**	**Plg-2**	**Plg-3**	**Plg-4**	**Plg-5**
Na_2O	5.8861	5.6472	5.6856	4.6089	4.9303	6.7932	6.035
MgO	0.0173	0.0426	0.0969	0.0819	0.1261	0.0389	0.1157
Al_2O_3	21.5995	27.2649	27.5064	29.1969	21.6868	25.8641	26.7944
SiO_2	64.0839	57.1323	56.4169	52.9221	64.7745	59.9523	56.7736
K_2O	6.0486	0.5911	0.4243	0.3109	6.6062	0.7393	0.4161
CaO	3.2644	9.3555	9.7039	11.6765	2.0168	7.2477	9.383
TiO_2	0.2957	0.2141	0.2241	0.1497	0.1441	0.2038	0.2453
Cr_2O_3	0.003	0.0000	0.0000	0.0077	0.0000	0.0000	0.0038
MnO	0.0056	0.0000	0.0034	0.0033	0.0136	0.0013	0.0069
FeO	0.3097	0.461	0.8602	0.8058	0.5975	0.5871	0.9946
Total	101.51	100.71	100.92	99.76	100.90	101.43	100.77
Na	3.8972	3.7665	3.7925	3.1271	3.2822	4.475	4.0306
Mg	0.0088	0.0218	0.0497	0.0427	0.0645	0.0197	0.0594
Al	8.6932	11.0538	11.1529	12.0417	8.7759	10.3569	10.878
Si	21.8841	19.6531	19.4091	18.5195	22.2406	20.3695	19.5566
K	2.6351	0.2594	0.1862	0.1388	2.8937	0.3205	0.1828
Ca	1.1944	3.4481	3.5769	4.3779	0.742	2.6384	3.463
Ti	0.0759	0.0554	0.058	0.0394	0.0372	0.0521	0.0635
Cr	0.0008	0.0000	0.0000	0.0021	0.0000	0.0000	0.001
Mn	0.0016	0.0000	0.001	0.001	0.0039	0.0004	0.002
Fe	0.0884	0.1326	0.2475	0.2358	0.1716	0.1668	0.2865
O	61.5204	61.6109	61.5269	61.474	61.7888	61.6011	61.4765
Total	100	100	100	100	100	100	100

CURRICULUM VITAE

ALİCAN AKTAĞ

EDUCATION:

2015-2022	Ph.D., Department of Geological Engineering, METU
	Supervisor: Assoc. Prof. Dr. Kaan Sayıt
2011-2014	M.Sc., Department of Geological Engineering, Munzur University
	Supervisor: Prof. Dr. Ayten Öztüfekçi Önal
2005-2009	B.S., Department of Geological Engineering, Mersin University

PROFESSIONAL EXPERIENCE:

2014-2022	Research/Teaching Assistant, Department of Geological Engineering, METU
2010-2014	Research/Teaching Assistant, Department of Geological Engineering, Munzur University

MEMBERSHIPS & SCIENTIFIC ACTIVITIES

Chamber of Geological Engineers (UCTEA)	2014- present
Geological Society of America (Student Member)	2011- 2012

GRANTS

2012-2014	The Scientific and Technological Research Council of Turkey (TUBITAK) 1001 – Scholarship

COURSES ASSISTED

METU, GEOE207	Principles of Mineralogy and Petrography
METU, GEOE210	Petrography
METU, GEOE213	Mineralogy
METU, GEOE304	Igneous and Metamorphic Petrology

PUBLICATIONS

3) Aktağ, A., Sayit, K., Peters, B.J,. Furman, T., Rickli, J., 2022. Interaction of C-like asthenospheric melts and sub-continental mantle lithosphere beneath eastern Turkey**,** Lithos (In revision).

2) Aktağ, A., Önal, A.Ö., Sayit, K., 2019. Geochemistry of the post-collisional Miocene mafic Tunceli Volcanics, Eastern Turkey: Implications for the nature of the mantle source and melting systematics. Geochemistry. https://doi.org/10.1016/J.GEOCH.2018.11.004.

1) Çimen, O., Toksoy-Köksal, F., Öztüfekçi-Önal, A., **Aktağ, A**. 2016. Depleted to Refertilized Mantle Peridotites Hosting Chromitites within the Tunceli Ophiolite, Eastern Anatolia (Turkey): Insights on the Back Arc Origin. Ofioliti. Vol. 41 (1), 1-20.

ABSTRACTS

12) Önal, A., **Aktağ, A.,** Toksoy-Köksal, F., Çimen, O., Öztüfekçi Önal, A. Tunceli İlindeki Kromit Yataklarının Jeolojik Özellikleri. Uluslararası Katılımlı Doğu Anadolu Jeoloji Sempozyumu (DAJEO'2015), Van, Eylül 2015.

11) Öztüfekçi Önal, A., Karaoğlu, Ö., Kürüm, S., Savaşçın, M. Y., **Aktağ, A.,** Lustrino, M., Agostini, S. Doğu Anadolu Yığışım Karmaşığı Batısında, Tunceli-Mazgirt Yöresi Neojen Volkanizmasının Jeolojik, Petrografik ve Jeokimyasal Özellikleri. 1. Türkiye Volkanoloji Çalıştayı, Ankara, Ekim 2016.

10) Kürüm, S., Öztüfekçi Önal, A., Karaoğlu, Ö., Savaşçın, M. Y., **Aktağ, A.,** Lustrino, M., Agostini, S., Di Guiseppe. Çemişgezek-Pertek (Tunceli) Neojen Volkanizmasının Petrografik-Jeokimyasal Özellikleri. 1. Türkiye Volkanoloji Çalıştayı, Ankara, Ekim 2016.

9) Öztüfekçi Önal, A., Çimen, O., Toksoy-Köksal, F., **Aktağ, A.,** Önal, A. Tunceli İlindeki Kromit Yataklarının Petrojenetik Özellikleri. Uluslararası Katılımlı Doğu Anadolu Jeoloji Sempozyumu (DAJEO'2015), Van, Eylül 2015.

8) Çimen, O., Öztüfekçi-Önal, A., Toksoy-Köksal, F., **Aktağ, A.,** Önal, A. Tunceli (Doğu Anadolu) Kromitlerinin Jeokimyası Üzerine İlk Veriler, 6. Jeokimya Sempozyumu, Mersin Üniversitesi, Mersin, Mayıs 2014.

7) Aktağ, A. ve Öztüfekçi Önal, A. Pertek (Tunceli) Doğusundaki Volkanitlerin Jeolojisi ve Jeokimyası. 6. Jeokimya Sempozyumu, Mersin Üniversitesi, Mersin, Mayıs 2014.

6) Öztüfekçi-Önal, A., Toksoy-Köksal, F., Zaccarini, F., Çimen, O., **Aktağ, A.,** Önal, A. First description of platinum group minerals (PGM) in ultramafic rocks of the Ovacık and Pülümür ophiolitic complex, Tunceli, Turkey. EMAS 2014 Regional Workshop 2014, Leoben, Austria.

5) Çimen, O., Sayıt, K., Göncüoğlu, M.C., Öztüfekçi Önal, **A. Aktağ,** A. MORB- and SSZ-type mafic rocks from the eastern part of the Ankara-Erzincan-Sevan-Akera Suture Belt: Preliminary geochemical data. Goldchmidt 2014 Sacramento, USA.

4) Öztüfekçi Önal, A., Örgün Tutay, Y., Önal, A., **Aktağ, A**., Çimen, O. Tunceli'deki Cevherleşmeler ve Madencilik Faaliyetlerinin Su Sistemine Etkileri. 2. Tıbbi Jeoloji Çalıştayı, Akdeniz Üniversitesi, Antalya, Aralık 2013.

3) Zabcı, C., Sançar, T., **Aktağ, A.,** Çetinkaya, F., Akçar, N. Ovacık Fayı'nın (Tunceli) Holosen? Etkinliği Hakkında Ön Bulgular. Aktif Tektonik Araştırma Grubu 16. Çalıştayı, 2012, İstanbul, Türkiye.

2) Aktağ, A., Öztüfekçi Önal, A., Sançar, T., Önal, A., Çimen, O. New Petrological Data From the Western Termination of East Anatolian Accretionary Complex (EAAC), Eastern Turkey. EGU General Assembly 2013 Vienna, Austria.

1) Zabcı, C., Sançar, T., **Aktağ, A.,** Akçar, N. Preliminary Results About the Quaternary Activiy of the Ovacık Fault, Eastern Turkey. EGU General Assembly 2013 Vienna, Austria.

PROJECTS INVOLVED

6) Elazığ Kuzeyindeki Kuvaterner Mafik Volkanizmanın Jeokimyasal Evrimi ve Manto Kaynak Karakterizasyonu, TÜBİTAK-ÇAYDAG 118Y280, Proje Yürütücüsü, (2019- Cont'd, 30.000 TL)

5) Malatya-Elazığ-Tunceli Bölgesindeki Neojen-Kuvaterner mafik Lavların Petrojenetik Evrimi (Doğu Anadolu, Türkiye), ODTÜ BAP Birimi, DKT-309-2018-3705, Proje Araştırmacısı, 2019 (Completed 2.900 TL)

4) Tunceli Güneyindeki Tersiyer Bazaltlarının Sr-Nd-Pb-Hf İzotop Jeokimyası: Volkanizmanın Manto Kaynak Özellikleri ve Etkilendiği Magmatik Süreçlere İlişkin Çıkarımlar, ODTÜ BAP Birimi, GAP-309-2018-2761, Proje Araştırmacısı, 2019 (Conmpleted, 10.000 TL)

3) Tunceli ili Krom Yataklarının Petrojenetik Özellikleri, Tunceli Üniversitesi BAP Birimi, Proje No: MFTUB013-09, Proje Araştırmacısı, 2013 (Completed, 15.000 TL)

2) Tunceli Civarındaki Tersiyer Volkanizmasının Petrojenik-Jeodinamik Evrimi ve Doğu Anadolu Yığışım Karmaşası Üzerindeki Volkanizma İle İlişkisi. Proje No: TÜBİTAK-ÇAYDAG 112Y10, Bursiyer (2012-2014), 2015, (Completed, 253.000 TL)

1) Tunceli İli Civarındaki Genç Dönem Volkanik Kayaların Jeolojik Konumu, Petrografik ve Jeokimyasal Özelliklerinin İncelenmesi. Tunceli Üniversitesi BAP Birimi, Proje No: YLTUB011-18, Proje Araştırmacısı, 2011 (Completed, 5.000 TL)